Zelfheling en microstructuur van cementgebonden materialen met microvezels en superabsorberende polymeren

Self-Healing and Microstructure of Cementitious Materials with Microfibres and Superabsorbent Polymers

Didier Snoeck

Promotoren: prof. dr. ir. N. De Belie, prof. dr. P. Dubruel
Proefschrift ingediend tot het behalen van de graad van
Doctor in de Ingenieurswetenschappen: Bouwkunde

Vakgroep Bouwkundige Constructies
Voorzitter: prof. dr. ir. L. Taerwe
Faculteit Ingenieurswetenschappen en Architectuur
Academiejaar 2015-2016

UNIVERSITEIT GENT

ISBN 978-90-8578-845-4
NUR 955
Wettelijk depot: D/2015/10.500/89

Supervisors

Prof. dr. ir. Nele De Belie
Ghent University, Department of Structural Engineering

Prof. dr. Peter Dubruel
Ghent University, Department of Organic and Macromolecular Chemistry

Research Institutes

Magnel Laboratory for Concrete Research
Department of Structural Engineering
Faculty of Engineering and Architecture

Polymer Chemistry and Biomaterials Group
Department of Organic and Macromolecular Chemistry
Faculty of Sciences

Ghent University

Examination committee

Prof. dr. ir. Luc Taerwe (chairman)
Ghent University, Department of Structural Engineering

Prof. dr. ir. Geert De Schutter (secretary)
Ghent University, Department of Structural Engineering

Prof. dr. Sandra Van Vlierberghe
Ghent University, Department of Organic and Macromolecular Chemistry

Prof. dr. Veerle Cnudde
Ghent University, Department of Geology and Soil Science

Col. Prof. dr. Peter Lodewyckx
Royal Military Academy, Department of Chemistry

Prof. dr. ir. Ole Mejlhede Jensen
Technical University of Denmark, Department of Building Materials

Research funding

As a Research Assistant of the Research Foundation-Flanders (FWO-Vlaanderen), D. Snoeck wants to thank the foundation for the financial support.

Dankwoord

First of all, I would like to thank you, the reader, for showing interest in this work and taking the time to read it.

Na vier jaar onderzoek is de tijd aangebroken om het meest gelezen stukje tekst van dit doctoraatsmanuscript te schrijven. Het biedt de mogelijkheid om even stil te staan en velen te bedanken die bijgedragen hebben bij het in tot stand komen van dit werk.

"The journey of a thousand miles begins with a single step."

– Lao Tzu

Uiteraard is er een begin aan deze tocht. Deze was mijn masterproef welke handelde over zelfheling in cementgebonden materialen. Direct werd mijn interesse in het gebied van wetenschappelijk onderzoek aangewakkerd en diende enkel nog een beurs aangevraagd te worden. Daarom wens ik het FWO te danken voor het verkregen aspirantenmandaat.

Een doctoraatsthesis is natuurlijk ook niet mogelijk zonder mijn beide promotoren. Prof. dr. ir. Nele De Belie wens ik uitermate te bedanken voor de begeleiding, het vele leeswerk en voor de interessante discussies. Nele, bedankt voor de mogelijkheid om wetenschappelijk onderzoek uit te voeren, het stimuleren om het onderzoek in het buitenland voor te stellen op internationale congressen en om me te laten proeven van de wetenschappelijke betonwereld in al haar facetten. Uw deur stond – letterlijk – altijd open en ik apprecieer het steeds snelle handelen. Prof. dr. Peter Dubruel wens ik te danken om mijn interesse in de polymeerchemie verder uit te breiden.

Het onderzoek werd voornamelijk verricht in het Laboratorium Magnel voor Betononderzoek en het Laboratorium voor Polymeerchemie en Biomaterialen. Prof. dr. ir. Luc Taerwe en prof. dr. Peter Dubruel ben ik erkentelijk voor het ter beschikking stellen van de infrastructuur en de technieken. Aan de andere leden van het professorenkorps; prof. dr. ir. Geert De Schutter, prof. dr. ir. Stijn Matthys en prof. dr. ir. Robby Caspeele richt ik ook een woord van dank voor hun advies, bijvoorbeeld inzake wetenschappelijke dienstverlening.

Er waren ook vele helpende handen beschikbaar in het labo. Ik wil daarom het technisch personeel (Bart, Dieter, Jan, Marc, Nathan, Nicolas, Peter L, Peter VdB, Sandra, Stefan, Tom en Tommy) bedanken voor de hulp en assistentie bij de proeven en het inplannen ervan. Ook het administratief personeel (Christel, Marijke en Viviane) wil ik spreekwoordelijk in de bloemetjes zetten om alles in goede banen te leiden op vlak van dienstverlening, het regelen van de dienstreizen en de financiële kant van het verhaal te bolwerken.

De leden van de examencommissie wil ik van harte bedanken voor hun waardevolle opmerkingen en suggesties; prof. dr. ir. Luc Taerwe, prof. dr. ir Geert De Schutter, prof. dr. Sandra Van Vlierberghe, prof. dr. Veerle Cnudde, Col. prof. dr. Peter Lodewyckx en prof. dr. ir. Ole Mejlhede Jensen.

I would like to thank Col. prof. dr. Peter Lodewyckx and dr. Leticia Velasco from the Royal Military Academy for our numerous discussions in the field of sorption of both cement-based and carbon materials.

In particular, I want to thank prof. dr. ir. Ole Mejlhede Jensen for his very warm welcome in Lyngby during my research stay at the Technical University of Denmark. We had numerous scientific and non-scientific discussions. I want to thank you for letting me enjoy the professionalism and your seemingly endless enthusiasm. Mange tak!

"The most exciting phrase to hear in science, the one that heralds new discoveries, is not 'Eureka!' but 'That's funny...'"

– Isaac Asimov

Uiteraard gebeurt onderzoek niet zonder slag of stoot. Stroomonderbrekingen, meerdere storingen in stikstofaanvoer en plotse tegenstribbelingen van toestellen zorgden voor interessante plotwendingen. Ook waren sommige toestellen niet beschikbaar waardoor ik naar andere oorden diende uit te wijken. Dit gebeurde al vanaf de allereerste dag. Mijn eerste officiële werkdag als doctoraatsbursaal was namelijk in Villigen aan het Paul Scherrer Instituut. Een onvergetelijk avontuur waarbij 24/24u neutronenradiografie tot een goed einde werd gebracht.

Tijdens mijn doctoraat had ik de mogelijkheid veel bij te leren door het volgen van cursussen en het bijwonen van conferenties. Allen gaven ze een nieuw beeld en inkijk op de wereld. Ze waren ieder op zich een leerrijke ervaring en een verrijking. Nieuwe wetenschappelijke ideeën en connecties bleken een groot pluspunt.

Ik had ook de mogelijkheid om in andere laboratoria te werken, zoals het Laboratorium voor Nucleaire Wetenschappen, Farmaceutische Technologie, Geologie, Microbiële Ecologie en Technologie (LabMET), Materiaalkunde, Microsysteem Technologie (imec), X-stralen Tomografie (PProGRess; UGCT), Fysica en Sterrenkunde, Textielkunde, Organische Chemie, Anorganische Chemie, Fysische Chemie,... Het was steeds interessant nieuwe invalshoeken te krijgen op het onderzoek en ook nieuwe experimenten en methoden uit te proberen.

Mijn thesisstudenten (Nele, Pierre-André, Stijn, Bavo, Kenny, Alexander, Sander, Laurence en Núria) wil ik bedanken voor hun inzet bij het maken van hun masterproef.

"You've achieved success in your field when you don't know whether what you're doing is work or play."

– Warren Beatty

Op het einde kijk je met voldoening terug op een prachtige tijd. Die tijd vloog voorbij. Dit zeker door de toffe werksfeer en collega's. Vele collega's zijn de revue gepasseerd; met wie ik een bureau gedeeld heb, met wie ik oefeningenlessen en examens verzorgd heb, met wie ik een ongelooflijke tijd beleefd heb tijdens congressen en met wie ik vele activiteiten buiten de werkuren heb mogen beleven. Deze leuke momenten zijn onvergetelijk.

Ook de vele boeiende gesprekken over gemeenschappelijke interesses zoals ruimtevaart, films en wetenschap zijn een meerwaarde gebleken. De vele quizzen die we samen deden waren ook aangename verpozingen.

Ik vond het altijd tof deel uit te maken van onze onderzoeksgroep 'Beton en Milieu'. Het was altijd aangenaam vergaderen en de teambuilding activiteiten zullen ook altijd bijblijven.

"A journey is best measured in friends, rather than miles."

– Tim Cahill

Tijdens mijn doctoraatsonderzoek heb ik het genoegen gehad vele mensen vanuit alle hoeken van de wereld te mogen leren kennen. Velen van hen reken ik nu onder mijn vrienden.

Adelaide, Alessandro, Ali, Anibal, Aniello, Arn, Arne, Benoît, Bert, Bjorn, Brenda, Charlotte, Chris, Corina, Cornelia, Desirée, Dirk, Dorletta, Eleni, Elke, Emmanuel, Farid, Filipe, Florent, Hai Dang, Han, Hugo, Jeroen, Jianyun, João, Jolien, Jonas, Joris, Julia, Kai, Karel, Kenny, Kim, Kizzy, Kunpeng, Lijie, Limin, Mathias, Mieke, Mu, Natalia, Nicky, Peter, Philip, Pieter, Pieterjan, Quoc, Raul, Ravi, Romy, Ruben S, Ruben VC, Sandra, Sara, Serge, Steffen, Stijn, Tim, Wenhao, Willem, Wouter, Xiang, Yang, Yihua, Yun, Yury, Yusuf, Zhijun, Zhiqiang; *many of you have become friends!*

Special thanks to my office mates Limin, Eleni, Kunpeng, Han, Yihua, Nicky and Mieke for always keeping a fun atmosphere and collegiality.

De mooie momenten die ik naast mijn doctoraat mocht beleven, heb ik vooral te danken aan mijn vrienden. Hierbij denk ik aan mijn vrienden uit het middelbaar en voornamelijk de 'Grieken' Jeroen, Tim en Wouter. Het is altijd plezant om met jullie af te spreken! Ook uit de hogere studies de tennisvrienden Robin en Valerie, en onze zogenaamde 'Groep van Acht' Bram, Michiel, Philippe, Pieter, Tom VA, Tom VDS, en Yoeri. Het was altijd tof in de les te zitten en samen alles te overbruggen. De laatste groep die ik wens te danken is de 'Groep van Aalst'. Ik, als Merelbekenaar, kwam er plotsklaps bij, werd heel warm onthaald en jullie zijn stuk voor stuk vrienden geworden. Zeker bedankt aan Dennis, Gerrit, Maarten, Romina, Tom VA, Thomas, en alle anderen!

Naast mijn vriendenkring ben ik ook dankbaar aan mijn familie. Ik kon altijd rekenen op mijn ouders Dirk en Katrien in het najagen en verwezenlijken van mijn dromen. Dankjewel voor alle steun! Ook mijn broer, Jean-Philippe, bedankt voor alles.

En uiteraard Dorien. Weinig woorden kunnen omschrijven wat jij voor mij betekent. Ik besef iedere dag meer en meer hoeveel geluk ik met je heb en ik kijk uit naar ons leven samen!

Didier Snoeck, October 2015

"It is good to have an end to journey toward;
but it is the journey that matters, in the end."

– Ernest Hemingway

Table of contents

Nomenclature

Symbols

a_f	Cross-sectional area of the fluid column [m²]
a_g	Flow rate coefficient [-]
A	Surface area of the sample subjected to flow [m²]
A_{BET}	BET interception constant [-]
a/b/c	Constant coefficient [-]
c	BET constant [-]
β	Affinity coefficient [-]
B	Coefficient of capillary water penetration [$m \cdot h^{-1/2}$]
BFS/C	Blast-furnace-slag-to-cement ratio [-]
Δm	Mass difference [g]
$\Delta m/m$	Mass difference ratio [-]
ΔV	Volume difference [ℓ]
$\Delta V/V$	Volume difference ratio [-]
d	Pore diameter [µm]
d_c	Length of the crack in the flow direction [m]
d_p	Diameter of barrow mesopores [nm]
dm/dt	Mass increase criterion [g/s]
ε_{cu}	Strain at the peak stress [%]
ε_{fc}	Strain at the first-cracking-strength [%]
E	Modulus of elasticity [GPa]
E	Wave energy through mortar [J]
E_0	Characteristic activation energy of adsorption [J]
E_{ref}	Reference wave energy through a container filled with water [J]
E/E_{ref}	Energy ratio [-]
FA/C	Fly-ash-to-cement ratio [-]
g	Gravity constant [m/s²]
γ	Surface energy [N/m]
h	Height of the fluid column on the inlet [m]
h_0	Initial pressure head [m]
h_f	Remaining pressure head [m]
I	Absorption [mm]
I_0	Intensity of the incident ray [$mA^{-1} \cdot cm^{-2} \cdot s^{-1}$]
I_{BET}	BET interception constant [-]
I_{dry}	Intensity of the attenuated beam in the dry state [$mA^{-1} \cdot cm^{-2} \cdot s^{-1}$]
I_p	Pressure gradient (h/d) [-]
k	Coefficient of water permeability [m/s]
k_{app}	Apparent gas permeability coefficient [m²]
l_s	Length of the crack at a right angle of the flow direction [m]
L	Height of the specimen [m]
m	Mass of the sample [g]
m%	Mass percent relative over cement weight [%]
m_1	Mass of maximum packed dry particles [g]
m_2	Known mass of dry particles [g]

m_a	Mass of the adsorbent [g]
m_d	Dry mass [g]
m_h	Hydrostatic mass [g]
m_s	Saturated mass [g]
m_t	Mass at time t [g]
MW_{CH}	Molecular weight of portlandite [g·mole^{-1}]
MW_{H2O}	Molecular weight of water [g·mole^{-1}]
ν	Kinematic viscosity [m²/s]
υ	Adsorbed gas quantity [m³]
υ_m	Monolayer adsorbed gas quantity [m³]
n	Number of replicates [-]
N_a	The Avogadro constant [mole^{-1}]
Ø	Diameter [m]
p	Equilibrium pressure [Pa]
p_0	Saturation pressure [Pa]
P_1	Upstream pressure [Pa]
P_2	Downstream pressure [Pa]
q	Heat production rate [J/g/h]
Q	Cumulative heat production [J/g]
Q_f	Flow rate [ml/s]
ρ_1	Porosity accessible to water [-]
ρ_2	Amount of absorbed water [-]
ρ_{app}	Apparent volumetric mass [kg/m³]
$\rho_{hydrogel}$	Density of the hydrogel [kg/m³]
ρ_{fluid}	Density of the fluid [kg/m³]
ρ_w	Density of water [kg/m³]
σ_{cu}	Peak stress [MPa]
σ_{fc}	First-cracking-strength [MPa]
$\sigma_{release}$	Release stress [MPa]
$\sigma_{residual}$	Residual stress [MPa]
Σ	Attenuation coefficient of the sample [cm^{-1}]
Σ_w	Attenuation coefficient of water [cm^{-1}]
s	Adsorption cross section [m²]
S/B	Sand-to-binder ratio [-]
S_{BET}	Specific surface area [m²/g]
Spl/B	Superplasticizer-to-binder ratio [-]
θ	Contact angle [°]
t	Time [s]
t_s	Thickness of the sample [m]
t_w	Thickness of the water layer [m]
t_f	Measured flow time [s]
T	Temperature [K]
T_s	Specimen thickness [m]
u	Vertical displacement [m]
V	Molar volume of adsorbate gas [mole]
v%	Volume percent [%]

V_1	Maximum volume reading dry particles [ℓ]
V_2	Volume of packed wet particles [ℓ]
V_{meso}	Volume of mesopores [mm³/g]
V_{micro}	Volume of micropores [mm³/g]
w	Crack width [µm]
wt%	Weight percentage [%]
W	Volume filled at a relative pressure of p/p_0 [m³]
W_f	Total working force [J]
W_0	Micropore volume [m³]
(w/b)	Water-to-binder ratio [-]
$(w/b)_e$	Effective water-to-binder ratio [-]
(w/c)	Water-to-cement ratio [-]
$(w/c)_{add}$	Additional water-to-cement ratio [-]
$(w/c)_{eff}$	Effective water-to-cement ratio [-]
$(w/c)_{tot}$	Total water-to-cement ratio [-]
w_{dry}	Dry weight [g]
WL_{CaCO3}	Weight loss of CO_2 from $CaCO_3$ [%]
WL_{CH}	Weight loss of portlandite [%]
$WL_{original\ CO2}$	Weight loss of CO_2 from original constituents [%]
w_{wet}	Saturated weight [g]
x	Penetration depth [cm]
x_0	Initial penetration through surface pores [cm]

Chemical abbreviations

AA	Acrylic acid
AFm	Monosulphoaluminate
AFt	Ettringite
AH	Acetic anhydride
Al^{3+}	Aluminium ion
Al_2O_3	Aluminium oxide
AM	Acrylamide
BMA	Bismethacrylate
BP	Benzoylperoxide
C_3A	Tricalcium aluminate
C_2S	Dicalcium silicate
C_3S	Tricalcium silicate
C_4AF	Tetracalcium aluminoferrite
Ca^{2+}	Calcium ion
$CaCl_2$	Calcium chloride
$CaCO_3$	Calcium carbonate
CH	Calcium hydroxide
CH_3	Methyl
CH_3CO	Acetyl
CH_3COOK	Potassium acetate
CaO	Calcium oxide
$Ca(OH)_2$	Calcium hydroxide/Portlandite

C-A-S-H	Calcium aluminium silicate hydrates
$CDCl_3$	Deuterated chloroform
Cl^-	Chloride ion
-CONH-	Amide linkage
$-CONH_2$	Amide group
-COOH	Carboxylic acid group
C-S-H	Calcium silicate hydrates
CO_2	Carbon dioxide
CO_3^{2-}	Carbonate ion
Et_3N	Triethylamine
Et_3NH^+	Protonated triethylamine
F127	Pluronic F127
Fe^{3+}	Iron ion
Fe_2O_3	Ferric oxide
H	Hydrogen
H^+	Proton
HCl	Hydrochloric acid
HCO_3^-	Hydrogen carbonate ion
Hg	Mercury
H_2O	Water
H_2SO_4	Sulphuric acid
Irg	Irgacure
K^+	Potassium ion
KCl	Potassium chloride
KI	Potassium iodide
KNO_3	Potassium nitrate
K_2SO_4	Potassium sulphate
LiCl	Lithium chloride
Me	Methyl
Mg^{2+}	Magnesium ion
$MgBr_2$	Magnesium bromide
$MgCl_2$	Magnesium chloride
Na	Sodium
Na^+	Sodium ion
NaBr	Sodium bromide
NaCl	Sodium chloride
NaOH	Sodium hydroxide
Na_2SO_4	Sodium sulphate
$-NH_2$	Amidogen
O	Oxygen
O^-	Oxygen ion group
O^{2-}	Oxygen ion
O_2	Oxygen
-OH	Hydroxide group
OH^-	Hydroxide ion
PAA	Poly(acrylic acid)

PE	Polyethylene
PEG	Polyethylene glycol
PEO	Polyethylene oxide
PAA	Polyacrylic acid
PLA	Polylactic acid
Plu	Pluronic
PMA	Polymethacrylate
PMMA	Poly(methyl methacrylate)
PP	Polypropylene
PPO	polypropylene oxide
PU	Polyurethane
PVA	Polyvinyl alcohol
PVC	Polyvinylchloride
Si	Silicon
SiC	Silicon carbide
SiH_4	Silanes
SO_2	Sulphur dioxide
TAIC	Trichloroacetylisocyanate
TEA	Triethylamine
UH	Unhydrated cement

Abbreviations

60	Storage at a relative humidity of 60%
90	Storage at a relative humidity of more than 90%
AC	Air content
ANOVA	Analysis of variance
BET	Brunauer-Emmett-Teller
BJH	Barrett-Joyner-Halenda
BFS	Blast-furnace slag
BSE-SEM	Backscattered electron – scanning electron microscopy
B_s	Bacterial spores
B_v	Bacterial vegetative cells
CCD	Charge-coupled device
CD	Critical diameter
CF	Cement filtrate
CF	Cottonised flax
CRA	Cracked
DE	Diatomaceous earth
DR	Dubinin-Radushkevich
DVS	Dynamic vapour sorption
DW	Demineralized water
ECC	Engineered cementitious composites
EDS	Energy-dispersive spectroscopy
FA	Fly ash
F-drying	Freeze-drying
FRC	Fibre-reinforced concrete

FRCC	Fibre-reinforced cementitious composites
^{1}H-NMR	Proton nuclear magnetic resonance
HTPP	High tenacity polypropylene
HPFRCC	High-performance fibre-reinforced cementitious composites
IC	Internal curing
MC	Multiple cracking
µCT	X-ray computed microtomography
MFCFRCC	Multiple-fine-cracking fibre-reinforced cementitious composites
MIP	Mercury intrusion porosimetry
N-	Mercerization or alkalisation treatment
NH	Non-retted hemp
OPC	Ordinary Portland cement
QNI	Quantitative neutron imaging
REF	Reference
RH	Relative humidity
RF	Retention factor
S	Silane primer
SAF	Superabsorbent fibre
SAP	Superabsorbent polymer
SAPs	Superabsorbent polymers
SCM	Supplementary cementitious material
SCMs	Supplementary cementitious materials
SEM	Scanning electron microscopy
SG	Silica gel
SH	Slightly-retted hemp
SHCC	Strain hardening cementitious composites
Spl	Superplasticizer
SPV	SAP pore volume
TGA	Thermogravimetric analysis
TF	Technical flax
TPV	Total pore volume
TRC	Textile reinforced concrete
UNC	Uncracked
UV	Ultraviolet
wd	Wet/dry cycles

Samenvatting

Deze doctoraatsverhandeling focust op drie hoofddelen. Ten eerste worden de kinderziektes door het inmengen van superabsorberende polymeren besproken. Ten tweede wordt de minder gebruikte sorptie techniek geoptimaliseerd. Ten laatste wordt een slim zelfhelend material onafhankelijk van de omgevings-condities ontworpen.

Beton kan je de dag van vandaag niet zomaar wegcijferen uit het dagelijkse leven. De grootste bouwwerken zijn namelijk opgetrokken uit beton en dat geeft ons een gevoel van zekerheid en stevigheid. Beton is echter bros. Beton kan goed druk opnemen, maar als het onderhevig is aan trek, kan er scheurvorming optreden zonder grote rekvervorming. Deze scheuren brengen de duurzaamheid in het gedrang als je het materiaal niet tijdig herstelt en daardoor kunnen de kosten torenhoog oplopen. Zeker wanneer schadelijke stoffen het beton binnendringen en vernielen.

Hoe kunnen we dit oplossen?

Een antwoord vind je bij jezelf. De mens heeft namelijk de eigenschap zichzelf te herstellen. Een wonde zal na verloop van tijd helen en achteraf zie je geen schade meer. Ook beton kan deze eigenschap hebben. We dienen dit enkel te stimuleren. De twee helingsmechanismen zijn de calciumcarbonaat kristalvorming en de verdergaande hydratatie van cement en andere bindmiddelen. Als we nu deze twee mechanismes zouden bevorderen, dan zou er een materiaal verkregen worden dat zichzelf perfect zou helen en zou resulteren in een lagere herstelkost.

De bouwstenen voor heling zijn aanwezig in een weldoordachte samenstelling. De mengeling werd geoptimaliseerd door het variëren van het type bindmiddel en de water/bindmiddel factor. Een vliegas/cement factor van 1, een zand/bindmiddel gehalte van 0.35, een water/bindmiddel gehalte van 0.30, een superplastificeerder/ bindmiddel gehalte van 0.0097 en twee volumeprocent aan met olie gecoate polyvinylalcohol microvezels bleken de ideale verhoudingen. De scheurwijdte in beton kan beperkt worden door het inmengen van microvezels, waarbij meervoudige scheurvorming optreedt. De vezelversterkte materialen zijn duurzaam en beschikken over een betrouwbare ductiliteit onder trek en een scheurbeperkende capaciteit om lokale brosse scheurvorming te voorkomen. De gevormde kleine scheuren kunnen wel heling vertonen en het materiaal kan volledig herstellen. Verschillende vezeltypes werden bestudeerd, waaronder synthetische microvezels en natuurlijke vezels als groen alternatief. De autogene heling was onafhankelijk van het vezeltype en hing voornamelijk af van de initiële scheurwijdte. Kleine scheuren (<30 µm) heelden volledig, iets grotere (50-150 µm) slechts gedeeltelijk en grote scheuren (>150 µm) vertoonden geen noemenswaardige vorm van zelfheling.

Het gebruik van vlas- en hennepvezels leidde tot verstevigingsgedrag en meervoudige scheurvorming. De beste resultaten werden verkregen in mengsels met technisch vlas, waarbij de gemiddelde scheurwijdte 28 µm bedroeg en er 0.76% rek optrad. De mengelingen werden geoptimaliseerd en de natuurlijke vezels werden chemisch behandeld om de ductiele capaciteit en de duurzaamheid in

alkalisch milieu te verbeteren. Een alkalisatie met 2 massapercent NaOH van technisch vlas en lichtgerote hennep leidde tot scheurwijdtes van 28 en 53 µm, respectievelijk. Een behandeling met een waterafstotend middel, benzoylperoxide, azijnzuur of acetylering verbeterde de eigenschappen niet. De nieuwe bevindingen tonen het potentieel van deze natuurlijke vezels. Het grootste nadeel blijft de degradatie in een alkalisch milieu daar de onbehandelde vezels nauwelijks sterkte vertonen na zes maand opslag in cementfiltraat. De chemische behandeling met alkalisatie verbeterde de weerstand en de treksterkte bleef behouden. Globaal blijken de vlas- en hennepvezels een goed alternatief voor synthetische vezels bij toekomstig gebruik in gebouwen.

Zonder water is er geen heling. Het water is voorradig door het inmengen van superabsorberende polymeren (SAPs). Superabsorberende polymeren zijn ketens met geladen groepen, verbonden door verschillende crosslinks. Verschillende commercieel verkrijgbare polymeren werden onderzocht op hun zwellend gedrag, kinetiek en degradatie, samen met een eigen gesynthetiseerd polymeer. Ze zijn in staat tot 500 keer hun eigen gewicht aan vloeistoffen en tot vier keer hun eigen gewicht in vocht vanuit de omgeving op te nemen. Dit werd bestudeerd door middel van filtratieproeven en dynamische vocht sorptie proeven. In een alkalisch milieu zoals beton zijn de polymeren slechts in staat een vijfde van hun zwelgedrag in water te vertonen. Dit komt door de afscherming van geladen groepen door de kationen die in de poriënvloeistof aanwezig zijn. Ook is er een sterke complexatie van divalente en trivalente ionen met de geladen groepen van het polymeer, waardoor er extra crosslinks optreden en dus ook minder zwelling.

Door hun zwellend gedrag zullen superabsorberende polymeren een deel van het mengwater opnemen. Vandaar werd steeds extra water toegevoegd om aan dit verlies in verwerkbaarheid tegemoet te komen. Dit water wordt tijdens verharding aan de matrix gegeven, waardoor de autogene krimp volledig wordt gecompenseerd. In mengsels waarbij cement deels vervangen is door vliegas of hoogovenslakken, is de initiële totale krimp hoger dan in mengsels met puur cement. Het gebruik van SAPs elimineert deze krimp, onafhankelijk van de samenstelling van de mengeling. Achteraf blijven lege macroporiën achter, welke de sterkte beïnvloeden. Net doordat deze polymeren water opnemen, verlaagt de effectieve water/cement factor waardoor de microstructuur ook verandert en denser wordt. Niet de totale maar de effectieve water/cement factor is belangrijk in geval van capillaire porositeit. Het toevoegen van extra water moet dus overwogen worden wanneer superabsorberende polymeren gebruikt worden, zeker als een gelijkwaardige microstructuur gewenst is. Achteraf zal dit extra water ook wel zorgen voor verdergaande hydratatie. Dit zal voor een kleine reductie (niet significant) aan capillaire poriën zorgen. Door de studie van de intensiteit van de fluorescentie bij slijpplaatjes, kwam de densere microstructuur aan het licht in mengsels met superabsorberende polymeren zonder extra mengwater. Dit komt dus door het gradueel afgeven van opgenomen mengwater aan de cementgebonden matrix. Elektronenmicroscopie toonde ook aan dat dezelfde microstructuur werd gevonden in mengsels met eenzelfde effectieve water/cement factor. Kwikporosimetrie en helium pyknometrie leidden tot dezelfde conclusies op het vlak van capillaire microstructuur.

Het onderzoek naar de invloed van de superabsorberende polymeren op de microstructuur gaf beter inzicht in de transporteigenschappen en zelfheling van het cementgebonden materiaal. Vochttransport kan hierbij niet begrepen worden zonder kennis van de vochtfixatie in de poriën. Waterdamp sorptie is daarom belangrijk. Twee methodes worden gebruikt om vochttransport te bestuderen. Deze zijn de statische en dynamische waterdamp sorptie test. De dynamische methode om de micro- en meso-porositeit te bestuderen wordt niet vaak gebruikt voor cementgebonden materialen en vele vragen rijzen over de proefstuk-voorbereiding, meettechniek en interpretatie van de verkregen sorptie isothermen. Verschillende parameters werden daarom bestudeerd om waardevolle informatie te verkrijgen en de techniek te optimalizeren. Verschillende drogingsmethodes en modellen (Barrett-Joyner-Halenda en Dubinin-Radushkevich) werden toegepast op cementgebonden materialen. Waterdamp sorptie is een nieuwe veelbelovende techniek om extra informatie te geven over en inzicht te bieden in de microstructuur van cementgebonden materialen, al dan niet met SAPs. De ideale drogingstechniek, die de microstructuur behoudt en enkel het ongebonden water verwijdert, bestaat spijtig genoeg niet. Elke drogingstechniek beïnvloedt de microstructuur op haar eigen manier. Water sorptie gaf extra experimenteel bewijs dat de beste technieken vacuüm droging en de vloeistofextractie met isopropanol zijn. Vriesdrogen veranderde de microstructuur door thermomechanische krachtswerking. Het drogen in een oven verwijderde deels het gebonden water en dehydrateerde C-S-H, monosulfoaluminaat en ettringiet. Ook was er sprake van differentiële expansie en capillaire krachtswerking door terugtrekkende watermenisci waardoor de texturele eigenschappen veranderden. Het drogen in een geventileerde oven en in lucht leidden tot carbonatatie, opnieuw de microstructuur nefast beïnvloedend. Het drogen in een oven is dus een ongeschikte drogingstechniek om de fragiele microstructuur van een cementgebonden materiaal te behouden. Methanol reageerde met C-S-H (enkel bij opwarming) maar isopropanol bleek inert te zijn ten opzichte van de cementgebonden componenten.

De micro- en mesoporiën in proefstukken met superabsorberende polymeren werden onderzocht met dynamische vocht sorptie proeven. Cement pasta's met SAPs en zonder extra mengwater vertonen een lichte daling in het aantal micro- en mesoporiën en hebben een vergelijkbare microstructuur als mengsels met dezelfde effectieve water/cement factor. Wanneer extra mengwater gebruikt wordt, is er geen significant verschil in geval van de microporiën en een lichte stijging in het gehalte aan grote mesoporiën.

De buigtrek-, druk- en splijtsterkte hangen voornamelijk af van de macroporiën. In het geval van de buigtreksterkte is er geen duidelijk verschil (extra mengwater heeft zowel een positieve als negatieve invloed), maar de drukstrekte is lager als extra mengwater gebruikt wordt. Superabsorberende polymeren blijken de vorst/dooi resistentie te verhogen daar ze voor minder verwering zorgen door de vorming van een uniform verspreid poriënnetwerk wanneer extra mengwater wordt gebruikt. Geen extra mengwater verhoogde de resistentie nog verder. De globale verbetering is gelijk aan deze wanneer een conventionele luchtbelvormer toegepast wordt. De sterkte bij gebruik van deze luchtbelvormer daalde echter significant, zelfs nog meer dan bij gebruik van SAPs met extra mengwater.

Gaspermeabiliteitsmetingen toonden aan dat proefstukken met SAPs een verhoging in gaspermeabiliteit vertonen. De macroporiën blijven steeds toegankelijk hoewel de omringende matrix dens is. Een toename in gaspermeabiliteit van 15 en 41% werd verkregen bij het gebruik van 0.5 en 1 massaprocent aan SAP ten opzichte van het cementgehalte, respectievelijk.

Door overmatige scheurvorming kunnen ongewenste agressieve stoffen of vloeistoffen via de scheuren naar binnen treden en zo het beton van binnenuit aantasten. Superabsorberende polymeren zwellen na contact met een vloeistof en blokkeren de scheur waardoor ze de indringing van agressieve stoffen verhinderen. De permeabiliteit kon bestudeerd worden door middel van water permeabiliteitstesten (zowel onder lage als hoge druk), capillaire absorptieproeven en neutronen radiografie. Proefstukken met superabsorberende polymeren vertoonden een daling in permeabiliteit (van $1{\cdot}10^{-7}$ to $1{\cdot}10^{-10}$ m/s vergeleken met $1{\cdot}10^{-5}$ m/s voor gescheurde referentieproefstukken zonder SAPs), wat het zelfdichtend effect bewijst. Kleine SAPs (100-200 µm in diameter) zijn niet doeltreffend om een scheur te dichten. Ze zijn niet in staat een 200 µm scheur te overbruggen. Te grote SAPs (>700 µm) zijn ook niet efficiënt daar er slechts een lokale dichting optreedt. De ideale grootte is 500 µm. Concluderend zijn SAPs in staat om de vloeistofstroom een halt toe te roepen, zo de opname van schadelijke stoffen te verminderen, en dus mogelijk te leiden tot een verhoging van de duurzaamheid en levensduur van de constructie op lange termijn.

Het herstel in mechanische eigenschappen werd bestudeerd door herhaalde vierpuntsbuigproeven op verschillende leeftijden (na 7 dagen, 28 dagen, 3 maanden en 1 jaar) van de proefstukken. De proefstukken werden eerst belast tot een rek van 1% en werden dan opgeslagen in drie verschillende helingscondities. De eerste is een combinatie van nat/droog cycli waarbij proefstukken eerst een uur in water werden gebracht en vervolgens de overige 23 uur in een standaard laboratorium conditie met een relatieve vochtigheid van 60%. De tweede conditie is de opslag onder een relatieve vochtigheid van meer dan 90% en de derde onder 60% relatieve vochtigheid. De proefstukken werden dan belast tot falen. Sommige proefstukken werden opnieuw belast tot 1% rek en opgeslagen in helingscondities vooraleer belast te worden tot falen. Dit was om de herhaalbaarheid van zelfheling te bestuderen. Alle proefstukken werden microscopisch onderzocht op hun scheurdichtende capaciteit en de samenstelling van de helende producten werd bepaald door middel van een elektronenmicroscoop uitgerust met een elementaire detector. Het materiaal zonder superabsorberende polymeren in nat/droog cycli is in staat om totale visuele heling te vertonen in scheuren tot 30 µm. Wanneer de polymeren wel werden ingemengd, bleken scheuren van 100 µm en groter volledig te dichten, hoofdzakelijk door calciumcarbonaat kristallisatie. De polymeren helpen het dichten van grotere scheuren waardoor het materiaal sneller en beter herstelt. Ze zwellen na het in contact komen met een vloeistof, geven de opgenomen vloeistof af voor zelfheling en realiseren zo een herwonnen dichtheid van het beton. Na hun afgifte van vocht kunnen de superabsorberende polymeren opnieuw vocht opnemen en afgeven, wat zorgt voor een gesloten keten. In een relatieve vochtigheidsconditie is er enkel zichtbare heling waarneembaar in proefstukken met superabsorberende polymeren. Hun vochtopname lijkt

voldoende om een lichte vorm van autogene heling te stimuleren. Deze vorm van heling bestaat voornamelijk uit verdergaande hydratatie en de puzzolane activiteit van vliegas. De gevormde helingsproducten werden driedimensionaal gevisualiseerd door middel van X-stralen microtomografie. Het gehalte aan kristallen in nat/droog cycli hangt af van de positie in de scheur. Een kleine regio van 0 tot 800-1000 µm diep in de scheur werd volledig geheeld wanneer superabsorberende polymeren gebruikt werden. In het inwendige van de scheur was de hoeveelheid aan helingsproducten lager.

Deze helingsproducten; hebben ze enige vorm van sterkte?

Het herstel in sterkte diende bestudeerd te worden. Eerst en vooral moet er gezegd worden dat de sterkte van de materialen met één massapercent aan SAPs en het referentie-materiaal onderling geen significant verschillende sterkte vertonen. Hogere gehaltes aan superabsorberende polymeren zouden leiden tot lagere sterktes door meer gevormde macroporiën. In nat/droog cycli is er een sterkteherstel van 45% in proefstukken zonder superabsorberende polymeren en geen heling bij relatieve vochtigheden van 60% en meer als 90%. Met deze polymeren is er echter een gedeeltelijke heling van 25-40% bij een relatieve vochtigheid van 60% en 40-55% herstel bij meer dan 90%. De vochtopname door de polymeren lijkt voldoende om enige vorm van zelfheling te stimuleren bij relatieve vochtigheden. Deze nieuwe en interessante eigenschap kan zelfheling binnenshuis stimuleren waar regen of water niet voorhanden is. De polymeren vervullen zo de voorwaarde voor de aanwezigheid van water. In nat/droog cycli kan het materiaal met superabsorberende polymeren volledig herstellen en 70-100% van de mechanische eigenschappen wordt herwonnen. De herwinning in mechanische sterkte blijft deels behouden gedurende verschillende belastingen. In nat/droog cycli, is de herwinning na de tweede belasting 28%. Bij het gebruik van superabsorberende polymeren is dit nog steeds 66%. Een gehalte van één massapercent ten opzichte van het cementgehalte aan SAPs bleek het beste resultaat te geven. De sterkte daalde hierbij niet noemenswaardig en de zelfdichtende en zelfhelende eigenschappen waren superieur.

Zelfheling zorgt voor een volledige of gedeeltelijke herwinning in mechanische eigenschappen na scheurvorming. Door zelfheling moeten geen manuele reparaties meer toegepast worden. Dit verhoogt de betrouwbaarheid en bedrijfszekerheid van constructies.

Samenvattend zorgt de combinatie van microvezels en superabsorberende polymeren voor verbeterde zelfhelende eigenschappen, waardoor het materiaal minder onderhoud en kosten vergt. Meervoudige scheurvorming, zelfdichting en zelfheling onder de vorm van verdergaande hydratatie en calciumcarbonaat kristalvorming, zullen de duurzaamheid verhogen. Op deze manier wordt een betrouwbaar materiaal verkregen, onafhankelijk van de omgevingscondities.

xx

Abstract

This doctoral thesis focuses on three main parts. First, the teething problems due to mixing in superabsorbent polymers are addressed. Secondly, the under-used technique for sorption measurements to characterize the porous structure is optimized. Finally, a smart self-healing cementitious material independent from conditions is designed.

Concrete is an excellent material to take up compressive forces. But, due to the low tensile strength, concrete is very brittle. When tensile forces are acting, the concrete may crack. This cracking leads to the ingress of water, and with that, to the ingress of potentially harmful substances. These substances will enter the cracks and will cause the deterioration of concrete from inside out. In this way, the durability of concrete is endangered. If you do not repair it in time, the costs will rise sky high.

But how can we solve this?

Well, we do not need to look too far, because we, humans, are the answer. We are able to heal cuts, bruises and broken bones and this property is also available in concrete. You only need to improve it.

The two main mechanisms for this biomimicry are the formation of calcium carbonate crystals and further hydration of both cement and pozzolanic materials like fly ash. If you would stimulate these properties, you would get a material which could perfectly heal itself and which will thus result in less repair costs. Building blocks for this healing using a well-thought mixture need to be present. The mixture composition was optimized to obtain the best autogenous healing capacity. The best overall self-healing mixture had a fly-ash-to-cement ratio of 1, a sand-to-binder ratio of 0.35, a water-to-binder ratio of 0.30, a superplasticizer-to-binder ratio of 0.0097 and 2 v% of oil-coated polyvinyl alcohol microfibres. The amount of microfibres led to strain-hardening and multiple cracking. Micro-fibre reinforced strain-hardening cementitious materials are durable and provide reliable tensile ductility and crack-controlling capability to prevent localized cracking failure often observed in concrete structures. The small cracks are interesting in terms of autogenous healing where only small cracks are able to heal completely. Different fibre types were studied, including synthetic types and the cheaper natural fibres as a green replacement for synthetic microfibres. Autogenous healing was independent of the fibre type but was mainly dependent on the initial crack width. Small crack widths (<30 µm) healed completely. Wider cracks (50-150 µm) only partially healed. Larger cracks (>150 µm) did not show a noteworthy form of autogenous healing.

The use of flax and hemp fibres in cementitious composites resulted in mixtures with tensile strain-hardening and extensive multiple cracking properties. The best overall results were found in the technical flax mixtures, giving an average crack width of 28 µm and a multiple cracking amount of 0.76%. The properties were further improved by chemically treating the fibres prior to mixing. The best results were obtained by mercerization with 2 m% NaOH of technical flax and slightly-retted hemp, providing respective average crack widths of 28 µm and

53 µm. A treatment with a silane primer, with benzoylperoxide, with acetic acid or with acetylation was not useful in terms of multiple cracking. The findings show the great potential of flax and hemp fibres for use in cementitious composites. The most important downside to the use of these fibres remains the degradation in alkaline cementitious environment, as almost no strength remained after storing the untreated natural fibres in cement filtrate for six months. Chemical treatment with mercerization improved the resistance of the natural fibres in an alkaline environment and the tensile properties were still present. Generally, flax and hemp fibres appear to be a good replacement for synthetic fibres and flax/hemp-fibre reinforced cementitious materials are an interesting alternative for future building applications.

Water needs to be present for autogenous healing as well and is provided by superabsorbent polymers (SAPs). These polymers have a polymer chain with electrically charged groups, interconnected with crosslinks. Different commercially available polymers were studied, together with an in-house synthesized hydrogel on their swelling behaviour, kinetics and degradation and shelf life. Exposed to demineralized water, they are able to take up three hundred times their own weight in water and four times their weight in moisture. This was investigated by using the filtration method and dynamic vapour sorption. In an alkaline environment, however, there is five times lower swelling due to charge-screening effects by cations like calcium ions and complex formation of divalent and trivalent ions with the carboxylate groups.

Because the superabsorbent polymers swell, they will absorb part of the mixing water. Additional water was therefore used to counteract the uptake of mixing water by the superabsorbent polymers. During hardening, they will release their stored water for internal curing, leading to a reduction and total mitigation of autogenous strain. In both fly ash and blast-furnace slag systems, where part of the cement is replaced by supplementary cementitious materials, the initial total amount of autogenous shrinkage is lower compared to an ordinary Portland cement mixture with a water-to-binder ratio of 0.30. At later ages, the rate of autogenous shrinkage is higher compared to ordinary Portland cement mixtures. Internal curing by means of SAPs seems to be successful, independent of this long-term higher rate of shrinkage in mixtures with supplementary cementitious materials. After internal curing, empty macro pores remain. The internal curing will also lead to the densification of the cementitious matrix. Not the total water-to-cement ratio, but the effective water-to-cement ratio is important in case of the capillary porosity. Additional water thus needs to be considered when using superabsorbent polymers if one aims to maintain approximately the same global microstructure. But afterwards, the additional water will cause further hydration too. This will cause a small reduction (not significant) of the amount of capillary pores. A comparison of the luminosity of thin sections under fluorescent light revealed the densification of the cementitious matrix in mixes containing SAPs and without additional water due to the uptake of mixing water during setting and the release of the mixing water afterwards. The same microstructural properties were found between the reference mixture and mixtures with SAPs and additional water, with the same effective water-to-cement ratio by using scanning electron

microscopy. The additional water will cause the formation of approximately the same global microstructure. Mercury intrusion porosimetry and helium pycnometry led to the same conclusions on the capillary porosity.

The study on the influences on the microstructure led to a better understanding of the moisture movements in the composite, and also for self-healing in standard laboratory conditions. Furthermore, moisture transport processes cannot be understood without the knowledge of the moisture fixation in the concrete pore system. Water vapour sorption is therefore a key parameter. There are two important methods for characterizing water vapour transport processes; using semi-equilibrium or dynamic gravimetric methods. The latter method, however, is not frequently used in concrete applications and a lot of questions remained regarding sample preparation, measuring procedure and interpretation of the sorption isotherms. Therefore, several parameters were investigated to optimize the method and to obtain valuable information concerning the effect of humidity on self-healing. Different drying techniques and models (Barrett-Joyner-Halenda and Dubinin-Radushkevich) were applied to cementitious materials. The ideal drying technique, which can preserve the microstructure and can remove only the non-bound water does unfortunately not exist. All drying techniques affect the microstructure in their own way. Water vapour sorption has given additional experimental evidence that the best techniques to dry the cementitious samples are vacuum-drying and the solvent-exchange-method with isopropanol. Freeze-drying changed the microstructure due to thermo-mechanical stress in the inner C-S-H. Oven-drying removed part of the non-evaporable water, dehydrated C-S-H, monosulfoaluminate and ettringite phases, and caused thermo-hydric stresses due to differential expansion. Capillary stresses due to receding water menisci also induced a modification of the textural properties of the sample. Oven-drying and air-drying proved to cause carbonation, which has its impact on the microstructure. Also, oven-drying at 105°C and air-drying in the presence of silica gel led to the removal of part of the C S-H phase, thus modifying the structural and textural properties of the sample. Oven-drying is thus an unsuitable drying technique to preserve the fragile microstructure of cement-based materials. Methanol reacted with C-S-H (only upon heating) but isopropanol seemed to be inert with cementitious compounds.

The micro- and mesopores of samples with SAPs were studied by means of dynamic vapour sorption. Cement pastes with SAPs and without additional water show a slight decrease in the micro- and mesopore range and have a similar microstructure as a cement paste with the same effective water-to-cement ratio. Cement pastes with SAPs and with additional water show no significant difference in the micropore range and a slight increase in larger mesopore range.

The bending, compressive and splitting strength are mostly governed by the formation of macro pores by the SAPs. In case of bending strength, there is no conclusive difference (additional water has both positive as negative effects on the bending strength properties), but the compressive strength is lower if additional water is used. Superabsorbent polymers were also able to increase the freeze-thaw resistance as they caused less scaling due to the formation of an evenly-distributed pore system, when using additional water. When SAPs without additional water

were used, the performance even improved considerably further. The overall improvement was hereby similar to that obtained with conventional air entrainment. However, when using an air-entraining agent, the strength decreased significantly, even more compared to using SAPs with additional water.

Gas permeability measurements of specimens with SAPs show an increase in gas permeability. The macro pores are still penetrable even though the surrounding cementitious matrix is denser. An increase of 15% and 41% in gas permeability was found for 0.5 m% and 1 m% of SAP by weight of cement, respectively.

Due to the swelling ability of the superabsorbent polymers, they are able to seal a crack. In this way, the water flow is prevented. The permeability could be visualized by means of low-pressure and high-pressure water permeability tests, capillary absorption tests and neutron radiography. Specimens containing SAPs show a decrease in permeability (from $1{\cdot}10^{-7}$ to $1{\cdot}10^{-10}$ m/s compared to $1{\cdot}10^{-5}$ m/s for cracked reference samples without SAPs), proving the self-sealing effect of SAPs. Small SAPs (100-200 µm in diameter) are ineffective in terms of sealing. They are unable to bridge a 200 µm wide crack and to completely seal it. Too large SAPs (>700 µm) are also not efficient as only distinct locations can be sealed. The best size is approximately 500 µm. In summary, SAP particles are able to prevent water movement through a crack, thus reducing the uptake of harmful substances, most likely leading to an enhanced long-term durability and normal service life.

The regain in mechanical properties was investigated as well by performing repeated four-point-bending tests at different ages (7 days, 28 days, 3 months and 1 year). To study the influences of superabsorbent polymers on the self-healing properties, the specimens were first loaded under four-point-bending until 1% of strain, and were then stored in three different curing conditions. The first one was storage in wet/dry cycles where the specimens are stored in water for an hour, and 23 hours in standard laboratory conditions with a relative humidity of 60%. The second curing regime is storage at a relative humidity of more than 90% and the third at a relative humidity of 60%. Then, specimens were reloaded until failure. Also, to study the repeatability of autogenous healing, some specimens were reloaded with an additional 1% strain and are cured again. After this second healing period, the specimens were loaded until failure. In the meantime, specimens were microscopically observed and backscattered-electron scanning electron microscopy was used to study the formed healing products. The material is able to visually heal itself perfectly. In wet/dry cycles, cracks up to 30 µm in specimens without superabsorbent polymers were closed completely. When mixing in superabsorbent polymers, cracks up to 100 µm and further were able to close in wet/dry cycles, mainly due to calcium carbonate crystallization, as microscopically observed and by means of elemental analysis by scanning electron microscopy. So, superabsorbent polymers are able to take up water, to hold it and to provide it to the cementitious matrix for self-healing. After providing the water to the cementitious matrix, the superabsorbent polymers are able to take up water again, resulting in a closed loop. Even at a relative humidity condition, parts of the cracks were visually closed in specimens with superabsorbent polymers, proving that their moisture uptake capacity seems to be sufficient to promote some autogenous healing. This healing was mainly further hydration and pozzolanic activity of the

fly ash. The healing products were visualized three-dimensionally by means of X-ray computed microtomography. The extent of healing in wet/dry cycles depends on the position along the crack depth. A shallow region about 0 till 800-1000 µm from the surface is completely healed when using SAP particles. In the interior of the specimen, the healing amount was less.

But, these healing materials; are they strong enough?

Therefore, the regain in mechanical properties was investigated. First of all, the strength is approximately the same when using one mass percent of SAPs. If larger amounts would be used, the strength would decrease due to the formation of more macro pores. There is healing up to 45% of specimens without superabsorbent polymers and at a relative humidity of 60% and more than 90%, there is no healing. But, when using superabsorbent polymers, there is partial healing at relative humidity conditions; 25-40% at a relative humidity of 60% and 40-55% at more than 90%. So, the moisture uptake by the superabsorbent polymers seems to be enough to promote autogenous healing in standard laboratory conditions. This new feature can promote self-healing materials indoors and for structural components that are not exposed to rain. In this way, superabsorbent polymers may be used as a replacement for the environmental condition (water) to introduce crack-healing, even in air. In wet/dry cycles, the material heals perfectly and regain of 70-100% of its mechanical properties is achieved. To a certain degree the autogenous healing capability of cementitious materials is maintained during subsequent loading cycles. In wet/dry cycles, after the second healing cycle, the regain in first-cracking-strength is 28%. When superabsorbent polymers are used, the second regain is still 66%. Introducing 1 m% of SAP relative to the cement weight gives the best results, considering no decrease in overall mechanical properties of the virgin material, which are similar as for the reference, and the superior self-sealing and self-healing capacity.

Self-healing provides a complete or partial healing of the mechanical properties after crack formation. This happens in situ, meaning that no action has to be undertaken like manual repair. This improves the reliability and the lifetime of structures, reducing the maintenance costs.

To conclude, the smart material by the combination of microfibres and superabsorbent polymers will promote multiple cracking and self-healing. Also, the superabsorbent polymers will swell and this will result in a decrease of water ingress. The material thus has self-sealing properties. Due to its self-healing effect, by further hydration and calcium carbonate crystallization, the material will increase the durability and this will result in less maintenance costs needed. In this way, a smart cementitious material which is reliable and independent from the conditions is acquired.

Chapter 1

Introduction

| Cracks in concrete are inevitable. How should we solve this problem?

Chapter redrafted after (Snoeck & De Belie, 2015b).

"Look deep into nature,
and then you will understand everything better."

– *Albert Einstein*

1.1 Introduction

Concrete is a material which can cope with high compressive stresses, but has a low tensile strength. Adding reinforcements increases the strength in tension but the composite will crack nevertheless. Cracking in plain concrete is thus inevitable. It can be the result of one or a combination of factors such as drying shrinkage, thermal contraction, restraints, differential settlement, and applied loads. Cracks are aesthetically unwanted and they will cause durability issues as they form a pathway for intruding potentially harmful substances. After crack formation and water intrusion, the pH will drop in the vicinity of reinforcements, leading to steel corrosion and possible structural declination. The ingress of chlorides will accelerate corrosion by de-passivating the protective film around reinforcements. Intruding carbon dioxide (CO_2) will react with the calcium hydroxide $Ca(OH)_2$ in the pore fluid causing a decrease of the pH and thus de-passivation and increased corrosion. The ingress of sulphates can result in the formation of ettringite, a subsequent volume expansion and a damaged microstructure. All these deteriorating processes need to be stopped before it is too late (Figure 1.1).

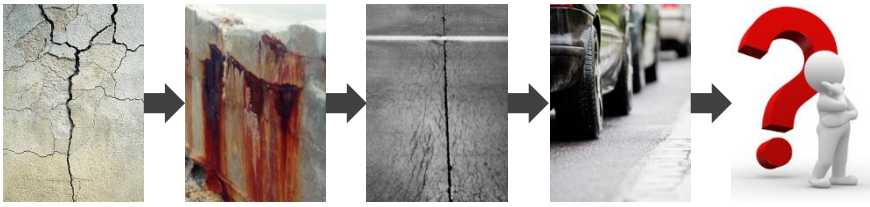

Figure 1.1. Problem statement due to cracking in concrete; how to solve this?

The amount of cracking can be controlled after taking the causes into account and repairs can be applied to seal the cracks from intrusion. But these repairs are time-consuming and costly. It would therefore be beneficial if the material would heal on its own. The self-healing concrete should hereby provide a complete or partial regain of the mechanical properties after crack formation. This happens in situ, meaning that no interaction has to be undertaken like manual repair. This would improve the reliability and the lifetime of structures.

Autogenous healing, which will be discussed later-on, can only close small cracks. A way to obtain these small cracks in concrete is the use of microfibres. In the first part of this chapter, the history of fibre-reinforced cementitious composites will be addressed. Different advantages and disadvantages of using different fibres in cementitious materials will be covered like the effects on degradation, steel corrosion and crack width restriction. The second part will be a close-up of autogenous healing and the need for attaining a complete healing of a cementitious composite. The third part will focus on the basic knowledge on the optimization of self-healing with the addition of microfibres. The future of this kind of self-healing cementitious materials with fibres will be discussed at the end.

1.2 From straw in bricks to use of microfibres in cementitious materials

1.2.1 Microfibres through history

Fibre-reinforced composites are used frequently nowadays and its properties have been used for a long time. One of the first written references to fibre reinforced composites can be found in the Biblical book Exodus (Bentur & Mindess, 1990):

> *Pharao praecepit ergo in die illo praefectis operum et exactoribus populi dicens nequaquam ultra dabitis paleas populo ad conficiendos lateres sicut prius sed ipsi vadant et colligant stipulam. - Exodus 5 (6-7)*
> That same day Pharaoh gave the order to the slave drivers and overseers in charge of the people that they are no longer to supply the people with straw for making bricks and that the people should go and gather their own straw. - Exodus 5 (6-7)

In ancient times the Egyptians, Sumerians, Babylonians and other civilizations used straw or horse hair to reinforce clay bricks. In this way, the bricks were stronger and were more durable in time. In the case of the Babylonians, this reinforcement could be beneficial in view of the liability of the constructor. Think about the Code of Hammurabi, a Babylonian law code, in which the builder is responsible for good practice and would lose his life if the owner of the house was killed due to poor construction. The use of reinforced materials was therefore imposed and the composites are still used today.

In 1963, fibre reinforced concrete found its way to the scientific community (Romualdi & Batson, 1963; Romualdi & Mandel, 1964) and since then, the material has been intensively studied. Review papers on fibre reinforced cement-based composites can be found in (Zollo, 1997) and (Brandt, 2008). Generally, fibre reinforced concrete is a material containing dispersed randomly oriented fibres. There are several materials which can be used in cementitious materials: natural fibres (e.g. akwara, bamboo, cellulose fibres, coconut husk, elephant grass, flax, hemp, jute, malva, musamba, plantain, sisal, sugar cane bagasse, water-reed, wood), glass fibres, carbon fibres, metal fibres (e.g. alumina, steel), and synthetic fibres (e.g. acrylic, aramid (Kevlar), nylon, polyester, polyethylene, polypropylene, polyvinyl alcohol) (Agopyan et al., 2005; Andonian et al., 1979; Aziz et al., 1981; Baley, 2002; Batson, 1976; Bentur et al., 1985; Bentur & Mindess, 1990; Boghossian & Wegner, 2008; Bos et al., 2002; Brandt, 2008; Campbell & Coutts, 1980; Cohen & Menashi, 1986; Colombo et al., 2015; Coutts & Campbell, 1979; de Andrade Silva et al., 2014; Geymayer & Cox, 1970; Krelani, 2015; Larner et al., 1976; Lewis & Mirihagalia, 1970; Li et al., 1997; Orlowsky et al., 2005; Ozomaka, 1976; Racines, 1977; Romualdi & Batson, 1963; Romualdi & Mandel, 1964; Savastano Jr. & Agopyan, 1999; Sedan et al., 2008; Slate, 1976; Swift & Smith, 1979; Tolêdo Filho et al., 2000; Wang et al., 1987; Yilmaz & Glasser, 1991; Zollo, 1997). Also asbestos was used, but that material has been banned due to human health issues.

1.2.2 Glass, steel and natural fibres: degradation in an alkaline environment

One of the main concerns of the use of non-cementitious materials in a cementitious matrix is the (change in) alkaline environment. The strength of the composite may decrease and in case of the fibres, the bond with the matrix can change due to chemical and physical interactions, or the fibres may degrade. These interactions are due to the alkaline pore fluid (pH>13) combined with the intrusion of potentially harmful substances through a crack. The alkaline environment poses a threat for glass fibres (Larner et al., 1976; Orlowsky et al., 2005; Wei et al., 2010) and natural fibres (Akers & Studinka, 1989; Bentur & Akers, 1989; Bilba et al., 2003; Stamboulis et al., 2001; Van De Velde & Kiekens, 2001; Yang et al., 2006), but almost none for synthetic fibres. Si-O-Si bonds are destroyed in the glass network due to the alkaline environment (Wei et al., 2010). By making the glass fibres alkali resistant, this can be overcome (Bentur et al., 1985; Butler et al., 2011; Yilmaz & Glasser, 1991). Also natural fibres can be surface-treated (Bledzki et al., 2004; Sedan et al., 2008). On the other hand, the matrix can be modified too, to lower the alkalinity (Bijen, 1990; Cohen & Menashi, 1986) and thus the degradation in this alkaline environment. The degradation due to intrusion by substances changing the alkalinity occurs mainly with steel fibres due to corrosion (Kim et al., 2014). Generally, all above-mentioned degradation processes will eventually lead to a decrease in strength of the composite material.

A good review on cementitious building materials reinforced with vegetable fibres can be found in (Agopyan et al., 2005; Pacheco-Torgal & Jalali, 2011). In natural fibres, the molecular chains of hemicellulose degrade due to the alkaline environment. There are three main processes involving degradation in an alkaline environment (Gram, 1983). The first one is peeling off due to the reaction of alkaline cations with hydroxide groups OH^- of cellulose. However, due to the high degree of polymerization and the slow kinetics, this process is negligible. The second main process is called alkaline hydrolysis in which the molecular chains of hemicellulose are broken, resulting in a loss of strength (Aziz et al., 1981). The third one is the petrification of a natural fibre. In this process, the hollow part of the natural fibre, the lumen, is hardened with cement products (Savastano Jr. & Agopyan, 1999). By lowering the amount of alkali-sensitive hemicellulose by chemical or physical methods, the sensitivity decreases. As some natural fibres like flax or hemp have excellent strength properties, the natural fibres could be a low-cost solution to the demanding quest to obtain an alternative for the synthetic fibres (Aziz et al., 1981).

1.2.3 Synergetic interaction between fibre and cementitious matrix

One of the reasons why fibres found their way in the concrete technology is the replacement of reinforcements and the control in cracking behaviour. As concrete is a brittle material, reinforcements are placed when casting the concrete to take up the tensile loads. The reinforcements are located in distinctive places. Fibres on the other hand, are evenly distributed in the matrix. They are not able to withstand large tensile stresses, but due to their uniform distribution, they can control the cracking behaviour.

Before going into detail about the effects of synthetic fibres in cementitious materials, the interactions need to be understood. The properties of the cementitious matrix, the fibre and the transition zone between both are important. The three combined affect the properties of the cementitious composite. There are also three main factors regulating the bond between fibre and matrix (Bentur & Mindess, 1990). These are *1)* friction, *2)* anchorage due to deformations and *3)* physical and chemical adhesion. The bond can be measured with a simple pull-out test (Lin et al., 1999; Redon et al., 2001; Yang, 2008) or by investigating the protruding fibre length from a tensile fracture surface of the cementitious composite (Obla & Li, 1995). In the latter, the bond is linked to the protruding length as a long embedment will cause rupture of the fibres if the bond is too strong. In this way, the critical length can be determined.

When a fibre is pulled out, the bond with the matrix is theoretically lost, and pure friction takes over. However, there can be slip softening and slip hardening. The latter happens due to blockage in the fibre tunnel when a fibre is pulled out. The retaining forces of the fibres are dependent on the embedded length in the matrix. This is the length of a fibre at a side of a crack which is surrounded by plain material. If the embedded length is too small, the fibre will be pulled out without any slip hardening.

When a crack occurs due to tensile stresses, the fibres are pulled out. But in this way, the tensile forces are relocated through the fibre and the fibre will bridge the crack. This is visualized in Figure 1.2a. Fibres can either be partially debonded, transfer the load without debonding or can be pulled out (Redon et al., 2001). If the tensile capacity of the fibre exceeds the tensile capacity of the matrix and the embedment is strong enough, the material will be able to take up more forces. This will lead to multiple cracking (Figure 1.2b). If we would start from an un-cracked material (stage 1), micro cracks would form if the tensile capacity is reached (stage 2, crack suppression). Microfibres along the crack are pulled out (stage 3, crack stabilization) and are able to take up the load. If the tensile capacity of the microfibres exceeds the tensile capacity of the cementitious matrix, a crack will form at another location (stage 4, crack bridging). The same principle is repeated (stage 5-6) until the fibres are no longer able to take up the tensile stresses. At this point, the fibres are pulled out or rupture (stage 7, failure). So, instead of an incapability of transferring the load over a crack (Figure 1.2c left), the fibres are controlling the cracking behaviour (Figure 1.2c right) and transfer forces over the crack, leading to a local tensile-stress capability upon cracking.

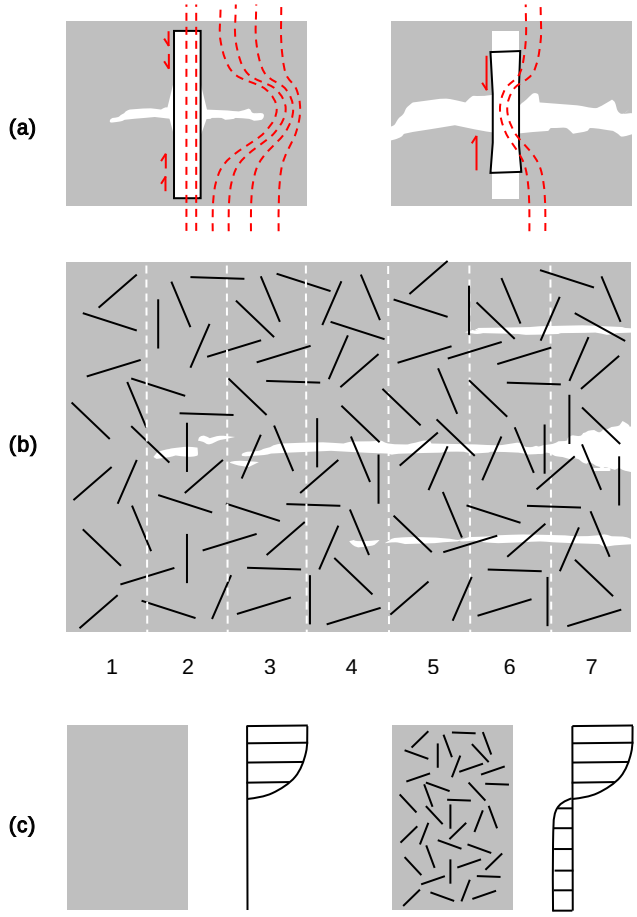

Figure 1.2. Schematic overview of the load transfer through a fibre **(a)**, the formation of multiple cracks **(b)**, and the ideal representation of the stresses in the material **(c)**.

The use of fibres may increase the overall strength since the stresses are transferred across the formed cracks (Aveston et al., 1971). So, when the first-cracking-strength is reached, the composite is still able to show additional strain. But this can be divided in strain-softening and strain-hardening behaviour. In the first, the fibres will not be able to transfer additional load and will be pulled out. In the strain-hardening case, the stress may alter due to the bridging action of the fibres. The forces which are transferred will be higher. This is shown in Figure 1.3. In this figure, three modes of failure are given: the brittle behaviour of a plain concrete material, strain softening (quasi-brittle) and strain hardening (Li, 2008). A brittle behaviour is characterized by a linear stress-strain curve followed by failure (sudden drop). A quasi-brittle material has a softening tail and this behaviour is often found in normal fibre-reinforced cementitious materials. With strain hardening, there is a linear elastic behaviour followed by a plastic behaviour until failure. In case of a hardening effect, both sides of a fibre may be pulled out

(Figure 1.2a) (Wang & Li, 2006), improving the ductile behaviour of the composite. Ductility is the deformation capacity under a specific load. Also, the toughness is improved due to debonding and energy absorption. The energy absorption, proportional to the area under the curve, will thus improve for example the earthquake resistance, impact resistance and the service life of dams (Kanda, 1998; Kunieda & Rokugo, 2006; Mechtcherine, 2012; Zhu et al., 2009).

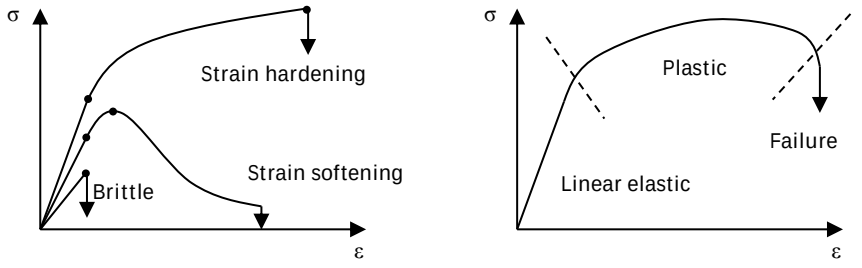

(a) **(b)**

Figure 1.3. Three modes of failure with a stress-strain curve **(a)** and the different subdivisions in the stress-strain curve **(b)**.

By mixing in fibres and designing the material in such a way, the brittle behaviour is minimized and the composite will show significant ductile strain-hardening behaviour. Several terms are addressing the material in literature. These are: FRC(C) (Fibre-reinforced concrete/cementitious composites), TRC (Textile reinforced concrete), ECC (Engineered cementitious composites), HPFRCC (High-performance fibre-reinforced cementitious composites), SHCC (Strain-hardening cementitious composites) and MFCFRCC (Multiple-fine-cracking fibre-reinforced cementitious composites) (Li, 2008), amongst others. The general research in literature has mainly focused on the use of synthetic microfibres, in particularly the polypropylene and polyvinyl alcohol fibre.

1.2.4 Synthetic microfibres with modifiable properties

In the following part, only the monofilament synthetic fibres are discussed as they are mostly un-influenced by degradation and corrosion and possess high multiple-cracking behaviour. Several synthetic fibres with their properties are listed in Table 1.1 (Bentur & Mindess, 1990; De Lhoneux et al., 2002; Wang et al., 1987; Yang, 2008; Zollo, 1997). In the table, acrylic and polyester fibres may degrade in an alkaline environment. The most used for receiving multiple-cracking behaviour are the polypropylene fibre and the polyvinyl alcohol fibre. These two types of fibres will be addressed in detail.

Table 1.1. Several types of synthetic fibres with their diameter [µm], density [$\cdot 10^3$ kg m^{-3}], tensile strength [MPa], modulus of elasticity [GPa], elongation at rupture [%] and bond [MPa] in comparison to the cementitious matrix.

Type of fibre	*Diameter [µm]*	*Density [t m^{-3}]*	*Strength [MPa]*	*Modulus of elasticity [GPa]*	*Elongation [%]*	*Bond [MPa]*
Cementitious matrix	**-**	**2.5**	**3-7**	**10-40**	**0.02**	**-**
Acrylic	20-350	1.16-1.18	200-600	5-10	2-50	
Aramid (Kevlar)	10-12	1.44	2000-3000	70-130	2-5	4.5
Nylon	23-400	1.14	800-1000	4-6	16-20	0.16
Polyester	10-200	1.34-1.39	200-1200	10-18	10-50	
Polyethylene	10-1000	0.92-0.96	80-600	5-31	3-100	0.11-0.63
Polypropylene	**20-400**	**0.9-0.95**	**100-*928***	**1-*11***	**8-25**	**0.2-1**
Polyvinyl alcohol	**10-650**	**1.3**	**1200-*1600***	**20-*40***	**5.7**	**< 2 (coated)**

** the values in italic are for high-tenacity polypropylene fibres and oil-coated polyvinyl alcohol fibres, respectively.*

Polypropylene fibres have a high melting point (165°C), a low manufacturing price (melt spinning) and a low bond with the cementitious matrix. Monofilament fibres are produced by extrusion, by pushing the polypropylene resin through a circular die. By doing so, the polymer crystals are aligned in one direction. This anisotropy is advantageous because the fibres are now strongly orientated in one direction and are thus stronger in that direction. Afterwards, the long fibre is cut into fibres with the appropriate length. The low bond with the matrix is beneficial as the fibres are thus pulled out more easily instead of being ruptured after cracking the cementitious composite. The low bond is due to the hydrophobic chemical structure of polypropylene. The fibres have, however, a low modulus of elasticity (1-8 GPa). Therefore, high-tenacity fibres were developed with a high modulus of elasticity (up to 11 GPa) and a high strength (italic values in Table 1.1). High-tenacity polypropylene fibres consist out of a core (high tensile strength) and an outer layer (improved surface properties) (De Lhoneux et al., 2002; Yang, 2008). Due to its high elongation, polypropylene is mainly used to restrain the plastic shrinkage at early ages. In that period, the modulus of elasticity of the fresh mixture is that of the fibres. When the mixture is hardening, the modulus of the matrix will become higher than the fibres, making them useless. But at the same time, micro cracks are prevented, reducing the plastic shrinkage and possible future macro cracking. Another use of the polypropylene fibre is for stress release during fire, as they melt during fire and create channels for relieving internal pressure (Brandt, 2008).

Polyvinyl alcohol fibres may not be thermo-plastically processed as the polypropylene fibre is and are processed by wet spinning. In this process, the resin is dissolved in water and spun in a salt-rich bath in which the polymer coagulates. Afterwards, there is a procedure of stretching and heat treatment to receive the needed strength. Polyvinyl alcohol fibres have OH^- groups affecting the bond with the matrix. This hydrophilic nature ensures a strong bond with the matrix but also a lower dispersion during mixing (Betterman et al., 1995; Zhou et al., 2012). Due to the strong bond with the matrix, the fibres will rupture instead of being pulled out. This is not beneficial for multiple cracking. A total of 4-6 v% (volume percent) of fibres needs to be mixed in to receive multiple cracking, but this amount is not workable (Li et al., 2002). Therefore, the fibres can be surface treated with oil, to lower the hydrophilic nature (Redon et al., 2001). A coating of 1.2% of oil (italic values in Table 1.1) is the optimal treatment for 2 v% of polyvinyl alcohol fibres. This will enhance the performance since the polyvinyl alcohol fibre both has a higher strength and a higher modulus of elasticity in comparison to a polypropylene fibre and the modulus of elasticity is approximately the same as for the cementitious matrix (Table 1.1). Also, the polyvinyl alcohol fibre has a better cracking restriction because the high elongation of the polypropylene fibre is not efficient.

Both these fibres are used as an additive of cementitious materials for optimal use of the so-called autogenous healing.

1.3 The biomimicry of healing a crack in a cementitious composite

Nature has always inspired humans. Trees are the example for efficient weight transfer to foundations of high rise buildings, a thistle for the Velcro hook-and-loop fastener, a gecko for adhesive properties, a lotus flower for hydrophobicity and non-wettable textiles. This biomimicry can also be found in self-healing cementitious materials. Consider the human power to heal itself of broken bones and cuts. The regenerated bones and tissue are nearly as strong as the original material. If this feature to heal cracks would be designed in cementitious materials, the costs for repair and maintenance could be reduced. Self-healing materials can repair damage without any external intervention. This feature is often called 'smart' as the structure needs to monitor and repair the damage. The self-healing mechanism should be pervasive (ready for activation where needed), stabile (active for the service life of a structure), economical (usable for large-scale production, i.e. not too expensive), compatible (no negative effect on the composites properties), reliable (usable in several environmental conditions), qualitative (mechanical properties as good as the plain material) and repeatable (multiple damage events can be healed) (Jonkers, 2008; Li & Herbert, 2012; Yang, 2008).

The self-sealing of cracks was already seen in the beginning of the 20th century as formed cracks in a bridge deck close due to a white precipitation (Abrams, 1913). This is called autogenous healing as cracks close due to material formed by the cementitious matrix itself. Healing can also be autonomic, by incorporating self-healing mechanisms inside the concrete material. In the latter case, the material to close a crack does not originate from the matrix itself, but from another source. Good reviews on self-healing can be found in (Joseph et al., 2011; Mihashi & Nishiwaki, 2012; Talaiekhozan et al., 2014; Tang et al., 2015; Van Tittelboom & De Belie, 2013; Wu et al., 2012) and in the book (de Rooij et al., 2013).

Generally, there is a subdivision in self-sealing and self-healing. Self-sealing states the closure of a crack, but possibly without strength regain. Self-healing includes additionally the regain in mechanical properties. Self-sealing approaches prevent the ingress of harsh chemical substances which may deteriorate the concrete matrix. This can be achieved by autonomous healing (e.g. inductive melting of a film pipe, release of encapsulated healing agents, use of shrinkable polymers or calcium carbonate precipitation by bacteria) and autogenous healing of concrete cracks (e.g. further cement hydration, calcium carbonate precipitation originating from components from the cementitious matrix) (as will be explained in the next paragraph). The autonomous healing efficiency depends on the crack width (availability of healing agents), the way of encapsulation (spherical or tubular capsules) and the amount of deposited reaction products (improved by incorporating calcium carbonate precipitating bacteria). The autogenous healing efficiency depends also on the amount of deposited reaction products (improved by matrix tailoring), but also on the availability of water (improved by the inclusion of superabsorbent polymers) and the crack width (restricted by adding microfibres). The self-sealing efficiency is generally evaluated by measuring the decrease in water permeability and air flow through a crack.

Self-healing includes the regain in mechanical properties after crack formation. The extent of regain depends on the type of additive, mix composition and the synergetic interaction between all components. The healing efficiency is usually evaluated by reloading the healed specimen and comparing the obtained mechanical properties with the original ones.

1.3.1 Autonomous crack healing

Autonomic healing can be by the use of a repair agent in a film pipe which melts under heating (Nishiwaki et al., 2006). The tube in the latter is made out of a thermoplastic film and the healing agent superglue is encapsulated herein. When a crack occurs, there will be an increased electrical resistance due to the breakage of the conductive path. This will cause a selective heating of the pipe and thus the release of the healing agent which fills the crack. The disadvantage is the embedment of the heating device and the external power supply. Other from outside activated mechanisms like this inductive heating include laser beam activation and ultrasonically induced friction (Nishiwaki et al., 2006).

Another autonomous healing mechanism is the use of encapsulated chemicals both in spherical and tubular capsules (Dry, 1994, 1996; Kessler et al., 2003; Li et al., 1988; Maes et al., 2014; White et al., 2001). Microsphere embedment is one way to promote self-healing. The spheres are uniformly distributed in the matrix and have a thin shell which can be easily broken when a crack occurs in the composite. The system can be composed out of a one-component or a two-component agent which needs to polymerize after contact with one another. This general principle is shown in Figure 1.4 (Cho, 2006). A healing agent and a solid chemical catalyst are dispersed in an epoxy matrix. If a crack runs through the capsules, the healing agent is released due to capillary forces. Exposure of the healing agent to the catalyst triggers polymerization and the crack faces are bound together. Parameters which are important are the wall thickness of the capsules and the strength (in function of breaking and manufacturing process) and the bonding between the matrix and the capsules (Kessler et al., 2003; White et al., 2001). Tube embedment is similar to microsphere embedment. The most used material is glass or some other brittle material. A two-component polyurethane as a healing agent may be used for this purpose (Hilloulin et al., 2015; Van Tittelboom et al., 2011a; Van Tittelboom et al., 2012a; Van Tittelboom et al., 2011b; Van Tittelboom et al., 2014; Van Tittelboom et al., 2015) and the crack filling with the foaming healing agent was visualized by means of X-ray computed microtomography (Figure 1.5). Shrinkable polymers, like shape-memory alloys which return to their initial shape upon heating, may also be used to close a crack (Jefferson et al., 2010). Glass tubes with one-part epoxy may be used as well (Thao et al., 2009; Trask & Bond, 2006) or a hollow pipe as a core to insert the healing agent (Mihashi et al., 2000), mimicking closely the bleeding-based healing mechanism in living things. More closely related to this animal healing is the use of a porous concrete, where the healing product can be inserted after crack formation (Sangadji & Schlangen, 2012, 2013). The bone self-healing process is hereby imitated by putting porous concrete internally in the concrete structure to create a porous network similar to 'spongious bone' (Figure 1.6).

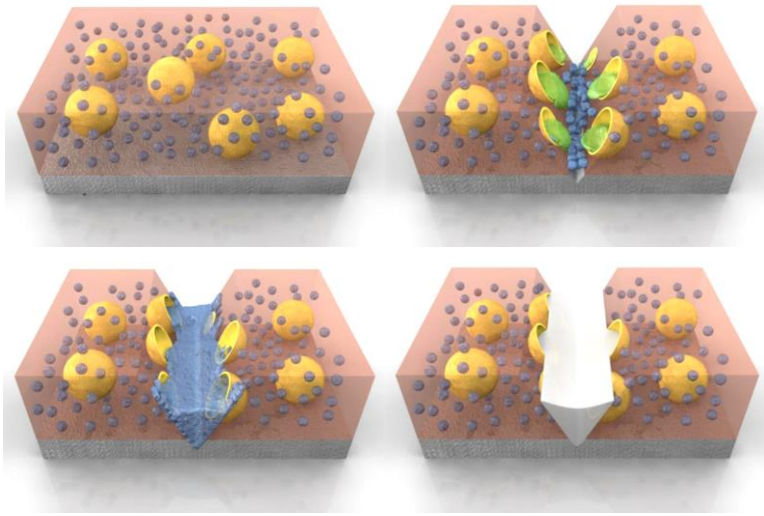

Figure 1.4. Autonomous repair of cracks in a composite material: general schematization, after (Cho, 2006).

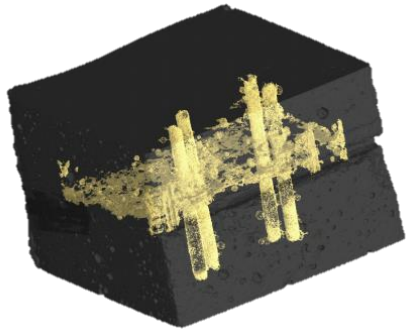

Figure 1.5. Two-component polyurethane healing after crack formation visualized by means of X-ray computed microtomography, after (Van Tittelboom et al., 2011b).

Figure 1.6. Porous concrete healing similar to spongious bone filled with epoxy, after (Sangadji & Schlangen, 2012).

Micro-organisms that induce calcite precipitation can also promote the self-healing of a crack (Gollapudi et al., 1995). This can also be considered as autonomous healing as bacteria, like Bacillus pasteurii (Bang et al., 2001), Bacillus cohnii (De Muynck et al., 2010) or Bacillus sphaericus (De Muynck et al., 2008a; De Muynck et al., 2008b; Van Tittelboom et al., 2010; Wang et al., 2012b), precipitate calcium carbonate to close a crack (as shown in Figure 1.7). The general idea is to incorporate dormant bacteria in the concrete matrix. When water enters a crack, the bacteria will become active, will start to multiply and will start to precipitate calcium carbonate. In case of calcinogenic bacteria, urea is hydrolysed and degraded to carbonate and ammonium (De Muynck et al., 2010). Ureolytic strains, decompose urea into carbon dioxide ions (Wang et al., 2012b; Wiktor & Jonkers, 2011). This is also done by the consumption of organic salts (like lactate) incorporated in the mixture into acetate, calcium carbonate and carbon dioxide. Bacterial calcium carbonate precipitation through denitrification is also possible as the afore-mentioned bacterial mechanisms are sometimes oxygen-limited and toxic side products may form (Erşan et al., 2015). The carbon dioxide, dissolved in water, has the additional benefit to react with calcium hydroxide to also form calcium carbonate and water. The latter also happens in the case of the autogenous healing method, which will be described in the next paragraph.

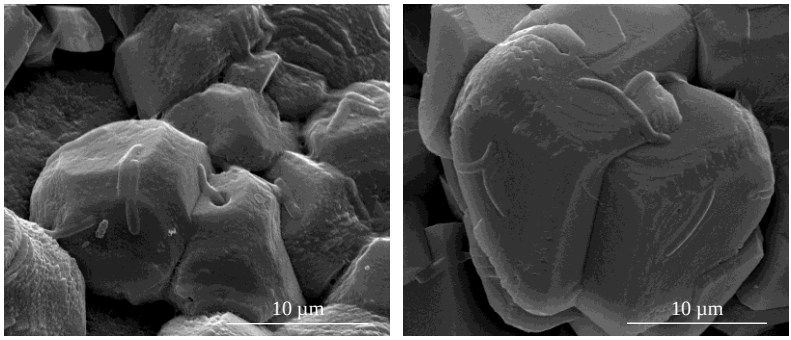

Figure 1.7. Scanning electron micrographs showing bacteria and $CaCO_3$ crystallization, after (Wang et al., 2012b).

A cementitious matrix is not the ideal environment for bacteria as there are no nutrients available. These nutrients also need to be incorporated in the matrix together with the dormant bacteria. The alkaline environment poses no direct treat for alkaliphile bacteria which can survive in the concrete matrix. However, the bacteria need to survive the mixing procedure and may not be crushed due to ongoing cement hydration and matrix densification (Jonkers et al., 2010). As a cement pore size of 1 µm is limiting the survivability of the bacteria (with a typical size of several micrometres as seen in Figure 1.7) and the pores in a cementitious matrix are of that dimension and below, the bacteria need to be protected. This can be done by immobilization in silica gel or polyurethane (Bang et al., 2001; Van Tittelboom et al., 2010; Wang et al., 2012b), on porous powders (like diatomaceous earth) (Wang et al., 2012a), in microcapsules (Wang et al., 2014c), by incorporation in porous granulates like lava or Argex, or by using air-entraining agents which

create larger pores (Jonkers et al., 2010). A strength regain up to 60% is possible (Wang et al., 2012b), but the immobilization reduces the strength.

As bacteria precipitate calcium carbonate, bacterial self-healing is often confused with autogenous healing. However, the cementitious matrix is not the only source for this precipitation, thus the mechanism with bacteria should be regarded as autonomous.

1.3.2 Autogenous crack healing

Concrete has the natural capacity of autogenous crack healing, as first found by the French Academy of Science in 1836 (as stated by (Hearn, 1998)). Four main mechanisms and their combined effect contribute to autogenous healing of concrete cracks (Edvardsen, 1999; Granger et al., 2007; Hearn, 1998; Homma et al., 2009; Jia et al., 2010; Lauer & Slate, 1956; Neville, 2002; ter Heide, 2005; van Breugel, 2007; Yang, 2008):

(a) Dissolved carbon dioxide in water may react with Ca^{2+} ions present in the concrete matrix to form calcium carbonate ($CaCO_3$) crystals;
(b) Loose particles or impurities may block the crack;
(c) Unhydrated cement grains present in the matrix and on the crack surfaces may further hydrate. Also, supplementary cementitious materials such fly ash or slag (Taylor, 1990) can further react through pozzolanic or latent-hydraulic activity;
(d) The matrix may expand due to swelling of calcium-silicate-hydrates (C-S-H).

All four mechanisms are shown in Figure 1.8 (ter Heide, 2005). The most significant mechanism is the calcium carbonate crystallization (Edvardsen, 1999; Homma et al., 2009; Jooss, 2001). In this case, a white material fills the crack. With a pH of the water higher than 8, the mechanism of calcium carbonate precipitation is (Edvardsen, 1999; Jooss, 2001):

$$CO_2(g) + 2\ OH^-(aq) \rightarrow CO_3^{2-}(aq) + H_2O(l) \quad (1)$$

$$Ca^{2+}(aq) + CO_3^{2-}(aq) \rightarrow CaCO_3(s) \quad (2)$$

$$CO_2 + 2\ OH^- + Ca^{2+} \rightarrow CaCO_3 + H_2O \quad (3)$$

For a pH between 7 and 8 (Edvardsen, 1999):

$$Ca^{2+} + HCO_3^- \rightarrow CaCO_3 + H^+ \quad (4)$$

Its sealing is dependent on the crack width and the water pressure but independent from the type of water (Edvardsen, 1999). The calcium carbonate crystallization is first surface controlled, but as the Ca^{2+} ions are exhausted in time, the precipitation becomes diffusion controlled. The Ca^{2+} ions then need to migrate through the cementitious matrix (Edvardsen, 1999).

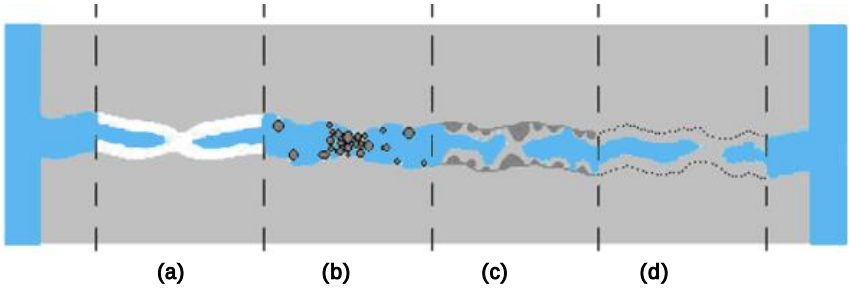

Figure 1.8. Different healing mechanisms responsible for autogenous crack healing: crystallization **(a)**, blockage by loose particles **(b)**, further hydration **(c)** and expansion of calcium-silicate-hydrates **(d)**, redrawn after (ter Heide, 2005).

The sealing capacity can be studied by means of a decrease in water permeability in time. In this test, the permeability coefficient is a function of the third power of the crack width (Edvardsen, 1999; Nanayakkara, 2003; Tsukamoto & Woener, 1991). The sealing of a crack is dependent on the crack width and the hydraulic gradient as the formed healing products may also be washed out (Aldea et al., 2000; Edvardsen, 1999; Lepech, 2006; Lepech & Li, 2005; Nanayakkara, 2003; Reinhardt & Jooss, 2003). The reduced permeability in cracked specimens is thus due to the combination of mechanical blocking and chemical precipitation of calcium carbonate (Clear, 1985). As the precipitation of the crystals is promoted by the use of a permeability test (Lepech, 2006), one should be critical referring to self-sealing and self-healing in that case.

In high-strength concretes with a low water-to-cement ratio, the healing is mainly due to the hydration of unhydrated cement grains on the crack surfaces. Using a low water-to-cement ratio, reservoirs of unhydrated cement grains are dispersed in the matrix, waiting for water to further hydrate. The stiffness of the new crystals is close to that of the primary calcium-silicate-hydrates (Granger et al., 2007; Jacobsen et al., 1995; Jacobsen & Sellevold, 1996). Also, the younger the material, the more healing will occur due to the higher amount of unhydrated particles. As the cement further hydrates in time, the healing material formed at early ages is a combination of $CaCO_3$, C-S-H and $Ca(OH)_2$. At later ages, the healing material is mainly $CaCO_3$ (Lauer & Slate, 1956; ter Heide, 2005). C-S-H are stronger than the weaker calcium carbonate. This C-S-H is therefore wanted as it will highly contribute to the regain in mechanical properties.

Water is needed in the above-mentioned healing mechanism to heal a specimen (Granger et al., 2007; Homma et al., 2009; Yang et al., 2009). The crack width and the mix composition seem to be important for the self-healing as they will determine the dispersion of the unhydrated cement grains in the matrix and at the crack faces. Water also needs to be present as the hydraulic (cement) and pozzolanic and latent-hydraulic reactions (binders like fly ash or blast furnace slag) need water. Pozzolans promote further hydration as these materials react with water and $Ca(OH)_2$ to form C-S-H. This mechanism lasts for a long period and is therefore beneficial for possible healing. Pozzolanic fly ash (Termkhajornkit et al., 2009; Van den Heede et al., 2014), blast-furnace slag (Van Tittelboom et al., 2012b), lime (Yildirim et al., 2014) or alkaline activators (Gruyaert et al., 2014) can be

added to receive more autogenous healing. Additives like expandable geo-materials (Ahn & Kishi, 2010) or crystalline admixtures (Ferrara, 2014; Ferrara et al., 2014; Krelani, 2015; Roig-Flores et al., 2015; Sisomphon et al., 2012) stimulate the crack healing capacity even further. The expansion will seal a crack and the additives significantly affect the rate of formation of re-hydration products.

Overall, there are three needed conditions for autogenous crack healing to occur. These are the presence of specific building blocks (e.g. chemical ions like Ca^{2+}, CO_2, unhydrated particles); the exposure to humid environmental conditions (e.g. wet/dry cycles, submersion in water) and small crack widths (< 50 µm) (Yang, 2008; Yang et al., 2009). Cracking and permeation inside a crack can induce the needed diffusive forces which can lead the free Ca^{2+} ions to the crack faces. This tendency causes the provision of the chemical buildings stones for the precipitation of healing products. However, the presence of the chemical ions decreases in time and will become exhausted. Water is available during raining and the effect of alternated rainy and dry periods is studied by performing wet/dry cycles. Cracks smaller than 50 µm show complete healing and cracks smaller than 150 µm only show partial healing (Yang, 2008). From the latter it can be concluded that autogenous healing is only efficient for healing narrow cracks. As the cementitious material has a problem with healing large 'fractures' or 'cuts' like the human body, the crack width should be restricted. The crack width should also be restricted to healable cracks in the frame of corrosion of reinforcements, especially in nuclear applications (Ramm & Biscoping, 1998). This is obtained by mixing in microfibres, as will be described later on.

1.4 Microfibre-reinforced composites with restricted crack widths

Engineering and nature are dual. In time, nature has developed efficient ways of living using the least amount of resources. This involves an optimal use of energy between the various living organisms. Engineering requests the efficient use of money, to obtain lower costs. If nature is interpreted and mimicked correctly, the efficiency in daily life would improve. The plain cementitious material can be adjusted by the addition of microfibres to receive a cost-efficiently self-healing material. Microfibres are able to control the cracking behaviour and to restrict the cracks. Not one large un-healable crack is formed, but several small healable cracks are formed.

1.4.1 Design of fibre-reinforced cementitious composites

The main research on fibre reinforced cementitious composites with polypropylene and polyvinyl alcohol fibres was done by V.C. Li. His engineered cementitious composites are able to give tensile strengths of 4.5 MPa, ultimate strains of 4% and limited crack widths of below 100 µm, with only a fibre volume of 2% of the total volume of the cementitious mixture (Li et al., 1997; Li et al., 2002; Mechtcherine et al., 2011; Mechtcherine et al., 2012; Yang, 2008; Yang et al., 2009). The ductility of the composite under four-point-bending is shown in Figure 1.9 (Li, 2008). Multiple cracking can be observed, which shows the power of this material.

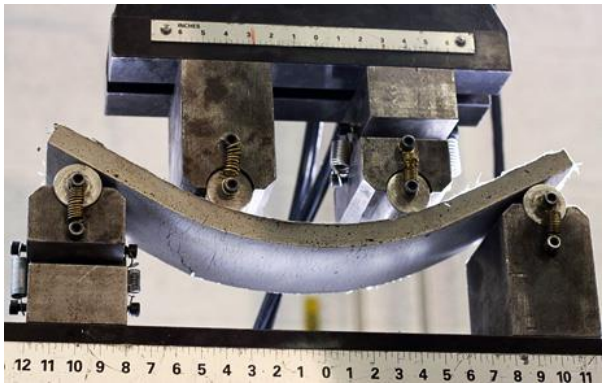

Figure 1.9. Multiple cracking and high ductility of the PVA-ECC M45 mixture when loaded under four-point-bending, after (Li, 2008).

There are two main strain hardening criteria: the first is the crack tip toughness need and the second the force need (Li & Leung, 1992; Li et al., 2002; Li & Wu, 1992; Wang, 2005; Yang, 2008). The former uses the concept of energy balance and is a statistical analysis of the combination of absorption, debonding, sliding and bridging action. It is a function of the bond with the matrix, the friction and the fibre characteristics. This criterion is for steady-state cracking. The net energy input by external work must be less than the energy consumed by bridging during the crack formation. This will be the driving force of crack formation after which fibre bridging will take over (Li et al., 1993). If the criterion is not met, there will be

unstable crack formation. This type of unstable crack is called a Griffith crack and in this type of cracking, the crack width varies over the length of the crack, especially at the midpoint of the crack (Figure 1.10; stepwise formation of the crack) (Li, 2008). This will cause fibre failure in that region and is thus unwanted. A stable (steady-state) crack is wanted with a constant crack opening at any location. In this way, there is optimal fibre bridging.

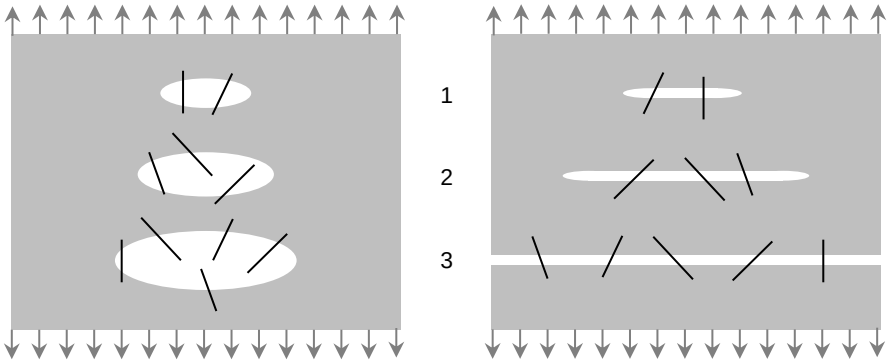

Figure 1.10. Formation of a Griffith type of crack **(a)** and a steady-state flat crack **(b)**.

The second criterion states that the matrix tensile cracking strength must be lower than the maximum fibre bridging strength. This criterion ensures the initiation of micro cracks from flaws before the tensile load exceeds the maximum fibre-bridging capacity. The time of crack formation is also important as less unhydrated particles are present at later ages (Qian et al., 2009; Qian et al., 2010), but the pozzolanic activity increases at the same time. Longer-aged cementitious materials lead to more cracks with narrower width (Kan & Shi, 2012) as the cementitious matrix is tougher due to further hydration.

Both criteria need to be met and they are a combination of the synergetic interaction between the cementitious matrix, the fibre and the interface. The properties can be altered by the holistic modification of the fibre geometry, treating the fibre surface and optimizing the matrix properties (Bentur & Mindess, 1990). The matrix toughness can be altered by changing the water-to-cement ratio, the type of aggregates and the use of supplementary cementitious materials and additives like fly ash, silica fume or blast furnace slag (Kunieda et al., 2012; Li, 2008; Yang, 2008). The interfacial bond can be altered by changing the fibre surface properties or the type of fibre (Li, 2008; Yang, 2008). Also, the length and the diameter of the fibres play a significant role. As long fibres are preferred, they may also cause less workability. The matrix can be tailored by changing the fracture toughness and by introducing flaws. These flaws will cause more cracking and thus higher multiple cracking as they affect the crack tip criterion. Several factors together will thus determine the strain-hardening effect of the composite. In the following part, the most-frequently-used cementitious strain-hardening composite is investigated.

1.4.2 Towards a ductile material with a good autogenous healing capacity

PVA-ECC mix 45 (M45) is used often as a typical strain-hardening cementitious composite (Yang, 2008). It is composed out of 571 kg/m³ cement, 685 kg/m³ fly ash, 456 kg/m³ sand, 332 kg/m³ water, 6.8 kg/m³ superplasticizer and 26 kg/m³ PVA fibres. The fly-ash-to-cement ratio is 1.2, the sand-to-cement ratio is 0.8 and the water-to-cement ratio is 0.58 (water-to-binder ratio of 0.26). Due to the low water-to-binder ratio, the amount of unhydrated particles is quite high, which can be useful for autogenous healing. The best sand-to-cement ratio is 0.6-0.8 (sand-to-binder ratio of about 0.35-0.4) in terms of strain capacity (Li et al., 2002). The sand has an impact on the matrix toughness and interfacial properties. A higher amount increases the toughness due to the increase of energy by the tortuous propagating crack. On the other hand, sand may act as crack initiator but this only has an inferior effect. Sand also increases the interfacial stress and fibre abrasion (Li et al., 2002). This results in less fibre-bridging action. The amount thus needs to be limited. The sand particle size is also of utmost importance as the above-mentioned factors are influenced by it (Şahmaran et al., 2009). Also, due to the balling effect of fibres together with larger sand particles, the porosity may increase. The ECC M45 mixture uses 12 mm long and 39 µm diameter polyvinyl alcohol fibres coated with 1.2% oil. Due to the hydrophilic nature of polyvinyl alcohol fibre, the bond with the cementitious matrix can be as high as 6 MPa. By coating the fibre with a thin layer of oil (Yang, 2008), the bond is reduced to lower than 2 MPa (Table 1.1). Coating the fibre with oil affects both of the above-mentioned criteria. In this way, the ductility is enhanced. Some physical properties are listed in Table 1.2 (Li, 2008). The first-cracking-strength is the strength at which a first drop in the stress strain curve occurs and a complete steady-state crack runs through the specimen. The ultimate tensile strength is the highest strength found during strain hardening and the ultimate tensile strain is the strain at which this stress is achieved.

Table 1.2. Typical mechanical properties of strain hardening cementitious composites.

Compressive strength [MPa]	*First-cracking-strength* [MPa]	*Ultimate tensile strength* [MPa]	*Ultimate tensile strain* [%]	*Modulus of elasticity* [GPa]	*Flexural strength* [MPa]
20-95	3-7	4-12	1-8	18-34	10-30

Self-healing of the cracked specimens prevails in a variety of environmental conditions, including conditioning temperature, water permeation and chloride submersion (Li & Li, 2011). Water needs to be present, ranging from complete submersion to cyclic wet-dry cycles (Hannant & Keer, 1983; Yang et al., 2009). The best healing and regain in mechanical properties occurred in water/dry cycles (submersion in water at 20°C for 24 hours and drying in laboratory air for 24 hours), followed by continuous submersion. A cycle at a certain relative humidity (stored in air) did not provide any form of healing (Yang, 2008; Yang et al., 2009).

Further hydration of cement grains needs water and the water also encourages the dissolution and leaching of calcium hydroxide from the concrete matrix to form self-healing crystals with the carbon dioxide dissolved in water. The latter has better crystallization possibilities at the crack mouth. An example of this autogenous healing is shown in Figure 1.11 (Jia et al., 2010). After only several wet/dry cycles, the material is able to self-seal and self-heal. A regain in air tightness is even possible (Gagné & Argouges, 2012).

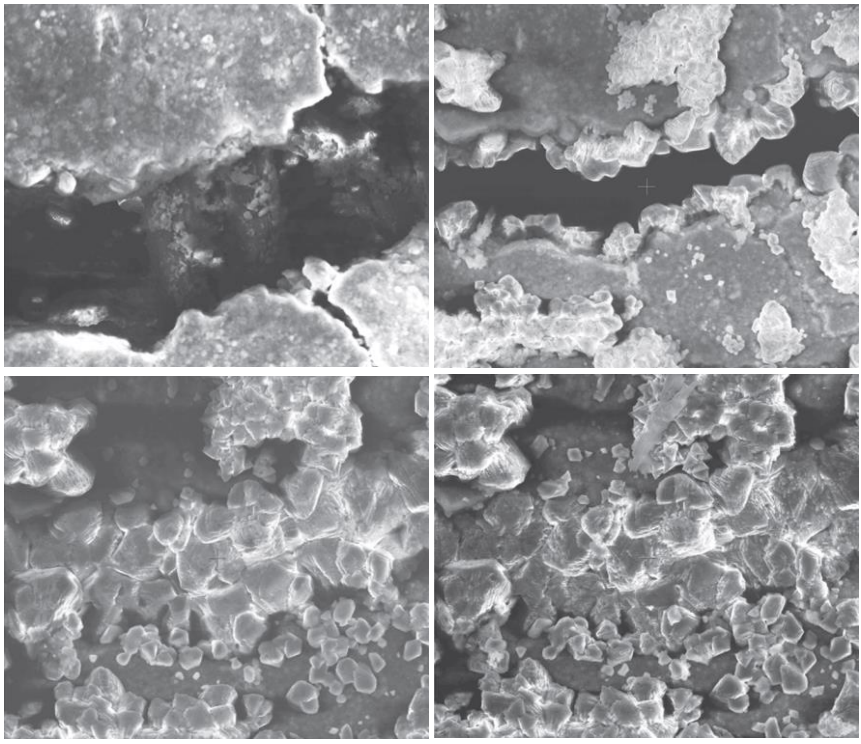

Figure 1.11. Autogenous healing of a crack mainly due to calcium carbonate crystallization after 0, 1, 2 and 3 wet/dry cycles, after (Jia et al., 2010).

Autogenous healing can be studied with varied testing methods. The most often used tests are mechanical reloading tests to evaluate the regain in mechanical properties. Renewed tension or bending tests reveal that the majority of the cracks tend to follow previous crack lines and propagate through the self-healing materials. This is due to the relatively weak nature of calcium carbonate crystals (Yang, 2008) and also the weak bond between primary and new-formed calcium-silicate-hydrate crystals. But, there may also be full recovery of the mechanical properties as cracks may form elsewhere as well (Yang, 2008). Microscopic analysis supports these findings and is complementary. To compare self-healing in different environmental conditions, the resonance frequency technology is also used recently but is not solid as the matrix around a crack may also change and a weight change in specimens (partly) saturated with water will change the resonant

frequency. This will not give objective data to compare self-healing in different environmental conditions. However, this technique is used and one needs to be careful when studying and reporting these results. Therefore, we have to be cautious when comparing the healing effect even using the same evaluation method. Also, in between different countries or laboratories, differences in test conditions apply, such as different healing conditions, different types of water, different imposed water pressure heads, differences in studied cracks (formed by shrinkage, direct tension, flexural tension, and so on) and the different sample age amongst others.

A self-healing material is often called a smart material. The definition states an interaction with the environment and the ability to respond to changes. Multiple cracks are formed and the material is healed after the imposed deformation. This corresponds with a tree, which will accrete material where the stresses are higher. The material is located in the region where it is needed more. In self-healing materials, the cracks will be closed with additional material too.

Mostly, only the outermost part of a crack is sealed with healing product. The bacterial-based self-healing can be visualized by means of X-ray computed microtomography (Wang et al., 2014a) and this technique can also be used for visualizing autogenous healing. Sealing by precipitation in high-strength low-permeability concrete was already studied by means of micro-focus X-ray CT (Fukuda et al., 2012). It was found that the precipitation occurred only near the surface of the specimen and only the first 0 till 50-200 µm of the 100 µm wide cracks was filled with precipitation. However, in the cited study, the test specimens were stored in the presence of seawater. The obtained healing could thus also be the combination of autogenous healing and salt formation (Palin et al., 2015). A recent µCT study (Fan & Li, 2015) gave results on the healing properties of strain-hardening materials. It was found that the extent and rate of healing strongly depended on the initial surface crack width. Also, the region of a crack close to the surface (from 0 to 50-150 µm below the surface) could be sealed quickly with crystalline precipitates. In deeper parts, the healing process takes longer and is more likely continued hydration and pozzolanic reactions. Jonkers (Jonkers, 2011) showed, in bacterial self-healing concrete, that precipitation mainly occurred near the crack rim leaving major parts of the 150 µm wide crack unhealed. He explained the precipitation at the crack rim due to the relatively high solubility of calcium hydroxide and hypotheses that calcium hydroxide first uses the carbon dioxide from intruding water in the crack, and afterwards the remaining calcium hydroxide would dissolve and diffuse out of the crack into the bulk water. Here it will react with carbon dioxide present near the crack rim resulting in the precipitation of larger quantities of calcium carbonate (Jonkers, 2011; Sisomphon et al., 2012).

Bacterial self-healing properties can be included in strain-hardening materials to allow wider cracks to heal (Sierra-Beltran et al., 2014). Alkali-resistant bacteria and a food source are hereby included and cracks up to several hundreds of micrometres are able to close. Strain-hardening materials, also those containing bacterial healing agents, are also used as a patch repair systems (Luković et al., 2014; Mechtcherine, 2013; Schröfl et al., 2015; Sierra-Beltran et al., 2014).

1.5 Improving and stimulating the autogenous healing capacity

A new topic is the investigation of the combined effect of microfibres and superabsorbent polymers (SAPs) (Kim & Schlangen, 2010). As those polymers swell in contact with water after crack formation, the crack is self-sealed (Lee et al., 2010a; Lee et al., 2010b). The water can then be released towards the cementitious matrix to stimulate the autogenous healing. This water supply complies with the water criterion needed for autogenous healing. It is even possible to synthesize the SAP resin in situ (Song et al., 2009). A precursor is hereby injected with initiator and cross-linker. Infrared radiation is used to make the precursor copolymerize. However, this sealing mechanism can only be applied afterwards. By incorporating SAP particles in the mix from the beginning, this can be overcome. SAP particles even act as pre-existing flaws to improve the performance and ductility of strain-hardening cementitious composites (Yao et al., 2011), further improving the narrow crack width criterion.

Cementitious materials are sensitive to crack formation and it would be beneficial if the material could stop the crack propagation, repair the damage and reach again the original liquid-tightness and/or strength. Therefore, a cementitious material with synthetic microfibres and superabsorbent polymers (SAPs) is proposed. The proposed healing mechanism is shown in Figure 1.12, an analogy to bone healing. Upon bone crack formation, there will be blood. This blood will cloth and the building blocks present in the blood will stimulate the formation of new bone fragments, leading to the regain in properties and reuse. In concrete, there will be water. This water will be stored by the SAPs and will be provided towards the cementitious matrix for healing. The crack is refilled and the material is able to ideally regain its properties.

The material has not been widely studied and most of the properties are still unknown. This dissertation will try to fill missing links, to connect loops and to give a general overview of this new self-sealing and self-healing material in all its aspects.

In this PhD dissertation, there will be three general objectives; designing a smart self-healing cementitious material independent from conditions, excluding the teething problems due to mixing in superabsorbent polymers and optimizing an under-used technique for sorption measurements. These objectives will be described in the next paragraph.

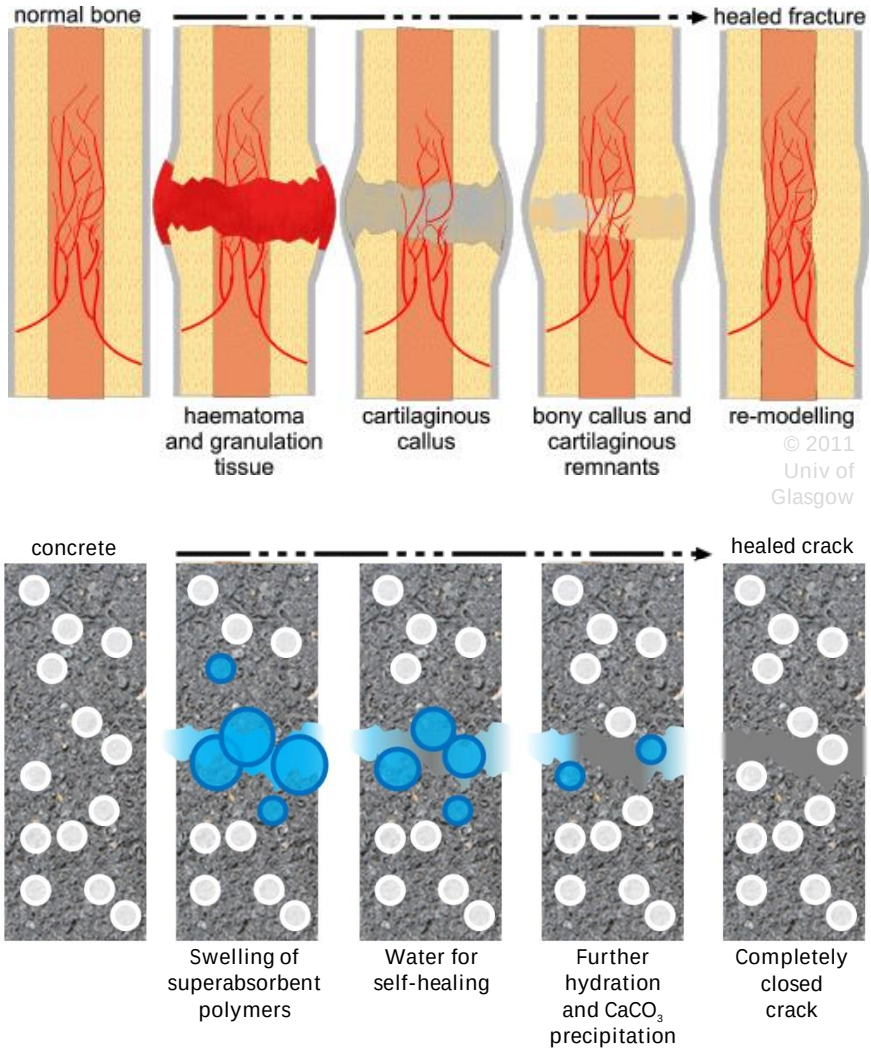

Figure 1.12. Use of superabsorbent polymers in cementitious materials to stimulate autogenous healing, as a bio-mimicry of bone healing.

1.5.1 Objective 1

Excluding the teething problems due to mixing in superabsorbent polymers

The concrete pore structure will change by mixing in SAP particles due to the uptake of mixing water. This needs to be studied, since the water-to-cement ratio changes. Macropores, after de-swelling of the SAP particles upon cement hydration, may cause a decrease in tensile strength. Part of the swelling capacity will be needed for filling of the pore and is thus lost for crack filling. One way to change the swelling is using pH-sensitive SAPs. The developed hydrogels would only swell when the pH drops from around 13 (concrete) to below 10 (in a crack). But in practice, when the pH in the crack would rise again, the SAPs will de-swell, resulting in an increase of water permeability. To have the best sealing (and healing for long-term durability) capacity, the SAP should swell in each fluid (with each pH) upon crack formation to effectively seal a crack.

The effect of SAPs on the microstructure and the water exchange between SAP and the matrix will be investigated. This will lead to a better understanding of the moisture movements in the composite, and also for self-healing in standard laboratory conditions. Furthermore, moisture transport processes cannot be understood without the knowledge of the moisture fixation in the concrete pore system. Water sorption is therefore a key parameter.

1.5.2 Objective 2

Optimizing an under-used technique for sorption measurements

There are two important methods for characterizing water vapour transport processes; using static or dynamic gravimetric methods (Dynamic vapour sorption: DVS). The principle of the static method consists of equilibrating the sample in a chamber with controlled temperature and humidity (e.g. desiccator with saturated salt solution) until constant weight. This method requires simple instrumentation and is often used as reference. Its drawback lies in the long time necessary to reach the near equilibrium state for each RH step. In the dynamic method humidity is usually controlled by mixing of humid and dry gas and near-equilibrium state is reached much quicker. The relative humidity is changed stepwise and mass changes are recorded. The method, however, is not frequently used in concrete applications and a lot of questions remain regarding sample preparation, measuring procedure and interpretation of the isotherms. Therefore, several parameters need to be investigated to optimize the method and to obtain valuable information concerning the effect of humidity on self-healing. Scanning and analysis of water vapour sorption isotherms can give useful information concerning the structure of porous materials like connectivity, inkbottle porosity, pore size distribution and specific surface area. DVS thus becomes a better tool for understanding relative humidity conditions on self-healing of concrete, if the method is clearly understood.

1.5.3 Objective 3

Designing a smart self-healing cementitious material independent from conditions

In this research, self-healing properties of cementitious materials are investigated. Self-healing provides a complete or partial restoration of the mechanical properties after crack formation. This happens in situ, meaning that no action has to be undertaken like manual repair. This improves the reliability and the lifetime of structures, reducing the maintenance costs. The mixture composition will be optimized to obtain the best autogenous healing capacity.

In order to activate the autogenous healing mechanisms, water needs to be present. As there is no healing in air, without presence of water, superabsorbent polymers will be mixed in. They are able to take up moisture from the environment and to provide it to the matrix for self-healing. Up to now, no other research has proven autogenous healing in standard laboratory conditions. This new feature can promote the use of self-healing materials indoors and for structural components that are not exposed to rain. In this way, SAPs may be used as a replacement for the environmental condition (water) to introduce crack-healing, even in air. The goal is to obtain an adaptable cementitious material which is independent from the ambient conditions.

The first focus relies on hindering the fluid flow by swelling of superabsorbent polymers after they are exposed to a humid environment. The second focus relies on healing of small cracks in fibre reinforced cementitious materials, restoring the mechanical properties. Cracks close through the combination of further hydration of unhydrated cement particles, precipitation of calcium carbonate and activation of the pozzolanic reaction of fly ash. Desorption of superabsorbent polymers triggers healing in the vicinity of crack faces. In this way, a smart cementitious material which is reliable and independent from the conditions is acquired.

1.5.4 Importance and impact

One of the main factors which endangers the durability in cracked concrete is the water movement through cracks. A smart cementitious material which has the property to prevent water movement in a crack would therefore have a clear added value. SAPs both self-seal (upon swelling) and self-heal a crack (by providing water to the cementitious matrix for further hydration of unhydrated cement grains and $CaCO_3$ precipitation). Superabsorbent polymers are a promising additive to be used in the building industry but may induce microstructural changes.

During this study, the fundamental interactions between water, superabsorbent polymers and cement-bound materials will be investigated in detail. A smart material will be designed which needs less repair and can heal itself completely in the presence of water and partially in the presence of humid air. The sealing and healing will allow a recovery of the water-tightness of the structure. The total uptake of potentially harmful substances hereby lowers, leading to an enhanced long-term durability and lower maintenance costs.

The in-depth study on the water sorption characteristics will lead to new insights regarding the effect of RH on the saturation degree and the microstructure

of cementitious materials. There are many questions regarding the water vapour sorption characteristics and this topic is an investigation on its own. Also, a profound understanding of the pore structure of cementitious materials gives insight in several properties including compressive strength, permeability and durability aspects.

The main topics in this PhD dissertation are interconnected with each other (Figure 1.13). In the next chapter, the superabsorbent polymers or hydrogels will be explained. In Chapter 3, the influences of the SAPs on the cementitious properties will be discussed with a focus on the microstructural properties of the cementitious matrix. Chapter 4 comprises the self-sealing effect by using SAPs and Chapter 5 the self-healing effect. In the end, conclusions, recommendations and perspectives will be given in Chapter 6.

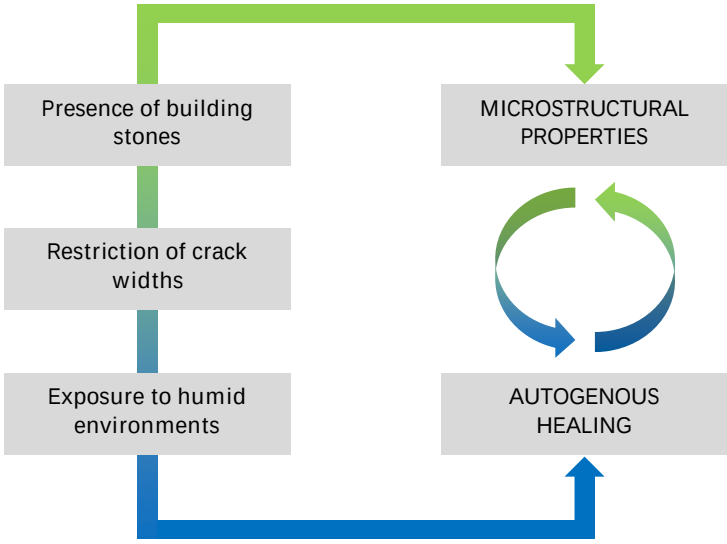

Figure 1.13. Interconnectivity between microstructural properties and autogenous healing.

1.6 Statistical analysis

All standard deviations shown are deviations on individual results. All statistical analysis in this dissertation was performed by using the program SPSS® (IBM) in order to compare the obtained results. Multiple averages were compared using an analysis of variance (ANOVA) test with a significance level of 5%. The homogeneity of the variances was controlled with a Levene's test. The *post hoc* test for data with homogenous variances was the Student-Newman-Keuls test. If no homogenous variances were obtained, a Dunnett's T3 test was used. For all tests, a significance level of 5% was applied. A minimum of three samples was always tested to receive statistically relevant results.

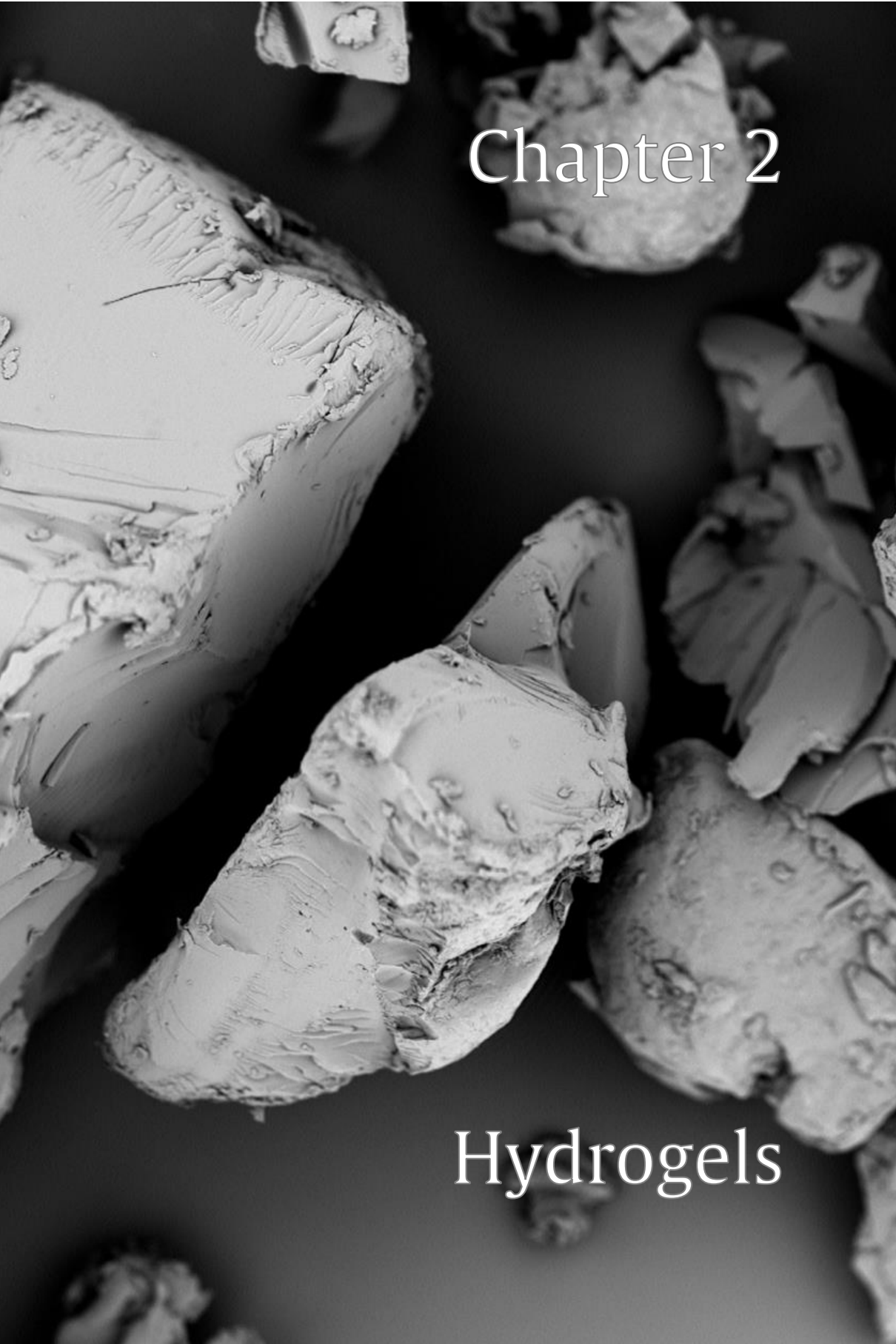

Chapter 2

Hydrogels

| Scanning-electron micrograph of bulk-polymerized superabsorbent polymers

Chapter partially redrafted after (Snoeck et al., 2015e).

"To enter the cosmos, to engage in an unprecedented duel with nature,
could one dream of anything more?"

– *Yuri Gagarin*

2.1 General aspects of superabsorbent polymers

2.1.1 What are superabsorbent polymers and hydrogels?

A superabsorbent polymer is a natural or synthetic water-insoluble three-dimensional network of polymeric chains cross-linked by chemical or physical bonding (Figure 2.1a). They are able to take up a significant amount (up to 500 times their own weight) of fluids from the environment dispersed throughout the structure. If this fluid is water, they are also often called hydrogels. Hydrogels are used nowadays in contact lenses, scaffolds in tissue engineering, smart sustained-release delivery systems, human health care products and other applications (Buchholz & Graham, 1998; Hennink & van Nostrum, 2002; Hoffman, 2002).

On a molecular level, water in a hydrogel is either bonding to hydrophilic groups (bond water) or is filling the space between the network chains, pores or voids (free water) (Figure 2.1b). What also may occur is a rearrangement of water around either hydrophobic or hydrophilic groups or a hydrophobic association of the hydrophobic groups. The physical law governing the swelling is the osmotic pressure exerted by the electrically charged polymeric groups. Hydrogel cross-linking, which is the density of junctions joining the chains into a permanent form, can be chemical (covalent bonds) or physical (hydrophobic/ electrostatic interaction or hydrogen bridges). Controlled cross-linking of the hydrogel structure is used to both retard the hydrogels degradation and improve their mechanical properties. High degrees of cross-linking also decrease the swelling capabilities due to a decrease in mobility.

The swelling of hydrogels is quite a complicated process which appears due to the osmotic pressure associated to the presence of hydrophilic groups (-OH, -CONH, -$CONH_2$, -COOH). When a balance between the osmotic pressure and the elastic retractive forces of the polymer matrix is reached, the equilibrium swelling capacity is attained. When either the osmotic pressure changes (e.g. due to deprotonation of acid groups in the network) or the cross-linking density changes (e.g. due to degradation of the network and thus decreasing the number of cross-linking points), this balance is broken and a change in the degree of swelling occurs (Juergen et al., 2012). The content of mobile counter-ions and of the strength of electrostatic repulsions between chain segments is very important considering the swelling capacity (Figure 2.1c).

Hydrogels can be either natural or synthetic and both of them can be combined. Examples of natural polymers are proteins like collagen and polysaccharides like chitosan, dextran and alginate. Natural hydrogels are biocompatible and biodegradable but display disadvantages such as low mechanical strength and batch variation. Cross-linked networks of synthetic polymers such as polyethylene oxide (PEO), polylactic acid (PLA), polyacrylic acid (PAA), polymethacrylate (PMA), polyethylene glycol (PEG) are also used (Gulrez et al., 2011). The most available ones are commonly made from petrochemical-based monomers such as vinyl acetate or acrylamide. Currently, the main producers of synthetic SAPs are BASF, Sumitomo Seika, Technical Absorbents, SNF Floerger and Evonik, amongst others. Those polymers were studied in this work.

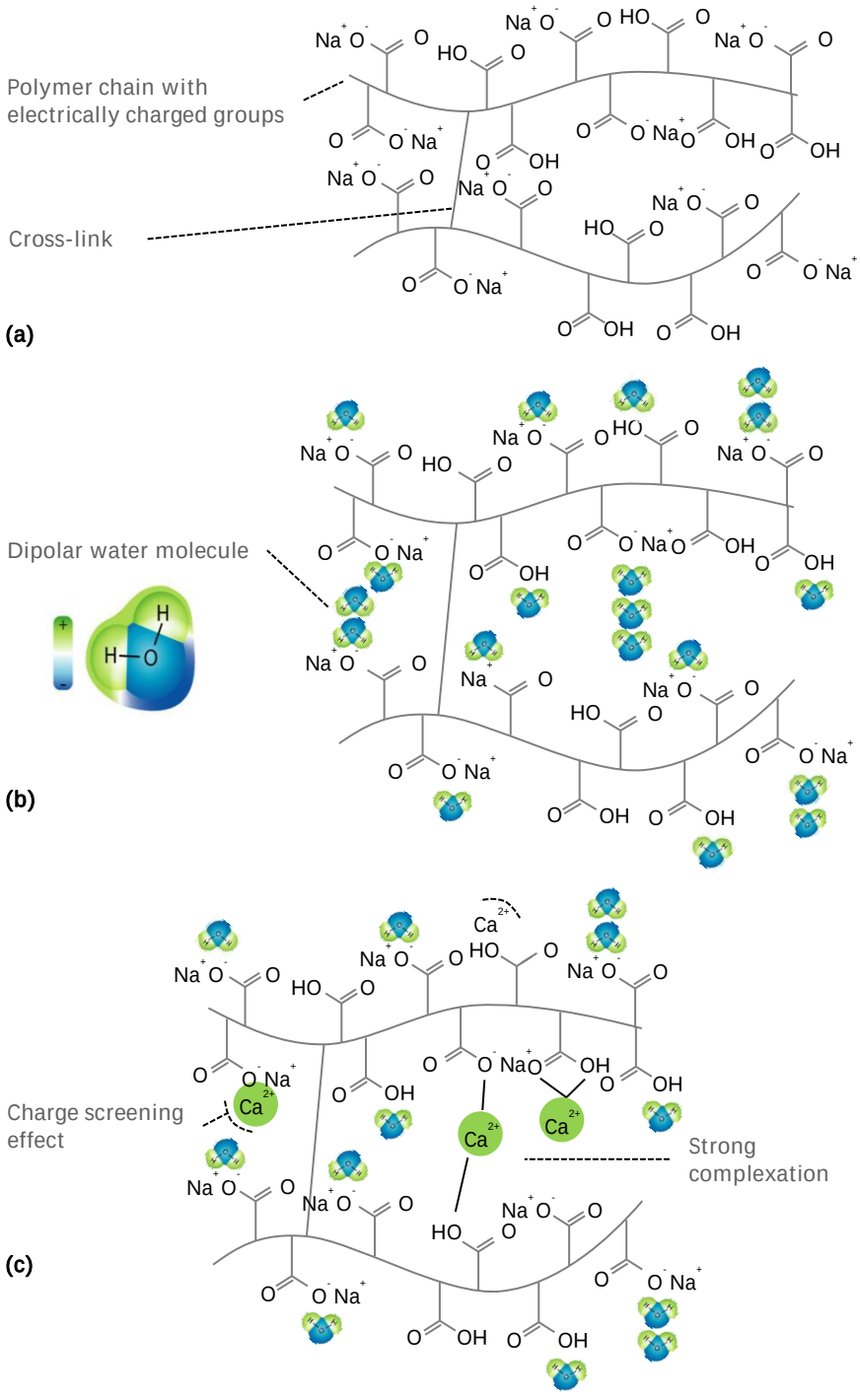

Figure 2.1. Schematic overview of the chemical structure of superabsorbent polymers **(a)**, the swelling mechanism **(b)** and the charge screening and strong complexation **(c)**.

2.1.2 Synthesis of superabsorbent polymers

The classical reaction for synthesis is free-radical polymerization, which mainly occurs with units having double bonds (vinyl units). Free-radical polymerization can be carried out in bulk, emulsion, suspension or solution processes. Bulk polymerization is carried out by adding an initiator to the pure monomer in the liquid state, after which polymerization starts. Emulsion polymerization initially starts with an emulsion incorporating water, monomer and surfactants. Droplets of monomer are hereby emulsified with surfactants in a continuous phase of water after which polymerization initiates. The suspension polymerization is a heterogeneous radical polymerization process that uses mechanical stirring to mix a monomer in a liquid phase while the monomers polymerize, forming spheres. Solution polymerization uses a monomer dissolved in a non-reactive solvent that contains a catalyst.

There are three major steps in the process of free-radical polymerization. The first one is the initiation of the chain. Free radicals needed to initiate the polymerization reaction can be generated through various kinds of pathways: by heating, by the use of a redox system or by the use of a photo-initiator. Initiators become incorporated into the polymer chain, usually at one end, and are consumed during the reaction. The second step is the propagation of the chain. Rapid growth of the chain occurs by monomers reacting with one active centre on the chain, which generates a new active centre. The third step is the termination of the reactive site to give completed macromolecules. The free radical centre on the polymer chain can be stopped by reacting with a similar centre or a nearby chain. Termination can also occur by means of side reactions, including non-productive reactions with monomers, impurities, solvents, initiators and/or polymer chain segments.

Redox polymerization is the most used mechanism for the free radical synthesis. It proceeds at high rates at relatively low temperatures and are generally performed in aqueous solution, suspension or emulsion. Emulsion is the most appropriate technique to produce fine and regular particles sizes. But, the structure of polymer chains is less easy to control compared with bulk and solution polymerizations.

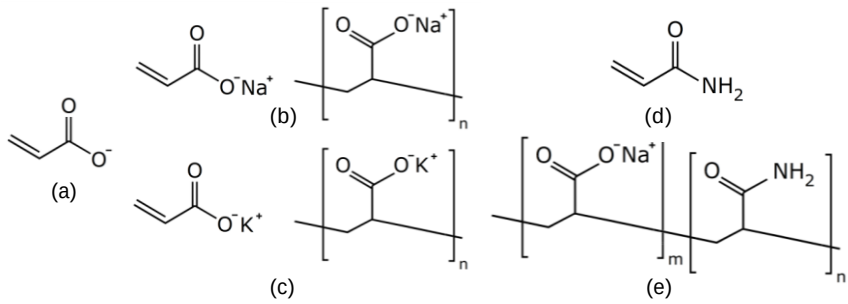

Figure 2.2. Acrylate **(a)**, (poly) sodium acrylate **(b)**, (poly) potassium acrylate **(c)**, acrylamide **(d)** and copolymer of acrylamide and sodium acrylate **(e)**.

Acrylic acid (AA), partly neutralized by sodium or potassium salts, and acrylamide (AM) are the most used monomers in the industrial production of SAPs (Figure 2.1a and Figure 2.2). They are considered to be non-renewable materials that are dependent on the petroleum industry. They have a better performance and longer functional life (up to minimally five years) compared to natural hydrogels.

Some hydrogels display reversible changes in swelling when exposed to physical, chemical or biochemical stimuli such as temperature, light or pH. These stimuli-based responses can be tailored by adjusting hydrogel composition, hydrophilicity of the network, shape, size and type/degree of cross-linking.

2.1.3 Swelling behaviour and proposed testing methods

2.1.3.1 Teabag and filtration method

The main property to be characterized for hydrogels is the swelling behaviour, which can basically be determined by comparing the ratio of the swollen polymer volume or mass to that of the dry state. The swelling capacity of SAPs can be determined in several ways (Jensen, 2011; Zohuriaan-Mehr & Kabiri, 2008), all based on mass or volume changes or the measurement of an indirect quantity. The absorption is hereby calculated as the volume increase relative to the original volume in dry state, divided by the relative density of the SAP and fluid, and expressed as g fluid absorbed per g SAP (Tanaka & Fillmore, 1979). An example of the indirect quantity is a measurement of the concentration change of an exposure liquid component, which is not absorbed by the SAP particles (Qi et al., 2008). By this indirect measurement, the amount of liquid absorption can be determined. The absorption of single SAP particles can be measured by gravimetric methods (difference in mass), as well as by optical microscopy. With optical microscopy, a fluid is gradually added to a single particle and the volume increase is quantified. This method, however, requires spherical particles, which is not the case when using bulk polymerized hydrogels with subsequent grinding. Also, the swelling capacity of small SAPs was impossible to measure.

The two most-extended methods are the teabag and the filtration method (Zohuriaan-Mehr & Kabiri, 2008). In the teabag method, a known amount of SAP is placed in a sealed permeable teabag and put in a test solution. After the swelling time the teabag is removed, hung up to remove excess liquid and then weighed again. The difference between the dry and the wet weight determines the absorption capacity or swelling. The fluid held by capillary forces between SAP particles, however, cannot be totally removed, even by centrifugation. This leads to a small but negligible overestimation of the absorption capacity, being a minor drawback of the tea bag method. The second used test, also based on gravimetric determination, is the filtration method. To assess the sealing capacity of SAP, the swelling capacity is calculated from the weight increase between the vacuum-dried state and the saturated state. A fluid is added to vacuum-dried SAP particles and the whole is filtered after one day (at equilibrium swelling of the SAPs). The amount of filtered fluid is recorded. To ensure there is no influence of the filter paper, the latter is saturated with the fluid prior to filtration. During performing the test, the whole is covered with a lid to minimize evaporation.

In both variations, the absorption capacity of the hydrogel is expressed by equation 2.1:

$$\text{Swelling capacity [g/g SAP]} = \frac{w_{sat} - w_{dry}}{w_{dry}} \tag{2.1}$$

where w_{wet} is the saturated weight and w_{dry} the dry weight. By dividing by the volumetric mass of the studied fluid, the volumetric swelling capacity is calculated.

Inter-particulate fluid may have a considerable effect on the obtained results but microscopic analysis revealed that this influence was negligible. In this test, a fluid was drop-wise added to an almost spherical particle. The initial size was recorded as well as the size of complete saturation. From the calculated volume increase, the absorption capacity was evaluated and compared to the values found by means of the actual filtration tests based on mass increase.

2.1.3.2 Packing swelling method to monitor in time

Another suitable method to study the degradation/absorption capacity in a fluid is the strategy described by (Jensen, 2011). He proposed to study the swelling of hydrogels through the volume increase, or decrease, of loosely packed particles by means of graduated cylinders. As swollen particles are heavier than the fluid itself, the packed amount can be recorded. This amount is linked to the absorption capacity, excluding the influence of capillary forces. The method provides a quick estimation of the water absorption capacity and the swelling can be monitored as a function of time. The particles should, however, be non-buoyant. The relationship between the volume and the mass of packed dry hydrogel particles was required. The latter was obtained by filling a cylinder to its maximum reading (V_1) with dry particles and recording the mass of the packed dry particles (m_1). Next, the studied fluid (in excess compared to the final swelling capacity) was added to a small amount of hydrogel particles with known mass (m_2). During the absorption, the particles were softly shaken to allow free swelling. After settlement due to gravity, the volume of the packed wet particles was read (V_2). Using equation 2.2, the water absorption capacity (g/g) can be calculated:

$$\frac{\rho_{fluid}}{\rho_{hydrogel}} \cdot \left(\frac{V_2}{V_1} \cdot \frac{m_1}{m_2} - 1 \right) \tag{2.2}$$

where $\rho_{hydrogel}$ is the density of the hydrogel and ρ_{fluid} is the density of the fluid.

This test is useful to study the level of packing in time, and thus the time effects like degradation and the possible loss or gain in swelling capacity.

Swelling and kinetics are dependent on the pH factor, degree of crosslinking, the ion concentration, the salinity, the temperature, amongst others (Andry et al., 2009; Lee et al., 2010b; Mark & Kroschwitz, 2003; Omidian et al., 1999; Rosa et al., 2013; Zohuriaan-Mehr & Kabiri, 2008).

2.1.3.3 Swelling behaviour in different test solutions

In this research, tests were carried out in five different solutions. These include demineralized water, tap water, cement filtrate solution (obtained by mixing 10 g of ordinary Portland cement CEM I 52.5 N in 100 g of demineralized water and subsequent filtration), artificial seawater (with 24 g NaCl, 5 g $MgCl_2$, 4 g Na_2SO_4, 0.7 g $CaCl_2$ and 0.8 g $MgBr_2$ for 1 L seawater) and a sulphate solution (with 50 g Na_2SO_4 for 1 L). These solutions were selected as they frequently occur in practice in concrete constructions such as tunnel elements, quays and other ground-retaining structures.

2.1.3.4 Moisture uptake by means of dynamic vapour sorption

Apart from fluids, the superabsorbent polymers are able to absorb moisture from the environment. Dynamic Vapour Sorption (DVS) is a technique to gravimetrically measure the moisture uptake capacity at different relative humidities (RH). Within a temperature-controlled housing, the flow of wet and dry N_2 gas is monitored. With increasing RH, the weight of a sample and reference container is determined by means of a Cahn microbalance during measurement inside the housing. The temperature used was 25°C. For the DVS analysis, approximately 5-10 mg of hydrogel was placed in the sample pan. A first step (RH of 0%) is necessary to start with a completely dry material. Afterwards, the humidity is varied stepwise (i.e. 60, 90 and 98% RH). Every subsequent step is initiated when the change of the sample mass as a function of time is lower than 0.002 wt%/min. To determine the equilibrium value at 98% RH, an extrapolation was used using equation 2.3, based on an analytical solution of the diffusion equation (Ahs, 2008; De Belie et al., 2010; Tada & Watanabe, 2005):

$$m(t) = a \cdot (1 - b \cdot exp(-c \cdot t)) \quad (2.3)$$

where m(t) is the mass of the sample at time t, and the coefficients a, b and c were determined by means of non-linear curve fitting on the obtained data before reaching equilibrium.

2.1.4 Kinetic behaviour and swelling time determination

Apart from equilibrium absorption, another parameter of interest is swelling time (swelling kinetics) of the SAP which is obtained by comparing different swelling measurements at consecutive time intervals. Another test is the so-called vortex test (Zohuriaan-Mehr & Kabiri, 2008). For this test, 100 g of demineralized water was added to a beaker. Then, a vortex was made using a magnetic stirrer (400 rpm). From the already obtained absorption capacity, the specific amount of SAPs to absorb 100 g of demineralized water was added to the beaker. The time was recorded until the vortex disappeared (n=10) (Zohuriaan-Mehr & Kabiri, 2008). Swelling measurements using filtration at consecutive time intervals were used to verify the result.

2.2 Types of investigated superabsorbent polymers

2.2.1 Commercially available superabsorbent polymers

In this dissertation, several commercially available SAPs were tested. Also one in-house (Ghent University) synthesized SAP (SAP C) was used and will be discussed in paragraph 2.2.2. Scanning electron microscopy images (Figure 2.3) and the details (Table 2.1) for all tested commercial SAPs are given. As can be seen, several types and sizes of polymers were tested, ranging from the irregularly shaped crushed polymers over spherical types till even extruded fibre types. The main SAPs are based on cross-linked poly(acrylic acid) (PAA). The production method and company are enlisted. The swelling capacity was determined by means of the above-mentioned filtration method (in demineralized water and cement filtrate). The swelling time was determined by means of the vortex method and the moisture uptake by means of dynamic vapour sorption tests. All SAPs were vacuum dried (10-50 mbar) to constant mass in a desiccator prior to testing.

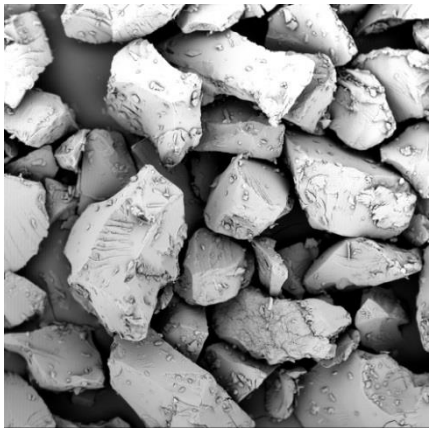

SAP A

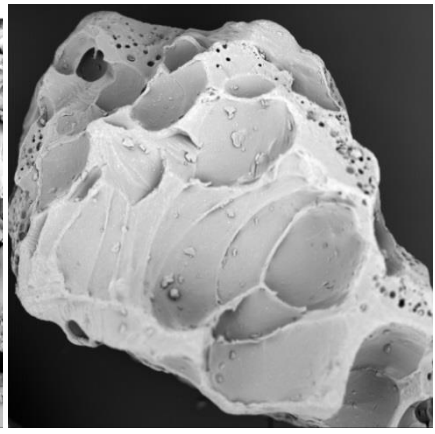

SAP B

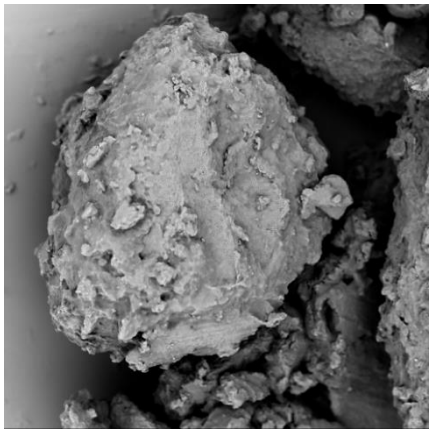

SAP C

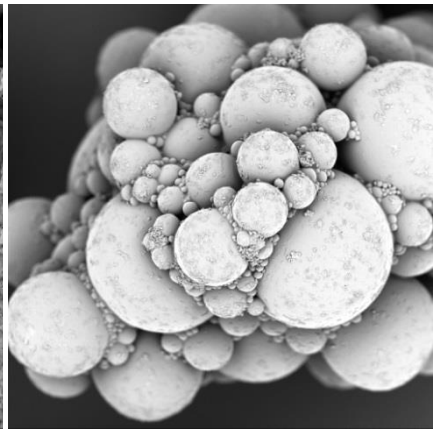

SAP D

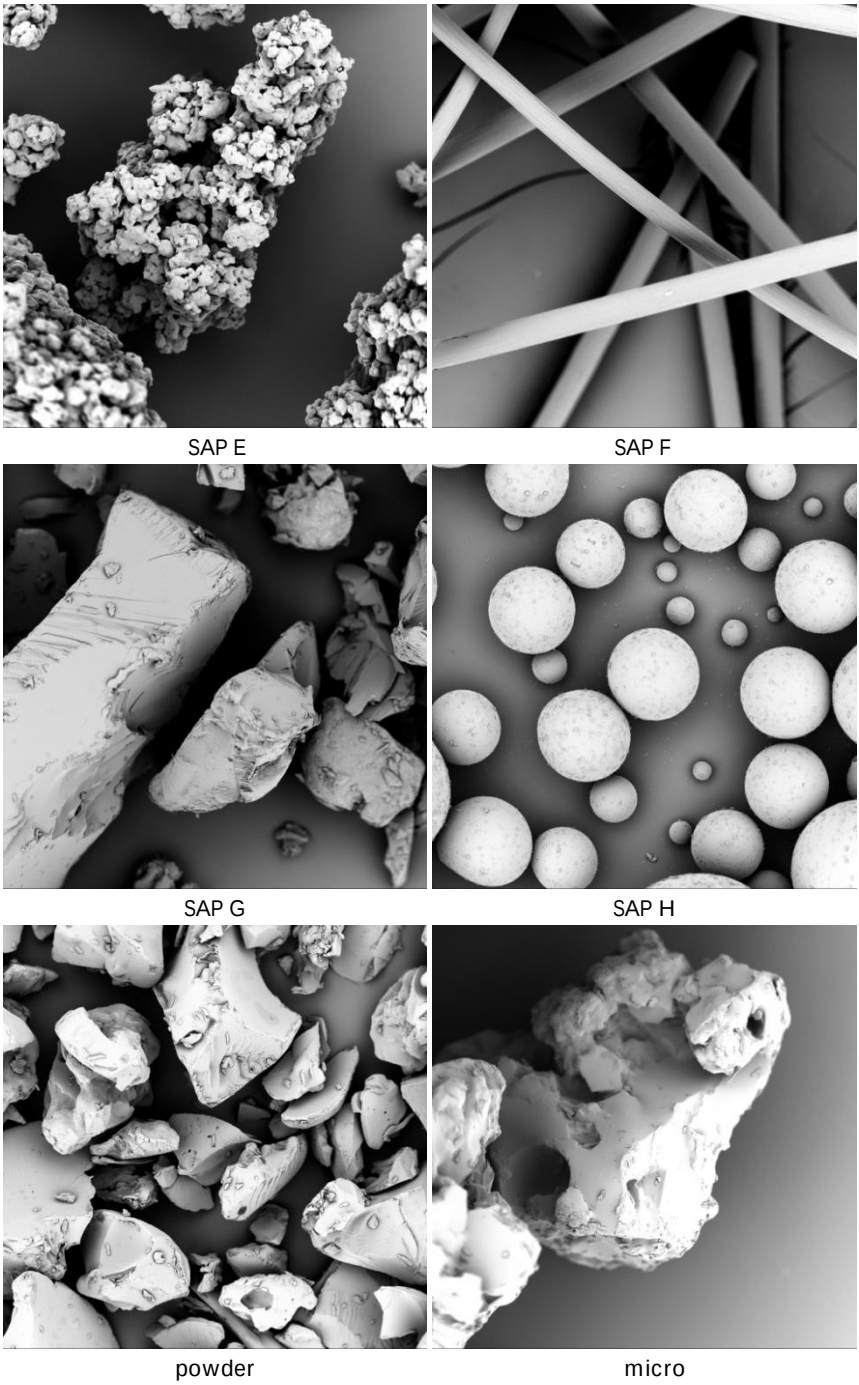

Figure 2.3. Different types of studied SAPs. The figures are 400 µm wide and the used magnification is ×600.

Table 2.1. Type of SAP, production method, company, size (n=500) [µm], swelling capacity in demineralized water [g DW/g SAP], in cement filtrate [g CF/ g SAP], swelling time [s] and moisture uptake [%] at 60/90/98% RH.

	Type of SAP	Production method	Company	Size [µm]	[g DW/ g SAP]	[g CF/ g SAP]	Swelling time [s]	Moisture uptake [%]
SAP A	copolymer of acrylamide - sodium acrylate	Bulk	BASF	100 ± 22	305 ± 4	61 ± 1	10	26/83/394
SAP B	cross-linked potassium salt polyacrylate	Bulk	BASF	477 ± 53	283 ± 2	58 ± 2	60	28/84/394
SAP C	Pluronic F127 bismethacrylate	Bulk	UGent	420 ± 148	20 ± 9	13 ± 6	205	2/43/178
SAP D	cross-linked sodium salt polyacrylate	Suspension	Sumitomo Seika	492 ± 79	351 ± 5	52 ± 2	55	37/105/306
SAP E	”	Suspension	Sumitomo	165 ± 32	390 ± 8	54 ± 1	4	42/99/229
SAP F	cross-linked acrylate copolymer	Extrusion fibre	Technical Absorbents	5.2 ± 0.3 mm • ø 27 ± 3 µm	165 ± 3	47 ± 1	8	30/89/389
SAP G	cross-linked acrylate copolymer	Bulk	SNF Floerger	157 ± 82	332 ± 6	47 ± 2	22	25/79/392
SAP H	”	Suspension	SNF	70 ± 34	281 ± 6	40 ± 5	36	31/93/264
Powder (p)	cross-linked potassium salt polyacrylate	Bulk	Evonik	190 ± 61	286 ± 1	58 ± 2	14	30/86/219
Micro (Mi)	”	Bulk	Evonik	486 ± 141	285 ± 2	59 ± 1	65	26/75/186
Medium (Me)	”	Bulk	Evonik	1200 ± 324	286 ± 1	52 ± 3	480	26/80/184
XL	”	Bulk	Evonik	3726 ± 996	173 ± 4	37 ± 2	n/a	19/73/172

One superabsorbent polymer was received in different sizes; powder, micro, medium and XL. Figure 2.4 gives an optical microscopic overview as scanning electron microscopy would not be able to show the complete XL particle. Next to the dry particles, a swollen particle is shown.

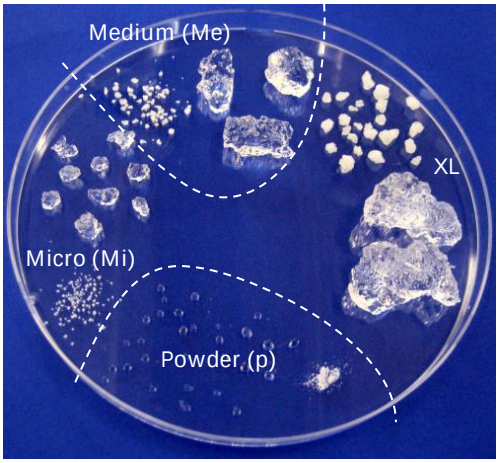

Figure 2.4. Different sizes of the SAP type from Evonik.

In the healthcare and hygienic industry, smaller particles are preferred over the larger particles. The largest particles are mostly used in ground-retaining applications to increase the utilizable water-holding capacity of soils to improve the plant growth. SAP D is used in the hygienic market and SAP E in the cable industry (in optic sea cables against water-tightness damage by boats or sharks).

The fibre type, also called SAF (superabsorbent fibre) is made by extruding the aqueous polymer solution into a hot air stream in order to dry and cure the polymer, resulting in filaments. These are then cooled and cut at specific lengths. The cut fibre is then dried and cross-linked. Yarns and fabrics can be made from these fibres. They have their application in the hygiene, medical, dental, packaging, agricultural and geotextile industry.

As already mentioned, the most important feature of the superabsorbent polymers is their ability to swell and retain a large amount of fluid. This is shown in Figure 2.5. A visualization of the absorption of a SAP B particle is shown in Figure 2.6 with steps of ten seconds. In this visualization a single water droplet was placed on the SAP. As intuitively can be seen, the polymer chains are expanding and storing the water within the polymer structure. The outer parts of a SAP particle take up the fluid and open the path for the inner part of the SAP to absorb water. The droplet of water is absorbed and the total absorption is still not reached. Afterwards, small droplets were carefully added until the SAP became fully saturated.

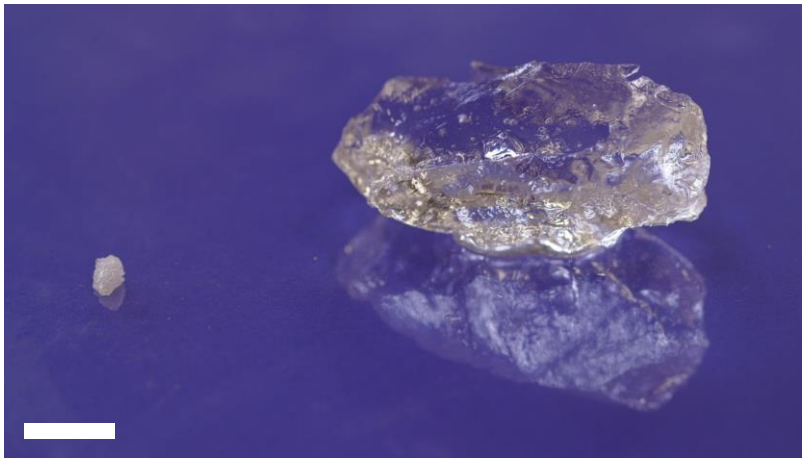

Figure 2.5. Close-up of an un-swollen and swollen SAP particle (XL). The scale bar amounts to 10 mm.

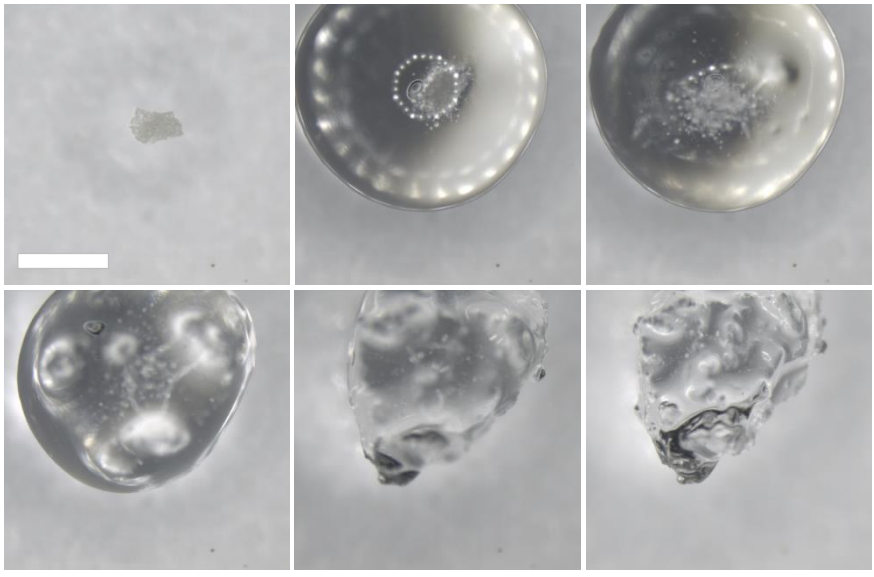

Figure 2.6. Visualization of the absorption of a SAP B particle by imposing a water droplet on top of a 500 µm dry SAP particle in steps of 10 seconds with a 1 mm scale bar.

The amount of absorbed water (Table 2.1) could be visualized in Figure 2.7. On the left-hand side, a small amount of particles is shown (1 g). On the right top part in the figure, the amounts of absorbable demineralized water and on the right bottom part, the amounts of absorbable cement filtrate by the respective SAPs.

These values are comparable to the ones found in literature (approximately 350 g/g in distilled water and 37 g/g in synthetic pore fluid (Jensen & Hansen, 2001, 2002); and respectively 200-300 g/g and 5-20 g/g (Lee et al., 2010b)) for the same types of SAPs (polyacrylates). SAP A and SAP B, both polyacrylates, are able to take up almost 300 times of their own weight in demineralized water.

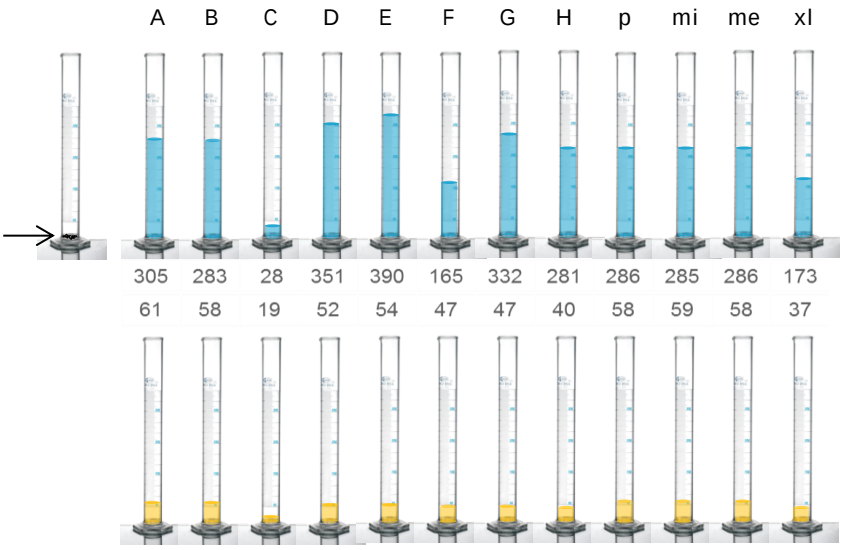

Figure 2.7. Schematic overview of the absorption capacity of the studied SAPs in demineralized water (top) and cement filtrate (bottom) [g fluid/g SAP]. In the top left of the figure, the initial dry weight is schematically shown.

In cement filtrate, this value is lower. This can be ascribed to the osmotic pressure which is a function of the polymer composition but also of the composition of the external fluid. When a SAP particle takes up fluid, the free volume expands. SAP particles consist of large chains cross-linked at certain points. Due to the ionic repulsion of the fluid and the acrylic groups of the SAP, the SAP particles swell. The charge on the carboxylate groups causes the osmotic pressure, responsible for the absorption capacity. On one hand, there is a charge-screening effect resulting from the dissolved cations K^+, Na^+, Mg^{2+} and Ca^{2+} in the filtrate (Figure 2.1c), reducing the osmotic pressure and thus the swelling capacity. Therefore, the ionic repulse of the negatively charged acrylic groups is lower and thus also the absorption decreases. On the other hand, divalent and trivalent ions (hard cations), e.g. Ca^{2+}, Mg^{2+} and Al^{3+}, have an additional effect on the swelling behaviour of SAP particles which are based on polyacrylates. Because of their strong complexation with carboxylate groups (hard anion, following the hard and soft acid and base principle of Pearson (Hancock & Martell, 1989)), they act as additional cross-linkers dramatically reducing the absorption capacity. The Ca^{2+} ions cause additional interlinking and as the concentration of ions outside the SAP increases, the osmotic pressure inside the gel decreases, leading to a reduced swelling of the SAP (Figure 2.1c). If an external fluid has a high amount of divalent or trivalent ions (like the filtered cement slurry), the osmotic pressure and thus the absorption capacity is lower. This effect was also reported by (Horkay et al., 2001; Schröfl et al., 2012).

Two types of SAP were mainly investigated in this research (both obtained from the company BASF). These include SAP A, being a copolymer of acrylamide and sodium acrylate (particle size 100.0 ± 21.5 µm (n=50)), and SAP B, a cross-linked potassium salt polyacrylate (particle size 477 ± 53 µm (n=50)). Both SAPs are bulk-polymerized and consist of irregular crushed particles. Results on their absorption capacity in different solutions (with their respective pH value), typical for the construction and building industry, are shown in Table 2.2.

Table 2.2. Mean diameter of SAP A and SAP B particles (n=50) [µm], density [kg/m³], absorption capacity of SAP (n=30) [g fluid/g SAP] in demineralized water; tap water and cement slurry with their pH, swelling time until full saturation of particles is achieved (n=6) [s], absorption capacity of SAP during mixing of a cement paste or mortar [g mixing water/g SAP] (See Chapter 3), and moisture uptake capacity by means of a dynamic vapour sorption test (DVS) [g moisture/g SAP] with standard deviations where appropriate.

Parameter/method	*pH*	*SAP A*	*SAP B*
Diameter		100.0 ± 21.5	476.6 ± 52.9
Density		700	700
ΔV demineralized water	6.5	305.0 ± 3.7	283.2 ± 2.4
ΔV tap water	6.8	163.9 ± 1.2	148.9 ± 0.9
ΔV NaOH-solution	13	72.5 ± 0.9	68.4 ± 0.7
ΔV cement slurry	12.8	61.0 ± 1.0	58.4 ± 1.7
ΔV seawater	6.3	30.0 ± 0.8	28.3 ± 0.9
ΔV HCl-solution	2.5	13.6 ± 0.5	12.7 ± 0.5
Swelling time		10 ± 2	60 ± 5
Δm/m during mixing		30.5	8.9
DVS at 60/90/98% RH		0.26/0.83/3.94	0.28/0.84/3.94

The value of absorption increases in the following order of fluids: HCl-solution, artificial seawater, filtered cement slurry, NaOH-solution, tap water and demineralized water. The mean reason for this is the charge-screening effect of the above-mentioned cations and the strong complexation by hard cations.

SAP B was almost spherical, so the absorption could also be determined by optical microscopic investigations (Leica S8 APO) and subsequent image analysis. With a syringe, water was carefully and gradually added to the SAP until an individual SAP particle became saturated. The absorption obtained in this way was 282.66 ± 7.51 g demineralized water/g SAP and 57.96 ± 3.05 g cement slurry/g SAP (n=10). Physical forces between SAP particles can distort the value of absorption obtained from the tea-bag method. In the latter method, SAP particles are placed in a tea-bag and submerged into a liquid. As the SAP cannot leave the tea-bag, the increase of mass after immersion is a measure for the absorption capacity. The absorption values found by microscopic investigation of one single SAP particle are not significantly different from those listed in Table 2.2 obtained by the filtration method. This shows that the absorption capacity obtained from filtration is a realistic value of absorption and the effect of physical forces between the SAPs is

negligible. It was found that the tea-bag method slightly overestimated the absorption capacity due to capillary forces acting in between the different SAP particles inside the tea-bag.

DVS measurements showed a moisture uptake up to four times their weight in a relative humidity (RH) of 98%. The values for SAP A and B are in accordance with the moisture absorption values found in literature for acrylic SAP (approximately 3 g moisture/g SAP with RH = 100% after (Jensen & Hansen, 2001, 2002)). This value seems to be negligible, but as further results will point out, the moisture uptake is important to sustain healing independent from ambient conditions.

SAP C (1050 kg/m³) is a completely different SAP compared to SAP A or SAP B and shows a lower absorption capacity. The different swelling capacity is due to a different chemical composition (see the next section; absence of specific charged groups). This causes a lower osmotic pressure and thus a lower absorption capacity.

The swelling starts immediately, but the swelling until complete saturation is different for the SAP particles. The swelling of SAP C takes twenty times longer than the swelling of SAP A, and three times longer than the swelling of SAP B (Table 2.1). This is due to a lower osmotic pressure due to another chemical composition of SAP C. SAP B, which is composed of larger particles than SAP A, showed a longer swelling time even though the composition was similar. Generally, the swelling time of all SAPs was found to be independent of the fluid used.

The swelling behaviour during mixing, however, will be different as in filtered cement slurry. This is due to the presence of heavy cement grains and sand particles which obstruct the swelling of the SAP because of the weight exerted by the surrounding material. Also, the synthetic fluid may be different compared to the real pore liquid. The swelling capacity in a concrete mix is mentioned to be about half the one in filtered cement slurry (Brüdern & Mechtcherine, 2010). This amount will be determined in Chapter 3 by comparing the workability and the formed microstructure. The results are also given in this table to easily compare the results later on.

All SAPs showed comparable swelling capacities (except for the lower value for SAP C and SAP F) and their shape and size are the most important differences. Their influences on the sealing capacity and healing capacity will be studied in Chapter 4 and Chapter 5, respectively.

SAP C was in-house made at Ghent University, to study a different type of superabsorbent polymer. The synthesis of this polymer has been described in the next paragraph.

2.2.2 Synthesis of Pluronic F127-bismethacrylate

Next to the commercial SAPs, an in-house SAP was produced as well (SAP C). This was done to include an SAP showing a different initial polymeric backbone but an acceptable swelling capacity as a comparison of the results obtained with commercial SAPs.

Pluronic® F127 was purchased from Sigma-Aldrich and dried using azeotropic distillation in toluene (Dean & Stark) during 2 hours. Methacryloyl chloride and triethylamine (TEA) were obtained from Sigma-Aldrich and distilled before use. 4-tert.butyl catechol and Celite® 545 were purchased from Sigma-Aldrich. 1-[4-(2-Hydroxyethoxy)-phenyl]-2-hydroxy-2-methyl-1-propane-1-one (Irgacure® 2959) was obtained from Ciba Specialty Chemicals N.V. (Groot-Bijgaarden, Belgium) (Vandenhaute et al., 2014).

First, all glassware was dry-flamed. The reaction occurred under argon atmosphere, otherwise water would react with methacryloylchloride in a nucleophilic acyl substitution. Dried Pluronic F127 (250.0 g, 19.86 mmol) was dissolved in 500 ml distilled toluene and cooled below 10°C in an ice bad. Then, triethylamine (TEA; 8.0 eq.; 158.88 mmol; 22.08 ml) and a radical inhibitor (4-tert.butyl catechol; 0.01 eq.; 0.1986 mmol; 33.01 mg) were added. Subsequently, methacryloyl chloride (8.0 eq., 158.88 mmol, 15.38 ml) was added dropwise to the cooled mixture under argon atmosphere and magnetic stirring to the terminal OH-groups of the Pluronic F127. The reaction mixture was vigorously stirred at 0°C for 12 h and subsequently at room temperature for 12 hours. Unreacted methacryloyl chloride and TEA were removed by rotational vaporization and the crude product was resuspended in toluene (500 ml). The solution was filtered over a Celite® layer on a glass filter to remove the triethylammonium chloride salts formed. The Pluronic F127 dimethacrylate bis-macromonomer was purified by precipitation in a mixture of pentane:diethyl ether (5:1; 2.5 l) and isolated via filtration followed by several washing steps using diethyl ether. The macromonomer was dried for 24 hours under vacuum and stored at -18°C, protected from light. The general reaction scheme depicting the functionalization of the OH-terminated PEO-PPO-PEO triblocks using methacryloyl chloride is given in Figure 2.8.

The functionality of Pluronic F127 bismethacrylate could be calculated by the use of proton nuclear magnetic resonance (^{1}H-NMR) spectroscopy. ^{1}H-NMR spectra were recorded using a Brüker 300 MHz. The spectrometer operated at 300 MHz to record ^{1}H spectra. All spectra were obtained at room temperature in deuterated chloroform ($CDCl_3$). The recorded spectra were analysed by the ACD/SpecManager software (Advanced Chemistry Development Inc.).

The expected peaks in the spectrum are listed in Table 2.3. The peaks related to hydrogen atoms on the unsaturated bond after the modification with methacryloyl chloride should appear at δ = 5.62 ppm (doublet, one proton) and δ = 6.18 ppm (doublet, one proton).

The monomer ratio of copolymers was determined by means of ^{1}H-NMR spectroscopy. There were two peaks to be considered (Figure 2.9); the 1.2 ppm signal of CH_3 (PPO) and the 3.25-4.3 ppm signal of CH_2 (PEO), CH_2 (PPO) and CH (PPO).

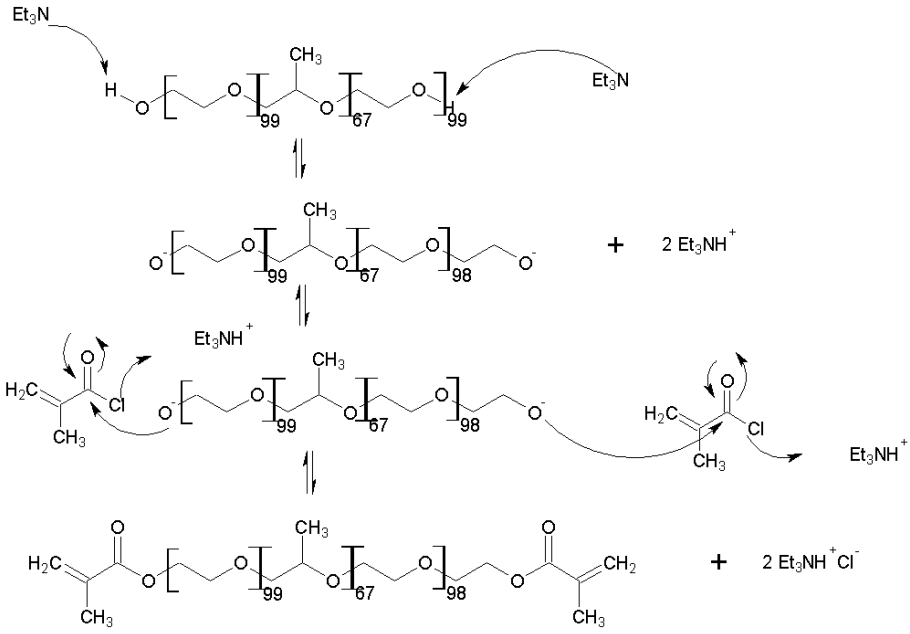

Figure 2.8. Reaction mechanism of Pluronic F127-bismethacrylate.

Table 2.3. Expected peaks in the ^{1}H-NMR spectrum [ppm].

H	*Peak*	*Explanation*
	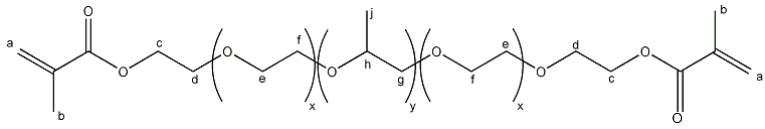	
H_j	1.2	CH_3 of PPO
H_b	1.9	CH_3 of methylacrylate-endgroup
H_e	3.25-3.6	CH_2 of PEO
H_f	3.25-3.6	CH_2 of PEO
H_g	3.25-3.6	CH_2 of PPO
H_h	3.25-3.6	CH of main chain PPO
H_d	3.6-3.9	CH_2 of PEO unit next to end-groups
H_c	4.5	CH_2 of PEO unit next to end-groups
H_a	5.62 and 6.18	Vinyl proton of the methacrylate group

If the signal of CH_3 is taken as reference, the following calculations can be made: Integration (H_h, main chain) = (Integration H_j, CH_3) = 3; Integration (H_{ef}) = Integration (H_{ef} + H_g, main chain) - 3 = 17.46 - 3 = x = 14.46; PPO/PEO= 1/ (x/4) = 0.2766; Theoretical ratio = 0.33 (67 / (2*99)). The experimental ratio (0.2766) has a

value close but not equal to the theoretical value (0.33). The integration of the hydroxyl end groups is often not quantitative due to exchange of the hydrogen with deuterium coming from the deuterated solvent. One can calculate the true number of PPO and PEO units by reaction with trichloroacetylisocyanate (TAIC). This causes a shift of the 2 H's next to the OH groups to 4.2-4.3 ppm. The integration of these is now an absolute standard (set to 4). The following calculations can now be made: True number of PPO units = 198.06/3 = 66 units, PPO/PEO= 0.2766 (previous ^{1}H-NMR); True number of PEO units: 66/0.2766 = 238 units. This means 119 units of PEO on each side of the PPO chain.

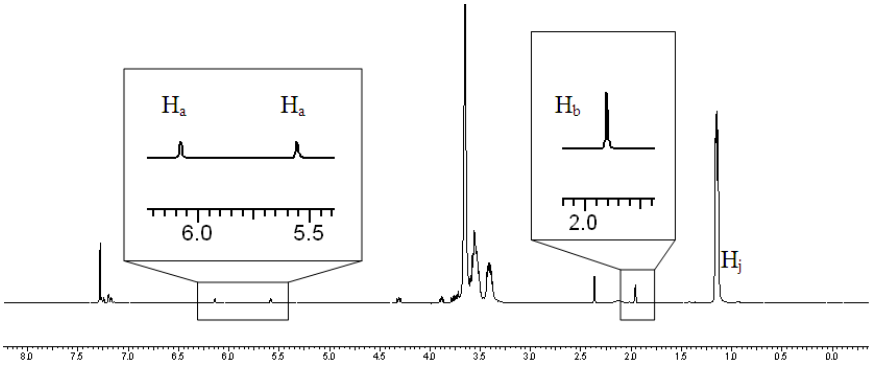

Figure 2.9. ^{1}H-NMR spectrum of methacrylate end-capped Pluronic® F127 BMA.

For Pluronic® F127 BMA, the degree of functionalization ranged from 95 to 100%, indicating that the functionalization strategy was successful.

Hydrogel films, based on methacrylate end-capped Pluronic® F127 (F127 BMA) were prepared starting from 10 ml aqueous hydrogel precursor solutions (25 and 30 wt%). A biocompatible photo-initiator (i.e. Irgacure® 2959, 2 mol% added relative to the amount of double bonds of the methacrylate end groups) was applied. The precursor solution was stirred and degassed followed by injection beween two glass plates covered by teflon release foil and separated by a silicon spacer (1 mm thickness). Since Pluronic® F127 BMA shows thermo-gelling behaviour upon heating above the critical gelation temperature (37°C for 10 wt% (Park et al., 2007), 20°C for 20 wt% and 5°C for 30 wt% (Meznarich, 2012; Wanka et al., 1994)), the glass plates were cooled in the freezer prior to use. The hydrogels films were exposed to UV-light for 20 minutes (365 nm, 8 mW/cm²) to enable complete chemical curing. Finally, the chemically cross-linked hydrogel films were released from the glass plates and hydrogel pellets (Ø 8 mm) and hydrogel granules (350-500 µm) were prepared. The Irgacure solution is used for its water-solubility. The Irgacure 2959 (80 mg) was dissolved in demineralized water and placed in an ultrasonic bath for 30 min. This solution was added to 3 ml 15 wt% Pluronic-BMA in amounts of 0.05, 0.08, 0.1 and 0.2 ml. After degassing the solution, 1 ml was injected in the UV-chamber and UV light was applied for 15 min, simultaneously synthesizing the four solutions. The initiation of Irgacure 2959 under UV light and the radical reaction is shown in Figure 2.10. The formed radicals will react with the polymeric chain to form the network (propagation).

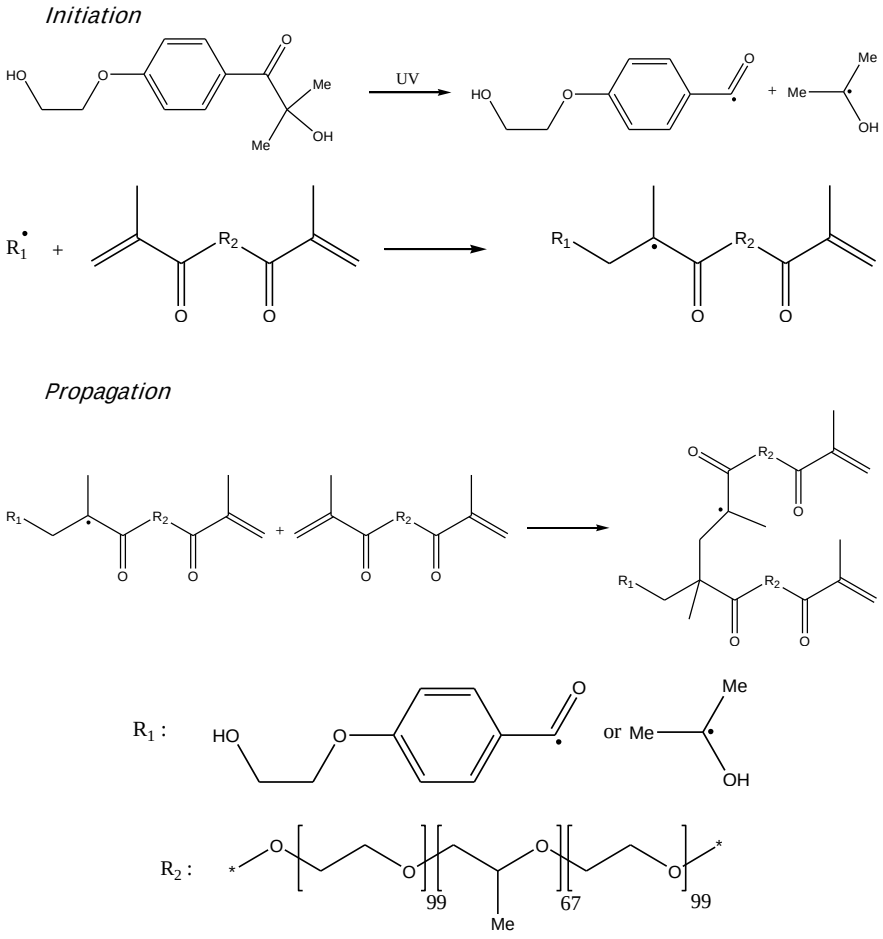

Figure 2.10. Reaction mechanism of the synthesis of the hydrogel.

Different networks were synthesized. These were 3 ml 15-20-25-30 wt% Pluronic-BMA with Irgacure solution of 0.05, 0.08, 0.1 and 0.2 ml. An amount of 80 mg of water-soluble Irgacure was hereby dissolved in 10 ml of demineralized water and was placed in an ultrasonic bath for 30 min. The higher the amount of Irgacure, the higher the solidity of the hydrogel, related to its functionality. The more Irgacure is added, the higher the crosslinking of the hydrogel. This higher cross-linking yield results in a stronger material. But, a too high amount of Irgacure may result in the formation of shorter polymeric chains and thus a less strong network. Also, a higher amount of Pluronic-BMA also results in a higher crosslinking of the hydrogel. The 15 wt% networks were not able to retain their shape after removal from the UV-chamber. The higher the amounts of wt% Pluronic-BMA, the more the networks could retain their shape.

After synthesis, the hydrogels were freeze-dried to remove water out of the network by means of sublimation. To obtain a specific range of particle sizes (depending on the actual absorption capacity, ideally this is 500 µm), polymerized

films were grinded using an IKA A11 basic grinder. The polymer powder was then sieved in the range of 350-500 µm. All hydrogel particles were subsequently vacuum-dried in a desiccator prior to testing for a minimal period of one week.

By using the same weight concentration of Pluronic-BMA (25 wt%) and varying the amount of the Irgacure solution, the cross-link density could by investigated. The solutions with Irg 0.2 swell more in comparison to the Irg 0.08 solutions. This finding is independent from the solution used. As there is more UV-initiator available in the Irg 0.2 solutions, there is more cross-linking of the network. This should lead to a restriction in swelling due to more cross-linking, but the Irg 0.08 solutions are not cross-linked as efficient as the Irg 0.2 solutions, leading to the higher value found for the Irg 0.2 solutions compared to the Irg 0.08 solutions.

Dynamic vapour sorption (DVS) measurements show that an increasing concentration (25 vs. 30 wt%) leads to less vapour and/or water absorption (see Table 2.4). This is due to the higher cross-linking degree which is responsible for a lower swelling capacity, restricting the increase in size due to swelling. The trend of the DVS measurements – i.e. swelling capacity of moisture and fluids – are alike to results found when using other types of hydrogels (Jensen & Hansen, 2002).

Table 2.4. Moisture uptake by means of DVS for the studied Pluronic® F127 hydrogels with different concentrations, with the absorption capacity on the right as a comparison.

Moisture uptake in	*60% RH [%]*	*90% RH [%]*	*98% RH [%]*	*Water [g fluid/g SAP]*
Pellet 25 wt% Freeze-dried	2.2	44.1	161.9	6.54 ± 0.04
Pellet 25 wt% air-dried first	2.2	43.6	155.2	6.22 ± 0.16
Particles/granules 25 wt%	2.2	42.6	177.6	15.40 ± 0.20
Pellet 30 wt% Freeze-dried	1.5	41.7	122.9	5.78 ± 0.20
Pellet 30 wt% air-dried first	1.4	35.7	75.0	5.57 ± 0.20
Particles/granules 30 wt%	1.4	37.6	100.2	10.65 ± 0.38

A comparison of air-drying to freeze-drying shows that the former induces the lower absorption value, both in fluids and in moist environments. The lower moisture uptake value found is due to the pre-drying in air, causing the SAP to swell less than if it would only have been freeze-dried. This is logical since more water is initially removed by freeze-drying. Also, there is partial degradation, leading to the loss in moisture uptake capacity. This is due to the hydrolysis of labile ester linkages (Antheunis et al., 2010; Li, 1999; Pielichowski & Flejtuch, 2005; Zweers et al., 2004). The higher value of water absorption when using particles is due to the larger surface area available during swelling and less dimensional restriction during swelling. When a pellet is steadily swelling, it is restricted in longitudinal direction. With particles, this is less the case and they are able to swell more freely in every direction, leading to the higher uptake of water. Even though the equilibrium has been reached in all samples, the uptake capacity is less when using larger hydrogel samples. From a practical point of view, particles are preferred, especially in building technology. Therefore, the focus in the next paragraph lies on particles rather than pellets.

2.3 Degradation and shelf-life

A very important factor is the possible degradation of the polymers. If this life span is too short (couple of months), they may lose their purpose as an additive in cementitious materials. The swelling method according to (Jensen, 2011) was used to study the degradation behaviour in time. Compared to the filtration tests, this method has its advantage as after filtration, the material cannot be reused without losing part of the material leading to erroneous results. Thus, to study the behaviour in a consistent way, the filtration method would require a high amount of hydrogels to study the swelling ability in time.

The first volume measurement was performed when the particles had settled, and then every hour during the first day, every day of the first week and subsequently every week. There is one main assumption for the Jensen method (Jensen, 2011), namely a similar packing of the dry particles and the wet particles after settlement in the fluid. The packing in the wet state is looser as the particles behave buoyant due to a small difference in density upon swelling and the settlement will act as a sieve separating different sizes of particles. For sake of comparison in time, this effect is not of order.

Besides studying the effect of possible degradation as a function of time in a solution, the hydrogels were also studied for their behaviour in air. Therefore, dried hydrogel particles were stored in standard laboratory conditions at a temperature of 20 ± 2°C and a relative humidity of 60 ± 5% for a total period of 105 days. Afterwards, the above-mentioned procedure was again applied on this 'aged' product and the samples were placed in the five different solutions and studied as a function of time.

Results on the absorption capacity in time show that the commercially available SAPs did not show degradation in time and that the new-synthesized hydrogel particles did show degradation in time (Figure 2.11). This figure shows two types of measurements, i.e. the tests started immediately in the fluids (at time zero) and the tests started on products stored in standard laboratory conditions (at 105 days). The first peak during the first days of measurement of the immediate first test is due to the settlement of the particles and the buoyant effect. It is also seen that the particles swell less in certain solutions. This is due to the strong charge screening effect and strong complexation of di-valent and tri-valent cations (especially Ca^{2+} present in the cement filtrate) with the carboxylic acid groups present in the hydrogel, following the hard and soft acid and base principle of Pearson (Hancock & Martell, 1989). This complexation causes additional cross-linking, thus reducing the absorption capacity. Covalent crosslinks are preferred as they are stable. The density of crosslinks depends on the production parameters of the hydrogels and this density is important to characterize the absorption capacity. As an increased crosslink density increases the mechanical properties, it may also lead to a lowering of the absorption capacity as the polymer chains in between the crosslinks are restricted in movement.

When put in another solution after these long storage periods (up to three years), the commercial polymers are able to swell again to full extent. The charge-screening effect therefore is more important compared to the strong complexation when studying the commercial types of SAPs. The swelling is thus reversible.

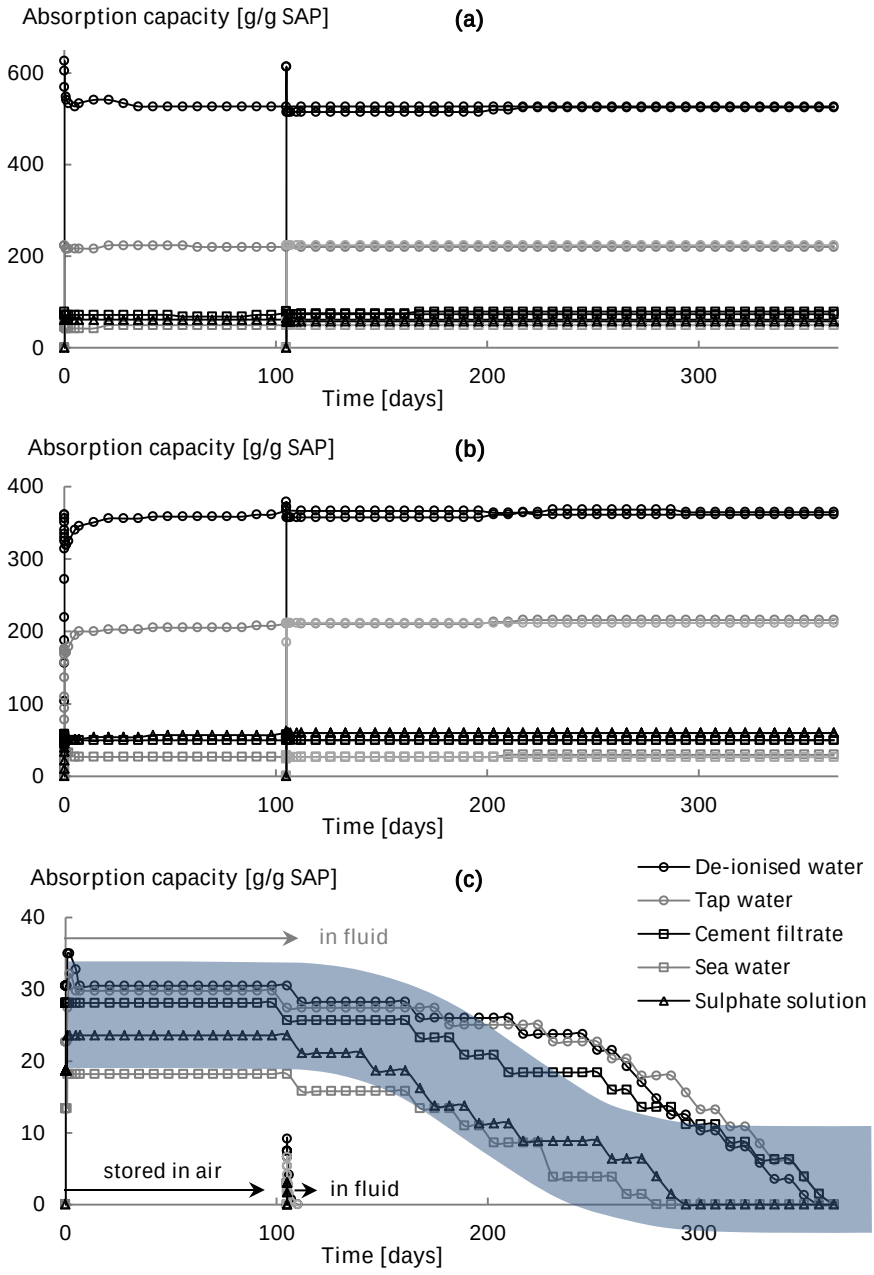

Figure 2.11. Degradation study/absorption capacity [g/g hydrogel] of the commercially available SAP A **(a)** and SAP B **(b)**, and Pluronic® F127 BMA hydrogel particles SAP C **(c)** (with a concentration of 25 wt%) as a function of time. The figure shows two tests: immediate testing in fluids at time zero and degradation tests at an age of 105 days on specimens stored for three months in standard laboratory conditions.

Around pH 3-9 there may be dissociation of acrylamide and above pH 9 the amide groups may start to hydrolyse. This is not the case for SAP A and SAP B. The same results were found with all other commercially available SAP samples, shown in Table 2.1.

When submerged in a fluid, degradation of the Pluronic hydrogels starts at approximately 3 months. This is due to the slow hydrolysis of labile ester linkages. The particles almost completely lose their capacity to swell when stored in standard laboratory conditions and the particles are not able to hold the swelling for several hours (small peak at 105 days in Figure 2.11). This is due to the strong and fast hydrolysis of labile ester linkages and natural oxidative degradation/aging of PEO chains when stored in standard laboratory conditions.

Tests on particles with three different concentrations (20-25-30 wt%) show that the particles with a higher concentration degrade slower in demineralized water (for sake of comparison only demineralized water was tested) (Figure 2.12). At higher concentrations, the amount of crosslinks is higher. The effect of degradation is thus delayed to some extent. The swelling is also higher with a lower concentration due to the lower amount of crosslinks.

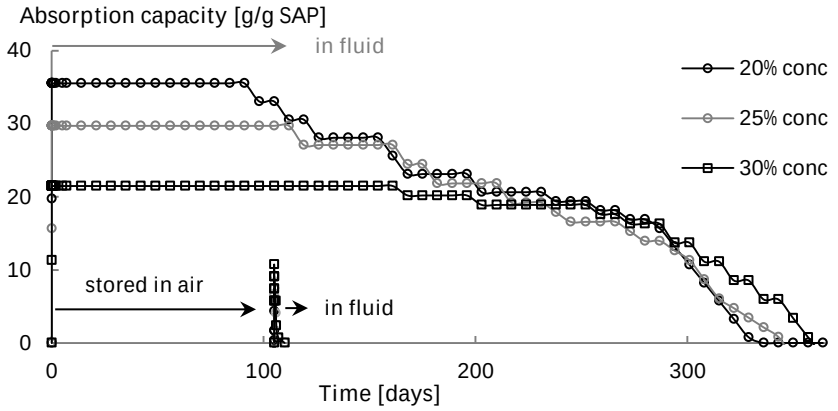

Figure 2.12. Degradation study/absorption capacity [g/g hydrogel] of the Pluronic® F127 BMA hydrogel (with a concentration of 20-25-30 wt%) in demineralized water as a function of time.

Overall, in cementitious systems used for self-sealing (Chapter 4) and self-healing (Chapter5), this property is unwanted as a stable polymer is needed to achieve sealing and healing at any time of crack occurrence. However, the repeatability of the swelling is not necessary for internal curing or freeze-thaw resistance (Chapter 3). Furthermore, the property of degradation could be useful in several biomedical applications where degradation is used as smart drug-delivery system.

2.4 Conclusions

In this Chapter, the properties and production methods superabsorbent polymers were described. Different methods to characterize the swelling behaviour, kinetic behaviour and moisture uptake have been proposed. It was found that the filtration method was a good measuring technique to determine the swelling capacity of the different types of SAPs, but it may be influenced by the particle size of the SAPs studied. The vortex method gave insight in the kinetics of swelling and dynamic vapour sorption was useful to calculate the total moisture uptake.

The studied commercial types show an absorption capacity of approximately 300 times their own weight in demineralized water, 40-60 times their weight in cement filtrate solution and up to four times their weight in moisture. The variation found in different solutions is mainly due to the occurring charge-screening effect by the present cations in the pore fluid and the strong complexation with the di- and tri-valent ions present in the pore solution.

A new type of SAP was successfully synthesized in-house to compare its results to those obtained when using commercial SAPs. The absorption values were lower but still acceptable and noteworthy.

Results of the absorption capacity in time show that the commercially available SAPs did not show degradation and that the new-synthesized hydrogel particles did show degradation in time due to the slow hydrolysis of labile ester linkages. This property is unwanted as a stable polymer is needed to achieve sealing and healing at any time of crack occurrence. Other applications, such as biomedical drug delivery, are nevertheless possible.

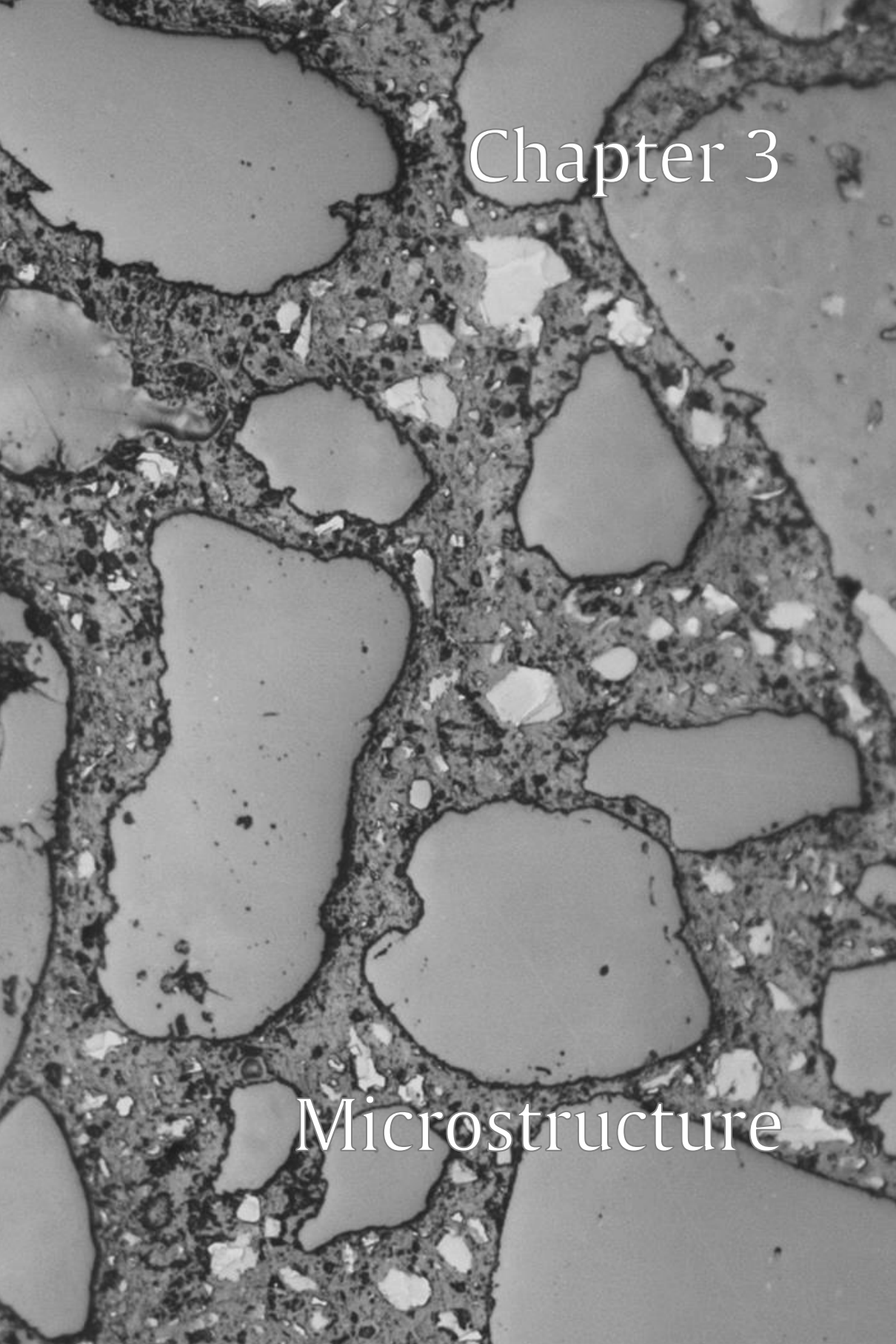

Chapter 3

Microstructure

| Polished mortar cross-section showing sand particles and cement paste products

Chapter redrafted after (Snoeck & De Belie, 2015a; Snoeck et al., 2015b; Snoeck et al., 2014a; Snoeck et al., 2014c, 2015f).

"The real voyage of discovery consists not in seeking
new landscapes, but in having new eyes."

– *Marcel Proust*

3.1 Properties at early age

Superabsorbent polymers (SAPs) have the feature to absorb up to 500 times their own weight in aqueous solutions due to osmotic pressure, resulting in the formation of a swollen hydrogel (Chapter 2 on hydrogels). Their long chains of linear polymers are interconnected at several points (crosslinks). Due to osmotic pressure, an aqueous solution is absorbed and the space in between the chains and the crosslinks (free volume) thus expands, causing the polymer to swell. Nowadays, due to this interesting and useful feature, they are used in the hygiene and medical industry as care articles or smart pills, and they can also be used for firefighting or food packaging (Buchholz & Graham, 1998). It was only a matter of time until this polymer also found its way as an additive in cementitious materials (225-SAP, 2012). SAPs can be used in cementitious materials for reducing the autogenous shrinkage (Assmann, 2013; Craeye & De Schutter, 2006; Igarashi & Watanabe, 2006; Jensen & Hansen, 2001, 2002; Mechtcherine et al., 2009; Mechtcherine et al., 2014), for changing the rheology of the fresh material (Jensen, 2008; Jensen & Hansen, 2001, 2002), for increasing the freeze/thaw resistance (Mönnig, 2005; Mönnig & Lura, 2007), for self-sealing (Lee et al., 2010b; Tsuji et al., 1999) and even to promote autogenous healing (Kim & Schlangen, 2010).

During preparation of a concrete mixture, the SAPs will take up mixing water. This swelling capacity is dependent on the composition of the mixture and the composition of the SAPs as the osmotic pressure force is dependent on the external fluid composition and the chemical structure, length and crosslinking degree of the SAP. The SAPs will thus form water-filled inclusions, useful for internal curing (Jensen & Hansen, 2001, 2002; Mechtcherine et al., 2009). The water present in the SAP will hereby be released into the cementitious matrix due to the drop in relative humidity. In this way, the internal relative humidity is maintained. The SAP particles shrink and an empty macro pore remains as shown by means of neutron tomography measurements (Trtik et al., 2010; Trtik et al., 2011).

Due to the uptake of mixing water by the SAPs, the workability decreases as less water is available in the mortar matrix itself, and partly swollen SAP particles obstruct the handling during fabrication of the specimens. This is mostly unwanted. Also, if the mixture would not be workable, the strength and the overall stability of the structure would not be certified.

In most applications, mostly additional water is added to compensate for the loss in workability as the SAPs will absorb mixing water during mixing. The amount of additional water added is hereby dependent on the mixture composition, the type and size of SAP. A study of the rheological behaviour of the mixture can determine the additional water needed (Mechtcherine et al., 2009; Schröfl et al., 2012). The additional water is then held by the SAPs and released in time, which is useful for internal curing by maintaining the relative humidity and the reduction in autogenous shrinkage. Afterwards, as the SAPs shrink back to their original size, they leave macro pores behind. These voids are interesting for increasing the freeze-thaw resistance as the voids act in the same way as if an air-entraining agent is added. Dudziak and Mechtcherine (2010) showed a reduction in workability of concrete with SAPs due to the absorption of mixing water by SAPs,

even if additional water was added to compensate for the water uptake by the SAP. Their calculations, however, were based on the swelling capacity of SAP in artificial pore-fluid and not on the real swelling capacity and behaviour in fresh mortar. Typical values added for studying the effects of internal curing are 0.3-0.6 m% SAPs by weight of cement.

The rate of release of water in time is affected by the density of anionic functional groups. A high density results in a quick release of water (Schröfl et al., 2012). If this water is released too soon, it leads to a significant decrease in compressive strength. But if this water is released at the ideal stage (beginning of concrete setting as the earliest point), this water would serve as internal curing water (Schröfl et al., 2012). It is thus very important to use a SAP with the ideal properties. If the water is released too fast (i.e. before setting), the microstructure will be completely different and if the water is released too late (i.e. after a couple of days onwards), the purpose of internal curing vanishes.

Another way to compensate the loss in workability is the use of a superplasticizer. But the latter may influence the hydration. One of the characteristics influencing the practical application is the possible delayed hydration. If the mixture has a long setting time, the formwork cannot be removed early. This effect will therefore result in a delay in the construction process. Most types of superplasticizer do have this effect. A superplasticizer not only affects the fluidity of a cement paste, but also causes a stiffness like pseudo-setting or a remarkable retardation of setting (Hanehara & Yamada, 1999). For example, in literature, the initial setting was found to be delayed 50% and the final setting 10-30% in time when using 1.5 m% of cement weight of polycarboxylic ether, modified polycarboxylate or melamine formaldehyde (Şahmaran et al., 2006). A polycarboxylate-type superplasticizer retarded the initial set by 1 h and the final set by 2 h in slag pastes (1 m% of binder weight) (Palacios & Puertas, 2005). A delay of 2 h in hydration time and an increase in heat evolution over several hours (3-17 h) was found when using 0.3 v% of superplasticizer (experimental superplasticizers based on polycarboxylic acid). The time between the main hydration peak and the shoulder attributed to the consumption of calcium sulphate seemed to be prolonged as well (Winnefeld et al., 2007). Data on the degree of delayed hydration caused by SAPs are scarce in literature. Dudziak and Mechtcherine (2010) showed that the final setting of specimens with SAPs, additional water - to compensate for the entrained water compared to SAP-less samples - and an increased amount of superplasticizer (0.37 wt% of cement weight), was postponed by 2-4 h.

In this section, a general overview of the effects of SAPs, superplasticizer and additional water on the early-age properties of a cementitious composite will be given.

3.1.1 Composition and fresh properties

3.1.1.1 Cement paste

A cement paste with a water-to-binder ratio (W/B) of 0.3 was made to study the influences on autogenous shrinkage. The cement used was CEM I 52.5 N (Chemical composition in Table 3.1). Furthermore, mixtures containing different amounts of supplementary cementitious materials were made (Properties in Table 3.1). The studied mixtures, all with a W/B=0.30, are the following (FA = fly ash; BFS = blast furnace slag, together with their percent replacement of the cement). The mixtures were mixed according to the Standard EN 196-1.

100% CEM I 52.5N; R0.30
85% CEM I 52.5N + 15% Class F fly ash; FA15
70% CEM I 52.5N + 30% Class F fly ash; FA30
50% CEM I 52.5N + 50% Class F fly ash; FA50
85% CEM I 52.5N + 15% blast-furnace slag; BFS15
70% CEM I 52.5N + 30% blast-furnace slag; BFS30
50% CEM I 52.5N + 50% blast-furnace slag; BFS50
15% CEM I 52.5N + 85% blast-furnace slag; BFS85

Table 3.1. Chemical composition of CEM I 52.5 N, Class F fly ash and Blast Furnace Slag [% (w/w)] and specific surface (Blaine fineness).

	CEM I 52.5 N	*Class F fly ash*	*Blast Furnace Slag*
	mass-%	*mass-%*	*mass-%*
CaO	63.12	2.47	40.38
SiO_2	18.73	49.34	34.35
Al_2O_3	4.94	24.55	11.36
Fe_2O_3	3.99	6.23	0.48
SO_3	3.07	0.30	1.65
MgO	1.02	1.73	7.57
K_2O	0.77	3.84	0.37
Na_2O	0.41	0.52	0.29
Cl^-	-	-	0.013
S^{2-}	-	-	0.77
Mn	-	-	0.165
Specific surface	390 $m^2 kg^{-1}$	330 $m^2 kg^{-1}$	400 $m^2 kg^{-1}$

Portland cement is made by heating limestone and clay to a temperature of about 1450°C to produce clinker. The clinker is mixed with gypsum and finely ground to make cement. The cement has typical 67% CaO, 22% SO_2, 5% Al_2O_3, 3% Fe_2O_3, and 3% of other components (Taylor, 1990). In traditional concrete, each of the cement minerals (C_3S, C_2S and C_4AF with C=CaO, S=SiO_2, A=Al_2O_3 and F=Fe_2O_3) reacts with water to form hydration products.

A fully hydrated cement paste has approximately 70% calcium-silicate-hydrates (C-S-H), 20% Portlandite $Ca(OH)_2$, 7% ettringite and 3% minor phases (St John et al., 1998). The phase composition of the CEM I 52.5 N calculated based on the formulas of Bogue, corrected with the amount of sulphur trioxide (SO_3) for C_3S is: 66.9 m% C_3S, 3.3 m% C_2S, 6.3 m% C_3A and 12.1 m% C_4AF.

The dosage of the superplasticizer was kept constant, to limit its influence on the setting and hydration properties as most superplasticizers cause retardation. The amount was 0.42 m% (mass percentage of binder weight) polycarboxylate superplasticizer (Glenium 51, conc. 35%, BASF). In these mixtures, SAPs were added in addition, as well as additional water to be absorbed to induce internal curing. Theoretically, an amount of $(W/B)_e$=0.054 is needed to effectively mitigate autogenous shrinkage in cement pastes with a W/B=0.30 (Jensen & Hansen, 2001). A reference mixture with W/B=0.354 to study the differences in self-desiccation was also prepared: R0.354.

FA15 with internal curing; FA15_A_e
FA30 with internal curing; FA30_A_e
FA50 with internal curing; FA50_A_e
BFS15 with internal curing; BFS15_A_e
BFS30 with internal curing; BFS30_A_e
BFS50 with internal curing; BFS50_A_e
BFS85 with internal curing; BFS85_A_e
100% CEM I 52.5N; R0.354

The theoretical calculation of the amount of entrained water is based on pure cement systems. As part of the cement is replaced by SCMs, deviations of this theoretical amount can occur. This was not the case, as will be shown later-on. The amount of mixing water absorbed was calculated from the flow values of the different mixtures, following the Standard EN 12350-5. A comparison of the flow value of mixtures with and without SAPs may tentatively be used to reflect the absorption of the SAPs in the mortar mixture (Mechtcherine et al., 2009; Mönnig & Lura, 2007; Schröfl et al., 2012). One needs to make sure that this amount is not overestimated as it may change the overall microstructure (Hasholt et al., 2012). Microscopic analysis confirmed the amount of entrained water and thus the amount of ideal additional water in the mixture. This was done by microscopically comparing the theoretical sizes of the SAP particles saturated by the uptake of the total amount of additional mixing water and the sizes of the macro pores formed in the hardened system. The method will be further described in detail in paragraph 3.2.1.1. The swelling time was fast enough (see values in Table 2.1) to ensure complete swelling by absorption of additional mixing water during mixing.

The amount of SAP to be added to receive an additional entrained water amount of $(W/B)_e$=0.054 was 0.22 m% (mass percentage of binder weight) SAP A (A_e) and 0.45 m% SAP B (B_e), respectively. Additionally, mixtures with 0.11 m% ($(W/B)_e$=0.027) and 0.33 m% ($(W/B)_e$=0.081) SAP A were studied, as well as a mixture with 0.225 m% ($(W/B)_e$=0.054) SAP B.

100% CEM I 52.5N with (W/B)=0.30 and $(W/B)_e$=0.054; A_0.054 or A_e
100% CEM I 52.5N with (W/B)=0.30 and $(W/B)_e$=0.027; A_0.027
100% CEM I 52.5N with (W/B)=0.30 and $(W/B)_e$=0.081; A_0.081
100% CEM I 52.5N with (W/B)=0.30 and $(W/B)_e$=0.054; B_0.054 or B_e
100% CEM I 52.5N with (W/B)=0.30 and $(W/B)_e$=0.054; B_h

All above-mentioned mixtures were used to study the effects on autogenous shrinkage as a low water-to-binder ratio highlights these results.

Cement pastes with a water-to-cement ratio of 0.50, 0.46, 0.41 and 0.35 were additionally made and cast to study the effects of SAPs on the vapour sorption properties. The cement used was CEM I 52.5 N (Chemical and phase composition in Table 3.1) and the standard used for the mixing procedure was EN 196-1. A varying amount of SAP expressed as mass percentage of cement weight (0.5 and 1 m%) and additional water were added on top. Dry SAP particles were added to the cement and were first dry mixed to ensure a homogenous dispersion in the cement. The amount of additional water depends on the type of SAP (30.5 g and 8.9 g mixing water/g SAP A and SAP B, respectively). The difference in mixing water uptake is due to the higher relative surface area available to mixing water due to the smaller particle size of SAP A (100 ± 22 µm) compared to the larger particle size of SAP B (477 ± 53 µm).

After one day of storage in a relative humidity of 95 ± 5% and a temperature of 20 ± 2°C, the samples were stored in water at 20 ± 2°C for a minimum period of 6 months to ensure a stable formation of the cementitious matrix. For mixes without SAPs, the code consists of the letter R (R for reference) followed by the water-to-cement ratio. For mixes with SAPs, the type of SAP is given first (A or B), followed by the amount of SAP (0.5 or 1 m% by weight of cement). In some cases these codes end with an 'a' which means that additional water was used. This amount allows to derive the additional water-to-cement ratio $(w/c)_{add}$ and the total water-to-cement ratio $(w/c)_{tot}$. The effective water-to-cement ratio $(w/c)_{eff}$ is the water-to-cement ratio taking into account the amount of water absorbed by the SAPs during mixing. Mixes with additional water thus have an $(w/c)_{eff}$ of 0.50, similar to the reference R0.50.

Additionally, the effects of supplementary cementitious materials on the sorption properties were also investigated. The cement was partly replaced with fly ash and blast-furnace slag and the mixtures FA15, FA50, BFS15, BFS50 and BFS85 were studied. The water-to-binder ratio was hereby kept constant at 0.50.

3.1.1.2 Mortar

The reference mortar mixture with a water-to-cement ratio of 0.50 was composed of Portland cement (CEM I 52.5 N) (510 kg/m³), silica sand 0/2 (1530 kg/m³) and water (255 kg/m³). In other mixtures, a varying amount of SAP expressed as mass percentage (m%) of cement weight, a polycarboxylate superplasticizer (Glenium 51, conc. 35%) and/or additional water (as shown in Figure 3.1 and Table 3.2) were added on top. For mixtures without SAPs, the code (see Table 3.2) consists of the letter R (R for reference) followed by the water-to-cement ratio. For mixtures with SAPs, the type of SAP is given first (A or B), followed by the amount of SAP (0.5 or 1 m% by weight of cement). In some cases these codes end with an '*a*' which means that additional water was used and no superplasticizer. In Table 3.2, the amount of additional water is also given. This amount can be derived to the additional water-to-cement ratio $(w/c)_{add}$ and the total water-to-cement ratio $(w/c)_{tot}$. The effective water-to-cement ratio $(w/c)_{eff}$ is the water-to-cement ratio disregarding the amount of water absorbed by the SAPs during mixing. Mixtures with additional water thus have a $(w/c)_{eff}$ of 0.50, similar to the reference (R0.50) used. In mixtures without the '*a*', superplasticizer was added. Those mixtures but now without superplasticizer have codes ending with '*/s*'. All compositions are shown in Table 3.3.

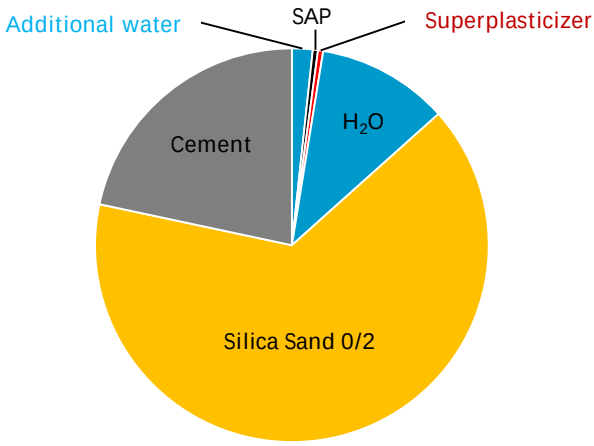

Figure 3.1. Schematic overview of the mortar composition based on the distribution of mass of material.

All SAPs were vacuum dried in a desiccator (10–50 mbar) prior to testing or mixing in the cement paste or mortar mixtures. Dry SAP particles were added to the cement and were first dry mixed to ensure a homogenous dispersion in the cement. After this dry mixing, the additional water was added together with the mixing water and superplasticizer.

Table 3.2. Studied mortar mixtures with their code, m% of SAP and corresponding water-to-cement ratios (additional, total and effective).

Code	*m% SAP [%]*	*$(w/c)_{add}$ [-]*	*$(w/c)_{tot}$ [-]*	*$(w/c)_{eff}$ [-]*
R0.50	0	0	0.5	0.5
R0.46	0	0	0.46	0.46
R0.41	0	0	0.41	0.41
R0.35	0	0	0.35	0.35
R0.46/s	0	0	0.46	0.46
R0.41/s	0	0	0.41	0.41
A0.5	0.5 SAP A	0	0.5	0.35
A0.5a	0.5 SAP A	0.15	0.65	0.5
A1	1 SAP A	0	0.5	0.2
A1a	1 SAP A	0.30	0.8	0.5
A0.5/s	0.5 SAP A	0	0.5	0.35
B0.5	0.5 SAP B	0	0.5	0.46
B0.5a	0.5 SAP B	0.04	0.54	0.5
B1	1 SAP B	0	0.5	0.41
B1a	1 SAP B	0.09	0.59	0.5
B0.5/s	0.5 SAP B	0	0.5	0.46
B1/s	1 SAP B	0	0.5	0.41

"'R' = reference, 'A' = SAP A, 'B' = SAP B, 'a' = additional water, '/s' = without superplasticizer, 'w/c' = water-to-cement

All compositions were mixed according to the standard NBN EN 196-1. The mixing procedure was as follows:

-30 – 0 s	Cement and SAPs (depending on the mixture composition) were dry mixed to ensure a homogeneous distribution of the SAPs in the mixture;
0 – 30 s	Immediately after contact of water (total amount with additional water depending on the mixture composition) with cement, mixing is started at 140 rpm and the superplasticizer (depending on the mixture composition) is added during the first 5 s;
30 – 60 s	Sand is steadily added;
60 – 90 s	The mixing speed is increased to 285 rpm;
90 – 180 s	During the first 30 s of a subsequent 90 s stop, the mortar is scraped from the walls and bottom part of the bowl;
180 – 240 s	Final mixing at 285 rpm.

Table 3.3. Studied mortar mixtures with their code, amount (kg/m³) of cement, sand, water, SAP, superplasticizer, additional water and corresponding flow value (mm).

Code	*Cement [kg/m³]*	Sand *[kg/m³]*	*Water [kg/m³]*	*SAP [kg/m³]*	Spl *[kg/m³]*	w_{add} *[kg/m³]*	*Flow [mm]*
R0.50	510	1530	255	0	0	0	210
R0.46	520.2	1560.6	239.3	0	1.0	0	210
R0.41	533.1	1599.4	218.6	0	3.1	0	220
R0.35	546.0	1638.0	191.1	0	12.8	0	200
R0.46/s	520.7	1562	239.5	0	0	0	180
R0.41/s	534.7	1604	219.2	0	0	0	120
A0.5	501.7	1505.2	250.9	2.5	13.8	0	200
A0.5a	475.3	1425.9	237.6	2.4	0	64.3	200
A1	499.5	1498.5	249.7	5.0	14.7	0	110
A1a	445.4	1336.2	222.7	4.5	0	119.6	210
A0.5/s	508.1	1524.4	254.1	2.5	0	0	110
B0.5	507.7	1523.0	253.8	2.5	1.0	0	210
B0.5a	498.2	1494.5	249.1	2.5	0	19.5	210
B1	504.7	1514.1	252.3	5.0	3.5	0	220
B1a	486.9	1460.6	243.4	4.9	0	38.2	220
B0.5/s	508.1	1524.4	254.1	2.5	0	0	195
B1/s	506.3	1518.9	253.1	5.1	0	0	140

Workability reflects the ease of mixing, transportation, placing and compaction to give a uniform material. There are some empirical tests to determine this ease. After mixing, the slump and flow can be measured following NBN EN 206-1; EN 12350-2 and EN 12350-5. The slump test provides a measure of the flow of concrete under its own weight. The flow test is analogous, but the material is spread by jolting a plate, on which the mortar is cast, 15 times at one jolt per second to receive a flow. The latter method was used in this research.

A comparison of the flow value of mixtures with and without SAPs can be used to reflect the absorption of the SAPs in the mortar mixture (Mechtcherine et al., 2009; Mönnig & Lura, 2007; Schröfl et al., 2012). The mixtures (Table 3.2, see amount of superplasticizer and additional water) were designed to have the same flow (210 mm). The amount of additional mixing water was increased in several mixtures with the same amount of SAP until a flow of 210 mm was reached. This mixture was then used. Subsequently, the same procedure was repeated for the different amounts and types of SAPs. In this way, the amount of mixing water absorbed by the SAPs could be determined. This amount of water uptake is 30.5 g mixing water/g SAP A and 8.9 g mixing water/g SAP B. The flow value was determined after 10 min of the initial contact of mixing water with the dry components, to ensure total absorption of mixing water by the SAPs. The SAP

swelling time, as determined by the vortex method (10 ± 2 s and 60 ± 5 for SAP A and SAP B, respectively), was fast enough for this assumption.

The flow characteristics were used to determine the amount of superplasticizer or additional water to be added. All mixtures had the same flow except the A1-mixture. In this mixture, the maximum amount of superplasticizer advised by the supplier BASF was added. Still, the flow was not as high as for the other mixtures (110 mm instead of 210 mm). The small size and high absorption capacity of SAP A have a negative impact on the workability of the mixture if high amounts of SAP A (1 m% or higher) are mixed in.

The fluid absorption of SAP in cement-based materials can also be measured by traditional air-void analysis. Due to swelling, SAP particles cause the formation of pores in cementitious materials. By measuring those voids, the absorption can be determined. Laustsen *et al.* (2010) used X-ray computed tomography to analyse SAP cavities in cementitious materials.

The amount of water absorbed by SAPs in the mortar mixture is less than in the filtered cement slurry (see Chapter 2). In filtered cement slurry the particles are able to take up fluids freely. Due to the smaller particle size of SAP A compared to SAP B, SAP A particles will swell more due to the higher relative access to mixing water even though their swelling time is a little bit higher compared to SAP B. This is related with the empirical formulation of (Brüdern & Mechtcherine, 2010), who also proposed that the absorption capacity of SAP in a concrete mix is about half of the absorption capacity in simulated pore solution. The difference between the absorption capacity in filtered cement slurry and in the mortar mix itself is due to the presence of solid particles which may restrict the swelling. Also, a different ion concentration may exist between filtered cement slurry and the pore fluid of the mortar mixture. Other factors may also influence the difference, for example the increase in workability by using the round-shaped fly ash.

The additional $(w/c)_{add}$, total $(w/c)_{tot}$ and effective $(w/c)_{eff}$ water-to-cement ratios are listed in Table 3.2. The $(w/c)_{add}$ ranged from 0.04 to 0.30. Schröfl *et al.* (2012) showed an additional water-to-cement ratio of 0.06 to 0.26 after comparing the workability of different mixtures with(out) SAPs (typically 0.3 m%) and with(out) additional water. They also stated that a too high absorptivity causes a too high increase in total water-to-cement ratio, changing the macroscopic mortar parameters. The mixture R0.20 (to compare it with the mixture A1) was not made in this research (if the highest recommended amount of superplasticizer would be added, the mixture would still not be workable enough), and the mixtures A1 and A1a were only used to compare the results with the mixtures B1 and B1a.

3.1.2 Setting properties

3.1.2.1 Determining the setting properties of cementitious materials

To determine the start and end of setting, a Vicat needle (EN 196-3) or a penetration resistance test (ASTM C403) can be used. These destructive tests are a little bit impractical as they are more discontinuous due to bigger time intervals in between measurements, even if they are automatized. By measuring the ultrasonic wave velocity through mortar, the start and end of setting can be determined too, but now in a non-destructive way and with a better precision (Robeyst et al., 2008). Changes in the ultrasonic pulse velocity permit to follow cement hydration and monitor the development of the microstructure at early age (Ye, 2003).

The system used in this research was the FreshCon system (Figure 3.2), an ultrasonic transmission system (Stuttgart University (Reinhardt & Grosse, 2004; Robeyst et al., 2009; Robeyst et al., 2008)) which can determine the wave velocity, the ultrasonic wave energy and the frequency content. The mortar container consisted of two poly(methyl methacrylate) (PMMA) plates tied together by four screws and spacers. The mould was a U-shaped rubber foam element with high damping properties. Also, the PMMA walls were large enough to prevent the waves from travelling around the sample. A contact agent (multi-purpose silicon grease) was used between the sensor and the protective wear cap to prevent the creation of air bubbles. The same grease was used between the protective wear cap and the mortar. The sample volume was about 35 cm^3 (Reinhardt & Grosse, 2004) and the mortar was covered with plastic foil during ultrasonic measurements to avoid water evaporation and thus shrinkage of the mortar.

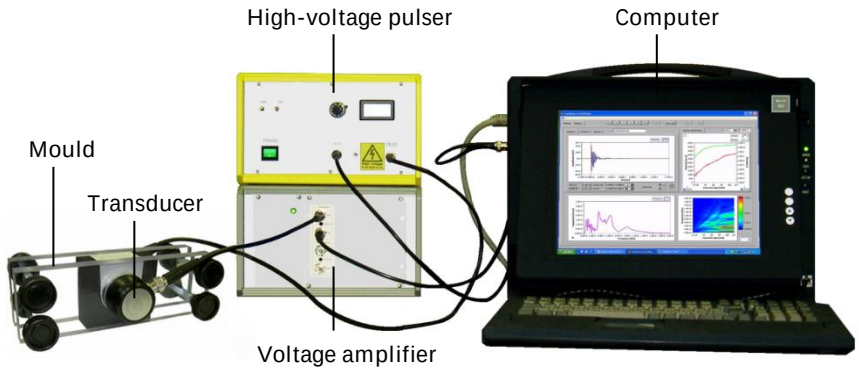

Figure 3.2. Schematic visualization of the ultrasonic equipment (FreshCon).

The ultrasonic wave velocity was measured through the opposite transducers at both sides of the mortar container. Every 5 min, an electric pulse was sent by the data-acquisition card from the computer through the amplifier (450 V for mortar specimens) to the piezoelectric transmitter generating the ultrasonic wave.

A semi-adiabatic calorimeter (Langavant) was coupled to the equipment. The change in temperature with time of hydration of the studied sample, the temperature of a completely hydrated reference sample in the calorimeter and the

temperature of the ambient environment were recorded by thermocouples. In this way, both ultrasonic and calorimetric measurements were simultaneously conducted and the temperature changes in the bulk material were investigated. In this test, the temperature rise of the hydrating sample in a heat-insulated flask was continuously measured and the cumulative heat production Q could be calculated following the method described in (Robeyst et al., 2009). The heat production rate q is the derivative of the cumulative heat production Q.

With the ultrasonic method, the initial and final setting time could be determined. The initial set states the time at which the plasticity and workability of the mixture is lost. The final set is the time at which the mixture has become rigid and solid. The equipment measures the percolation threshold, when a path of connected particles is formed between both transducers. As hydration proceeds, more bonds between the particles are made and clusters are formed. This goes on until the cement particles are connected firmly (Soroka, 1993).

The start and end of setting can be determined by comparing the acquired velocity and energy graphs. The boundaries for the start of setting used in literature for mortar samples are 800-980 m/s (Lee et al., 2004) and 1500 m/s (Kamada et al., 2005; Trtnik et al., 2008). For the end of setting respectively 1200-1400 m/s and 1750-1850 m/s are used. Also, Trtnik *et al.* (2008) and Robeyst *et al.* (2008) proposed that the inflection point (maximum of the first derivative of the velocity curve) indicates the start of an increase in penetration resistance. In this research, the start of setting was determined as the inflection point in the velocity graph and the time at which the energy ratio E/E_{ref} of 0.01 was reached in the energy spectrum (Robeyst et al., 2009) (in which E is the energy of a wave through the mortar and E_{ref} the energy through the container filled with water and with the same path length). The end of setting was determined as the time at which E/E_{ref} became 0.07 (Robeyst et al., 2009).

The penetration resistance test (ASTM C403) was used to check the FreshCon measurements. In the latter test, the start of setting is determined as the time at which the penetration resistance amounts to 3.5 MPa and the end of setting to 27.6 MPa. The specimens used for the ASTM C403 test followed the same temperature history as the specimens for ultrasonic pulse velocity measurements. They do have the same maturity at the same hydration time.

3.1.2.2 Influences on the setting properties

The flow characteristics were used to determine the amount of superplasticizer and additional water to be added (Table 3.3). All mixtures had the same flow except the A1-mixture (110 mm instead of 210 mm). In this A1-mixture, the maximum amount of superplasticizer advised by the supplier BASF was added. The workability of the mixtures without superplasticizer (/s) was also lower compared to the reference flow of 210 mm.

The amount of water absorbed by SAPs in the mortar mixture is less than in the filtered cement slurry (see Chapter 2), which is less than the value in demineralized water. The latter is due to the charge-screening effect and strong complexation (Hancock & Martell, 1989). The former difference is due to the fact that in filtered cement slurry the particles are able to take up fluids freely. Due to

the smaller particle size of SAP A compared to SAP B, SAP A particles will swell more due to the higher relative access to mixing water, i.e. the available surface area is higher. Also, solid particles may restrict the swelling and a different ion concentration may exist between filtered cement slurry and the actual pore fluid of the mortar mixture due to dissolution of atoms from the sand fraction for example. The difference is in correspondence with the empirical formulation of (Brüdern & Mechtcherine, 2010), who also proposed that the absorption capacity of SAP in a concrete mix is about half of the absorption capacity in simulated pore solution. They also used a smaller SAP like the SAP A type.

Figure 3.3a shows the wave velocity through the fresh mixture (R0.50). First, the velocity is low, and this corresponds to the dormant period where the velocity is merely a function of the air content in the fluid sample. The point where the velocity starts to increase is the end of the dormant period. At this point, a percolation cluster of solid particles is formed and this connectivity causes the rapid increase in velocity. The velocity will keep increasing due to further connections and pore filling by further hydration and finally, the velocity will reach an asymptotic value.

The inflection point in the graph (●) represents the initial setting time and this time is in good accordance to the time at which a penetration resistance of 3.5 MPa according to ASTM C403 (|) occurred. The inflection point states a more gradual increase in the velocity due to the start of setting. The inflection point of the velocity graph was found to be 1532 ± 43 m/s. This is in good accordance to 1500 m/s (Kamada et al., 2005; Trtnik et al., 2008). The time at which a penetration resistance of 27.6 MPa (¦) was reached, corresponded with a wave velocity of 2526 ± 83 m/s. This value is higher than the 1850 m/s boundary in (Kamada et al., 2005; Trtnik et al., 2008).

An analogous interpretation can be made based on the energy ratio shown in Figure 3.3b. The thresholds of E/E_{ref} = 0.01 (●) and 0.07 (○) are represented on the energy ratio graph. A very good correspondence exists between the energy-ratio thresholds and the penetration resistance thresholds = 3.5 (|) and 27.6 MPa (¦). The energy of the transmitted wave increases in time with further hydration of the mixture. When the mixture is hardened, the energy ratio reaches an asymptotic value.

The temperature developed during setting was recorded during the test and is shown in Figure 3.3c. The maximum in the semi-adiabatic temperature graph (Sample container) is reached after setting. In this graph, also two reference temperatures are shown. These are the temperature of the air-conditioned room and the reference sample under semi-adiabatic conditions.

The results of the wave velocity recordings of SAP A mixtures are shown in Figure 3.4a. The addition of SAPs with superplasticizer and without additional water (A0.5 and A1) postpones the setting as the curves are shifted to the right. The mixtures with SAPs and additional water (A0.5a and A1a) are in good correspondence with the reference mixture R0.50, having the same $(w/c)_{eff}$.

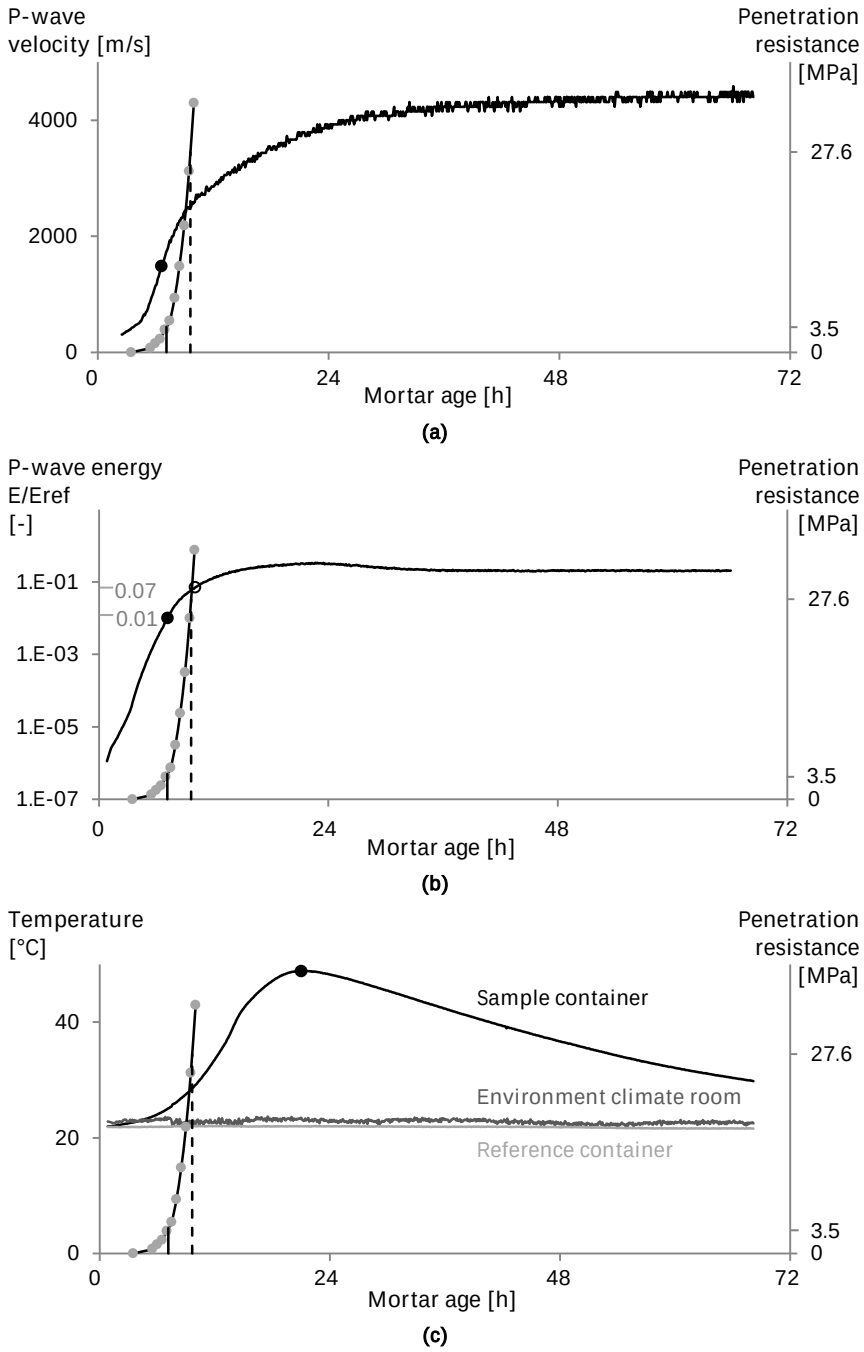

Figure 3.3. Comparison between velocity **(a)** / energy ratio **(b)** / temperature **(c)** graph (left axis) and penetration resistance of mortar mixture R0.50 (right axis, •). The inflection point (●) on the velocity graph, the thresholds of E/E_{ref} = 0.01 (●) and 0.07 (○) on the energy ratio graph, the maximum temperature (●) and the initial (|) and final (¦) setting times according to ASTM C403 are indicated.

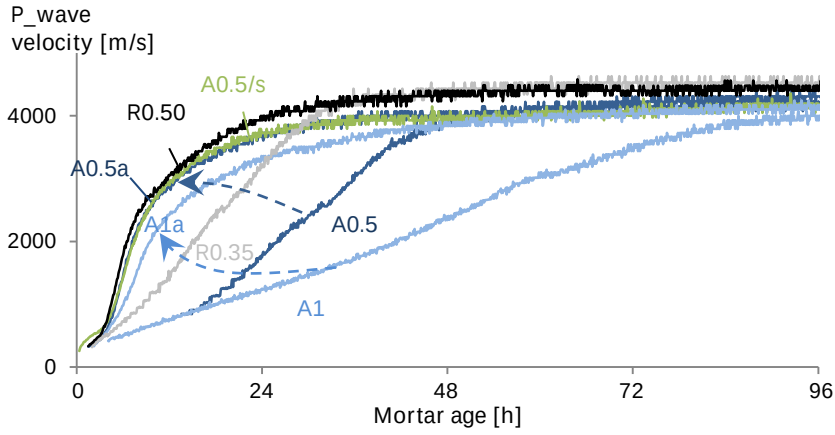

(a)

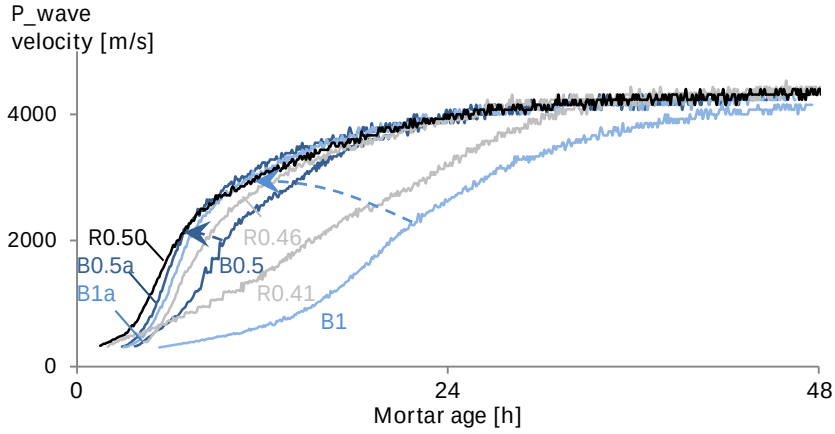

(b)

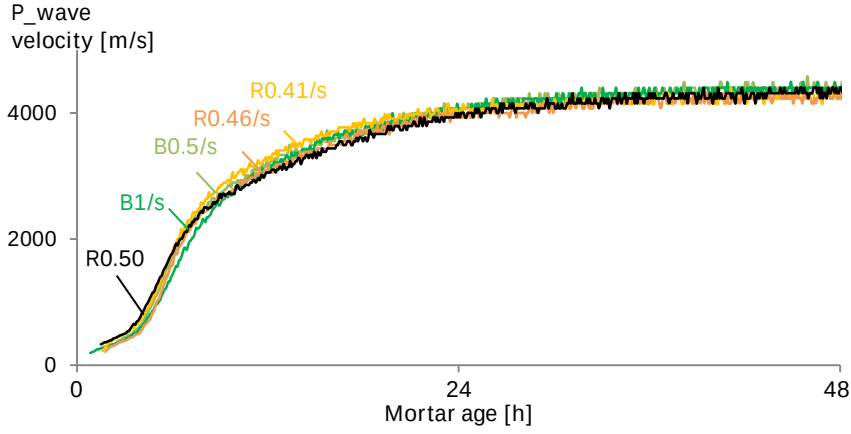

(c)

Figure 3.4. Velocity graphs of SAP A **(a)** and SAP B mixtures with superplasticizer **(b)** and without superplasticizer **(c)**, with appropriate references.

Additional water in mixtures with SAPs, to compensate for the mixing water uptake by SAP, thus gives approximately the same setting properties as the reference mixture R0.50. SAPs may have an effect on setting, but that would be through some monomers leaching out from the polymer. This effect on setting would be seen both with and without additional water. As this is not the case, the SAPs seem not to influence the setting properties.

After setting, the final velocity in the graphs is slightly different. An increase in m% of SAP lowers the final velocity. This may be due to a higher amount of macro pores. As the wave needs to travel around the voids, the velocity is lower. There is no noticeable difference between the reference samples. The SAPs thus are responsible for the decrease in final velocity after setting. The ultrasonic pulse velocity will also depend on the mixture composition, including the amount of aggregates in the unit volume. This explains the different end values of the ultrasonic pulse velocity curves. The sand content (see Table 3.3) namely shifts the maximum of the velocity (Aggelis & Philippidis, 2004).

Figure 3.4b gives the results for the SAP B mixtures. Again, the same trends are found. The addition of superplasticizer also postpones setting of the mixture. Additional water, however, shifts the setting process towards the reference mixture R0.50. Reference mixtures harden slightly faster compared to the corresponding mixtures with SAPs and additional water but leaching out of monomers in the SAPs is unlikely.

Again, reference mixtures tend to the same final velocity and the final velocity is lowered due to the inclusion of SAP particles in the mixture (the formation of macro pores) and the slightly different sand content.

Mixtures without superplasticizer seem to show the same setting properties compared to the reference R0.50 mixture (Figure 3.4c). The small shift in setting in the B1/s mixture may be due to internal curing during hardening. The end values are alike due to approximately the same amount of sand fraction in all mixtures.

The time of initial setting, final setting and the time at which the temperature reaches a maximum value, are shown in Figure 3.5 for all mixtures. In the reference mixtures, the setting is postponed slightly when a lower water-to-cement ratio is used, due the higher amount of superplasticizer. If no superplasticizer is used, the setting properties are alike. If superplasticizer is used in SAP mixtures, the setting is also postponed several hours. However, if additional water is added instead of superplasticizer, the setting is shifted back and becomes similar to the reference mixture R0.50. Additional water should therefore be used to limit the effect of superplasticizer on the hardening properties.

SAP B mixtures show less influence on the setting compared to SAP A mixtures, due to the lower swelling capacity and thus the lower amount of superplasticizer needed. The reason for the difference is the smaller particle size leading to more access to the mixing water of SAP A particles. This causes a higher water uptake during mixing. The A1 mixture shows poor hardening and was also the least workable even when the maximum amount of superplasticizer was added. If no additional water is added, the SAP B mixtures would be better compared to SAP A mixtures as a higher amount of SAP can be added and the setting properties are less impaired due to the use of superplasticizer.

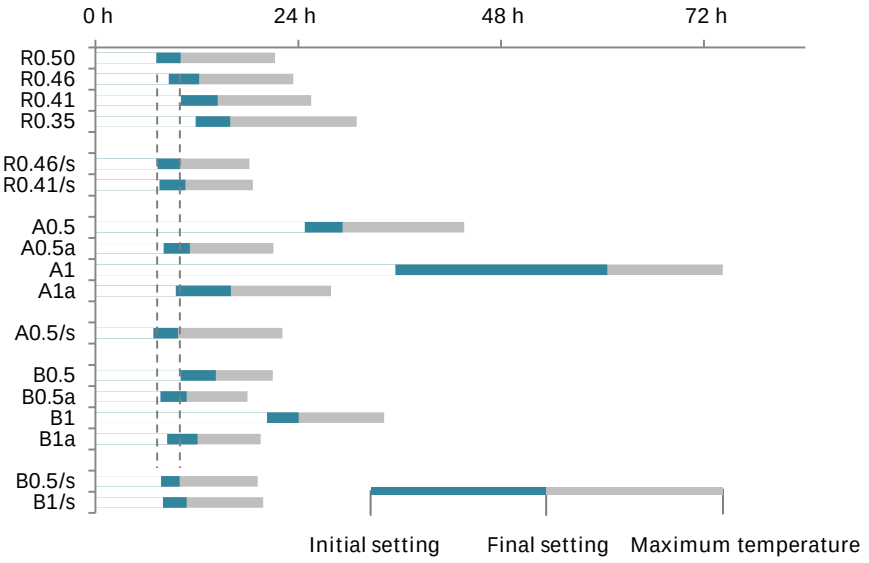

Figure 3.5. Time [h] of initial setting (E/E_{ref} = 0.01), final setting (E/E_{ref} = 0.07) and maximum temperature for all studied mixtures. The shown boundaries (dashed lines) are the initial and final setting time for the R0.50 mixture.

There is a good correlation between initial setting determined by the 0.01 criterion in the energy curve, the initial setting determined by the 3.5 MPa criterion in the penetration test, and the inflection point in the velocity graph, as shown in Figure 3.6. There is a slight difference in correlation if the inflection point is used for mixtures with the shortest time of initial setting after casting. The time at which the inflection point occurs, comes slightly earlier than the two other criteria. If the energy and penetration criteria are compared, the setting times are in perfect agreement with each other.

The correlation for mortar mixtures between the final setting determined by penetration resistance tests and by E/E_{ref} = 0.07 is shown in Figure 3.7. Again, there is a good correlation and this proves the applicability of the ultrasonic equipment to determine the initial and final setting.

Figure 3.8 shows the cumulative heat production Q and heat production rate q of all studied mixtures. Generally, one distinguishable peak in heat production rate can be seen for every mixture, followed by a shoulder attributed to the consumption of calcium sulphate. The heat production peak occurred later in case of mixtures with a lower water-to-cement ratio, due to the higher amount of superplasticizer used. If SAPs are mixed in, the $(w/c)_{eff}$ is lower compared to the R0.50 mixture, leading to a postponed heat production peak due to the use of approximately the same amount of superplasticizer. Additional water stimulates early hydration and the heat production peak occurred earlier. The swollen SAPs could hereby serve as a nucleation site for the precipitation of hydration products. Due to the inclusion of swollen saturated SAPs, the peaks of heat production are less intense in mixtures containing SAPs. This only seems a function of the amount

of SAPs and does not depend on whether additional water is used or not. SAP B shows less influence on the heat production compared to SAP A, but this is again mainly due to the amount of superplasticizer used.

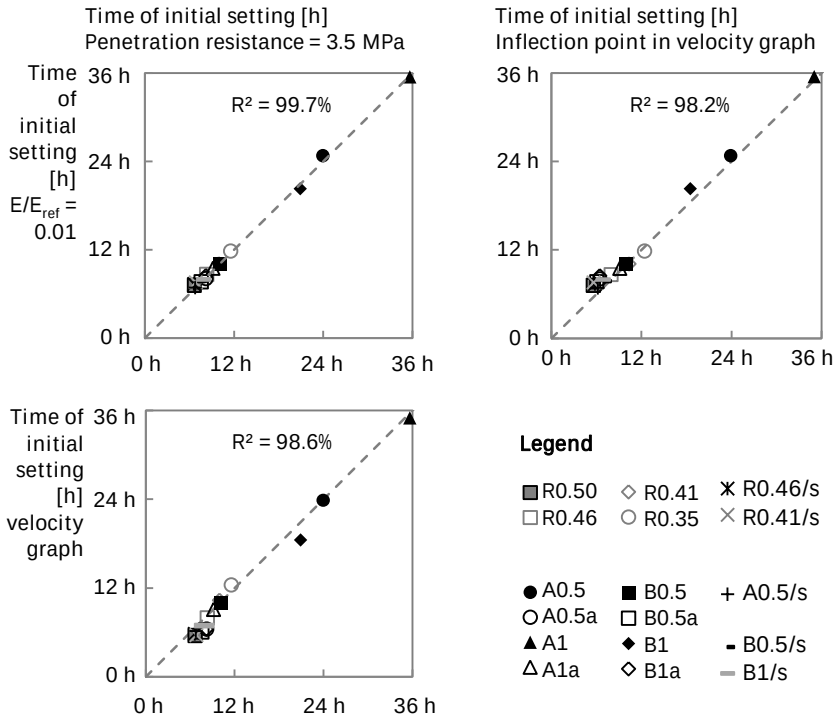

Figure 3.6. Correlation for mortar mixtures between the initial setting determined by penetration resistance tests, by the E/E$_{ref}$ = 0.01 criterion and by the inflection point in the velocity graph.

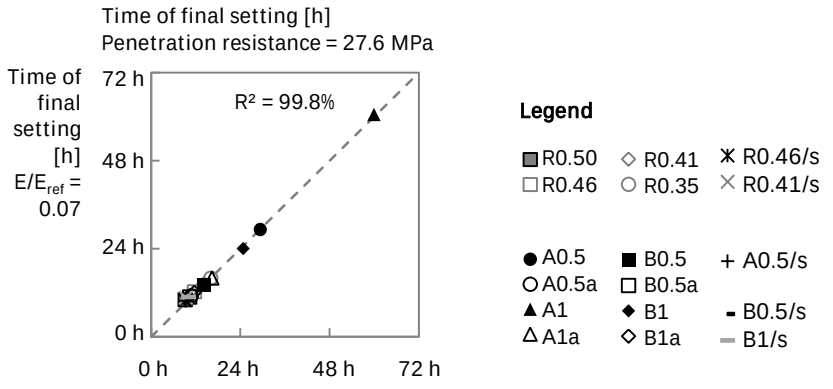

Figure 3.7. Correlation for mortar mixtures between the final setting determined by penetration resistance tests and by the E/E$_{ref}$ = 0.07 criterion.

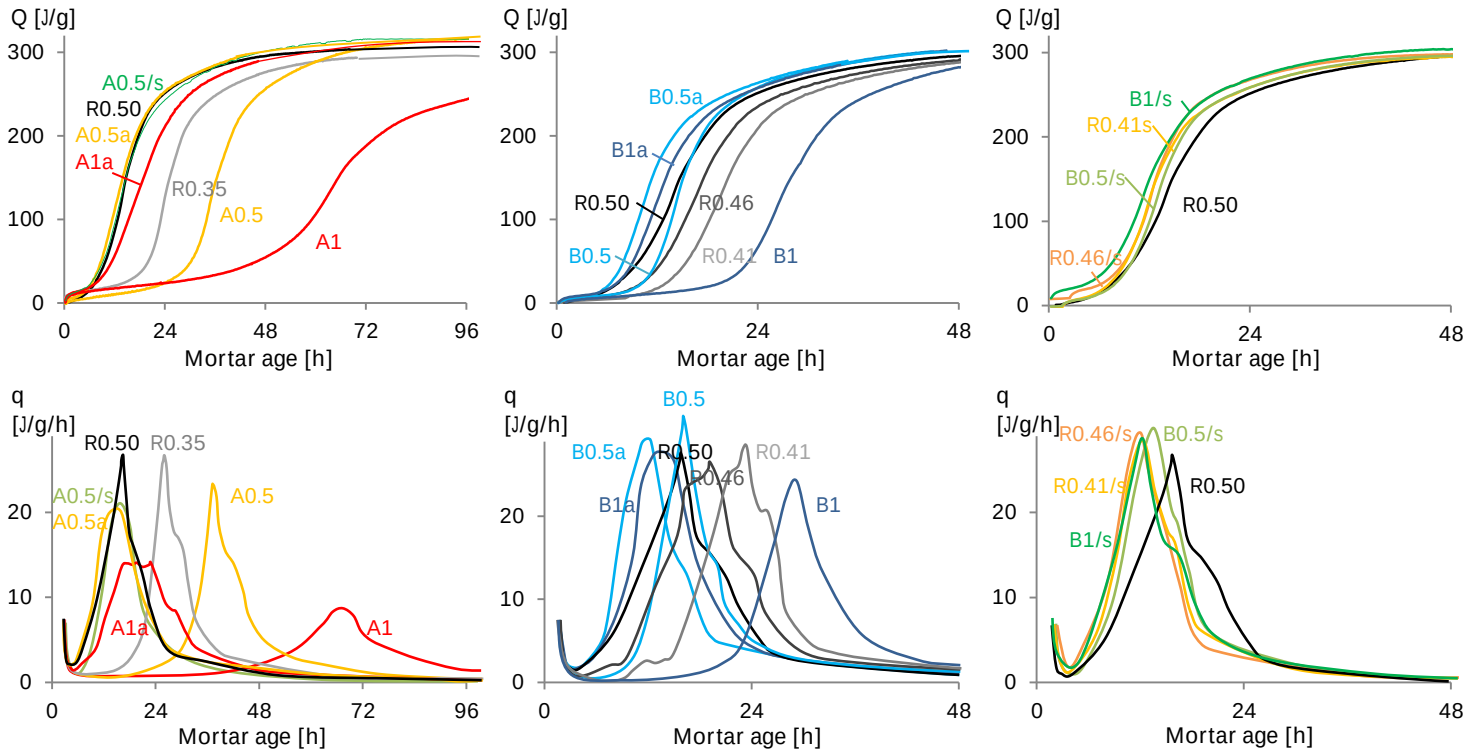

Figure 3.8. The cumulative heat production [J/g binder] versus equivalent mortar age at 20°C under semi-adiabatic conditions (upper figures) and heat production rate [J/g binder/h] (lower figures) for all studied mixtures.

3.1.3 Superabsorbent polymers and autogenous strain

3.1.3.1 General considerations

When fresh mortar is subjected to drying, contraction may take place. This plastic shrinkage may cause cracking during the first few hours after casting (Soroka, 1993). Other forms of shrinkage include autogenous shrinkage as a result of cement hydration, thermally-induced shrinkage and drying shrinkage due to the loss of water to the surroundings and shrinkage due to carbonation. As cement reacts with water hydration products will precipitate in the water-filled spaces between the solid particles in the cementitious material. The water in the remaining small capillaries forms menisci and exerts hydrostatic tension forces. These capillary forces reduce the distance between the solid particles, leading to autogenous shrinkage. Chemical and autogenous shrinkage are theoretically shown in Figure 3.9.

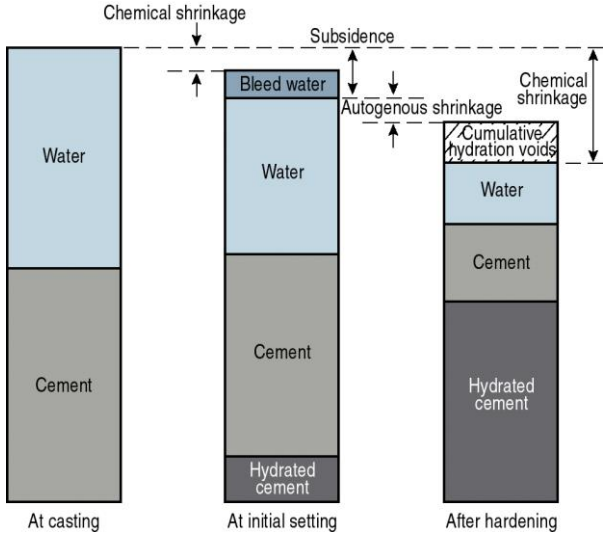

Figure 3.9. Definition of chemical and autogenous shrinkage.

Autogenous shrinkage may result in micro- and macro-cracks which impair strength, durability and aesthetics, especially in mixtures with a low water-to-binder ratio. During hardening, the internal relative humidity (RH) will drop in these mixtures and self-desiccation will occur if no external water source is present. This will lead to self-desiccation shrinkage. The cracks interconnect flow paths for water and gases, possibly containing harmful substances (Wang et al., 1997). For example, the ingress of water could induce steel corrosion, frost attack, chemical attack and internal expansive reactions, endangering the durability.

One should mitigate autogenous shrinkage to reduce the amount of shrinkage cracks to increase the service life of a structure. Internal curing is the provision of water within the specimens to maintain the internal RH during self-desiccation and it can mitigate plastic and autogenous shrinkage. Several materials can be used to promote internal curing in concrete: lightweight aggregates, pumice, expanded

clay, and superabsorbent polymers (SAPs) amongst others (Bentz & Weiss, 2011; Jensen & Lura, 2006). The application of SAPs for this purpose proved to be promising as autogenous shrinkage was reduced and even counteracted in time (Assmann, 2013; Craeye & De Schutter, 2006; Igarashi & Watanabe, 2006; Jensen & Hansen, 2001, 2002; Mechtcherine et al., 2009; Mechtcherine et al., 2014).

During preparation of a concrete mixture, the SAPs will take up mixing water. The SAPs will thus form water-filled inclusions, useful for internal curing (Mechtcherine et al., 2009). The water released due to self-desiccation during cement hydration can be used for further hydration and reduction of the autogenous shrinkage (Craeye & De Schutter, 2006). The water present in the SAP will hereby be released into the cementitious matrix due to the imminent drop in relative humidity. Due to this water release, the internal relative humidity is maintained. The SAP particles shrink and an empty macro pore remains as shown by means of neutron tomography measurements (Trtik et al., 2010).

In systems with a water-to-cement ratio of 0.3 complete hydration is not possible. The hydration stops at a minimum porosity of the cement gel (26-28%). The capillary water reacts until it is consumed and the cement starts to react with the harder bound gel water, causing the relative humidity to decrease and the cement paste to self-desiccate. With an additional (entrained) water-to-cement ratio of 0.054 through pre-described water-filled SAP inclusions, internal curing takes over and the self-desiccation is mitigated (Jensen & Hansen, 2001; Powers & Brownyard, 1948). There are less gas-filled micro pores and the degree of hydration is higher. Compared to a system with a water-to-cement ratio of 0.35, the maximum degree of hydration is the same and the overall porosity is the same as well. The difference is that in the SAP-entrained system, macro pores are more likely than the finer capillary pores present in the system without internal curing.

Brüdern and Mechtcherine (2010) showed (in uncracked concrete) internal curing due to the presence of SAP and a decrease of the autogenous shrinkage and self-desiccation by the gradual release of water from the SAP particles. Jensen and Hansen (2002) measured up to 3700 microstrains (µm/m) of shrinkage in reference cement paste in a period of 3 weeks. When SAPs were used, there was a successful mitigation of shrinkage and even some expansion. Igarashi and Wanatabe (2006) showed successful mitigation of shrinkage with an amount of 0.7% SAPs by mass of cement in a paste with a water-to-cement ratio of 0.25. Mönnig (2005) visualised the densification of the matrix around a SAP particle due to the larger amount of water available in time. The amount of entrained water that is needed to promote the internal curing effectively is 0.18 times the water-to-cement ratio (Jensen & Hansen, 2001). This entrained water is additionally added to the cementitious mix and held by the SAPs during mixing (Jensen & Hansen, 2001). The determination of this amount is based on the theory of Powers and Brownyard (Powers & Brownyard, 1948). The ideal amount of superabsorbent polymers to provide internal curing will be applied in this research. This amount will be based on the theoretical amount of entrained water needed for internal curing (Jensen & Hansen, 2001, 2002; Powers & Brownyard, 1948).

All abovementioned results were obtained for concrete made with ordinary Portland cement with or without silica fume (Jensen & Hansen, 2002). As nowadays

concrete structures are frequently made with binders containing other supplementary cementitious materials (SCM) like fly ash and blast-furnace slag, the effect of SAPs on the autogenous shrinkage results of those mixtures also needs to be studied in detail. Publications describing the effects of SAPs on internal curing and shrinkage mitigation for concrete with these SCMs, are scarce.

The cement clinker and supplementary cementitious materials hydrate simultaneously and influence one another. The concrete composition and pore fluid affect the overall hydration and pozzolanic reactions (by fly ash) are known to occur later as pozzolans need to react with the calcium hydroxide formed in cement hydration. Yan and Chen (2014) found that for mixtures with a water-to-binder ratio of 0.30 a reference with OPC (at 192 days) showed 320 µm/m shrinkage strain, FA15 (with 85% of cement and 15% of fly ash in the binder) 250 µm/m shrinkage strain, FA30 220 µm/m shrinkage strain and FA45 150 µm/m shrinkage strain. As the degree of hydration of fly ash increases, the autogenous shrinkage also increased in time (Termkhajornkit et al., 2005). De la Varga *et al.* (2012) found that autogenous shrinkage in high volume fly ash systems is lower than in non-fly ash mortar due to the fact that the fly ash systems contained a lower amount of cement, so that the initial reaction rate and water consumption was lower. Fly ash starts to react at later ages and consequently less autogenous shrinkage is monitored at early ages. At later ages, the rate of shrinkage is higher in fly ash mortars compared to pure cement systems. De la Varga *et al.* found 200 µm/m shrinkage strain for a mixture with cement and a water-to-binder ratio of 0.30, 100 µm/m shrinkage strain for FA40 (fly ash), 50 µm/m shrinkage strain for FA60, 20 µm/m expansion strain for FA60IC (internal curing) and 60 µm/m expansion strain for FA40IC at an age of 14 days. In the latter research, internal curing by means of lightweight aggregates proved to be promising to mitigate autogenous shrinkage in fly ash systems. However, the influence of the internal curing in mixtures containing fly ash should also be investigated at later ages than 14 days. This data is lacking in literature. Data from 14 days onwards would be very useful as the net overall shrinkage for fly ash systems may then exceed the one for the pure cement mixtures.

Blast-furnace slag is another commonly used addition in the building industry. Blast-furnace slag mixtures showed greater autogenous shrinkage than ordinary concrete in the research of (Lee et al., 2006). The higher the blast-furnace slag amount, the greater the autogenous shrinkage. They found 310 µm/m shrinkage strain for a cement mixture with a water-to-binder ratio of 0.32, 380 µm/m shrinkage strain for 32BFS30 (70% of cement and 30% of blast-furnace slag with a water-to-binder ratio of 0.32) and 420 µm/m shrinkage strain for 32BFS50 at an age of 200 days. Also, concrete made with BFS showed higher shrinkage in the first days than concrete made with Portland cement (Lura et al., 2001). Lura *et al.* (2001) addressed this phenomenon to the supposed denser structure of the BFS cement paste which showed smaller pores. These smaller pores lead to higher capillary forces for self-desiccation, increasing the autogenous shrinkage. One of the few studies found in literature, by (Wyrzykowski & Lura, 2014), focused on the effect of internal curing on ordinary Portland cement and blast-furnace-slag-blended cement pastes. They found for blast-furnace-slag-blended cement mixtures, that a

part of the autogenous shrinkage was eliminated due to internal curing, but the remaining shrinkage was very high. The shrinkage was approximately 1400 µm/m shrinkage strain for BFSC-REF (blast-furnace slag blended cement mixture), 600 µm/m shrinkage strain for BFSC-SAP (mixture with BFS and internal curing), 200 µm/m shrinkage strain for OPC-REF (ordinary Portland cement mixture) and 50 µm/m shrinkage strain for OPC-SAP at an age of 7 days. Results from 7 days onwards are again missing in literature.

In the following paragraph, the setting of mixtures with varying amounts of FA or BFS is studied by means of the Vicat needle test and the autogenous strain is monitored in time. Both manual and automated tests are hereby used to study the effects of internal curing by means of superabsorbent polymers on the early age and later age autogenous shrinkage properties.

3.1.3.2 Determining the autogenous shrinkage

To determine the time of final setting, the Vicat needle test following the Standard ASTM C191 – 08 was used (Method A: Reference Test Method using the manually operated Vicat apparatus). All components were stored at a temperature of 20 ± 1°C for at least one day before testing. Subsequently, the cement paste was made and poured into the sample containers. By periodically penetrating the thin cement paste with the 1-mm Vicat needle, the time between initial contact of cement and water and the time at which the needle did not leave a circular impression in the paste surface, was recorded and used as the time of final setting. This time was then used as the start of the autogenous shrinkage measurements, described in the next paragraph. The Vicat test was performed in triplicate for a better estimation of the time of final setting.

To measure the autogenous strain at constant temperature (20 ± 1°C) from the time of final setting until a specified age, the Standard ASTM C 1698 – 09 was followed.

First, a base for supporting a corrugated tube was mounted to a vibration table. Freshly mixed paste was poured in a corrugated mould which had little resistance to length change of the specimen and which was then sealed. The corrugated plastic tubes were made of low-density polyethylene with a length of 420 ± 5 mm and a diameter of 29 ± 0.5 mm. The wall thickness was 0.5 ± 0.2 mm. From the final setting onwards, the length of the specimen was monitored using a dilatometer at regular time intervals (Figure 3.10). Manual test moulds were tightly closed with two end plugs with a length of 19 ± 0.5 mm.

During the manual tests, the specimens were kept 30 mm minimally separated from other specimens to allow dispersion of the heat of hydration. A sliced tube was made to ensure a safe handling of all specimens and to limit mechanical disturbance during manual measurements. The sliced tube proved to be useful for this purpose and the manual tests were comparable to the automated tests, as the results will show later-on. The specimens were measured every half hour for the first 12 hours and then every hour for the subsequent 24 hours. Then, specimens were measured at least twice every day.

Figure 3.10. Specimens and sliced tube used for the manual autogenous shrinkage tests.

For the automated tests another type of end closures were used to seal the specimen at both ends. Specimens were placed in a polyalkylene-glycol thermobath which was held at 20°C during the whole testing period (Figure 3.11).

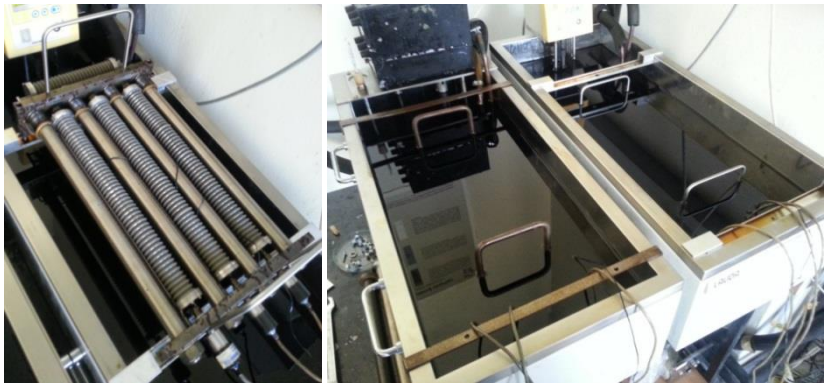

Figure 3.11. Specimens used for the automated autogenous shrinkage tests and automated autogenous shrinkage tests in a polyalkylene-glycol thermobath at 20°C.

The internal temperature was also monitored over time for the reference specimens by placing a thermocouple in the interior of separate specimens to record the hydration temperature (Figure 3.12). The short specimen is representative of the longer ones as the length is still approximately six times the diameter. The temperature curves are shown in Figure 3.13. The maximum temperature increase in the centre of the specimen was 0.6°C in the automated tests where the hydration temperature did not show a pronounced influence on the autogenous shrinkage values. The internal temperature increase in the manually tested specimens was higher than the internal temperature increase of specimens in the automated test, where all hydration heat is effectively dissipated in the surrounding, circulating fluid. As a consequence, the hydration rate in the manual specimens was higher and the hardening occurred faster. The autogenous shrinkage thus happened earlier in time. Nevertheless, the small additional peak of 3.5°C seemed to have little influence on the overall measurements (leading to a

temporary 70 μm/m strain and a time shift or acceleration of 1.5 hours using an activation energy of 33.5 kJ/mol) and the error was calculated to be approximately 1%, lower than the measuring error of the test, namely approximately 3%. So, the increase in temperature did not have a significant effect and all results were comparable.

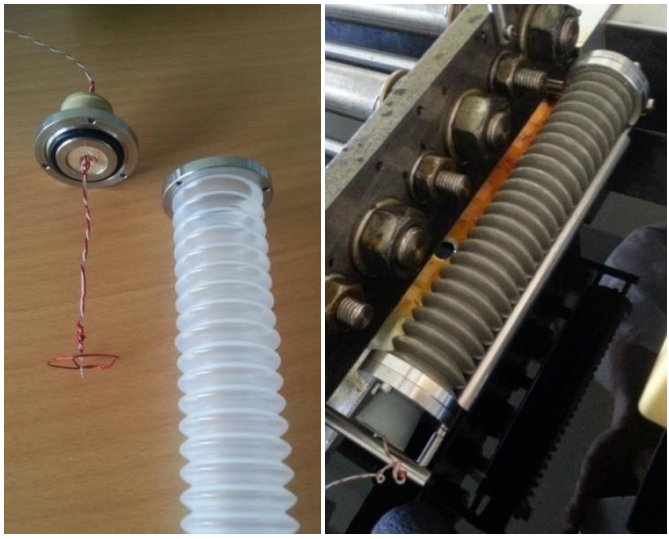

Figure 3.12. Thermocouple and separate specimen used for the internal temperature measurements.

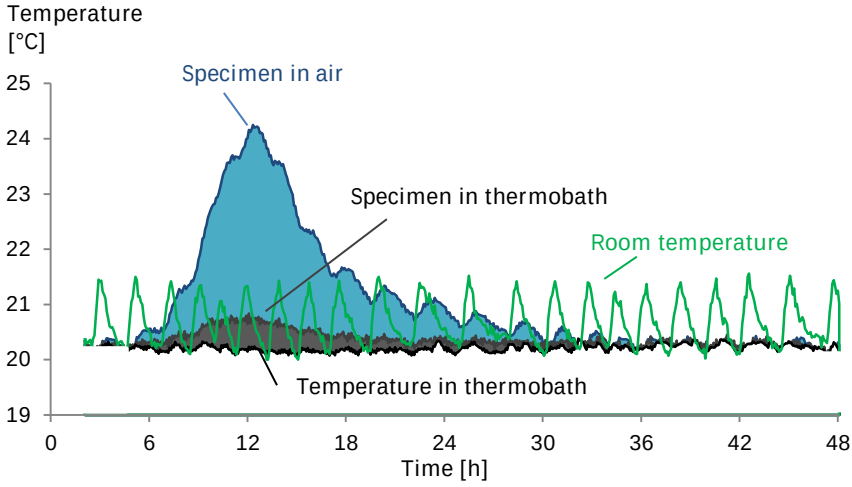

Figure 3.13. Measured temperature profiles during a manual and automated test, together with the room temperature and the temperature in the thermobath.

3.1.3.3 Influences on the autogenous shrinkage properties

Figure 3.14 shows the delay in setting caused by fly ash and blast-furnace slag systems as a function of the amount of supplementary cementitious materials relative to the amount of cement. This is due to the pozzolanic reaction which occurs at later ages due to the consumption of or activation by $Ca(OH)_2$, which needs to be formed from the cement hydration mechanism. The time of final setting was used as a starting point for the autogenous shrinkage measurements and the length used in the automated measurements is the length at final setting. As the Vicat needle test is unreliable around this point, one should be careful comparing the results as the rate of shrinkage is very high around this point of final set. Therefore, the test was done in triplicate and the results coincide within a quarter of an hour.

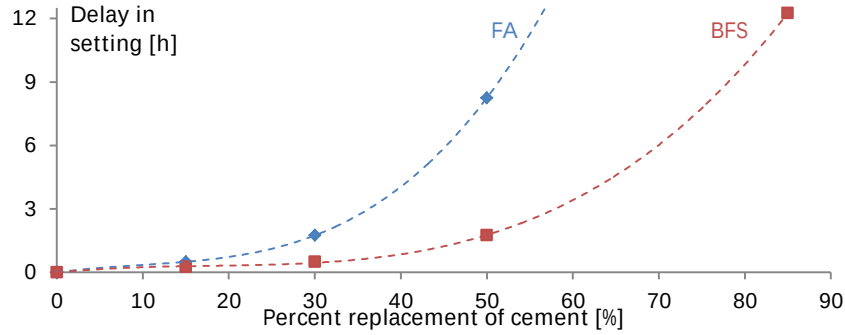

Figure 3.14. Delay in setting of the fly ash and blast-furnace slag systems as a function of the amount of supplementary cementitious materials replacement.

Figure 3.15a shows the results of the mixtures with a water-to-binder ratio of 0.30 and 0.354, and mixtures with a water-to-binder ratio of 0.30 and superabsorbent polymers for internal curing. Figure 3.15b visualizes a close-up of the results up to 7 days of age. Just after setting, there is a small expansion. This can be due to the re-absorption of bleeding water in the mixture or due to the crystallization pressure of calcium hydroxide (Sant et al., 2011). The effect was not prominent and almost no bleeding occurred.

There is less shrinkage strain in a mixture with a higher water-to-binder ratio (R0.354 compared to R0.30); which confirms that autogenous shrinkage strain is typical a more important problem in mixtures with a low water-to-binder ratio. This is due to the denser matrix formed in mixtures with a lower water-to-binder ratio, increasing the hydrostatic tension forces (capillary forces) and leading to the increase in self-desiccation and autogenous shrinkage. When using a certain amount of SAPs to include an entrained water-to-binder content of 0.027 (A_0.027), there is a small mitigation of autogenous shrinkage, but the overall shrinkage is still evident. When the theoretical ideal amount of SAPs for internal curing is added ((W/B_e)=0.054; sample A_e), autogenous shrinkage is completely mitigated and a expansion is observed after day 1. An even higher amount of SAP ($(W/B)_e$=0.081; A_0.081) leads to approximately the same curve.

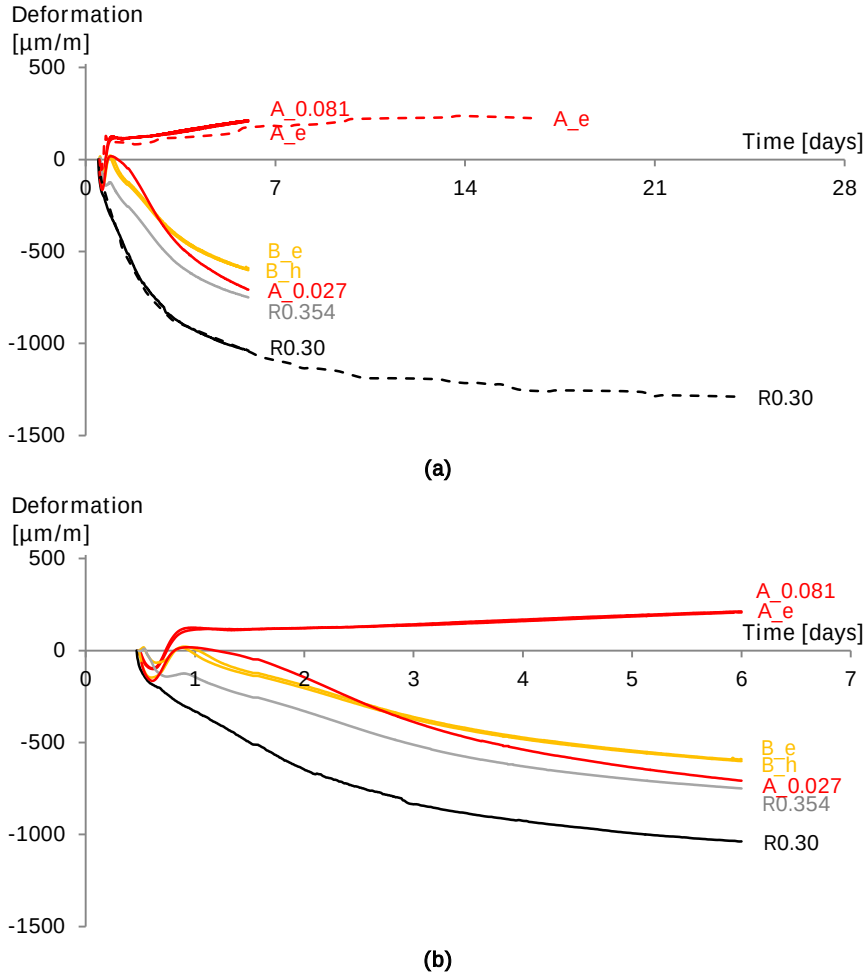

Figure 3.15. Autogenous strain [µm/m] for cement paste mixtures with and without entrained water by superabsorbent polymers, over 28 days **(a)** and 7 days **(b)**.
(--- = manual test curves; — = automated test curves)

There are differences in the effectiveness of SAPs for the mitigation of autogenous shrinkage. In some cases, the water may be released too fast to the cementitious matrix, or is not given to the matrix fast enough. This was possibly observed when using the bigger SAP B compared to SAP A. SAP A was able to eliminate autogenous shrinkage, but this was not the case for SAP B. Even though $(W/B)_e$=0.054, independent of the added amount autogenous shrinkage is still prominent (B_e and B_h). This can be explained by the too slow and only partial release of additional water to the cementitious matrix from SAP B. The curves are in close correspondence with the reference curve with a water-to-binder ratio of 0.354. Microscopic analysis showed that the macro pores did possess the expected size due to water retaining, so the additional water seemed to be held too long to ideally mitigate autogenous shrinkage. Also, if the polymer in the swollen state is

too large, it will not be able to supply all sites of the cement paste with curing water during hydration. Water close to the surface of the polymers is lost rapidly but water closer to the core must overcome more side-chains in the polymer, which interact with the water molecules through van-der-Waals forces. It is also important to consider the overall inter-particle spacing and water transport as only the cement paste within approximately 2 mm from the internal reservoir is provided with internal curing water (Trtik et al., 2011). The ideal size of the swollen state would be around 100-200 µm (Jensen & Hansen, 2002), a little bit lower than the 257 µm diameter for a swollen SAP A, but the 981 µm swollen SAP B seems to be too big. Therefore, in all other tests conducted considering the mitigation of autogenous shrinkage, SAP A was preferred over SAP B.

Comparing the manual discontinuous tests (dashed lines) with the automated continuous tests (solid lines), it is clear that the data corresponds well. In this way, the effects on the long term (between 7 and 28 days) could be studied by both techniques. The differences in thermal history did not have a significant influence, as mentioned before.

In time, the rate of autogenous shrinkage in the reference mixtures with a water-to-binder ratio of 0.30 and 0.354 decreases as most of the hydration products have been formed. At 21 days, autogenous shrinkage has almost stopped completely. The mixture with $(W/B)_e$=0.054 and SAP A seems to mitigate autogenous shrinkage completely at this age, proving the compatibility of SAP A with the mechanism of internal curing and the usefulness of the application of superabsorbent polymers to mitigate autogenous shrinkage in systems with ordinary Portland cement.

At early age, the pozzolanic fly ash accelerates cement hydration in fly ash systems. Then it acts as a substrate for crystal nucleation on which calcium-silicate-hydrate (C-S-H) phases and calcium hydroxide crystals can form preferentially. The formation of these additional C-S-H phases on the surface of fly ash particles leads to an increase in the amount of bound water relative to the cement content (Maltais & Marchand, 1997). Hydrates formed by the pozzolanic reaction densify the microstructure and shift the pore size distribution towards finer pores. In section 3.2.2.5, the fly ash systems show a slightly lower microporosity compared to a pure cementitious matrix. There was also a decrease of the narrow mesopores (pore sizes according to IUPAC classification). With increasing replacement of cement by fly ash, the amount of larger mesopores seemed to increase. This indicated pore densification when the supplementary cementitious materials' reaction caused a change of capillary pores towards gel pores. Also, in literature, a decrease in porosity and a shift towards finer pores was found (70 nm towards 40 nm threshold pore diameter as determined by means of MIP for a reference mixture and a mixture with 50% of fly ash, respectively) (Van den Heede, 2014). The same conclusion could be made considering the blast furnace slag mixtures. The microstructure in the BFS85 mixture was denser as part of the blast furnace slag was acting as filler. The densification was also described in literature for approximately the same mixtures where the capillary porosity decreases from 8.3% over 7.1% to 7.0% and the mean pore size was 34, 28 and 17 nm for REF, BFS50 and BFS85, respectively (Gruyaert, 2011).

Figure 3.16a shows the results for the fly ash systems. All mixtures have a water-to-binder ratio of 0.30 and the entrained water-to-binder amount is 0.054. The amount of shrinkage is less in fly ash systems due to the lower amount of cement at early age, as the initial reaction rate and water consumption is lower. This leads to less autogenous shrinkage at early ages. Only after a certain period, the pozzolanic reaction takes place, consuming the calcium hydroxide, increasing the autogenous shrinkage. This can be seen as the sudden increase in inclination of the shrinkage curve in time, i.e. the rate of autogenous shrinkage increases. The shift in inclination occurs after 8-9 days and the increase in shrinkage is clearly seen as the curve is shifted downwards. This corresponds to the time where calcium hydroxide started to be depleted due to the pozzolanic reaction (Baert et al., 2008; Jensen & Hansen, 1996).

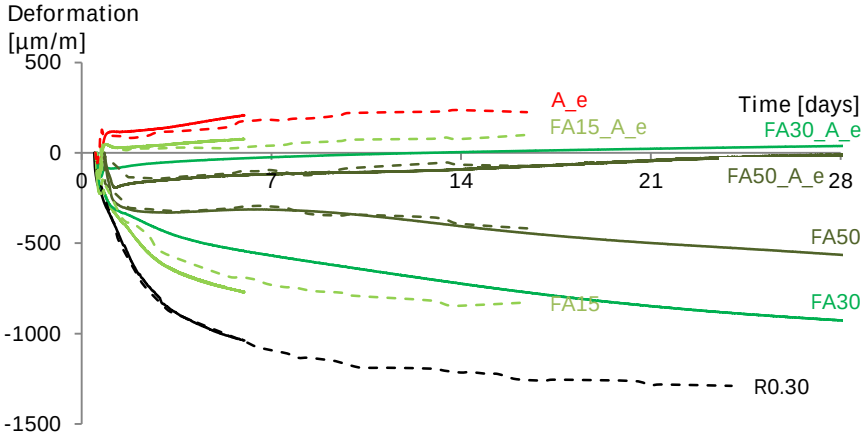

(a)

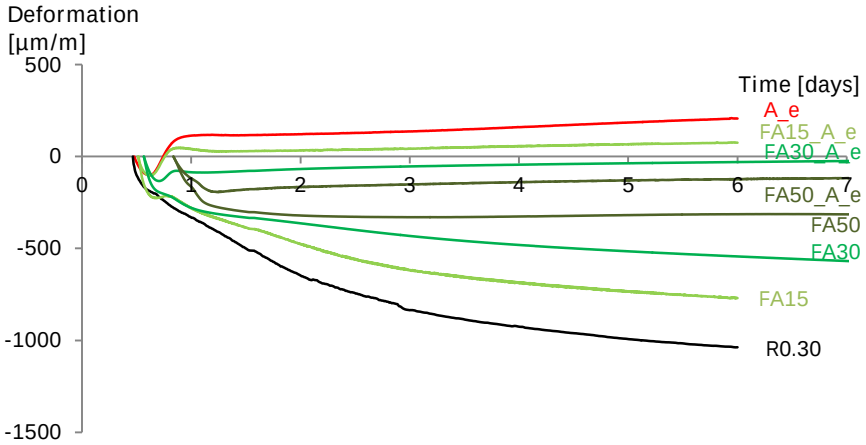

(b)

Figure 3.16. Autogenous strain [µm/m] for cement paste mixtures with and without fly ash and with and without entrained water by superabsorbent polymers, over 28 days **(a)** and 7 days **(b)**. (--- = manual test curves; — = automated test curves)

If one would only study Figure 3.16b, one could say that a FA50 system shows almost no shrinkage. This is not true as can be seen in Figure 3.16a for the long term, and confirms the importance of studying mixtures beyond 7 days when long-term reactions, such as the pozzolanic reaction, influence the autogenous shrinkage properties. If the amount of fly ash is high, i.e. 50% (FA50), the reaction degree of the fly ash decreases due to an insufficient amount of $Ca(OH)_2$ formed during cement hydration (Baert et al., 2008).

Compared to the results found by (Yan & Chen, 2014), the same trends can be found. They found a deformation of approximately 320, 250, 220 and 150 µm/m shrinkage strain at an age of 7 days for mixtures REF, FA15, FA30 and FA45 with a water-to-binder ratio of 0.30, respectively. In this research values of approximately 1100, 800, 600 and 300 µm/m shrinkage strain were found for R0.30, FA15, FA30 and FA50, respectively, which confirms the same trend as in literature. The values in this study are higher due to the difference in test setup and the different size of the specimens (100 × 100 × 350 mm^3 prisms in the research of (Yan & Chen, 2014)). Therefore, only a comparison can be made regarding the trend itself (qualitatively and not quantitatively). De la Varga et al. 2012) found values of approximately 200, 100 and 50 µm/m shrinkage strain, and 20 and 60 µm/m expansion strain at an age of 14 days for mixtures R0.30, FA40, FA60, FA60_IC and FA40_IC with a water-to-binder ratio of 0.30, respectively. They thus found a mitigation of the autogenous shrinkage but a small decrease of the rate of shrinkage in time after 10 days. No results were available from 14 days onwards.

In systems with fly ash and adequate internal curing, the autogenous shrinkage is mitigated (Figure 3.16). A small expansion is even noticed for some of the mixtures. In the FA50 system with internal curing, the increase in strain is more prominent after 14 days. This can be due to the higher relative amount of pozzolanic reaction as the amount of fly ash is higher compared to the other systems. A reaction degree of approximately 10% and 30% of fly ash is found in fly ash systems (FA50) after two weeks and three years, respectively (De Belie et al., 2011). If too high amounts of fly ash are used, not all fly ash will be consumed due to the insufficient amount of $Ca(OH)_2$ formed during hydration (Baert et al., 2008; De Belie et al., 2011). Generally, superabsorbent polymers are able to mitigate autogenous shrinkage in fly ash systems with a low water-to-binder ratio.

Figure 3.17a shows the results from the blast-furnace slag systems. As it is a slow reacting latent hydraulic material, the strain is lower at early age. Figure 3.17b shows a close-up of the results till 7 days of age. In the beginning there is less shrinkage, but after 5 days, the inclination of the autogenous shrinkage curve increases as the slag reaction starts to take place, i.e. the rate of shrinkage thus increases in time. Wyrzykowski and Lura (2014) showed a strain of approximately 1400, 600, 200, 50 µm/m shrinkage strain at an age of 7 days for mixtures with blast-furnace slag (approximately 66-80%; CEM III/B 32.5 N), blast-furnace slag with internal curing by means of SAPs, a reference mixture (CEM I 42.5 N) and an internally-cured mixture, respectively. The water-to-binder ratio was 0.30 in all mixtures. The trend between the ordinary Portland cement and the cement type blended with blast-furnace slag seems to be opposite as found in this research. Here, less strain was found in blast-furnace slag mixtures compared to the

autogenous strain of the R0.30 mixture. On the one hand, in paste with BFS the microstructure should be denser and the pores should be smaller. This would presumably lead to higher capillary forces, self-desiccation and more shrinkage (Lura et al., 2001). On the other hand, one would expect the slag reaction to occur mostly at later ages and hence the formation of the denser structure would occur also at later ages. It is the latter effect that is seen in this research. Also, the reaction degree boundary of blast furnace slag in blended cement is approximately 60-70% (Gruyaert et al., 2010), so not all blast furnace slag will react in the blast-furnace slag mixture. We want to point out that the used time zero in the research of (Wyrzykowski & Lura, 2014) was different to the one used in this research and it did not correspond with the time of final setting.

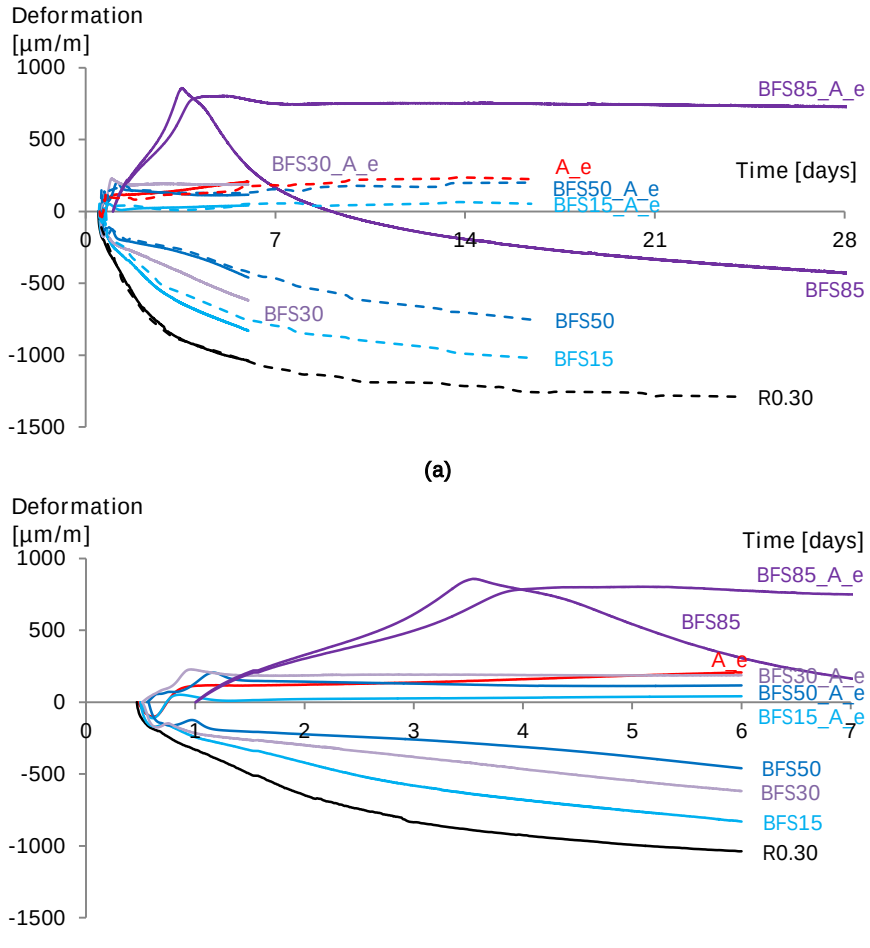

Figure 3.17. Autogenous strain [µm/m] for cement paste mixtures with and without blast-furnace slag and with and without entrained water by superabsorbent polymers, over 28 days **(a)** and 7 days **(b)**. (--- = manual test curves; — = automated test curves)

The mixtures with blast-furnace slag blended cement and internal curing in literature (Wyrzykowski & Lura, 2014) only showed partial mitigation of autogenous shrinkage and the remaining shrinkage was very high. Again, no results are available beyond 7 days. In this research, autogenous shrinkage is mitigated when using internal curing by means of superabsorbent polymers, in all blast-furnace slag systems. This again proves the use of internal curing, even independent from the cement type, being a pure ordinary Portland cement, fly ash or a blast-furnace slag system.

There is almost no shrinkage in BFS85 mixtures at early age, due to the low calcium hydroxide amount from the hydraulic reaction of the cement. There is even a vast expansion at early age. There is not enough $Ca(OH)_2$ to completely activate the slag reaction, so most of the blast-furnace slag acted as filler. In the beginning, there is expansion, but in time there is a prominent shrinkage due to the slow latent hydraulic reaction of blast-furnace slag. A partial re-absorption of bleeding water could also explain the expansion, but bleeding was not clearly observed in any of the specimens.

Mixtures with ordinary Portland cement without supplementary materials stop showing autogenous shrinkage in time. However, both fly ash and blast-furnace slag systems still show an increase in the autogenous shrinkage in time beyond 28 days, as can be seen in Figure 3.18. This is especially the case for the BFS85 system where the rate of shrinkage at 42 days is the highest, followed by the FA50 mixture. The mitigation by means of SAPs is still working at these ages as well, as no further shrinkage is noticed in time.

A final remark can be made. As the ion concentration in the pore fluid is different, the swelling capacity of the SAPs may be expected to be different between the mixtures. This is also highly dependent on the type of polymer. Here, however, no difference was found in flow characteristics between the different mixtures and it was concluded that the absorption of pore fluids was the same in all mixtures. This conclusion was also made by (Wyrzykowski & Lura, 2014).

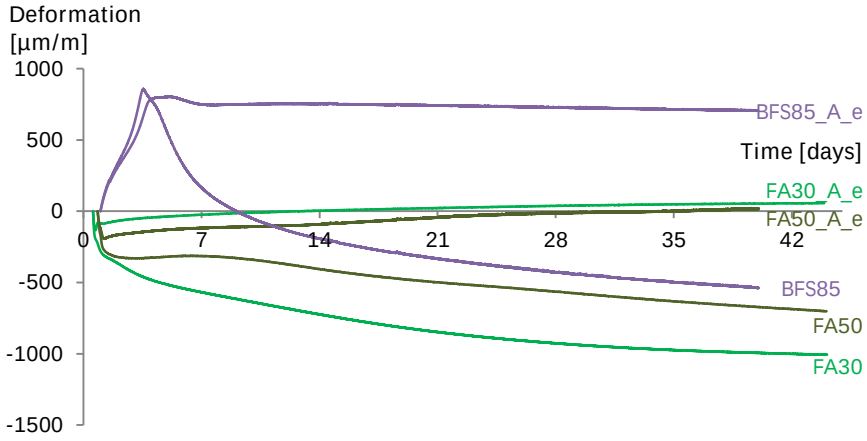

Figure 3.18. Long-term strain effects of fly ash and blast-furnace slag systems [µm/m].

3.2 Properties in hardened state

During hardening of the cementitious material, a heterogeneous and complex microstructure will be formed. In this thesis, the microstructure is defined as the pore structure from nano- to macroscale. Knowledge of the microstructure and properties of the individual components of cementitious materials and their relationship to each other is useful for the control of different properties like transport or strength.

As the available water influences the microstructural development and hardening, the water kinetics in samples with SAPs is a key parameter in the microstructural properties and moisture transport processes. Hydration of a mixture determines the microstructural development. Pastes with SAPs show less capillary porosity at later ages if additional water is used (compared to if no additional water is used). The water released from the SAPs results in continued hydration, thus decreasing the micro-porosity at later ages (Igarashi & Watanabe, 2006), except from the macro pores created by the SAPs. An X-ray tomography study (Lura et al., 2008) showed a reduction of the amount of smaller capillary pores. This is due to two effects: 1) Filling of the existing pores with hydration products due to internal curing and 2) Reduction of the initial micro-cracks in the interior of a cementitious matrix, as autogenous shrinkage is partially reduced. Mercury Intrusion Porosimetry (MIP) (Mechtcherine et al., 2009; Mönnig, 2005) showed a higher total porosity due to macro-pore formation in specimens with SAPs and additional water. If no additional water was added, the total porosity was lower for mixtures with SAPs (Mönnig, 2005). MIP does not directly measure the macro pores, since the range is narrow (working range of MIP; 0.1 nm < pore size < 100 µm), but macro pores do show up in the total porosity. The macro pores are hereby accessed only through smaller capillary pores, so that the volume is assigned to these narrower radii. Mixtures with the same effective water-to-cement ratio (ratio of the mixing water not held by the SAPs over the cement content), show the same capillary porosity (Reinhardt & Assmann, 2009). The latter researchers also found a lower water permeability of mixtures with SAPs and additional water (24 g water/g SAP based on the swelling capacity). The microstructure in between SAPs is denser due to internal curing and the macro pores do not interconnect. Therefore, the permeability is lower than of reference samples and this was also shown by using neutron radiography (see Chapter 4).

Microstructural properties directly affect the strength characteristics of the cementitious material. The flexural and compressive strength decrease when SAPs and additional water are added (Craeye & De Schutter, 2006; Igarashi & Watanabe, 2006; Jensen & Hansen, 2002; Lura et al., 2006; Mechtcherine et al., 2009). In these studies additional water was added until the same flow/slump was reached as a compensation for the loss of workability due to the water uptake of SAPs compared to reference mixtures, unless stated differently. The lower the water-to-cement ratio, the more the strength of the composite is influenced by the addition of SAPs (Igarashi & Watanabe, 2006), and this effect is more pronounced at early ages due to the higher total porosity at early ages (Dudziak & Mechtcherine, 2010; Mechtcherine et al., 2009). Internal curing leads to further hydration and the effect of SAPs on strength-loss is thus reduced at later ages. Theoretically, even a

complete hydration due to internal curing is possible (Powers & Brownyard, 1948). In Powers' model, however, complete hydration in saturated systems is only possible in systems above a certain water-to-cement ratio (0.42 (Jensen & Hansen, 2001; Powers & Brownyard, 1948)) and this complete hydration is not possible for cementitious materials with a very low water-to-cement ratio. This is because one gram of cement chemically binds 0.23 g water and will bind 0.19 g of gel water (Jensen & Hansen, 2001). The sum of both is 0.42 g. If this total amount of water is not available, total hydration is not possible unless water is provided from the surroundings during hardening.

Further hydration thus improves the mechanical properties but is mostly counteracted by the strength-loss caused by the SAPs (Lura et al., 2007). SAPs thus have both a positive and a negative effect on the mechanical properties. A decrease in strength is observed at earlier testing ages (<7 days) while sometimes increases are obtained at later ages (Bentz & Weiss, 2011), especially in systems with supplementary cementitious materials where the internal curing reservoirs are available for the longer term pozzolanic reactions. Also, the water-to-cement ratio has to be taken into account. At a value of 0.35 for example, the increased degree of hydration may counteract the strength loss due to macro pore formation (Hasholt et al., 2010). At higher water-to-cement ratios, this is not the case.

The structure of a cementitious material is affected by the apparent water-to-cement ratio. As SAPs take up the mixing water, the apparent water-to-cement ratio appears lower, resulting in a closely-packed matrix and subsequent hydration due to the release of that water. Samples without SAPs do not have access to this free water. Therefore, water penetration in samples with and without SAPs is different. The SAPs will swell inside the macro pores, blocking the free flow of water, but the overall effect of reduced permeation is due to the lower apparent water-to-cement ratio.

The effect of SAPs and additional water on the microstructural properties and moisture transport processes will be studied. The amounts of SAP sometimes are higher (up to 1 m%) compared to the amount needed for internal curing (typically 0.3-0.6 m%). The amount of SAPs was determined to obtain optimal self-sealing and stimulation of autogenous healing (see Chapters 4 and 5). The effects of high amounts of SAPs in mortar mixtures should therefore be investigated, especially in terms of porosity and strength. The combination of all characteristics will give a general overview of the effects of SAPs and additional water on the hardened-state properties of a cementitious composite.

3.2.1 Meso- and macro-porosity

To investigate the microstructure, the air voids and macro pores were studied by means of optical microscopy on thin sections impregnated with fluorescent resin. On the same thin sections, fluorescent microscopy was performed to study the local water-to-cement ratio. Finally, the capillary porosity and the different hydration products formed were studied by means of BackScattered Electron – Scanning Electron Microscopy (BSE-SEM) on polished sections. Mercury Intrusion Porosimetry (MIP) and helium pycnometry were used as additional testing methods to study the microstructure.

3.2.1.1 Air voids, macro-pore formation and water-to-cement ratio

To measure air content in the fresh mixture, the pressure gauge method was used (EN 1015-7). This value was compared with the other methods.

To study the amount of air voids, thin sections (40 mm × 25 mm × 25 µm) were prepared from a cubic specimen (cross-section 40 mm × 40 mm) at an age of 28 days. First, the specimens were cut to receive 40 mm × 25 mm faces, which were then glued on a glass slide with a thickness of 2.9 mm. The combined sample was cut and polished until a height of the specimen and glass of 10.1 mm was reached. Next, the specimens were impregnated under vacuum with a fluorescent epoxy. The excess epoxy was polished away and an object glass was glued on the smooth surface. Finally, the glass slides were cut off and the remaining part was polished until a thin section with 25 µm thickness was achieved. A cover glass was glued on top to protect the thin section. The thin sections were analysed with a Leica DMLP microscope with a DFC 295 camera under normal and fluorescent light.

Normal light was used to visualize the macro pores formed due to swelling of the SAP particles. Fluorescent light was used to quantify both the amount of air voids and macro pores. As the voids and pores were filled with fluorescent resin, they appeared as bright spots on a micrograph. These bright spots (diameter d > 40 µm) (based on the resolution of the microscope) served for quantification of the pores and were calculated using the image analysis program Adobe PhotoShop (n=10) (Figure 3.19). The size of the macro pores, measured twice perpendicularly for every macro pore (n=100), was studied as well as verification.

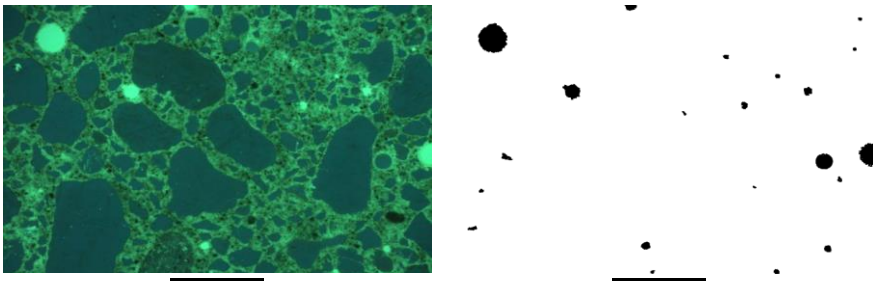

Figure 3.19. Image analysis of thin sections with fluorescent microscopy to determine the air voids and macro pores.

Figure 3.20 shows macro-pore formation due to the swelling of SAP B particles. The irregularity of the macro pore shapes originates from the initial irregular shape of the SAP particles. This irregular particle shape is determined by the production process. Here, SAP particles were fabricated by bulk polymerization followed by grinding. The macro pores, however, do not possess a high quantity of sharp edges which are stress inducers decreasing the strength. The un-swollen SAP particles do not adhere to the cementitious faces of the macro pore. They will not transfer loads, so they need to be considered as pores.

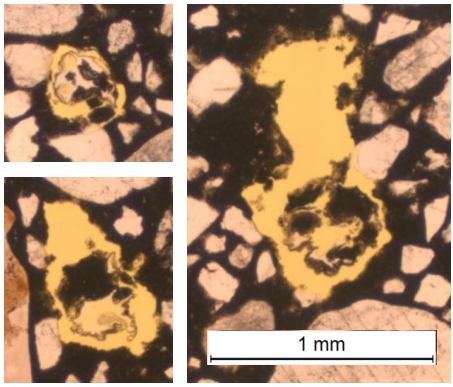

Figure 3.20. Optical micrograph of macro-pore formation due to the swelling of SAP B.

In case of a lower water-to-cement ratio in reference mixtures, there is a higher amount of voids due to entrapped air (Figure 3.21). If SAPs are added, macro pores are also present due to the shrinkage of the swollen SAPs. An increasing amount of SAPs results in an increased total volume of macro pores. This is observed in case of SAP A mixtures, but not clearly in case of SAP B mixtures when the SAP content is increased from 0.5 m% to 1 m%. This is due to the lower pore fluid uptake in SAP B mixtures, masking the effect of macro-pore formation. The scatter is high in mixtures with SAPs due to the irregularity of the macro pores in the thin sections. For the same type and amount of SAP in the mix and in case additional water is added, the amount of macro pores is approximately the same as if no additional water is added. Only in the A1 mixture, there are more pores, due to the poor workability and thus lower flow compared to the other mixtures. The amount of pores measured with the pressure gauge is less as the macro pores are considered as a solid material as they still hold the water during the first hours of hardening. The amount of pores by means of image analysis shows the same trend if one would add the theoretical amount of SAP macro pores (for example: 0.5 m% SAP B causes an additional 2.5% [volume of by mixing water saturated SAPs over the total volume of the mixture] volume-based amount of macro pores, while the value determined by means of image analysis equals to approximately 5%). Other research also proved the higher total porosity due to macro pore formation in specimens with SAPs and with(out) additional water (Laustsen et al., 2015; Mechtcherine et al., 2009).

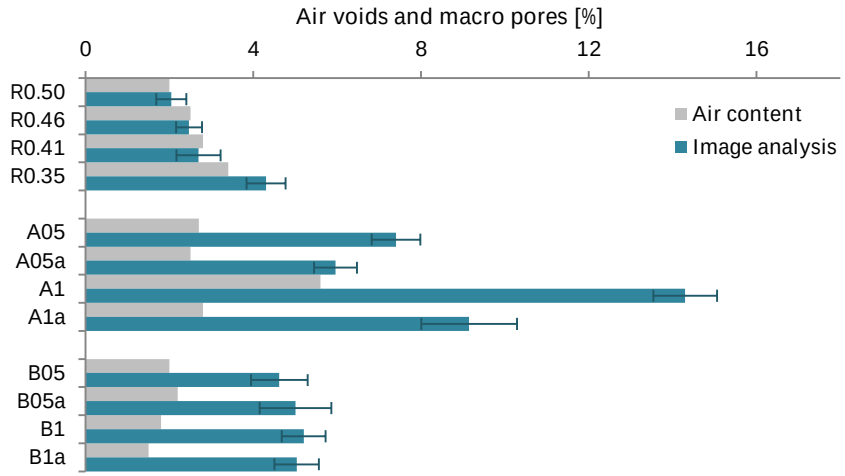

Figure 3.21. Air content (n=1) and percentage of air voids and macro pores determined by means of image analysis of optical micrographs on thin sections with standard deviation on mean values (n=10).

To verify the amount of additional water, a simple study can be conducted correlated to the amount of air pores, following the method described in (Laustsen et al., 2015). In SAP A mixtures, the amount of macro pores (obtained value for image analysis minus the obtained air content) is approximately 4.7% and 9.2% for respectively A0.5 and A1 mixtures (Figure 3.21). This leads to approximately 47 and 92 l/m³ water (assumed to be absorbed) which leads to an absorption capacity of 18-19 g mixing water/g SAP A. This value is lower than the value 30.5 g mixing water/g SAP A. SAP B mixtures showed a perfect correlation between the amount of pores and the recalculated amount of mixing water absorbed. The amount of macro pores is 2.5% and 3.9% for B0.5 and B1 mixtures, leading to an absorption capacity of 8-10 g mixing water/g SAP B (compared to 8.9 g mixing water/g SAP B).

An evaluation of thin section by means of image analysis will underestimate the pore volume and dried-out leftovers of the small SAP A are seen as solid parts. If a microscopic analysis is performed only considering the size of the macro pores, it was found that the sizes of macro pores were 270 ± 54 µm (n = 100) and 827 ± 173 µm (n = 100) for SAP A and SAP B mixtures, respectively. The sizes if 30.5 g mixing water/g SAP A and 8.9 g mixing water/g SAP B were used, were 281 ± 61 µm and 922 ± 102 µm respectively (theoretical size if perfect spherical particles are assumed). The differences are not significant and we can conclude that the amount of additional water is of the right order of magnitude.

3.2.1.2 Densification of the cementitious matrix on thin sections

Next, the water-to-cement ratio of the cement paste was compared for the fluorescent-epoxy-impregnated thin sections. A higher capillary porosity corresponds to a higher 'green' luminosity (Figure 3.19). The darker the image, the lower the effective water-to-cement ratio, and thus the denser the microstructure.

The luminosity was determined with the image analysis program Adobe PhotoShop on several acquired micrographs (n=10). In this measurement, the same light intensity and aperture was used to ensure a good comparison between the different fluorescent micrographs of the thin sections.

Another important microstructural property is the capillarity (0.2 µm < d < 40 µm). As the cementitious matrix is affected by the internal curing by the SAPs, the microstructure will be different. As the effective water-to-cement ratio is lower in specimens containing SAPs without additional water, densification of the cementitious matrix occurs. The densification is visualized in Figure 3.22 by means of fluorescent microscopy. In this figure, the effect of additional water is compared between a B1 and a B1a mixture. In the B1 mixture, densification occurs. The denser microstructure appears darker and is schematically pointed out by the red regions in the right-hand figure. The SAPs are present in the blue regions. However, if additional water is added, there is no densification of the cementitious matrix.

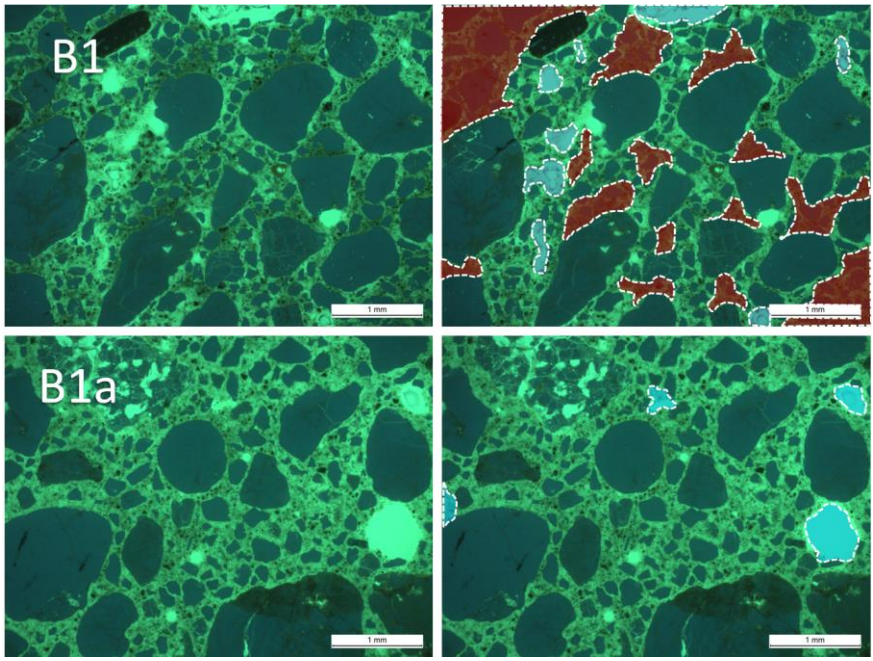

Figure 3.22. Densification of the cementitious matrix in between SAP B particles and the effect of additional water at an age of 28 days (top figures: B1, bottom figures: B1a). The red regions state the more dense structures, the blue regions the included SAP particles and their macro pores.

The different cementitious matrices of the mixtures are compared by their mean fluorescent luminosity. All specimens had the same thickness, so the amount of light passing through the specimens could be compared quantitatively. The mean value is shown in Figure 3.23. In reference samples, the luminosity decreases with decreasing water-to-cement ratio. Due to less mixing water, the solid particles are more compressed (the distances between the solid particles are

smaller) and the cementitious matrix is denser. Therefore, light cannot easily pass through the specimen and the mean luminosity is decreased.

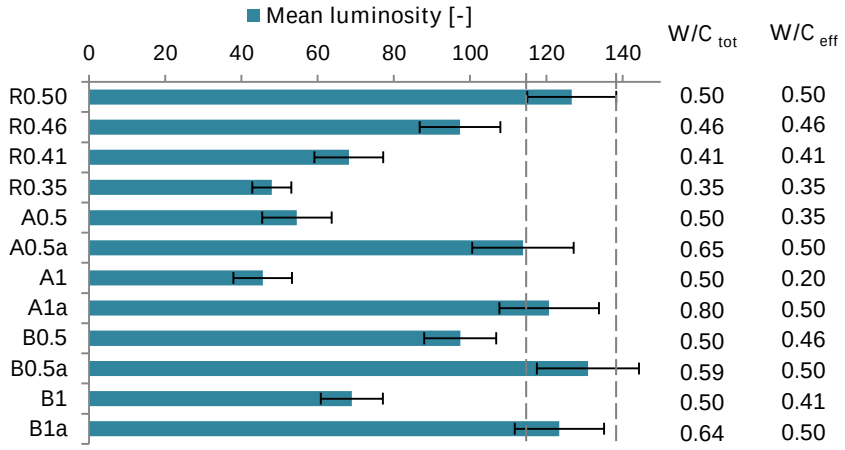

Figure 3.23. Calculated mean luminosity of the cementitious matrix by means of image analysis (n=10). The dashed lines represent the upper and lower standard deviation on a single measurement for the R0.50 mixture. The total and effective water-to-cement ratios are provided to compare the results.

When adding SAPs without additional water, the luminosity decreases. The particles will hold the mixing water until after settlement and release the water afterwards for further hydration. This causes densification of the matrix and thus a lower luminosity through the thin section. The lower porosity in mixtures with SAPs and without additional water is also found by (Mönnig, 2005).

Not the total water-to-cement ratio, but the effective water-to-cement ratio is important. The microstructure of the cementitious composite is a function of the spacing of the cement grains at setting and thus the effective water-to-cement ratio. Even when the retained water is provided by the SAP particles afterwards, the microstructure will still be completely different from the microstructure of a SAP-free specimen. The A0.5 mixture tends towards the R0.35 mixture and they possess the same effective water-to-cement ratio (B0.5 tends towards R0.46 and B1 towards R0.41). The mixtures with superabsorbent polymers, without additional water, show the same amount of luminosity as the respective reference samples with less mixing water. The luminosity of A1 is the darkest of all due to the high fluid uptake by SAP A. The A1 mixture should appear even darker, but due to the poor workability, there are more entrapped air voids, increasing the mean value of luminosity. If additional water is added to concrete containing SAPs, the luminosity shifts towards the R0.50 reference mixture with the same effective water-to-cement ratio (dashed lines). So, additional water should be added to the mixture with SAPs to obtain a similar mean fluorescent luminosity, and hence a similar capillary porosity, of the cementitious matrix. This additional water will cause the settlement of approximately the same global microstructure. But afterwards, the additional water will cause further hydration too.

3.2.1.3 Capillary porosity and formed hydration products (BSE-SEM)

The pore size distribution can be determined by measuring the pores in a random plane section of a specimen. The size distribution in 2D is not the same as the size distribution in 3D but it is generally accepted that this distribution is similar and comparable (Ye, 2003). Therefore, plane-polished sections are examined by means of BSE-SEM and subsequent image analysis.

Specimens were first broken into small pieces of approximately 1 cm. The pieces were submerged in isopropanol for 7 days at an age of 28 days to remove the water and thus to stop further cement hydration. The solvent was renewed every day, with a solution/sample volume ratio of 10:1 (Zhang & Scherer, 2011). Subsequently, the specimens were dried with silica gel in a vacuum container (RH = 3%) for another week. Finally, the specimens were dried further in a ventilated oven at 40°C until constant mass. The solvent-exchange method followed by ambient drying is the best known method for preserving the microstructure (Zhang & Scherer, 2011). A more in-depth investigation of the drying technique will be addressed in Section 3.2.2.4.

The sections were prepared by impregnating the specimens with a low-viscosity epoxy resin (100 g Conpox Harpiks BY 158 and 28 g of Hærder HY 2996) under vacuum and subsequent curing for 48 h at 40°C. The specimens were ground on a rotating wheel using a SiC abrasive paper (No. 320-grit) and water until the particles became uncovered. Subsequently, the specimens were impregnated for a second time. The specimens were then polished with SiC abrasive paper (No. 320-grit) and water until the same plane section became uncovered. Next, the specimens were polished with SiC abrasive paper (No. 2400-grit) and DP-lubricant brown (Struers). Subsequently, the specimens were polished with diamond paste (3 µm, then 1 µm and 0.25 µm) and methanol. In between each polishing step, the specimens were cleaned by submersion in methanol to remove all loose particles. At the end, the specimens were cleaned with a soft cloth to remove all impurities. This is a method based on (Snellings et al., 2012).

Prior to the electron microscope analysis, all samples were coated with a thin gold layer (approximately 20 nm) by means of plasma magnetron sputter coater (Figure 3.24a). Scanning Electron Microscope (SEM) analysis was performed on a JEOL JSM-5600 instrument equipped with a BSE detector operating at an acceleration voltage of 20 kV (Figure 3.24b). The BSE mode is an excellent way to visualize the capillary pores as they appear as dark areas when the BSE detector is used in the compositional contrast mode. The magnification used was x500. This is a good magnification to study the capillary porosity (0.2 µm < d < 40 µm). Only the cement paste was studied using SEM due to the magnification.

Grey level histograms were obtained with the image analysis program Adobe PhotoShop (n=10). Subsequently, the different phases were determined as the intensity is dependent on the atomic number of the phase. All images were taken with the same brightness and contrast and three regions were clearly distinguished based on grey levels (black 0-255 white): the pores from 0-17, the C-S-H (Calcium-Silicate-Hydrate) and CH (Calcium Hydroxide) products from 18-202 and UH (UnHydrated cement) from 203-255 (Figure 3.25). The boundaries were determined as the distinct changes in grey-level histogram.

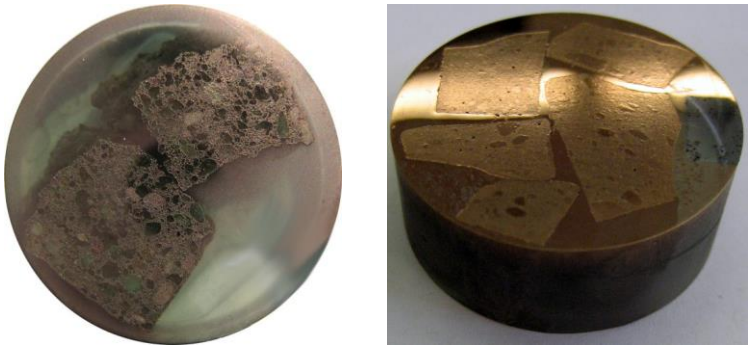

(a)

(b)

Figure 3.24. Polished sample after gold-coating **(a)** and gold-coating device and SEM equipment **(b)**.

The amount of small pores decreases with decreasing water-to-cement ratio in reference mixtures (Figure 3.26 and Figure 3.27). As there is less mixing water, there are more unhydrated products inside the matrix. When SAPs are added, the amount of small pores at later ages decreases due to the internal curing. As water is held by the SAPs and released afterwards, the amount of unhydrated products is initially less compared to the reference sample R0.50, but should become the same afterwards. This is not always the case. As SAP A provides the water for local densification due to the small particle size, some particles in the neighbourhood undergo more intense further hydration and some at further distance less (in mixtures without additional water). This explains the higher amount of unhydrated cement particles in the cementitious matrix in the presence of SAPs as the distance of water movement is limited (Bentz & Weiss, 2011). The A0.5 mixture behaves in the same way as the R0.35 reference mixture with the same effective water-to-cement ratio. Also the B0.5 and the B1 mixtures correspond to the R0.46 and R0.41 reference mixtures, respectively. The A1 mixture shows a very dense microstructure and a very high amount of unhydrated particles. This mixture was not workable and should be compared to a reference mixture with an effective water-to-cement ratio of 0.20. Due to the uptake of mixing water, the hydration and internal curing is different, especially in specimens containing smaller SAPs, which take up more mixing water due to their higher surface area available.

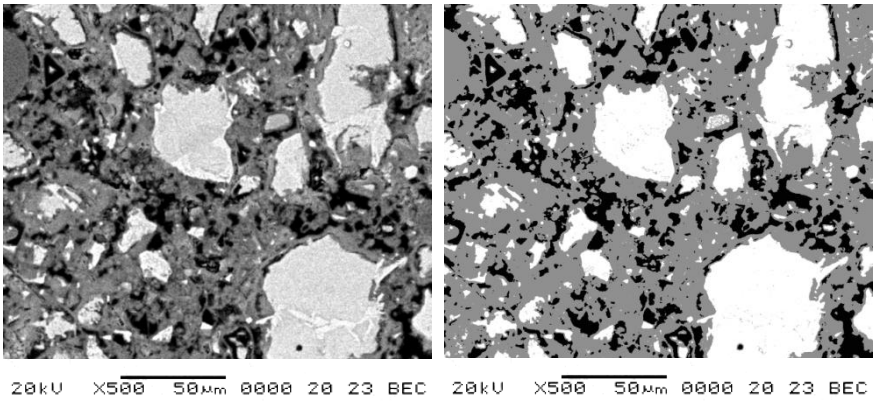

Figure 3.25. Original micrograph and image analysis of BSE-SEM micrographs to determine the different cementitious phases.

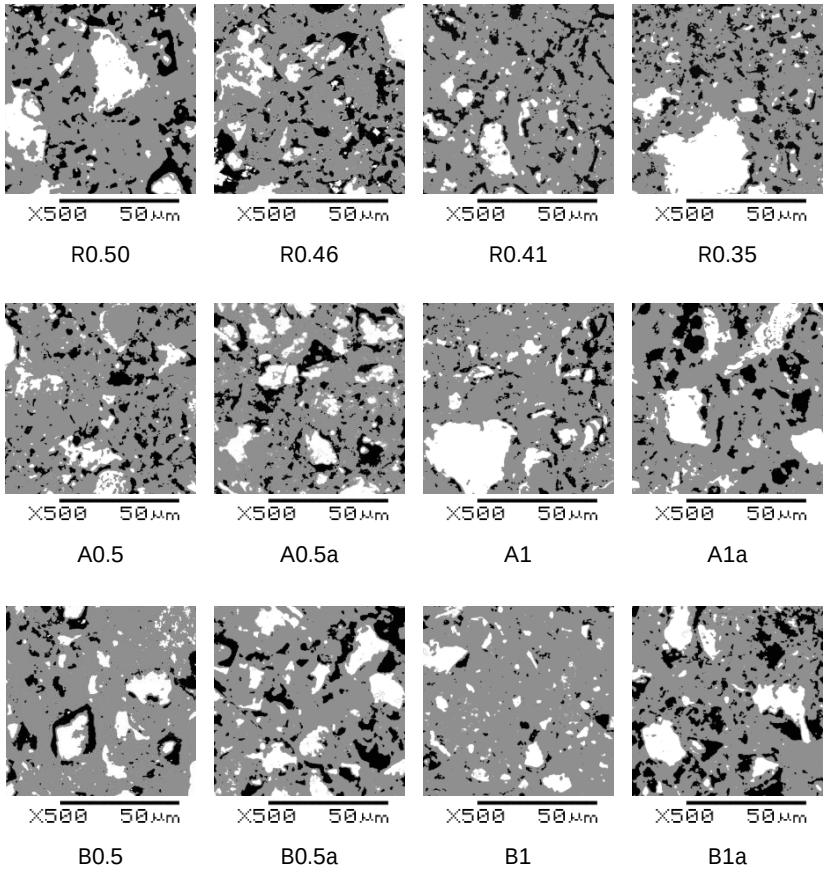

Figure 3.26. Grey-value micrographs obtained by BSE-SEM imaging. Black represents pores, grey C-S-H+CH (Calcium-Silicate-Hydrate and Calcium Hydroxide) and white UH (UnHydrated cement).

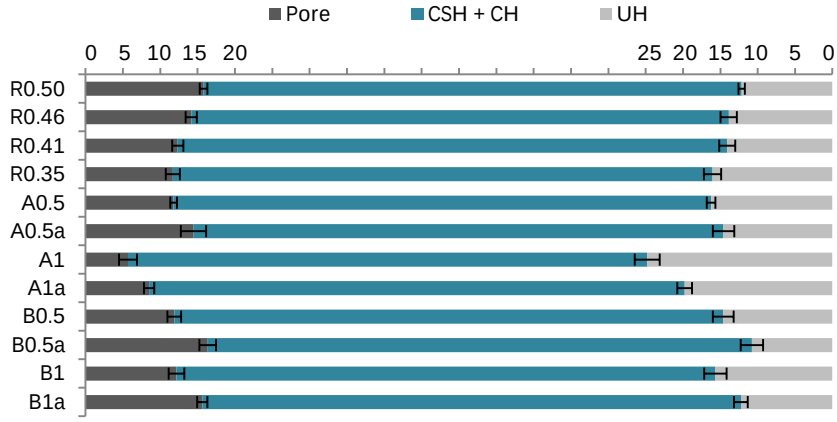

Figure 3.27. Analysis of the BSE-SEM micrographs as a quantification of the inner microstructure and formed products (n=10) (pores, Calcium-Silicate-Hydrate + Calcium Hydroxide and UnHydrated cement).

In specimens with internal curing, the amount of unhydrated cement is lower (Figure 3.26). Also, the overall size of unhydrated parts and the visible pores in the micrograph appear smaller. This points to further hydration.

If additional water is used, the matrix corresponds to the R0.50 reference mixture when considering the capillary pore microstructure. Due to the further hydration in SAP A mixtures, the amount of capillary pores is slightly lower. This is because the held water is provided to the cementitious matrix afterwards (but only very locally), filling the already formed pores. This effect is not as clear in SAP B mixtures due to the larger particle size, and thus the lower dispersion of the entrained water in the localized regions around the SAP particles. The effect of internal curing is higher in SAP A mixtures compared to SAP B mixtures. This is due to the smaller particle size of SAP A and thus a higher surface area exposed to the mixing water. If the total amount of entrained water in the SAPs is constant, small SAPs are also better distributed than large ones. The amount of unhydrated particles should be slightly lower than in the reference mixtures due to the further hydration following the release of retained mixing water by the SAP particles. This is the case in SAP B mixtures and not in SAP A mixtures. Additional water in mixtures with SAPs leads to more capillary porosity compared to mixtures without additional water, of the same order of magnitude as the R0.50 mix. The hydration degree in specimens with additional water is approximately the same as in R0.50 specimens. The further hydration caused by water release from SAPs also decreases the porosity at later ages in the research of (Igarashi & Watanabe, 2006).

3.2.1.4 Mercury intrusion porosimetry

To study the capillary porosity (in the range of 0.1 nm < d < 100 µm), Mercury Intrusion Porosimetry (MIP) was used (Pascal 140 and 440 series, Thermo Fisher Scientific Inc.). MIP is a method which is used frequently to study the effect on the microstructure. As a specific pressure corresponds to an aperture of a pore, and the amount of mercury intrusion approximates to the pores volume, the amount and size of the pores could be determined. MIP does not directly measure the amount of macro pores, since the range is narrow, but macro pores do show up in the total porosity. The macro pores are accessed only through smaller capillary pores, so that the volume is assigned to these narrower radii.

MIP, however, cannot provide a true pore size distribution as the mercury needs to pass through the narrowest pores in the network. Mercury intrusion porosimetry overestimates the volume of small pores due to the inkbottle effect as a large quantity of large pores is accessible only through smaller pores. MIP also damages the pore structure due to the high pressures and the results need to be handled with care (Diamond, 2000; Moukwa & Aïtcin, 1988; Olson et al., 1997). Gel foils are displaced and the pores are widened and neighbouring pores are closed (Taylor, 1990). But, the MIP method can give a first impression of the structure of the cementitious matrix (Gallé, 2003). With this test, the total pore volume, the retention factor (retained percentage due to the ink-bottle effect) and the critical diameter (most frequent diameter in the sample) could be determined.

In this test, a fluid is forced into a specimen. The pressure needed to force the liquid into a cylindrical pore is (Equation 3.1):

$$p = -4 \cdot \gamma \cdot \cos(\theta)/d \tag{3.1}$$

with p the pressure, γ the surface energy of Hg (0.483 $N \cdot m^{-1}$), θ the contact angle (140°) and d the nominal diameter of a pore. With a typical pressure of 400 MPa, a diameter of 3.5 nm can be intruded.

All samples were dried using the solvent-exchange method with isopropanol (cf. previous paragraph). Specimens with an age of 1 year were first broken into small pieces of approximately 1 cm. Approximately 1.5 g was used for MIP testing and a typical curve can be found in Figure 3.28.

The curve is in good accordance with results found in literature (Cook & Hover, 1999; Feldman & Beaudoin, 1991; Gallé, 2001; Ye, 2003). The critical diameter corresponds to values of 14 nm found by (Boel, 2006). Two peaks are noticed, one from the microporosity (around 14 nm) and a starting peak of nanoporosity (4 nm). The first peak is a characteristic of the outer C-S-H and the second of the inner C-S-H. Valckenborg studied the pore size distribution of a mortar by means of NMR. They proved a bimodal distribution with a first peak at 20 nm corresponding to capillary pores and a second peak close to 5 nm corresponding to C-S-H pores (Valckenborg et al., 2001).

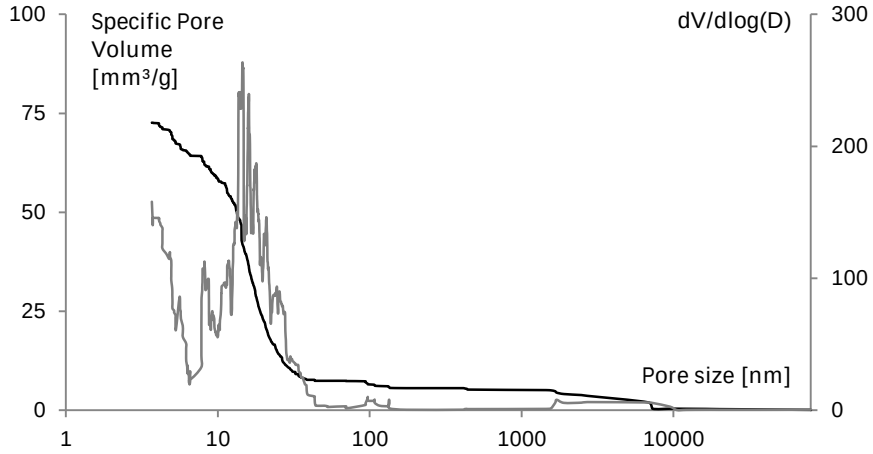

Figure 3.28. Typical specific pore volume and derivative by means of MIP tests.

MIP measurements cover pore ranges up to about 120 µm. The macro pores are bigger than this size and only the smaller pore sizes are shown with MIP measurements. The macro pores, however, do occur in the total porosity. Table 3.4 shows the total pore volume, retention factor, critical diameter, SAP pore volume and air content of the studied mixtures. The theoretical amount of SAP macro pores was calculated from the volume of SAPs and the amount of absorbed mixing water (30.5 and 8.9 g mixing water per g SAP A and SAP B, respectively). This amount was subtracted from the combined total determined by means of optical microscopy on thin sections (air content and macro pores) to calculate the amount of air voids.

Table 3.4. Total pore volume TPV [mm³/g] [%], retention factor RF [mm³/g], critical diameter CD [nm], SAP pore volume SPV [%] and air content AC [%].

Code	*TPV [mm³/g]*	*TPV [%]*	*RF [mm³/g]*	*CD [nm]*	*SPV [%]*	*AC [%]*
R0.50	66.7	18.9	39.3	18.6	-	2.0
R0.46	60.1	17.1	36.4	14.1	-	2.5
R0.41	53.5	15.2	31.8	9.6	-	2.7
R0.35	47.7	15.8	25.0	5.5	-	4.3
A0.5	59.5	19.3	29.8	5.4	6.1	1.3
A0.5a	79.6	23.6	29.8	16.0	6.1	0.9
A1	88.3	27.3	23.6	4.3	11.3	6.0
A1a	86.2	25.3	30.5	15.2	11.3	0.9
B0.5	64.2	19.4	37.6	14.0	2.6	2.0
B0.5a	71.3	22.6	36.6	19.2	2.6	2.4
B1	62.7	19.2	25.8	8.6	4.5	1.1
B1a	73.0	23.1	31.4	17.4	4.5	0.8

The total pore volume decreases with decreasing water-to-cement ratio. This is due to the denser matrix due to less mixing water. SAPs have the same effect and cause a densification of the matrix in between the SAP particles reducing the total pore volume but also form macro pores increasing the total pore volume. Especially in A1-mixtures, the pore volume increases. Additional water increases the total amount of pore volume as the macro-pore formation is highlighted and less densification occurred. Approximately the same conclusion can be drawn from the retention factor.

The critical diameter also decreases with decreasing water-to-cement ratio. When using SAPs, this diameter also decreases due to the densification of the matrix. As macro pores do not show up in MIP measurements, the found critical diameter is the one caused by densification. Additional water shifts this diameter back to the reference mixture R0.50. Mixtures with the same effective water-to-cement ratio show approximately the same critical diameter.

The values correspond to literature. In the work of (Reinhardt & Assmann, 2009), the mixtures M_1, M_2, M_{12}, M_3, M_{13} and M_{23} correspond to *R0.50*, *R0.41*, *B1a*, *R0.35*, *A0.5a* and *B0.5a*, respectively. Reinhardt and Assmann, however, look at the median pore radius, but the critical pore radius was preferred in this research. In their research, the SAP pore volume was also theoretically calculated with the swelling capacity during mixing and the air content was determined on the fresh mix. The amount of air content and the SAP pore volume in this research correspond to the values found by Reinhardt and Assmann: 0.7-3.4% and 2.8-6.6%, respectively (Reinhardt & Assmann, 2009).

The total porosity is more clearly visualized in Figure 3.29. The total pore volume ( ) can hereby be subdivided in capillary pores ( ), air voids ( ) and SAP pores ( ). The total sum of air voids and macro pores determined by means of optical microscopy ( ) was subtracted from the total pore volume. The remaining pores are the capillary pores, which are used to study the effect of the densification. The theoretical amount of SAP macro pores ( ) within the total sum of air voids and macro pores is shown as well. The dashed line visualizes the amount of capillary pores of the R0.50 reference mix.

Again, when adding SAPs without additional water, the total amount of pores increases. This is due to the macro pore formation. Additional water even increases the total porosity due to less densification. This is also found in literature. In mixtures with 0.6 m% of SAP and additional water to compensate for the loss in workability, the total porosity is approximately 6% higher than in plain material (Mechtcherine et al., 2009).

Mixtures with SAPs show less capillary porosity and more cement gel than a mortar without SAPs. The water released from the SAPs stimulated continued hydration, decreasing the porosity and thus causing a densification of the cementitious matrix.

Mixtures with the same effective water-to-cement ratio show the same amount of capillary porosity. Without using this additional water, the effective water-to-cement ratio is lower and these specimens with only SAPs show less capillary pores. SAPs thus cause a densification of the cementitious matrix and additional water counteracts this.

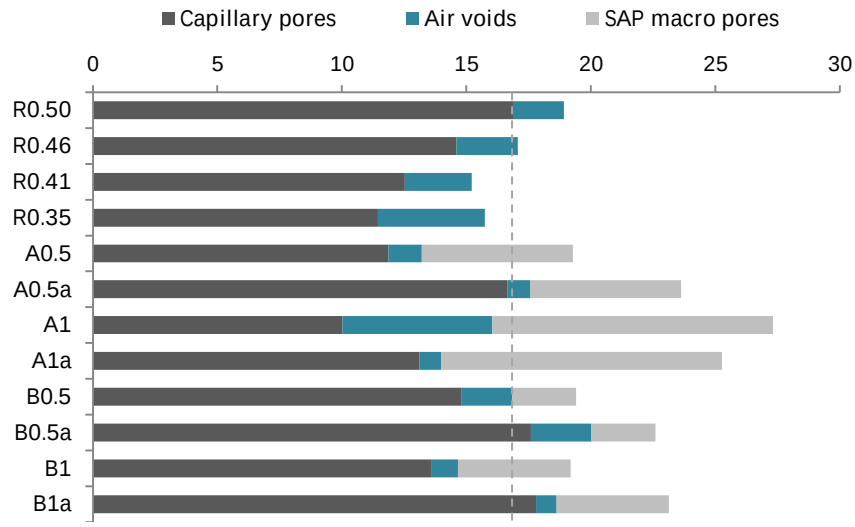

Figure 3.29. Amount of capillary pores, air voids and macro pores [%].

There is a small difference in amount of capillary porosity in SAP mixtures between the values obtained by MIP and by image analysis on BSE-SEM micrographs (Figure 3.30). The SAPs themselves do not appear dark in the BSE micrographs, so the BSE method slightly underestimates the amount of pores. An increasing amount of SAPs, leads to a bigger difference (A0.5 and A1). The same conclusions, however, can be drawn. Mixtures with the same effective water-to-cement ratio show nearly the same capillary porosity.

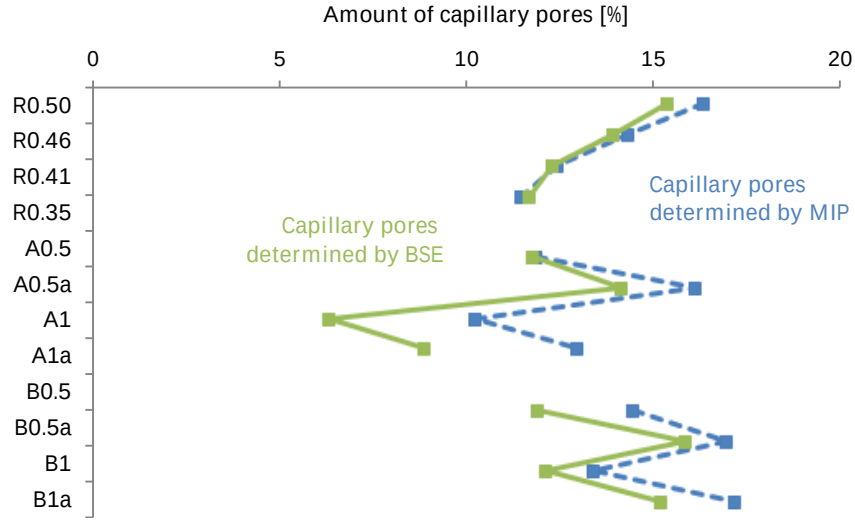

Figure 3.30. Comparison between the amounts of capillary pores [%] determined by means of BSE and MIP.

3.2.1.5 Helium pycnometry

The porosity was also determined by means of Helium pycnometry. A sample (4-7 g) of cement paste was placed in the measuring cell of the equipment (Accupyc 1330 Pycnometer, Micromeritics, Norcross, Georgia, US). After 10 purges with He-gas the chamber was pressurized to 1.34 bars (19.5 psig). The equilibration rate to proceed to the next step was set at 0.34 mbars/min (0.005 psig/min). The volume of the sample was determined ten times, and based on the average volume its absolute density was calculated. The true density was determined on bigger samples by means of weighing.

The results found by means of Helium pycnometry are given in Figure 3.31. In this figure, the theoretical amount of SAPs has been subtracted from the obtained value. The amount of macro pores has hereby been theoretically determined by calculating the volume of macro pores through the total uptake of water during mixing. As the water is released towards the cementitious matrix, a macro pore of approximately the size of the SAP particle and water uptake volume remained. The SAP particles do not adhere to the pore walls.

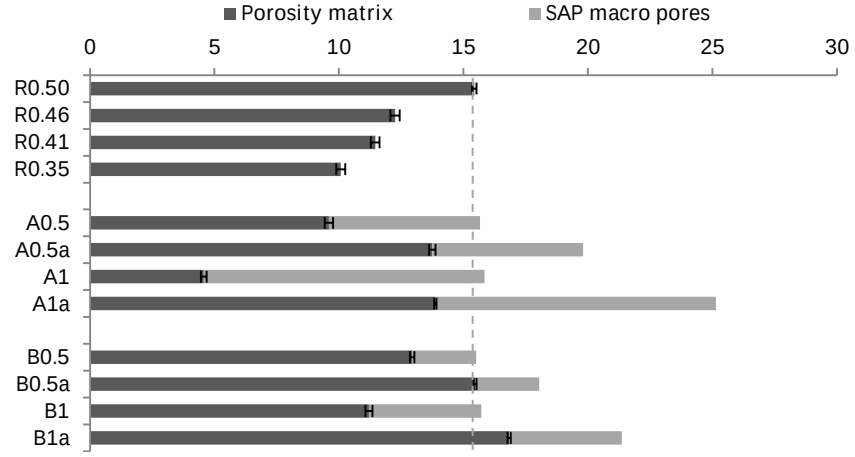

Figure 3.31. Amount of pores and SAP macro pores [%] found by Helium pycnometry.

When adding SAPs without additional water, the total amount of pores was approximately the same as the amount of pores found in the reference mixture R0.50. This is due to the macro-pore formation combined with densification. Additional water even increased the total porosity due to less densification. The results show that the mixtures with SAPs and without additional water show the same porosity of the cementitious matrix as a reference specimen with the same effective water-to-cement ratio (thus after subtracting the theoretical amount of SAP macro pores). If additional water is added, the total porosity is shifted upwards, but the porosity of the matrix is approximately the same as the R0.50 reference mixture. These results correspond to the results obtained by means of mercury intrusion porosimetry and by means of backscattered scanning electron microscopy.

The capillary porosity (0.2 µm < d < 40 µm) changes when using SAPs. As the cementitious matrix is affected by the internal curing by the SAPs, the microstructure will be different. As the effective water-to-cement ratio is lower in specimens containing SAPs without additional water, densification of the cementitious matrix occurs as the cementitious matrix in between the SAPs is denser. The water released from the SAPs hereby stimulated continued hydration. Additional water should be used to receive a similar capillary porosity of the cementitious matrix. Mixtures with the same effective water-to-cement ratio show nearly the same capillary porosity. The amount of pores is slightly lower in SAP A mixtures and this may be due to the local use of the entrained water by the SAPs filling the already formed pores. This effect is not as clear in SAP B mixtures due to the larger particle size of SAP B compared to SAP A, masking the overall effect.

3.2.2 Micro- and meso-porosity by means of dynamic vapour sorption

At some level the behaviour of every material is related to its microstructure (Jennings & Bullard, 2011). One of the most important properties of a cement paste is thus the developing pore structure. Other cementitious material characteristics (e.g. strength and permeability) can be derived based on the knowledge of the total pore volume, the pore size distribution, the specific surface area and the pore connectivity (Powers & Brownyard, 1948; Taylor, 1990).

Concrete contains a continuous network of pores and the pore structure will undergo densification with time due to ongoing hydration. Due to this proceeding hydration, the pore structure will change. Pores in a cementitious matrix can be classified in various ways. One possibility is the classification as gel pores (< 10 nm), capillary pores (10 nm – 10 µm) and voids (> 10 µm) (Espinosa & Franke, 2006; Mindess & Young, 1981; St John et al., 1998). Sometimes, those fractions are even further subdivided. Besides the differentiation between pores, there also exist three types of water related to the different pore sizes. First, there is the pore water in the capillary pores, which are a few hundred nanometres in size. Secondly, the interlayer water which is held by the gel pores by capillary tension and strong hydrogen bonds to the calcium-silicate-hydrates (C-S-H). The size of the gel pores is in the order of nanometres. The gel is a three-dimensional build-up of C-S-H layers with physically adsorbed water molecules and interlayer water between the sheet structure (Espinosa & Franke, 2006). Removal of this water by drying can cause considerable microstructural shrinkage. The third type of water is the chemically bound water, which is part of the chemical structure of the hydrated phases, and can only be removed by hydrate decomposition. Besides capillary and gel pores, voids are also a classification of pores. Another way of classifying pores is according to *micro-* (< 2 nm), *meso-* (2 - 50 nm) and *macro-* (> 50 nm) pores (originally proposed by (Dubinin, 1960) and subsequently officially adopted by the (IUPAC, 1972)). The latter is generally used for porous materials and is used in the present research.

Moisture transport processes cannot be understood without the knowledge of the moisture fixation in the concrete pore system. Water vapour sorption (i.e. the relation between moisture content and relative humidity) is therefore a key parameter. But, the moisture sorption isotherm is a function of the age, the moisture history, the temperature, etc. So, it is of great importance to know the extent and history of the drying process while performing a water vapour sorption test.

The condensation of gases on free surfaces is called adsorption. The penetration into the mass is called absorption. The term sorption is the combination of adsorption on the surface, absorption in the solid and capillary condensation in the pores. When a surface is exposed to a vapour, the surface will start to adsorb the vapour.

Also and comparatively with other sorption techniques, the use of water adsorption has some advantages, among them are: *i)* it can be performed at room temperature, *ii)* water has a small kinetic diameter (i.e. 0.28 nm) which allows it to enter pores even smaller than the ones accessible to CO_2 and N_2, and *iii)* for some kind of materials it is sensitive to surface chemistry. Moreover, it is not necessary

to submit the sample to a degassing protocol prior to the measurement, thus avoiding the partial removal of the ettringite phase.

The water release by the SAPs resulted in continued hydration, decreasing the microporosity, not taking into account the macro pores. Pastes with SAPs and without additional water show less capillary porosity when hardened (Igarashi & Watanabe, 2006). This was confirmed by means of an X-ray tomography study, showing a reduction of the amount of smaller capillary pores due to the filling of existing pores with hydration products and the reduction of initial micro cracks caused by the now mitigated autogenous shrinkage (Lura et al., 2008). The capillary porosity should hereby be the same for mixtures with the same effective water-to-cement ratio (ratio of the mixing water not held by the SAPs over the cement content) (Reinhardt & Assmann, 2009). The microstructure in between SAPs is denser due to internal curing and the macro pores do not interconnect. Therefore, the permeability is lower than for reference samples and this was also shown by using neutron radiography. All above-mentioned studies conclude on capillary pores (10 nm – 10 µm). However, it would also be interesting to study the effects in the micro- (< 2 nm) and mesopore (2 – 50 nm) range.

The attainable magnification of the methods described in Section 3.2.1, however, were too low (0.2 µm < d < 40 µm) to study the pores in these ranges. These specific ranges can be studied by means of water sorption and moisture transport processes, using the moisture fixation in the concrete pore system. Water sorption is hereby the relation between moisture content and the state of the moisture (relative humidity RH). Generally, water molecules are first adsorbed on the primary sites of the material (mainly oxygen-containing groups). The adsorbed water molecules then act as secondary sites for further sorption of water to form a cluster. As the relative pressure increases, those clusters grow and finally merge to fill the micropores. Once the micropore system is completely filled, further adsorption in the mesopores will take place. The studied specific surface area and the pore size distribution provide a relationship between the total amount of physically and chemically bound water and RH. This relationship is called the moisture sorption isotherm.

The effects of superabsorbent polymers and additional water on the microstructure and textural properties were approached using water vapour adsorption isotherms, obtained by both static as well as dynamic water vapour sorption tests. In this way, knowledge is gained on the effects of the SAPs on the sorption properties, namely the formed microstructure of cementitious materials. In addition, thermogravimetric analysis was used to elucidate on carbonation of the cementitious material. The influence of supplementary cementitious materials like fly ash and blast-furnace slag was also investigated.

First, however, the influence of different drying techniques on the measuring technique needed to be addressed in detail.

3.2.2.1 Storage conditions and sample preparation

After one day of storage at a relative humidity of 95 ± 5% and a temperature of 20 ± 2°C, the cement pastes (see paragraph 3.1.1.1) were demoulded and stored in water at 20 ± 2°C for a minimum period of 6 months to ensure a stable formation of the cementitious matrix and to avoid carbonation. An important leaching effect needed to be considered. As the volume ratio water-sample was low (1:2), the water became saturated with calcium hydroxide. The leaching was therefore limited to the exterior of the samples. This exterior part was removed and only the interior was used to study the effects on the microporosity. After being stored in water for 6 months, the samples were crushed and stored again in demineralized water for a minimum of 1 hour. This ensured the polymers would swell to their full extent. Subsequently, the crushed part was wet-sieved between 500 and 1000 µm. Circular movement during sieving on the 500 µm sieve separated the lighter small polymer particles from the paste particles (resemblance with gold panning, see Figure 3.32). As the SAPs are not as heavy as the paste and do not adhere to the cementitious matrix, circular movement will collect heavy particles in the middle of the sieve and will cause less-dense particles (SAPs) to move towards the edge. The paste particles were collected and the whole was rinsed. The 1000 µm fraction left-overs were crushed once more and wet-sieved according to the above-mentioned method. The wet-sieving was generally repeated on the collected paste particles until no SAPs were visible anymore during sieving.

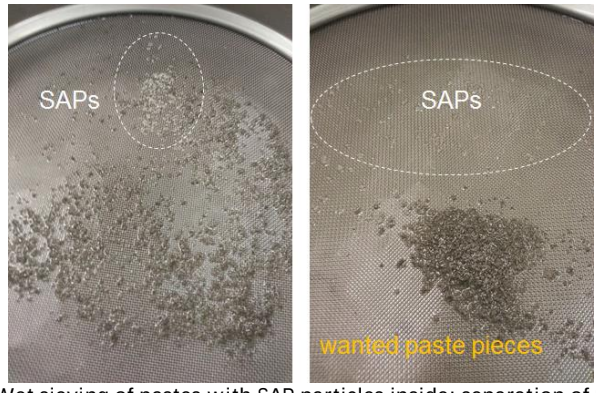

Figure 3.32. Wet sieving of pastes with SAP particles inside; separation of SAP particles.

The moisture sorption isotherm curve is dependent on the extent and history of the drying process. In this work, different drying techniques were studied. It was found that the solvent-exchange method in isopropanol followed by vacuum-drying at 20 ± 2°C (stored in the solvent with a solution/sample volume ratio of more than 100/1 for one week and subsequently vacuum-dried for two weeks) showed the least influence on the microstructural properties (See Section 3.2.2.4). The final collected samples were thus stored in isopropanol for one week and vacuum dried for two additional weeks in the presence of soda lime to exclude the effect of contact with carbon dioxide (CO_2) and the effects of carbonation. The soda lime was replaced every day.

3.2.2.2 Static and dynamic vapour sorption and used models

The water vapour sorption test can be conducted statically, and is often considered as a reference method (Baroghel-Bouny, 2007). The cement paste particles (0.05 g) were then stored in the presence of saturated salt solutions which govern the relative humidity inside a desiccator. The samples were first vacuum dried for two months at 20 ± 2°C. The desiccator was placed in a conditioned room at 20 ± 2°C and at atmospheric pressure. The desiccator's volume was high enough compared to the volume of the specimens in order not to disturb the ambience controlled by the salts and not to delay the equilibrium. Soda lime was placed in the desiccator to eliminate carbonation. The desiccator was taped to exclude air movement.

Every salt-storage step lasted for a minimum of a month and until the mass increase was lower than dm/dt < 0.0001 g/day (only measured in the last two days), with both requirements to be fulfilled. The minimum storage time to obtain equilibrium above 76% RH was two months due to the slower equilibration at a higher relative humidity. The time step ensured a stable equilibrium of the moisture status of the studied samples. Empty containers were used as reference containers.

The relative humidity was then increased from 3% to 97% relative humidity (RH). The following pure salts were used, with the corresponding RH:

Silica Gel		3% RH
Lithium chloride	LiCl	12% RH
Potassium acetate	CH_3COOK	23% RH
Magnesium chloride	$MgCl_2$	33% RH
Sodium bromide	NaBr	59% RH
Potassium iodide	KI	69% RH
Sodium chloride	NaCl	76% RH
Potassium chloride	KCl	86% RH
Potassium nitrate	KNO_3	93% RH
Potassium sulphate	K_2SO_4	97% RH

The Dynamic Vapour Sorption Apparatus used was from Surface Measurement Systems, London, UK (Figure 3.33). The general principle of a sorption measurement is shown in Figure 3.33a. The most important part is the humidity-controlled sample chamber and the microbalance module. By measuring the mass change as a function of time with changing relative humidity (RH) of the sample versus an empty reference, sorption isotherms can be calculated. The humidity is regulated by mixing humid and dry nitrogen gases. Figure 3.33b shows storage of samples in the presence of soda lime and the material studied next to the DVS equipment.

The temperature was set to 20°C, and the mass criterion to proceed to the next RH step was dm/dt < 0.002 wt%/min. The RH levels at which samples (5–10 mg) were subsequently equilibrated included 98-90-80-70-60-50-40-30-20-10-5-2-1-0% RH. Wet samples underwent two desorption-adsorption cycles. Dried cement pastes were first conditioned at 0% RH inside the DVS equipment followed by two adsorption-desorption cycles.

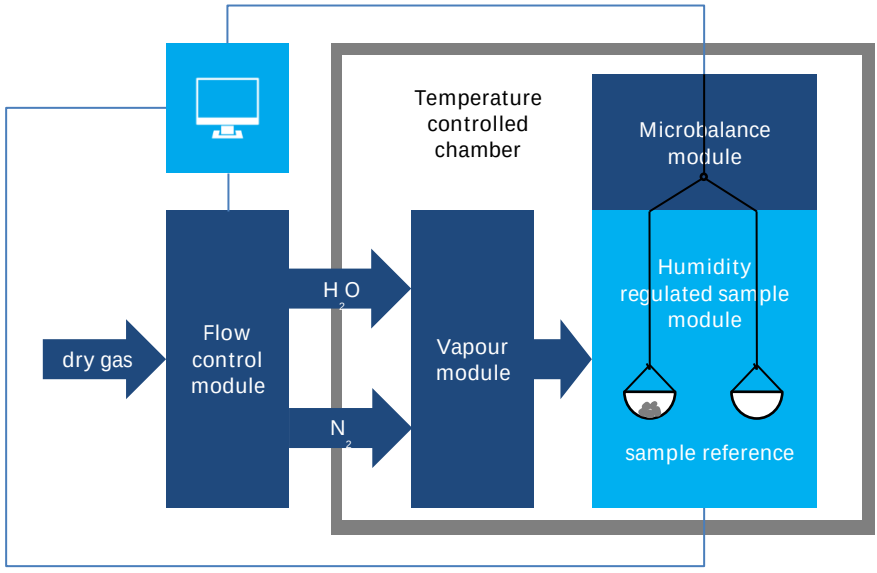

(a)

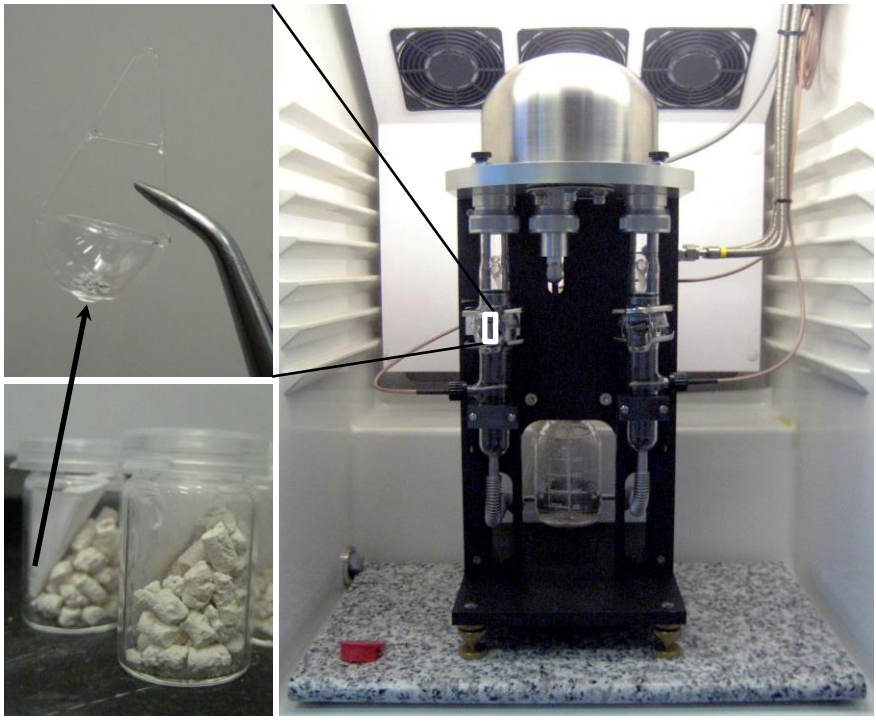

(b)

Figure 3.33. Schematic overview of the Dynamic Vapour Sorption (DVS) methodology **(a)** and the used equipment, where samples stored in the presence of soda lime are put into the sample container and the whole is put in the DVS equipment **(b)**.

The effect of the samples size was studied by performing DVS experiments with different granulometry. These were 250 - 500, 500 - 1000, 1000 - 2000 and 2000 - 5000 µm. The larger the particle size, the longer the time required for equilibration of the masses while increasing or decreasing the RH. If the sample is too big, the time to reach equilibrium is much higher and impracticable. Only the first two size classes proved to be acceptable. Practically, however, if a sample is too small, carbonation may occur and handling is less straightforward. In literature, the most frequent sample sizes are: 500 – 1000 (De Belie et al., 2010), 600 – 1180 (Garci Juenger & Jennings, 2001), 800 - 1000 (Baroghel-Bouny, 2007) and 600 – 1200 µm (Korpa & Trettin, 2006). Therefore, a sample size of 500 - 1000 µm was used in the present work. The effect of the equilibration time was studied by imposing longer times to reach the equilibrium. Since negligible differences were found at longer equilibrium times, it was confirmed that the selected criterion (dm/dt < 0.002 wt%/min) ensured the reliability of the experiments.

The type of branch of the water sorption isotherms taken into account to calculate the microstructural properties is a point for discussion. The adsorption branch is not entirely correct as the menisci formation is delayed. The desorption branch is not usable due to delayed evaporation or pore emptying (Everett, 1979; Gregg & Sing, 1982; Korpa & Trettin, 2006). As a consequence, the obtained pore size distributions will not exactly represent the real pore structures, but some general conclusions can be derived. In this research, and taking into account the shape of the measured isotherms, the most frequently used adsorption curve was studied.

Although the understanding and modelling of water isotherms in porous materials have been extensively researched, the underlying mechanism of water adsorption is not yet fully elucidated to date and remains the object of discussion (Furmaniak et al., 2008). Therefore, the interpretation of the experimental water sorption isotherms is not always straightforward. Notwithstanding, some classical models (described below) can be applied in order to calculate the textural parameters of the materials from their water isotherms. The obtained results may differ from reality, but they are still relevant and useful for comparative studies.

The BJH (Barrett, Joyner and Halenda) method (Barrett et al., 1951) allows the determination of the pore size distribution in the mesopore range (2 - 50 nm) from experimental isotherms using the Kelvin model of pore filling (Baroghel-Bouny, 2007; Gregg & Sing, 1982). In the Kelvin model, both capillary and adsorbed water phases exist in cylindrical pores and iterative step-by-step calculation leads to the pore size distribution (Baroghel-Bouny, 2007).

The micropore volumes (< 2 nm) have been calculated by applying the Dubinin-Radushkevich (DR) equation (Dubinin, 1975). It is used to describe the adsorption in microporous materials, mostly for activated carbons and zeolites. The equation is based on the assumptions of a change in potential energy between the gas and adsorbed phases, and the characteristic energy of the solid (Nguyen & Do, 2001) with the Polanyi model (Gil & Grange, 1996; Wood, 2001). The adsorption potential hereby corresponds to the change in vapour pressure (Polanyi model) (Gil & Grange, 1996; Wood, 2001), leading to the Dubinin-Radushkevich equation (Equation 3.2):

$$\ln(W) = \ln(W_0) - \left(\frac{R \cdot T}{\beta \cdot E_0}\right)^2 \cdot \ln^2\left(\frac{p^0}{p}\right) \quad (3.2)$$

where W_0 is the micropore volume, W the volume that has been filled at a relative pressure of p/p_0, E_0 the characteristic activation energy of adsorption for a reference vapour, β the affinity coefficient, R the gas constant and T the temperature (293 K). The DR equation was applied at low relative humidities (1-10% RH).

There is still a lot of controversy regarding the correct value to be used for the affinity coefficient β (Wood, 2001). Cement pastes have been studied less, compared to activated carbons (data in (Wood, 2001)), so more research has to be performed in this area before being able to infer the E_0 value from the DR equation applied to water isotherms. In this study, a value of 0.39 has been used and the DR equation was applied at the adsorption values at 1, 5 and 10% RH.

The physical adsorption of vapour molecules on a solid surface was explained by the BET theory (Brunauer-Emmett-Teller) (Brunauer et al., 1938; Gregg & Sing, 1982). This model is an extension of the Langmuir theory (Langmuir, 1916) from monolayer molecular adsorption to multilayer adsorption. The BET equation considers that the rate of adsorption onto surface sites is equal to the rate of evaporation from occupied sites, but it also assumes that the energy of adsorption for the second and subsequent layers is equal to that of liquefaction, and the total number of molecules adsorbed is the sum of all the adsorbed layers. Although this model has some drawbacks, it has been widely used ever since. In this regard, one of the limitations of the BET method is that it can only be applied in porous samples if these possess an open porosity (Odler, 2003), which is the case for cementitious materials. With the BET theory, the specific surface area accessible to water molecules (S_{BET}) was calculated within the low RH range (10, 20 and 30% RH) of the adsorption isotherms. In the BET theory for multilayer adsorption, following hypotheses are made: *i)* there is an infinitely physical adsorption in layers, *ii)* there is no interaction between the layers, and *iii)* the Langmuir theory can be applied to each layer. The BET equation is formulated in equation 3.3:

$$\frac{1}{\upsilon \cdot [(p_0/p) - 1]} = \frac{c-1}{\upsilon_m \cdot c} \cdot \frac{p}{p_0} + \frac{1}{\upsilon_m \cdot c} \quad (3.3)$$

where p is the equilibrium pressure, p_0 the saturation pressure, υ the adsorbed gas quantity, υ_m the monolayer adsorbed gas quantity and c the BET constant. This is linear relationship is only valid for $0.05 < p_0/p < 0.35$. If I_{BET} and A_{BET} would be the y-intercept and slope of the curve respectively, following equations 3.4 can be used:

$$\upsilon_m = \frac{1}{I_{BET} + A_{BET}} \qquad c = 1 + \frac{A_{BET}}{I_{BET}} \qquad S_{BET} = \frac{\upsilon_m \cdot N_a \cdot s}{V \cdot m_a} \quad (3.4)$$

where N_a is the Avogadro constant, s the adsorption cross section, V the molar volume of the adsorbate gas and m_a the mass of the absorbent.

From the isotherms, the C-S-H gel amount can be calculated as the ratio of the water amount adsorbed by the hardened cementitious material to the water amount adsorbed by the C-S-H, following the method described in (Baroghel-Bouny, 2007). The value of RH at 20% was chosen as multilayer adsorption occurs, without excessive condensation in the gel pores. It is calculated as the ratio of water adsorbed at 20% RH (instead of 22.8% RH in (Baroghel-Bouny, 2007)) to the water amount adsorbed by the C-S-H at a certain RH. The latter value was determined in (Baroghel-Bouny, 2007; Olson & Jennings, 2001) and is 0.219 $g \cdot cm^{-3}$ at 22.8% RH (by using 2.6 $g \cdot cm^{-3}$ for the C-S-H density in this state, according to (Olson & Jennings, 2001)) and 0.26 $g \cdot cm^{-3}$ at 20% RH (Olson & Jennings, 2001). In this study, both values are used as an interval for the C-S-H content determination.

3.2.2.3 Thermogravimetric analysis

The TGA instrument used in this investigation is a TGA Q50 Thermogravimetric Analyser. A sample was hereby gradually heated at a rate of 10°C min^{-1} till 900°C under a controlled nitrogen (N_2) atmosphere. The mass loss due to degradation of the material was recorded and used to check whether the samples showed carbonation or not. The samples used were the same as used for the dynamic vapour sorption tests.

The amount of physically bound water, chemically bound water and portlandite could be quantified using thermogravimetric analysis. The amount of physically bound water was calculated as the difference between the weight percent (wt%) at 105°C minus the starting value. The chemically bound water will mainly be driven off at temperatures above 105°C. It was determined by the mass loss between 105°C and 900°C minus the loss due to dehydration of the portlandite and the loss due to decarbonation.

When portlandite CH decomposes to CaO and H_2O (dehydroxylation of $Ca(OH)_2$), a mass loss is recorded around 420°C. Taking into account the molecular weight of portlandite (MW_{CH}) and water (MW_{H2O}), the weight loss in percent (WL_{CH}) can be converted to the amount of CH according to the first part of equation 3.5. However, due to the decomposition of calcite in CaO and CO_2 (decarbonation of $CaCO_3$) around 680°C and the fact that calcite originates on the one hand from the original components ($WL_{original\ CO2}$) and on the other hand from the chemical reaction between CH and CO_2, an additional term is added to calculate the total CH content irrespective of carbonation (with MW_{CO2} the molecular weight of carbon dioxide). All amounts were expressed relative to the final mass at 900°C.

$$CH(\%) = WL_{CH}(\%) \cdot \frac{MW_{CH}}{MW_{H_2O}} + \left(WL_{CaCO_3}(\%) - WL_{originalCO_2}(\%)\right) \cdot \frac{MW_{CH}}{MW_{CO_2}} \qquad (3.5)$$

This CH value may be slightly overestimated as part of the $CaCO_3$ also originates from the carbonation of C-S-H (Borges et al., 2010). This effect is negligible for Portland cements and is more pronounced when one uses supplementary cementitious materials.

3.2.2.4 Influence of different drying techniques

Generally, all drying techniques more or less dehydrate C-S-H and ettringite. A strong drying method may remove interlayer water from C-S-H which re-enters when the RH increases again (De Belie et al., 2010). Drying causes the restructuration of low-density C-S-H and a collapse below 40% RH as well as the conversion of loosely-packed C-S-H to denser C-S-H. Drying enhances the chemical ageing, meaning that the degree of polymerization of the silicate chains has increased and the C-S-H has changed irreversibly towards stiffer, stronger and denser ones (Olson & Jennings, 2001). Incomplete water removal likely leaves plugs or residual water in the narrowest choke points, resulting in a complete pore blockage in some areas of the paste (Diamond, 2003; Gallé, 2003). During chemical aging, C-S-H tends to link with each other, causing a compression of the hydrates. A strong drying step accelerates this reaction because the C-S-H are brought closer together (Espinosa & Franke, 2006).

The four main drying techniques described in literature to dry cementitious materials are discussed hereafter:

Freeze-drying

In freeze-drying (F-drying), the ice sublimates, causing less capillary stresses. Some investigations even showed a preservation of the pores in the fine pore region ($r < 5$ nm) (Konecny & Naqvi, 1993; Korpa & Trettin, 2006). For that reason, this drying technique is used frequently for MIP and TGA measurements (Collier et al., 2008) as it also stops hydration. However, F-drying may also change the microstructure (Zhang & Scherer, 2011). It causes damage, due to thermo-mechanical stress in the inner C-S-H porosity (Collier et al., 2008; Gallé, 2001; Konecny & Naqvi, 1993). So overall, the literature is not conclusive on the effects of F-drying.

Oven-drying

Oven-drying is widely used because it is a fast drying technique. Oven-drying, however, damages and alters the microstructure significantly, even to a greater extent than freeze-drying (Gallé, 2001). For example, oven-drying at 105°C removes unbound water but the capillary hydrostatic stresses due to surface tension of the receding water menisci generate a collapse of the fine pores (Beaudoin & Tamtsia, 2004; Gallé, 2001; Garci Juenger & Jennings, 2001; Korpa & Trettin, 2006) as C-S-H is partly dehydrated at 105°C (Taylor, 1990). Oven-drying also leads to the decomposition of monosulphoaluminate (AFm) and ettringite (Aft) phase at 60°C ((Zhang & Glasser, 2000) as cited by (Zhang & Scherer, 2011)). It thus causes ettringite and C-S-H to lose a significant amount of non-evaporable water (Gallé, 2001; Moukwa & Aïtcin, 1988). Drying at 50°C coarsens the pore structure due to the polymerization of silicate anion chains and the development of a cohesive structure in C-S-H (Aono et al., 2007). Generally, oven-drying thus results in large capillary porosity due to capillary stresses, cement hydrates (ettringite, AFm and C-S-H) desiccation, and micro-crack generation due to thermo-hydric stresses and the differential thermal expansion of the composition.

Vacuum-drying

Vacuum-drying is a slow technique and Zhang & Glasser ((Zhang & Glasser, 2000) as cited by (Gallé, 2001; Zhang & Scherer, 2011)) already observed that

ettringite and monosulphoaluminate may degrade (structural and physical collapse of hydrates like AFm and AFt phases), causing damage to the pore structure and increasing the pore volume ((Zhang & Glasser, 2000), as quoted by (Collier et al., 2008)).

Solvent-exchange method

Solvent-exchange methods replace the water by a solvent during submersion of a sample in the solvent. The solvent is afterwards removed by ambient drying or vacuum-drying. The solvent-exchange methods show the best results in preserving the microstructure as they stress the microstructure less (Collier et al., 2008; Feldman & Beaudoin, 1991; Konecny & Naqvi, 1993) and they are therefore used to stop the hydration and to study the microstructure. However, it remains possible that a solvent replacement creates chemical artefacts in the specimens by reaction with hydration products or through strong adsorption. Upon heating, methanol for example will react with C-S-H to form CO_2 and this is reflected in a higher carbonate peak (Beaudoin et al., 1998; Day, 1981; Feldman & Beaudoin, 1991). It binds with hydrating and mature cement paste. Some researchers stated that there might be a possible reaction of isopropanol with calcium hydroxide (Beaudoin, 1987), but in general, it is accepted that isopropanol does not react with cement (Feldman & Beaudoin, 1991) as does methanol.

Which drying technique is the optimal is feed for discussion. Zhang & Glasser (2011) have summarized pros and cons of the various drying techniques available as follows:

To preserve microstructure:

solvent-replacement > vacuum-drying > F-drying > oven-drying

To preserve composition:

F-drying > oven-drying > solvent-replacement

To save time:

oven-drying > F-drying > solvent-replacement

The effects of different drying techniques on the microstructure were approached using a supplementary technique, namely water vapour adsorption isotherms. In this way, knowledge is gained on the effects of the drying techniques on the sorption properties, namely the formed microstructure of cementitious materials. In addition, thermogravimetric analysis was used to elucidate carbonation.

Several drying techniques were studied. These include:

- *no-drying (20 ± 2°C)*: specimens are stored in water;
- *freeze-drying*: specimens are dried in liquid nitrogen and placed in a freeze-dryer instantaneously for two weeks;
- *oven-drying at 40°C*: for two weeks (ventilated oven);
- *oven-drying 105°C*: for two weeks (not ventilated oven);
- *air-drying in the presence of silica gel (20 ± 2°C)*: for one month;
- *vacuum-drying (20 ± 2°C)*: for two weeks at 0.1 bar;
- *the solvent-exchange method in methanol and isopropanol followed by vacuum-drying (20 ± 2°C)*: stored in the solvent (solution : sample volume ratio more than 100 : 1) for one week and subsequently vacuum-dried for two weeks.

In addition, ground specimens were stored for six months in water and six months in air to ensure complete carbonation for comparison with a changed microstructure.

The obtained derivatives of the TGA curves are shown in Figure 3.34. There is a high mass loss between 50 - 500°C due to the release of water from cement binding phases, like C-S-H. Generally, four peaks are visible, corresponding to ettringite (AFt) at approximately 60°C, monosulphoaluminate (AFm) at 120°C, portlandite (dehydroxylation of $Ca(OH)_2$) at 420°C, and calcite (decarbonation of $CaCO_3$) at 680°C.

TGA results from carbonated cement pastes (dashed line in Figure 3.34) correspond to the profiles found in (Villain et al., 2007). The TGA curve of the samples stored in water only shows a minor form of carbonation (saturated in Figure 3.34a). Oven-drying in a ventilated oven (40°C) and in air with silica gel caused significant carbonation, even though the soda lime was replaced regularly every day. Oven-drying at 105°C resulted in almost no carbonation, as the air was not ventilated and soda lime was able to extract most of the carbon dioxide from the air. Vacuum-drying did not induce any significant carbonation and F-drying caused partial carbonation (Figure 3.34b). Specimens dried with the solvent-exchange method followed by vacuum-drying (Figure 3.34c) also showed almost no carbonation (isopropanol) and partial carbonation (methanol). As methanol, upon heating, will react with C-S-H to form CO_2, this is reflected in a higher carbonate peak (Day, 1981). This heating was caused by performing TGA analysis and would typically not happen at room temperature.

Oven-drying at 105°C removed part of the non-evaporable water, dehydrated C-S-H, monosulphoaluminate (AFm) and ettringite (AFt) phases as the peaks till 200°C in Figure 3.34a lie lower compared to all other drying techniques.

These findings are also reflected in the calculation of the total amount of CH through portlandite and CH through the carbonation peak (Figure 3.35a). The total amount of portlandite is approximately the same for all mixtures (17-19%). Figure 3.35a indicates that the carbonation increases with the following drying techniques: F-drying, oven-drying at 105°C, the solvent-exchange method with methanol, oven-drying at 40°C in a ventilated oven, drying in the presence of silica gel and the totally carbonated specimen. The other drying techniques (vacuum drying and the solvent-exchange method with isopropanol) did not show significant carbonation compared to the non-dried sample. The explanation of the higher amount of carbonation, reflected by using methanol, is given above.

The amount of physically bound water left (Figure 3.35b) reflects the strength of the drying technique. It is clear that the oven-drying technique at 105°C causes a significant reduction in physically bound water compared to other drying techniques as it is a strong drying technique. The lower value of drying in the presence of silica gel is due to the change of the microstructure by carbonation, thus leading to a different adsorption in the interior. Moreover, drying in the presence of silica gel occurs near 3% RH, and the physically bound water in samples dried in the presence of silica gel is thus still present in a higher extent compared to samples dried with the other drying techniques. Only the F-drying, vacuum-drying and the solvent-exchange methods show the same amount of physically

bound water. The amount of physically bound water in saturated specimens could not be determined as there was still a lot of free water present during testing due to the continuous storage under water.

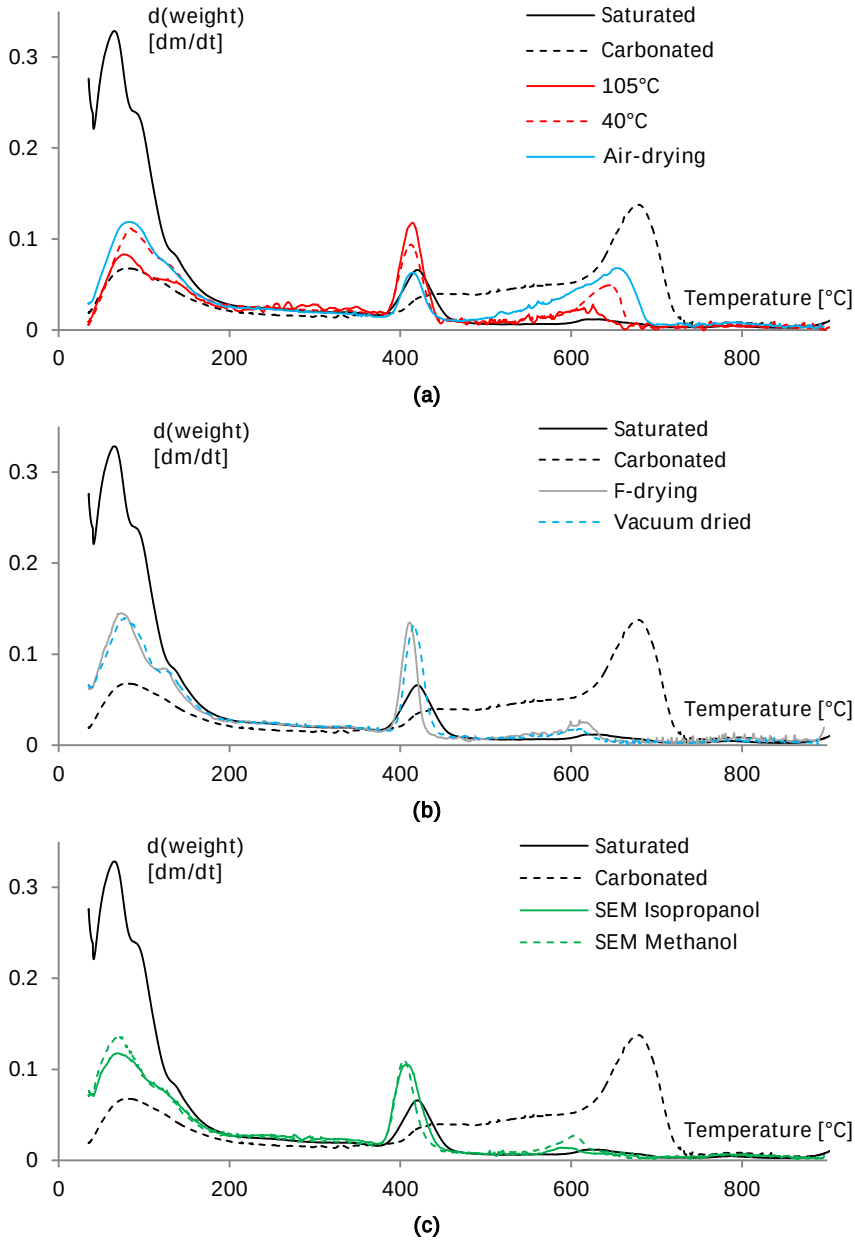

Figure 3.34. Thermogravimetric analysis (TGA) showing partially carbonation of air- and oven-dried specimens **(a),** no carbonation of F- and vacuum-dried specimens **(b)** and no carbonation of specimens dried with solvent-exchange **(c)**. The curves show the derivative of the TGA weight curve as a function of the temperature.

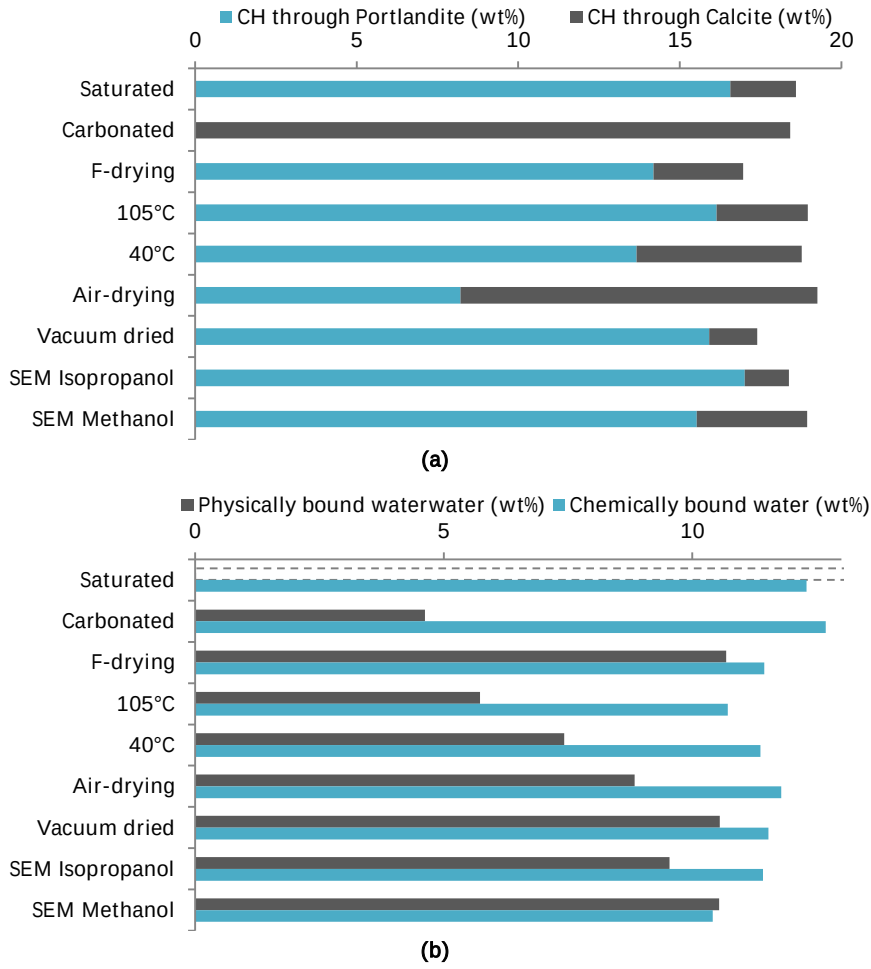

Figure 3.35. Thermogravimetric analysis results [wt%] of the portlandite content **(a)** and the physically bound water and chemically bound water **(b)** of all specimens studied.

The amounts of chemically bound water present do not seem to differ much, except for the oven drying at 105°C and the solvent-exchange method with methanol. During drying at high temperatures, part of the chemically bound water is removed. The lower value, when using methanol, can be explained by the fact that methanol is anticipated to react with the original constituents (Day, 1981).

Taking into account that water is likely to impair the mechanical properties and durability of concrete structures, water vapour adsorption measurements constitute an essential tool when characterizing the properties of cement-bound materials.

The obtained water vapour sorption curves are shown in Figure 3.36 and are in correspondence with the ones found by (Baroghel-Bouny, 2007). The repetition in testing falls between the boundaries and accuracy of the test.

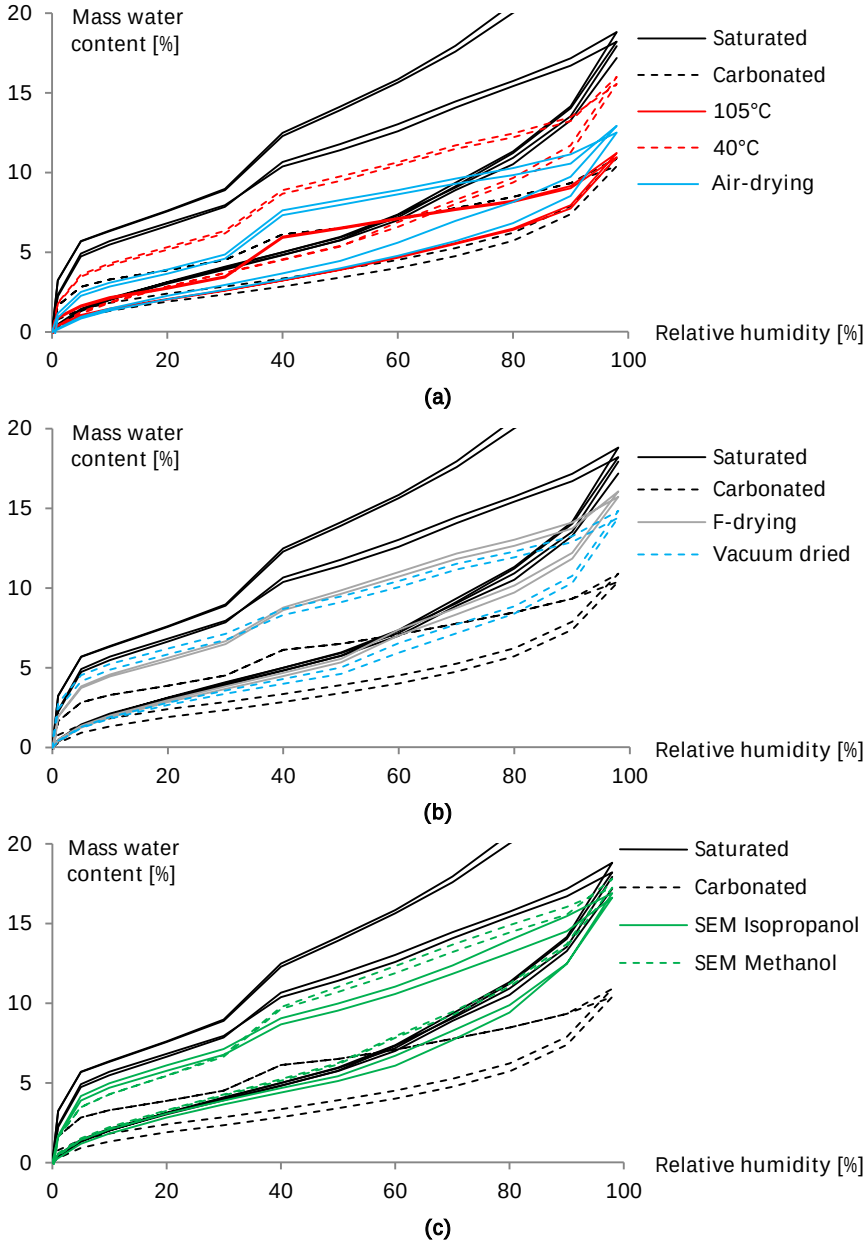

Figure 3.36. Influence of the drying on the obtained sorption curves: air- and oven-drying **(a)**, F- and vacuum-drying **(b)**, and solvent-exchange followed by vacuum-drying **(c)**. The curves show the mass water content as a function of the relative humidity.

The shape of the isotherms gives us valuable information regarding the pore structure of the samples. The water molecules are firstly adsorbed at the narrow micropores and the sorption mechanism will gradually proceed through the further filling of the pores of increasing size. Thus, the low water uptakes in the

first part of the isotherm and the steep rises of the slope of the adsorption curve at relative pressures above 50% indicate that these samples are mainly comprised of mesopores. There also are not that much bigger pores present as there is no huge water uptake at a high relative humidity (>96%).

However, in the case of the carbonated specimen and the samples dried in the presence of silica gel and oven-dried at 105°C, the slope of the isotherms is almost linear until high relative pressures. This result, coupled with the fact that their total water uptake is lower than for the rest of the specimens, indicates that the drying technique has provoked a partial collapse of the porous structure. Also, with increasing the degree of carbonation, the porosity of the specimens is reduced. In this regard it has been previously stated that carbonation reduced the porosity among the capillary mesopores in the outer C-S-H (10 - 100 nm) (Thiéry et al., 2011). It is also worth it to mention that the specimens dried by solvent-exchange, especially in the presence of methanol, lead to practically identical isotherms than in the case of the saturated sample, thus indicating that this drying technique preserves the microstructure and sorption properties of the material.

In all the cases, the isotherms exhibit a very pronounced hysteresis loop. This phenomenon is still under investigation and nowadays there are two feasible theories. The first one is the existence of ink-bottle pores: during the desorption process small pores will constrict the openings to larger pores such that the adsorbed water in the larger pores is not released until the relative pressure corresponds to that of the smaller pore radius. An alternative approach suggests that during the adsorption or/and desorption process the water is in a metastable state leading to the assembly of water molecules into different molecular structures during adsorption and desorption (Ohba & Kaneko, 2007). It is clearly observed that the desorption branch of the obtained isotherms presents a steep decrease at RH < 40%, this being attributable to the existence of ink-bottles pores in these materials and the occurrence of cavitation. In this regard, if diameter of the pore entrance is smaller than a certain critical width, the mechanism of desorption from the pore body involves the spontaneous nucleation and growth of gas bubbles in the metastable condensed fluid (cavitation). In this case, the body empties while the pore neck remains filled. When this occurs, the pressure of desorption depends on the adsorbate and temperature and it is not correlated with the size of connecting pores. Hence, pore size distributions calculated from the desorption branch of the hysteresis loop are artificial and they do not reflect the real pore sizes (Thommes, 2010). The structure of the C-S-H is also important (Adolphs, 2008).

A deeper study of the isotherms has been carried out by applying different models. As it has been previously explained, the mesopore size distributions have been calculated by the BJH method applied to the adsorption branch and the obtained profiles are shown in Figure 3.37. The results confirm that the porous network of the materials is mainly formed of narrow mesopores (d_p ~ 5-6 nm), where the curves present a maximum. As expected, all profiles are co-alike except for the ones corresponding to the specimens air-dried in the presence of silica gel, oven-dried at 105°C and the carbonated one, where the obtained pore size distribution is flatter. This result evidences that these two drying techniques are not adequate since the porous structure of the original sample has been modified.

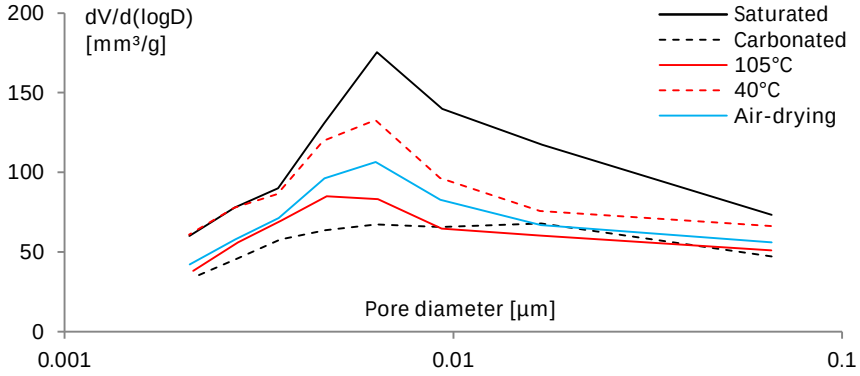

(a)

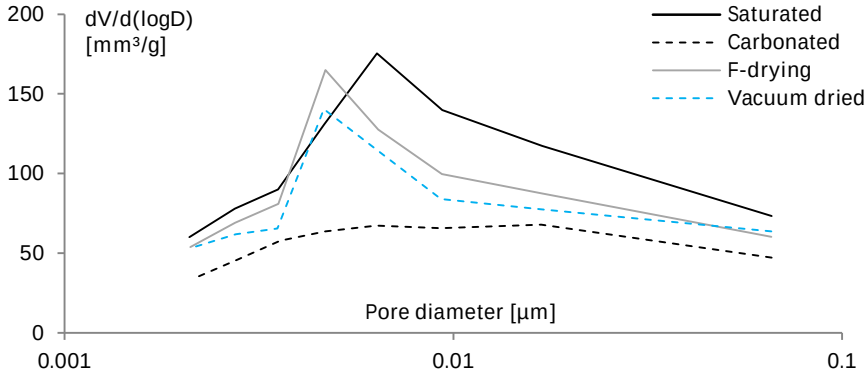

(b)

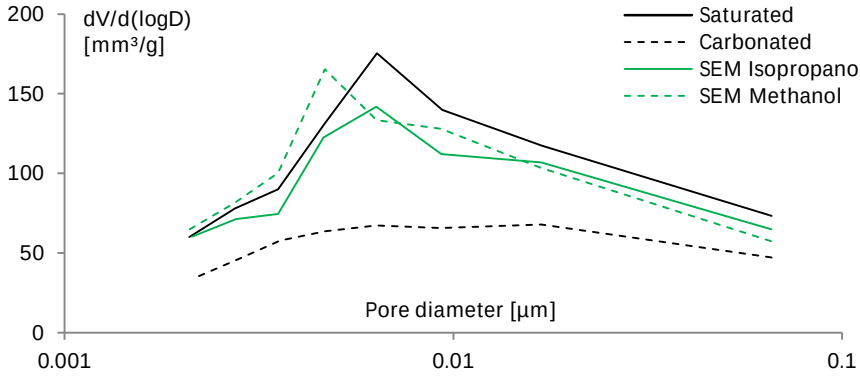

(c)

Figure 3.37. Influence of the drying on the calculated microstructure with the BJH method: air- and oven-drying **(a)**, F- and vacuum-drying **(b)**, and solvent-exchange followed by vacuum-drying **(c)**. The curves show the pore size distribution as a function of the pore diameter, with V the volume of the pores and D the diameter.

The volumes of micro and mesopores are presented in Figure 3.38. As it is clearly seen, the micropore volumes (calculated by the DR formulism) are much lower in comparison with the volume of mesopores. In fact, and for all the samples, the volume of micropores only accounts for approximately the 20% of the total pore volume.

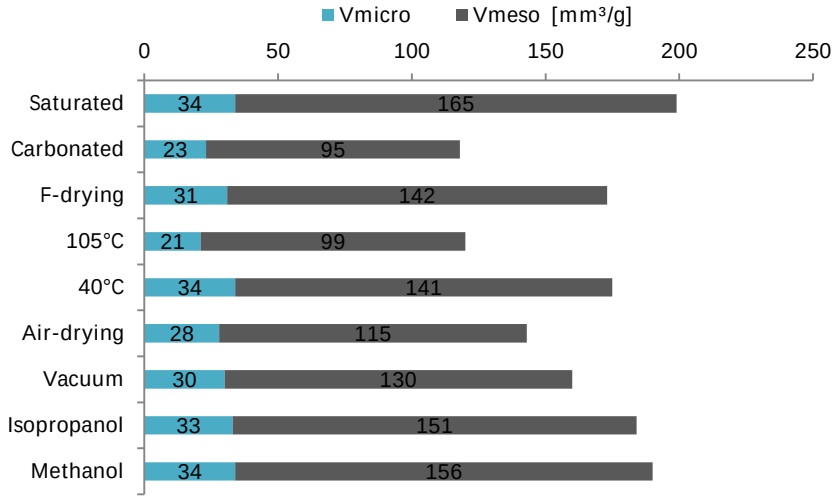

Figure 3.38. Amount ($mm^3 \cdot g^{-1}$) of micropores calculated with the DR-method and amount of mesopores calculated with the BJH-method. (IUPAC pore classification: micropores (< 2 nm), mesopores (2-50 nm) and macro pores (> 50 nm))

The C-S-H gel amounts are shown in Figure 3.39. It is clear that the prominent changes are recorded in the same mixtures as above. The lower values reflect the densification of the C-S-H due to the loss of physically bound water (Figure 3.35b) which causes the C-S-H to change from loose-packed C-S-H to denser ones. These results perfectly match with the ones obtained by water adsorption. Thus, the three samples with the lowest water uptake are also the ones that present the lowest C-S-H gel amount. Considering that the C-S-H is comprised of gel pores and that it is the main phase responsible for the development of the porosity in cementitious materials, when using invasive drying techniques, not only the chemical composition of the material but also its porous microstructure is affected.

The S_{BET}-values are shown in Figure 3.40. Typically, the S_{BET}-values range from 77 – 138 m²/g. These values are in good correspondence with Baroghel-Bouny and others researchers (Baroghel-Bouny, 2007; Odler, 2003; Powers & Brownyard, 1948), who report on values ranging from 80 to 143 m²/g.

A higher water removal does not result in a larger specific surface area and more accessible porosity (Korpa & Trettin, 2006), which is also visible if one compares the value found for an oven-dried (105°C) specimen to all other values for the specific surface area. Several authors observed that the minimum surface area was obtained for oven-dried samples at high temperatures (Garci Juenger & Jennings, 2001; Korpa & Trettin, 2006). When applying oven-drying at 105°C, the

amount of removed water is higher (see also Figure 3.35b) but the surface area is smaller. This can be interpreted as a possible pore collapse or pore alteration. As more water is removed, finer pores are accessed, but some gel pores cannot be accessed due to pore collapse. As a result, not the original pore structure is studied as the microstructure is changed.

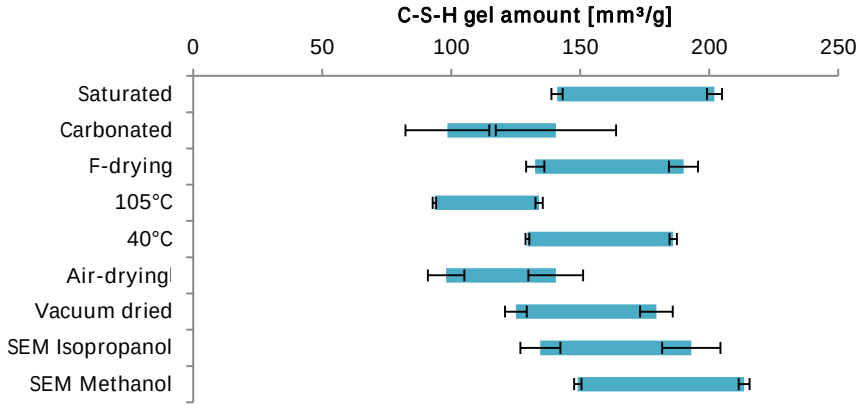

Figure 3.39. C-S-H amount for all samples after specific drying regimes, with deviations on the boundaries.

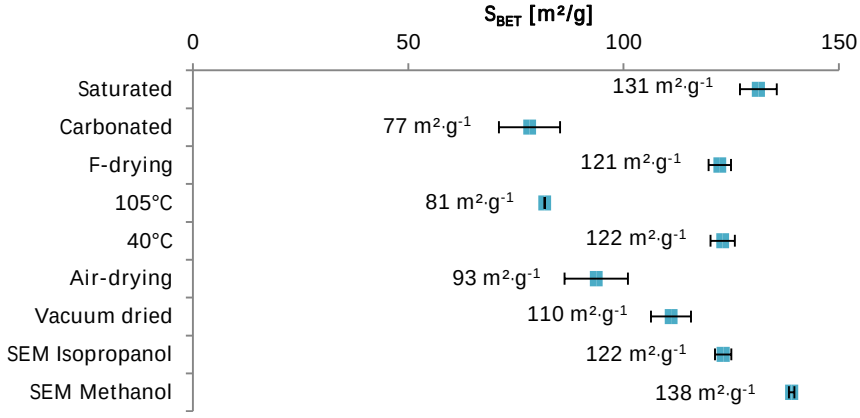

Figure 3.40. Obtained specific surface area S_{BET} for all studied drying techniques.

The lower values for carbonated specimens and drying in air can be explained by the degree of carbonation. Hence, and in accordance with results from literature (Thomas et al., 1996), an inverse correlation is obtained between the surface area and the amount of calcium carbonate present in the sample. In addition, methanol-calcium ion products have a high surface area which can affect the isotherm determination (Beaudoin, 1987). The latter explains the highest value of S_{BET} for the solvent-exchange method with methanol.

Based on the obtained results, the effect of the different drying techniques on the microstructural properties of the specimens is summarized as follows. Oven-drying causes capillary hydrostatic stresses due to the surface tension of the receding water menisci and removed part of the non-evaporable water. This results from the dehydration of C-S-H and causes the collapse of the monosulphoaluminate (AFm) and ettringite (AFt) phase at 60°C (Zhang & Glasser, 2000). In fact, the thermogravimetric profile of the specimen oven-dried at 105°C shows, together with the carbonated sample, the lowest amount of these two phases (Figure 3.34). Generally, oven-drying results in cement hydrates (ettringite, AFm and C-S-H) desiccation, and micro-crack generation due to thermo-hydric stresses and the differential thermal expansion of the composition. Capillary stresses due to receding water menisci may also induce a modification of the textural properties of the sample. The pore collapse will cause a decrease of the amount of the smallest pores present as capillary pressure increases with decreasing pore size. The effect of cracking and microstructure alteration increases with increasing drying temperature (40°C compared 105°C). It removes the bound water from ettringite and does not preserve the microstructure as the amount of pores when dried at 40°C is higher compared to drying at 105°C. Oven-drying is thus an unsuitable drying technique to preserve the fragile microstructure of cement-based materials. Air-drying in the presence of silica gel has to be avoided since it causes the carbonation of the material and, therefore, the modification of its microstructural properties. Vacuum-drying may lead to the structural and physical collapse of hydrates including AFm and AFt phases (Zhang & Glasser, 2000). However, and considering the found results, it seems an acceptable drying technique that preserves the amount of physically bound water and avoids carbonation. Finally, the solvent-exchange methods followed by vacuum-drying causes the smallest change in microstructural properties, thus being the most suitable ones for the drying of cement-based materials. Among both of them, isopropanol exchange should be selected when submitting the sample at high temperatures, since methanol reacts with C-S-H.

If the percentage of water mass obtained in the sorption isotherms is divided by the S_{BET}-value, the average thickness of the water film adsorbed on the solid surface is found (bold black curve of non-dried specimens in Figure 3.41). This curve can be compared to the ones suggested by (Hagymassy Jr. et al., 1969) (solid grey and blue curves). The t-curve is the statistical thickness of the film adsorbed on nonporous adsorbents as a function of the relative pressure (Hagymassy Jr. et al., 1969).

All curves obtained are between the boundaries of the t-curves from (Hagymassy Jr. et al., 1969). They found that below the statistical thickness of a monomolecular water layer (3 Å) or thus a RH of approximately 23%, the strongly bound water is removed from the C-S-H. Moreover, a linear relationship exists between 12 - 63% RH. The equilibrium water amount adsorbed is proportional to the C-S-H amount. From 63% RH onwards, a significant condensation takes place which implies the overall filling of pores (Baroghel-Bouny, 2007).

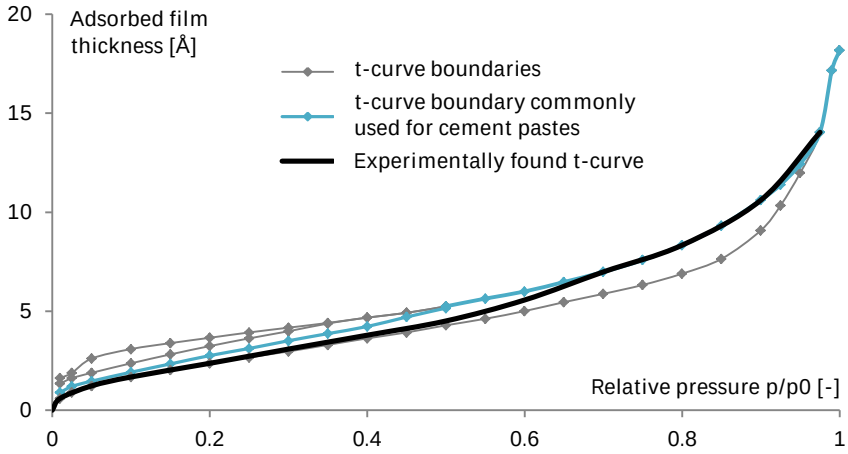

Figure 3.41. Obtained t-curve compared to the curves used by Hagymassy Jr.

For cementitious materials, the blue curve is used as proposed by (Hagymassy Jr. et al., 1969). It can be seen that this curve is slightly higher in values than the one found by recalculating it from the sorption isotherms. Up to 63% RH, this curve should be shifted downwards.

The conclusions are summarized in Table 3.5. The ideal drying technique, which can preserve the microstructure and can remove only the non-bound water, does unfortunately not exist. All drying techniques affect the microstructure in their own way. Water sorption has given additional experimental evidence that the best techniques to dry the cementitious samples are vacuum-drying and the solvent-exchange method with isopropanol.

Table 3.5. Conclusion of the effects of the drying techniques and carbonation.

	No Carbonation	*No reduction of free water*	*No change in microstructure*	*Overall conclusion*
Saturated	++	++	++	++
Carbonated	--	--	--	--
F-drying	+	++	+	+
105°C	+	--	--	--
40°C	-	-	+	-
Air-drying	--	+	-	--
Vacuum dried	++	++	+	++
Isopropanol	++	++	++	++
Methanol	-	++	++	+

3.2.2.5 Influence of supplementary cementitious materials

Figure 3.42 gives the mixtures with cement partly replaced by supplementary cementitious materials (FA and BFS). The sample preparation and storage condition is discussed in paragraph 3.2.2.1. The drying technique was solvent-exchange method in isopropanol followed by vacuum-drying at 20 ± 2°C. The water vapour sorption isotherms of fly ash systems show the same overall microporosity compared to a pure cementitious matrix. Only, with increasing replacement of cement by fly ash, the amount of larger mesopores seems to increase. This is seen as the steeper rise from a relative humidity of 80% onwards for the FA50 mixture. The FA85 mixture was impossible to make as there is not enough binder available for a stable microstructure during hardening.

The same conclusion can be made considering the blast-furnace slag mixtures. The amount of smaller pores seems to be slightly higher compared to the reference mixture. Again, the amount of larger mesopores is higher. The microstructure is denser in the BFS85 mixture, where not all the slag is consumed and part is acting as a filler. The isotherm remains flat but at higher relative humidity, it becomes steeper and a high amount of mesopores can be expected.

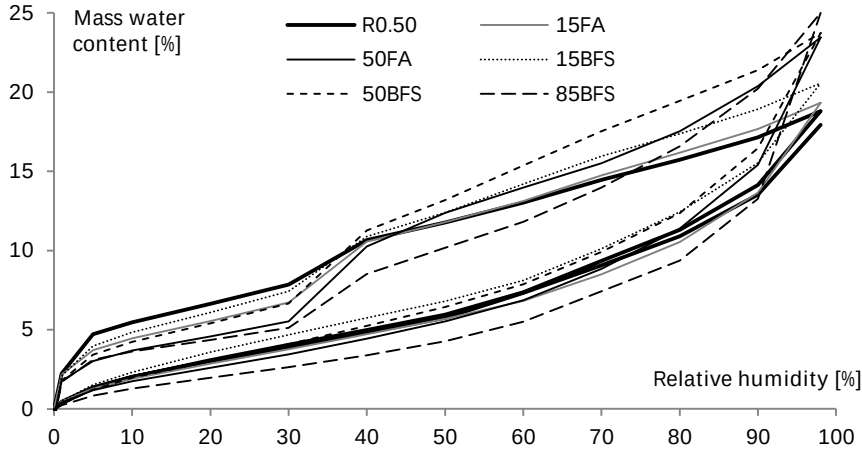

Figure 3.42. Water vapour sorption isotherms for specimens with supplementary cementitious materials.

The calculated microstructure (BJH method) for supplementary cementitious materials mixtures are shown in Figure 3.43. All materials show an anticipated peak of narrow mesopores at 5-6 nm, which is typical for a cementitious material.

When supplementary cementitious materials like fly ash are present, the portlandite is consumed, producing calcium-silicate-hydrates (C-S-H). They contribute to the formation of the binding phases in the cementitious matrix and thus influence the resulting pore structure. Overall, mixtures with supplementary cementitious materials show more mesopores than a cement paste with the same effective water-to-binder ratio. This could indicate pore densification when the supplementary cementitious materials' reaction causes a change of capillary pores towards gel pores. In case of fly ash, there is a decrease of the narrow mesopores.

This is a property which is inherent to a cementitious matrix which is partly replaced by fly ash. For example, at early age, the pozzolanic fly ash accelerates cement hydration. Then it acts as a substrate for crystal nucleation on which C-S-H phases and calcium hydroxide crystals can form preferentially. The formation of these additional C-S-H phases on the surface of fly ash particles leads to an increase in the amount of bound water relative to the cement content. Hydrates formed by the pozzolanic reaction densify the microstructure.

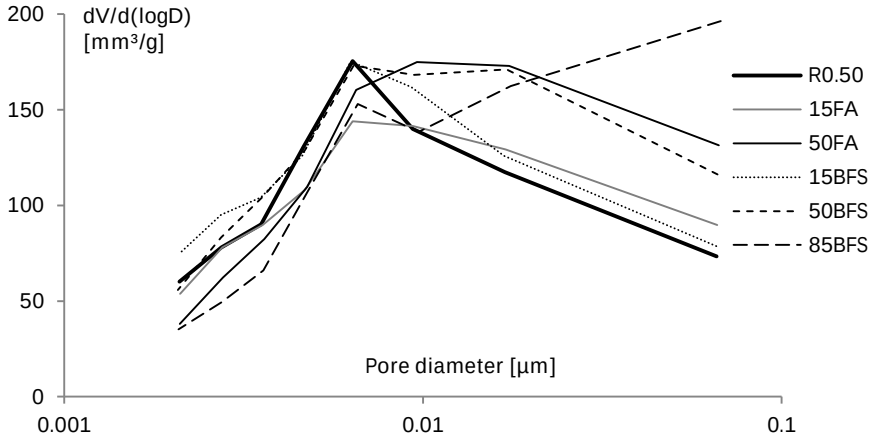

Figure 3.43. Calculated microstructure (BJH method) for specimens with supplementary cementitious materials.

In blast-furnace slag mixture, only a small increase in amount of narrow mesopores is found. However, in the BFS85 mixture, the amount of small mesopores is less. In this mixture, there is not enough portlandite to activate all slag (also partly the case in the BFS50 mixture). The remaining part of the slag is considered to be filler.

The micropore and mesopore volumes are quantitatively shown in Figure 3.44. The micropore volumes, as determined by means of the DR method, are 29, 27, 38, 35 and 22 mm³/g for FA15, FA50, BFS15, BFS50 and BFS85 mixtures, respectively. The amount of micropores is lower than the amount of mesopores, which is typical for a cementitious material. The same conclusions can be drawn.

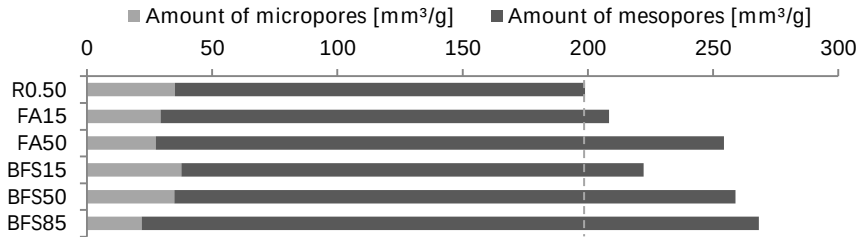

Figure 3.44. Amount of micropores calculated with the DR-method and the amount of mesopores calculated with the BJH-method for specimens with SCMs.

3.2.2.6 Influence of superabsorbent polymers

The sample preparation and storage condition is discussed in paragraph 3.2.2.1. The amount of SAPs added in this research is relatively high (0.5-1 m%), as those amounts are mostly used to receive self-sealing and self-healing rather than to mitigate autogenous shrinkage (typical amounts of 0.3-0.4 m%). These higher amounts of SAPs will influence the cementitious matrix even more and will accentuate the influences of the SAPs from a microstructural point of view.

The obtained derivatives of the TGA curves are shown in Figure 3.45, where four general peaks clearly are visible. The first at approximately 60°C corresponds to decomposition of ettringite, the second at 120°C to monosulphoaluminate, the third at 420°C to portlandite and the fourth to calcite.

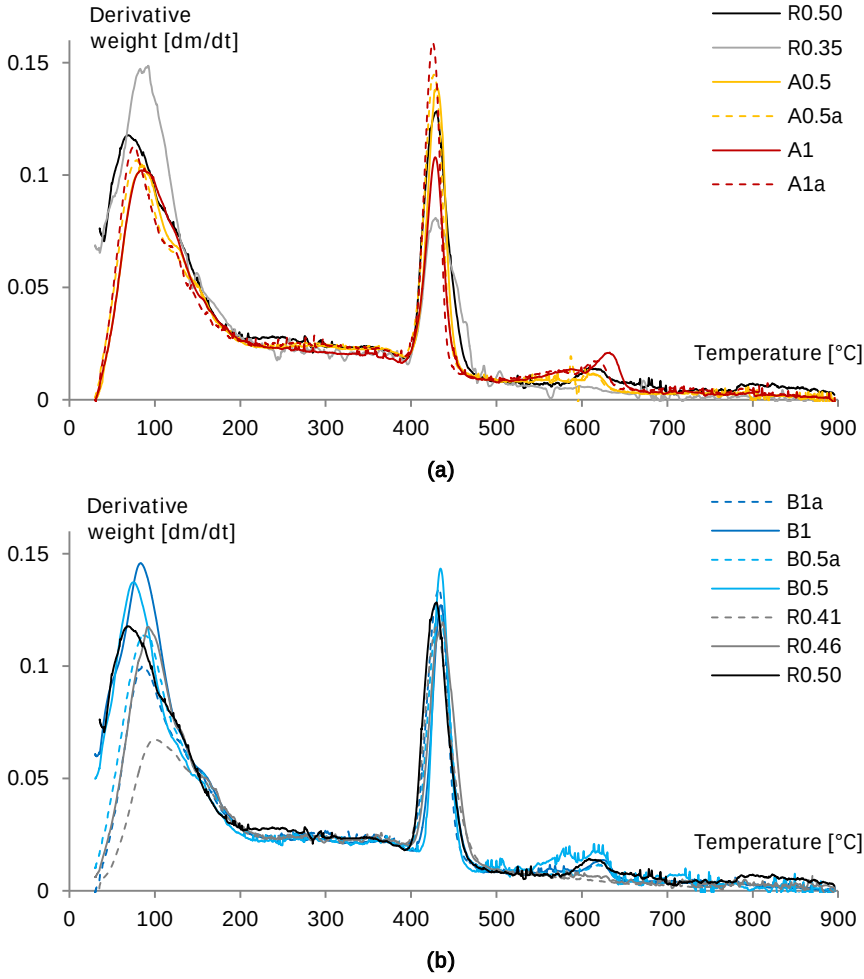

Figure 3.45. Thermogravimetric analysis (TGA) of specimens with SAP A **(a)** and SAP B **(b)** with their respective references. The curves show the derivative of the TGA weight curve as a function of the temperature.

All samples only show a minor degree of carbonation, which proves that the storage in the presence of soda lime is efficient to reduce the amount of carbonation and to almost completely prevent it. The specimens are rather small, so carbonation can occur quickly, but this was not the case in this research due to the use of soda lime.

Some researchers attribute the small peak at 680°C to a reaction of the solvent with a hydration product. Other solvent-exchange methods, like methanol, do induce 'carbonation'. Methanol, upon heating, will react with the C-S-H to form CO_2 and this is reflected in a higher carbonation peak (Beaudoin et al., 1998; Day, 1981; Feldman & Beaudoin, 1991). There might also be a small reaction of isopropanol upon heating with calcium hydroxide (Beaudoin, 1987), but in general, it is accepted that isopropanol does not react with the mature cement paste (Feldman & Beaudoin, 1991). The small peak observed in Figure 3.45 could partly be explained by this small but insignificant reaction as well. The reaction will not occur at room temperature as is the case in the vapour sorption tests.

The total amount of calcium hydroxide (CH) present as portlandite and as calcite is shown in Figure 3.46a. A decrease in water-to-cement ratio results in a decrease of the amount of CH. Using SAPs without additional water also causes a decrease of the CH content but the use of additional water compensates for this decrease. Figure 3.46a also indicates that the carbonation is limited in all mixtures.

The amount of chemically bound water in C-S-H is given in Figure 3.46b. The amounts of chemically bound water present do not seem to differ too much. However, the same trend as mentioned above for CH can be seen. The mixtures with the same effective water-to-cement ratio seem to behave similarly.

Taking into account that water is likely to impair the mechanical properties and durability of concrete structures, water vapour sorption measurements constitute an essential tool when characterizing the properties of cement-bound materials. The obtained water vapour sorption curves are shown in Figure 3.47 for the static water vapour tests and in Figure 3.48 for the dynamic water vapour measurements. The standard deviation on the static water vapour sorption values is the standard error on single values for five repetitions. Only one adsorption curve is given for the dynamic water vapour sorption tests as the replicates for these kinds of tests fall between the measurement error boundaries of the specific nature of the water vapour test.

First, the shape found by means of the static and dynamic water vapour test methods is alike and provides information regarding the pore structure of the cement paste. The overall magnitude of the mass increase is similar for both tests. When increasing the relative humidity, first water will be adsorbed starting at narrow micropores and then at pores with increasing size. So, the steep rise from a RH of 60% onwards, and especially above 80% RH, indicates that all samples show mainly mesopores. This is typical for a cementitious material.

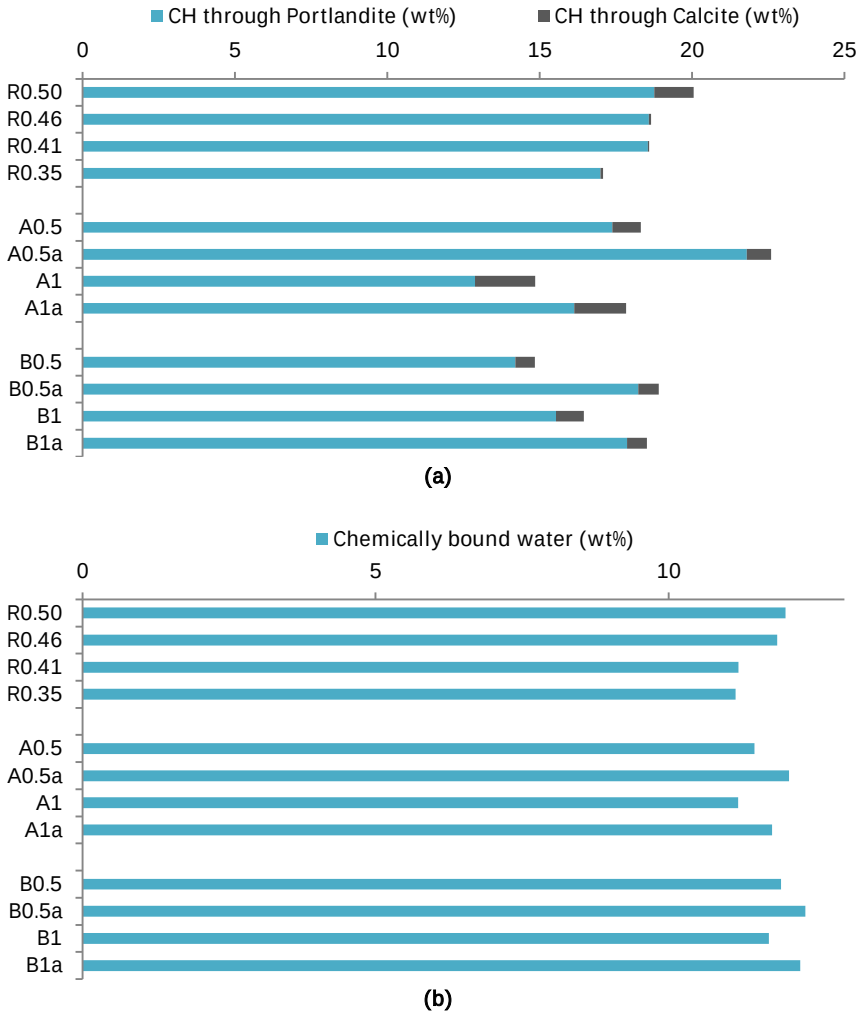

Figure 3.46. Thermogravimetric analysis results [wt%] of the portlandite content **(a)** and the chemically bound water **(b)** of all specimens studied.

The results for pure SAPs (Figure 3.47a) show that the material is able to take up moisture to a high extent from a relative humidity of 90% onwards. The values correspond to the values found with dynamic vapour sorption (not shown in a figure). SAP A particles are able to extract 25.6%, 83.1% and 393.8% of their weight in moisture from the air in an environment with 60, 90 and 98% RH, respectively. SAP B particles are able to extract 28.1%, 84.0% and 394.1%, respectively. This property to extract moisture is especially useful for self-healing purposes as the moisture can be provided towards the cementitious matrix for further hydration and calcium carbonate crystallization (see Chapter 5).

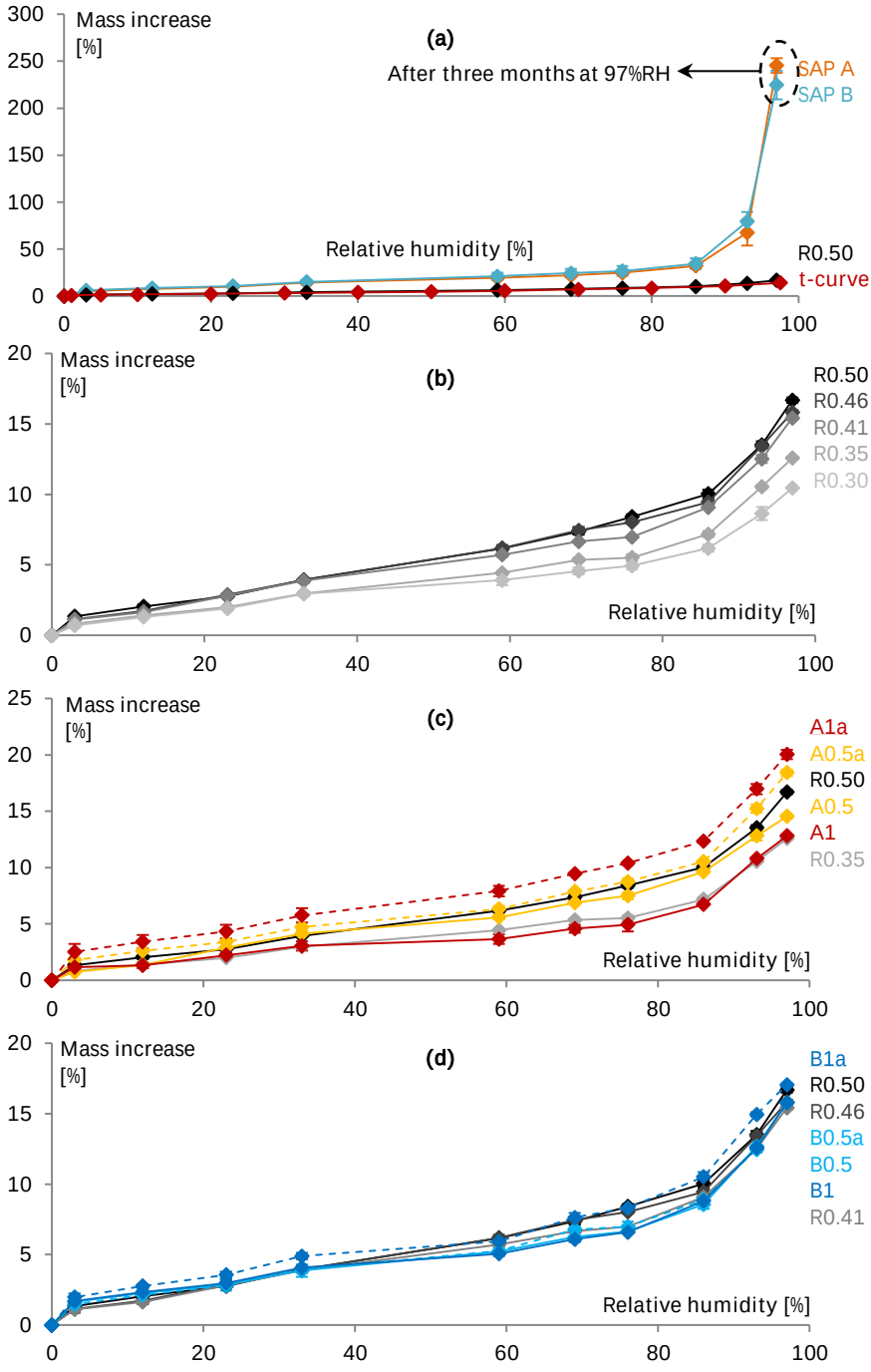

Figure 3.47. Static water vapour sorption results for superabsorbent polymers **(a)**, for specimens with a different water-to-cement ratio **(b)**, mixtures with SAP A **(c)** and SAP B **(d)** with their respective references. The curves show the mass water content as a function of the relative humidity.

The reference curve for the static water vapour sorption (R0.50) is put next to the t-curve found in literature (Hagymassy Jr. et al., 1969) in Figure 3.47a. The t-curve is an adsorption curve proposed for cementitious materials. Both correspond within the measuring error of the test itself. This served as a verification of the test results.

The static water vapour sorption results shown in Figure 3.47b point out that the sorption curve is shifted downwards with a decrease in water-to-cement ratio. As the water-to-cement ratio decreases, the capillary porosity is reduced and the pore network becomes finer. This leads to the lower water contents found in the water vapour sorption isotherms. The curves are also shifted downwards when using SAPs without additional water (Figure 3.47c-d for SAP A and SAP B, respectively). This already points to the expected densification of the cementitious matrix due to internal curing and the lower effective water-to-cement ratio. When using additional water, the curves are shifted upwards towards the reference curve with the same effective water-to-cement ratio. In case of SAP A, the curves are shifted too high, but in case of SAP B, the curves always coincide with the references with the corresponding effective water-to-cement ratios. Additional water thus seems to counteract for the densification caused by the uptake of mixing water by the SAPs and internal curing afterwards.

The static water vapour sorption tests, however, take a significant amount of time. Even though carbonation is prevented by the use of soda lime, there is still a high possibility of carbonation. TGA showed almost no carbonation. The total measuring time was one and a half year for one adsorption branch. With dynamic water vapour sorption, this is only half a week for one adsorption-desorption curve. As the test is performed in a nitrogen environment, there is no possibility for carbonation during the test itself.

Longer equilibration times are needed when performing the static measurements, thus favouring the entry of water molecules in the narrowest micropores (Lodewyckx, 2010). Consequently, higher water uptakes are obtained for the static measurements. However, and taking into account that these materials do not present a highly developed microporosity, the differences between the uptake values obtained by both techniques are minimal. The cement will also partially hydrate further due to the long measuring time.

The results for dynamic water vapour sorption are shown in Figure 3.48. Again, there is a steeper increase above a relative humidity of 50% pointing towards a material mainly comprised of mesopores. The slope of the isotherm for the A1 mixture is almost linear until high relative pressures. As the final vapour sorption at 98% RH is also lower than for the other specimens, this less steep increase points towards a densification of the cementitious matrix and a reduction in the amount of mesopores. The shape of the obtained isotherms indicates that these samples display a type II isotherm with a type H4 hysteresis loop according to the IUPAC classification (Brunauer et al., 1940), characteristic of meso- and macro-porous materials with a limited development of the porosity.

All isotherms show a pronounced hysteresis loop. In this regard, the position, the extension and the width of the hysteresis loop is influenced by three-dimensional factors such as pore shape and pore connectivity.

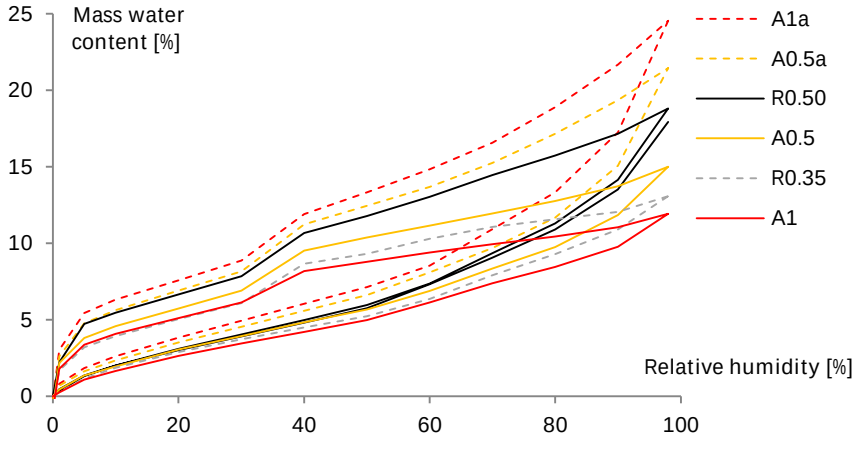

(a)

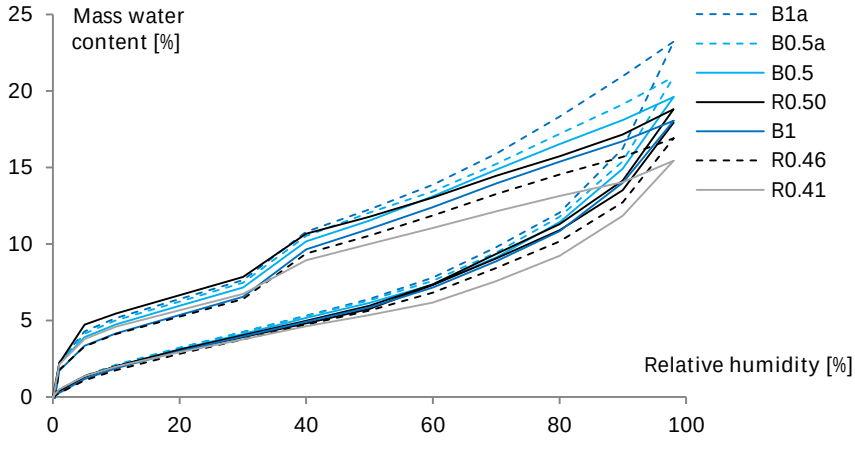

(b)

Figure 3.48. Dynamic water vapour sorption results for mixtures with SAP A **(a)** and SAP B **(b)** with their respective references. The curves show the mass water content as a function of the relative humidity.

The mesopore size distributions have been calculated using the BJH method applied to the adsorption branch of the dynamic water vapour sorption isotherms and are shown in Figure 3.49. As expected for a cementitious material, the materials are mainly formed of narrow mesopores with a size of 5-6 nm. Due to the denser matrix when lowering the water-to-cement ratio, the curves are shifted downwards. The hydration products which are then formed cannot grow expansively and will develop a tight cluster and thus denser matrix (Garci Juenger & Jennings, 2001).

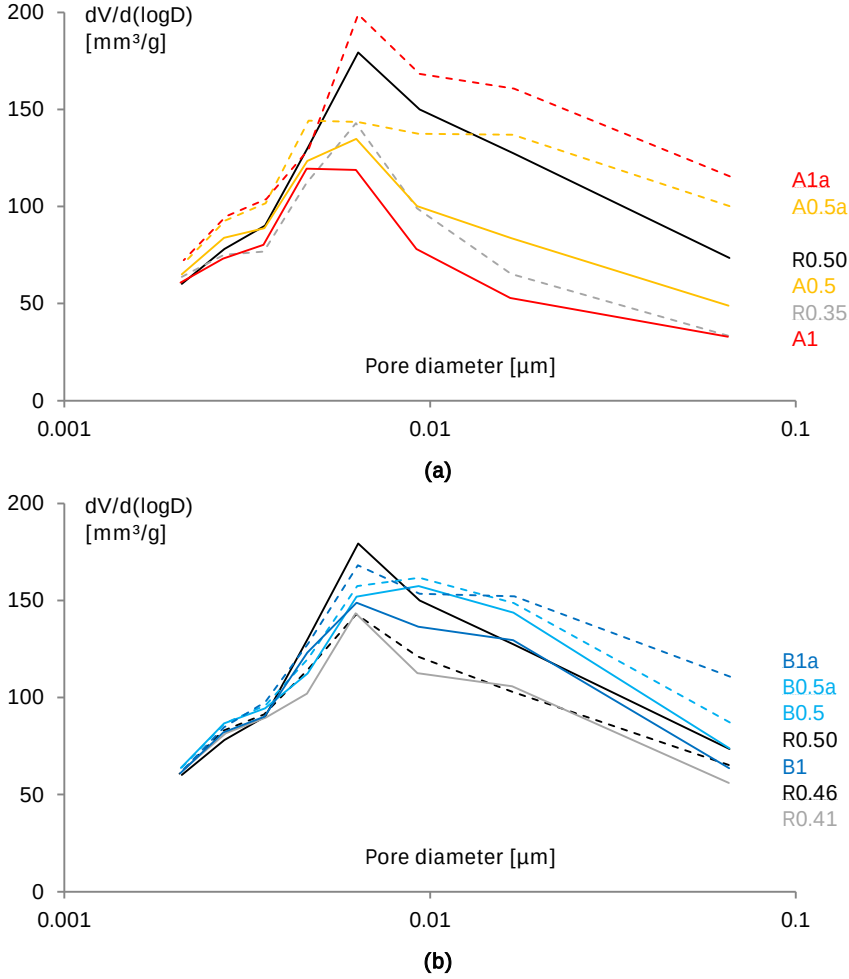

Figure 3.49. Calculated microstructure with the BJH method for mixtures with SAP A **(a)** and SAP B **(b)** with their respective references. The curves show the pore size distribution as a function of the pore diameter, with V the volume of the pores and D the diameter.

This is also the case in mixtures with SAPs but without additional water. The curves are shifted to the respective mixtures with the same effective water-to-cement ratio. This is for example the case for the A0.5 mixture which should be compared with the R0.35 matrix. The results show that cement pastes with SAPs and without additional water show a slight decrease in the narrow and larger mesopore range compared to the R0.50 reference. If mixtures with SAPs and without additional water are compared with the respective references with the same $(w/c)_{eff}$, it can be concluded that there is a slight increase in the larger mesopore range. The smaller mesopore range is similar.

If additional water is used, the curves are shifted upwards towards the reference R0.50, which should give a matrix with the same effective water-to-cement ratio. Cement pastes with SAPs and with additional water show no significant difference in the narrow mesopore range and a slight increase in larger mesopore range.

The amount of micropores calculated with the DR method and the amount of mesopores calculated with the BJH method are given in Figure 3.50 and Table 3.6. The micropore volume (DR) is much lower compared to the mesopore volume (BJH). This is an intrinsic property of cementitious materials. The amount of micropores is less than 20% of the studied pore volume by means of dynamic water vapour sorption. The amount of micropores is approximately the same for mixtures with the same effective water-to-cement ratio. Use of SAPs thus leads to a denser matrix as if the water-to-cement ratio would be lowered. Additional water leads to the same micropore matrix as if no SAPs were used. The amount of mesopores of mixtures with the same effective water-to-cement ratio is slightly higher in mixtures with SAPs with or without additional water. The C-S-H gel amount, also given in Table 3.6, decreases when the water-to-cement ratio lowers. When comparing the mixtures with the same effective water-to-cement ratio, the gel amount is slightly higher in mixtures with SAPs with or without additional water. This is possibly due to the further hydration caused by internal curing after the cementitious matrix is formed. The higher values for the C-S-H gel amount reflect the densification of the C-S-H due to the release of mixing water by the SAPs. The C-S-H is mainly comprised of gel pores, and is therefore mostly seen when using the water sorption technique.

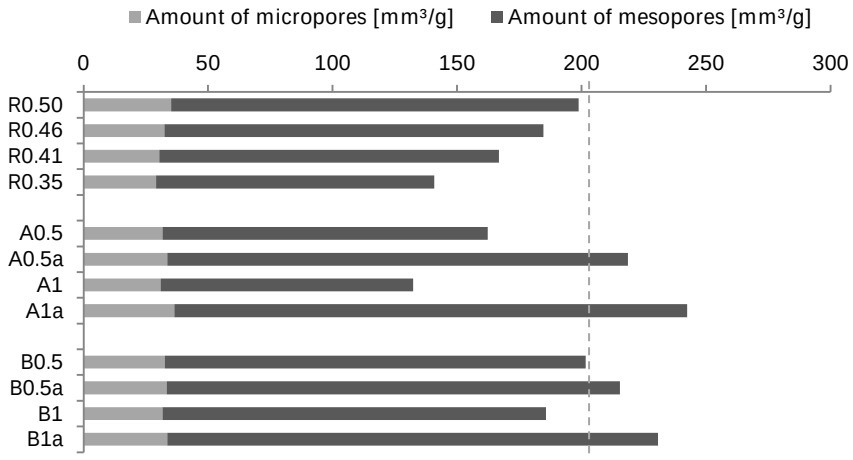

Figure 3.50. Amount of micropores calculated with the DR-method and the amount of mesopores calculated with the BJH-method. (IUPAC pore classification: micropores (< 2 nm), mesopores (2-50 nm) and macro pores (> 50 nm).

Table 3.6. C-S-H amount, specific surface area (S_{BET}), micropore and mesopore volumes. (IUPAC pore classification: micropores (< 2 nm), mesopores (2-50 nm) and macro pores (>50 nm).

	C-S-H gel amount [mm³/g]	*Specific surface area (S_{BET}) [m²/g]*	*Mesopore volume [mm³/g]*	*Micropore volume [mm³/g]*
R0.50	141 – 202	131	164	35
R0.46	139 – 195	130	152	32
R0.41	134 – 191	126	136	30
R0.35	132 – 189	124	112	29
A0.5	140 – 200	132	131	32
A0.5a	150 – 219	147	185	34
A1	120 – 172	118	101	31
A1a	160 – 230	158	206	36
B0.5	143 – 204	140	169	33
B0.5a	148 – 211	141	182	33
B1	137 – 196	136	154	32
B1a	146 – 209	144	197	34

The specific surface area S_{BET} (Table 3.6) follows the same trend as the C-S-H amount. The same conclusions can be drawn. In the studied mixtures, the S_{BET}-values range from 118 to 158 m²/g, similar to values found in literature.

The hardened cement paste undergoes some structural changes during variation of relative humidity which can affect the determination of the S_{BET} value (Adolphs et al., 2002; Chappuis, 1999; Völkl et al., 1987). However, this latter effect was found to be almost negligible in this case.

Summarizing, it can be stated that the results inferred from both static and dynamic techniques lead to the same main conclusions regarding the influence of the use of SAPs and additional water on the textural properties of the cementitious materials. The results obtained reveal that water sorption can be used as a characterization technique of the porous structure of cementitious materials, thus overcoming the inconveniences of nitrogen adsorption: cryogenic circumstances and the possible modification of the composition of the material during the required outgassing pre-treatment. Also, water has a smaller kinetic diameter than N_2 (0.28 versus 0.36 nm, respectively) that permits its entry into pores that are not accessible to nitrogen (ultramicropores) (Verhoeven & Lodewyckx, 2001), Moreover, and after it has been demonstrated that water sorption gives information about the surface chemistry of some kind of materials (i.e. activated carbons) (Lodewyckx et al., 2013), a thorough modelling of these isotherms is expected to broaden their applicability towards the surface characterization of cements.

3.2.3 Mechanical properties

If one uses a new material, the strength should be certified. The superabsorbent polymers, additional water and superplasticizer do have an influence on the strength properties. In the next paragraphs, the influences on mortar and concrete will be investigated.

3.2.3.1 Flexural and compressive strength

The flexural strength was measured by means of a three-point-bending test and the compressive strength by means of a compression test (NBN EN 196-1) on 160 × 40 × 40 mm³ mortar beams with the testing machine Walter+Bai DB 250/15. The mechanical properties were studied at 2, 7 and 28 days after casting. Before testing, the samples were stored at a relative humidity of more than 95% and a temperature of 20 ± 2°C until the age of testing.

The strength will depend on the mixture composition, including the amount of aggregates in the unit volume. Generally, a lower water-to-cement ratio in SAP-free reference samples results in a higher strength. This can also be seen in Figure 3.51. This is due to the densification of the matrix similar to the one which can be seen in Figure 3.22.

The mixtures with SAP A and without additional water only have a barely noticeable strength after 2 days. The reason for the delayed setting and hardening, is the result of the amount of superplasticizer.

The bending strength (Figure 3.51a) of the composite is dependent on the total amount of air voids and macro pores in the cross-sectional area of the tensile plane. Due to the higher amount of air voids and macro pores in SAP A mixtures compared to SAP B mixtures (Figure 3.21), the bending strength is lower. Also, the internal curing provided by the SAPs increases the strength. Internal curing by the additional water in mixtures with 1 m% SAP would increase the bending strength at 28 days (so not at early ages, but at later ages). But, the macro pores will cause a localized lower strength, possibly decreasing the additional strength gain (for example A0.5 and B0.5 compared to A0.5a and B0.5a). Also, premature partial release of water by the SAPs before setting results in a higher effective water-to-cement ratio and thus a higher capillary porosity and lower strength (Schröfl et al., 2012). An increase in m% of SAP leads to a decrease in strength. This is due to more macro-pore formation by the swelling of the SAP particles. If 2 m% of SAP B would be used, the strength would be even much lower. The bending strength is thus mostly governed by the formation of macro pores by the SAPs.

The compressive strength (Figure 3.51b) is also affected. As the macro pores are irregular in shape (bulk polymerization of SAP followed by grinding), the compressive loads are not transferred by dome action, as would be the case for spherical SAPs. This causes the compressive strength to be lower. The additional water has both positive as negative effects on the strength properties.

Adding additional water to specimens with SAP results in lower compressive strength values. The decrease in compressive strength is of the same order of magnitude as the decrease in strength between the according reference mixtures. The capillary pore structure is the same as in the reference R0.50 mixture

(Figure 3.27) in specimens with SAPs and additional water, so the macro pores are responsible for the decrease in strength as they are stress inducers due to their irregular shape. This was also found by other authors (Craeye & De Schutter, 2006; Igarashi & Watanabe, 2006; Jensen & Hansen, 2002; Lura et al., 2006; Mechtcherine et al., 2009) as a higher total porosity at early ages, as explained by (Dudziak & Mechtcherine, 2010; Mechtcherine et al., 2009). The strength loss is reduced at later ages due to the further hydration. As previously mentioned, further hydration may improve the mechanical properties but is mostly counteracted by the strength-loss caused by the SAPs (Lura et al., 2007). SAPs thus have both a positive and a negative effect on the mechanical properties, which was also studied in (Esteves, 2012).

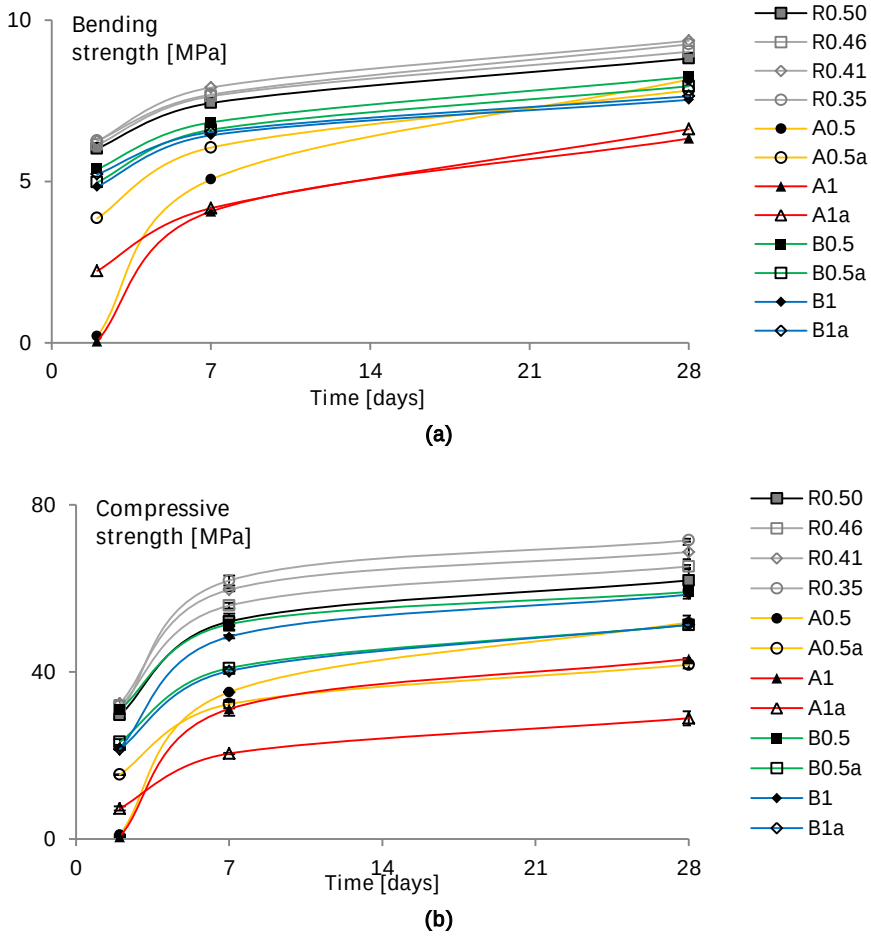

Figure 3.51. The development of the bending strength (n=3) **(a)** and the compressive strength (n=6) **(b)** as a function of time for the studied mixtures, with standard deviations of single measurements.

Another interesting paper on this subject is the one by (Hasholt et al., 2012). She suggests that the reduction in strength may be caused by an overestimation of the SAP water absorption during mixing. As found in Chapter 2, the value for SAP A (30.5 g mixing water/g SAP A) is indeed high. But following the microscopic analysis, the sizes of the macro pores seem to correlate with the theoretical expected sizes. When the water-to-cement ratio is more than 0.42 (Hasholt et al., 2012), the water from the superabsorbent polymers is not needed to mitigate autogenous shrinkage. The formation of macro pores thus may lead to a reduction in strength. Below a water-to-cement ratio of 0.42, the maximum hydration is increased and the strength is increased as the decrease due to macro pore formation is mostly counteracted (Hasholt et al., 2012). This is only the case if the ideal amount of superabsorbent polymers to mitigate autogenous shrinkage is added. In this research, the amounts were higher as these are the needed amounts to receive self-sealing and self-healing.

The strength demands in EN 197-1 and PTV 603 are the following: the strength at 2 days should be ≥ 20 N/mm² and at 28 days ≥ 52.5 N/mm² (based on the certified strengths needed to obtain CEM I 52.5N). Only the reference mixtures and SAP B mixtures and A0.5 meet these demands. SAP B mixtures thus show an acceptable decrease in overall strength. For the SAP A mixtures, only A0.5 mixtures show an acceptable strength decrease.

All other SAPs mentioned in Chapter 2 were also studied on their strength properties. The tensile strength at 28 days of age of SAP C mixtures, however, was 3.4, 3.5, 2.4, 2.5 MPa for C0.5, C0.5a, C1 and C1a, respectively. The compressive strengths were 16.8 ± 0.7, 17.6 ± 0.2, 9.2 ± 0.1 and 9.8 ± 0.3 MPa, respectively. SAP C mixtures show a high decrease in strength due to the plasticizing effect of the polymers in the mixtures. This is possibly due to a partial removal of the solvent used to produce these superabsorbent polymers. The amount of additional water was 2 g mixing water/g SAP C.

Table 3.7 provides the results of the strength at an age of 28 days for all studied mixtures with different types of SAPs and additional water to compensate for the loss in workability. The influences on the strength are mainly linked to the mixing water uptake. And again, an increase in the amount of SAP leads to a higher reduction in strength. The influence of SAP D on the tensile strength is similar to the one of SAP B, even though the almost double uptake of mixing water. This is due to the rounder shape of SAP D compared to the irregular rough shape of SAP B. SAP E, more irregular compared to SAP D due to the collapsed shape and with a very fast swelling time, reduces the tensile strength more. Due to the balling effect and the possible lower dispersion of the SAP fibre type (SAP F/SAF), the strength is lower. The mixing water uptake of SAP G is highest compared to all SAPs, leading to the highest reduction in strength. Due to the zero uptake of mixing water and the spherical shape of SAP H, the tensile strength is less reduced in a mixture containing SAP H. No significant differences can be found when comparing the tensile strengths of mixtures with different sizes of SAPs. Only a trend can be seen. This is, the smaller the particle size, the higher the reduction in strength is. This is due to the higher quantity of pores, as was also found by (Mönnig, 2009).

Table 3.7. Absorption of mixing water [g/g SAP], tensile strength [MPa] and compressive strength [%] for mixtures with different types of SAPs when using additional water to compensate for the loss in workability.

Code	Mixing water absorption [g/g SAP]	Tensile strength [MPa]	Compressive strength [MPa]
REF		8.8 ± 0.2	61.9 ± 2.6
A0.5	30.5	7.8 ± 0.2	41.7 ± 0.9
A1	30.5	6.6 ± 0.3	28.9 ± 1.7
B0.5	8.9	8.0 ± 0.1	51.2 ± 1.1
B1	8.9	7.6 ± 0.2	51.3 ± 0.4
C0.5	2.0	3.5 ± 0.8	17.6 ± 0.3
C1	2.0	2.5 ± 0.9	9.8 ± 0.3
D0.5	16	7.8 ± 0.2	58.0 ± 1.3
D1	16	6.6 ± 0.3	46.0 ± 1.2
E0.5	16	7.2 ± 0.7	47.5 ± 1.4
E1	16	4.7 ± 0.1	31.0 ± 1.5
F0.5	32	6.4 ± 0.3	45.2 ± 0.8
F1	32	5.6 ± 0.3	36.9 ± 1.7
G0.5	45	5.7 ± 0.1	37.3 ± 1.3
H0.5	0	6.7 ± 0.7	56.5 ± 1.8
H1	0	7.3 ± 0.5	56.6 ± 2.1
Po0.5	40	5.2 ± 0.2	30.2 ± 0.9
Mi0.5	21	6.1 ± 0.2	41.5 ± 2.5
Me0.5	10	5.4 ± 0.4	43.7 ± 2.1
Me1	10	4.5 ± 0.7	27.6 ± 0.5
XL0.5	10	5.5 ± 0.7	60.8 ± 3.4
XL1	10	5.4 ± 0.9	48.2 ± 2.4

The same conclusions can be drawn when investigating the compressive strength. Due to the fast swelling of SAP E and the collapsed structure of the SAP itself, the compressive strength is lower. The lower dispersion of SAP F and the noticed balling effect during mixing, leads to a lower overall strength. Due to the higher mixing water uptake by SAP A, G and Powder, the strength is decreased. But, due to the lower mixing water uptake by SAP H, the strength is not lowered. Also, as SAP H is spherical, compressive stresses can be transferred by dome action, leading to the higher strength and no significant difference when using a higher amount of SAP. When comparing Po0.5, Mi0.5, Me0.5 and XL0.5, a significant increase in strength is noticed. This is mainly due to the difference in size. On one hand in case of a smaller particle this will cause a higher mixing water uptake due to the higher available surface area. Furthermore, a higher amount of stress initiators will be present in case of the smaller particle sizes. But, when the size is too large, structural impracticalities occur. Due to the delayed uptake of mixing water due to the spacial restrictions, they tend to break the cementitious matrix when it is hardening, leading to extremely large pores. This is aesthetically unwanted and inferior in case of durability aspects.

The observed microstructures through air void analysis are shown in Figure 3.52. The material was prepared and calculated based on the Standard EN 480-11.

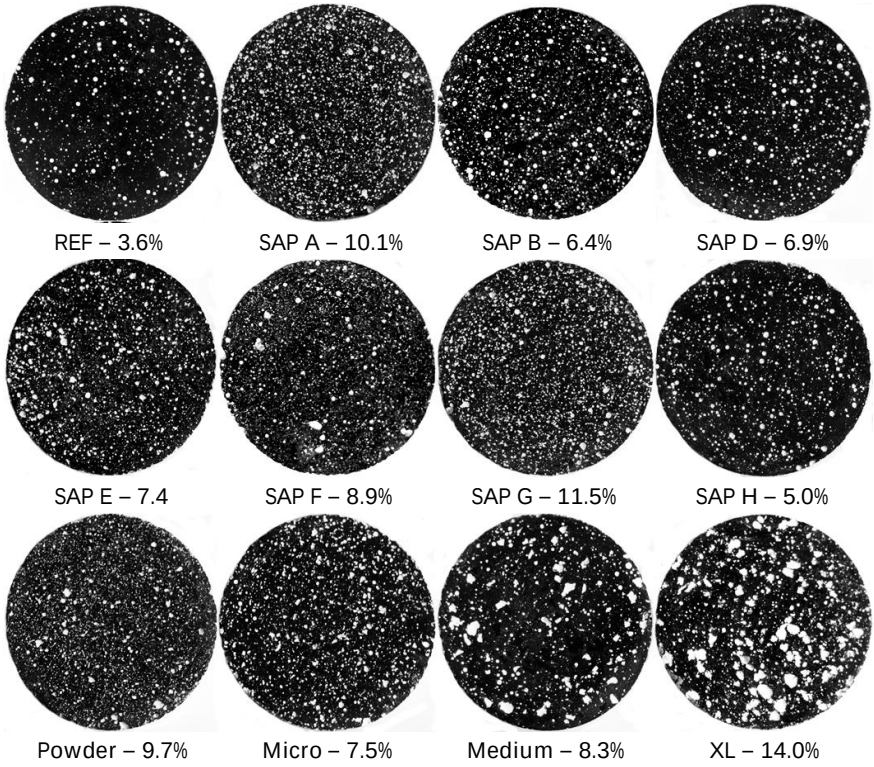

Figure 3.52. Observed air voids through air void analysis of all studied mixtures with 0.5 m% of SAPs, with their respective determined porosity.

A cylindrical specimen was hereby cut perpendicular to the longitudinal axis and the surface was then ground and polished to produce a smooth flat surface finish. The specimen surface was treated to produce a better contrast between the air voids and the cementitious matrix. First, black ink was applied on the surface. Then, the surface was covered with fine barium sulphate powder which was pressed in the air voids. The excess white powder was then removed and the specimens could be microscopically studied. The air void structure was hereby examined by scanning along a series of traverse lines parallel to each other. The air voids intersected by the traverse lines were recorded and the total porosity could be determined.

As can be seen from the quantitative air void porosity in Figure 3.52, the amount of pores is closely linked to the amount of added water as these are mainly macro pores. The more water is added, the more pores are visually seen. This is on its turn closely related to the strength, as discussed above. SAP A, SAP G and powder mixtures show the highest amount of pores due to the small size of the SAPs. SAP B, SAP D and SAP H show the lowest influence due to their larger shape and the spherical form of SAP D and SAP H. Increasing the size of SAPs leads to the formation of larger macro pores as well. The XL mixture was less practicable due to the formation of very large pores.

3.2.3.2 Freeze-thaw properties of concrete with SAPs

Superabsorbent polymers (SAP) can be used to change the pore structure. SAP particles introduce a system of fine, evenly distributed air voids after release of their absorbed water. SAPs can thus also function as air pore entraining agents, increasing the freeze-thaw resistance, the durability and the density. They can extract water of the fresh concrete mixture causing the stiffening of the paste which is accompanied by a reduction of the capillary porosity. Cavities will remain as empty pores. The appropriate size-designed pore systems could improve the durability in terms of freeze/thaw resistance.

These tests were carried out as a Round-Robin test in the frame of the RILEM Technical Committee 225-SAP "Applications of Superabsorbent Polymers in Concrete Construction". The concrete composition and SAPs were determined by the project leader. For the ease of comparative reasons, the names remained unchanged. The basic composition is based on ordinary concrete in road construction with a water-to-cement ratio of 0.45; 350 kg/m³ CEM I 42.5 N, 157.5 kg/m³ water, 690 kg/m³ quartz sand 0/4, 188 kg/m³ gravel 2/8, 1003 kg/m³ gravel 8/16 and an amount of superplasticizer. The sand fractions were determined in such a way that the resulting grading curve would be in the range between A and B according to the denomination of the standard grading curves of EN 1045-2. As a superplasticizer, a commercial product based on β-naphthalene sulphonate (BNS), was used (Woerment FM30/BV30 from BASF; 1.2 g/cm³). The spread diameter should be between 420 and 480 mm for all mixtures to be in the consistency class F3 (soft) as specified in EN 1045-2. This was the case for all mixtures, except for the higher water-to-cement ratio of 0.50, which was more fluid even though no superplasticizer was used. Bulk-polymerized SAPs (two types) were added on top at 0.15 m% of cement weight. Both SAPs are able to take up approximately 300 g demineralized water and 33.3 g mixing water per g SAP. Their sizes are 180 ± 45 µm (SAP 3) and 70 ± 21 µm (SAP 4). The corresponding macro pores should be 882 ± 220 µm (SAP 3) and 343 ± 103 µm (SAP 4). The amount of additional water was 17.5 kg/m³ to receive a $(w/c)_{tot}$ of 0.50. To retain consistency class F3, the dosage of superplasticizer was increased. Additionally, mixtures with SAPs but without additional water and a mixture with the additional water on top but without SAPs were made. A comparative reference incorporating a conventional air-entraining agent (AEA) was used. The air-entraining agent was a commercial product (LP75 from BASF) and was simply added on top (but first homogeneously mixed with the mixing water). The amount of air entrainer was 0.025 m% (by weight of cement). The different mixtures are shown in Table 3.8. REF I and REF II have water-to-cement ratios of 0.45 and 0.50, respectively. SAP1/2 is a SAP3/4 mixture without additional water, containing SAPs. AEA is a mixture containing the air-entraining agent.

The mixing procedure comprised 2 min homogenization of the dry powders, and the dry SAPs in the respective mixtures, at low speed (Rotating pan mixer Zyklos 50 ℓ). In the following 30 s, water was added. The whole was mixed for 1 minute and the superplasticizer was added in the next 15 s, followed with an additional 2 min of mixing at high speed.

Table 3.8. Studied concrete mixtures with nomenclature.

	REF I	SAP 3	SAP 4	REF II	AEA	SAP 1	SAP 2
$(W/C)_{tot}$	0.45	0.50	0.50	0.50	0.50	0.45	0.45
$(W/C)_{add}$	-	0.05	0.05	-	-	0.05	0.05
$(W/C)_{eff}$	0.45	0.45	0.45	0.50	0.50	0.40	0.40
SAP 3		x				x	
SAP 4			x				x
AEA					x		

All results on the mechanical properties and the used standards are listed in Table 3.9. The Young's modulus was determined on cylindrical specimens with a diameter of 150 mm and a height of 300 mm. First, the specimen was loaded till one third of the compressive strength, then unloaded till 0.5 MPa, again loaded till one third of the strength, again unloaded, then a 30 s resting period was taken into consideration and the stress and strain were measured. The specimen was again loaded to one third of the strength and there was a 30 s resting period until the stress and strain were measured again. Using these stresses and strains, the modulus of elasticity could be determined. The loading speed was 0.5 ± 0.2 MPa/s.

The fresh concrete air content was approximately 3% for all mixtures (possibly due to the use of specific aggregates), instead of the AEA mixture which needed to show 6-7% of air content. Due to this high amount of entrained air, the fresh concrete density and volumetric mass were lower compared to the other mixtures.

When using SAPs and additional water, the strength decreases within an acceptable range. This corresponds to the results found on mortars. Increasing the water-to-cement ratio without adding SAPs, the strength also decreases within the range of the SAP mixtures without additional water. Using an air-entraining agent decreases the strength to a high extent, especially due to the entrained air content. When using SAPs and no additional water, the effective water-to-cement ratio decreases, thus increasing the strength. The combined effect with the strength reduction by the SAPs leads to a material with approximately the same strength as the REF I mixture. The same conclusions can be drawn on the results found for the modulus of elasticity and the splitting tensile strength.

The test to determine the freeze-thaw resistance was the slab test according to the Standard EN 12390-9 on cylindrical specimens of 100 mm in diameter and 80 mm high, with the temperature cycle as in Figure 3.53.

The results are shown in Figure 3.54 after 7, 14, 28, 42 and 56 cycles. The limit for freeze/thaw-resistant concrete is 1.5 kg/cm² after 28 cycles. The REF II mixture showed the highest scaling as the mixture was especially susceptible due to the high water-to-cement ratio. The next mixture is REF I. Both SAP 3 and SAP 4 show a lower scaling but not as good as the AEA mixture, and they are not significantly different in terms of scaling. Both, however, almost meet the requirements of 1.5 kg/cm² after 28 cycles. The SAP 1, SAP 2 and AEA do meet this requirement. The difference between SAP 1/2 and SAP 3/4 is due to the lower apparent water-to-cement ratio. This causes a further increase in the freeze/thaw resistance as the strength is increased.

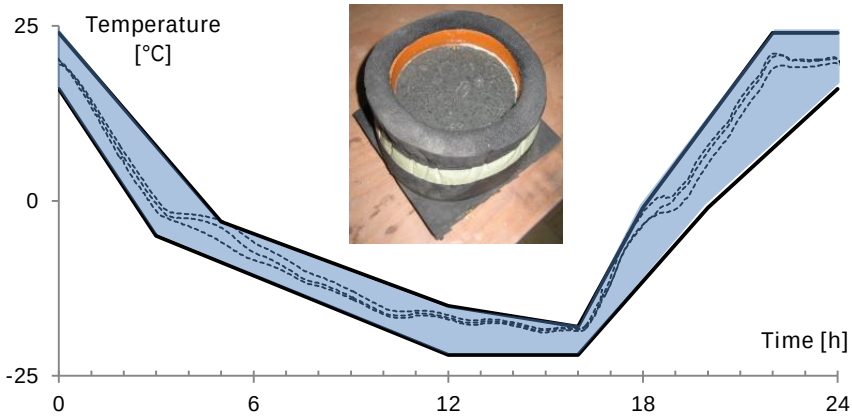

Figure 3.53. Followed temperature cycle for freeze-thaw testing.

The rate of scaling, especially after 28 cycles, also showed that the reference mixtures deteriorated more rapidly compared to the mixtures with SAPs, again proving their increased freeze/thaw resistance.

The changes in mass loss for SAP-containing mixtures in comparison to the SAP-free concrete (REF I) after 28 freeze/thaw cycles are 60% for SAP 3, 50% for SAP 4, 95% for SAP 1, 92% for SAP 2, 97% for AEA and -26% for REF II. There thus was a considerable improvement in the materials performance due to the use of SAPs in terms of decreasing mass loss after a given number of freeze/thaw cycles. SAPs are thus also interesting in terms of improving the freeze/thaw resistance.

Without de-icing salts, the results were not statistically different from each other and almost no scaling was found (Figure 3.54). This is because the test without de-icing salts is less severe compared to the test with de-icing salts. There is, however, a small trend visible. Again, mixtures containing SAPs are able to increase the freeze/thaw resistance.

The air voids and spacing factor are important parameters to be considered when studying the freeze/thaw resistance. An automated air-void analysis according to the Standard EN 480-11 was performed. All specimens show a spacing factor of 0.100-0.150 mm. The cumulative air content for all studied mixtures is given in Figure 3.55 (average of two 100 × 150 mm² samples). The traversed length was 1200 mm. If one would start from the initial size of the superabsorbent polymers and the amount of additional water (33.3 g mixing water/g SAP for both SAPs with a SAP bulk density of 700 kg/m³), one could calculate the final swollen size of the SAP particles in the concrete. SAP 3 with an initial size of 180 ± 45 µm attains a swollen size of 670 ± 167 µm µm. For SAP 4, this is 70 ± 21 and 260 ± 78 µm, respectively. These can be found in the automated air void analysis. The AEA mixture shows typical additional pores with pore sizes of approximately 250 µm.

Table 3.9. Mechanical properties of the studied mixtures. The results show averages and standard deviations on the single results.

	REF I	SAP 3	SAP 4	REF II	AEA	SAP 1	SAP 2	Standard
Flow [mm]	430	430	430	525	440	420	430	EN 12350-5
Superplasticizer amount [kg/m³]	0.315	0.315	0.315	0	0.067	1.26	1.418	-
Fresh concrete air content [%]	3	3.7	3.3	2.3	6.6	3.3	3.5	EN 12350-7
Fresh concrete density [kg/m³]	2375	2325	2344	2363	2219	2350	2331	EN 12350-7
Volumetric mass [kg/m³]	2365 ± 15	2312 ± 4	2323 ± 4	2353 ± 7	2231 ± 6	2378 ± 3	2349 ± 19	-
Compressive strength [MPa]	57.8 ± 0.7	49.3 ± 1.0	48.6 ± 0.8	52.0 ± 0.9	33.8 ± 1.4	58.0 ± 1.0	50.0 ± 2.1	EN 12390-3
Modulus of elasticity [GPa]	35.1 ± 0.7	34.6 ± 0.8	34.2 ± 1.3	34.4 ± 1.4	31.7 ± 1.0	36.5 ± 0.9	35.9 ± 0.5	DIN 1048-5
Splitting tensile strength [MPa]	3.67 ± 0.25	3.35 ± 0.12	3.48 ± 0.40	3.35 ± 0.09	2.64 ± 0.35	3.99 ± 0.28	3.71 ± 0.25	EN 12390-6

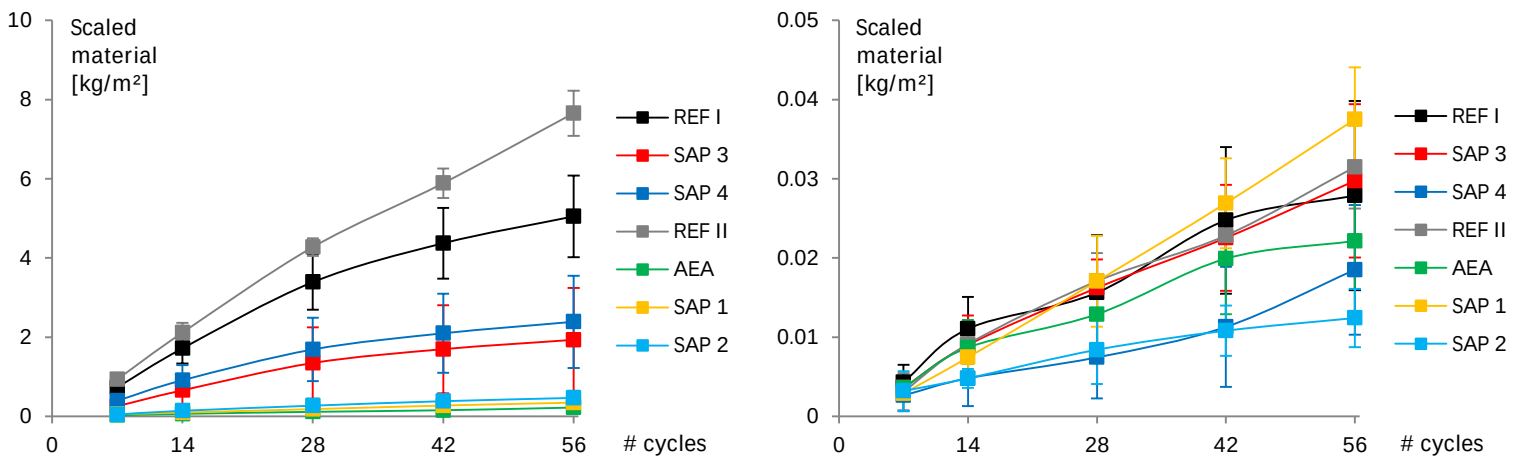

Figure 3.54. Freeze-thaw results with (left) and without (right) de-icing salts.

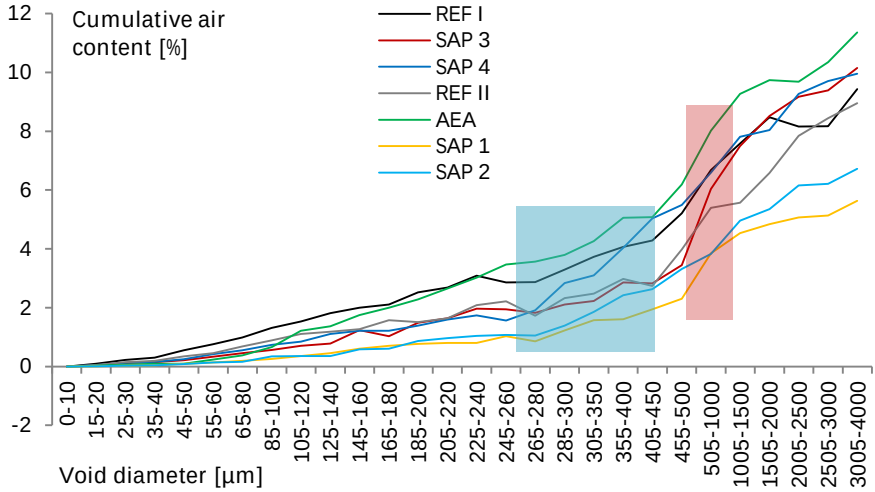

Figure 3.55. Cumulative air content of the studied samples.

3.3 Conclusions

Chapter 3 comprises the influences on the fresh and hardened properties of cementitious materials with or without superabsorbent polymers. The following points give the overall conclusions.

General conclusions

The method of comparing the different flow values to determine the amount of additional superplasticizer or additional water is a good way to counteract the loss in workability and the change in microstructure due to the uptake of mixing water by the SAPs. The amount of mixing water absorbed by the SAP seemed to be independent of the mixture composition. The experimentally determined amounts of additional water to be added are valid for the cement, fly ash and blast-furnace slag mixtures.

The storage of cement paste near soda lime prevented carbonation so the actual microstructure could be studied.

Setting and hardening

There is a good correlation between the setting and hardening results found from penetration resistance tests and ultrasonic wave transmission measurements. The setting is postponed when a polycarboxylate superplasticizer is used. The results show that one needs to be careful in the use of specific types of superplasticizer as a compensation for the loss in workability, as they may drastically delay setting. If additional water is used (to compensate for the loss in workability), the setting is approximately the same as for a reference sample without SAPs and with the same effective water-to-cement ratio. The SAPs do not

show an influence as monomers should leach out to obtain this effect, and this was not the case. SAP B mixtures show less influence on the setting compared to SAP A mixtures because of their larger particle size and lower amount of superplasticizer needed. If no additional water is added, SAP B should be selected instead of SAP A as a higher amount of SAP can be added and the setting properties are less impaired.

Autogenous shrinkage

Results of manual, discontinuous tests coincide well with the automated continuous tests for measuring the autogenous shrinkage in time. Both in fly ash and blast-furnace slag systems, where part of the cement is replaced by SCMs, the initial total amount of autogenous shrinkage is lower compared to an ordinary Portland cement mixture with a water-to-binder ratio of 0.30. This is due to the slower reaction of the supplementary cementitious materials. At later ages, the rate of autogenous shrinkage is higher compared to ordinary Portland cement mixtures. It is therefore important to study the effects of autogenous shrinkage on the long term, rather than stopping at an age of 7 days. These additional results prove to be useful as the (rate of) shrinkage of all mixtures changes differently with time. Internal curing by means of SAP A seems to be successful, independent of this long-term higher rate of shrinkage in mixtures with SCMs.

The swollen size of SAP A (257 µm mean diameter) is preferable considering the mitigation of autogenous shrinkage compared to the swollen size of SAP B (981 µm mean diameter). This is most likely due to the ideal release of mixing water for internal curing and better distribution of the smaller SAP particles. SAP A is able to mitigate autogenous shrinkage in mixtures with a water-to-binder ratio of 0.30, with or without fly ash and/or blast-furnace slag as a supplementary cementitious material.

Drying procedure

The ideal drying technique, which can preserve the microstructure and can remove only the non-bound water does unfortunately not exist. All drying techniques affect the microstructure in their own way. Water sorption has given additional experimental evidence that the best techniques to dry the cementitious samples are vacuum-drying and the solvent-exchange-method with isopropanol. Freeze-drying changed the microstructure due to thermo-mechanical stress in the inner C-S-H. Oven-drying removed part of the non-evaporable water, dehydrated C-S-H, monosulfoaluminate (AFm) and ettringite (AFt) phases, and caused thermo-hydric stresses due to differential expansion. Capillary stresses due to receding water menisci may also induce a modification of the textural properties of the sample. Oven-drying and air-drying proved to cause carbonation, which has its impact on the microstructure. Also, oven-drying at 105°C and air-drying in the presence of silica gel led to the removal of part of the C S-H phase, thus modifying the structural and textural properties of the sample. Oven-drying is thus an unsuitable drying technique to preserve the fragile microstructure of cement-based materials. Methanol reacted with C-S-H (only upon heating) but isopropanol seemed to be inert with cementitious compounds. The porosity is reduced the

most with increasing degree of carbonation. Carbonation reduced the porosity among the outer C-S-H (10 - 100 nm). A higher water removal does not result in a larger specific surface area and more accessible porosity. In oven-drying, the amount of removed water is higher but the surface area is smaller. This can be interpreted as a possible pore collapse or pore alteration.

Microstructural properties

Not the total water-to-cement ratio, but the effective water-to-cement ratio is important in case of the capillary porosity. Additional water thus needs to be considered when using superabsorbent polymers if one aims to maintain approximately the same global microstructure. But afterwards, the additional water will cause further hydration too. This will cause a small reduction (not significant) of the amount of capillary pores. A comparison of the luminosity of thin sections under fluorescent light revealed the densification of the cementitious matrix in mixes containing SAPs and without additional water due to the uptake of mixing water during setting and the release of the mixing water afterwards. The same microstructural properties were found between the reference mixture and mixtures with SAPs and additional water, with the same effective water-to-cement ratio by using scanning electron microscopy. The additional water will cause the formation of approximately the same global microstructure. Mercury intrusion porosimetry and helium pycnometry led to the same conclusions on the capillary porosity.

Results from the static and dynamic water vapour sorption experiments could be compared and similar results were obtained. The static tests are time-consuming and the dynamic test is a fast test to determine the sorption properties of the material. The agreement between the results obtained by the two sorption techniques reveals that water sorption can be used as a characterization technique of the porous structure of cementitious materials. Cement pastes with SAPs and without additional water show a slight decrease in the micro- and mesopore range and have a similar microstructure as a cement paste with the same effective water-to-cement ratio. Cement pastes with SAPs and with additional water show no significant difference in the micropore range and a slight increase in larger mesopore range. Dynamic water vapour sorption, together with the Dubinin-Radushkevich and Barrett-Joyner-Halenda models, is a promising technique to characterize the pore stricture in the micro- and mesopore range of cementitious materials.

Mechanical properties

The bending and compressive strength are mostly governed by the formation of macro pores by the SAPs. In case of bending strength, there is no conclusive difference (additional water has both positive and negative effects on the bending strength properties), but the compressive strength is lower if additional water is used. SAP B mixtures show an acceptable decrease in overall strength. For the SAP A mixtures, only the A0.5 mixture has a good strength due to the high mixing water uptake (as is also the case for SAP G and Powder). The newly-synthesized SAP C did not show promising results due to a plasticizing effect of the polymers. A

more round shape (SAP D and SAP H) is beneficial in terms of strength as the polymers act less as stress initiators. A rough formed SAP (like the collapsed SAP E) reduced the strength more. The fibre type (SAP F) led to a balling effect, decreasing the overall strength of the material. Also, too small particle sizes are less beneficial in terms of strength when comparing the same SAPs but with different sizes (Powder, Micro, Medium and XL). A too large particle would also lead to a too high porosity, which is unwanted in case of durability aspects. The most ideal size is 500 µm.

Superabsorbent polymers were also able to increase the freeze-thaw resistance as they caused less scaling due to the formation of an evenly-distributed pore system, when using additional water. When SAPs without additional water were used, the performance even further improved considerably. The overall improvement was hereby similar to that obtained with conventional air entrainment. However, when using an air-entraining agent, the strength decreased significantly, even more compared to using SAPs with additional water in a mixture.

Chapter 4

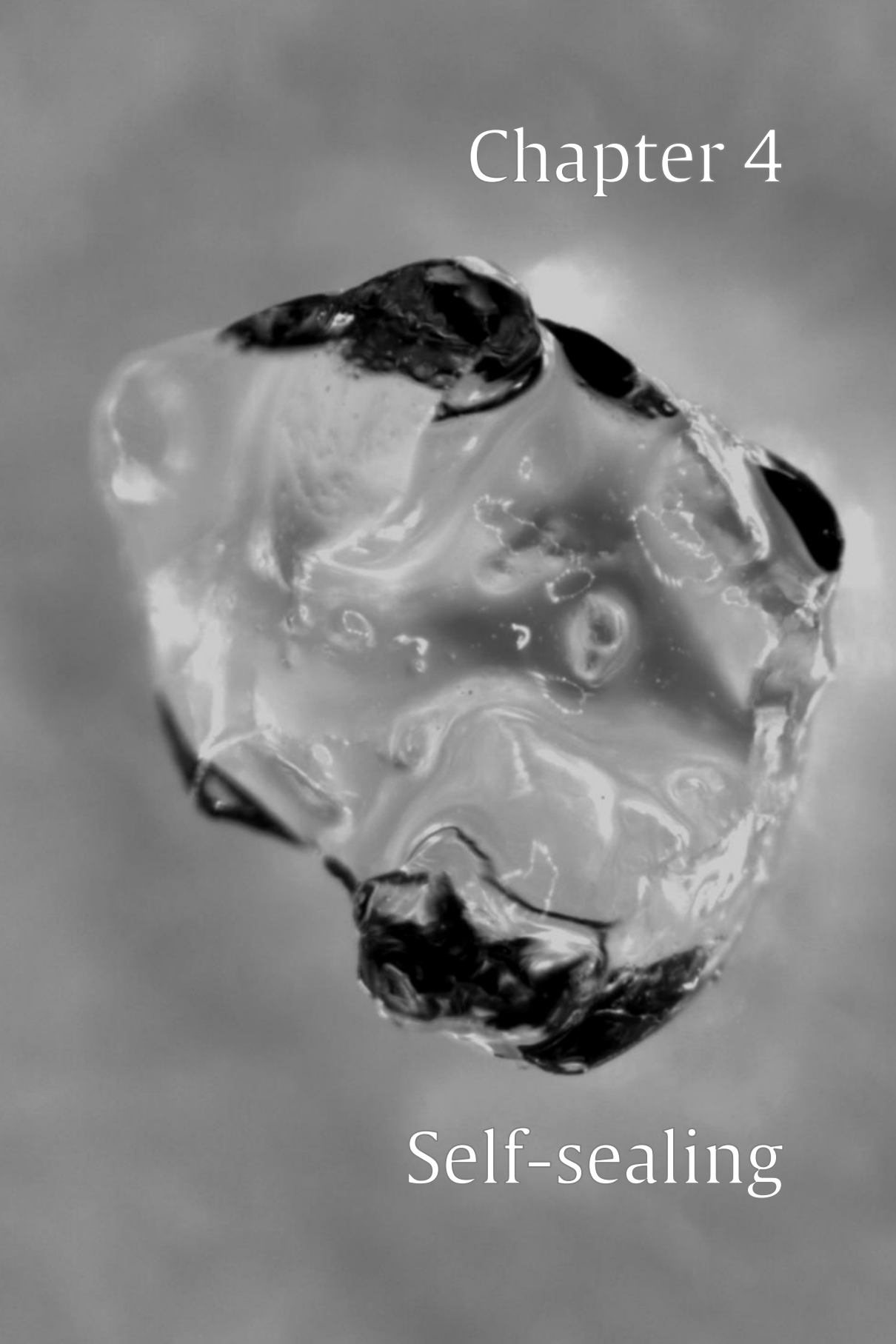

Self-sealing

| Superabsorbent polymer particle swollen to full extent, ready to seal a crack

Chapter redrafted after (Snoeck et al., 2012a; Snoeck et al., 2012b; Snoeck et al., 2014b).

"Je n'ai point d'espoir de sortir par moi de ma solitude.
La pierre n'a point d'espoir d'être autre chose que pierre.
Mais de collaborer, elle s'assemble et devient temple."

– Antoine de Saint-Exupéry – Citadelle

4.1 Introduction

Concrete is prone to cracking and the cracks interconnect flow paths for water, possibly containing harmful substances (Wang et al., 1997). Water can move in different states and therefore water is usually referred to as moisture. The moisture movement is a combination of water vapour in the pores, liquid water in larger pores, bound water at the pore walls and bound water in the gel (Nilsson, 2002). The ingress of water could induce steel corrosion, frost attack, chemical attack and internal expansion, endangering the durability of a structure. One of the main factors which endangers the durability in cracked concrete is the water movement through cracks. A smart cementitious material which has the property to stop or to partially prevent water movement in a crack would therefore have a clear added value.

Concrete has a passive healing capacity of its own, also called autogenous healing (Chapter 5). Unhydrated cement particles always remain present in a hardened concrete matrix. As water flows into the cracks, continued hydration of these unhydrated cement grains produces new C-S-H, which can result in sealing of small cracks. Another mechanism of autogenous crack healing is the precipitation of calcium carbonate ($CaCO_3$) which also blocks the crack. These forms of crack healing are studied in great detail by (Edvardsen, 1999) who observed a decrease in water permeability in cracked concrete specimens due to autogenous crack healing and performed an intensive study on the laws which govern the nucleation and crystal growth processes. Lepech (2006) also proved autogenous crack sealing by the precipitation of $CaCO_3$ by means of energy-dispersive X-ray spectroscopy as a decrease in water permeability in time was noticed. The decrease in permeability hereby demonstrated the potential of the autogenous healing as there is less intrusion of durability-decreasing substances and thus a probability of an increased service-life of the concrete structure.

As superabsorbent polymers are able to swell with mixing water during mixing, they will cause the formation of macro pores, a densification and thus a change in microstructure. This will cause the air permeability to be different. Furthermore, due to their swelling capacity, upon contact with fluids, they may cause a decrease in permeability of cracked cementitious materials. Lee *et al.* (2010a; 2010b) investigated the incorporation of SAP in concrete in order to obtain self-sealing properties. When liquids enter a crack, SAP particles along the crack faces will swell and block the crack. This is reflected in a decrease of water permeability through a crack. Song *et al.* (2009) synthesized a superabsorbent resin in situ to repair concrete leakage, but this was manual repair.

The swelling also takes place during mixing as water is absorbed by the SAP particles. The incorporation of SAP therefore changes the local water-to-cement (w/c) ratio because water is retained during hardening and is steadily provided to the cementitious matrix for internal curing and further hydration. This effect causes the matrix to have a lower water-to-cement ratio and thus denser matrix in between SAP particles (Reinhardt & Assmann, 2009) (also see Chapter 3). This densification leads to a decrease in permeability. To obtain an unchanged matrix, extra water can be added (Reinhardt & Assmann, 2009).

The matrix itself affects moisture movements in concrete. And, since water could induce potential steel corrosion or even cracking due to the swelling effect of water during freezing periods, a lot of research has focussed on ways to determine the moisture distribution in concrete. There are many test methods to measure the water distribution in cement-based materials, both destructive and non-destructive (Phillipson et al., 2007; Roels et al., 2004; Zhang et al., 2011b). These are gravimetric methods (drilling and carbide meters), electrical techniques, thermographic imaging and heat pulse, nuclear magnetic resonance spectroscopy, humidity sensors (McCarter & Vennesland, 2004), and radiation attenuation techniques (X-ray, γ-ray (Nizovtsev et al., 2008) and neutron radiography (Vontobel et al., 2006)).

In this research, air permeability tests, low-pressure and high-pressure water permeability tests, capillary water absorption tests and neutron radiography are used to visualise the self-sealing effect by the superabsorbent polymers.

4.2 Mortar composition

The same mortar composition and nomenclature as in Section 3.1.1.2 is valid. These mixtures were used for the air permeability, the low-pressure water permeability, the high pressure water permeability, the capillary water absorption measurements and neutron radiography measurements. Also, in some mix codes, first the m% of and the type of SAP is given, followed by CRA for cracked specimens or UNC for uncracked specimens to state the difference between cracked and uncracked specimens. These codes were 0 – CRA, 1A – CRA, 0.5B – CRA, 1B – CRA, 2B – CRA, 1C – CRA and 2C – CRA for the studied cracked specimens and 0 – UNC, 1A – UNC, 1B – UNC and 1C- UNC for the uncracked specimens.

Additionally, another mixture (ideal mixture to obtain self-healing, see Chapter 5) was also used for the low-pressure permeability tests. These mortar mixtures were based on the mixture composition of (Li, 2008; Yang et al., 2009). The mixtures contained 571 kg/m³ CEM I 52.5 N, 685 kg/m³ Class F fly ash, 456 kg/m³ fine silica sand, 332 kg/m³ water, 10 kg/m³ polycarboxylate superplasticizer (Glenium 51, conc. 35%, BASF), 1 v% of Polyvinyl-Alcohol (PVA) fibres from Redco, and a varying amount of SAP. A superplasticizer was used to compensate for the loss in workability. These additional mixtures were used for the low-pressure water permeability measurements to study the difference in composition.

4.3 Air permeability

For gas permeability measurements, a cylindrical specimen (Ø 150 mm × 50 mm) was drilled from a small mortar slab (200 mm × 200 mm × 70 mm) at an age of 28 days. The top and bottom surface were levelled and the specimens were stored at 20 ± 2°C and 95 ± 5 %RH until the age of 3 months. The curing condition and measurement thereafter are based on (116-PCD, 1999). The specimens were placed in a permeameter cell and a rubber tube was inflated to seal the side. In that way, a unidirectional flow was obtained. At the start of the test, the specimen was subjected to an oxygen flow at 2 bar until a steady-state flow was reached (after 30 min for each step). Afterwards, the pressure was increased to 3 bar and 4 bar subsequently. The latter value was used in the discussion further-on. For this test, only one specimen was used as the size of the specimen was noteworthy compared to the amount of SAP needed and available for testing.

Starting from the Hagen-Poisseuille formula for laminar current of a compressible fluid through a porous mass under static regime, it is possible to calculate the apparent gas permeability coefficient k_{app}, [m²] using equation 4.1.

$$k_{app} = \frac{4.04 \cdot P_2 \cdot Q_f \cdot L \cdot 10^{-16}}{A \cdot (P_1^2 - P_2^2)} \tag{4.1}$$

where Q_f the flow rate [ml/s], L the height of the specimen [m], A the cross-section of the specimen [m²] and P_1 and P_2 the upstream and downstream pressure [Pa]. The test was conducted at 20 ± 2°C with a dynamic viscosity of the oxygen gas of $2.02 \cdot 10^{-5}$ N·s·m^{-2}. The downstream pressure P_2 is equal to the atmospheric pressure (1 bar or 10^5 N·m^{-2}).

Gas permeability measurements of specimens with SAPs show an increase in gas permeability (Figure 4.1). As the mixing water is released with time, macro pores will be formed and only a part of the pore is filled with the dry SAP particle. Upon crack appearance and water intrusion, the SAPs will first need to fill the remaining macro pore before actual sealing of a crack. For gas permeability, this first sealing of the macro pore does not occur. The moisture uptake (cf. Chapter 2) is not sufficient to even fill up the remaining macro pore, so the macro pore still needs to be considered as penetrable. That is one of the reasons why the air permeability in specimens containing SAPs is higher compared to the reference sample. However, due to the release of mixing water during hardening, the matrix around a SAP particle may appear denser and the 'shell' is thus less penetrable compared to the macro pore itself. However, in this study, it was found that the gas permeability in specimens with SAPs was higher compared to reference mixtures.

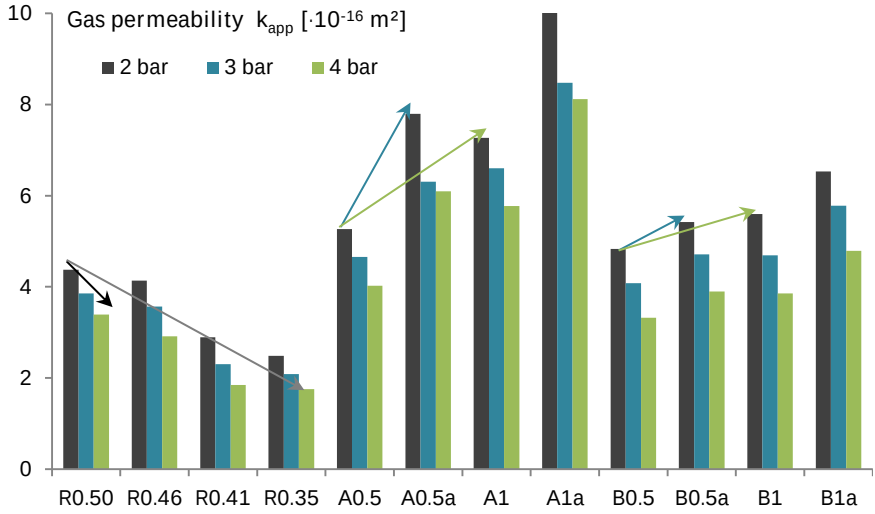

Figure 4.1. Gas permeability value k_{app} [m²] at 2, 3 and 4 bar of the studied specimens.

SAP A mixtures, which were the least workable due to the high mixing water uptake, show a higher gas permeability compared to the SAP B mixtures. SAP A mixtures show an increase of 80% and 140% for 0.5 m% and 1 m%, respectively. An increase of 15% and 41% was found for 0.5 m% and 1 m% SAP B, respectively. The values correspond more or less to literature (Reinhardt & Assmann, 2009). There it was found that in mixtures with the same effective water-to-cement ratio and comparable to SAP B mixtures, the gas permeability was increased with 0-50%. In mixtures comparable to SAP A mixtures but with a distinct lower effective water-to-cement ratio, the gas permeability was also increased with 50-150%, depending on the amount added.

Results in literature also show that the permeability apparently is decreased when using a bigger particle (Reinhardt & Assmann, 2009). There it was stated that a smaller number of pores do not create a continuous structure. The larger pores seem less accessible for gases. As the surface is less dependent on the size of the particle (in case of a spherical particle in function of the diameter to the second power) as is the volume (third power of the diameter), the pores seem less accessible for oxygen flow in case of bigger particles used. This seems also the case if one compares SAP A with SAP B macro pores: 270 ± 54 µm and 827 ± 173 µm, respectively (see paragraph 3.2.1.1).

4.4 Low-pressure water permeability

To determine the water movement through a specimen, several methods can be used, both destructive and non-destructive. A possibility is the use of a water permeability test set-up. However, in this method, the crack sealing potential of SAP particles cannot be visualized, only measured. The decrease in water permeability is a measure for the sealing capacity. The low-pressure water permeability test used, is the one described by (Aldea et al., 1999; Aldea et al., 2000; Van Tittelboom et al., 2011b) (Figure 4.2). First, cylindrical specimens (Ø 78 mm × 20 mm, n=5; with 1 v% of microfibres or two metal curved fibres perpendicular to the loading direction) were cracked at an age of 7 days by means of a crack-width-controlled splitting test (Walter+Bai DB 250/15). The crack width was controlled with one Linear Variable Difference Transducer (LVDT) (Solartron AX/0.5/S with an accuracy of 1 µm). The crack opened with a velocity of 0.001 mm/s and splitting was stopped when a 300 µm crack width was reached. After unloading, the residual crack width was 150-200 µm.

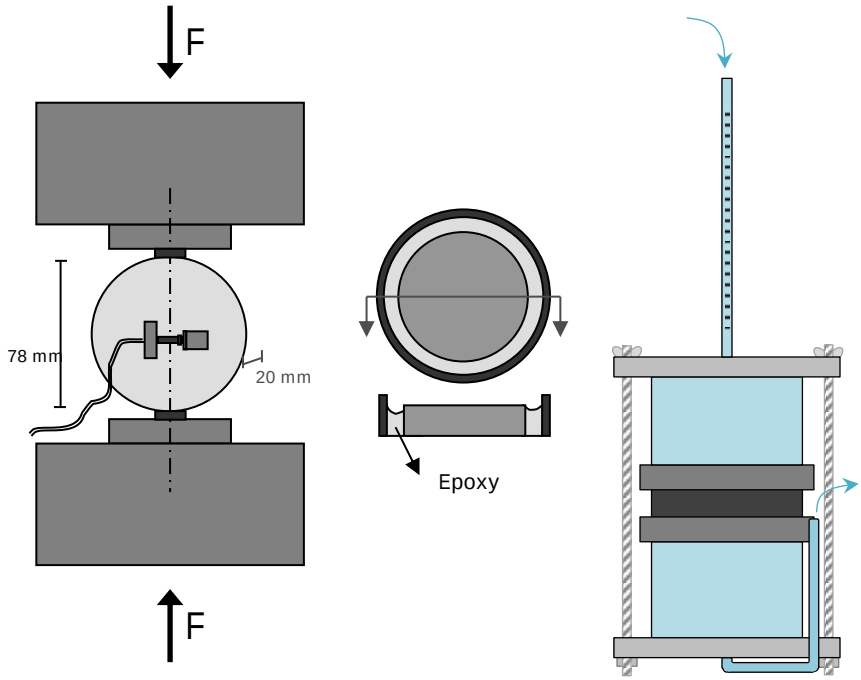

Figure 4.2. Low-pressure water permeability: splitting test, sample preparation and test set-up.

After splitting, the samples were glued with epoxy into a PVC-tube. This ensured a unidirectional flow during the test later-on to exclude the side effects during the permeability tests. The samples were vacuum saturated with demineralized water and placed into the water permeability test set-up at an age

of 28 days. The self-sealing efficiency was then measured as the decrease in water permeability. For this, the coefficient of water permeability k [m/s] was calculated according to equation 4.2, starting from Darcy's law:

$$k = \frac{a_f \cdot T_s}{A \cdot t_f} \cdot \ln\left(\frac{h_0}{h_f}\right) \tag{4.2}$$

where a_f = cross-sectional area of the fluid column [m²]; T_s = specimen thickness [m]; A = surface area of the sample subjected to the flow [m²]; t_f = measured time [s]; h_0 = initial pressure head [m]; and h_f = remaining pressure head [m].

The water permeability is related to the third power of the crack width (k/w³), according to the formula of Tsukamoto (Edvardsen, 1999; Tsukamoto & Woener, 1991) according to a parallel-plate theory of fluid dynamics. The formula is given in equation 4.3:

$$k = \frac{a_g \cdot I_p \cdot l_s \cdot g}{12 \cdot \nu} \cdot w^3 \tag{4.3}$$

where a_g is a flow rate coefficient indicating the smoothness of the crack surface as the concrete faces are not parallel $(0 \leq a_g \leq 1)$ [-], I_p is the pressure gradient (h/d_c) [-], h is the height of the fluid column on the inlet [m], d_c is the length of the crack in the flow direction [m], l_s is the length of the crack at a right angle to the flow direction [m], g is the gravity constant [m/s²] and ν is the kinematic viscosity [m²/s].

The real boundaries in literature for a_g are 0.04 and 0.53 (Edvardsen, 1999). The formula of Tsukamoto does, however, have a high variability in the small crack width range. In this study, the crack widths exceed the 100 µm boundary given by (Homma et al., 2009) and therefore the formula of Tsukamoto is assumed to be valid. In the formula of Tsukamoto, the value of 0.22 for a_g is obtained by the mathematical calculation of the lowest residual sum of squares. Edvardsen (1999) calculated a specific value of 0.25 as the experimental a_g which is in good accordance to the value found in this investigation (0.22).

Permeability readings for all specimens were taken every day. Because the measurements were not immediately constant, they were repeated until a steady-state flow was reached. This steady-state flow was reached when subsequent measurements were almost constant in time. During the measurements, the specimens remained completely submerged. On the thirtieth day (at an age of 58 days), the average coefficients of water permeability of the samples were compared.

During the test, water will react with unhydrated cement grains and the concrete will swell. This causes a densification of the matrix. Also, possible remaining air bubbles will have to leave the specimen, causing a small drop in k-value after the first measurements. By measuring continuously in time and determining the value of water permeability k at 30 days in the test set-up (age of 37 days), these influences are overcome.

Figure 4.3 shows the splitting strength of the cylinders used in the low-pressure water permeability tests. The splitting strength decreases significantly with increasing m% of SAP B. This is due to the macro-pore formation due to the uptake of mixing water and the gradual release afterwards. These macro pores will decrease the available surface area in the cross-section for taking up tensile forces during the Brazilian splitting test. SAP A particles seem to reduce the strength more compared to SAP B particles. This is due to their small particle size which causes a lower workability during mixing, but this is also due to the formation of relatively more pores in the tensile cross-sectional area compared to a smaller amount of larger pores in SAP B specimens. The available area is thus lower and this causes a reduction in strength which is substantial. Due to the lower water absorption and large particle size of SAP C, the splitting strength is not significantly different compared to the strength of a SAP-less mixture. As the SAP C particles take up less water, the macro pores will not be as large as for the SAP B specimens. These findings for SAP C are not corresponding to the results found in paragraph 3.2.3.1 on mortar prisms, as in this case no plasticizing effect was found. This is due to another batch of Pluronic F127 between different syntheses.

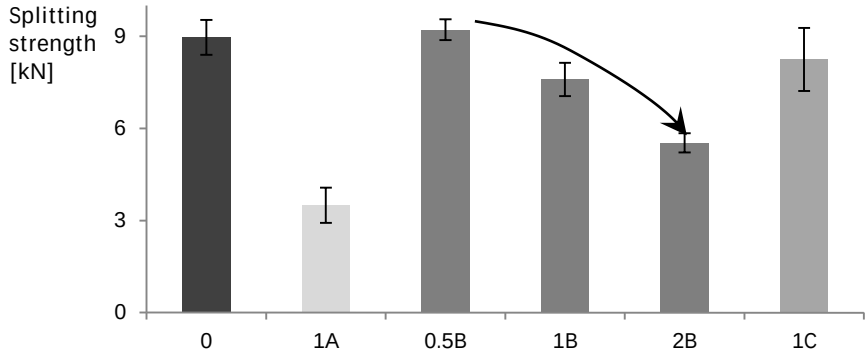

Figure 4.3. Splitting strength [kN] of the cylindrical specimens used in the low-pressure water permeability tests. The error bars show the standard deviations on single results.

The low-pressure coefficients of water permeability (k) in time are shown in Figure 4.4 for the self-healing mixtures. A very small drop of k in time is noticed. Specimens containing SAP, initially show a decrease in permeability. This is mainly due to the swelling effect of SAPs and blockage of the crack by SAPs. Further decrease in water permeability is due to the further blockage by loose particles and SAPs, autogenous healing and densification of the matrix. The SAP B particles are able to seal the crack more effectively in comparison to SAP A and SAP C. The difference noticed between SAP A and SAP B is due to the smaller particle size of SAP A. As SAP A has a dry particle size of 100 µm, it is not able to seal a 190-220 µm crack effectively, even in completely swollen state. Their expanding diameter does not reach over the total crack and water may flow in between the swollen particles. It is also possible that a SAP A particle which starts to swell is washed out of the crack before actual crack blockage occurs. The bigger SAP B, with a size of

477 µm, is not likely to be washed out and is able to seal a crack in a more effective way compared to the smaller SAP A. The difference noticed between SAP B and SAP C is due to a lower absorption capacity of SAP C (See Chapter 2). As the particles swell less, they result in less crack sealing.

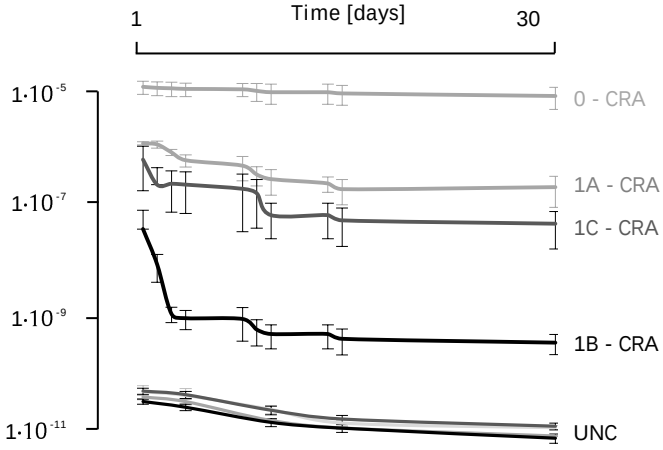

Figure 4.4. Water permeability k [m/s] in time of the cracked (CRA) and uncracked self-healing specimens.

The final low-pressure coefficients of water permeability (k) in time are shown in Figure 4.5 for the self-healing mixtures. Cracked specimens without SAP particles have a final k value of $1{\cdot}10^{-5}$ m/s. Specimens containing SAPs, however, show a decrease in permeability (from $1{\cdot}10^{-7}$ to $1{\cdot}10^{-10}$ m/s compared to $1{\cdot}10^{-5}$ m/s). This is mainly due to the swelling effect of SAPs and blockage of the crack by the SAPs. Increasing the amount of SAP B results in a higher amount of SAP particles available to seal a crack. An amount of 0.5 m% SAP B is not sufficient to receive complete crack blockage, but the double amount is. A too high amount of SAPs, however, causes a decrease in strength (as seen in Figure 4.3) as more macro pores are formed. These pores need to be filled and part of the self-sealing effect is lost. Also, the difference between 1B-CRA (cracked specimens with 1 m% of SAP B) and 2B-CRA (cracked specimens with 2 m% of SAP B) is possibly due to the formation of more internal cracks due to the more porous cementitious matrix. The permeability of a sealed crack with 1 m% SAP B ($1{\cdot}10^{-10}$ m/s) is almost as good as the value noticed for an uncracked specimen ($1{\cdot}10^{-11}$ m/s). So, 1 m% of SAP B can efficiently seal a crack from intruding fluids. This proves the sealing capacity when using SAPs in cementitious materials.

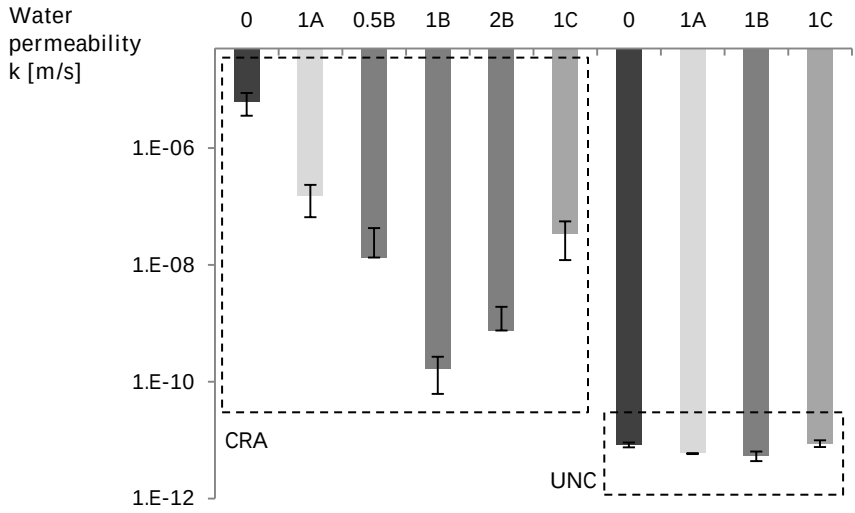

Figure 4.5. Water permeability k [m/s] at 30 days of the cracked (CRA) and uncracked (UNC) specimens in the low-pressure water permeability test set-up. The error bars show the standard deviation on single results.

Yang (2008) measured a permeability coefficient of $1 \cdot 10^{-6}$ m/s in a sample with a crack width of 200 µm, which is approximately the one found for cracked reference samples. A decrease in water permeability is observed for specimens containing SAP, in agreement with (Lee et al., 2010a; Lee et al., 2010b) who also measured a decrease in permeability. SAP B in an amount of 1 m% relative to the cement weight provided the highest decrease in permeability over time. A higher amount of SAP B caused a coarser matrix (due to the formation of macro pores) and lower strength and thus more pathways for water to migrate. Since also the mechanical properties decrease with increasing m% of SAP B, 1 m% of SAP B can be selected as best option to obtain self-sealing mortar. It is clear that, by the use of SAPs, the permeability of cracked mortar (crack width of 150-200 µm) is decreased with a factor up to 10^4. Due to the swelling effect of the SAPs, the crack will be filled by the hydrogel formed, as can be seen in Figure 4.6, an example when using SAP B. This crack filling leads to the blockage of that crack and thus the reduction in permeability as the water flow is reduced or even stopped completely at distinct places.

It was also found that due to the swelling effect of the SAPs, the reduced water movement speed, which is critical to obtain autogenous healing, is optimal as cracks are able to close due to deposited crystals. In reference specimens, the amount of autogenous healing – inherent part of a cementitious system – is less compared to the specimens with SAPs. As the water speed is high in reference samples, possible healing products are likely to be washed out as the criteria for autogenous healing described in (Edvardsen, 1999) are not optimal. In water-retaining structures like quays or cellars the SAPs may prove to be useful as the flow will be reduced, sealing the cracks, but the crack may by sealed by deposited crystals as well.

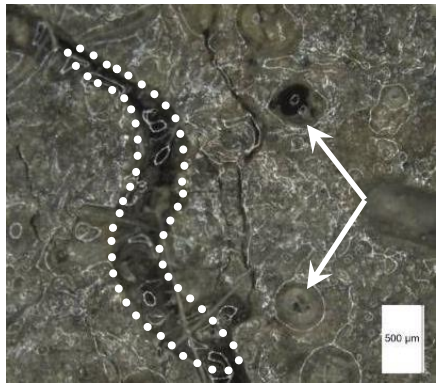

Figure 4.6. Blockage by SAP B (1B) of a crack and macro pores (as indicated crack area and arrows, respectively; the scale bar shows a distance of 500 µm).

The permeability of a sealed crack with 1 m% SAP B is almost as good as the value noticed for an uncracked specimen. Uncracked specimens with SAPs even show less permeability (Figure 4.7). The value for 1A-UNC (uncracked specimens with 1 m% of SAP A) and 1B-UNC (uncracked specimens with 1 m% of SAP B) seem to be lower than the value for 0-UNC (uncracked specimens without SAPs) and 1C-UNC (cracked specimens with 1 m% of SAP C) (Figure 4.7). This is mainly due to the modification of the matrix porosity by SAP. This was also seen by (Reinhardt & Assmann, 2009). Due to taking up mixing water, the SAP will give their water-to-the cementitious matrix, but only after a period of time. This will result in a matrix with a lower apparent water-to-cement factor in between SAPs and thus in a change in microstructure and permeability. Afterwards, the absorbed water is released for internal curing, making the microstructure even denser. Furthermore, the SAPs in pores will swell upon contact with water, and the permeation is lowered in the SAP cavities (macro pores). However, the overall effect of the reduced permeation is mostly due to the lower water-to-cement ratio. SAP C seems not to change the microstructure as much as SAP A or SAP B, due to the smaller absorption capacity of SAP C. This will result in less internal curing, a lower water retention and thus a smaller influence on the microstructural properties of the cementitious matrix. That is why the values for 0-UNC and 1C-UNC are similar.

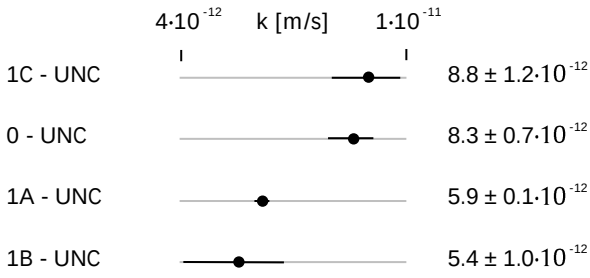

Figure 4.7. Detailed water permeability k [m/s] at 30 days of the uncracked mixtures.

The influence of a different matrix was investigated using another mixture composition (found in paragraph 4.2). The water permeability for the standard mortar mixtures is shown in Figure 4.8. As a comparison, the permeability coefficients of comparable self-healing mixtures (see Chapter 5) are given as well. A decrease in water-to-cement ratio does not lead to a decrease in water permeability in cracked specimens. The cementitious matrix is of less concern when studying these cracked specimens. When using SAPs, the permeability decreased substantially. This result was already described earlier. However, when adding additional water, the permeability is slightly higher compared to mixtures with additional superplasticizer. This is due to the change in microstructure and the slightly different cementitious matrix composition (See Chapter 3).

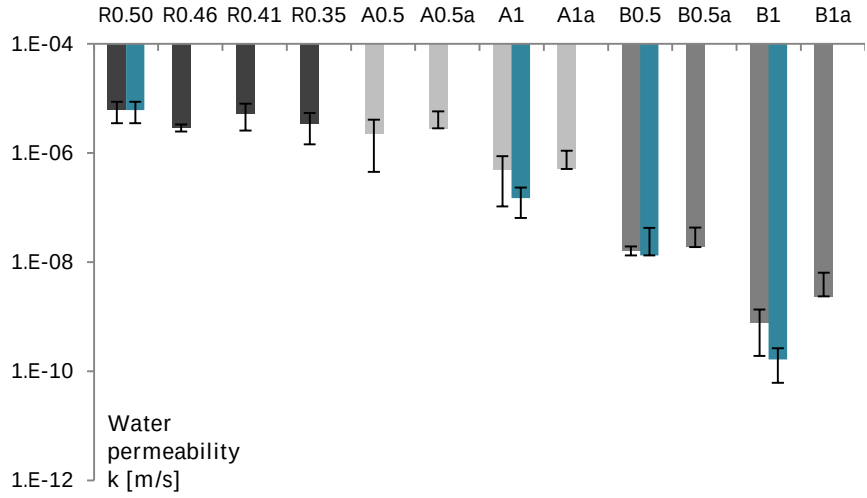

Figure 4.8. Mean water permeability k [m/s] at 30 days of the cracked standard-mortar mixtures (grey tones) and self-healing mixtures (blue) in the low-pressure water permeability test set-up. The error bars show the standard deviation on single results.

The effect of the change in microstructure is more clearly seen in uncracked specimens. The results from the low-pressure water permeability tests are shown in Figure 4.9. Here, the coefficient of water permeability k after 28 days of submersion is given to exclude remaining air bubbles or possible leakage at the start of the test. As the variability in the test is large, only trends can be evaluated. The obtained values correspond to values of uncracked specimens in literature (Reinhardt & Assmann, 2009; Van Tittelboom et al., 2011b). With a decreasing water-to-cement ratio, there is a reduced water permeability, due to the denser microstructure. If SAPs are added, the permeability is lower. This effect is attributed to two different reasons: *i)* the swelling of the SAP particles inside macro pores, but even more to *ii)* the densification of the cementitious matrix due to internal curing. When using additional water, the matrix is approximately the same (see Chapter 3). The permeability, however, is slightly lower. Generally, the effect of SAPs on the microstructural development is the key parameter in water transport processes.

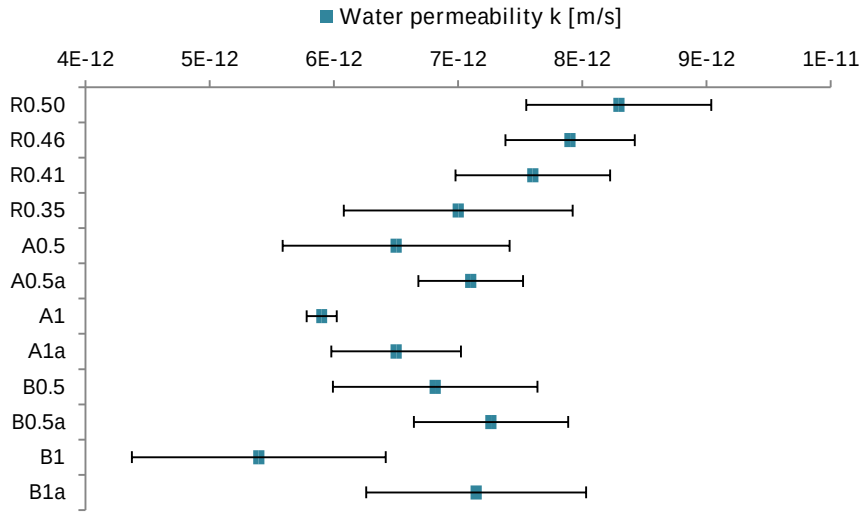

Figure 4.9. Water permeability value k [m/s] for the studied uncracked mixtures.

To investigate a real situation, simulated sea water was used as well in these low-pressure water permeability tests. The test conditions were the same as described earlier. Not to induce damage or corrosion of the test setup, this test was only conducted over a total period of several days (one week). Approximately the same results were found when using sea water instead of demineralized water. The sealing effect by the SAPs was the same in sea water and the same conclusions may be drawn. However, in time, salt crystals present in the sea water may start to deposit in the crack, reducing the overall flow, as other healing products based on salts may be formed as well (Palin et al., 2015). This would further decrease the overall water permeability.

The use of different types of SAPs and their influence on the low-pressure water permeability at 28 days of testing is shown in Table 4.1. An increase in amount of SAPs results in a further decrease in water permeability. The smaller SAPs, such as SAP E, SAP H and Powder, are unable to bridge the approximately 200 µm wide cracks. It is possible that those SAPs are partially washed out from the wide crack. This would lead to the low water permeability found in E1, where part of the SAPs may cluster to block the crack from intruding fluids. SAP G, also a fine SAP, tends to lead to a sealing of the crack. This is possibly due to a partial blockage of the SAP after being dislodged. SAP F, the fibre type, is also unable to efficiently block a crack. This is mainly due to the form of the SAP as only a part of the SAP will be able to swell towards the crack faces. SAP D and Micro are able to seal a crack. Their size is ideal to self-seal a crack and both SAPs are comparable to SAP B. The Medium form is too large to seal a crack. Only some distinct SAP particles are hereby exposed to the water and the water flow occurs in between the blocked regions. The rough crack faces restrict the extreme deformations of the Medium SAP to fill up a crack. Also, the middle part of the SAP may not be exposed to water.

Table 4.1. Water permeability value k [m/s] after 4, 12 and 30 days for all studied mixtures with different types of SAP.

	k [m/s] after 4 days	k [m/s] after 12 days	k [m/s] after 30 days
D0.5	$8.0 \pm 2.0 \cdot 10^{-7}$	$2.7 \pm 1.4 \cdot 10^{-7}$	$1.9 \pm 1.0 \cdot 10^{-7}$
D1	$2.6 \pm 0.7 \cdot 10^{-8}$	$1.4 \pm 0.6 \cdot 10^{-8}$	$7.1 \pm 3.3 \cdot 10^{-9}$
E0.5	$2.5 \pm 0.4 \cdot 10^{-6}$	$1.4 \pm 0.2 \cdot 10^{-6}$	$6.2 \pm 1.0 \cdot 10^{-7}$
E1	$9.3 \pm 3.5 \cdot 10^{-8}$	$4.5 \pm 0.6 \cdot 10^{-8}$	$9.6 \pm 0.2 \cdot 10^{-9}$
F0.5	$2.5 \pm 0.8 \cdot 10^{-6}$	$1.8 \pm 0.6 \cdot 10^{-6}$	$7.4 \pm 2.6 \cdot 10^{-7}$
F1	$1.4 \pm 0.6 \cdot 10^{-7}$	$6.4 \pm 2.6 \cdot 10^{-8}$	$1.3 \pm 0.7 \cdot 10^{-8}$
G0.5	$7.2 \pm 1.6 \cdot 10^{-8}$	$2.4 \pm 0.8 \cdot 10^{-8}$	$2.7 \pm 1.9 \cdot 10^{-8}$
H0.5	$9.1 \pm 2.8 \cdot 10^{-7}$	$3.1 \pm 0.1 \cdot 10^{-7}$	$1.3 \pm 0.1 \cdot 10^{-7}$
H1	$1.9 \pm 0.5 \cdot 10^{-7}$	$1.0 \pm 0.3 \cdot 10^{-7}$	$3.8 \pm 1.6 \cdot 10^{-8}$
po0.5	$4.6 \pm 2.2 \cdot 10^{-7}$	$3.8 \pm 2.1 \cdot 10^{-7}$	$2.0 \pm 1.1 \cdot 10^{-7}$
µi0.5	$4.3 \pm 2.1 \cdot 10^{-8}$	$3.4 \pm 1.7 \cdot 10^{-8}$	$1.9 \pm 0.9 \cdot 10^{-8}$
Me0.5	$4.6 \pm 0.9 \cdot 10^{-7}$	$2.1 \pm 0.4 \cdot 10^{-7}$	$6.8 \pm 0.2 \cdot 10^{-8}$
Me1	$1.7 \pm 0.3 \cdot 10^{-7}$	$8.7 \pm 3.1 \cdot 10^{-8}$	$6.4 \pm 2.3 \cdot 10^{-8}$

4.5 Deposition of calcium carbonate and further hydration

During the low-pressure water permeability tests, stalactites were formed on the bottom of the specimens around the cracks (Figure 4.10). These are washed-out products and needed to be investigated on their composition.

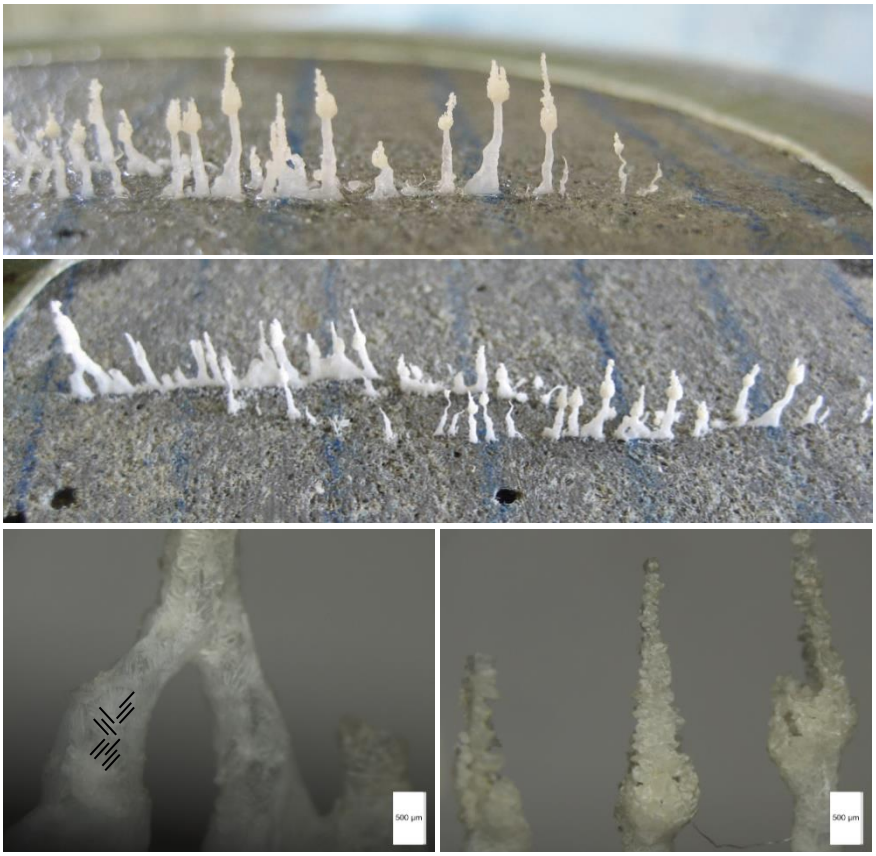

Figure 4.10. Formation of stalactites with a maximum height of 11 mm after a low-pressure water-permeability test at the outlet of the crack of a specimen containing SAP B. The scale bars amount to 500 µm.

Also, domes were visible on the surface of dried specimens after permeability testing (Figure 4.11). These are pure $CaCO_3$-crystals by the reaction of CO_2 dissolved in the Ca^{2+}-rich fluid in the SAP. The SAPs shrink again by yielding fluid to the precipitation reaction, the matrix and by vaporization. Only the domes are left behind. The crack faces of the specimens showed further hydration and a distinct formation of white crystals.

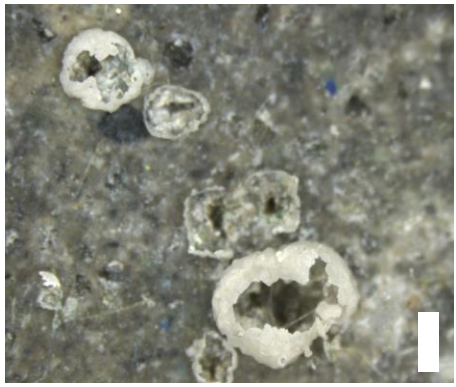

Figure 4.11. Formation of $CaCO_3$ domes on the sample surface after shrinking of SAP. The height of the scale bar is 500 µm.

Thermogravimetric analysis (TGA) with a Hi-Res TGA 2950 Thermogravimetric Analyser was conducted to determine the composition of the white crystallization found in the permeability tests and the degradation temperature of pure SAPs. The crystals were carefully removed from the specimens and approximately 0.01 g was used in the TGA. During the analysis, the temperature was gradually increased (10°C/min) and the mass decrease was measured by a Cahn microbalance until a temperature of 1000°C was reached. Measurements were performed under a controlled Helium atmosphere.

The outlet of the crack in every specimen showed a large quantity of stalactites after performance of the permeability tests. Thermogravimetric analysis (TGA) showed that the stalactites consisted of $CaCO_3$ and washed-out hydration products (see Figure 4.12 for the REF and B1 samples; A1, B0.5 and B2 are analogous to B1). The degradation temperature of pure $CaCO_3$ is 700-750°C (Tiwari, 2008). At this temperature, $CaCO_3$ decomposes to CaO and CO_2. The degradation peak is also visible in the first derivative (black) of the TGA curve (grey) in Figure 4.12. The degradation of pure $Ca(OH)_2$ starts at 320°C, peaks at 480°C and stops at 510°C, after (Beaudoin et al., 2006), which is also visible. $Ca(OH)_2$ decomposes to the solid CaO with the formation of H_2O.

TGA was also conducted on virgin SAP, as can be seen in Figure 4.13, but the degradation peaks of the material (250-450°C, 600°C and 900°C) were not found in the TGA curves of the stalactites, supporting the conclusion that SAP effectively seal the crack without dissolving or being washed-out. If this would be the case, the SAP peaks would be visible in the TGA curves of the stalactites. The peak below 100°C can be attributed to adsorbed moisture.

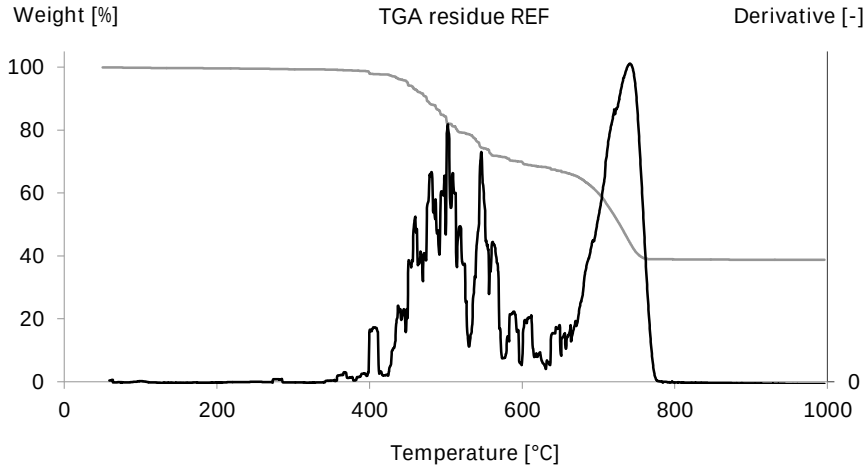

(a)

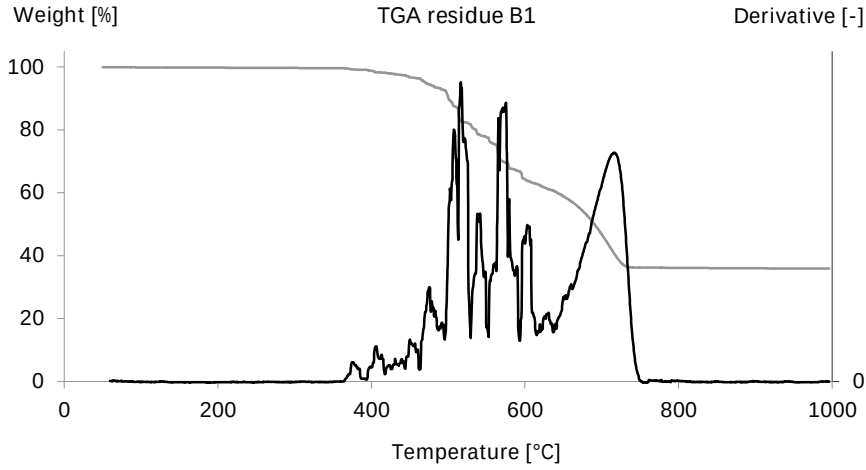

(b)

Figure 4.12. TGA of the stalactites obtained in the permeability tests of REF samples without SAP **(a)** and samples with 1 m% SAP B **(b)** (TGA of A1, B0.5 and B2 are analogous to TGA residue B1) in grey with the derivative as a measurement of the weight loss in black.

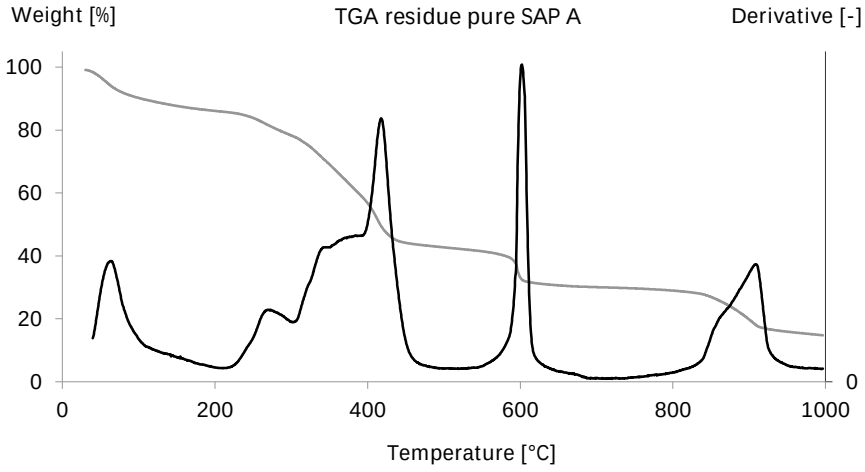

(a)

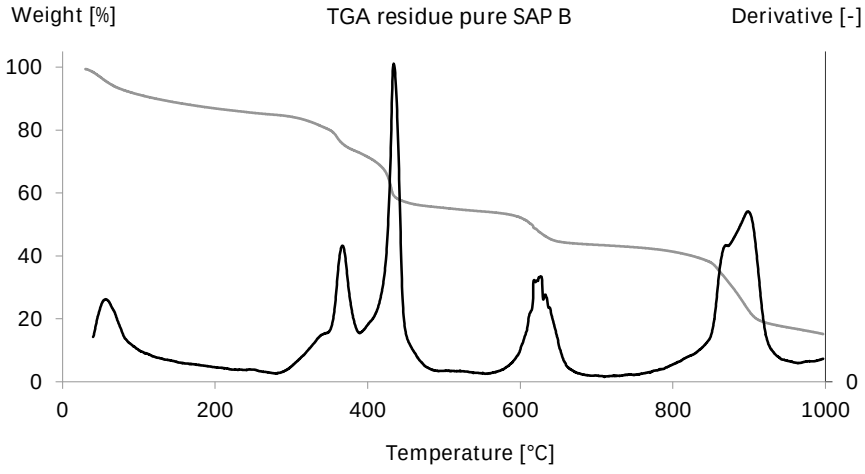

(b)

Figure 4.13. TGA of pure SAP A **(a)** and SAP B **(b)** in grey with the derivative as a measurement of the weight loss in black.

4.6 High-pressure water-permeability

The effect of SAPs on uncracked specimens was also studied by means of a high-pressure permeability set-up (NBN EN 12390-8). The machine used was a Water impermeability tester type WUP 6-M of the company Testing. For these tests, large cylindrical specimens (Ø 100 mm × 100 mm, n=3) were glued with epoxy into a hollow prism (200 mm × 200 mm × 150 mm) (Figure 4.14). These composite specimens were then saturated with water under vacuum at an age of 27 days. Then, the specimens were placed into the test set-up at an age of 28 days and water was applied under pressure to the bottom surface of the hardened concrete. First, 1 bar of water pressure was applied for 1 day to ensure that there was no leakage in the set-up. Subsequently, 5 bar water pressure was applied until maximally 1 l had come through the specimen. At specific time intervals, the amount of water that passed through the specimen was recorded for a total time of 28 days.

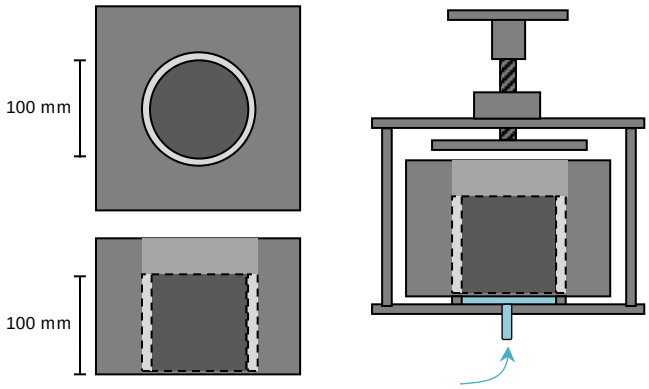

Figure 4.14. High-pressure water permeability: sample preparation and test set-up.

As the low-pressure water permeability values for uncracked specimens were not all significantly different, high-pressure water permeability tests were performed. The results with a water pressure of 5 bar are shown in Figure 4.15. In this figure, the x-axis is put in logarithmic scale. In time, the amount of water leaking through a specimen increases. After only one day, SAP-less specimens have transmitted 1 l of water. Incorporating SAP A leads to a denser matrix and blockage due to swelling, and the permeability is less. SAP B mixtures show the best result as the water impermeability is maintained during 28 days. SAP C mixtures, however, show an opposite effect. Due to the high-pressure, they were not able to withstand the water penetration and the water found easy pathways for migrating through the macro pores. This is possibly due to the low mechanical strength typical for these types of hydrogels as a plasticizing effect was seen. SAP C is thus not as efficient as SAP A or SAP B to seal a crack from intruding fluids at high pressures.

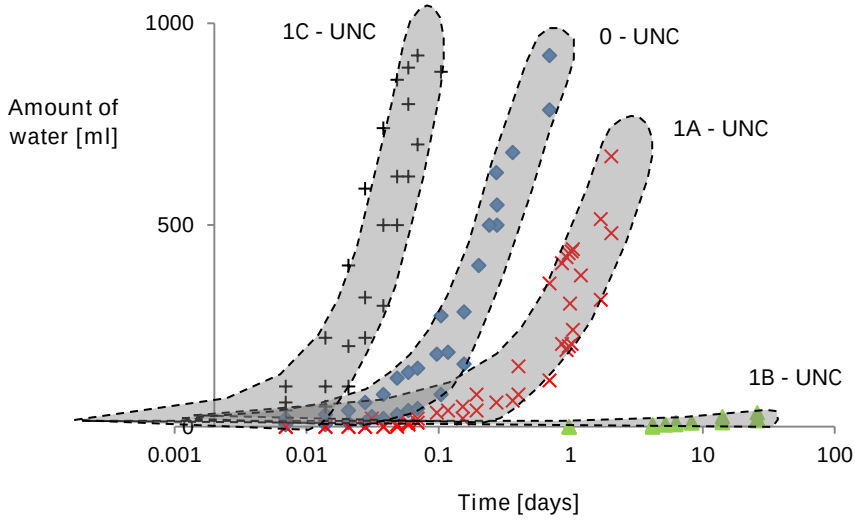

Figure 4.15. Amount of water through a specimen [ml] as a function of time of the uncracked specimens in the high-pressure water permeability test set-up at 5 bar water pressure. The dashed lines show the interval of three specimens.

4.7 Capillary water absorption

The standard used to determine the capillary water absorption on cylindrical specimens (diameter of 100 mm and 50 mm high) was ASTM C 1585-04 (Figure 4.16). This test method is used to determine the rate of absorption (sorptivity) of water due to capillary suction by mortar by measuring the increase in the mass of a specimen resulting from absorption of water as a function of time when only one surface of the specimen is exposed to water. The test specimens were first made according to EN 196-1 and were cured for 28 days at 20 ± 2°C and 95 ± 5 % RH. They were then stored in an environmental chamber at 50 ± 2°C and 80 ± 3 % RH for three days. The specimens were then stored for a minimum of 15 days at 23 ± 2°C and the dry mass was determined. The sides of the specimens were taped with aluminium foil and the end that will not be exposed to water was sealed with a loosely attached plastic sheet. The specimen was then placed in a pan with water where the water level was 2 mm above the supports.

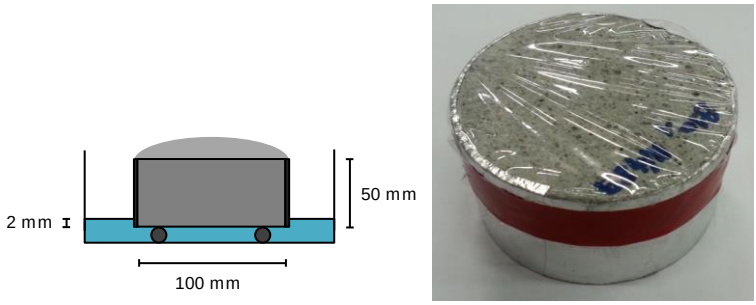

Figure 4.16. Test set-up of the capillary water absorption tests (left) and used sealed specimens (right).

The mass was then recorded after 60 ± 2 s, 5 min ± 10 s, 10 ± 2 min, 20 ± 2, 30 ± 2, 60 ± 2, every hour up to 6 hours ± 5 min, once a day up to 3 days followed by three measurements at least 24 h apart during days 4 to 7 and one final measurement at least 24 h after the measurement at 7 days. The absorption I was determined as the change in mass divided by the product of the cross-sectional area of the test specimen and the density of water, following equation 4.4.

$$I = \frac{m_t}{A \cdot \rho_w} \tag{4.4}$$

where I is the absorption, m_t the change in mass at time t [g], A the exposed area [mm²] and ρ_w the density of water [g/mm³].

The initial rate of water absorption [mm·s$^{-1/2}$] was defined as the slope of the line that is the best fit to I plotted against the square root of time [s$^{1/2}$], using all the points from 1 min to 6 h. The secondary rate of water absorption [mm·s$^{-1/2}$] was calculated using all the points from 1 d to 7 d.

After conducting the capillary water absorption tests, the specimens were first vacuum saturated with water for 24 hours. The first 4 hours, the specimens were put in a chamber at 25 mbars at 20 ± 2°C. Afterwards, water was added till the specimens were completely submerged. The specimens were then hydrostatically weighed (m_h) and the saturated mass was determined (m_s). The specimens were then stored at 105 ± 5°C for 7 days until constant mass (mass difference < 0.05% after 24 h). The dry mass was then determined (m_d). The apparent volumetric mass, the porosity accessible to water and the amount of water absorbed were determined used following equations.

The apparent volumetric mass: $$\rho_{app} = \frac{m_d}{m_s - m_h} \quad (4.5)$$

The porosity accessible to water: $$\rho_1 = \frac{m_s - m_d}{m_s - m_h} \quad (4.6)$$

Amount of water absorbed: $$\rho_2 = \frac{m_s - m_d}{m_d} \quad (4.7)$$

The results for the capillary water absorption tests for SAP A and SAP B (standard mixtures in paragraph 4.2) are shown in Figure 4.17. All results derived from the samples are shown in Table 4.2. With decreasing water-to-cement ratio, the capillary absorption and the initial and secondary rate of water absorption decrease. When using SAPs without additional water, the absorption is also lower, but higher than the absorption by a reference mixture with the same effective water-to-cement ratio. This is due to the water uptake by the SAPs during weighing the specimens as this water is held. This causes a higher mass and thus higher value for absorption. The same conclusions can be made considering the use of additional water. Again, the absorption is slightly higher compared to the reference R0.50 mixture with the same effective water-to-cement ratio. With additional water used, the decrease in absorption is compensated, even overcompensated. This is again due to the absorption by the SAPs, holding the water, thus increasing the mass during weighing when not put in the water.

Capillary action is inversely related to the pore radius. With a larger pore size, such as a macro pore, the capillary action is decreased until gravity is overcome. But, SAP pores get filled with water due to the swelling action of the SAPs and thus cause an increase of mass during measurement. The moisture content also influences the results but all specimens followed the same curing conditions and could be compared. The curves flatten over time. The reason is that gravity interferes with capillary action. Also, the cementitious matrix partly swells, causing a partial and local densification.

In literature, a decrease in rate of water absorption is also found for a decrease in water-to-cement ratio (Reinhardt & Assmann, 2009). The mixtures with SAPs and additional water, show a partial decrease in rate of water absorption, which is only found for mixtures with superplasticizer in this research. Here a partial increase in rate of water absorption is found when compared to a reference mixture with the same effective water-to-cement ratio.

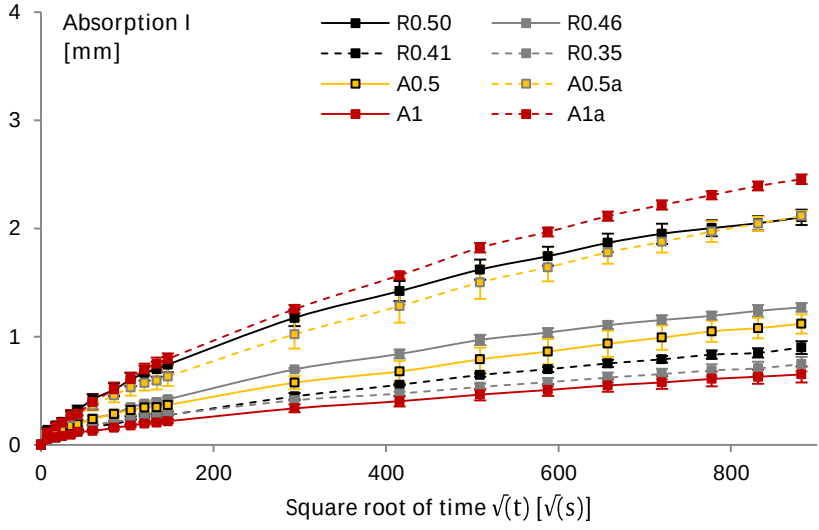

(a)

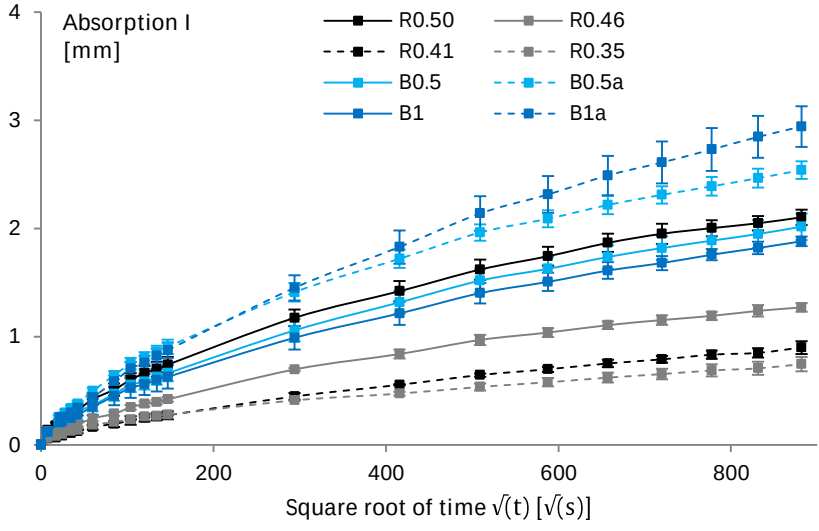

(b)

Figure 4.17. Capillary water absorption tests for SAP A **(a)** and SAP B **(b)**.

The same results as in Section 3.2.3.2 can be found considering the bulk density. The main differences are due to the macro-pore formation by the SAPs and their caused densification when no additional water is used. The density is lower when using additional water. The values are comparable as found in Section 3.2.3.2.

The accessible porosity and the water absorption accessibility show the same trends. With a decrease in water-to-cement ratio, there is also a decrease in porosity accessible. With SAP addition without additional water, this accessible porosity is comparable to the respective references with the same effective water-to-cement ratio. With additional water, this porosity shifts towards the R0.50 value, with a comparable microstructure (similar results as found in Chapter 3).

Table 4.2. Rate of initial and secondary water absorption [$\cdot 10^{-3}$ mm$\cdot$s$^{-1/2}$], bulk density [kg/m³], accessible porosity [%] and water absorption when fully saturated [%].

	Initial rate	*Secondary rate*	*Bulk density*	*Accessible porosity*	*Water absorption*
R0.50	4.40 ± 0.38	1.74 ± 0.01	2169 ± 21	7.7 ± 0.7	3.6 ± 0.4
R0.46	2.40 ± 0.05	1.03 ± 0.04	2215 ± 22	6.8 ± 0.6	3.1 ± 0.3
R0.41	1.60 ± 0.24	0.79 ± 0.11	2301 ± 27	4.4 ± 0.5	1.9 ± 0.2
R0.35	1.52 ± 0.07	0.58 ± 0.11	2373 ±12	2.7 ± 0.2	1.1 ± 0.1
A0.5	1.97 ± 0.30	0.99 ± 0.11	2217 ± 4	4.2 ± 0.2	1.9 ± 0.1
A0.5a	3.70 ± 0.51	1.97 ± 0.11	2071 ± 25	7.9 ± 0.7	3.8 ± 0.4
A1	1.13 ± 0.10	0.57 ± 0.09	2125 ± 1	4.3 ± 0.4	2.0 ± 0.2
A1a	4.93 ± 0.37	2.18 ± 0.16	1941 ± 23	9.9 ± 1.1	5.1 ± 0.6
B0.5	3.73 ± 0.31	1.71 ± 0.05	2167 ± 7	7.2 ± 0.5	3.3 ± 0.2
B0.5a	5.29 ± 0.48	2.01 ± 0.04	2144 ± 9	7.7 ± 0.2	3.6 ± 0.1
B1	3.52 ± 0.52	1.58 ± 0.16	2162 ± 7	6.4 ± 0.1	3.0 ± 0.1
B1a	5.21 ± 0.32	2.64 ± 0.16	2064 ± 11	8.6 ± 0.7	4.2 ± 0.4

The same conclusions can be drawn when using different types of SAPs with additional water (Table 4.3). For all SAPs, due to their water uptake, the rate of absorption is overcompensated, as is the final absorption value after 9 days. Again, the increase is mainly due to the storage of water in the SAPs when performing capillary absorption tests. This amount should be subtracted to show the absorption through the cementitious matrix itself.

Table 4.3. Rate of initial and secondary water absorption [$\cdot 10^{-3}$ mm$\cdot$s$^{-1/2}$], final absorption after 9 days [mm], bulk density [kg/m³], accessible porosity [%] and water absorption when fully saturated [%] for all studied mixtures with different types of SAPs.

	Initial rate	*Secondary rate*	*Final absorption*	*Bulk density*	*Accessible porosity*	*Water absorption*
D0.5a	7.0 ± 0.3	1.2 ± 0.1	2.48 ± 0.10	2180 ± 8	8.7 ± 0.2	3.9 ± 0.1
D1a	7.6 ± 0.3	1.5 ± 0.1	2.77 ± 0.09	2163 ± 19	9.4 ± 0.6	4.2 ± 0.3
E0.5a	6.5 ± 0.3	1.1 ± 0.1	2.43 ± 0.10	2153 ± 17	7.9 ± 0.1	3.6 ± 0.1
E1a	7.2 ± 0.2	1.6 ± 0.1	2.70 ± 0.07	2106 ± 19	8.8 ± 0.3	4.1 ± 0.2
F0.5a	6.8 ± 0.3	1.3 ± 0.1	2.59 ± 0.10	2205 ± 11	9.0 ± 0.5	4.0 ± 0.2
F1a	7.9 ± 0.3	1.6 ± 0.1	3.11 ± 0.09	2136 ± 19	10.6 ± 0.4	4.8 ± 0.2
G0.5a	5.5 ± 0.2	1.7 ± 0.1	2.51 ± 0.05	2072 ± 27	10.9 ± 0.3	5.2 ± 0.2
H0.5a	4.6 ± 0.2	1.5 ± 0.1	2.04 ± 0.06	2240 ± 18	7.8 ± 0.6	3.4 ± 0.3
H1a	4.2 ± 0.3	1.4 ± 0.1	1.92 ± 0.09	2259 ± 12	7.7 ± 0.4	3.3 ± 0.2
po0.5a	7.1 ± 0.2	2.0 ± 0.1	3.12 ± 0.07	2124 ± 7	10.2 ± 0.2	5.1 ± 0.1
µi0.5a	7.0 ± 0.4	1.8 ± 0.2	2.99 ± 0.12	2120 ± 5	8.9 ± 0.4	4 ± 0.2
Me0.5a	6.6 ± 0.1	1.7 ± 0.1	2.86 ± 0.04	2131 ± 23	8.6 ± 0.3	3.8 ± 0.1
Me1a	7.7 ± 0.2	2.0 ± 0.1	3.29 ± 0.06	2100 ± 10	10.0 ± 0.6	5.1 ± 0.3

Compared to the reference R0.50 in Table 4.2, only H0.5 and H1 tend to show the same rates and final value. This is due to their spherical shape and low uptake of mixing water. Their matrix is comparable to the reference one. The highest increase in initial and final rate can be found in mixtures containing SAP F, SAP G, Powder and Medium. This is due to their high water uptake during mixing. Increasing the amount of SAPs also shifts the rates and final absorption upwards.

The bulk density values show the expected tendencies. Due to the macro pore formation, the density decreases as after hardening empty macro pores remain. The higher the initial water uptake during mixing, the larger the influence on the density is.

The accessible porosity and the water absorption accessibility also show the same above-mentioned trends. The results were alike to the ones on air void analysis found in paragraph 3.2.3.1 when using different types of superabsorbent polymers. The lowest influences were found when using SAP H. The highest when using SAP F, SAP G and Powder. Increasing the amount of SAPs also increases the accessible porosity and water absorption.

4.8 Neutron radiography

The microstructure and water permeability can be studied by means of neutron radiography. As for neutron radiography thermalized neutrons are used, hydrogen attenuates more in comparison to concrete or aluminium. Water partly consists out of hydrogen and therefore neutrons are the ideal way to visualize the distribution of water in the pores of concrete with a high resolution. Zhang *et al.* (2010a) investigated the effectiveness of integral water repellent concrete to prevent the ingress of water and salt solutions. Neutron radiography proved to be a good method both to visualise water saturated areas inside a steel-reinforced concrete specimen. Kanematsu *et al.* (2009) also investigated water migration into cracked concrete by means of neutron radiography and observed a higher water content, indicating a more porous zone, at reinforcements. Cnudde *et al.* (2008) used neutron radiography to investigate the effect of porosity in natural stones on the water penetration depth. Neutron radiography also proved to be a very good way to determine the volume change of big SAP particles (Trtik et al., 2010; Trtik et al., 2011).

4.8.1 Studied specimens and neutron beam line with test set-ups

Neutron radiography was used to visualize and to quantify the water penetration into concrete through cracks. Two types of tests were performed. The first type was a capillary water absorption test; the second was a permeability test. The studied mixtures (without additional water) are shown in Table 4.4.

Table 4.4. Studied mortar samples with their code, m% of SAP, method of crack formation and residual crack width [µm] with standard deviation (n=3).

Specimen	*Code*	*m% SAP*	*Cracking*	*Crack width*
prism	0 - CRA	0	3 point bending	221 ± 66
	0 - UNC	0	n/a	n/a
	1B - CRA	1 m% SAP B	3 point bending	255 ± 33
	1C - CRA	1 m% SAP C	3 point bending	246 ± 44
	1C - UNC	1 m% SAP C	n/a	n/a
	2C - CRA	2 m% SAP C	3 point bending	224 ± 21
cylinder	0 - CRA	0	Splitting	148 ± 12
	1B - CRA	1 m% SAP B	Splitting	149 ± 14
	1C - CRA	1 m% SAP C	Splitting	146 ± 9

Every tested prism originated from a 300 × 100 × 100 mm³ mortar beam, reinforced with nine steel bars with a diameter of 2 mm (Figure 4.18). Three bars were alternatively positioned in the moulds at 25 mm, 50 mm and 75 mm height. The samples were demoulded 24 hours after casting and were stored at a relative humidity of more than 90% and a temperature of 20 ± 2°C until the age of 7 days. At that age, the beams were sawn along the main axis into three equal prisms of 300 × 100 × 25 mm³.

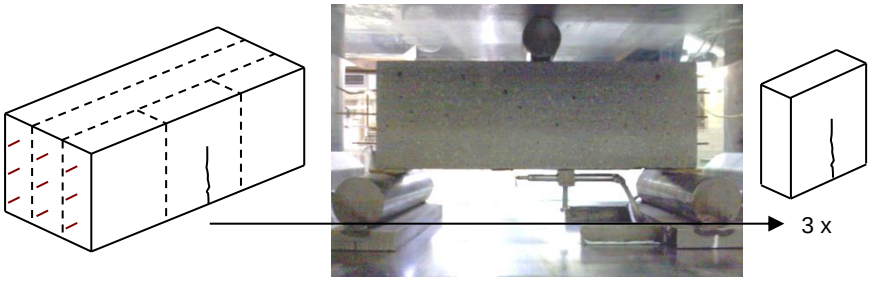

Figure 4.18. Schematization of the saw planes of the specimens and the test setup and testing machine used for the three-point-bending test.

By means of a crack-width-controlled three-point-bending test, a crack was created in the mortar prisms at an age of 7 days (Figure 4.18). The specimens were placed on two 40 mm Ø steel bars over a span of 280 mm. A third 30 mm Ø steel bar was placed in the middle on top of the specimens to apply the force. The crack width was measured with a linear variable differential transformer (LVDT) with a measurement range of 5 mm and an accuracy of 5 µm. The LVDT was positioned at the bottom of the specimen and measured the deformations over a span of 40 mm. The crack width was increased with a velocity of 0.5 µm/s until a crack of 400 µm was reached. After unloading, the residual crack width was about 200 µm. Microscopic analysis was used to measure the cracks. The stereomicroscope used was a Leica S8 APO with a DFC 295 camera. The crack height reached 70-80 mm and was not significantly different between the test series.

Specimens used for the neutron radiography tests, consisted of one 100 × 100 × 25 mm³ sample obtained after sawing one 300 × 100 × 25 mm³ prism the day after crack formation. A minimum of three samples for each test series was always tested to receive statistical relevant results. All samples were dried in an oven at 50°C for 16 days to exclude moisture, prior to testing. The total height, width and length of the specimen were determined by means of a slide gauge with an accuracy of 0.02 mm. The lower surface contained the crack mouth through which the water will penetrate. All surfaces, except the bottom and top faces of the specimens, were covered with self-adhesive aluminium foil to induce unidirectional water flow during the test. This minimizes the evaporation of moisture from the sides and the disappearance of the entrapped air sideways as only unidirectional flow is wanted. The specimens were tested at an age of 28 days.

Small cylindrical specimens were cast into a PVC-tube with an inner diameter of 10 mm. The tubes were filled to approximately 20 mm in height. The different sample types are listed in Table 4.4. The samples were demoulded after 48 hours and stored at a relative humidity of more than 90% and a temperature of 20 ± 2°C until the age of 7 days. The specimens were wrapped with self-adhesive aluminium foil along the height. The top and bottom circular planes remained open. The foil reached over the ends of the specimen to obtain two reservoirs that could be used as inlet or outlet. Then, the specimens were manually cracked by means of a screw jack. The setup is analogous to the one used in the Brazilian splitting test. The force was manually and slowly increased until a crack was formed through the

longitudinal axis of the cylinder. The aluminium foil provided sufficient stability to maintain a constant crack opening. Crack widths were measured by means of optical microscopy (Table 4.4). The samples were stored at standard laboratory conditions until the age of 28 days. Three samples for each test series were tested.

The beam used in this investigation was a neutron beam with a proton current of 1.5 mA at the measuring station NEUTRA, the thermal neutron radiographic facility at the Swiss spallation source SINQ of the Paul Scherrer Institute (PSI) (Lehmann et al., 2001) (Figure 4.19).

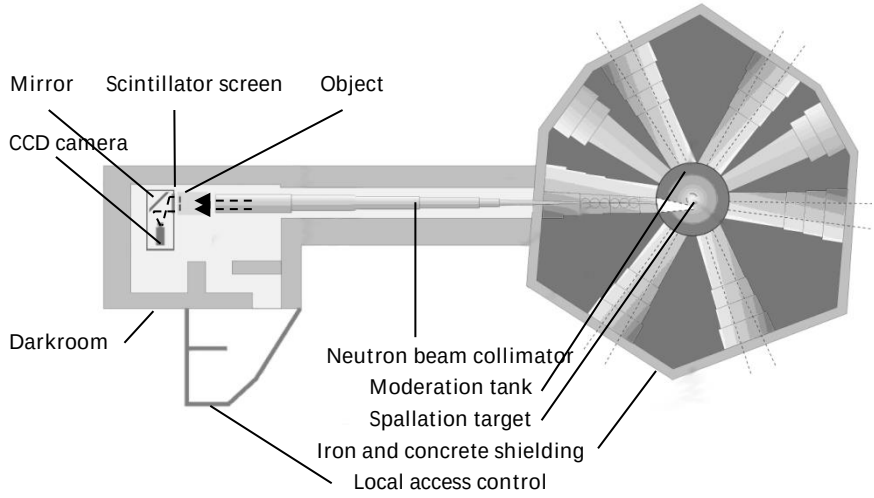

Figure 4.19. NEUTRA beam line with various parts.

The NEUTRA beam line consisted of a neutron source, in which neutrons were created by means of spallation of lead after being bombarded by protons. The neutrons were moderated and slowed down by heavy water. A collimator parallelized the neutron beam and led it towards the object space. The neutron beam travelled through the studied object, the 100 µm scintillator screen as neutron-to-light converter, hit a mirror in the dark room and was recorded by a CCD camera, an AF-S NIKKOR 50 mm lens of Nikon with a CCD-size of 2048 pixels. Digitization of the output of the detector resulted in an array of intensity values, corresponding to the grey values of the pixels of the obtained image. The pixel size obtained with an exposure time of 30 s was 0.1515 mm/pixel and with an exposure time of 3 s, 0.302 mm/pixel. The relation between the intensity values and composition of the sample is described by the law of exponential attenuation in equation 4.8, also known as the Beer-Lambert law.

$$I_{dry} = I_0 \cdot \exp\left(-\Sigma \cdot t_s\right) \tag{4.8}$$

where I_{dry} is the intensity of the attenuated beam which travelled through the sample in the dry state [$mA^{-1} \cdot cm^{-2} \cdot s^{-1}$], I_0 is the intensity of the incident ray [$mA^{-1} \cdot cm^{-2} \cdot s^{-1}$], Σ is the attenuation coefficient of the sample [cm^{-1}] and t_s is the thickness of the sample [cm].

For a wet sample, the law states:

$$I_{wet} = I_0 \cdot \exp\left(-\Sigma \cdot t_s - \Sigma_w \cdot t_w\right) \tag{4.9}$$

with Σ_w the attenuation coefficient of water and t_w the thickness of the water layer.

As each pixel had its own intensity value; cracks, materials edges, defects, etc. were distinguishable from neighbouring pixels due to differences in grey values. Also, water was visible (t_w) as water attenuates more in comparison to the plain cementitious material.

Before the start of the capillary absorption tests, the specimens were weighed with a Sartorius BP 3100 S balance. Four samples were placed into two water basins onto line supports and water was added through two pipes during the test (Figure 4.20). The addition of water was stopped when specimens were approximately 3.5 mm immersed. Post-processing revealed an immersion of 3.48 ± 0.38 mm. The two pipes, shown in Figure 4.20, were connected with a submersible pump which was activated from outside the neutron bunker during the test. The samples were positioned with the crack surface facing downwards. The scintillator screen is visible at the background.

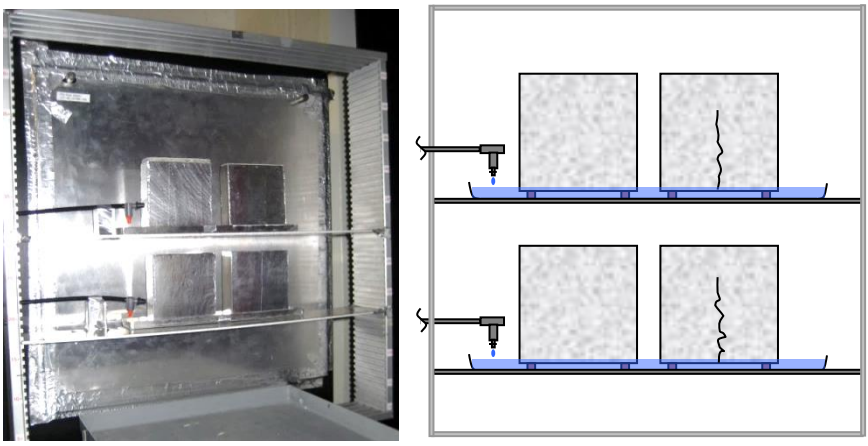

Figure 4.20. Schematization of the test setup used for capillary water absorption tests with neutron radiography.

First, dry images with both an exposure time of 3 s and 30 s were taken. The submersible pump was activated and with steps of 5 s (3 s exposure time + processing delay) 200 radiographs were taken. After ending this series, images were taken every 35 s with an exposure time of 30 s to receive a higher resolution. At one hour testing, images were taken with an interval of 5 min until the total measured time was four hours. In this way, the water penetration due to capillary suction in the cement-based material could be followed as a function of time. After the measurement, the specimens were weighed again to quantify the amount of absorbed moisture. This value was divided by the length and width of the bottom contact surface to receive the total water uptake per square meter.

The cylindrical specimens, used for the water permeability test, were positioned as shown in Figure 4.21a, and the upper reservoir was filled with water during the test. The water head applied was 20 mm, the total height of a specimen. With an exposure time of 3 s, every 5 s an image was taken to investigate the time needed for emptying the reservoir through the crack.

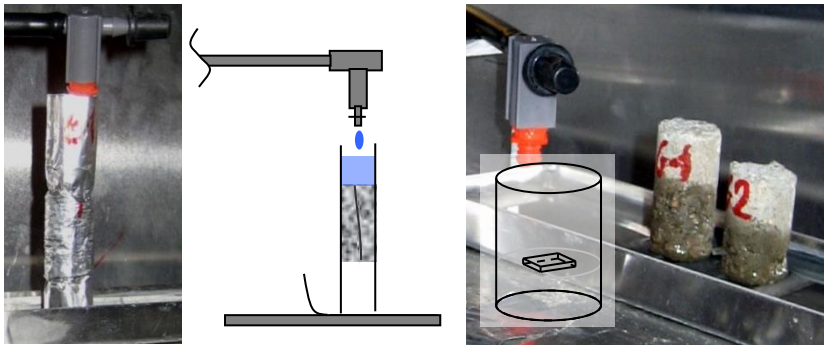

(a) (b)

Figure 4.21. Schematization of the test setup used for water permeability tests with neutron radiography **(a)** and small capillary tests with SAP platelets **(b)**.

Furthermore, small cylindrical samples (Ø 10 mm × 20 mm, n=3) were first filled with reference material for 10 mm and a 5 x 5 x 1 mm³ platelet of SAP C was positioned in the middle of the sample. The sample was then filled to the top with reference material. These samples would undergo capillary tests to visualize the absorption in a cementitious material by means of neutron radiography (Figure 4.21b). The difference in grey levels after processing radiographs with an exposure time of 30 s is a qualitative measurement for the water absorption of the single large SAP C particle.

4.8.2 Scatter deviations and image analysis

Each image obtained with neutron radiography needed to be filtered with the image correction tool "Quantitative Neutron Imaging" (QNI) (Hassanein, 2006) for qualitative information. The reason for this processing is that the exponential law of attenuation is influenced by several deviations. The QNI program takes into account the CCD dark current, the background scattering, the sample scattering, the spectral effects, the intensity and the flat field correction. The program uses Monte-Carlo simulations to describe the scattering distribution of the neutron beam. The main reason for occurring deviations is that the neutrons are not only absorbed or undisturbed passed by the samples atoms, but they can be scattered. Many relevant materials (e.g. water) have even a much higher probability for scattering than for absorption. The scattered neutrons can hit the detector, where they provide a too high measured value. This pretended high transmission is misunderstood as a too small thickness or density of the measured sample.

A further reason for the deviation from the exponential law of attenuation is the poly-energetic spectrum of the neutron beam. Since most of the cross sections

increase for lower energies in the thermal region, it is not possible to give a general value for them. Also the cross sections of the detector materials are dependent on the energy. These spectral effects affect the effective cross section, used for the evaluation of the quantitative mass thickness from the measured neutron flux.

The first deviation taken into account is the so-called *CCD dark current*. The surroundings of the test setup within the NEUTRA bunker leads to surrounding scattering. This scattering is unwanted since this surrounding scattering may not have travelled through the sample. By an appropriate test setup with a minimum of material and materials with less attenuation, a large quantity of the surrounding scattering can be avoided. The surrounding scattering is estimated by taking a dark current image with the shutters closed. This dark radiograph is divided from the object radiographs. The correction also takes into account the amount of electronic noise or noise from the camera system.

During measurements with the neutron beam, some rays may be scattered from the mirror or the camera setup. These rays may hit the object from behind and can be scattered again, resulting in an increase of the measured flux. This *background scattering* can be estimated by replacing the sample by a body which is opaque for neutrons (no neutrons will pass). The measured flux in the opaque region is the criterion for background scattering. The value of the flux is scaled to the intensity of the sample and subtracted from it.

Another reason for processing is that neutrons are scattered next to the measured absorption of neutrons by the object. Water for example is a material which also has a probability for scattering, next to absorption. The scattered neutrons hit the detector elsewhere, resulting in higher measured values. These altered values lead to a lower thickness of the measured substance, an underestimation of the moisture content. The opposite is also true. Parts where neutrons are scattered (water) seem to have a higher transmission, leading to miscomprehension of the moisture distribution. This deviation is taken into account by *sample scattering*. The binning for this step was taken to 15 pixels.

Spectral effects also need to be considered. These effects are caused by the NEUTRA spectrum and the experimental test setup. The proper setup needed to be loaded into the post-processing software.

Each obtained image needs to be scaled to one another, because the neutron flux varies in time. For this *intensity* correction, the same rectangular region between the samples (no material, no attenuation) is highlighted and scaled to 1 (no attenuation).

Also an influence to the exponential law of attenuation is the poly-energetic spectrum of the neutron beam. The cylindrical parallel neutron beam gives lower energy in the outer perimeter of the cylindrical shape. This results in a brighter conic region in the centre of a recorded picture as the detector is sensitive for these energy deviations. The poly-energetic deflection is filtered by dividing the raw data by a *flat field* image with only the neutron beam and without studied objects. An eventual inhomogeneity of the detector is also taken into account by this correction. Influencing parameters are the neutron energy spectrum, the sample material, the pixel size, the thickness of the sample, the detector type and the distance between the sample and the detector.

4.8.3 Water content profiles during capillary absorption

After post-processing of the radiographs, the measured wet states were divided by the dry states as a qualitative measurement of the moisture distribution and content. The water content profiles along vertical and horizontal rectangles as a function of time could be determined in this way. These rectangles are shown in Figure 4.22. The profiles were made at 0 s, 5 s, 30 s, 1 min, 5 min, 15 min, 30 min, 1 h, 2 h and 4 h in measuring time.

The mean penetration in a crack is determined as the uppermost point of the water distribution profile in a specimen. The mean penetration depth in the cementitious matrix was determined as the inflexion point of the water content profile. Some inflexion points are shown in Figure 4.22. These points were the approximate distance from the crack at which a uniformly distributed water content could be presumed. The penetration depth of water as a function of time x(t) could be predicted by equation 4.10 (Zhang et al., 2011b) where B is the coefficient of capillary water penetration [$m \cdot h^{-1/2}$]. If the penetration depth was plotted as a function of the square root of contact time [h], straight lines were obtained. From the slope of the fitted lines, the coefficient of capillary penetration B could be calculated.

$$x(t) = B \cdot \sqrt{t} \tag{4.10}$$

During the initial phase, contact with water in surface pores lead to initial water absorption. This was taken into account by the constant x_0 [m] (Wittmann et al., 2011):

$$x(t) = B \cdot \sqrt{t} + x_0 \tag{4.11}$$

Both the horizontal (cracked specimens) as the vertical (uncracked specimens) coefficient of capillary penetration B were calculated.

Figure 4.22 gives the horizontal and vertical moisture distribution of a cracked sample without SAP. The dark areas in a divided radiograph represent zones with penetrated water. By capillary action water is quickly absorbed from the surface high into the crack of the specimen. Once water has filled the crack, water penetrates by capillary action horizontally out of the crack into the mortar. The horizontal penetration process is approximately symmetric with respect to the position of the crack. The reinforcements of the composite material can be recognized as the lighter areas as they do hardly absorb any water. The position of the steel reinforcement bars is clearly reproduced by the pronounced drop of water content in the profile. The descending moisture content in the vertical moisture distribution profiles (pointed out by a circle) represents the skin effect (Zhang et al., 2011a). This effect states that the zone close to the surface is richer in hardened cement paste and therefore more porous.

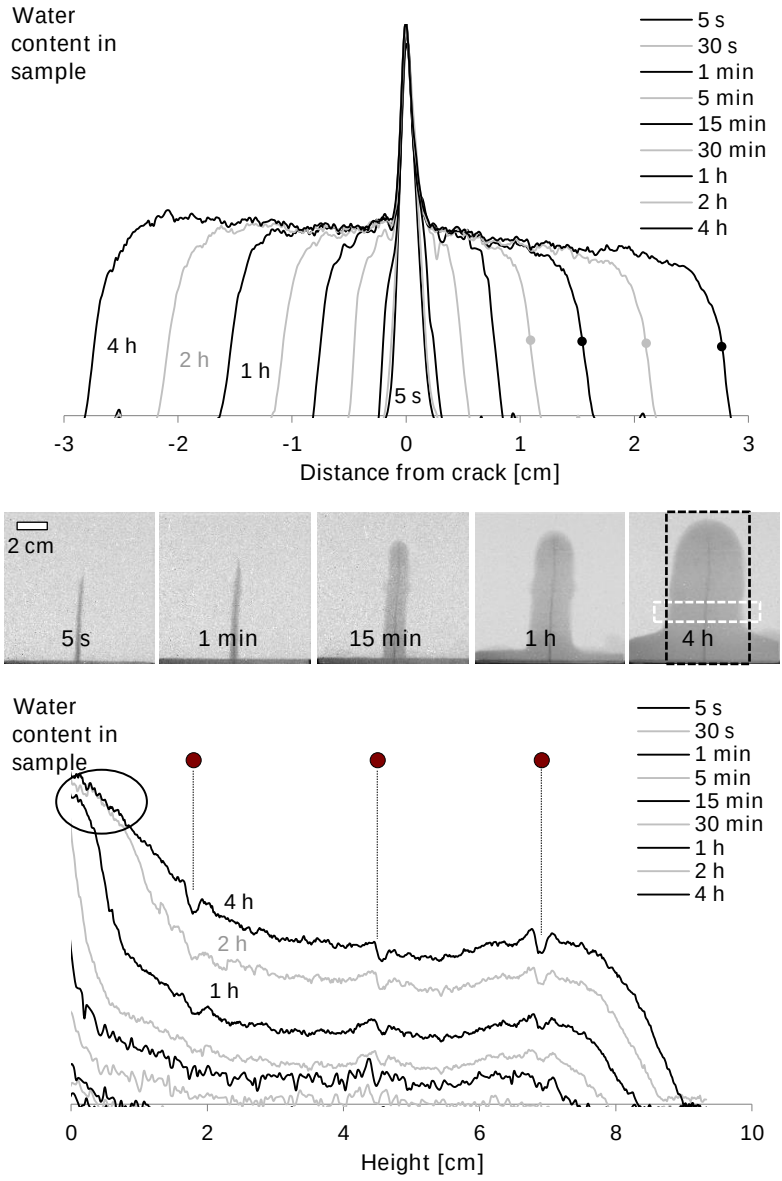

Figure 4.22. Horizontal (top) and vertical (bottom) moisture distribution through a cracked sample without SAP addition (0 - CRA) with visualization at 5 s, 1 min, 15 min, 1 h and 4 h after water contact. The white dashed rectangle is used for mean horizontal moisture distribution quantification and the black dashed rectangle for mean vertical moisture distribution. Points in the upper part are the used inflexion points, circles in the lower part are the locations of reinforcements.

The total moisture distribution after 4 hours contact with water of the different test series is shown in Figure 4.23. SAP particles reduce the moisture uptake in a crack, due to their swelling capability. Samples containing SAP show also in total a lower water uptake (Figure 4.24). Cracked samples without SAP take up most water, followed by the cracked specimens containing 1 m% SAP B and SAP C. Samples containing 2 m% SAP C even show a lower uptake in comparison to samples containing 1 m% SAP C. Further optimisation of the amount of SAP, taking into account the effect on both the mechanical properties of the virgin material and the self-sealing efficiency, is therefore necessary.

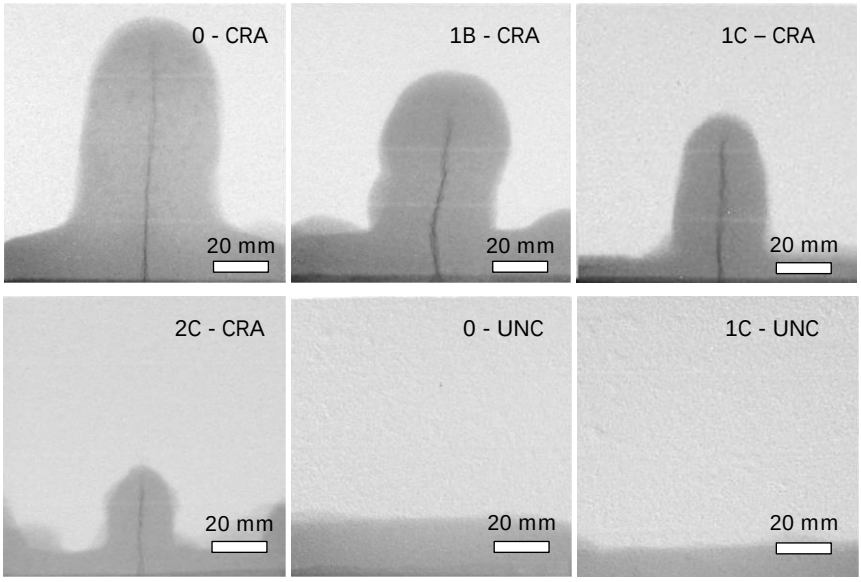

Figure 4.23. Water content with neutron radiography after 4 hours of contact with water for cracked samples without SAP addition, 1 m% SAP B, 1 m% SAP C, 2 m% SAP C samples and uncracked samples without SAP and uncracked 1 m% SAP C samples.

Assuming that the macro pores formed by SAP do not interconnect and the pores are perfect spheres, the amount of SAP needed for crack sealing can be estimated. The absorption of SAP B in mortar is 8.9 g mixing water/g SAP and the formed macro pores have sizes of 827 ± 173 µm (see paragraph 3.2.1.1). Assuming that the crack runs through the macro pores, as they act as stress initiators, the SAP particles will be available for swelling. The swelling of SAP B, after making contact with tap water upon crack formation is 148.9 g fluid/g SAP. This causes a volume increase up to a diameter of 2.25 mm. Part of this volume (sphere with a diameter of 0.827 mm = 0.30 mm³) fills the macro pores. The remaining volume of 5.68 mm³ (sphere with diameter of 2.25 mm minus the macro pore filling) is therefore provided for crack sealing. Assuming that the extra volume will expand equally in every direction of a 250 µm wide crack (Table 4.4), the cylindrical-shaped expanded SAP particle within the crack would have a diameter of 5.38 mm. Assuming that there is a simple hexagonal close packing lattice of the particles (homogenous distribution of SAP particles) in a straight crack and only SAPs in

open pores (where the crack ran through) are exposed, there must be a total of five particles (for a total crack length of 25 mm) available in a region of approximately $5.38 \cdot 6^{1/2} \cdot 3^{-1} \times 0.827 \times 25$ mm³ (hexagonal coefficient; macro pore size; crack length). This gives an amount of 2.19 kg/m³ to be mixed in (density of the SAPs of 700 kg/m³). As this is a theoretical calculation and the packing is imposed, the used amount of 1 m% SAP B (5.1 kg/m³) gives more certainty to obtain complete crack blocking. The same calculations for SAP C result in a theoretically necessary amount of 14.74 kg/m³ (density of 1050 kg/m³), which is higher than the 2 m% SAP C used (10.2 kg/m³). The good sealing effect of 2 m% SAP C (Figure 4.24) is possibly due to a freer movement of the swollen SAP C particles in the crack as the absorption is lower than for SAP B.

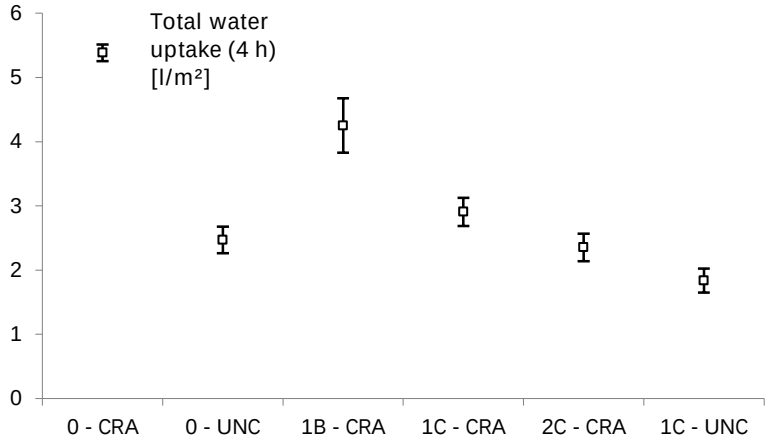

Figure 4.24. Total water uptake with standard deviation (n=3) after 4 hours of contact with water per square meter as the quantity of water uptake over the total bottom surface area [l/m²] by difference in mass by means of a balance, showing a decrease in specimens containing SAP.

The cracks in samples without SAPs filled rapidly (within 5 seconds) up to a height of 5 cm (Figure 4.25). Complete filling of the 7-8 cm high cracks occurred within 15 min. In samples containing SAPs, the water penetration height was less than the total crack height, even after 4 h of water absorption testing (notice that the total crack heights were not significantly different in samples with or without SAPs). As previously mentioned, swelling of SAP occurs rapidly and this limits water penetration into the crack. The water penetration heights of specimens containing 1 m% SAP B and 1 m% SAP C are not significantly different from each other. Due to a higher absorption capacity and ditto volume change, the specimens containing SAP B should give a better crack closure (cf. theoretical calculations above). The variability in the results of SAP B samples, however, is too high to make this conclusion. Two specimens gave high penetration, and one specimen gave a lower penetration as expected.

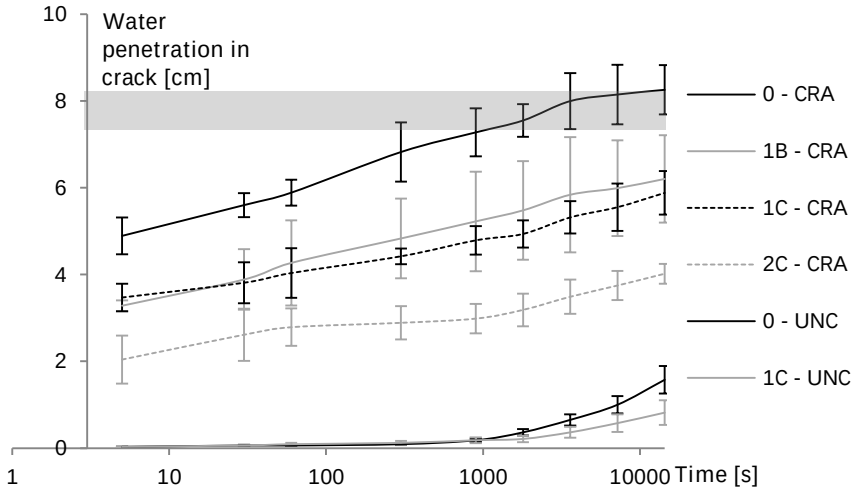

Figure 4.25. Superabsorbent polymers are able to stop water penetration in a crack due to their swelling ability. The grey zone between 7-8 cm gives the maximum crack height. As a comparison, the penetration in plain uncracked material is also given.

SAP particles swell due to the uptake of mixing water (Reinhardt & Assmann, 2009). This results in a lower apparent water-to-cement ratio, and thus a lower porosity and lower permeability of the matrix. The structure of a cementitious material is thus affected by the apparent water-to-cement ratio. The SAP particles later on release the absorbed water to the matrix for further hydration due to internal curing, but the samples without SAPs have no access to this free water. Therefore, samples without SAP cannot be considered as reference samples to compare the water penetration in the matrix of the cementitious material as the structure of the samples with and without SAPs and without additional water is not comparable. Due to a lower porosity in samples containing SAPs, there will logically be a reduced water penetration (Cnudde et al., 2008). This is clearly visible in the uncracked specimens (0 - UNC and 1C - UNC), as water penetrates less in samples containing SAPs. Reinhardt and Assmann (2009) stated that the large-sized fraction of SAP pores were not relevant for capillary suction, as capillary rise is inversely proportional to the pore radius. Therefore, the moisture will travel mostly in between SAP particles, and the lower water-to-cement ratio will induce less water penetration in the matrix material. Furthermore, the SAP pores will also attract the water, and the permeation is lowered in those pores due to swelling of SAPs. However, the overall effect of the reduced permeation is due to the lower water-to-cement ratio.

The coefficient of capillary penetration B, both horizontally and vertically determined, is visualized in Figure 4.26. It can be seen that the rate of horizontal capillary water suction out of the crack and the vertical capillary suction from the adjacent water reservoir are approximately equal. Gravity has no influence on the rate of penetration in the initial stage. The measurements for the material without SAPs (12.2 ± 0.2 mm·h$^{-1/2}$) are similar to the ones found by (Zhang et al., 2011b): 11.1 mm·h$^{-1/2}$ and (Wittmann et al., 2011): 14 mm·h$^{-1/2}$ for concrete with w/c=0.6 at

an age of 28 days). As samples containing SAPs have a denser matrix, their coefficient of penetration is lower than the one noted for samples without SAPs (4-7 $mm \cdot h^{-1/2}$ lower). This conclusion can be drawn for the horizontal penetration in cracked samples, as well as for the vertical penetration in uncracked samples. The coefficient of penetration B can also be compared to the work of (Reinhardt & Assmann, 2009). They found a value of 13.5 $mm \cdot h^{-1/2}$ (approximately the same value as 12.2 ± 0.2 $mm \cdot h^{-1/2}$) for samples without SAPs (w/c = 0.5). However, by mixing in SAPs without additional water, the matrix is changed. To investigate this, the coefficients of penetration of two additional mixtures were compared. Samples with corrected water-to-cement ratio of 0.36 had a coefficient B of 5.8 $mm \cdot h^{-1/2}$ and samples containing SAPs 9.1 $mm \cdot h^{-1/2}$ ($w/c_{tot} = 0.5$ and $w/c_{eff} = 0.36$). Samples with water-to-cement ratio correction show a lower coefficient of penetration in comparison to samples containing SAPs with the same capillary pores (determined by means of mercury intrusion porosimetry). The SAPs in the macro pores take up water, causing a higher coefficient B. They concluded that the penetration of water in the material is mainly due to the change of porosity, which is due to a lower water-to-cement ratio.

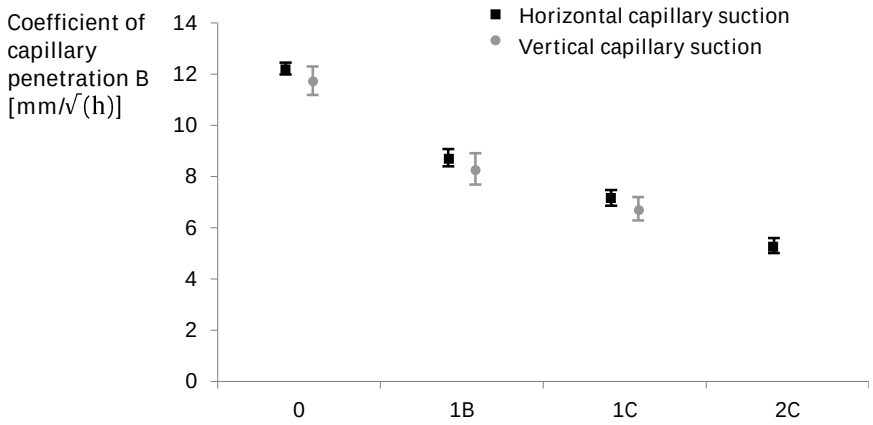

Figure 4.26. The equal horizontal and vertical coefficient of capillary penetration B [$mm \cdot h^{-1/2}$] for all studied samples with standard deviation (n=3).

The water absorption in the material could also be calculated from the data set and could be investigated (Figure 4.27). These results are closely linked to the capillary absorption tests. Again, the rate of water absorption is lower when using SAPs (and superplasticizer to compensate for the loss in workability). A critical note needs to be made as the neutron radiography readings are based on references before testing. Reference dark images should be made before every micrograph to correctly calculate these small amounts of absorbed water. A qualitative comparison, however, could be made.

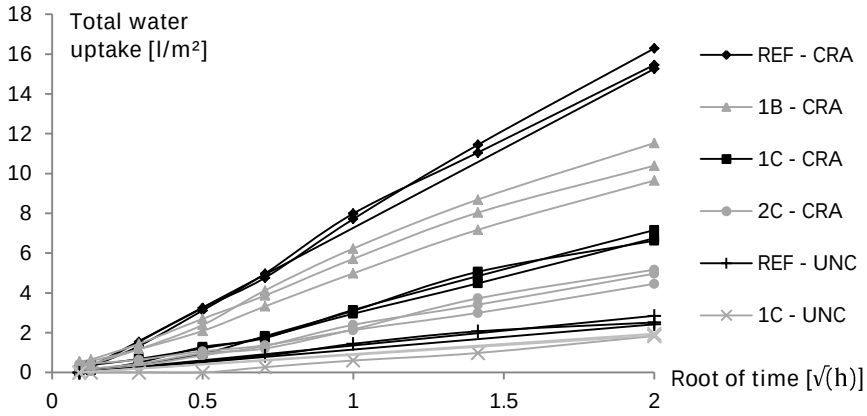

Figure 4.27. Calculated total water uptake by means of neutron radiography.

The main reason for the reduced capillary water uptake is the change in microstructure as superplasticizer and not additional water was added to the mixture. Due to swelling of the SAP particles, there is internal curing, but also a lower effective water-to-cement ratio (Reinhardt & Assmann, 2009). This causes a densification of the matrix, resulting in a low capillarity. The swelling of the SAP particles inside the macro pores is also one factor that hinders the water uptake, but not the main one. As the water movement is stopped in macro pores by the swelling action of the SAPs, the main water transport goes through the cementitious matrix. The latter water transport is hindered by the denser matrix, reducing the permeability.

4.8.4 Water permeability by means of neutron radiography

Figure 4.28 shows the water permeability in time of the cracked samples without SAP and the cracked samples containing 1 m% SAP B and 1 m% SAP C. Visualizing the water permeability with neutron radiography shows that SAP particles are able to seal a crack (Figure 4.28). In Figure 4.28a, the water head in specimens without SAPs decreases rapidly in time. In Figure 4.28b-c, however, the water head in specimens with SAPs decreases only slightly in time. It is clearly visible that water permeated through a specimen without SAP particles after only 40 s, but even after 480 s, there was still a substantial water head in case of specimens which contained SAP particles. Samples containing SAP are able to close the crack due to swelling of the SAP particles at the crack faces. The decrease in water permeability is a measure for the self-sealing capacity. The water level above the crack with SAP B does not lower a lot. SAP C samples, however, experience a small leakage of water. This is due to the lower absorption capacity and the longer swelling time of SAP C in comparison to SAP B. The blockage effect is still pronounced.

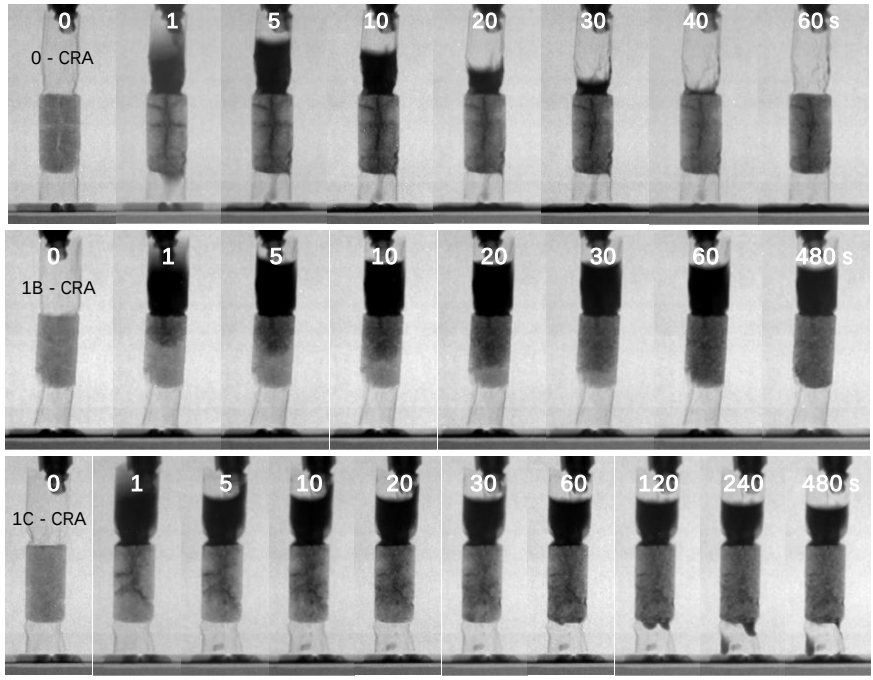

Figure 4.28. Water permeability of the samples without SAP and samples containing 1 m% SAP B and SAP C. In the upper part of the respective figures, the time [s] is given.

Figure 4.29 represents the water head in a clear way as a function of time. This figure confirms that SAP B particles are able to close the crack instantaneously, whereas SAP C particles need 5 s to close the crack. The small slope of the curves state the ability to retain the closure of the cracks. After the initial leakage, the slope becomes more or less similar for the SAP C samples as for the SAP B samples.

In Figure 4.28, it can be clearly observed that the SAP B particles swell, sealing the crack. Water thus needs to penetrate through the matrix and this only happens steadily. In SAP C specimens, the crack was first filled with water. As SAP C particles absorb less water than SAP B particles, the crack is not as efficiently sealed and part of the water penetrates the specimen in time. Also, the swelling of SAP C (205 s) takes five times longer than the swelling of SAP B (60 s). This explains the first drop in water level compared to the dashed line (the initial water head) and thus the small initial leakage through the specimen. This is the reason why the crack is first filled with water as the effect of the swelling of the SAP particles is postponed. After some time, these SAP C particles are also able to effectively seal a crack from intruding water. In time, there is a small decrease of the water head. This is possibly due to evaporation during the test and a small reduced self-sealing effect of the SAP particles due to the dissolution of Ca^{2+}-ions in the intruding fluid. As the osmotic pressure thus decreases, the swelling also decreases and part of the absorbed water by the SAP particles is released. This was also seen in the absorption capacity measurements as the charge-screening effect and strong complexation of di- and tri-valent ions present in the pore fluid (Chapter 2). The rate at which the leakage happened was 650 µm/s for cracked reference samples, 3 µm/s for cracked samples containing 1 m% SAP B and 6 µm/s for cracked specimens containing 1 m% SAP C. The crack widths were the same, and SAPs are thus able to seal a crack from intruding water flow. This is mainly due to the swelling of SAP particles along the crack faces.

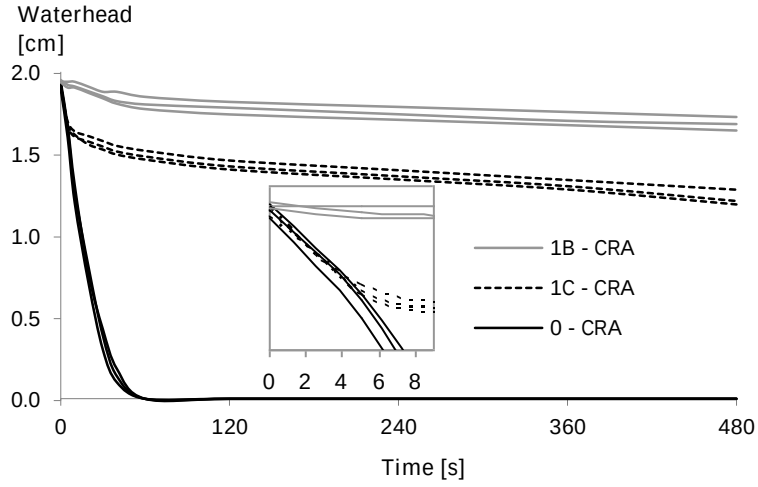

Figure 4.29. Water permeability of the samples containing no SAP and samples containing 1 m% SAP B and SAP C in function of time. An enlargement of the first ten seconds is also provided.

4.8.5 Visualisation of SAPs in the cementitious matrix

It is also possible to visualize three different larger SAP C particles in the matrix (Figure 4.30). Due to the exposure time, it was impossible to efficiently visualize the smaller particles. As the resolution is 0.302 mm/pixel, the particles (from 100 to 500 µm) would occur as only one pixel, or as blurred flocks. Larger particles, like a 5 x 5 x 1 mm³ platelet of SAP C, were easy distinguishable and recognizable. The figure shown is one obtained after post-processing by dividing the value from the wet state with the one from the dry state. Thus, only water is shown on this figure. This water is the water in the cementitious matrix by capillary absorption and the water absorption of SAP C platelets. The particles want to expand and appear dark due to the uptake of water. The absorption of SAP particles in concrete is smaller than in filtered cement slurry because there are restrictions in dimensions and the fluid inside concrete may differ from the artificial cement slurry. In the absorption measurements (see Chapter 2), the SAP particles can move freely in the fluids. This is not the case in hardened concrete and these restrictions are seen as the edges of the very dark parts of the image. The platelet is not able to swell more with water as it is dimensionally restricted.

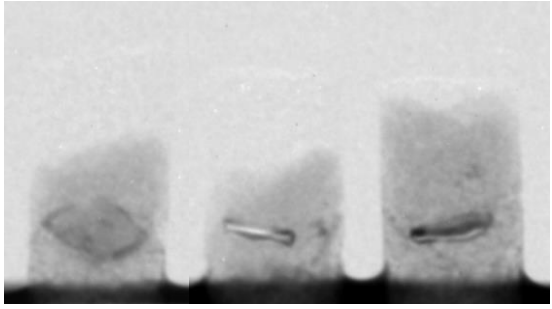

Figure 4.30. Water absorption visualizations of three different 5 x 5 x 1 mm³ platelets of SAP C by means of neutron radiography.

4.9 Conclusions

The main conclusions considering the permeability of samples containing superabsorbent polymers are given in this paragraph.

Gas permeability measurements of specimens with SAPs show an increase in gas permeability. The possible moisture uptake by the SAPs is not sufficient to fill up the remaining macro pores, so the macro pores are still penetrable even though the surrounding cementitious matrix is denser. SAP A mixtures with 0.5 m% and 1 m% SAP A by weight of cement show an increase of 80% and 140% of the gas permeability, respectively. An increase of 15% and 41% was found for 0.5 m% and 1 m% SAP B, respectively.

Splitting tests revealed a decrease in strength with increasing amount of superabsorbent polymers (SAPs), as was also found when performing bending and compressive strength tests in Chapter 3.

When cracking occurs and water enters a crack, the SAPs will swell and block the crack, resulting in a decrease in water permeability. In this way, the water flow is prevented. The drop in water permeability was both shown by low-pressure and high-pressure water permeability tests as well as neutron radiography. Specimens containing SAPs show a decrease in permeability (from $1{\cdot}10^{-7}$ to $1{\cdot}10^{-10}$ m/s compared to $1{\cdot}10^{-5}$ m/s for cracked reference samples without SAPs. The permeability through cracked specimens was independent from the mixture composition.

Neutron radiography is a powerful non-destructive test technique to determine the water distribution and the penetration depth of water in concrete cracks as a function of time and with a high spatial resolution. The water head in the small permeability tests remained approximately constant, proving the self-sealing effect of SAPs. SAP particles are thus able to retain the fluid within their structure and the crack is sealed autonomously. In this way, harmful substances dissolved in fluids will penetrate the structure to a lower extent.

SAP C was not able to efficiently seal a crack, especially at high water pressure. SAP B is able to withstand both low-pressure and high-pressure water permeability tests and an amount of 1 m% of SAP B proved to be most efficient, taking into account the effect on both the mechanical properties (see Chapter 3) and the self-sealing efficiency. The low-pressure water permeability of cracked samples with 1 m% of SAP B was found to be nearly the same as for un-cracked specimens.

Small SAPs (smaller than 150 µm in diameter) such as SAP A, SAP E, SAP G, SAP H and Powder, are ineffective in terms of sealing. They are unable to bridge a 200 µm wide crack and to completely seal it. The fibre-type SAP F is also not able to completely seal a crack due to its restricting form. The Medium and XL forms are too large and only distinct locations can be sealed. SAP B, SAP D and Micro are able to seal a crack.

Calcium carbonate was deposited in the cracks when performing the low-pressure water permeability tests. This will lead to a self-healing effect, which will be discussed in detail in Chapter 5.

With decreasing water-to-cement ratio, the capillary absorption decreases. When using SAPs without additional water, the absorption is also lower, but higher than the absorption by a reference mixture with the same effective water-to-

cement ratio. This is mainly due to the water uptake by the SAPs during weighing the specimens as this water is held. This causes a higher mass and thus higher value for absorption. The same conclusions can be made considering the use of additional water. The initial and secondary rate of water absorption, bulk density, accessible porosity and water absorption accessibility also show the same trends. Furthermore, with SAP addition without additional water, the porosity is comparable to the respective references with the same effective water-to-cement ratio. With additional water, this porosity shifts towards the value of the reference mixture with the same effective water-to-cement ratio, with a comparable microstructure. These results were similar to the ones found in Chapter 3.

When studying neutron micrographs, mortar samples containing SAPs show a lower total moisture uptake in a crack in comparison to samples without SAPs. Cracked samples without SAPs take up most water, followed by the cracked specimens containing 1 m% SAP B and SAP C without using additional water. The water penetration in the matrix of the cementitious materials is mainly affected by a decrease in porosity caused by a lower apparent water-to-cement ratio if no additional water is added to compensate for initial mixing water absorption by the SAPs.

In summary, SAP particles are able to prevent water movement through a crack, thus reducing the uptake of harmful substances, most likely leading to an enhanced long-term durability and normal service life.

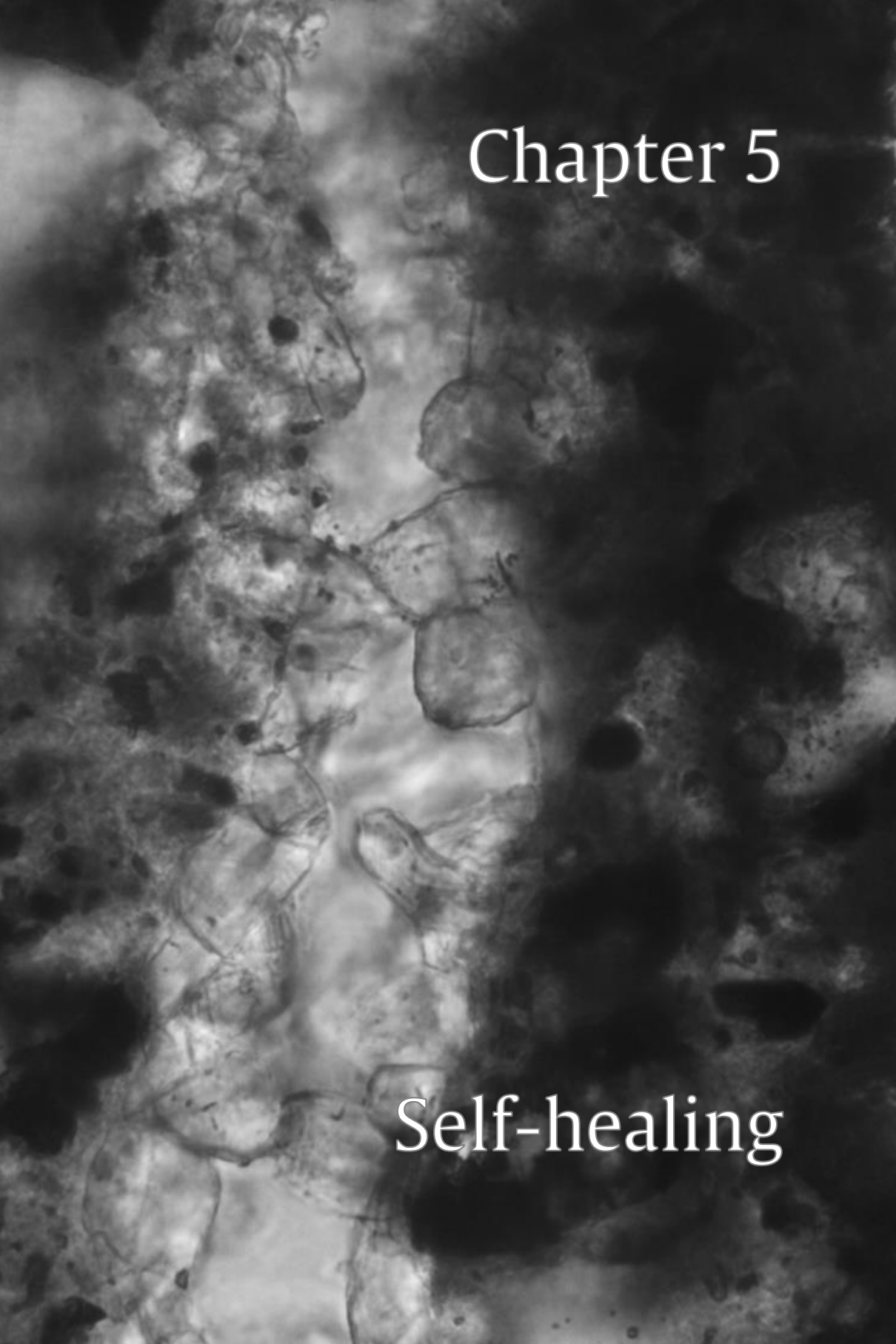

Chapter 5

Self-healing

| Thin section of formed precipitation products in a crack after healing

Chapter redrafted after (Snoeck & De Belie, 2012, 2015c; Snoeck et al., 2015a; Snoeck et al., 2015d; Snoeck et al., 2014b).

"*Calida umoris ieiunitas aquae repente satiata confervescit et vehementer efficit ea coire celeriterque unam soliditatis percipere virtutem.*

The great want of moisture quickly supplied by water binds and strongly cements them, and also imparts a rapid solidity."

– *Vitruvius*

5.1 Introduction

Cracking in concrete occurs commonly due to the relatively low tensile strength. However, concrete has a passive healing capacity of its own, also called autogenous healing (as described in Chapter 1).

Self-healing is a hot topic nowadays (van Breugel, 2007). Autogenous healing was already studied in the mid ninetieth century (by the French Academy of Science in 1836 as stated by (Hearn, 1998)). The autogenous healing property was again studied by (Hearn, 1998) in water-retaining structures, i.e. culverts and pipes. He made a distinction between self-sealing due to blockage and self-healing due to further hydration. This is important to know as a possible temporal self-sealing effect may not lead to a regain in mechanical properties. After this first specific publication, autogenous healing was studied in detail by many other researchers (Edvardsen, 1999; Granger et al., 2007; Homma et al., 2009; Li & Li, 2011; Li, 2008; Neville, 2002; ter Heide, 2005; Yang, 2008; Yang et al., 2009). It was concluded that the main healing mechanism at the surface was calcium carbonate ($CaCO_3$) (Edvardsen, 1999) and calcium hydroxide ($Ca(OH)_2$) precipitation. Unhydrated cement particles always remain present in a hardened concrete matrix. As water flows into the cracks, continued hydration of these unhydrated cement grains produces new strong calcium-silicate-hydrates (C-S-H) crystals (Granger et al., 2007), which can result in sealing of small cracks. The main mechanism of autogenous crack healing is the precipitation of calcium carbonate ($CaCO_3$) which also blocks the crack. These forms of crack healing are studied in great detail by (Edvardsen, 1999) who observed a decrease in water permeability in cracked concrete specimens due to autogenous crack healing. Lepech (2006) also proved autogenous crack sealing by the precipitation of $CaCO_3$ by means of energy-dispersive X-ray spectroscopy. Generally, it can be stated that autogenous healing is ascribed to the following four healing mechanisms and their combination (Homma et al., 2009; ter Heide, 2005):

i) further reaction of the hitherto unhydrated cement;
ii) closing of the cracks due to blocking by cement particles, hydration particles, loose particles and impurities (inferior mechanism (Neville, 2002));
iii) expansion of the calcium-silicate-hydrate (C-S-H) in concrete at the crack faces; and
iv) precipitation of $CaCO_3$ by the mechanisms given in equations (5.1-5.2) (Edvardsen, 1999).

$$8 < pH_{water} \qquad Ca^{2+} + CO_2 + 2\,OH^- \rightarrow CaCO_3 + H_2O \qquad (5.1)$$

$$7 < pH_{water} < 8 \qquad Ca^{2+} + HCO_3^- \rightarrow CaCO_3 + H^+ \qquad (5.2)$$

Ca^{2+}-ions in the matrix react with carbon dioxide (CO_2) or hydrogen carbonate (HCO_3^-) dissolved in water to form $CaCO_3$. The crystallization rate within the crack is dependent on the crack width and the water pressure, but independent of the concrete composition and the type of water (Edvardsen, 1999).

Recent reviews on self-healing cementitious materials in general (Joseph et al., 2011; Talaiekhozan et al., 2014; Van Tittelboom & De Belie, 2013) and self-healing in strain-hardening cementitious materials (Mihashi & Nishiwaki, 2012; Wu et al., 2012) have been published.

There are three needed conditions for autogenous crack healing to occur. These are the presence of specific chemical ions (Ca^{2+}, CO_2, etc.); the exposure to humid environmental conditions (wet/dry cycles, submersion in water, etc.) and restricted crack widths. The restriction in crack width may be 5-10 µm (Jacobsen et al., 1995), 50 µm (Yang, 2008), 100 µm (Reinhardt & Jooss, 2003), 200 µm (Edvardsen, 1999), 205 µm (Aldea et al., 2000) or 300 µm (Clear, 1985) depending on the mixture composition and the test conditions. For the proposed material in this research, the 50 µm criterion is most important. Cracks in strain-hardening cementitious materials smaller than 50 µm show complete healing and cracks smaller than 150 µm only show partial healing according to (Yang, 2008). From the latter it can be concluded that autogenous healing is only efficient for healing of narrow cracks. Cracks in high-strength cementitious materials need to be small in order to be completely healable. If not, the products available in the mortar mix are consumed before the crack is effectively closed. However, a dedicated material design can promote the autogenous healing capacity. Two possible mechanisms and their combined effect are investigated in this study.

The first mechanism is the introduction of microfibres to obtain fibre-reinforced cementitious materials with a high tensile ductility, as studied by (Li, 2008; Yang, 2008) (See Chapter 1). These composites exhibit tensile strain-hardening behaviour achieved by matrix multiple cracking. The studied material in this research is an ultra-ductile fibre-reinforced cementitious material optimized through the use of micromechanics in order to attain high tensile ductility and tight micro-cracks at moderate fibre contents. (2 v% or less) (Li, 2008; Li et al., 1988; Li et al., 1993; Li et al., 1997; Li et al., 2002; Li & Wu, 1992; Wang & Li, 2006; Yang et al., 2009; Yao et al., 2011). The extreme strain capacity of this material (beyond 3%) is several hundred times that of traditional concrete and its toughness is similar to that of aluminium alloys (Maalej et al., 2012). Due to the use of microfibres, the crack widths are restrained within the healable range (30-50 µm for complete healing after wet/dry cycles, smaller than the 150 µm criterion for no healing (Yang, 2008; Yang et al., 2009)). The main purpose of the fibres is to provide a controlled way of cracking and to increase the fracture toughness of the brittle cementitious matrix through bridging action during both micro- and macro-cracking of the matrix.

Self-healing prevails in a variety of environmental conditions even when the composite is deliberately damaged by tensioning to several percentages strain. Autogenous healing has been demonstrated in these strain-hardening cementitious materials and the healing products were mainly $CaCO_3$, $Ca(OH)_2$ (Qian et al., 2009; Qian et al., 2010) and calcium-silicate-hydrates (C-S-H) (Kan & Shi, 2012). Autogenous healing of these cementitious materials can provide a solution of the cracking problems found in building constructions and it is a potential solution for obtaining a sustainable concrete infrastructure. But the healing is limited (as water needs to be present) and needs to be stimulated. At 95% relative humidity (RH),

there was no healing visible and it was concluded that the presence of water as curing medium was essential (Lauer & Slate, 1956). In a humid environment, so without the presence of liquid water, the material indeed does not show any form of healing (Yang et al., 2009).

Small crack widths are a great advantage when using fibres in cementitious materials, as all the cracks may heal and mechanical properties recover. Manual repair is only applied after a certain time, but self-healing happens *in situ*, starting just after crack formation. So, no manual repair after crack formation needs to be undertaken. This improves the reliability and the lifetime of a structure. The potential of the autogenous healing lies in the fact that there is less intrusion of durability-decreasing substances and thus a probability of an increased service-life of the concrete structure.

The second healing mechanism is the use of superabsorbent polymers (SAPs; See Chapter 2), improving/promoting the obtained autogenous healing capacity. The use of SAPs to promote autogenous healing is dual. SAP particles swell due to mixing-water uptake during the mixing process and shrink during hardening of the cementitious material, leaving behind macro pores (Yao et al., 2011). These macro pores act as initial flaws and promote multiple cracking. Secondly, SAP-particles are very useful for autogenous healing as they absorb water during wet periods and slowly release it during dry periods. When liquids enter a crack, SAP particles along the crack faces will swell and block the crack. Also, as the SAPs swell, they will initially seal a crack from intruding fluids, thus increasing the durability (Lee et al., 2010a; Lee et al., 2010b). Kim and Schlangen (2010) showed that SAPs can contribute to the internal healing of a crack after performing wet/dry cycles. By absorbing fluids from the surroundings, water is available for healing. Formation of new cracks was noticed upon reloading the samples containing SAPs and regain of mechanical properties was shown. Specimens containing SAPs cured in air showed almost no healing.

The aim of the current research is to investigate the ability of SAPs to promote self-sealing and self-healing in microfibre-reinforced concrete under realistic conditions of wet-dry cycles, and in air with medium or high relative humidity. A regain in mechanical properties is aimed for. In this way, a smart cementitious material which is reliable and less independent from external conditions will be acquired.

5.2 Mortar composition, mixing procedure and storage

The studied mortar mixtures were based on the mixture of V.C. Li that is composed of ordinary Portland cement (CEM I 52.5 N; Holcim) (571 kg/m³), fly ash (Class F; OBBC) (685 kg/m³), fine quartz sand M34 (456 kg/m³; Sibelco; D_{50} = 170 µm), water (332 kg/m³), a polycarboxylate superplasticizer (Glenium 51, conc. 35%; BASF), and 2 v% (volume percent) of polyvinyl alcohol fibres (15 dtex; 8 mm cutting length; 12 cN/dtex tenacity; Kuraray) (after (Li, 2008; Li et al., 1997; Yang, 2008)). Amounts of 0.5 v%, 1 v% and 1.5 v% of microfibres were studied as well but only from 2 v% onwards, the multiple cracking was optimal. Higher amounts were not practical. In other mixtures, a varying amount of SAP expressed as mass-percentage (m%) of cement weight was added on top of the reference mixture without SAPs.

All amounts were varied to obtain the most ideal mixture. The studied mixtures contained CEM I 52.5 N, Class F fly ash (FA/C = 0/0.5/1) or blast furnace slag (BFS/C = 0/0.5/1), fine silica sand M34 (S/B = 0.35), water (W/B = 0.30/0.35/0.40), polycarboxylate superplasticizer Glenium 51 (Spl/B = 0.0097), different amounts of microfibres (0/0.5/1/2 v%), different types of fibres, a varying amount of SAPs expressed as mass percentage (m%) of cement weight (0/0.5/1 m%), different types of SAPs and additional water (or superplasticizer) to compensate for the loss in workability (See Chapter 3). A maximal amount of 0.5-1.6 litres per 100 kg of cementitious material of superplasticizer may be used. The amount of additional water or superplasticizer was determined in function of the flow of the mixture. Every mix used had a flow of 175 mm. The densities are 3140 kg/m³ for cement, 2250 kg/m³ for fly ash, 2900 kg/m³ for blast-furnace slag, 2650 kg/m³ for silica sand, 1000 kg/m³ for water, 1100 kg/m³ for superplasticizer, 1300 kg/m³ for PVA fibres and 700 kg/m³ for SAPs.

The most ideal mixture in terms of autogenous healing had a FA/C ratio of 1 and a W/B of 0.30 (as results will show later-on). The best properties were obtained by using 2 v% of synthetic oil-coated PVA fibres from Kuraray. The compositions (with superabsorbent polymers where applicable) are shown in Table 5.1 and visually and schematically represented in Figure 5.1. 'REF' states a mixture without SAPs, '0.5A/0.5B/1B' a mixture with 0.5 m% SAP A and SAP B and 1 m% of SAP B, respectively. The '1A' mixture was not studied as it was an inferior mixture (following the results found in Chapter 3).

Table 5.1. Mortar composition of the most ideal mixture [kg/m³]; C stands for cement, and FA, S, W, Spl and PVA for fly ash, sand, water, superplasticizer and PVA fibres respectively. The water is divided to show the amount of additional water W_{add}.

[kg/m³]	C	FA	S	W +W_{add}	Spl	PVA	SAP A	SAP B
REF	608	608	426	365	11.8	26	-	-
0.5A	554	554	388	332 +85	10.7	26	2.77	-
0.5B	590	590	413	354 +26	11.4	26	-	2.95
1B	572	572	400	343 +51	11.1	26	-	5.72

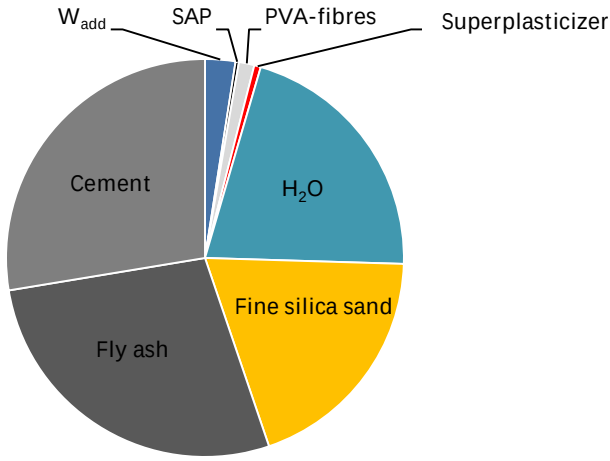

Figure 5.1. Mortar composition of the strain-hardening mixture '1B', representing the visual mass amounts.

The first step in the mixing procedure was dry mixing of cement, fly ash and possibly SAPs (depending on the mixture composition) with a standard mortar mixer for 30 s until they were equally distributed. Water and superplasticizer were then added to the dry mixture and it was mixed during 30 s at 140 rpm. The fine silica sand was next added and the composition was again mixed during 30 s at 140 rpm. To ensure a homogeneous dispersion of all components, the speed was increased for the following 30 s to 285 rpm. The edges of the bowl were scraped during 30 seconds and there was a resting period of 60 s. Subsequently, at a speed of 140 rpm, microfibres were slowly added during 30 s. The final step was mixing for 60 s at 285 rpm. Moulds (160 × 40 × 10 mm^3 samples) were filled and the samples were compacted by jolting 60 times. The samples were demoulded after 24 hours and were stored at a relative humidity of 95 ± 5% and a temperature of 20 ± 2°C until the age of 28 days. Series used within this study, consisted of minimum three samples.

The respective sample codes in every paragraph will state the studied parameter (type of fibre, type of composition, different amounts) and will be explained in detail.

5.3 Four-point-bending test and healing conditions

Fibre-reinforced composites exhibit multiple-cracking behaviour, and this was examined using a four-point-bending test. Series used for four-point bending tests, consisted of minimally three 160 × 40 × 10 mm³ samples with 2 v% of polyvinyl alcohol (PVA) fibres. By means of a four-point-bending test (Figure 5.2), multiple cracks were created in the mortar prisms at an age of 7, 14, 28 days, 3 months and 1 year. The cracking occurred under standard laboratory conditions at a relative humidity of 60%. The servo-hydraulic testing system (Walter+Bai DB 250/15) ensured a displacement-controlled test (0.0015 mm/s to imitate a quasi-static load). The displacement was increased until the maximum multiple cracking capacity was reached or till 1% strain at the bottom of the specimen. The vertical displacement u was altered with this loading speed and the force-displacement curves were recorded. The unloading speed was 5 N/s. Force-displacement curves obtained through the software Proteus® 10.1 were transformed into stress-strain curves by relating the vertical displacement to the strain in the curved lower surface of the prisms during bending by means of trigonometry.

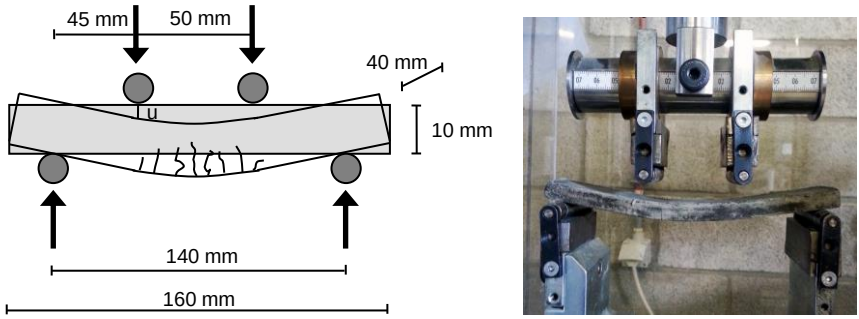

Figure 5.2. Schematization of the test setup and testing machine used for the four-point-bending test.

After cracking, the samples were cured for 28 days under three conditions:

i) wet/dry cycles during which samples were stored alternately for one hour in water and 23 hours in air at a RH of 60% and 20 ± 2°C;

ii) at a relative humidity of more than 90% and 20 ± 2°C, and;

iii) at a relative humidity of 60% and 20 ± 2°C.

After a period of 28 days, the specimens were tested again in four-point-bending and the mechanical properties obtained during the first and the second loading cycle were compared (Figure 5.3). In between both loading cycles, microscopic observations were performed by means of a stereo microscope (Leica S8 APO mounted with a DFC 295 camera) to study the extent of autogenous healing and this at regular time intervals (after 3, 7, 14 and 28 cycles). Control specimens were not cracked at an age of 28 days but underwent the same curing conditions as other specimens. After 56 days, the control specimens were cracked and immediately reloaded until final failure.

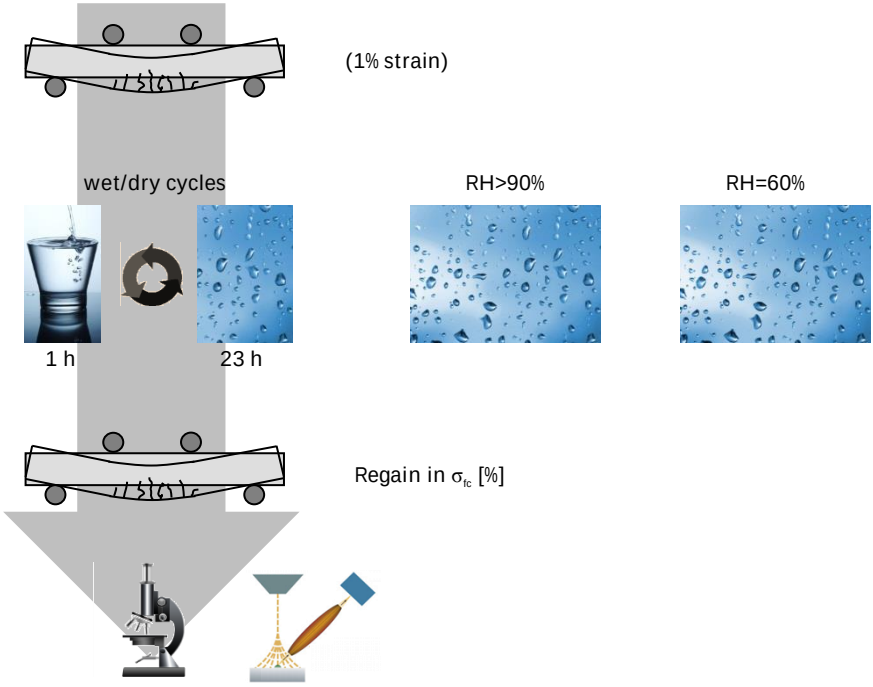

Figure 5.3. Schematic overview of the testing program for autogenous healing of specimens broken by means of four-point-bending.

The sample codes are given in Table 5.2. The first part of the code states the amount of SAPs used. This can be '0' for a mixture without SAPs, and a number followed by a letter which gives the amount of SAPs in m% and the type of SAP. The second part of the codes states the healing condition. This can be '60' for healing at 60% RH, '90' at more than 90% RH and 'wd' for wet/dry cycles.

Table 5.2. Explanation of the different samples codes.

Sample code	*m% SAP** [%]	*SAP type*	*Curing*
0 - 60	0	-	RH = 60%
0 - 90	0	-	RH > 90%
0 - wd	0	-	wet/dry
0.5A - 60	0.5	A	RH = 60%
0.5A - 90	0.5	A	RH > 90%
0.5A - wd	0.5	A	wet/dry
0.5B - 60	0.5	B	RH = 60%
0.5B - 90	0.5	B	RH > 90%
0.5B - wd	0.5	B	wet/dry
1B - 60	1	B	RH = 60%
1B - 90	1	B	RH > 90%
1B - wd	1	B	wet/dry

An automatic wet/dry cycle (Figure 5.4) was used to mimic realistic conditions such as raining. These were 12 (or 1) h in water and 12 (or 23) h in standard laboratory conditions. A timer ensured the activation of a pump at specific times and water was steadily pumped from one basin to the next one. The cracked faces were put upwards as this would drain the water out of the crack. If the specimens would be put on their sides, an irregular healing pattern would be achieved. If they would be put with the crack face downwards, capillary action would keep the water in the crack and the healing products would preferentially form at the crack surface. This would give a misleading picture of the occurring amount of healing. As the crack surface is microscopically studied, the actual healing should be studied with the crack surface facing upwards.

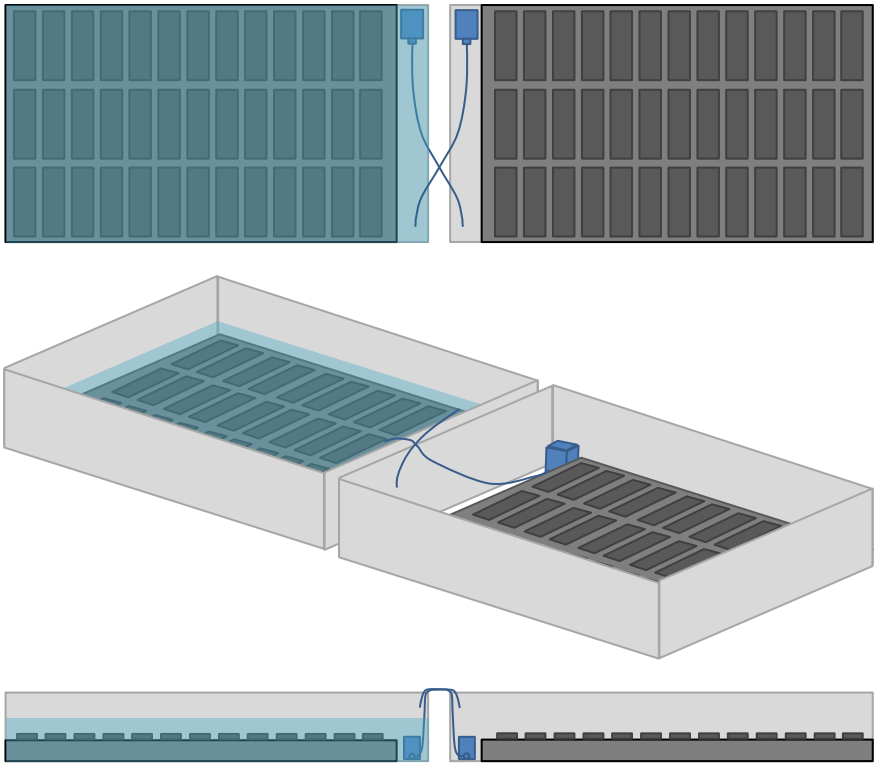

Figure 5.4. Wet/dry cycles, where cycles of 12 (or 1) h in water and 12 (or 23) h in standard laboratory conditions were performed.

The mechanical parameters investigated in the stress-strain curves were the modulus of elasticity E (slope of the stress-strain curve), the stress at the point of formation of the first crack (the strength at which the first drop in the stress-strain curve occurred), further called first-cracking-strength (σ_{fc}), the peak stress (σ_{cu}), the total working force W_f (surface under the stress/displacement curve) as a measurement of multiple cracking (the strain increase over the hardening branch) (MC). The preloading was manually stopped at the release stress ($\sigma_{release}$) which was

smaller than σ_{fc} to ensure a maximum use of *MC*, or at 1% of strain. All parameters are shown in Figure 5.5. The first-cracking-strength is the first kink in the stress-strain curve and it is characterised by a drop due to an unstable extension in the matrix fibre tunnel. Multiple cracking was characterised as the strain at σ_{cu} (ε_{cu}) minus the strain at σ_{fc} (ε_{fc}).

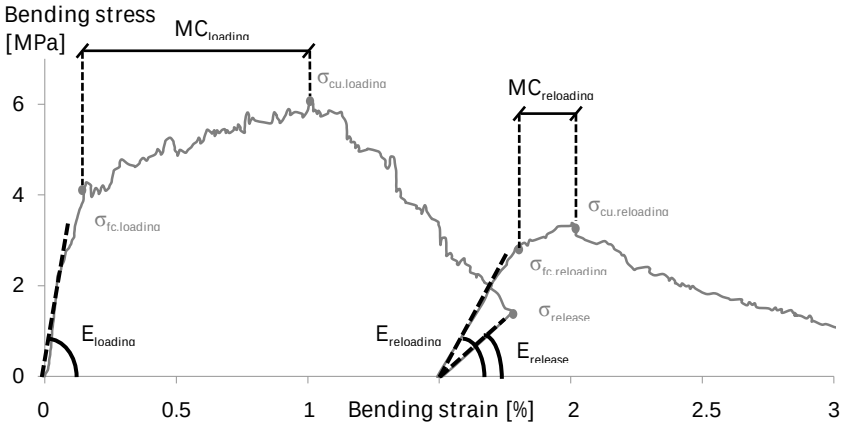

Figure 5.5. Investigated parameters shown on a typical stress-strain curve.

The self-healing capacity was determined as the regain of *E*, σ_{fc}, σ_{cu} and *MC* after reloading the specimens until complete failure, using the equations 5.3-5.6. The amount of visual closure of a crack was established by means of the stereomicroscope and was determined with equation 5.7, where *w* is the crack width.

Regain of E $$\frac{E_{reloading} - E_{release}}{E_{loading} - E_{release}} \quad (5.3)$$

Regain of σ_{fc} $$\frac{\sigma_{fc,reloading} - \sigma_{release}}{\sigma_{fc,loading} - \sigma_{release}} \quad (5.4)$$

Regain of σ_{cu} $$\frac{\sigma_{cu,reloading} - \sigma_{release}}{\sigma_{cu,loading} - \sigma_{release}} \quad (5.5)$$

Regain of *MC* $$\frac{MC_{reloading}}{MC_{loading}} \quad (5.6)$$

Visual closure $$\frac{w_{loading} - w_{healed}}{w_{loading}} \quad (5.7)$$

5.4 Restriction of crack width

When 2 v% PVA-fibres were mixed in, the amount of multiple cracking and the ductility of the specimen were noteworthy (Figure 5.6). When a crack forms, bridging action of the fibres takes over and the stress can be augmented forcing the sample to crack elsewhere. This process continues until the weakest link becomes the fibre bridging action instead of the strength of the cementitious matrix. Then, a previously opened crack widens and the composite has reached its final possible strain. This phenomenon is named multiple cracking. A maximum of 15 mm vertical displacement was manageable and the corresponding crack width varied between 6-104 µm. Before strain softening, the cracks varied in the range of 6-36 µm. After multiple cracking, one previously formed crack opened, thus resulting in the 6-104 µm crack width range, as one large final crack (in case of total loading) was formed.

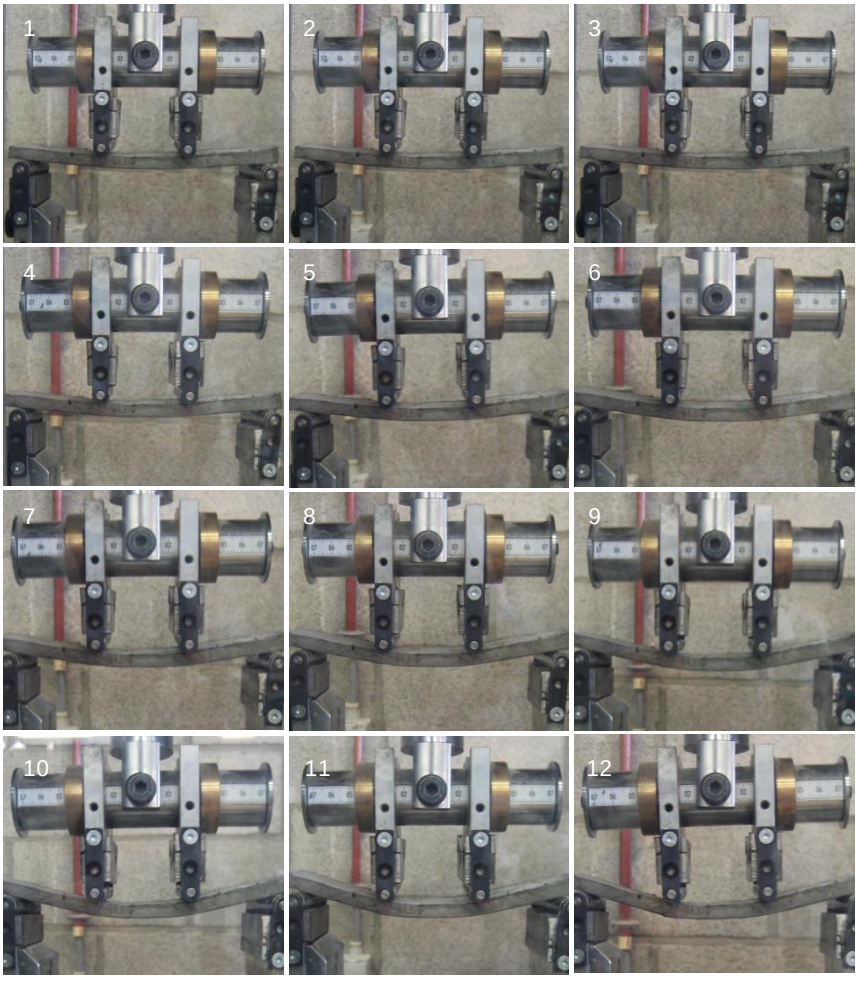

Figure 5.6. Ductility in steps of 1 mm vertical displacement, up to 12 mm total vertical displacement. In the top corner, the vertical displacement [mm] is given.

5.5 Presence of building blocks and fibres

5.5.1 Microscopic observations

The main healing mechanisms found when microscopically studying the specimens stored in wet/dry cycles are shown in Figure 5.7. These are further hydration (a-b), calcium carbonate crystallization (c-d) and the combination of both (e-f). As the mixture is showing a strain-hardening behaviour, this healing led to a total closure of all cracks (e).

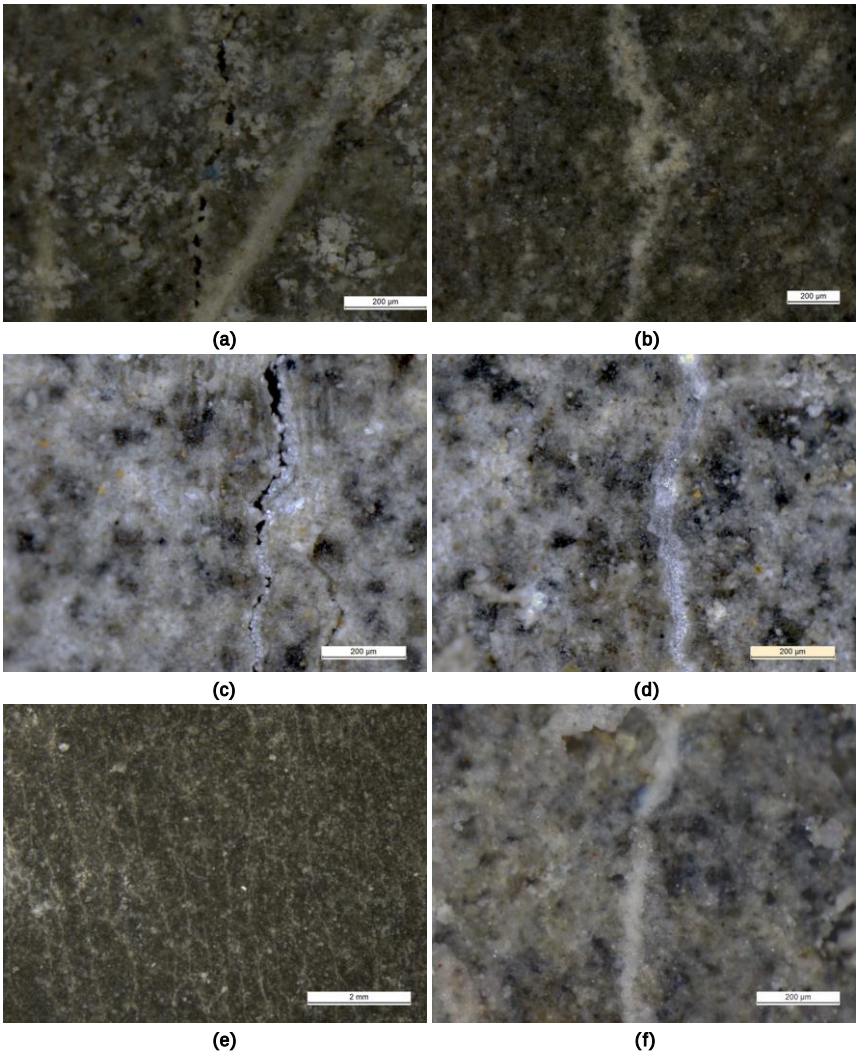

Figure 5.7. Autogenous healing mechanisms showing partial **(a)** and further hydration **(b)**, partial **(c)** and full calcium carbonate crystallization **(d)** and the combination of both in a number of cracks **(e)** and close-up **(f)**.The scale bars amount to 200 µm (a-d; f) and 2 mm (e).

In nature, animals and trees can usually heal small bodily damage. This is also the case in fibre-reinforced cementitious composites as they have the ability to keep the crack thin by the bridging action of the fibres. Small cracks were able to partially close with a whitish substance. This is the $CaCO_3$ crystallization and the further hydration. However, sometimes the healing was not visible over the whole crack. This is due to a severe wet/dry cycle with a small wet step of 1 h.

5.5.2 Influence of synthetic fibres

The precipitation of $CaCO_3$ is facilitated by the microfibres as they act as a nucleation site where the $CaCO_3$-crystals can attach, which was also noticed in microscopic investigations by (Homma et al., 2009). This is also visible in large cracks, but only when a crack is small enough the precipitation can cover the whole opening of the crack. Closer to the crack tip, however, there is a lower distance between the crack faces. This gives the opportunity of crack bridging by healing materials inside. Even though almost no healing is visible at the crack surface, the inner part of a crack can be healed, resulting in some regain in mechanical properties.

Both PP and PVA fibres are used as an additive of cementitious materials for optimal use of autogenous healing. Four types of synthetic microfibres were studied. These include a pure polyvinyl alcohol (PVA) fibre from the Belgian company Redco nv (slightly oil-coated; fibre length 6 mm), an 1.2% oil-coated PVA fibre from the Japanese company Kuraray (fibre length 8 mm), a bicore polypropylene (PP) fibre (fibre length 6 mm) and a monofilament PP fibre (fibre length 8 mm), both from the Belgian company Redco nv. The density of the PVA is 1300 kg/m³ and of the PP 910 kg/m³.

All samples were four-point-bended until failure. When a crack forms, microfibres will bridge a crack and due to fibre action, the stress can still increase until the weakest part of the bridging fibre does not manage to take up the additional forces. The first-cracking-strength was 4.9 ± 0.4 MPa for the pure PVA, 5.0 ± 0.4 MPa for the oil-coated PVA, 4.4 ± 0.4 MPa for the bicore PP and 3.7 ± 0.3 MPa for the monofilament PP fibre mixture. Due to the lower bond with the matrix by the PP fibres, the first-cracking-strength is lower.

Figure 5.8 shows the crack pattern with clear multiple cracking. All cracks were through-going, which is typical for steady-state cracks which are formed when performing four-point-bending tests on mixtures with incorporated synthetic microfibres. The crack width did not vary significantly over the total crack length and all microscopic properties were alike over the total length. The most-frequent crack width in pure PVA samples is narrowest (15 µm). This is due to the high bond with the cementitious matrix. Oil-coating them leads to an increase in overall crack width (18 µm). In PP bicore mixtures, the crack width is around 50 µm and in PP monofilament around 70 µm. Microfibre-reinforced composites show crack widths between 20-80 µm (Li, 2008) when oil-coated PVA-fibres are used.

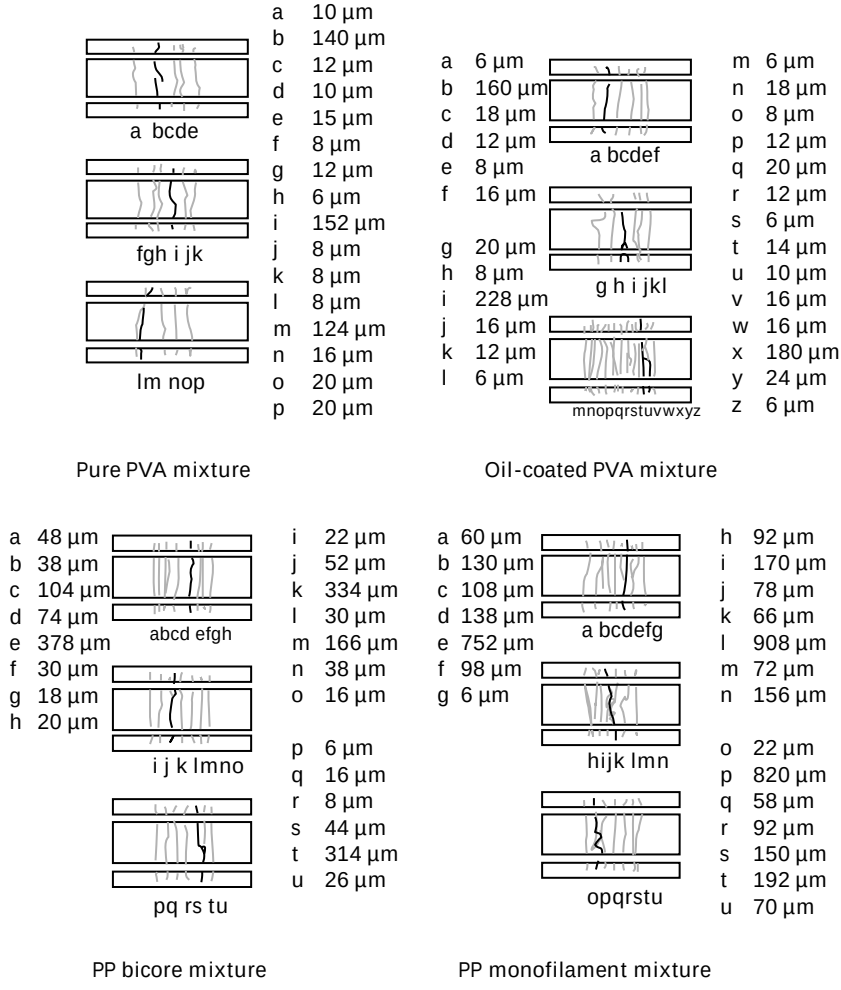

Figure 5.8. Crack pattern of the studied specimens.

An inherent feature is the pronounced strain-hardening found when using synthetic microfibres. The multiple cracking amount (strain) at 28 days of age was 0.81 ± 0.32 % for the pure PVA, 2.92 ± 0.61 % for the oil-coated PVA, 3.25 ± 0.63 % for the bicore PP and 4.22 ± 0.37 % for the monofilament PP fibre mixture. The strain was determined until strain-softening occurred so that the widening of the cracks was not added to the multiple cracking amount.

Microscopic results revealed the nucleation of healing products on the fibres, stimulating the healing of a crack. This resembles to the stitching of a crack at first and the subsequent total healing. All fibre types show this form of nucleation. An example for the untreated pure PVA fibre is shown in Figure 5.9. This is due to the alkaliphilic nature of the fibre, attracting the $CaCO_3$ crystals. But, as can be seen, not the complete crack has been closed due to healing. In literature, the boundary is 30-50 µm (Yang, 2008), so the widest latest-formed cracks do not heal efficiently over the whole of the crack. In the pure PVA mixture, all other cracks (< 30 µm) were healed.

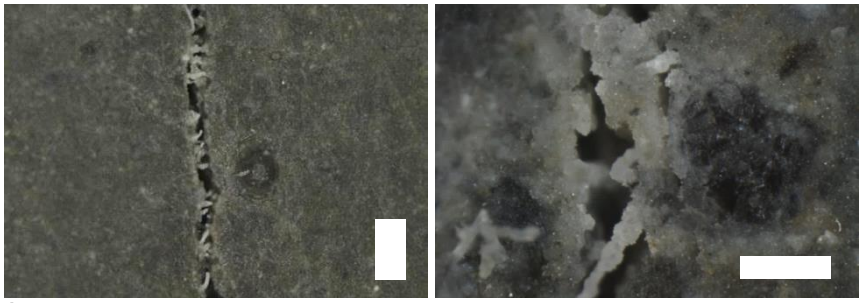

Figure 5.9. Nucleation of $CaCO_3$ on pure PVA fibres. *The scale bar is 500 µm high (left-hand side) and 200 µm in length (right-hand side)*

Compared to the pure PVA fibre, the oil-coated fibre showed a little bit more healing product nucleation (Figure 5.10). This is possibly due to the treatment with oil. The difference, however, is not significant. In Figure 5.10, the nucleation can be studied as a function of the number of wet/dry cycles. Already a vast amount of crystals is formed after 3 wet/dry cycles. After 14 wet/dry cycles, this amount does not change in time as the building blocks for autogenous healing are consumed in time. In the oil-coated PVA mixture, all cracks < 30 µm were healed.

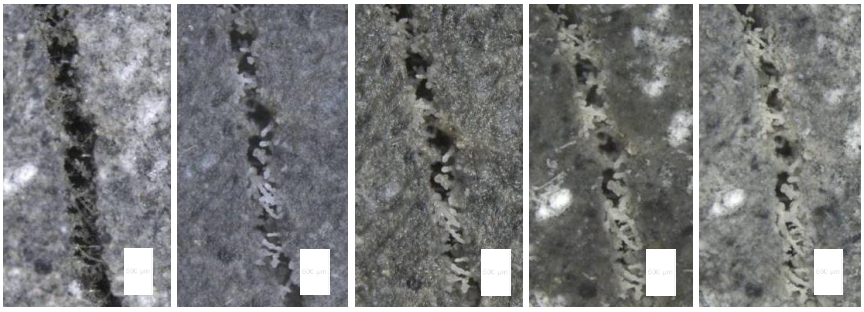

Figure 5.10. Nucleation of $CaCO_3$ on oil-coated PVA fibres (crack width 280 µm) after 1, 3, 10, 17 and 27 wet/dry cycles. *The scale bars are 500 µm high.*

Far more nucleation is seen on PP fibres (Figure 5.11). This is due to the polar groups at the fibre surface which attract $CaCO_3$ crystals. This will lead to a more sustainable and better healing condition. The amount of nucleation on both types of PP fibres does not differ significantly. The final crack widths of samples with PP

fibres, however, is larger compared to mixtures with PVA fibres. This is due to the very low bond with the cementitious matrix, causing the microfibres to be pulled out instead of matrix tunnel blockage. Overall, all other cracks were also larger (Figure 5.8). This is not beneficial for autogenous healing to occur as the mechanism shows less healing as a function of the crack width. Narrower cracks are thus preferred. Also, the polyvinyl alcohol fibre has a better cracking restriction because the high elongation of the polypropylene fibre is not efficient.

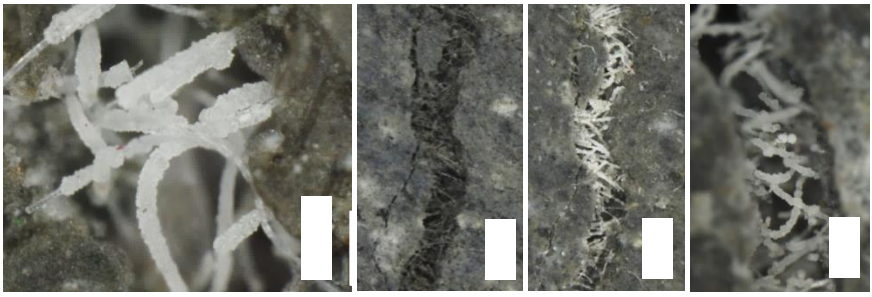

Figure 5.11. Nucleation of $CaCO_3$ on PP monofilament fibres (first) and PP bicore fibres (last three figures; crack width of 334 µm) after three wet/dry cycles. *The scale bar amounts to 200, 500 µm, 500 µm and 200 µm, respectively*

The difference in mechanical behaviour of the PP fibres is due to the form of the fibre. The bicore fibre is smooth and long and the monofilament is more curved after being pulled-out (Figure 5.12). This additionally causes the monofilament PP fibre mixture to show larger crack widths compared to the bicore PP fibre mixture. Due to the bicore nature, the fibre is also stronger (De Lhoneux et al., 2002).

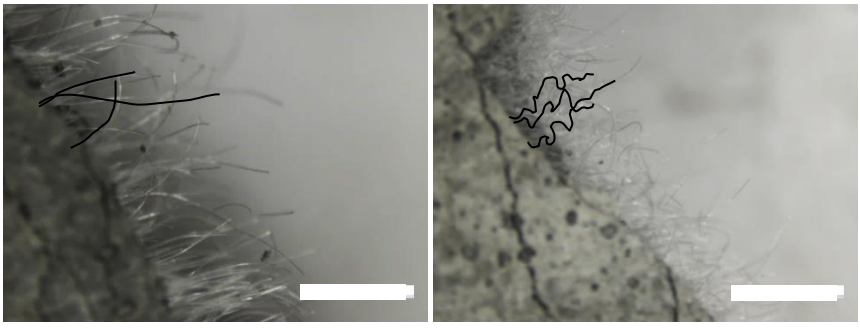

Figure 5.12. Pulled out PP bicore (left-hand side) and PP monofilament (right-hand side) fibres. *The scale bar amounts to 2 mm*

In literature, the better self-healing precipitation around fibres was explained by the high polarity of synthetic microfibres, inducing nucleation (Nishiwaki et al., 2012).

The best fibre type was the oil-coated PVA fibre from Kuraray, considering the restriction in crack width and the optimal multiple cracking and ductility. This fibre was selected and further studied.

5.5.3 Natural fibres as a green replacement for synthetic microfibres

5.5.3.1 Background

Synthetic microfibres have already demonstrated their ability to increase the durability of a cementitious material. A proper mixture design can produce cementitious composites which exhibit tensile strain-hardening and multiple cracking, while minimizing the crack width (Li et al., 1988; Li et al., 1997; Wang et al., 1987; Yang, 2008).

Natural fibres may also be used to receive multiple cracking and autogenous healing. The use of natural 'green' fibres is very attractive for two main reasons. Firstly, the production of natural fibres can occur at low cost and with a limited ecological impact. The concrete industry in particular is prone to high carbon dioxide emissions and would thus benefit from the use of renewable, eco-friendly natural materials. As environmental problems and future oil shortages increase, opportunities for the production of fibres from non-petroleum renewable sources will increase. Also, because of photosynthesis, the cultivation of natural fibres reduces the amount of carbon dioxide (CO_2) and increases the amount of oxygen (O_2) in the atmosphere, thereby reducing the impact of the greenhouse effect. Also some plant varieties, such as flax, thrive in a variety of climatic conditions and are therefore easy to cultivate. Secondly, some natural fibres have particularly good mechanical properties, as is especially the case for hemp and flax fibres. The use of these natural fibres in concrete compared to synthetic microfibres is therefore an object of great interest.

Flax is primarily cultivated for its seeds from which oil is obtained. Plant stems are often considered as waste material, e.g. sisal pulp and banana pulp (Savastano Jr. et al., 2000). But the fibres in stems can be used in fibre reinforced composites with good mechanical properties; particularly flax fibre which is one of the most durable and strong natural fibres (Boghossian & Wegner, 2008). The production of flax fibres uses little energy and flax needs little fertiliser and chemical pesticides, so its cultivation offers an environmental pause which can be used to maintain soil quality and bio-diversity within crop rotations.

The polymers found in natural fibres are cellulose, hemicellulose, lignin and pectin (Figure 5.13). Lignin and pectin act as the bonding agents (Baley, 2002b; Bledzki & Gassan, 1999; Bledzki et al., 2004; Sal'nikov et al., 1993). The fibres contain chains of cellulose that are wrapped together by microfibrils and have a polygonal cross-section. In the middle a central channel, the lumen, is found (Sedan et al., 2008b). The mechanical properties of natural fibres depend on the crystal structure, the cellulose, the degree of crystallisation and polymerisation, the angle of the microfibrils, the porosity and the size of the lumen. Fibre strength reduces with the moisture content, and the stiffness diminishes with increasing uptake of water in the fibre pores since it reduces the cohesion of the fibrils. The lumen is partly responsible for the water uptake (Baley, 2002b). The tensile strength and modulus of elasticity decrease as the fibre diameter increases (Bodros & Baley, 2008). The difference between natural and synthetic fibres is the water uptake; natural fibres are more hydrophilic in nature. In cementitious composites this ensures a better bond with the cement matrix (Boghossian & Wegner, 2008).

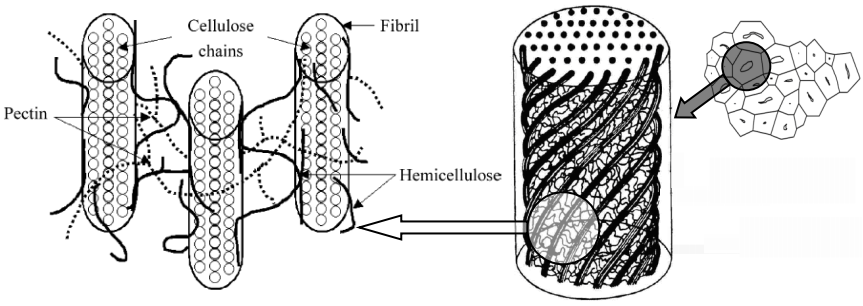

Figure 5.13. Polygonal cross-section of natural fibres with microfibrils and polymers after (Baley, 2002b) and (Sedan et al., 2008b).

The one metre long technical fibre inside a typical flax stem (Figure 5.14) consists of bundles of elementary fibres bound together with pectin and hemicellulose. Due to the bundling effect, the strength of the technical fibre is 57% of the strength of the elementary fibre (Bos et al., 2002b; Bos, 2004). The stress-strain curve shows an initial non-linear elastic behaviour. This is attributed to the orientation and sliding of the microfibrils (10-11°) with the axis of strain (Baley, 2002b). The mechanical properties of the flax fibres show higher variability due to the natural origin. The term flax fibre describes the material flax. Technical and elementary fibres are a subset of this general term. Some properties of the elementary flax fibre are listed in Table 5.3.

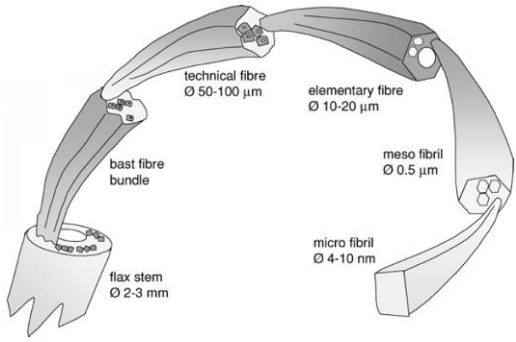

Figure 5.14. Composition of a flax stem after (Baley, 2002b; Bodros & Baley, 2008).

Table 5.3. Mean mechanical properties of elementary flax (Baley, 2002b; Bodros & Baley, 2008; Boghossian & Wegner, 2008; Bos et al., 2002b; Bos, 2004) and PVA-fibres (Li, 2008).

	Elementary flax fibre	PVA-fibre
Diameter	10-60 µm	39 µm
Tensile strength	840-1800 MPa	806-1620 MPa
Modulus of elasticity	50-100 GPa	21.8-60 GPa
Maximum strain	1.8-3.2%	6%
Water uptake	95%	
Density	1500 kg m^{-3}	1300 kg m^{-3}

Although flax fibres have excellent strength properties, they also have negative characteristics. The durability of flax fibres (both technical and elementary fibres) in alkaline environments is endangered due to the deterioration of the hemicellulose (Bentur & Akers, 1989; Stamboulis et al., 2001). Also, hemicellulose seems to prevent some cement hydration (Bilba et al., 2003). Therefore, the cottonisation of flax used for reinforced cementitious composites is proposed in this research. The process of cottonisation by carding reduces the amount of technical fibres and alters the amount of elementary fibres. The pectin and hemicellulose are partly removed, giving promising characteristics.

The technical and cottonised flax fibres are compared in this research with synthetic uncoated polyvinyl alcohol (PVA) fibre. As the hydrophilic nature of the PVA-fibre gives a strong chemical bond with the cement matrix originating from a hydroxyl group in the molecular chain of the PVA-fibre, the PVA-fibres might be coated with 1.2% of oil (Li, 2008; Yang, 2008; Yang et al., 2009). This coating results in a hydrophobic PVA-fibre. The mean mechanical properties of the uncoated PVA-fibre are given in Table 5.3.

5.5.3.2 Materials and methods

Both technical flax and cottonised flax in cementitious materials were investigated as an alternative to synthetic PVA fibres with the aim to obtain a more ductile material. The addition of the fibres should restrict the crack widths and enhance autogenous self-healing. The investigated characteristics are the mechanical properties and the regain in mechanical properties due to self-healing, after performing four-point-bending tests. The loss in hemicellulose and pectin due to cottonisation, which would improve the durability of flax in an alkaline environment, was investigated by means of thermogravimetric analysis (TGA) of technical and cottonised flax fibres.

The PVA-fibres with a length of 6 mm and the flax fibres were obtained from the Belgian companies Redco nv and Debruyne nv, respectively. The technical fibre had been cut into approximately 50 mm long pieces. The raw material required further processing. This included cutting it into 20-30 mm long fibres and removing of all the clay and unwanted natural materials as dirt. The three types of fibres are shown in Figure 5.15. As can be seen, the cottonised flax appears to have smaller fibres compared to the technical flax and has a "woollier" look. The diameters are the same as in Figure 5.14. Some unwanted natural materials were visible and this ratified the need for further processing.

The investigated mixtures are shown in Table 5.4 and are based on the ideal self-healing mixture described in paragraph 4.2. In the sample codes, the type of fibre is given first: 'PVA' stands for the polyvinyl alcohol fibre, 'TF' for the technical flax fibre and 'CF' for the cottonised flax fibre. The, the amount (0.5/1/2 v%) of microfibres is given. The samples were prepared, mixed, stored, cracked at an age of 28 days and healed for 28 days as described in paragraph 5.3. The wet/dry cycle had a 12 hours wet and 12 hours dry condition.

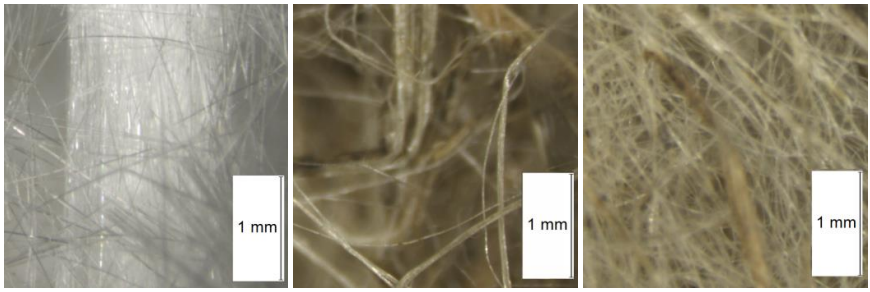

(a) (b) (c)

Figure 5.15. Typical view of PVA-fibres **(a)**, technical flax fibres **(b)** and cottonised flax fibres **(c)**. The scale bars are 1 mm in height.

Table 5.4. Studied mortar samples with their code, volume percent of fibres, amount of superplasticiser and method of crack formation (n=3).

Specimen code	v% of fibres	Superplasticiser	Cracking
PVA2 C	2 (26 kg m^{-3})	15 kg m^{-3}	no cracking
PVA2	2 (26 kg m^{-3})	15 kg m^{-3}	four-point bending
PVA1	1 (13 kg m^{-3})	10 kg m^{-3}	four-point bending
PVA0.5	0.5 (6.5 kg m^{-3})	5 kg m^{-3}	four-point bending
TF1 C	1 (15 kg m^{-3})	15 kg m^{-3}	no cracking
CF1 C	1 (15 kg m^{-3})	15 kg m^{-3}	no cracking
TF1	1 (15 kg m^{-3})	15 kg m^{-3}	four-point bending
CF1	1 (15 kg m^{-3})	15 kg m^{-3}	four-point bending
TF0.5	0.5 (7.5 kg m^{-3})	7.5 kg m^{-3}	four-point bending
CF0.5	0.5 (7.5 kg m^{-3})	7.5 kg m^{-3}	four-point bending

The control specimens (indicated with 'C' in the end) were not cracked at an age of 28 days by means of four-point-bending and underwent the same storage and healing conditions as the cracked specimens. They were cracked at an age of 56 days, when the other samples were reloaded.

Older uncracked specimens (indicated with '9' in the end in the following results) were used to investigate the pozzolanic activity of fly ash and the effect of cottonisation on the first-cracking-strength. The specimens underwent wet/dry cycles up to an age of 56 days and were then stored in a relative humidity of 60%. After 9 months, the samples were cracked using a four-point-bending test and the first-cracking-strength was compared.

The determining factor of the workability was the step of fibre addition during processing. The workability decreased as the amount of fibres increased. The workability of mixtures with flax fibres was lower than for the mixtures with the synthetic PVA-fibres. That is due to the higher fluid uptake by the flax fibre. Due to the smaller diameters, and thus larger surface area, of cottonised flax (*CF*), the workability of mixtures with *CF* was lower than of the mixtures with technical flax fibres (*TF*). Only a maximum of 1 v% flax fibres was manageable. If the amount was greater, the mix was too stiff, leading to an inadequately compacted product.

Mixtures with PVA-fibres hardened after a day and the specimens could be demoulded. As hemicellulose partly prevents cement hydration (Bilba et al., 2003), the hardening of mixtures with technical flax lasted two days. The specimens could not be demoulded after one day but demoulding was possible on the subsequent day. However, the hardening of mixtures with cottonised flax was comparable to a mixture with PVA-fibres. This points to the removal of a large amount of hemicellulose by the cottonisation process as hemicellulose slows the cement hydration (see later-on). Cement hydration was therefore mostly unchanged in mixtures with cottonised flax. To ensure the hydration, the use of cottonised flax fibres is therefore better than the use of technical flax fibres for the adopted conditions of curing.

Microscopic observations after crack formation showed that the crack always ran through points on the specimen where the remains of bast fibres are positioned (Figure 5.16). Generally, to enhance the formation of multiple cracks, micro defects can be added. Bast fibre remains function as crack initiators, as can be seen in Figure 5.16a. These bast fibres do not bind with the cement matrix and are pulled out completely after loading until failure (Figure 5.16b). The extracted length was sometimes 15 mm.

Specimens of *PVA2 C* and *PVA2* exhibited multiple cracking with the formation of 5-6 cracks with an average crack width of 6-30 µm and a pronounced strain hardening effect. The loading was stopped beyond the point of maximum multiple cracking, resulting in an opening of a previously formed crack. The crack widths in samples containing slightly oil-coated PVA-fibres (6-30 µm) are smaller than those for samples containing oil-coated PVA-fibres (20-80 µm according to (Li, 2008; Yang, 2008). This was due to the more hydrophilic nature of coated PVA-fibres compared with the slightly coated PVA-fibres.

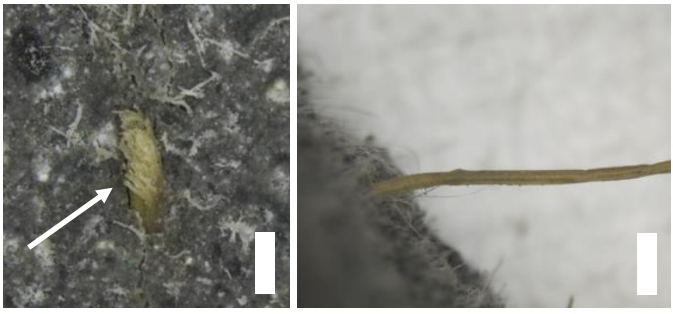

(a) (b)

Figure 5.16. Bast fibre remains as crack initiators (white arrow) **(a)** and totally pulled out bast fibre **(b)**. The white scale bars are 500 µm in height.

5.5.3.3 Mechanical properties and regain

Table 5.5 summarises the different mechanical parameters and their regain. In the next sections, each property is discussed. Specimens *PVA2 C* had a higher E-modulus than other PVA-mixtures. Control specimens were not pre-cracked, so this points to further hydration of the binder in the wet/dry cycles. There was a significant difference between *CF1* and *PVA1* with *CF1* showing the higher E-modulus, but none between *TF1* and *PVA1*. On a significance level of 8.4% there was a difference between the two mixtures with flax. On this level, it can be concluded that mixtures with cottonised flax showed a higher modulus of elasticity than those with technical flax fibres. This is compared with the findings of experiments with flax fibres found in the literature. Bodros and Baley (2008) observed an increase in tensile strength and E-modulus with a decrease in fibre diameter. As the process of cottonisation of flax lowers the amount of large diameters and increases the amount of small diameters, the strength and stiffness properties increased.

There was more regain in stiffness in specimens of *PVA1* and *PVA0.5* than *PVA2*. This is because the strain induced at pre-cracking of the *PVA2* specimens was larger due to multiple cracking capability. The final crack width in *PVA2* specimens was larger due to a higher bridging capacity of more fibres. Mixtures with a similar amount of flax fibres showed a lower regain in stiffness but did not differ from each other.

There is no significant difference of peak stress at different volume percent of PVA-fibres. The peak stress of control specimens is higher than the corresponding stress for the test specimens. This is due to further hydration, of both the Portland cement and the pozzolanic fly ash. Samples with flax fibres show a lower peak stress than those with PVA-fibres. Specimens of *CF0.5* differed at a significance level of 9.1% from *TF0.5* and *CF1* at 24.6% from *TF1*. However, *CF1 C* differed significantly from *TF1 C*. Therefore, mixtures with cottonised flax show a tendency for higher peak loads than those with technical flax fibres.

The regain of the peak load of control specimens was slightly negative as shown by the flattening of the stress-strain curves. There was no significant difference between the natural fibres. All mixtures showed similar recovery with regard to the peak load. A higher regain was found for the *PVA1* and *PVA2* mixtures. Lowering the volume percent of natural fibres gave a lower amount of total working force. There was not enough bridging capacity to induce multiple cracking at low amounts of fibres. Mixtures with 1 v% technical flax fibre had a better multiple cracking capability than those with 1 v% cottonised flax fibres. The difference between the flax fibres was due to the higher amount of bast fibres and the higher amount of technical fibres which have lower bonding capacity with the cement matrix in the mixture *TF1*. This resulted in the formation of two cracks in a mixture with technical flax. Due to slip in the matrix tunnel, the fibres blocked the opening crack. The mixtures with PVA fibres did show a pronounced strain-hardening effect and multiple cracking with small healable cracks. Paragraph 5.5.4 will focus on how to improve the strain-hardening capacity of mixtures with natural fibres.

Table 5.5. Mean value at 28 days (56 days for the controls 'C' and 9 months for durability testing '9') and mean regain at 56 days with the standard deviation of the modulus of elasticity, the peak stress, the total working force and the first-cracking-strength of the mixtures.

Code	Modulus of Elasticity [MPa]	Regain in elasticity [%]	Peak Stress [MPa]	Regain in peak stress [%]
PVA2	57 ± 3	15 ± 4	6.0 ± 0.8	35 ± 7
PVA1	57 ± 2	43 ± 6	5.9 ± 0.6	41 ± 10
TF1	60± 6	16 ± 4	4.2 ± 0.4	17 ± 6
CF1	69 ± 6	14 ± 3	4.7 ± 0.7	25 ± 5
PVA0.5	53 ± 5	28 ± 5	5.6 ± 0.2	27 ± 4
TF0.5	55 ± 9	17 ± 2	4.1 ± 0.4	23 ± 4
CF0.5	69 ± 5	20 ± 5	4.8 ± 0.5	26 ± 6
PVA2C	76 ± 5	-1 ± 2	7.4 ± 0.4	-5 ± 1
TF1 C	56 ± 6	-1 ± 1	5.0 ± 0.5	-4 ± 2
CF1 C	64 ± 5	-1 ± 1	6.1 ± 0.5	-4 ± 1
TF1 9	70 ± 11		10.2 ± 0.3	
CF1 9	80 ± 14		12.2 ± 0.7	

Code	Total working force [J]	Regain in working force [%]	First-cracking-strength [MPa]	Regain in first-cracking-strength [%]
PVA2	0.9 ± 0.1	25 ± 4	4.4 ± 0.4	40 ± 7
PVA1	0.2 ± 0.1	31 ± 3	4.1 ± 0.7	27 ± 5
TF1	0.4 ± 0.1	23 ± 2	4.8 ± 0.7	16 ± 4
CF1	0.2 ± 0.1	18 ± 2	4.8 ± 0.6	28 ± 8
PVA0.5	0.2 ± 0.1	26 ± 3	4.3 ± 0.6	7 ± 2
TF0.5	0.1 ± 0.1	19 ± 2	3.9 ± 0.5	22 ± 4
CF0.5	0.1 ± 0.1	11 ± 2	4.6 ± 0.6	30 ± 6
PVA2C	0.8 ± 0.1	13 ± 1	5.8 ± 0.5	-13 ± 5
TF1 C	0.4 ± 0.1	12 ± 2	4.7 ± 0.5	-7 ± 2
CF1 C	0.2 ± 0.1	9 ± 2	6.1 ± 0.5	-6 ± 1
TF1 9	0.1 ± 0.1		10.2 ± 0.3	
CF1 9	0.1 ± 0.1		12.2 ± 0.7	

The control mixtures gave a regain in working force of 12% due to the smoothing of the stress-strain curves at immediate reloading at 56 days. Also *CF0.5* specimens showed no regain in working force because it had almost none in the beginning. The difference between the technical and the cottonised flax fibre was due to the fact that the cottonised flax-fibre-reinforced composite did not exhibit great multiple-cracking behaviour.

Control mixtures always showed a higher first-cracking-strength because of further hydration. The only significant difference between the mixtures was found between *CF1 C* and *TF1 C*. The control mixture with cottonised flax fibre showed a higher first-cracking-strength than that with the technical flax fibre. This was possibly due to the better hardening of the mixtures with cottonised flax, compared to the mixtures with technical flax. After 9 months (*TF1 9* and *CF1 9* in Table 5.5), the first-cracking-strength kept rising due to the pozzolanic activity of the fly ash. The first-cracking-strength in specimens containing technical flax (*TF1 9*) was significantly lower than the strength of specimens with cottonised flax (*CF1 9*). A conclusion about degradation of flax cannot be drawn with this test.

The regain of the first-cracking-strength did not differ significantly. There was a maximum regain of the stress at crack initiation of 40% for *PVA2*. Mixes *PVA1*, *CF0.5* and *CF1* all showed a similar regain of around 30%. The regain for *TF0.5* was somewhat lower, but not significantly different. The differences in strength regain between *CF1* and *TF1* were significant. This was due to a larger crack width in *TF1* specimens compared to *CF1* specimens. Wider cracks need to heal more in comparison to smaller cracks, so *TF1* specimens healed less.

Microscopic investigation of the cracks showed similarities between mixtures with PVA and flax fibres. The crack closure through autogenous self-healing is independent of the fibre type, and is completely determined by the initial crack width. So, the use of natural flax fibres and the process of cottonisation did not change the self-healing capacity. In Figure 5.17, a micrograph before and after healing of a 24 µm wide crack is shown. Cracks narrower than 30 µm closed completely; but cracks with widths between 30 µm and 150 µm closed partially.

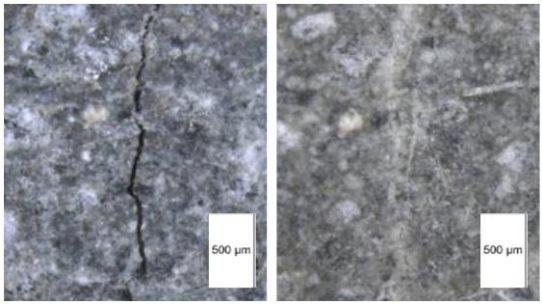

Figure 5.17. Visual closure of a 24 µm wide crack within a *PVA0.5* sample, before and after curing in wet/dry cycles. The scale bars are 500 µm in height.

5.5.3.4 Cottonisation to reduce the alkaline deterioration

Yang *et al.* (2006) used a simple way to determine the amount of hemicellulose, cellulose and lignin. They used TGA to determine the weight loss of three components. They characterised the pyrolysis of hemicellulose to start at 220°C until 315°C with a maximum value at 260°C. Cellulose decomposed in a range of 315 to 390°C with a maximum at 355°C. Lignin, however, decomposes at a very slow rate. A total of about 67 % weight loss was reached at 850°C.

The TGA used in this investigation was a Hi-RES TGA 2950 thermogravimetric analyser. A sample was gradually heated with 10°C min^{-1} until 1000°C was reached. The mass loss due to degradation of the material was recorded in function of increasing temperature under a controlled atmosphere (He). With this data, the amount of hemicellulose, cellulose and lignin could be determined.

The derivative of the TGA curves (Figure 5.18) is a measurement of weight loss as a function of temperature. The first peak is caused by the evaporation of water; this is also seen in (Yang et al., 2006). The small second peak is caused by hemicellulose and pectin; the third pronounced peak is cellulose, the main component of flax. The fourth peak is the further degradation of flax. Lignin is measured as the residue at the end. The amount of lignin in technical flax is 3%. The amount of lignin in cottonised flax was zero as all material is degraded at 600°C.

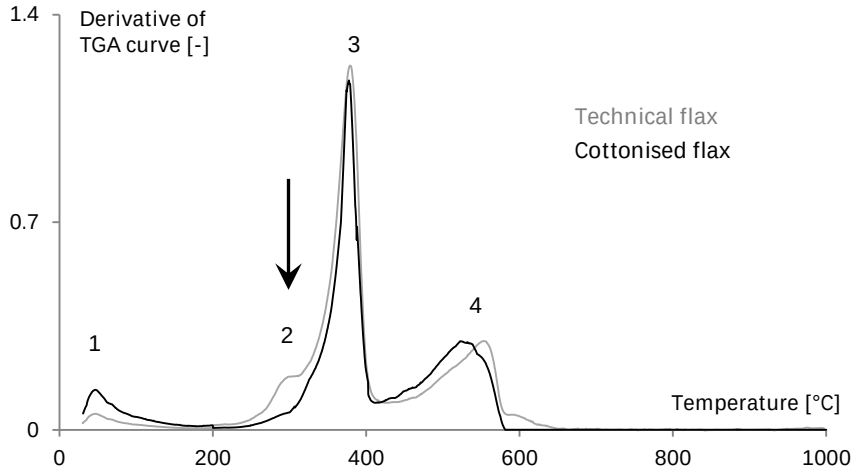

Figure 5.18. TGA showing the removal of pectin and hemicellulose if cottonisation is applied (loss of the second peak).

The hemicellulose peak was more flat in the derivative of the TGA for cottonised flax. This reduced peak points to a lowering in the amount of hemicellulose and pectin. A similar decrease was also seen by (Van De Velde & Kiekens, 2001) as a function of the degree of retting. Cottonisation thus partly removes hemicellulose and pectin.

5.5.4 Chemically treating the natural fibres to obtain multiple cracking

Paragraph 5.5.3 already proposed the use of natural 'green' fibres to induce strain-hardening. Unfortunately natural fibres have a few disadvantages, such as their high water absorption (Boghossian & Wegner, 2008) and their susceptible nature to degradation (Agopyan et al., 2005; Pacheco-Torgal & Jalali, 2011). This degradation can occur in several ways. Exposure to moisture can cause biodegradation after only three days, and, more importantly, cellulosic fibres deteriorate in an alkaline environment (Bentur & Akers, 1989; Gram, 1983; Stamboulis et al., 2001), which is the case in cementitious materials. The main polymers in natural fibres are cellulose, hemicellulose, lignin and pectin (Baley, 2002a; Bledzki & Gassan, 1999). The hydrophilic hemicellulose is mostly responsible for the water absorption (Davies & Bruce, 1998), but also for thermal and biodegradation (Aziz et al., 1981; Sahed & Jog, 1999). Lignin and pectin are thermally stable, but are responsible for UV-degradation (Sedan et al., 2008a). Also, the hollow part of the natural fibre, the lumen, may harden with cement products, the so-called petrification (Savastano Jr. & Agopyan, 1999).

To overcome these disadvantages, the fibres may be chemically treated. A chemical treatment may reduce the amount of hemicellulose, lignin, pectin and natural oils covering the surface of the fibre, thus changing their behaviour and roughness (Li et al., 2007; Mwaikambo & Ansell, 2002). By chemically treating the natural fibres, the fibre surface is modified, the fibres are cleaned and most of the impurities are removed. This will change the synergetic interaction between the natural fibre and the cementitious matrix. A treatment of the hydrophilic fibres (due to their hydroxylic groups) to obtain hydrophobic properties, will lead to a reduction of the water absorption of the fibres and thus also the biological deterioration in humid environments. Physical treatments, such as cottonisation may partly remove hemicellulose and pectin (Pickering et al., 2007), leading to a reduction of the degradation in an alkaline environment. Some treatments may improve the mechanical properties and the interaction with the cementitious matrix due to the change in surface and roughness properties (Bledzki & Gassan, 1999). This may possibly lead to an increase in ductile behaviour.

Two typical natural fibres will be studied: flax and hemp. Flax is mainly used for linen, but flax is one of the strongest and most durable natural fibres (Boghossian & Wegner, 2008). That is why they are so attractive to be used as a reinforcing fibre in composite materials. The technical flax fibre has a fibre diameter of 50-100 µm and is composed out of elementary fibres with a diameter of 10-20 µm (Bos et al., 2002b). Elementary fibres are hereby glued together by pectin and hemicellulose (Baley, 2002b). Cottonisation may partly remove pectin and hemicellulose, improving the overall susceptible nature to degradation. Another strong and stiff fibre is the hemp fibre and this fibre is already commonly used as a reinforcing material in the car industry (Pickering et al., 2007). The structure and architecture of the fibre is mostly comparable to the flax fibre. Again, smaller fibres are held together by pectin and hemicellulose (Sedan et al., 2008a; Van De Velde & Kiekens, 2001). By means of retting, the technical fibres come loose from the stem of the fibre. Pectin is hereby decomposed, without ideally removing the lignopectin which holds the elementary fibres together.

Multiple cracking and self-healing have only scarcely been studied in cementitious composites with flax and hemp fibres. As found in the previous paragraph, cementitious materials reinforced with cottonised flax did not show any form of strain hardening. Only some partial multiple cracking was observed in mixtures containing technical flax fibres and results considering autogenous crack healing proved to be promising. As a result, a proper mixture design still needed to be determined. One of the biggest drawbacks is also the workability of the mixtures. This is due to the high uptake of water by the natural fibres during mixing.

The application of flax and hemp fibres in cementitious composites was examined, with a focus on inducing multiple cracking under four-point-bending. The mechanical properties of the natural fibres themselves, as well as of the cementitious composites and the degradation of the natural fibres in alkaline environments were studied. The fibres were also chemically treated with several different techniques to study their influence on the strain-hardening multiple cracking capability and to improve the overall (self-healing) properties. As some natural fibres like flax or hemp have excellent strength properties, the natural fibres could be a low-cost solution to the demanding quest to obtain an alternative for the synthetic fibres.

5.5.4.1 Four types of natural fibres

One synthetic fibre, the polyvinyl alcohol (PVA) fibre coated with 1.2 m% oil, from Kuraray (Japan), was used as a reference. The natural fibres consisted of four basic types: technical flax (TF), cottonised flax (CF), non-retted hemp (NH) and slightly-retted hemp (SH) (Figure 5.19). The flax fibres were obtained from Debruyne nv and the hemp (Santhica 27 type) from Galle Linen nv in cooperation with Inagro, all Belgian companies and organizations. The raw natural-fibre material was hand-processed and cut into separate fibres with approximately 2 cm fibre length. The fibre amount was 0.5, 1, 1.5 or 2 v% (volume percent of the mixture). The average diameters of the natural fibres are 103 ± 47 µm for technical flax fibres, 62 ± 27 µm for cottonised flax fibres, 174 ± 50 µm for non-retted hemp and 149 ± 43 µm for slightly-retted hemp. Chemically treating (see later-on) the fibres leads to no significant increase in or reduction of the fibre diameter.

Fibre contents of more than 1 v% could not be achieved without hydrating the fibres with additional water prior to mixing (see methods, procedures and results found in paragraph 5.5.3). Using this hydrating step, mixtures were able to be made with fibre contents of 1.5 v% and 2 v%. The latter 2 v% was used in all further-described results. Higher amounts were not achievable, as again the workability was inferior due to already high mixing-water absorption by the natural fibres.

Three different pre-treatments with water were studied to improve the handling of the natural fibres during mixing. These include a maximum pre-hydration with additional water (7.2/9.0/5.3/3.7 g additional water/g TF/CF/NH/SH, respectively), a minimal pre-hydration by carefully squeezing out the fibres after being soaked in mixing water and the pre-hydration with mixing water itself. The flow value of all mixtures was determined using the Standard EN 1015-3 (for all mixtures, an average flow value of 150 ± 10 mm was found).

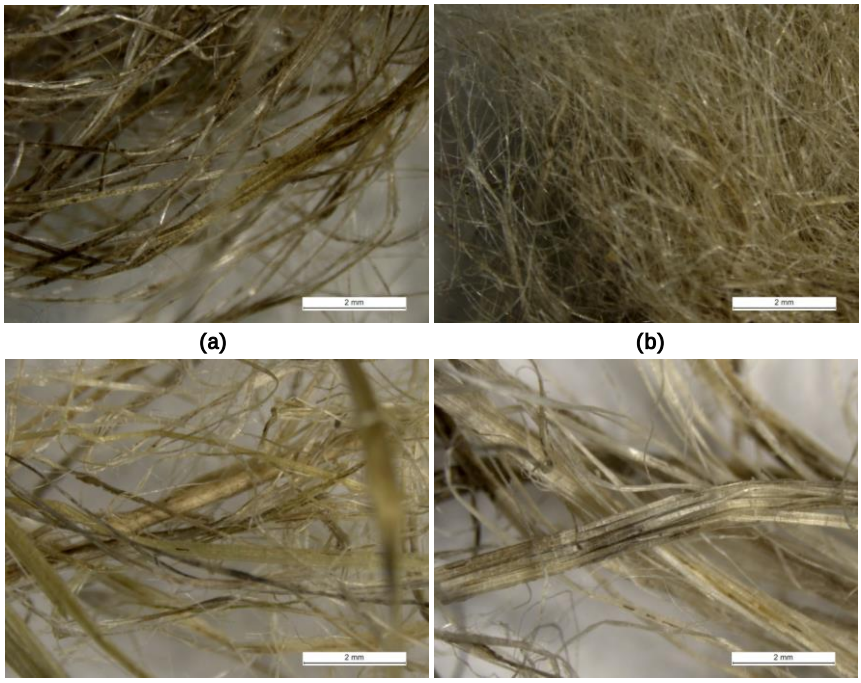

Figure 5.19. Micrographs of technical flax TF **(a)**, cottonised flax CF **(b)**, non-retted hemp NH **(c)** and slightly-retted hemp SH **(d)**. The scale bar amounts to 2 mm.

5.5.4.2 Used chemical treatments and degradation study

The different chemicals used (together with their abbreviations) were the following:

Silane-Prime impregnable silane primer (S), Klaas Coatings Pty Ltd;

A pre-weighed amount of natural fibres were cut on their respective lengths and were saturated with the silane primer Si-Prime for a period of 1 hour. Afterwards, the fibres were rinsed with water and were dried for 24 hours at standard laboratory conditions at 20 ± 2°C.

Benzoylperoxide (BP), Merck Schuchardt OHG;

The treatment was done as described in (Joseph et al., 1996). Alkali-treated fibres (NaOH at 10 m% during 1 hour) were soaked with 6% solution of benzoylperoxide in acetone for 30 min. The solution was decanted and the fibres were air dried at 20 ± 2°C for 24 hours.

Alkalisation or mercerization (N2, N6, N10), BDH Prolabo, VWR;

Alkalisation or mercerization is a chemical treatment with sodium hydroxide (NaOH). Three types of mercerization (submersion of fibres in 2/6/10 m% NaOH) were studied. Natural fibres were put for a total period of 24 hours in these solutions and were then rinsed with water until the water was pH-neutral and were dried for 24 hours at 20 ± 2°C before being mixed in the composite.

Acetic acid (AA), BDH Prolabo, VWR;

The fibres were put for 1 hour in an acetic acid solution and were then rinsed with water until the water was pH-neutral and were dried for 24 hours at 20 ± 2°C before being mixed in the composite.

Acetylation with acetic anhydride (AH), BDH Prolabo, VWR.

The treatment of the fibres was done as described in (Nair et al., 2001). The raw fibres were immersed in acetic acid (1 hour) and finally in acetic anhydride containing two drops of concentrated sulphuric acid (H_2SO_4) (1 hour). The fibre was then filtered and dried for 24 hours at 20 ± 2°C.

Due to the natural origin, biological and chemical degradation of the fibres is a possibility. Therefore, the properties in the alkaline environment were studied. The natural fibres and the chemically-treated natural fibres were stored during one and six months in cement filtrate (mixing 10 g of CEM I 52.5 N in 100 ml of demineralized water for 24 hours and subsequent filtration, pH = 12.8) in dark conditions at 20 ± 2°C to exclude any thermal or UV-degradation. Reference fibres were stored dry. The fibres were then tested by means of displacement-controlled tensile tests according to BISFA Standards. All fibres were first dried at 40°C for 24 hours and were acclimatised at 60% RH and 20 ± 2°C for 48 hours prior to testing. The tensile tests (TexTechno Favimat with a 1200 cN cell; Figure 5.20) were conducted on minimally 30 fibres. The test parameters were: a span length of 10 mm, pre-tensioning at 0.5 ± 0.05 cN/tex and a loading speed of 5 mm/min. Measurements showing even a minor form of slip were excluded. Additionally, there was a strength loss criterion of 3% to exclude limited slip. Afterwards, the tensile strengths and strains at failure were studied, together with the modulus of elasticity as determined between 1 and 1.5% strain. The 1-1.5% strain boundary was chosen as there is a non-linear elastic phase due to the angle of the micro-fibrils present in natural fibres before 1% of strain.

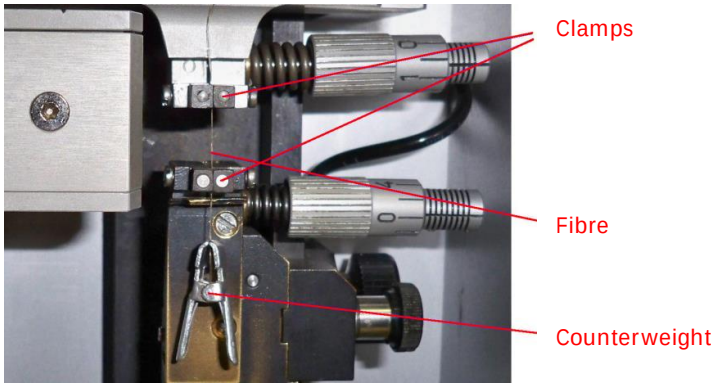

Figure 5.20. Test setup used to determine the (natural) fibre strength properties. The clamping length amounts to 10 mm.

5.5.4.3 Mechanical properties of the reinforced composite

The same procedure as described in paragraph 5.5.3.2 is valid. At an age of 28 days, the 2 v% PVA mixture showed 6-10 cracks with an average crack width of 29 ± 9 µm after performing four-point-bending (Table 5.6). This material served as a reference. A mixture with natural fibres should show the similar behaviour; a high ductility with small healable cracks.

Maximal pre-hydration in mixtures containing natural fibres led to no multiple cracking as the surrounding matrix was too weak due to the high additional water amount. Pre-hydration with mixing water led to partial formation of multiple cracking but the overall matrix near the natural fibre itself seemed to be weak. Minimal pre-hydration with mixing water by gently squeezing out the fibres led to the best results. Those were studied further in this research.

Natural fibre addition retards hardening of the cementitious matrix. This is due to the presence of hemicellulose (Bilba et al., 2003) and pectin (Sedan et al., 2008a). The following trend was found in order of increasing influence on the setting: CF < TF < NH = SH. Cottonisation partly removes hemicellulose and pectin , leading to the smaller influence on the setting compared with technical flax. Hemp fibres have generally higher amounts of pectin (18-20 m%) compared with flax (2-4 m%) (Batra, 1988; Mwaikambo & Ansell, 2006). Also, the fibre diameter of the hemp fibres is larger, and thus higher amounts of lignin and pectin, which bundle the elementary fibres, will be present in hemp.

If the embedded length is too small, the fibre will be pulled out without any slip hardening. Therefore, a fibre length of 2 cm was used in this research. Lengths of 0.5 and 1 cm did not show better results and longer fibres led to a too high reduction in workability.

The typical stress-strain curves for mixtures with 2 v% of natural fibres are shown in Figure 5.21 (left). Multiple cracking was achieved for all fibre types, except for slightly-retted hemp. A clear strain hardening is observed and the sudden drops in stress-strain curves are due to the formation of new cracks. The studied parameters are given in Table 5.6.

The best results in mixtures with the basic fibres were achieved using technical flax fibres (TF), giving an average of 4.7 cracks per sample, with an average crack width of 28 µm and a multiple cracking amount of 0.76% (Table 5.6). The average crack width is comparable to the one with synthetic microfibres, but the ductility is only a third (but noteworthy). The average crack width in specimens containing cottonised flax fibres (CF) is 24 µm, with non-retted hemp (NH) 161 µm and with slightly-retted hemp (SH) 158 µm. A possible explanation for the difference in crack width is that the chemical bonding between hemp fibres and the cementitious matrix is insufficient to induce proper fibre-bridging action. The hemp fibres contain a lower amount of cellulose compared to flax fibres, leading to less hydroxyl groups available for a decent bond with the cementitious matrix compared to flax fibres. Also, due to retting, the SH fibres are smoother, causing less friction and less force transfer through fibre action. This is not beneficial to receive small healable cracks.

Table 5.6. The modulus of elasticity, the amount of multiple cracking, the first-cracking-strength, the ultimate strength, the average crack width, the number of cracks and the regain in first-cracking-strength for the studied mixtures (n = 3). The green, yellow and red colours depict preferred, acceptable and unwanted properties, respectively.

Code	Modulus of Elasticity [GPa]	Multiple cracking [%]	First-cracking-strength [MPa]	Ultimate strength [MPa]	Average crack width [µm]	Number of cracks [-]	Regain in first-cracking-strength [%]
PVA	5.7 ± 0.3	2.4 ± 0.1	4.4 ± 0.4	6.0 ± 0.5	29 ± 9	8.3 ± 1.2	40 ± 7
TF	7.0 ± 0.4	0.8 ± 0.1	4.1 ± 0.3	6.2 ± 0.4	28 ± 17	4.7 ± 0.8	37 ± 6
CF	6.8 ± 1.0	0.3 ± 0.1	3.0 ± 0.2	3.2 ± 0.2	24 ± 6	1.7 ± 0.8	43 ± 9
NH	6.3 ± 0.5	0.3 ± 0.1	3.9 ± 0.4	4.0 ± 0.4	161 ± 38	2.3 ± 0.6	12 ±10
SH	5.8 ± 0.7	0.1 ± 0.1	3.9 ± 0.4	4.0 ± 0.3	158 ± 44	1.6 ± 0.8	-
TF - S	5.9 ± 0.6	0.1 ± 0.1	5.0 ± 0.3	5.1 ± 0.4	-	1	-
TF - BP	7.9 ± 1.0	0	3.8 ± 0.1	3.8 ± 0.1	-	1	-
TF - N2	7.1 ± 0.8	1.0 ± 0.1	3.6 ± 0.4	5.1 ± 0.8	28 ± 12	7.5 ± 0.3	40 ± 4
TF - N6	7.2 ± 0.9	0.5 ± 0.1	3.4 ± 0.3	3.8 ± 0.4	55 ± 14	3.4 ± 0.6	23 ±12
TF - N10	7.3 ± 0.3	0	4.0 ± 0.3	4.0 ± 0.3	-	1	-
TF - AA	6.1 ± 0.6	0.2 ± 0.1	5.1 ± 0.2	5.7 ± 0.3	25 ± 13	1.6 ± 0.6	-
TF - AH	7.5 ± 0.6	0.4 ± 0.2	5.0 ± 0.3	6.4 ± 0.8	29 ± 13	3.5 ± 0.6	35 ± 9
CF - S	6.2 ± 0.5	0.1 ± 0.1	3.5 ± 0.1	3.9 ± 0.2	27 ± 9	1.3 ± 0.3	-
CF - BP	7.9 ± 0.5	0	4.2 ± 0.4	4.2 ± 0.4	-	1	-
CF - N2	7.0 ± 0.8	0.4 ± 0.1	3.9 ± 0.1	4.5 ± 0.4	26 ± 8	2.7 ± 0.6	36 ± 8
CF - N6	6.7 ± 1.0	0	3.9 ± 0.3	4.0 ± 0.3	-	1	-
CF - N10	7.8 ± 0.7	0	5.4 ± 0.4	5.4 ± 0.4	-	1	-
CF - AA	7.2 ± 0.5	0.1 ± 0.1	3.4 ± 0.3	3.6 ± 0.3	29 ± 8	1.7 ± 0.3	-
CF - AH	6.6 ± 0.2	0.1 ± 0.1	4.3 ± 0.5	4.6 ± 0.5	29 ± 9	1.7 ± 0.6	-

NH - S	6.1 ± 0.2		0			4.3 ± 0.2		4.3 ± 0.2		-			1		-	
NH - BP	5.9 ± 1.0		0.1 ± 0.1			3.6 ± 0.5		5.7 ± 0.5		158 ± 42			1.6 ± 0.6		-	
NH - N2	7.9 ± 0.9		0.7 ± 0.1			3.5 ± 0.6		5.9 ± 0.5		81 ± 24			2.9 ± 1.2		17 ±12	
NH - N6	7.1 ± 0.2		0.1 ± 0.1			4.1 ± 0.2		4.2 ± 0.2		162 ± 18			1.3 ± 0.3		-	
NH - N10	6.3 ± 0.5		0			4.6 ± 0.2		4.6 ± 0.2		141 ± 9			1.3 ± 0.3		-	
NH - AA	8.0 ± 0.3		0			4.9 ± 0.4		4.9 ± 0.4		-			1		-	
NH - AH	7.4 ± 0.1		0.1 ± 0.1			4.2 ± 0.4		4.4 ± 0.3		-			1		-	
SH - S	5.7 ± 0.4		0.1 ± 0.1			4.2 ± 0.2		4.3 ± 0.2		128 ± 10			1.7 ± 0.6		-	
SH - BP	5.8 ± 0.2		0			4.2 ± 0.3		4.2 ± 0.3		-			1		-	
SH - N2	7.5 ± 0.8		0.9 ± 0.3			3.9 ± 0.4		4.4 ± 0.3		53 ± 16			6.8 ± 0.5		26 ±15	
SH - N6	7.4 ± 0.3		0.4 ± 0.2			4.6 ± 0.1		4.8 ± 0.1		162 ± 32			2.0 ± 0.1		9 ± 5	
SH - N10	7.0 ± 0.9		0			4.7 ± 0.2		4.7 ± 0.2		126 ± 10			1.3 ± 0.3		-	
SH - AA	6.8 ± 0.7		0.3 ± 0.2			3.9 ± 0.2		3.9 ± 0.2		160 ± 21			1.6 ± 0.5		-	
SH - AH	7.3 ± 0.4		0			5.0 ± 0.2		5.0 ± 0.2		129 ± 49			1.6 ± 0.9		-	

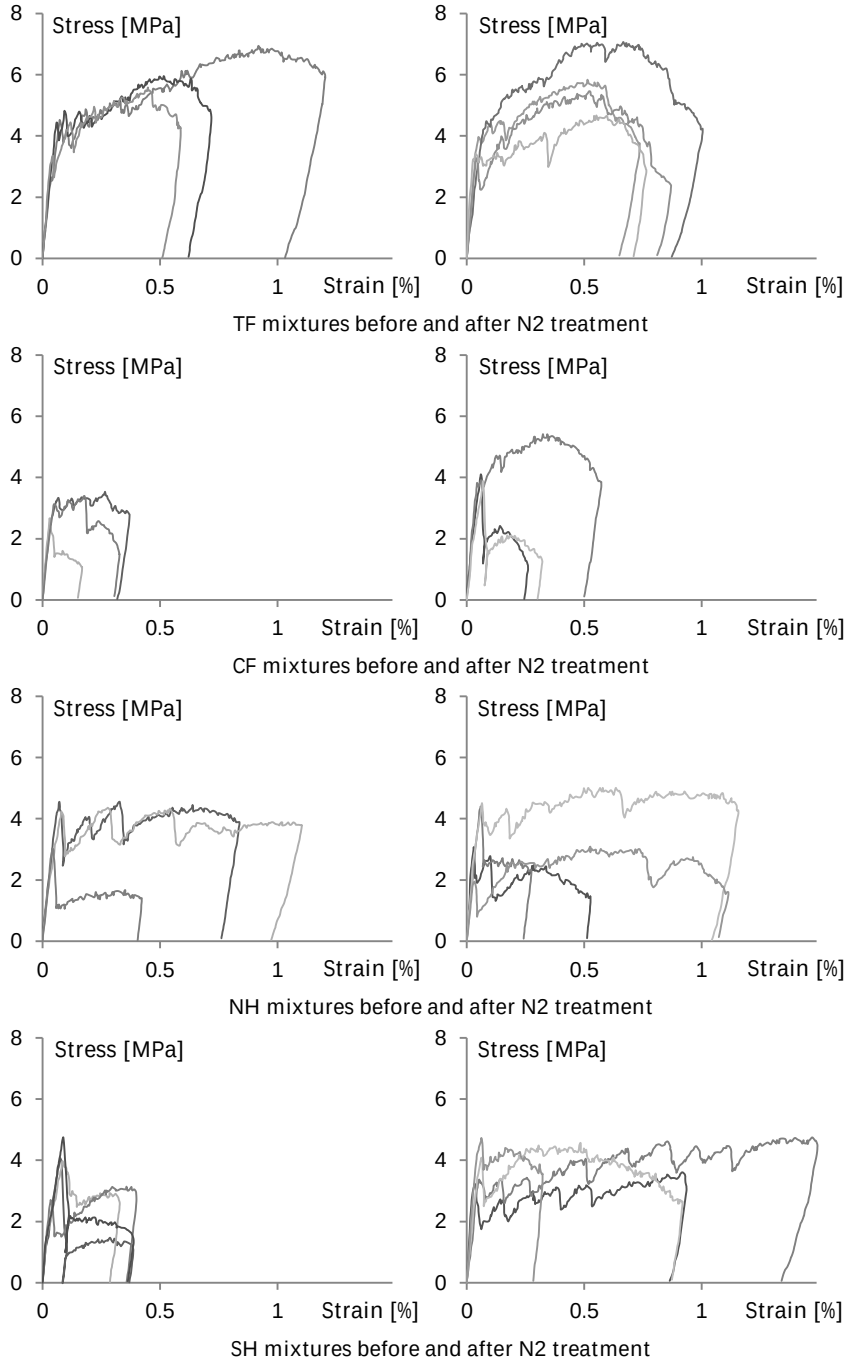

Figure 5.21. Typical stress-strain curves obtained for the mixtures with the four types of studied natural fibres, showing strain hardening after treatment with 2 m% NaOH.

Natural fibres can be chemically treated to tackle some of their pitfalls such as their bio-degradation and degradation in an alkaline environment. This will improve the fibre roughness and thus the synergetic interaction between fibre and cementitious matrix. The different chemical treatments will be addressed below.

The modulus of elasticity was determined from the stress-strain curves. Between the different chemically-treated mixtures, there is no significant difference in modulus of elasticity (significance level of 69% for TF, 40% for CF, 27% for NH and 21% for SH mixtures, respectively). There is no significant difference between the first-cracking-strengths of the basic materials compared to the synthetic PVA fibre. Only the cottonised flax mixture tends to show a lower strength. In all cases, the strength before and after chemical treatment were alike, proving the compatibility of the chemical treatment with the natural fibres.

Silane primer (S)

A chemical treatment with silanes (SiH_4) reduces the amount of hydroxylic groups on the surface of the natural fibre and changes the interface. In the presence of moisture, silane will react with the hydroxylic groups to form silanoles and thus stable covalent bonds. The treatment will reduce the water uptake of the fibres (Bilba et al., 2003) as the hydrophobic properties are increased. Both effects on the strength are possible: an increase due to the covalent bonding in between fibres and a decrease due to the reduction of the crystallinity of the natural fibre (Sawpan et al., 2011).

The treatment does not seem to improve the ductile behaviour as there is less multiple cracking observed. Only the slightly-retted hemp fibre mixture improved. The basic mixture, however, did not show any form of ductile behaviour. Overall, the treatment is not suited to receive strain hardening in the mixtures.

Benzoylperoxide (BP)

The peroxide treatment leads to free radicals which interact with the hydrogen molecules on the cellulose surface of the natural fibre. This will reduce its hydrophilicity and gives a modified fibre roughness (Paul et al., 1997; Sreekala et al., 2000). Free radicals from peroxides will react with the hydroxylic groups on the surface of natural fibres. This will increase the tensile strength properties of the fibres and was also found in literature (Paul et al., 1997; Sreekala et al., 2000).

There was no significant improvement in the ductile behaviour, so this technique is also not suited to improve the ductility in the mixtures.

Alkalisation or mercerization (N2, N6, N10)

Alkalisation or mercerization is a chemical treatment with sodium hydroxide (NaOH). NaOH is the most used chemical substance to bleach and to clean surfaces of natural fibres. It removes hemicellulose, lignin, pectin and natural oils which cover the natural fibres (Mwaikambo & Ansell, 2002). It also depolymerizes cellulose to shorter chains (Nishiyama & Okano, 1998; Zeronian & Nevell, 1985) and increases the surface roughness of the fibre (Li et al., 2007). The addition of NaOH hereby causes the ionisation of hydroxyl groups on the surface. Mercerization may increase the tensile strength of the natural fibres. This may be due to the increase in crystallinity of the cellulose (Sawpan et al., 2011). The increase in modulus of elasticity is due to the densification of the walls of the fibre due to the removal of non-cellulose materials. This leads to a better packing and a

preferential orientation of the cellulose chains towards the tensile forces (Bledzki & Gassan, 1999; Pickering et al., 2007). A concentration of 6 m% of NaOH should lead to the best and optimal results considering the mechanical properties (Mwaikambo & Ansell, 2002). A too high amount of NaOH, however, may reduce the fibre properties (Mwaikambo & Ansell, 2006; Pickering et al., 2007).

The best multiple cracking results were obtained with the mercerization (2 m% NaOH) of TF and SH, providing respective average number of cracks of 7.5 (1.02% MC) and 6.8 (0.91% MC) per sample, with average crack widths of 28 µm and 53 µm, respectively (Table 5.6). The mercerization enlarges the surface roughness, removes impurities, leads to an ionization of the hydroxylic groups and changes the structure of cellulose. This causes the difference in strength and surface properties in a cementitious matrix. Alkalisation results in a consistent improvement of the multiple cracking amount and ductility. The amount of 2 m% seems to be enough as a too high amount results in less multiple cracking. This is due to a higher modification of the cellulosic crystal structure. The amount of cracks is 2-4 in samples with non-treated fibres, compared to 7-8, 2-3, or 1-2 in samples with all fibre types chemically treated with 2%, 4% and 10% NaOH, respectively (except for cottonised flax and non-retted hemp).

The effect of mercerization on the first-cracking-strength is shown in Table 5.6. The strong increase in strength when using mercerization (10 m% NaOH) with cottonised flax can be due to nodule formation on the fibres, increasing the bond of the natural fibres with the calcium-rich cementitious matrix. This effect is also seen in the hemp mixtures.

Acetic acid (AA)

By treating the natural fibres with acids, hydrolysis may lead to shorter chain lengths and reduces the mechanical properties of the natural fibre. Acetic acid leads to a small form of alkalization (Rong et al., 2001). A modification with acids removes impurities, lowers the hydrophilic nature and results in a rougher surface. In this research, there was no positive influence on the ductile behaviour when using the acetic acid treatment.

Acetylation (AH)

Acetylation makes natural fibres more hydrophobic due to the reaction of hydroxylic groups with acetyl groups (CH_3CO). It reduces the moisture uptake capacity and thus the bio-degradation (Bledzki & Gassan, 1999; John & Anandjiwala, 2008; Kalia et al., 2009). Acetylation changes the hygroscopic nature of the fibres and the adhesion with the surrounding cementitious matrix. The ductile behaviour is similar to or lower than for mixtures with untreated fibres.

A treatment with silanes, acids and acetylation led to an increase in first-cracking-strength in technical flax mixtures. In cottonised flax mixtures the strength was higher after a treatment with 10 m% NaOH and acetylation. Mixtures with non-retted hemp did not show a form of significant different first-cracking-strengths (significance level of 40%). Only acetylation led to a higher strength in mixtures containing slightly-retted hemp.

The ultimate bending strength is reduced with peroxide treatment and N6 and N10 in technical flax mixtures. An increase is found with N10 and acetylation in CF mixtures. No significant differences are found in NH and SH mixtures (50% level).

5.5.4.4 Mechanical properties of the natural fibres

The strength results of the fibres are shown in stress expressed as cN/tex (the conversion to MPa is cN/tex·ρ_{fibre} = MPa with ρ_{fibre} = 1500 kg/m³) (Table 5.7). Due to the natural origin of the fibres, the standard deviation on the single results is noteworthy. The mechanical properties did show a high variation. This is due to natural defects and dislocations which occur regularly in natural fibres and determine the mechanical properties. Zones containing kink bands will hereby preferentially break upon tensile loading.

Table 5.7. Tensile strength, modulus of elasticity and tensile failure strain of the studied natural fibres, after being degraded in an alkaline environment (C) and after being chemically treated (n>30).

Fibre	Tensile strength [cN·tex^{-1}]	Modulus of elasticity [cN·tex^{-1}]	Tensile strain [%]
TF	55 ± 12	2089 ± 179	2.9 ± 0.3
CF	32 ± 10	1580 ± 208	2.3 ± 0.3
NH	34 ± 16	1306 ± 297	2.9 ± 0.2
SH	65 ± 30	1796 ± 372	3.6 ± 0.4
TF(C)	10 ± 4	648 ± 129	1.4 ± 0.2
CF(C)	12 ± 8	562 ± 165	2.0 ± 0.3
NH(C)	14 ± 4	497 ± 114	2.2 ± 0.4
SH(C)	10 ± 6	473 ± 109	2.1 ± 0.3
SH - S	57 ± 20	1168 ± 310	4.5 ± 0.6
SH - S(C)	45 ± 26	1555 ± 504	2.8 ± 0.4
SH - BP	21 ± 8	1226 ± 640	5.1 ± 0.6
SH - BP(C)	41 ± 20	908 ± 295	4.1 ± 0.5
SH - N2	53 ± 20	1419 ± 263	3.6 ± 0.4
SH - N2(C)	73 ± 40	1082 ± 387	4.9 ± 0.6
SH - N6	46 ± 18	1303 ± 545	5.4 ± 0.7
SH - N6(C)	50 ± 26	1086 ± 329	4.4 ± 0.6
SH - N10	35 ± 12	572 ± 82	6.0 ± 0.7
SH - N10(C)	53 ± 32	1164 ± 358	4.5 ± 0.5
SH - AA	36 ± 14	1537 ± 389	2.2 ± 0.4
SH - AA(C)	44 ± 20	1312 ± 489	2.9 ± 0.4
SH - AH	77 ± 31	1686 ± 352	3.8 ± 0.5
SH - AH(C)	64 ± 24	1149 ± 314	4.2 ± 0.4

Measurements of the mechanical properties of the natural fibres showed that TF (821 ± 365 MPa) and SH (972 ± 451 MPa) had significantly larger tensile strengths compared to CF (457 ± 130 MPa) and NH (561 ± 246 MPa) (Table 5.7). The largest stiffness was exhibited by TF (30 GPa) and the largest strain capacity by SH (3.6%), also explaining the larger crack width as seen after four-point-bending in specimens containing hemp fibres. Literature reports strength values between 345

and 2000 MPa for flax fibres (Batra, 1988; Bledzki & Gassan, 1999), mostly between 800 and 1500 MPa, which is also the case in this study (821 ± 365 MPa). The values for the cottonised flax fibres (457 ± 130 MPa), however, are lower compared to literature. In principle, the value should be higher compared to technical fibres due to the bundle-effect (Bos et al., 2002a; van der Zwaag, 1989). But, the mechanical processing of cottonisation to receive elementary fibres, damages the structure of the fibres, reducing the strength. They are also more susceptible to natural defects like kink bands due to their small size. Hemp fibres show strengths of 210 till 900 MPa (Li et al., 2007; Mwaikambo & Ansell, 2002). The found values for non-retted hemp (561 ± 246 MPa) and slightly-retted hemp (971 ± 451 MPa) correspond to these values. The higher value found in slightly-retted fibres is somewhat unexpected. As lignopectin dissolves due to retting, the overall strength should decrease. But, as the fibre diameter is less compared to the green hemp, this could explain the higher found value. Also, the used span length of 10 mm is low, thus less kink bands may be present when testing the material.

Values in this study correspond to values found in literature for the modulus of elasticity (12-100 GPa) and the strain (1-4%) (Batra, 1988; Bledzki et al., 2004; Boghossian & Wegner, 2008; Davies & Bruce, 1998). The strain at failure of the bundle fibres should be higher as more lignopectin is tested. This was the case for TF (2.9% strain) compared to CF (2.3%). The finer SH is stronger due to the partial removal of pectin and hemicellulose due to retting. This leads to individual stronger fibres without impairing the overall strength. The modulus of elasticity (30-70 GPa (Li et al., 2007; Mwaikambo & Ansell, 2006)), is lower than the TF fibres. This is due to the lower spiral angle of the microfibrils of the hemp fibres (Stamboulis et al., 2001). The strain at failure of the fibres (typically 1.6-4%) should be higher compared to flax due to the angle of the microfibrils. This is the case for SH (3.6%) but not entirely significant for NH (2.9%).

Due to the degradation in an alkaline environment (storage in cement filtrate for six months), the tensile properties decreased substantially. Almost no strength remains after degradation. There were no significant differences (significance level of 37.6%) between the different natural fibres. The slightly higher value after six months exposure to cement filtrate in CF fibres compared to TF can be explained by the partial loss of pectin and hemicellulose. In natural fibres, the overall tensile strength loss may be due to the change of cellulose to shorter polymeric chains (Mwaikambo & Ansell, 2006; Pickering et al., 2007). By chemically treating the natural fibres, they are protected from this alkaline environment and the tensile properties are still present. Combination of chemical treatment and exposure to cementitious filtrate induced better mechanical properties than for the non-exposed chemically-treated fibres, possibly due to calcium-nodule formation on the fibres. Only the results for the SH fibres are shown.

When using 10 m% of NaOH solution, the efficiency to counteract the degradation in cement filtrate is clearly visible as the strength value is higher compared to the strength value of the untreated fibre in cement filtrate. On the other hand, too high concentrations of NaOH degrade cellulose to shorter cellulose chains, reducing the tensile strength and the modulus of elasticity (Li et al., 2007; Pickering et al., 2007). A too high increase of mercerization thus tends to reduce

the fibre properties (Pickering et al., 2007), as can be seen in Table 5.7 (decreasing strength from N2 to N10). Due to the more plastic nature of the cellulose in the walls of the natural fibre, the tensile strain increases.

The results for the degradation on the mechanical properties of the natural fibres in an alkaline environment pointed out that the retting of hemp did not have the expected positive influence. Normally, it should reduce degradation due to the partial decrease of the degradable pectin and hemicellulose. Cottonisation should also lead to a better resistance against degradation due to the decrease of those polymers. This was seen in the results as the tensile strength, stiffness and strain at failure were still present even after long-term exposure to an alkaline environment but the results were not significantly different compared to technical flax fibres.

5.5.4.5 Autogenous healing in natural-fibre-reinforced materials

Autogenous healing was observed through microscopic examination of the cracks. After 14 days of healing time, the specimens were microscopically monitored on their crack closing ability. The crack width was hereby measured at the same fixed points. For every crack, the crack width was measured in intervals of 500 µm along the crack (n=10) and the average value was used. There was not a high scatter on the results.

Figure 5.22a shows the crack closure capacity as a function of the crack width for all specimens selected based on the best strain-hardening and crack width properties. All studied cracks are put in one figure to show the overall trend. Great variability was detected in the self-healing of the cracks, as some small cracks did not heal entirely and some larger cracks showed a large amount of crack filling. As anticipated, the mixtures with optimal multiple cracking capacity had the smallest crack widths. Consequently the best self-healing occurred in those mixtures, especially in mixtures reinforced with technical flax (see Table 5.6). It was found that cracks up to 30 µm healed completely and up to 150 µm only partially.

The autogenous healing seemed to be independent of the type of fibre, as can be seen in Figure 5.22b. Here, the average values together with their deviations (on single results) are shown. In intervals of 5 µm, the average values (solid lines) were determined, together with the respective standard deviations (dashed lines) on the single results in an interval of 5 µm. Then, those results were plotted as a scattered region, to obtain the green region for the natural fibres and the blue region (with the bold blue lines) for the synthetic PVA fibres.

The trend is the same and there is no significant difference. The only difference is the nucleation of crystals on the synthetic fibres. These were not considered to be part of the crack healing, only until the healing products completely bridged a crack.

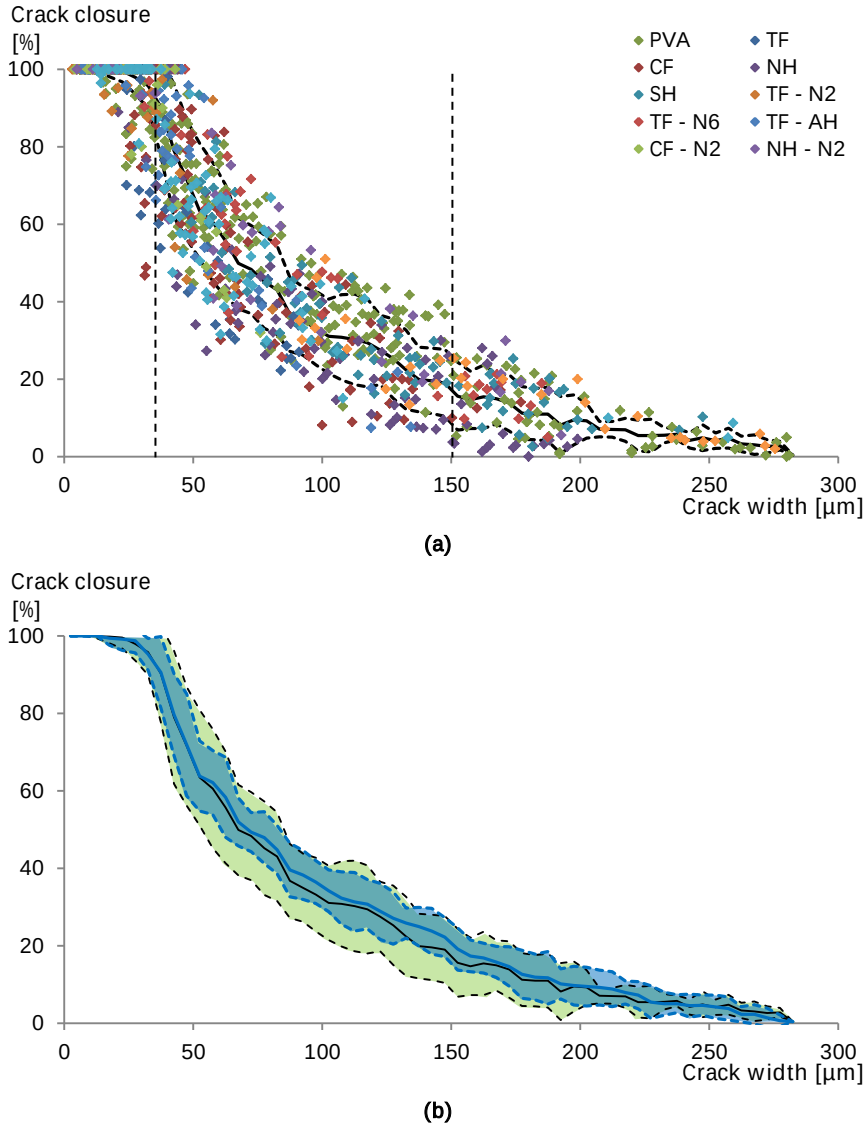

Figure 5.22. Crack closure as a function of the crack width for all specimens **(a)** showing the distribution of the results with the mean average and the standard deviation boundaries on the single results in intervals of 5 µm for mixtures with natural fibres (green region) and synthetic fibres (blue region with bold blue lines) **(b)**.

Generally, it was found that cracks up to 30 µm were able to close in wet/dry cycles and cracks larger than 50 µm did only show some minor form of crack closure. Also literature reports the 30 µm or 50 µm boundary (Yang, 2008) for complete autogenous healing. Hemp fibre mixtures overall show a larger crack width (Table 5.6), which is unwanted to receive optimal autogenous healing.

Figure 5.23 shows a crack of approximately 30 µm in a specimen containing technical flax fibres. Mostly, the cracks close rapidly after only 3-4 wet/dry cycles.

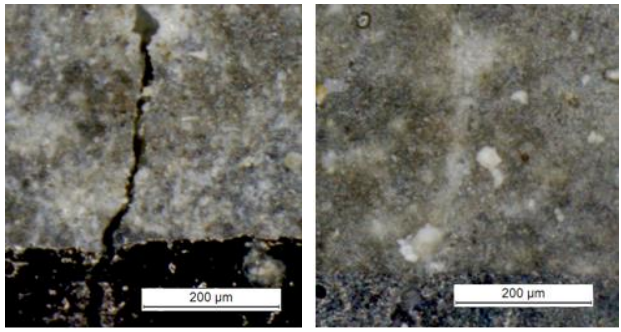

Figure 5.23. Micrographs of a crack before **(a)** and after autogenous healing **(b)** in a specimen containing technical flax. The scale bar amounts to 200 µm.

The hydrophilic natural fibres act as a nucleation site on which the calcium carbonate crystals may grow. This can be seen in Figure 5.24 on a technical flax fibre in a wide crack after seven wet/dry cycles. Furthermore, exposure to a cementitious environment leads to the formation of nodules on the surface of hemp fibres (Sedan et al., 2008a). This could lead to the change in surface roughness as described above. Due to the higher roughness after chemical treatment (2% NaOH) of the natural fibres, the healing products were able to grow in a higher extent on these fibres, leading to a higher amount of total crack healing (up to cracks of 40 µm). However, when increasing the m% of NaOH, this effect diminishes. Nucleation was seen in SH rather than NH due to the retting of the fibre and the better surface and roughness, beneficial for the calcium carbonate crystal adherence.

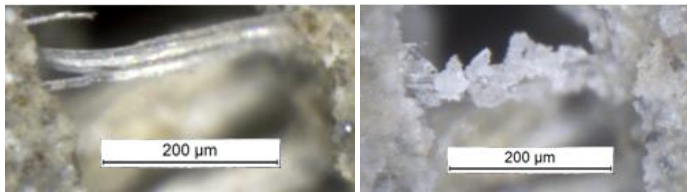

Figure 5.24. Micrograph of nucleation effects on technical flax TF before and after seven wet/dry cycles. The scale bar amounts to 200 µm.

Based on the found results, only the promising mixtures were studied for their regain in mechanical properties. The criterion used was a multiple cracking amount of more than 0.25%. All mixtures showing an average crack width of approximately 30 µm did show a regain in mechanical properties of 35-40% (Table 5.6). Those mixtures are the PVA, TF, CF, TF-N2, TF-AH and CF-N2 mixtures. A crack width of 50 µm approximately only led to a regain of 25% of the first-cracking-strength (TF-N6 and SH-N2 mixtures). Larger cracks up to 150 µm only showed a regain of 10% or lower (NH, NH-N2 and SH-N6 mixtures). The healing capacity is thus mainly dependent on the initial crack width.

5.5.5 Matrix modification, influence of different binders and age

To find the most-ideal mixture for autogenous healing, some parameters were varied (see paragraph 5.2). These were the replacement of cement by fly ash (FA/C = 0/0.5/1) or blast-furnace slag (BFS/C = 0/0.5/1). The sand-to-binder (S/B = 0.35) was kept constant. The water-to-binder ratio was varied as well (W/B = 0.30/0.35/0.40). Those varying parameters should give the most information and influences in terms of autogenous healing as a function of the composition. The most ideal mixture will be selected and used to study the influences of superabsorbent polymers.

The autogenous healing was studied by means of performing four-point-bending tests at several ages (7 days, 28 days, 3 months and 1 year). This should also give information about the extent and type of autogenous-healing mechanism responsible for visual crack closure and the regain in mechanical properties as a function of time. The results considering the average crack width, maximum crack width, number of cracks, multiple-cracking amount, first-cracking-strength and the regain in first-cracking-strength are given in Table 5.8. In this table, the results of the cement mixtures are given first, followed by the fly-ash-blended cement types and the blast-furnace-slag-blended mortars. The crack width, maximum crack width and the regain in first-cracking-strength were determined only on specimens loaded till 1% of initial strain. The number of cracks and multiple-cracking amount were determined on specimens loaded until failure. The first-cracking-strength was determined using the strengths of all studied specimens as this parameter is independent on the loading history.

Multiple cracks needed to be created and an amount of 2 v% of PVA is sufficient to show a pronounced amount of multiple cracking and strain-hardening. When a crack forms, PVA fibres will bridge a crack and due to fibre-bridging action, the stress can still increase until the weakest part of the bridging fibre does not manage to take up the additional forces. The stress keeps augmenting until a previously created crack widens, lowering the stress. This leads to a substantial amount of cracks and thus ductility. In specimens loaded until total failure, sometimes more than 15-20 cracks were formed, showing the high ductility. This is an inherent feature of the pronounced strain-hardening found when using synthetic microfibres.

All cracks were through-going, which is typical for steady-state cracks which are formed when performing four-point-bending tests on mixtures with incorporated synthetic microfibres. The crack width did not vary significantly over the total crack length and all microscopic properties were similar.

All mixtures showed a pronounced strain-hardening effect and multiple cracks were formed. By microscopically studying these cracks, the crack widths could be determined. Most important is the range of crack widths (mean value) and the largest crack. The latter is important as that crack width is mostly the limiting factor for the regain in mechanical properties. If there is one large crack compared to the other cracks, this crack will preferentially open even if the other cracks are ideally and perfectly sealed and healed by healing products.

Table 5.8. Mean values for the crack width [µm], the maximum crack width [µm], the number of cracks [#], the amount of multiple cracking [%], the first-cracking-strength [MPa], and the regain in first-cracking-strength [%] for the studied blended cementitious mixtures, together with their respective standard deviations on single results (n=3). The mixture codes are comprised with a letter (C stands for cement, F for fly ash and B for blast-furnace slag), followed by the amount of replacement of cement by SCMs (SCM/C=0.5 or 1) and the water-to-binder ratio (W/B=0.30/0.35/0.40). The results are shown as a function of time (after 7 days, 28 days, 3 months and 1 year).

		Crack width [µm]	Maximum crack width [µm]	Number of cracks [#]	Multiple-cracking amount [%]	First-cracking-strength [MPa]	Regain in first-cracking-strength [%]
C0030	7 days	18 ± 7	54	9-15	2.7 ± 0.2	5.5 ± 1.2	48 ± 9
	28 days	17 ± 8	44	8-11	2.0 ± 0.4	5.9 ± 0.9	40 ± 8
	3 months	16 ± 6	31	8-12	2.1 ± 0.6	6.5 ± 1.0	35 ± 4
	1 year	16 ± 8	35	4-7	1.2 ± 0.5	8.0 ± 1.2	34 ± 3
C0035	7 days	21 ± 10	50	8-18	3.0 ± 0.2	5.2 ± 1.3	48 ± 7
	28 days	20 ± 11	46	10-14	2.2 ± 0.4	5.2 ± 1.1	40 ± 7
	3 months	18 ± 11	39	8-18	2.0 ± 0.7	6.2 ± 0.4	36 ± 6
	1 year	14 ± 6	24	6-8	1.5 ± 0.4	5.9 ± 0.5	32 ± 5
C0040	7 days	16 ± 10	48	12-16	2.2 ± 0.2	3.6 ± 0.6	50 ± 8
	28 days	13 ± 11	44	10-12	2.4 ± 0.5	3.7 ± 0.9	38 ± 8
	3 months	15 ± 11	41	5-11	1.2 ± 0.6	4.3 ± 1.4	31 ± 7
	1 year	12 ± 6	30	5-7	0.6 ± 0.5	4.6 ± 0.5	27 ± 3

F0530	7 days	22 ± 7	44	18-24	2.2 ± 0.6	3.9 ± 0.1	53 ± 8
	28 days	22 ± 8	40	8-10	1.6 ± 0.3	5.9 ± 0.7	52 ± 8
	3 months	17 ± 10	29	5-11	1.1 ± 0.6	6.4 ± 0.9	47 ± 7
	1 year	13 ± 7	39	5-6	1.0 ± 0.5	6.8 ± 0.6	40 ± 1
F0535	7 days	25 ± 14	50	8-10	2.1 ± 0.4	3.8 ± 0.1	43 ± 8
	28 days	22 ± 17	48	11-14	1.7 ± 0.4	4.7 ± 0.4	40 ± 5
	3 months	22 ± 11	37	6-12	1.9 ± 0.4	5.8 ± 0.8	43 ± 7
	1 year	24 ± 13	49	5-12	1.6 ± 0.4	5.5 ± 0.6	37 ± 9
F0540	7 days	25 ± 12	58	4-8	2.1 ± 0.2	2.9 ± 0.1	49 ± 7
	28 days	26 ± 14	60	10-13	2.3 ± 0.5	4.0 ± 0.6	42 ± 8
	3 months	23 ± 12	55	8-15	1.9 ± 0.8	4.1 ± 0.8	36 ± 6
	1 year	16 ± 9	43	4-5	1.0 ± 0.5	4.5 ± 0.7	27 ± 2
F130	7 days	24 ± 12	49	24-30	5.4 ± 0.6	4.5 ± 0.3	59 ± 9
	28 days	20 ± 11	42	10-18	2.9 ± 0.6	4.8 ± 0.6	45 ± 7
	3 months	16 ± 10	35	8-12	2.4 ± 0.4	5.4 ± 0.5	42 ± 5
	1 year	11 ± 7	30	6-12	1.8 ± 0.5	6.0 ± 0.5	35 ± 6
F135	7 days	21 ± 7	55	16-18	2.9 ± 0.5	3.3 ± 0.3	53 ± 8
	28 days	19 ± 7	54	10-17	2.3 ± 0.5	4.1 ± 0.6	43 ± 5
	3 months	17 ± 8	47	7-14	1.9 ± 0.5	4.4 ± 0.9	44 ± 2
	1 year	17 ± 8	43	8-12	2.1 ± 0.5	4.4 ± 0.6	41 ± 8
F140	7 days	24 ± 10	56	6-8	2.5 ± 0.2	2.5 ± 0.1	59 ± 8
	28 days	22 ± 15	46	9-14	2.5 ± 0.4	3.6 ± 0.5	54 ± 7
	3 months	16 ± 8	36	6-17	2.0 ± 0.6	3.9 ± 0.7	49 ± 6
	1 year	16 ± 7	30	4-5	0.9 ± 0.4	4.0 ± 0.2	43 ± 6

B0530	7 days	32 ± 13	51	8-12	2.4 ± 0.3	4.9 ± 0.4	46 ± 8
	28 days	29 ± 11	55	9-12	2.1 ± 0.5	5.1 ± 0.9	41 ± 7
	3 months	25 ± 16	46	8-11	2.0 ± 0.8	6.0 ± 1.0	44 ± 7
	1 year	26 ± 12	56	4-5	0.6 ± 0.3	6.7 ± 0.4	32 ± 6
B0535	7 days	31 ± 13	64	9-15	2.3 ± 0.2	4.3 ± 0.3	51 ± 8
	28 days	30 ± 15	64	12-17	2.4 ± 0.5	4.8 ± 0.4	49 ± 8
	3 months	32 ± 14	57	7-11	2.4 ± 0.6	4.9 ± 0.9	45 ± 8
	1 year	26 ± 11	47	7-9	1.7 ± 0.5	6.0 ± 0.7	32 ± 2
B0540	7 days	31 ± 12	65	8-18	2.8 ± 0.2	3.9 ± 0.3	53 ± 4
	28 days	31 ± 16	64	10-16	2.7 ± 0.5	4.0 ± 0.8	46 ± 7
	3 months	28 ± 10	59	8-11	2.2 ± 0.6	4.4 ± 0.5	43 ± 3
	1 year	22 ± 11	45	8-10	2.2 ± 0.5	4.2 ± 0.6	43 ± 3
B130	7 days	33 ± 15	68	10-16	3.3 ± 0.4	4.0 ± 0.2	57 ± 8
	28 days	37 ± 21	64	10-12	2.4 ± 0.5	5.5 ± 0.7	43 ± 7
	3 months	31 ± 15	49	7-10	2.2 ± 0.6	6.2 ± 0.6	42 ± 7
	1 year	28 ± 9	33	6-10	0.7 ± 0.5	7.6 ± 0.9	36 ± 8
B135	7 days	31 ± 12	64	15-25	4.0 ± 0.6	3.2 ± 0.3	57 ± 3
	28 days	26 ± 19	54	10-16	2.4 ± 0.4	3.5 ± 0.7	48 ± 7
	3 months	29 ± 10	43	7-12	1.6 ± 0.6	4.7 ± 0.8	42 ± 8
	1 year	22 ± 9	37	6-10	0.4 ± 0.4	5.7 ± 0.3	37 ± 8
B140	7 days	28 ± 15	58	6-9	2.5 ± 0.2	2.3 ± 0.3	51 ± 6
	28 days	26 ± 12	52	10-18	2.8 ± 0.4	3.0 ± 0.7	45 ± 7
	3 months	29 ± 17	47	7-12	1.7 ± 0.3	3.6 ± 0.8	37 ± 6
	1 year	22 ± 5	22	5-10	1.7 ± 0.5	4.0 ± 0.8	34 ± 5

With increasing age, the crack width decreases. This is due to the stronger cementitious matrix with time due to hardening and thus the more fibre-pull-out force needed, leading to the lower pull-out length of the separate fibres and thus lower crack width. This was also found in literature (Kan & Shi, 2012; Yang et al., 2011). The differences between the different mixtures are mainly due to the differences in matrix properties. The differences in crack width are not significantly different, but sometimes a lower crack width is found in fly-ash systems. Generally, the crack widths are lower than in literature (16 cracks with average diameter of 39 µm and maximum of 60 µm at an age of 3 days (Yang et al., 2011) and average crack width of 29-35, 24-31 and 15-17 µm after 3 days, 28 days and 3 months, respectively (Kan & Shi, 2012; Yang et al., 2007a)) due to a different mixture composition, the use of different raw materials and possible differences in age. The same conclusions can be drawn about the largest crack width.

The blast-furnace slag mixtures tend to show a higher mean crack width compared to the cement references and the fly-ash mixtures. In literature, a smaller crack width is observed when combining limestone powder with blast-furnace slag (Zhou et al., 2010).

A higher water-to-binder ratio tends to increase the mean and maximum crack width. This is likely due to the less-strong cementitious matrix. A lower water-to-binder ratio was not workable and a higher water-to-binder ratio led to segregation of the mixture which was also unwanted.

Most of the mixtures are within the wanted 30 µm crack width boundary to show optimal autogenous-healing opportunities, if loaded till 1% of strain.

The number of cracks and the amount of multiple cracking are closely related. As the cracks are almost constant, a higher amount of cracks leads to a higher amount of multiple cracking. The higher the ductility, the better is the possible autogenous-healing capacity. The highest ductility is found when cracking the specimens at an age of 7 days, and decreases with increasing age. This is due to the hardening of the cementitious matrix in time, reducing the ductile capacity. This is mainly due to the stronger matrix, influencing the crack-tip and strength criterion to obtain strain-hardening cementitious materials (Chapter 1). With increasing water-to-binder ratio, the amount of multiple cracking (and number of cracks) decreases. This is due to the change in strength criterion. A lower water-to-binder ratio is thus wanted. This lower ratio is also more preferential and beneficial in terms of autogenous healing as more building blocks will be available upon crack formation. Using fly ash increases the multiple-cracking behaviour. This is due to the smaller and rounder shape of the fly ash, increasing the self-compacting properties and the strain-hardening behaviour. An even higher amount of fly ash would decrease this property. Replacement of part of the cement by blast-furnace slag also tends to increase this multiple-cracking ductility but is not optimal for a water-to-binder ratio of 0.30, but rather at 0.35. The highest ductility is found in the F130 mixture (FA/C=1 and W/B=0.30), followed by the B135, B130, C0035 and F135 mixtures. The strain capacity follows the same trend as in literature and the values for the strains are comparable (Kan & Shi, 2012; Yang et al., 2007a; Yang et al., 2011).

The influence of the age on the strength criterion to obtain a strain-hardening cementitious material is also reflected in the value of the first-cracking-strength. The strength increases in time during hardening, which is logical. All strength values are within the same range and are typical values for strain-hardening cementitious materials (Li, 2008; Yang, 2008; Yang et al., 2007a; Yang et al., 2009). The regain in mechanical properties, in this case the first-cracking-strength, when storing specimens in wet/dry cycles is dependent on the age of the specimen. The older the specimen, the lower the regain in mechanical properties is. This is due to the further hydration and stiffening of the cementitious matrix in time. This leads to a lower amount of available building blocks for the autogenous-healing mechanisms. The amount of healing also tends to decrease with increasing water-to-binder ratio, but the differences are not statistically significant. Again, this reduces the amount of available building blocks as less unhydrated particles remain within the cementitious matrix. However, using fly ash and blast-furnace slag, increases the amount of regain in mechanical properties. The pozzolanic reaction by the fly ash and the latent-hydraulic reaction of the blast-furnace slag seem promising for the autogenous healing. Fly ash continues to hydrate after 28 days, and the hydrated products may heal the cracks, increasing the self-healing ability. This was also found by (Jacobsen et al., 1995; Termkhajornkit et al., 2009; Zhou et al., 2011). In the long term, $Ca(OH)_2$ may not exist anymore due to carbonation, explaining the lower regain in mechanical properties at later ages as the pozzolanic reaction slows down.

At early age there is more further hydration combined with calcium-carbonate crystallization and from 3 months onwards, the main healing mechanism is the precipitation of $CaCO_3$. This was also seen in literature (Van Tittelboom et al., 2012b). The amount of white precipitated healing products was higher in specimens with a higher water-to-cement ratio. This is due to the higher amount of available $Ca(OH)_2$ which is used for the $CaCO_3$ precipitation. This is the case in the reference samples and the samples with fly ash. The samples with blast-furnace slag are the other way around.

A remark can be made. The matrix is composed out of C-S-H, CH and alkali oxides. If more C-S-H is formed, the pH value is expected to decrease, especially when high amounts of fly ash are available in the composite. The formation of $CaCO_3$ could hereby be limited (due to the reduced pH level). This was not the case in the studied mixtures in this research. The pH value of the intruding fluid inside a crack is dependent on the fluid composition itself rather than the mixture composition. In time, the leaching out of products may change the pH-value.

The specimens with fly ash closed better in comparison with the samples with pure cement and blast-furnace-slag-blended mortars. Better visual healing is achieved with a lower water-to-cement ratio and with fly ash. The best results are obtained with 0030, F0530, F0535, F130 and F135. The F0530 and F130 mixtures showed the best overall results considering the visual healing.

The best overall mixture (considering all aspects) was F130 and this mixture was studied in detail in different curing conditions. It possesses a high strain-hardening effect and small healable cracks. Superabsorbent polymers were also included and their effects were also studied in great detail.

5.6 Superabsorbent polymers to provide the necessary water

To study the effects of superabsorbent polymers on the autogenous healing properties, the mixtures in paragraph 5.2 (Table 5.1) were used.

Internal-water supply by means of SAPs has a positive influence on the amount of stimulated autogenous healing. SAPs can sustain hydration by yielding their absorbed water and provide water for the formation of healing products. Deposition of crystals is not only due to further hydration, but mainly due to precipitation of $CaCO_3$ crystals. In this case, CO_2 dissolves in water to react with Ca^{2+} present in the mortar matrix.

By examining the crack width before and after curing, the percentage of crack closure can be quantified. The microscopic visual crack closure of reference specimens without SAPs in wet/dry cycles, at a relative humidity of more than 90% and at a relative humidity of 60%, is shown in Figure 5.25. Figure 5.26 gives the results for specimens containing superabsorbent polymers stored in the same healing conditions. Both figures are set aside each other for comparative reasons.

Results show that cracks up to 30 µm heal completely and up to 150 µm heal partly when specimens without SAPs are subjected to 28 wet/dry cycles. The cracks steadily close in time. Also Li *et al.* proved this, but their limit was 50 µm instead of 30 µm (Li, 2008; Şahmaran et al., 2013; Yang, 2008). They also showed that, in the presence of air (without any water available), samples cannot heal. Figure 5.25 shows that at a relative humidity of more than 90%, there is only partial and minor healing. At 60% RH, the formation of healing products in a crack is non-existing.

In specimens with SAPs, however, some healing occurred as crack closure was noticed visually (1B - 60 and 1B - 90). This means that SAPs are able to provide water to the cementitious matrix for healing. SAPs are thus able to fulfil the criterion about exposure to environmental conditions. SAPs are able to take up four times their weight in moisture from the environment (Chapter 2). Due to possible suction of the mortar matrix, the water is provided to the cementitious matrix. This causes autogenous healing to occur as further hydration of the hitherto unhydrated cement grains.

Storing pure cement in humid conditions only ages the cement. But when SAPs are added as well, some hard hydrated parts in the vicinity of the SAPs are found. This led to the conclusion that SAPs are able to provide water towards the cementitious matrix due to possible small changes in relative humidity.

Cracks smaller than 30 µm exposed to wet/dry cycles healed completely both with and without SAPs. Cracks between 50 µm and 150 µm healed partly in samples without SAP, but for samples containing SAP B, even a 138 µm crack closed completely after 28 wet/dry cycles (Figure 5.27). With superabsorbent polymers, there is a higher amount of formed healing products in a crack. So, not only narrow cracks up to 30 to 50 µm are able to heal, but cracks up to 130 µm and further. On the inner part of the crack faces the same white material was noticed as at the surface, which can be attributed to the precipitation of $CaCO_3$. Cracks larger than 200 µm showed almost no healing. This is more or less in correspondence with findings of (Yang, 2008) on the same mixture without SAPs, who observed total healing of cracks smaller than 50 µm and partial healing of cracks up to 150 µm.

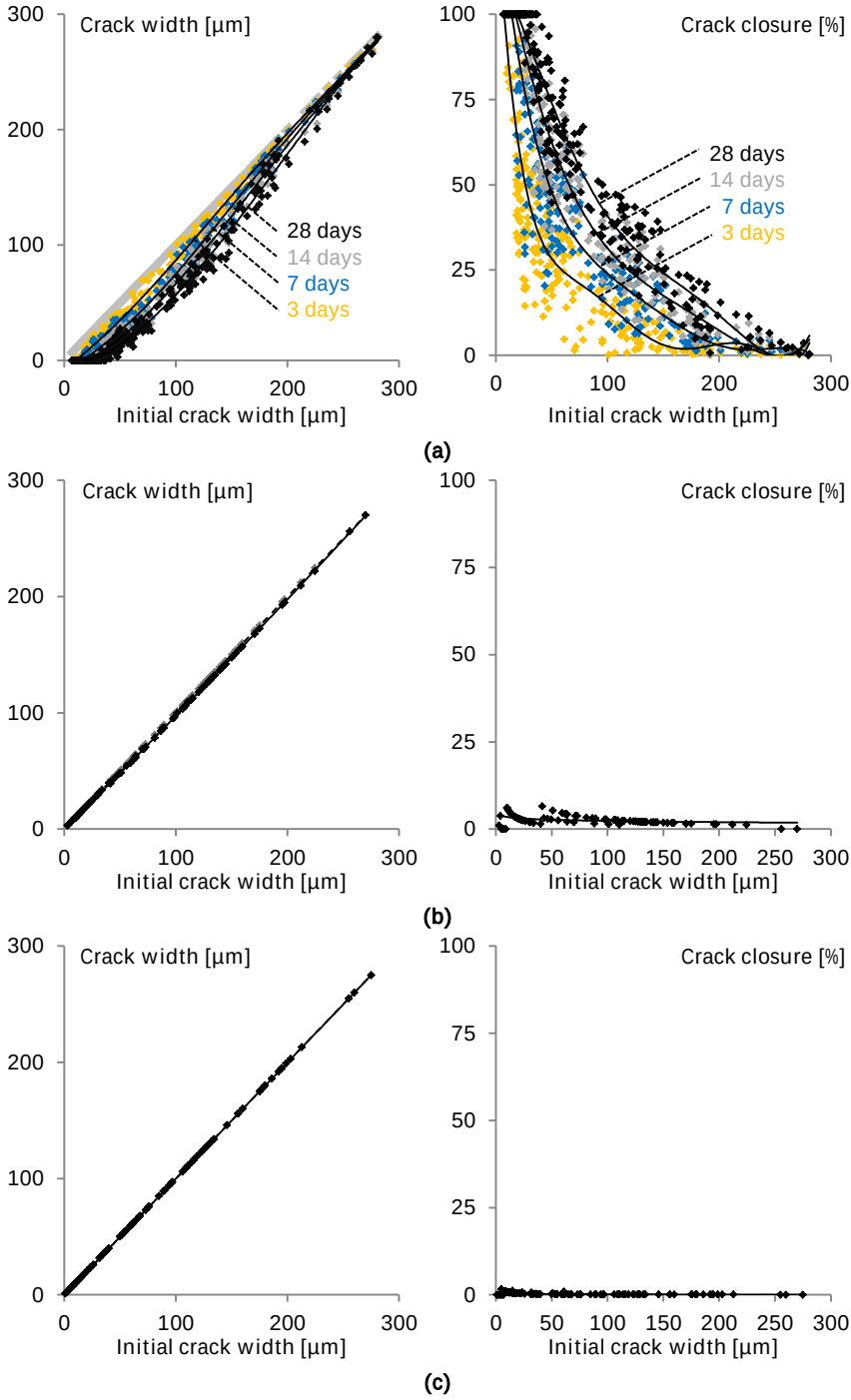

Figure 5.25. Specimens without SAPs healed in wet/dry cycles (after 3, 7, 14 and 28 cycles) **(a)**, at a relative humidity of more than 90% (28 days) **(b)** and at 60 % (28 days) **(c)**, showing the crack closure as a function of the initial crack width.

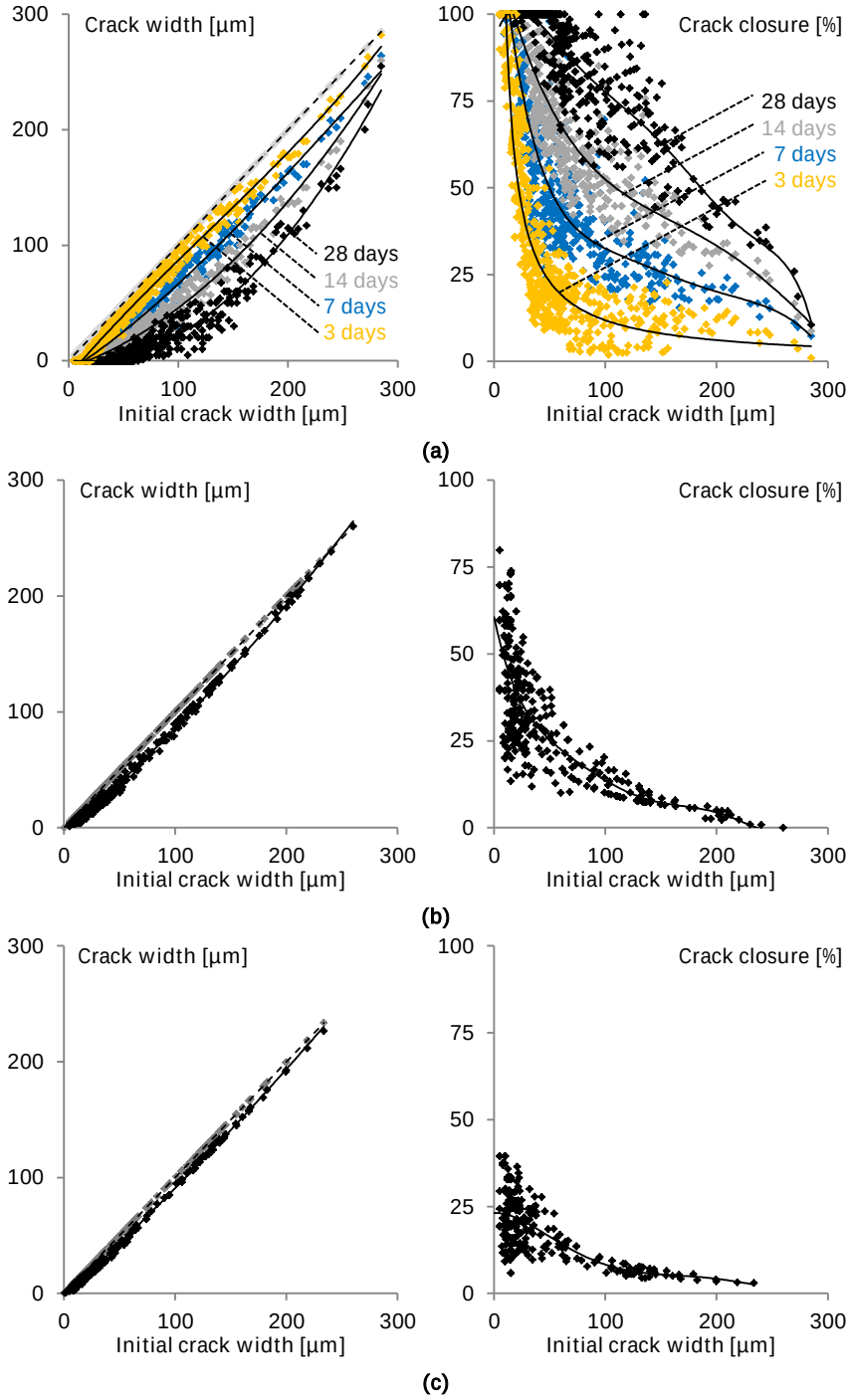

Figure 5.26. Specimens with 1 m% SAP B healed in wet/dry cycles (after 3, 7, 14 and 28 cycles) **(a)**, at a relative humidity of more than 90% (28 days) **(b)** and at 60 % (28 days) **(c)**, showing the crack closure as a function of the initial crack width.

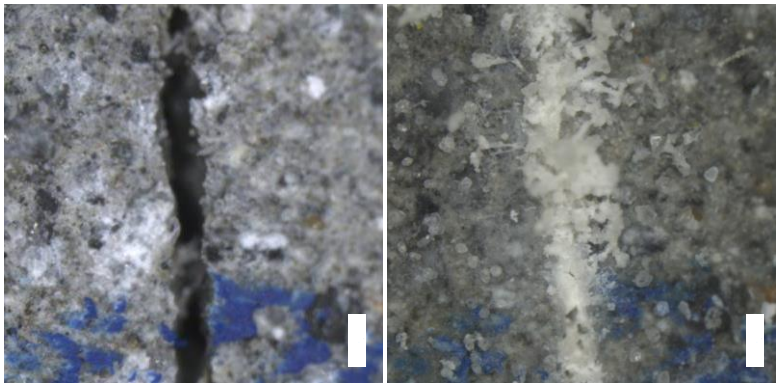

Figure 5.27. Total healing of a 138 µm crack of a specimen containing 1 m% SAP B after wet/dry cycles. The scale bars have a height of 200 µm.

Comparing the different healing conditions (Figure 5.28), storing the specimens in wet/dry cycles gives the highest amount of crack closure due to the higher available amount of water for autogenous healing. Using superabsorbent polymers enhances/promotes this healing as again more water and/or moisture is available. The water is thus an important factor in terms of autogenous healing and superabsorbent polymers are able to fulfil this condition as they are able to provide water towards the cementitious matrix in dry period as well. Up to 30 µm crack widths, 100% of the total crack is able to visually close in SAP and REF specimens. At a RH>90% this is reduced to 40-50% in SAP specimens and only 5% in REF specimens. At a RH=60%, 20% of the crack is still able to close in SAP specimens and there is almost no (0%) healing in REF specimens.

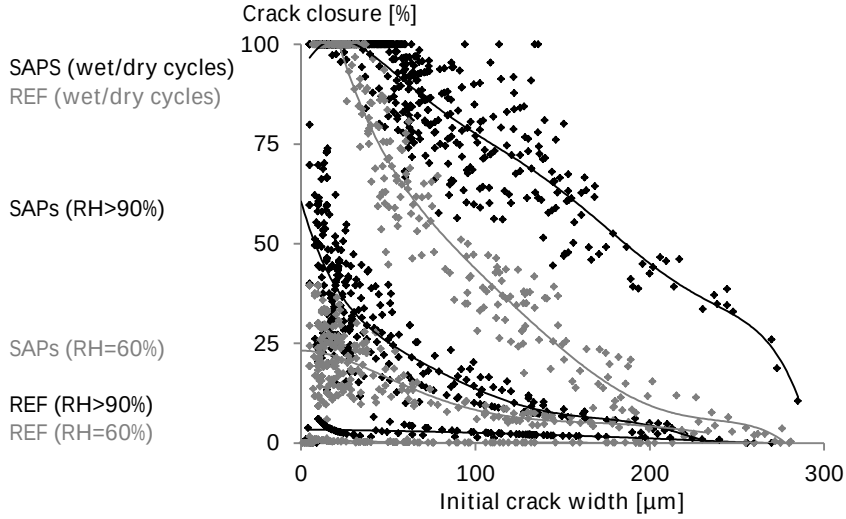

Figure 5.28. Closure of the cracks [%] after curing as a function of initial crack width [µm] by performing microscopic analysis for the different healing conditions.

The cracks close at a specific rate when the specimens are stored in wet/dry cycles (Figure 5.29). In reference samples this rate is 15-8-5-5 µm after 3-7-14-28 days, thus 5 µm/day (15/3) after 3 days, 2 µm/day (8/(7-3)) after 7 days, 0.7 µm/day (5/(14-7)) after 14 days and 0.4 µm/day (5/(28-14)) after 28 days. For specimens containing SAPs, this is 15-25-15-15 µm and thus 5 µm/day after 3 days, 6 µm/day after 7 days, 2.1 µm/day after 14 days and 1.1 µm/day after 28 days. The rate is different because SAPs are able to provide their absorbed water towards the cementitious matrix even in dry periods. This steady release of water is ideal and beneficial to promote autogenous healing in the form of further hydration and/or calcium carbonate crystallisation. The latter mechanism is most occurring.

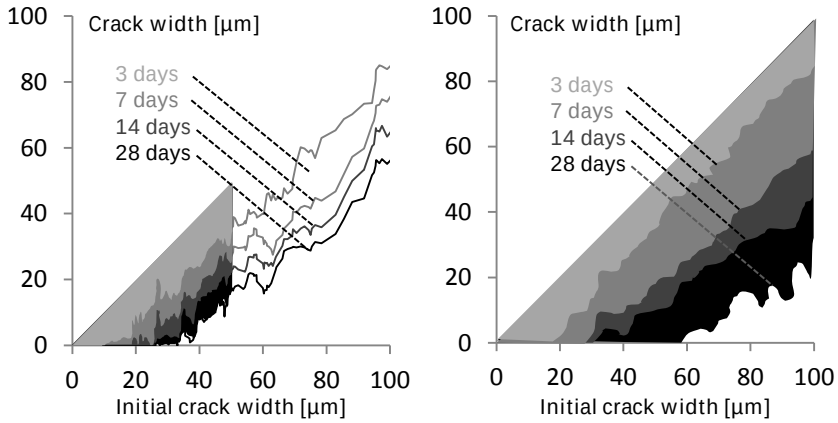

Figure 5.29. Rate of crack closure after 3, 7, 14 and 28 wet/dry cycles for reference samples (left) and specimens containing SAPs (right).

To conclude, the main healing mechanism is the formation of calcium carbonate crystals, which is enhanced by the use of superabsorbent polymers (Figure 5.30). Together with water and dissolved calcium dioxide, the white $CaCO_3$ are deposited in the crack, completely sealing it from intruding aggressive substances.

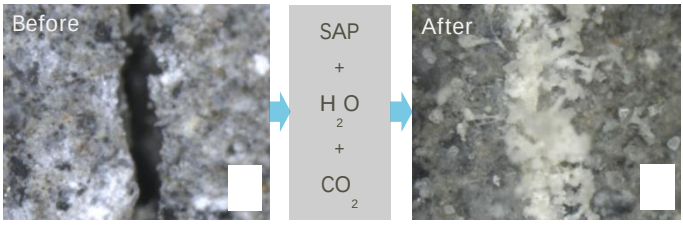

Figure 5.30. For specimens containing SAP particles, cracks up to 130 µm can close due to autogenous crack healing. The scale bars have a height of 200 µm.

Cracks may close with deposited crystals, but what about the strength of the new material? To answer this question, the properties of the basic material need to be investigated.

5.7 Regain in mechanical properties with SAPs

5.7.1 Promoting self-healing by means of SAPs

Important properties are the strength and the regain in strength of the cementitious materials with and without superabsorbent polymers. The studied mixtures are described in paragraph 5.2 in Table 5.1. The studied basic mixture was REF (F130), which showed the best results in terms of ductility, crack widths, strength and autogenous healing. The SAPs were added to further improve this autogenous healing, independent from ambient conditions. Additional water was used to compensate for the loss in workability.

To study the regain in mechanical properties, the strain at the bottom of the specimen was limited to 1%. All specimens in this study showed four to five cracks when loaded to 1% strain. The crack width was hereby always limited to 30 µm in all specimens, which is ideal for autogenous healing. The cracks were measured in the unloaded residual stage and there was strain in the matrix itself as well.

Not only are cracks able to visually close (previous paragraph), the composite is able to regain some of its mechanical properties. All results are shown in Table 5.9. In this table, the crack width, maximum crack width, number of cracks, multiple-cracking amount, first-cracking-strength and the regain in first-cracking-strength in the three different storage conditions are given. The three storage conditions are storage in wet/dry cycles (1 hour in water and 23 hours in standard laboratory conditions), at a relative humidity of more than 90% and at a relative humidity of 60%. The temperature was always 20 ± 2°C and the healing period was 28 days, as described in paragraph 5.3. The total number of cracks, multiple-cracking amount and part of the first-cracking-strengths were determined on specimens loaded until failure to induce complete strain hardening.

From the results from the last paragraph, we expect a full regain in mechanical properties in the specimens stored in wet/dry cycles, and partial healing in specimens containing superabsorbent polymers when stored at a relative humidity condition. The reference samples without superabsorbent polymers are expected to show no regain in mechanical properties in a moist environment as no water will be present to induce autogenous healing.

The mean crack widths are not statistically significant from each other between the different mixtures and decrease with age. This is due to the hardening of the cementitious matrix. The maximum crack width is also not statistically different. Superabsorbent polymers do not have an influence on the properties of the cementitious matrix when additional water is used; they only facilitate multiple cracking and the cracks are alike. Due to this facilitating, the amount of cracks is slightly higher in specimens loaded until failure, as is the amount of multiple cracking. There is no significant difference at an age of 7 days, but from 28 days onwards, the amount of multiple cracking is increased in specimens containing SAPs. A very fine cracking pattern is found at 7 days, with specimens showing up to 30 cracks. This is beneficial as at this loading, one single large crack would be formed if no microfibres were used. This is a strong positive influence to receive a high regain in mechanical properties and this is even further improved by using SAPs.

Table 5.9. Mean values and standard deviations for the crack width [µm], the maximum crack width [µm], number of cracks [#], the amount of multiple cracking [%], the first-cracking-strength [MPa], and the regain in first-cracking-strength [%] for the studied cementitious mixtures based on F130 with superabsorbent polymers, with their respective standard deviations on single results (n=3).

		Crack width [µm]	Maximum crack width [µm]	Number of cracks [#]	Multiple-cracking amount [%]	First-cracking-strength [MPa]	Regain in first-cracking-strength [%] wet/dry cycles	Regain in first-cracking-strength [%] RH>90%	Regain in first-cracking-strength [%] RH=60%
REF	7 days	24 ± 12	49	24-30	5.4 ± 0.6	4.5 ± 0.3	59 ± 9	7 ± 2	1 ± 1
	28 days	20 ± 11	42	10-18	2.9 ± 0.6	4.8 ± 0.6	45 ± 7	7 ± 1	1 ± 1
	3 months	16 ± 10	35	8-12	2.4 ± 0.4	5.4 ± 0.5	42 ± 5	7 ± 1	1 ± 1
	1 year	11 ± 7	30	6-12	1.8 ± 0.5	6.0 ± 0.5	35 ± 6	6 ± 1	0 ± 1
0.5A	7 days	23 ± 10	51	20-30	5.1 ± 1.2	4.9 ± 0.4	74 ± 9	49 ± 7	27 ± 6
	28 days	18 ± 10	40	7-18	3.5 ± 0.4	4.9 ± 1.5	65 ± 2	51 ± 3	29 ± 9
	3 months	16 ± 9	32	6-14	2.6 ± 0.4	5.3 ± 2.2	59 ± 2	46 ± 2	28 ± 9
	1 year	10 ± 6	28	8-15	2.2 ± 1	5.6 ± 2	45 ± 1	33 ± 3	19 ± 4
0.5B	7 days	22 ± 10	50	13-19	4.9 ± 0.2	4.6 ± 0.5	72 ± 4	58 ± 5	33 ± 2
	28 days	19 ± 11	41	8-18	3.5 ± 0.3	5.1 ± 1.1	69 ± 3	54 ± 3	35 ± 7
	3 months	17 ± 9	34	7-16	2.8 ± 0.4	5.2 ± 1	65 ± 6	44 ± 2	26 ± 2
	1 year	11 ± 8	28	8-16	2.5 ± 0.3	5.5 ± 2	53 ± 2	44 ± 5	21 ± 4
1B	7 days	21 ± 9	46	20-30	5.5 ± 0.1	4.7 ± 0.4	87 ± 6	61 ± 4	45 ± 8
	28 days	21 ± 10	42	14-24	3.8 ± 0.4	4.9 ± 0.9	86 ± 8	64 ± 8	44 ± 2
	3 months	13 ± 10	30	10-25	3.1 ± 0.2	5.3 ± 1.8	81 ± 8	62 ± 9	43 ± 3
	1 year	12 ± 6	28	8-21	2.6 ± 0.6	5.5 ± 1.3	65 ± 5	54 ± 3	32 ± 2

SAP particles form macro pores due to desorption of the SAPs during cement hydration. Such a system of voids facilitates multiple cracking. Samples containing SAPs showed an alteration of the multiple-cracking behaviour. Besides reopening of the previously formed cracks, even new cracks were formed. Some new cracks were not located in the vicinity of previously healed cracks. Healing of the cracks resulted in regained mechanical properties and a total healing of prisms was observed. Air voids – and thus also SAP macro pores – act as crack initiators, so the crack path likely follows the position of macro pores. The SAPs are thus available for swelling upon crack formation as the crack runs through the formed pore.

With increasing age, the building blocks will become exhausted. This will also lead to a lower amount of autogenous healing as the healing relies on the amount of unhydrated cement particles, $Ca(OH)_2$, unhydrated parts of the pozzolanic fly ash and the amount of leachable Ca^{2+} ions present in the matrix. As already found previously, the healing mechanism changes in time due to the changing availability of building blocks. At early age, more further hydration will occur but later-on, the calcium-carbonate crystallization will govern the overall healing.

At an age of 7 days and 28 days of healing, the self-healing mechanism is mostly the stitching of the crack by further hydration and calcium carbonate around SAPs, which results in dome formation as well (Chapter 4). In samples with an age of 28 days, there is a little bit more $CaCO_3$ in the crack. With a sample age of 3 months, there is mainly $CaCO_3$ on the crack faces. New formed cracks seem strong enough and sometimes new cracks are formed, or follow other pathways than the previously formed and healed cracks.

The first-cracking-strength of the different test series (0 and 1B) cracked at 7 days and stored at different healing conditions for 28 days can be compared (Figure 5.31). No significant differences exist between the stress values measured for samples with and without SAPs. SAPs have a dual effect on the strength (Hasholt et al., 2012) (see Chapter 3). On one hand they will increase the strength due to the further hydration by the release of mixing water in time during hardening of the cementitious matrix (i.e. due to internal curing). But, on the other hand, they will decrease the strength due to the formation of macro pores (see Chapter 3). Both influences combined leads in this case to an equivalent first-cracking-strength in these strain-hardening mixtures with a low water-to-binder ratio. Overall, the strength is not significantly different between all studied samples. The amounts of SAPs were limited to 0.5 m% and 1 m% in case of SAP A and SAP B, respectively. These amounts did not show a decrease in mechanical properties.

When incorporating 1 m% SAP A, however, the strength decreases (Table 5.10). The difference noticed between the strength of samples with SAPs is due to the smaller particle size of SAP A (100 ± 21 µm) compared to SAP B (477 ± 59 µm). By mixing the same weight of small particles compared to the same weight of large particles, the surface area available for taking up tensile forces is reduced more, as more particles may intersect the tensile plane. A cross section of a sample containing a large amount of small SAP A particles showed a greater reduction of the available area of solid material due to the formation of macro pores, than a sample containing the same amount of larger SAP B. Mönnig (2009) also found that

the particle size has an influence on the tensile strength. Two mixtures with the same SAP volume (same density of SAP A and SAP B) but with small and large particle sizes, will lead to a reduced tensile strength of the samples with small particles due to more summarized void cross-sections in a random plane. Also, the smaller but not perfect spherical particles could act as stress inducing voids (Mönnig, 2009). A SAP B content of 1 m% relative to the cement weight gives analogous properties of the first-cracking-strength compared to the REF-samples without SAPs. The first-cracking-strength, however, decreases with increasing m% of SAP due to a decrease of the matrix surface area. If the amount of SAP B is increased further, the strength would also decrease substantially (Table 5.10). A higher amount of SAPs would lead to an unwanted significant decrease in strength. A sample containing 4 m% of SAP B was porous due to the formation of a large number of macro pores and had low mechanical properties (more than 50% reduction of first-cracking-strength). This amount of superabsorbent polymers is rather high compared to literature, as only 0.3-0.6 m% SAP (Jensen & Hansen, 2002) or 0.4 m% SAP (Brüdern & Mechtcherine, 2010) is used to reduce the shrinkage by internal curing (also see Chapter 3). In this investigation, the amount of SAP was altered up to 4 m% only to investigate the self-healing properties. This mass percent is approximately ten times higher than the beneficial amount of SAPs for internal curing and thus not to impair the mechanical properties too much.

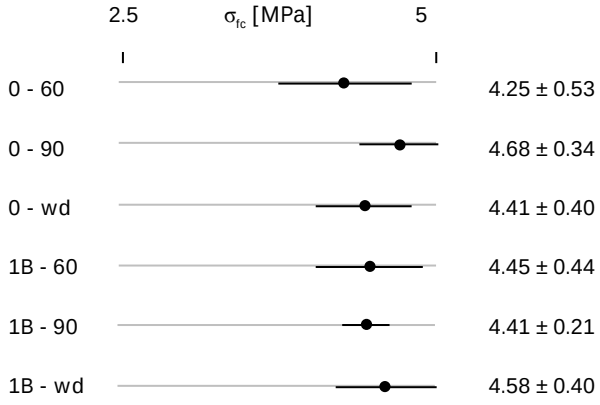

Figure 5.31. First-cracking-strength [MPa] for the different investigated mortar specimens; error bars indicate the standard deviation on the single values (n=3).

Table 5.10. Mean values and standard deviations for (regain in) first-cracking-strength and peak strength for virgin and healed specimens stored in wet/dry cycles with 1A containing 1 m% of cement weight SAP A and 2B, 4B containing 2 m%, 4 m% SAP B.

	σ_{fc} [MPa]	regain σ_{fc} [%]	σ_{cu} [MPa]	regain σ_{cu} [%]
1A	3.1 ± 0.4	78.9 ± 5.3	4.9 ± 0.3	52.5 ± 7.6
2B	2.9 ± 0.3	116.5 ± 13.3	5.1 ± 0.5	73.2 ± 9.0
4B	1.5 ± 0.2	243.1 ± 34.5	3.0 ± 0.8	108.6 ± 13.4

After cracking, the specimens were stored in several curing conditions to study the effects on autogenous healing in mixtures with and without SAPs. In the meantime, the specimens were thus microscopically monitored in time. By microscopically studying the crack before and after the healing, the amount of autogenous healing products could be quantified (previous paragraph). It was found that cracks up to 30 µm were able to close complete in wet/dry cycles. This 30 µm criterion is more severe compared to the 50 µm criterion found in literature (Yang et al., 2009). SAPs have an additional effect on the healing capacity as their water is released steadily to the cementitious matrix during dry periods. Even cracks up to 138 µm were able to close completely. This is mainly due to the crystallization of $CaCO_3$, as can be seen in a larger crack of a totally-cracked specimen in Figure 5.32. The microfibres themselves are also useful to promote autogenous healing as they serve as a nucleation site for $CaCO_3$ crystals, as also seen by (Homma et al., 2009).

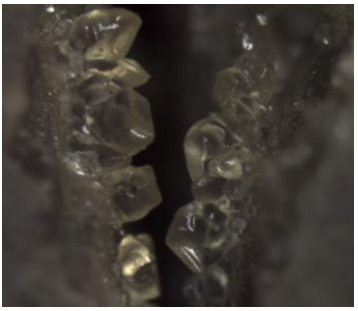

Figure 5.32. Crystal growth (mainly calcium carbonate) inside a 100 µm crack.

The regain in mechanical properties is certainly the case in wet/dry cycles where abundant water is available for the autogenous healing mechanisms of further hydration and calcium-carbonate crystallization. The surfaces of the SAPs and the microfibres act as a nucleation site for the crystals, thus closing the cracks completely. Thermogravimetric analyses proved the existence of $CaCO_3$ as the main healing mechanism. Storage in an environment with a relative humidity of more than 90% only showed visual closure of cracks for samples containing SAPs (Figure 5.28). SAP particles manage to take moisture out of a humid environment and provide it to the cementitious matrix for crack healing. Also cracks of specimens stored at a relative humidity of 60% only healed if the samples contained SAPs. This is similar to internal curing and is reflected in regained first-cracking-strength. After reloading in four-point-bending, the regain in first-cracking-strength was calculated (Figure 5.33). Without the presence of water, specimens without SAPs do not heal. This was also seen in previous investigations of (Yang, 2008). Cracked specimens containing 1 m% SAP B do show healing as there is a regain in mechanical properties (1B – 60/90). The crack closure (Figure 5.28) gives approximately the same value as the regain in first-cracking-strength (in %).

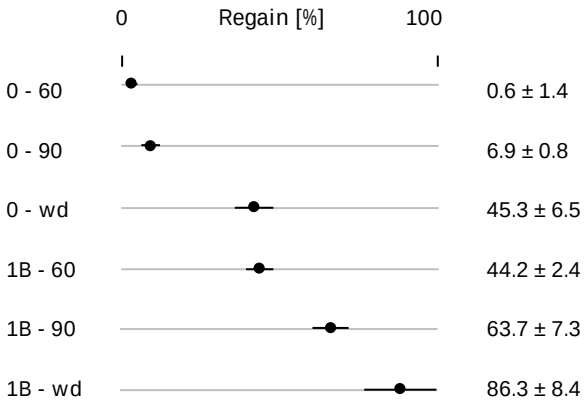

Figure 5.33. Regain of the first-cracking-strength [%] for the different investigated mortar specimens with an age of 28 days after performing wet/dry cycles and storage in a relative humidity (RH) of more than 90%; error bars indicate the standard deviation on the single values of three individual specimens.

Reference samples in wet/dry cycles show a regain of about 45%, which is comparable to values found in literature of 40% (Yang et al., 2009) and 42% (Yang, 2008). If reference samples are stored in a climate room with a certain relative humidity, there is almost no autogenous healing as water is not present to form the healing products. The values found in literature (Yang, 2008) for storage in a relative humidity of more than 90% (23% regain in first-cracking-strength) and in a relative humidity of 60% (13% regain in first-cracking-strength), correspond very well to the values found for specimens without SAPs in this research: 20% and 7%, respectively.

The incorporation of SAPs in this investigation, however, promotes self-healing in air of sufficient relative humidity. The samples with SAPs do show a regain in strength when stored in a relative humidity of more than 90%. The moisture uptake by SAPs (up to four times their own weight in moisture; cf. the DVS values of moisture uptake at 90 and 98% RH in Chapter 2) seems to be sufficient to promote a certain degree of autogenous healing, especially in the interior of the crack in the form of further hydration. In the relative humidity condition of more than 90%, the material with 1 m% SAP B shows a regain of 60%. There, further hydration occurred, leading to the regain in mechanical properties. At the crack mouth, the crack was still clearly open and only at some distinct places, there was some bridging of a crack by healing products. At reloading, previously created cracks reopened and no new cracks were formed until all cracks reopened. Newly formed cracks were only the case when the specimens were stored in wet/dry cycles.

A higher amount of SAPs, without decreasing the strength, leads to a higher amount of promoted autogenous healing due to more steadily-available water in time. Using 1 m% SAP B leads to a regain of 80-90% in wet/dry cycles and sometimes, a new crack is formed instead of the reopening of a healed crack, which shows a total regain of the mechanical properties at that distinct place. In the

interior mostly further hydration occurred and more pronounced $CaCO_3$ crystals mixed together with hydration products were formed at the crack mouth.

When specimens with 1 m% of SAP are subjected to wet/dry cycles, the amount of healing is higher compared to the healing of samples without SAPs. However, increasing the m% of SAP B gives more healing due to more release of absorbed water. The regain is high in specimens with very high amounts of SAPs due to the initial low strength (Table 5.10). The material still shows a pronounced healing capacity but is less applicable in frame of strength properties. Due to further hydration and precipitation of $CaCO_3$, the amount of healing of specimens with 2 m% and 4 m% of SAP B exceeds 100% (if compared to the initial strength of the specimen) for the first-cracking-strength but the absolute strength value is approximately the same.

The best combined result considering the mechanical properties and the healing capacity in all curing conditions is obtained by using 1 m% SAP B relative to the cement weight.

The same conclusions as for the first-cracking-strength could be drawn by investigating the peak strength and modulus of elasticity values.

5.7.2 Different types of superabsorbent polymers

Different types and sizes of superabsorbent polymers were studied on their influence on the autogenous healing properties.

The results considering the different types and sizes of SAPs are shown in Table 5.11. Only the XL SAP was not studied as it gave the worst results considering the macro structure of the cementitious material (Chapter 3). In the table, the amount of mixing water, first-cracking-strength, the regain in first-cracking-strength after being stored at a relative humidity of 60%, of more than 90% and in wet/dry cycles, and the amount of multiple cracking are given.

The amount of absorbed mixing water seems to be dependent on the size of the particles. As smaller particles have a higher surface area available for absorption of mixing water, their value is higher (SAP A, SAP G and Po). SAP H, which was small but spherical, did not have such a pronounced influence on the workability and no water needed to be added. This is due to the small round shape of the particle, less obstructing the workability. A fibre type such as SAP F did show an influence due to the balling effect, obstructing the handling. As a higher amount of water is added in those mixtures, the strength was lower. Also, this is due to the formation of a high amount of macro pores which act as stress inducers in the mixture. The lowest strength is found in the SAP C mixture (see Chapter 3). The mixtures which showed the least influence on the strength parameters are A0.5, B0.5, B1, D0.5, D1 and E0.5.

The regain in strength is comparable for all mixtures. One needs to bear in mind that the regain is determined based on the initial strength of the material. Two criteria for optimal self-healing need to be met. These are no reduction in strength and optimal autogenous healing and regain in mechanical properties. For example; even though the Mi1 mixture shows optimal healing, this is healing of cracks with a lower initial strength. Therefore, the B1 mixture is better.

In wet/dry cycles, the reference showed healing of approximately 45% of the first-cracking-strength and almost none when stored at humid conditions. Mixtures with SAPs showed 60-90% regain in mechanical properties when stored in wet/dry cycles, 30-50% when stored at a relative humidity of more than 90% and 20-40% at 60% RH. SAPs thus promote autogenous healing.

By using SAPs, the ductility is increased as the SAPs act as flaws facilitating the multiple cracking. This was the case in all mixtures except mixtures containing SAP C, SAP E and SAP F. SAP C was showing a plasticizing effect leading to a very weak matrix, responsible for the decrease in ductility. SAP E caused a non-significant difference. SAP D and E have a more irregular form and induce higher stress concentrations. SAP F showed a balling effect of the separate superabsorbent-polymer fibres, reducing the overall mechanical properties. A fibre type bundles together and causes a weaker specimen and lower strength. When studying the different sizes (Po, Mi and Me), a smaller particle size leads to a higher form of ductile behaviour. Prisms with a high MC value (SAP A, SAP B, SAP G, H, Po and Mi) show more healable cracks.

The best overall mixture is B1. There, the strength is not reduced significantly, the regain in mechanical properties (in all conditions) is optimal and the strain-hardening effect is noteworthy.

Table 5.11. Absorption of mixing water [g/g SAP], first-cracking-strength [MPa], regain in first-cracking-strength [%] when stored at a relative humidity of 60%, more than 90% and in wet/dry cycles and amount of multiple cracking [% strain].

Code	Mixing water absorption [g/g SAP]	First-cracking-strength σ_{fc} [MPa]	Regain in σ_{fc} (RH=60%) [%]	Regain in σ_{fc} (RH>90%) [%]	Regain in σ_{fc} (wet/dry cycles) [%]	Amount of multiple cracking [% strain]
REF		5.5 ± 0.6	1.0 ± 0.9	3.5 ± 3.1	46.5 ± 7.2	3.2 ± 1.1
A0.5	30.5	5.4 ± 0.8	28.9 ± 5.6	40.3 ± 7.2	60.0 ± 6.2	3.8 ± 0.8
A1	30.5	3.1 ± 0.8	32.6 ± 4.8	45.2 ± 5.3	76.7 ± 6.5	4.8 ± 0.7
B0.5	8.9	5.6 ± 0.7	32.2 ± 4.3	42.0 ± 4.8	72.7 ± 5.3	5.1 ± 0.6
B1	8.9	5.3 ± 0.5	37.6 ± 4.6	50.2 ± 3.9	86.7 ± 7.8	5.6 ± 0.8
C0.5	2.0	1.9 ± 0.5	30.0 ± 5.0	42.0 ± 4.0	56.0 ± 8.0	1.8 ± 0.6
C1	2.0	1.1 ± 0.5	32.0 ± 6.0	46.0 ± 6.0	60.0 ± 6.0	1.1 ± 0.9
D0.5	16	5.5 ± 0.7	34.2 ± 7.0	43.0 ± 5.3	64.6 ± 6.9	3.2 ± 1.0
D1	16	5.4 ± 0.8	29.7 ± 5.1	40.5 ± 6.4	57.9 ± 5.0	3.8 ± 1.0
E0.5	16	5.4 ± 0.8	25.4 ± 11.1	32.8 ± 7.1	46.8 ± 7.4	2.1 ± 0.8
E1	16	5.0 ± 0.8	27.3 ± 7.7	42.5 ± 3.0	64.3 ± 3.2	3.0 ± 1.0
F0.5	32	4.7 ± 0.5	32.3 ± 5.3	44.4 ± 8.6	62.7 ± 9.2	2.4 ± 0.6
G0.5	45	4.3 ± 0.5	28.5 ± 7.2	38.2 ± 9.4	56.8 ± 2.9	4.4 ± 1.1
H0.5	0	5.2 ± 0.6	29.0 ± 3.1	50.1 ± 4.6	69.0 ± 2.6	4.3 ± 1.2
H1	0	4.9 ± 0.5	34.0 ± 3.2	49.0 ± 3.7	66.0 ± 8.0	4.1 ± 0.9
Po0.5	40	4.1 ± 0.4	31.3 ± 11.8	44.6 ± 7.8	70.0 ± 7.1	5.4 ± 0.5
Mi0.5	21	4.1 ± 0.8	33.9 ± 6.2	51.2 ± 1.7	73.8 ± 8.6	5.0 ± 1.1
Mi1	21	3.7 ± 0.5	38.7 ± 14.1	47.8 ± 9.4	86.8 ± 2.8	5.3 ± 1.3
Me0.5	10	4.5 ± 0.8	37.0 ± 2.2	45.8 ± 6.4	65.0 ± 5.0	3.2 ± 1.0
Me1	10	3.8 ± 0.7	34.4 ± 13.1	39.8 ± 1.2	71.7 ± 7.8	3.9 ± 1.2

5.8 Repeated autogenous healing

5.8.1 Durability performance

If the self-healing material is used in practice, several robustness criteria need to be met. These are: a long shelf life, pervasiveness, economical advantage, stability, quality, reliability, versatility and repeatability (Li & Herbert, 2012; Yang, 2008). The focus here lies on repeatability after the first healing action due to autogenous healing, which is related with quality and reliability.

If we consider Figure 5.34a for a traditional structure, the durability performance of a construction is higher than the required performance. But, if there is excessive loading and/or cracking, this durability parameter may shift to lower values and degradation may occur. If one does not notice the failure and does not repair, the construction may decline (if the durability performance drops below the required performance line). The increases in durability performance are preventive and essential maintenance to rehabilitate the structure. The dashed curve shows the costs. The costs will increase stepwise in time due to maintenance monitoring and manual repair (van Breugel, 2007).

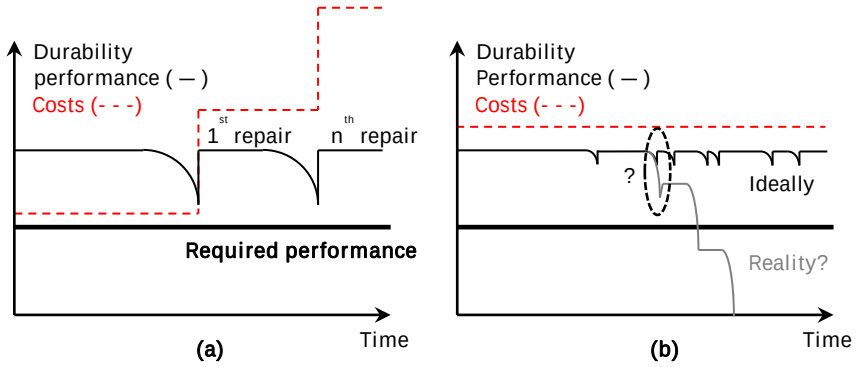

Figure 5.34. Durability performance and costs as a function of time for manual repair in a traditional structure **(a)**, and for an (ideal) autogenously healing material **(b)**. Figure redrafted after (van Breugel, 2007).

If an ideal self-healing material would be used, the durability could be guaranteed (Figure 5.34b) without human intervention. But, in the case of autogenous healing, the amount of available building blocks is consumed in time, thus limiting the possibility of renewed crack healing (indicated by means of a question mark in Figure 5.34b). So, the question rose whether this autogenous healing could be repeated. What will happen when autogenously healed specimens are again subjected to cracking? The possibility of a repeatable autogenous healing is therefore investigated by performing repeated four-point-bending tests on self-healing materials.

5.8.2 Repeated four-point-bending and optical microscopy

To study the repeatability of autogenous healing, the mixtures in Table 5.1 were used. The sample preparation, four-point-bending test and storage conditions described in paragraph 5.3 apply.

The specimens were first preloaded at an age of 28 days and the strain at the bottom side of the specimen was limited to 1%, theoretically calculated from the curvature and the vertical displacement during loading. This strain is lower than the maximum possible strain upon failure of such a strain-hardening specimen, so the service cracks could be studied before opening due to pull-out of the fibres. After a period of 28 days of healing, the specimens were reloaded in four-point-bending (again, the strain was limited to 1%) and the mechanical properties, obtained during the first and second loading cycle, were compared (Figure 5.35a). These properties are: the first-cracking-strength, the modulus of elasticity, the amount of multiple cracking, the regain in first-cracking-strength, the regain in modulus of elasticity and the total amount of multiple cracking. The first-cracking-strength was defined just before the first drop in stress due to an unstable extension in the matrix fibre tunnel. The modulus of elasticity is defined as the slope of the stress-strain curve before actual first cracking. The amount of multiple cracking was defined as the strain at the bottom of the specimen starting from the strain related to the first-cracking-strength until the point of reloading or strain-softening (where there is no longer strain-hardening, but a decrease in strength in time due to failure of the fibre bridging action). The testing regime for repeated healing actions is shown in Figure 5.35b.

After another 28 days of curing, the specimens were reloaded for a second time, till failure in the third loading cycle. From the additionally obtained stress-strain curves, the first-cracking-strength and regain in first-cracking-strength were again compared to the original and previous curve of first loading, using equation 5.8:

$$\text{Regain in } \sigma \text{ at first/second reloading} = \frac{\sigma_{1^{st}/2^{nd}\,reloading}}{\sigma_{preloading}} \tag{5.8}$$

where $\sigma_{preloading}$ is the first-cracking-strength at preloading, $\sigma_{first\ reloading}$ at reloading the specimen for the first time and $\sigma_{second\ reloading}$ at second reloading (Figure 5.35a).

The regain in Young's modulus is calculated with the following equation 5.9:

$$\text{Regain in E at first/second reloading} = \frac{E_{1^{st}/2^{nd}\,reloading} - E_{1^{st}/2^{nd}\,residual}}{E_{preloading} - E_{1^{st}/2^{nd}\,residual}} \tag{5.9}$$

where $E_{preloading}$ is the modulus of elasticity at preloading, $E_{first\ reloading}$ at reloading the specimen for the first time, $E_{second\ reloading}$ at second reloading, $E_{first\ residual}$ the residual modulus at preloading and $E_{second\ residual}$ at first reloading (Figure 5.35a). The residual modulus was calculated between the point at start of unloading and the point of total unloading.

The total amount of multiple cracking was determined till the point of strain-softening, assuming an already imposed strain from the previous loading parts.

Figure 5.35a represents the stress-strain curves of a specimen healed in wet/dry-cycles and three loading cycles are visible. The first loading part is the preloading (strain from 0% until 1%), the second part is the first reloading (an additional strain of 1%) and the third part is the second reloading (until failure).

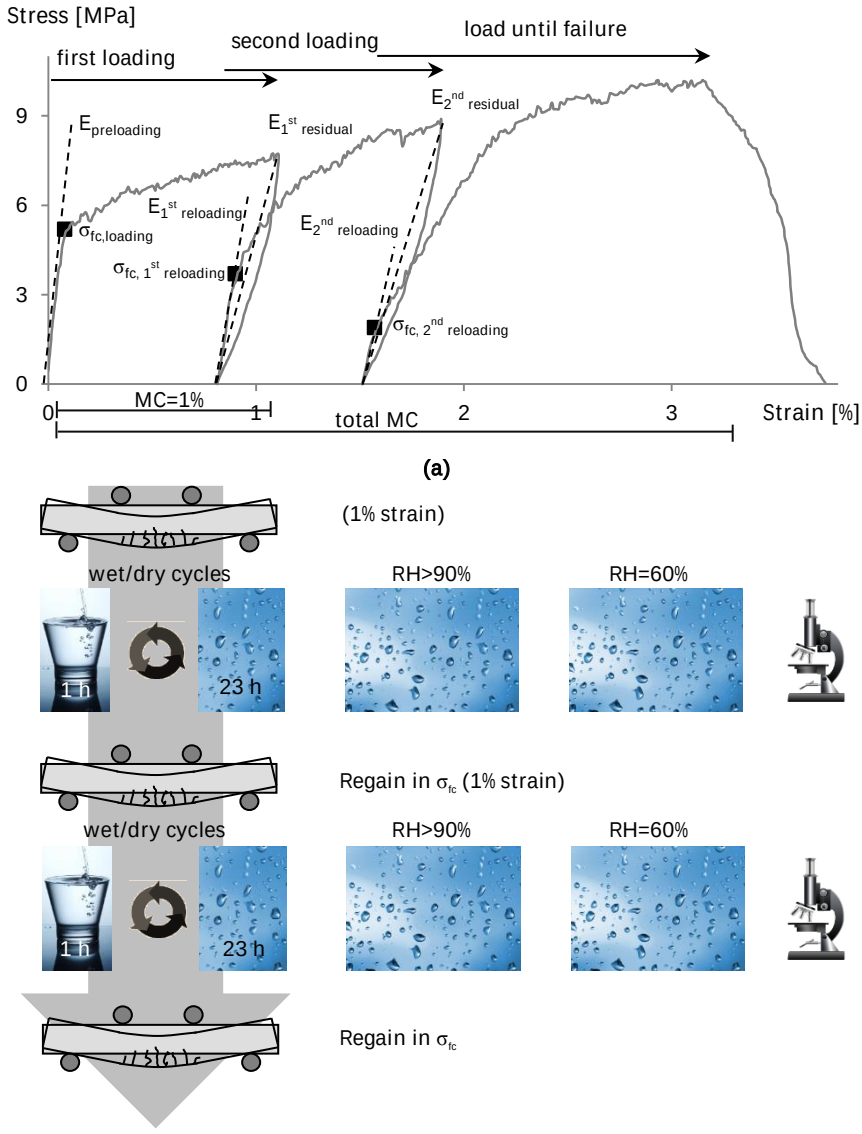

Figure 5.35. Typical stress-strain curve with the different cracking and healing stages, together with the indication of first-cracking-strengths σ_{fc} and the slopes of the curve at every stage **(a)**, and followed testing regime for repeated healing cycles **(b)**.

After preloading and before healing, initial microscopic observations were performed by means of a stereo microscope (Leica S8 APO optical microscope mounted with a DFC 295 camera). During the healing periods, additional microscopic observations were performed at regular time intervals and the crack width was measured and studied in time. The visual closure hereby served as a qualitative measurement for the autogenous healing capacity.

Some specimens were loaded until failure at the first and second cycle, to study the effect of autogenous healing on larger cracks. As the regain in mechanical properties of the failed specimens is low, these specimens were only used to perform microscopic analysis and to study the limit of autogenous healing.

Thin sections (40 mm × 10 mm × 25 µm) were prepared from studied four-point-bending specimens after storage in healing conditions (at a total age of 56 days) (Figure 5.36). First, the plain mortar specimens were cut to receive 40 mm × 10 mm faces, which were then glued on a glass slide with a thickness of 2.9 mm. The combined sample was cut and polished until a height of the specimen and glass of 10.1 mm was reached. Next, the specimens were impregnated under vacuum with a fluorescent epoxy. The excess epoxy was polished away and an object glass was glued on the smooth surface. Finally, the glass slides were cut off and the remaining part was polished until a thin section with 25 µm thickness was achieved. The epoxy ensured stable handling of the whole specimen and the healing products were untouched. A cover glass was glued on top to protect the thin section. The thin sections were analysed with a Leica DMLP microscope with a DFC 295 camera. Normal light, polarized light and fluorescent light were used to visualize the formed crystals in a crack and the change in microstructure around the crack faces.

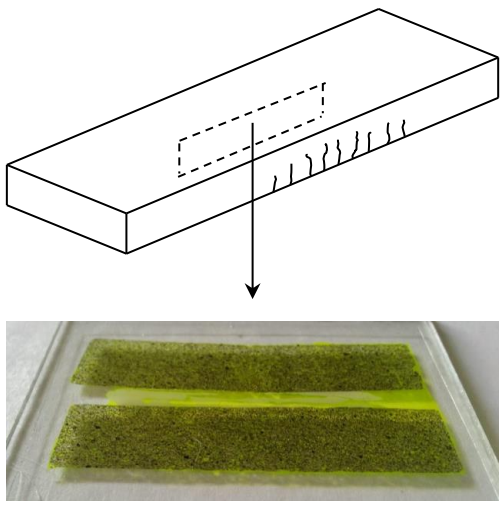

Figure 5.36. Schematic overview of the location of the thin section in a specimen used for four-point-bending.

5.8.3 Microscopic observations after first and second loading

Due to the addition of microfibres, multiple cracking was observed, giving all samples a ductile strain-hardening behaviour (Figure 5.35a). The crack width is hereby a very important parameter. If large cracks are formed, the building blocks for self-healing will be consumed after some time and the autogenous healing will no longer be optimal. In this research, the crack widths were limited to 30-50 µm, as was also the case in (Yang, 2008). The mean crack widths were 24.0 ± 12.2 µm in case of specimens without SAPs. Due to the addition of SAP particles, this multiple cracking behaviour was enhanced as the total maximum strain was increased. The macro pores formed by the SAPs act as crack initiators, increasing the ductile behaviour. Also, the crack width was approximately the same (23.7 ± 13.4 µm for specimens with SAPs). Due to partial reopening of the cracks at first reloading and the formation of new cracks, the crack width increased slightly (to 25.7 ± 15.9 µm for specimens without SAPs and 25.5 ± 15.6 µm for specimens with SAPs).

By examining the crack width before and after healing, the percentage of crack closure could be quantified. Figure 5.37a shows the visual crack closure in function of the initial crack width after the first healing cycle for mixtures with and without 0.5 m% of SAP A, stored in different healing conditions.

Results show that cracks up to 30 µm are able to heal completely at the crack mouth and up to 150 µm heal partly when specimens are subjected to wet/dry cycles (as found in paragraphs 5.6 and 5.7). Specimens used to study the self-healing capacity were limited to 1% strain. As mentioned above, the crack widths were thus limited. The larger crack widths found in Figure 5.37a originate from specimens which were loaded until failure. Due to the higher loading strain, the crack widths were larger in those specimens. These crack widths were studied on their healing capacity as well to obtain results for partial healing and the boundary criterion for ideal autogenous healing in the studied strain-hardening cementitious materials. That criterion was found to be 30 µm.

Specimens healed under wet/dry cycles exhibit the best healing as a fair amount of water is available for autogenous healing (Figure 5.37a). If superabsorbent polymers are added as well, the amount of healing with wet/dry cycles is slightly higher (Figure 5.37a-c). This is due to the fact that SAPs are able to seal a crack from intruding fluids, reducing the flow when put under water and thus establishing better circumstances for autogenous healing. The better circumstances are due to the lower fluid flow and thus less washing out of the healing products, as also found by (Edvardsen, 1999). Secondly, water is also available during the dry periods of the wet/dry cycle, thus increasing the possibility of autogenous crack healing. At a relative humidity of more than 90%, the healing is far less compared to the healing condition with wet/dry cycles as no water is present. However, specimens with superabsorbent polymers show partial healing. As SAPs are able to extract moisture from the environment and then provide the necessary water for further hydration of unhydrated binder particles in the crack. At a relative humidity of 60%, only the mixtures with SAPs show partial healing. The visual crack closure is important as a completely closed crack will be beneficial as harmful substances may no longer enter a crack in the future.

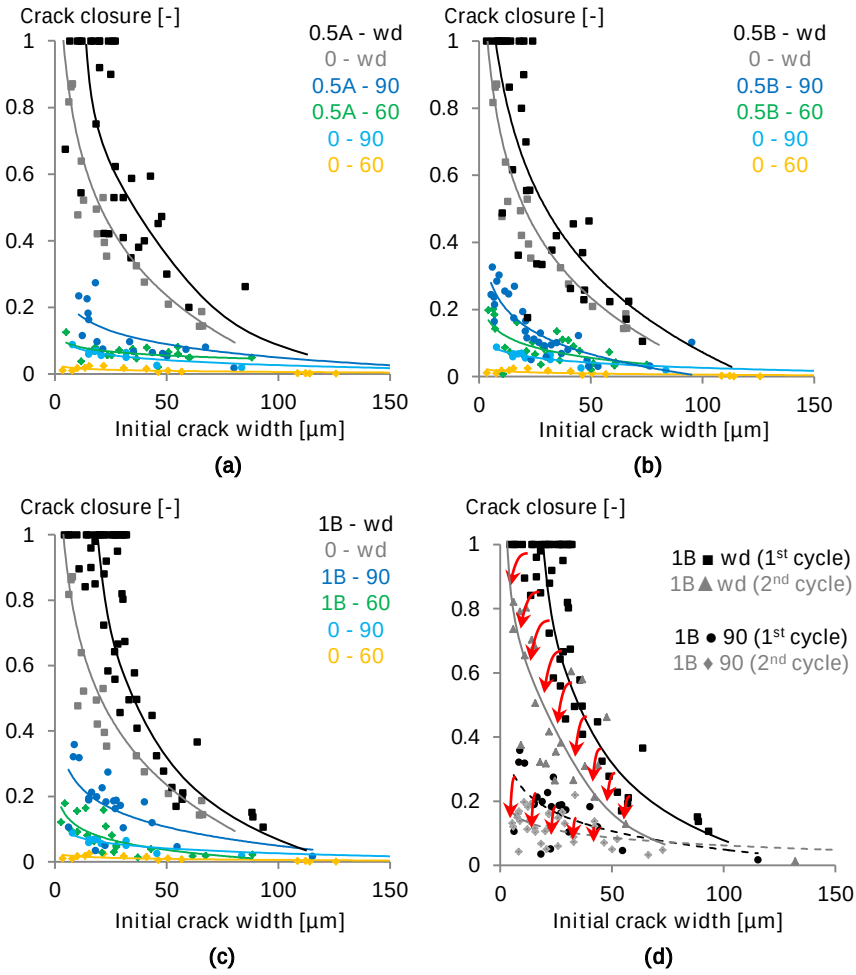

Figure 5.37. Crack closure [-] after the first healing stage as a function of initial crack width of 0.5A **(a)**, 0.5B **(b)** and 1B **(c)**, and a comparison between the first and second healing stage of 1B **(d)**.

The mixtures 0.5A (Figure 5.37a) and 0.5B (Figure 5.37b) show the same visual closure at the crack mouth. Their differences are not significant. A doubling of the amount of SAPs (0.5B; Figure 5.37b and 1B; Figure 5.37c) leads to better properties and visual closure in 1B-mixtures. The results in Chapter 4 showed that 1B provides the best results considering self-sealing.

After the first healing period, most of the building blocks for self-healing, i.e. unhydrated cement particles and Ca^{2+} ions are consumed, reducing the possibility for autogenous healing. Specimens with SAPs in the second wet/dry cycle for example show an inferior visual closure of the crack compared to the same specimens in the first healing cycle (Figure 5.37d). This already points out that the regain of mechanical properties upon the second healing will be lower compared to the first healing.

5.8.4 Mechanical properties and regain

The strength of the new material was investigated by analysing the results from the loading experiments. The first-cracking-strength of all studied mixtures is shown in Figure 5.38a. The same conclusions as in paragraph 5.7 can be made.

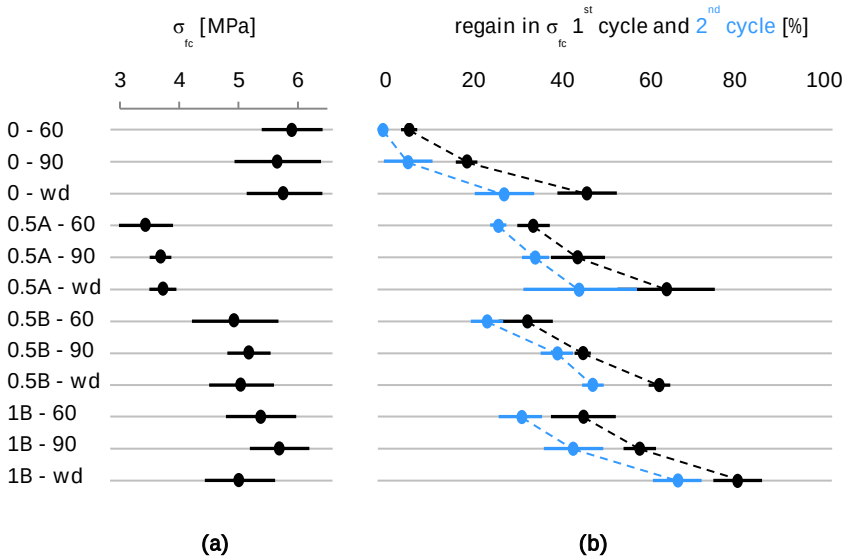

Figure 5.38. Mean first-cracking-strength σ_{fc} at 28 days with standard deviation **(a)** (n=3), and regain in first-cracking-strength after the first and second healing period **(b)** for all studied mixtures.

Samples with SAPs show a higher regain in first-cracking-strength than the SAP-free samples under all studied healing conditions (Figure 5.38b). The new findings agree to the ones found in paragraph 5.7. SAP particles not only tend to increase the healing capacity during the first healing stage (from 46% to 75% in wet/dry cycles), but also during the second healing stage (Figure 5.38). The regain is still 66% at second reloading. Without the superabsorbent polymers, this value was only 28% (wet/dry cycles). A possible explanation is the storage of a calcium-rich fluid (i.e. the pore solution) in the swollen superabsorbent polymers. This provides the possibility of the formation of the $CaCO_3$ crystals in the crack. If superabsorbent polymers are not present, this fluid is expected to be washed out from a crack upon drying. The crystal formation was also visible at the face of the specimens containing SAPs. Dome-like structures were formed, proving the theory of retained pore solution, used during the crystallization process. The dome structures were also found after performing low-pressure water permeability measurements (Chapter 4). By providing this retained pore solution to the matrix, the autogenous healing is promoted, both in the first and in the second healing stage. This autogenous healing was mostly present at the surface, but also in the interior of a crack as could be visually seen at the crack faces after loading until failure.

The same conclusions can be drawn if the modulus of elasticity of the different mixtures is compared (Figure 5.39). As was the case for the regain in first-cracking-strength, the regain in modulus for the samples healed in wet/dry-cycles is higher than for those healed in an environment with a RH > 90% or RH = 60%. When using SAP particles, the overall healing is increased (from 19% to 70% in wet/dry cycles). Upon second reloading, the crystals are assumed to be less strong and the regain is also less. The regain in mean modulus of elasticity in 1B-mixtures is still higher than for the reference samples without SAPs upon first reloading. The regain in modulus can also be due a stronger matrix and higher bond with the microfibres (Li et al., 2002). The study of the modulus of elasticity was only used as a verification of the results found by comparing the regain in first-cracking-strength.

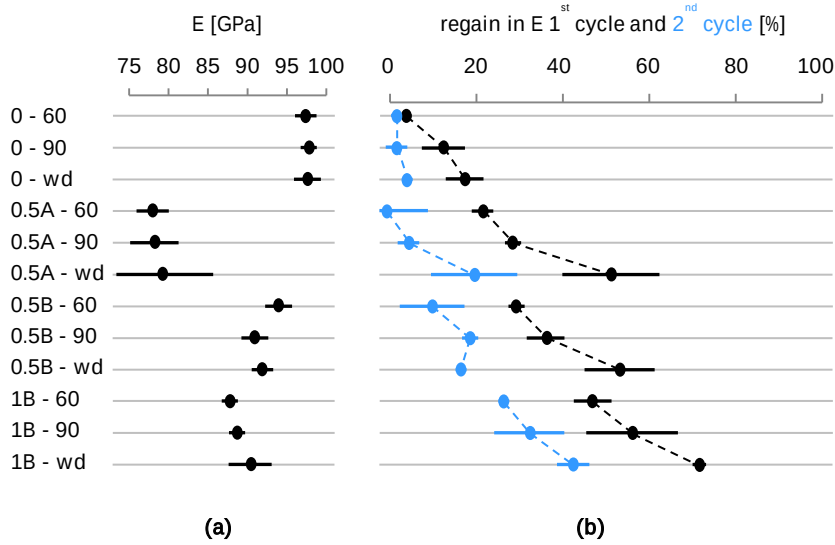

Figure 5.39. Mean modulus of elasticity E at 28 days with standard deviation **(a)** (n=3), and regain in modulus after the first and second healing period **(b)** for all mixtures.

The amount of multiple cracking is visualized in Figure 5.40a. This is the strain of specimens completely loaded until failure, without imposing several loading cycles. Specimens without SAPs show a strain of 2%, which is a normal value for these kind of strain-hardening materials (Li et al., 1997). Due to the use of SAPs, the amount of multiple cracking increases. This is due to the presence of crack initiators, facilitating the formation of additional cracks before failure of one of the already bridged cracks. A higher amount of SAPs leads to a higher amount of multiple cracking. This statement, however, is only valid as the strength is not significantly impaired. Due to healing, the total amount of multiple cracking is increased (Figure 5.40b). This is only significantly the case when stored in wet/dry cycles, especially considering the 1B-mixtures. Again the same trends are visible. The storage in wet/dry cycles leads to better healing properties compared to >90% RH and =60% RH. SAPs again seem to stimulate autogenous healing which on its turn leads to enhanced mechanical properties.

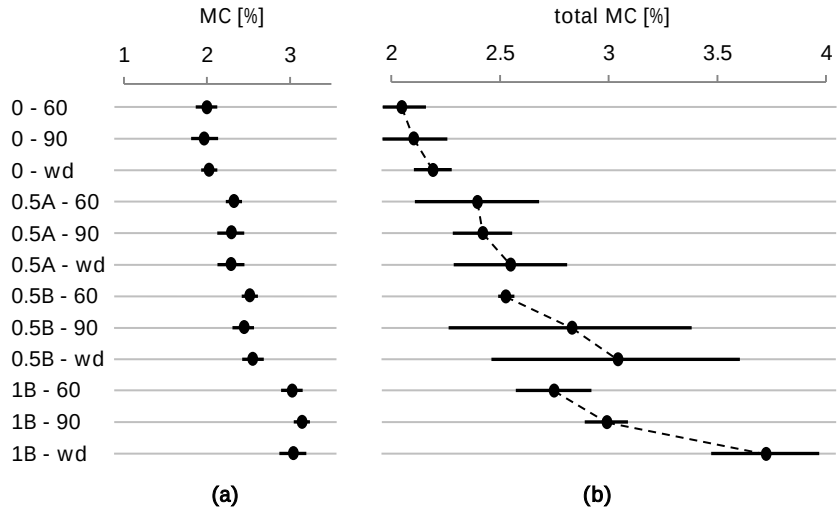

Figure 5.40. Mean amount of multiple cracking at 28 days with standard deviation **(a)** (n=3), and total amount of multiple cracking after imposing two times 1% strain **(b)** for all studied mixtures.

5.8.5 Thin-section analysis of healing products inside a crack

Figure 5.41 shows micrographs of thin sections of the interior of a crack of a specimen with and without SAP particles at the crack mouth. Abundant crystal formation can be seen in specimens stored in wet/dry cycles (Figure 5.41a-b). Crystals are mainly formed where hydration products are present at the crack faces. At the lighter parts (i.e. the sand particles) at the crack faces, there is less crystal formation. As $CaCO_3$ primarily needs Ca^{2+} ions, those cannot be provided by the sand particles, explaining the lower amount of crystals found at the sand particle edges. Also, a small difference in colour can be seen in different crystal clusters. The darker crystal formation is likely to be a mix of $CaCO_3$ and $Ca(OH)_2$, formed by further hydration. The pure white crystals are likely to be pure $CaCO_3$. At the crack mouth, the crystals are able to bridge the crack, leading to the regain in mechanical properties. The crystals are formed from 400 till over 1000 µm inside the crack (Figure 5.42). In the interior of a crack, the amount of crystals is less and only at some distinct places, the crystals bridge a crack, mostly in the vicinity of a fibre (as they act as a nucleation site for the $CaCO_3$ crystals). As the crack is sealed at the surface from intruding water, the crystallization comes to a hold in the interior of the crack. Also, the closer towards the crack tip, the more further hydration compared to $CaCO_3$ crystallization is found as the CO_2 will preferably be used at the surface where it dissolves in the water layer during the wet/dry cycles. Also Fan & Li (2015) showed that the region close to the surface had a high amount of crystalline products ($CaCO_3$). At greater depths, there was a lower amount of healing products (especially further hydration and pozzolanic reactions). In this research, it is also mostly $CaCO_3$ which is formed (crack mouth), but also a small part of further hydration (interior of crack and crack tip). Both mechanisms combined lead to up to 75% recovery of strength found in Figure 5.38.

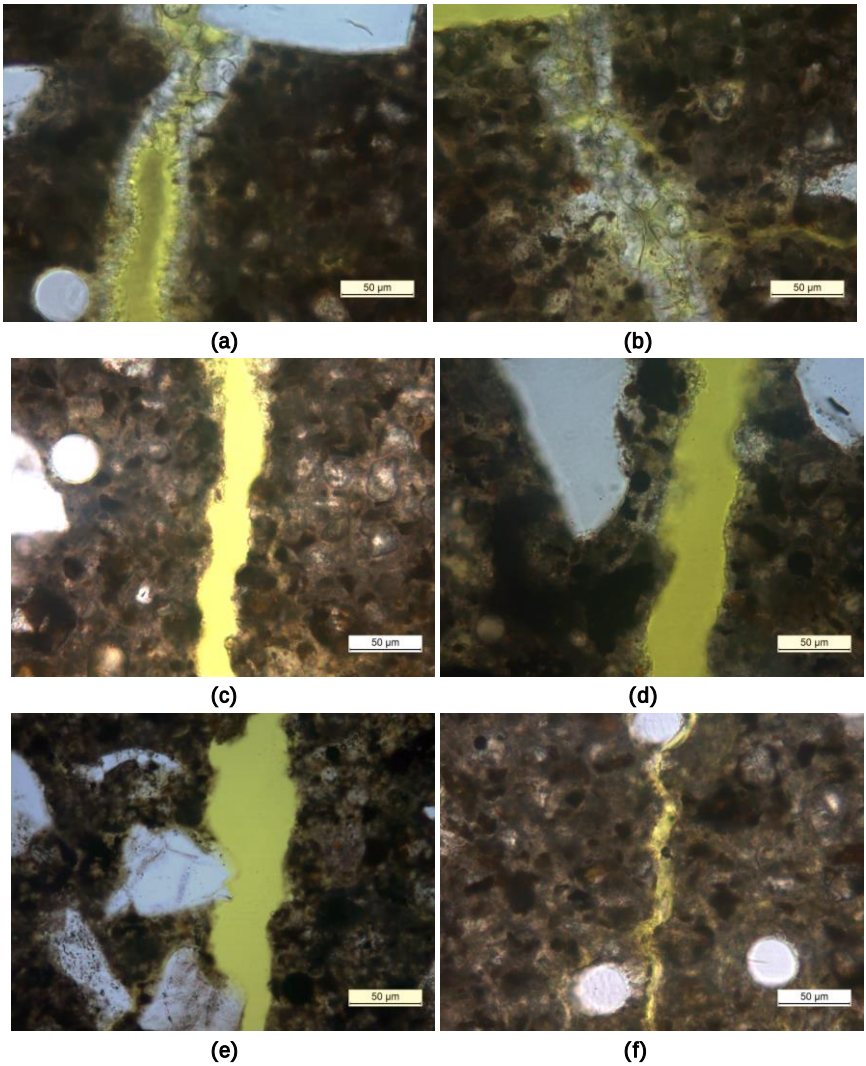

Figure 5.41. Thin sections of a crack in a reference cementitious material **(a, c, e)** and in a cementitious material with superabsorbent polymers mixed in **(b, d, f)** under cross-polarized light, showing crystal formation at the crack faces when stored in wet/dry cycles **(a-b)**, partial healing in the presence of SAPs when stored in a room at >90% **(c-d)** and =60% **(e-f)**. All micrographs were taken at the crack mouth. The scale bar shows a distance of 50 µm.

Jonkers (2011) showed, in bacterial self-healing concrete, that precipitation mainly occurred near the crack rim leaving major parts of the crack unhealed. His research was conducted on specimens with a 150 µm crack width, substantially higher than the 30-50 µm crack width region studied here. He explained the precipitation at the crack rim due to the relatively high solubility of calcium hydroxide. He hypotheses that calcium hydroxide first uses the carbon dioxide from intruding water in the crack, and afterwards the remaining calcium hydroxide

would dissolve and diffuse out of the crack into the bulk water. Here it will react with carbon dioxide present near the crack rim resulting in the precipitation of larger quantities of calcium carbonate (Jonkers, 2011; Sisomphon et al., 2012).

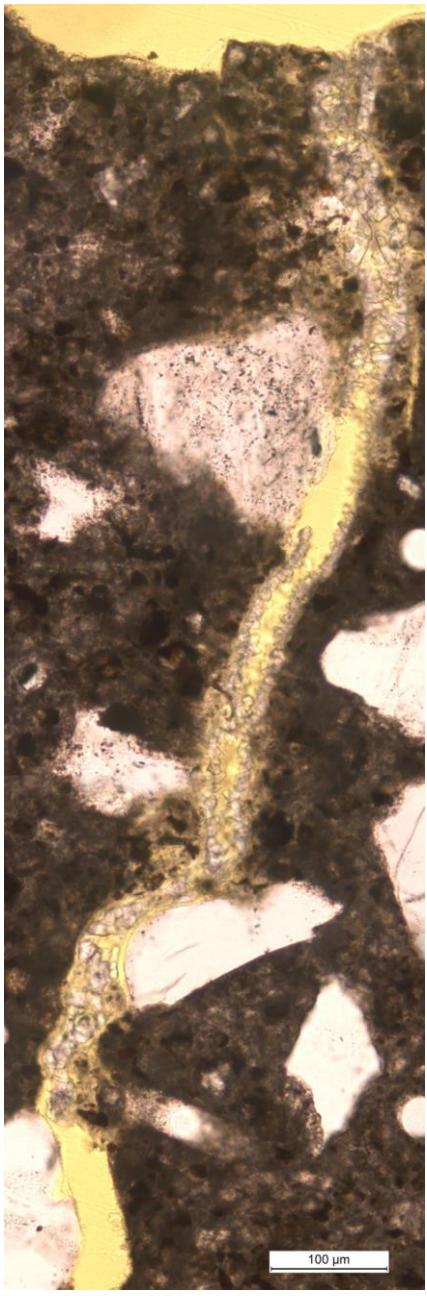

Figure 5.42. Thin section of the interior of a crack filled with healing products. The scale bar is 100 µm.

The healing mechanism of $CaCO_3$ crystals shows teeth-like structures in the interior of a crack, expanding towards each other and eventually making a solid bridge of a crack (Figure 5.41a). The amount of crystals is higher in specimens containing SAPs (Figure 5.41b) compared to specimens without SAPs (Figure 5.41a). This is possibly due to the slow release of water to the cementitious matrix during dry periods by the swollen SAP particles near the crack face. In a storage condition of >90% RH and =60% RH, almost no healing is found in specimens without SAPs (Figure 5.41c and Figure 5.41e). As no water is present to form autogenous healing products, no precipitates can be found. When investigating thin sections of specimens containing SAPs, partial crystal formation is found at the crack faces (Figure 5.41d) and further hydration may occur (Figure 5.41f) due to the release of extracted moisture by the SAP particles. This further hydration is beneficial in small cracks and at the crack tips, where a small amount of healing products is able to bridge a crack.

Ca^{2+} ions are consumed at the crack faces after the first healing period. This is connected to the results of the visual crack closure and the regain in mechanical properties. The visual crack closure is about 20% lower when the specimens are reloaded for a second time. An example of healing at second reloading is shown in Figure 5.43. During the first reloading, only a limited number of new cracks are formed. The previous-healed cracks thus mostly reopen and there is a limited possibility for a renewed autogenous healing of the crack. In the second healing stage, Ca^{2+} ions present in the interior of the matrix need to diffuse towards the crack face. So, the crystallization becomes diffusion-controlled instead of surface-controlled. This limits the speed of possible crystallization and thus autogenous healing and regain in mechanical properties.

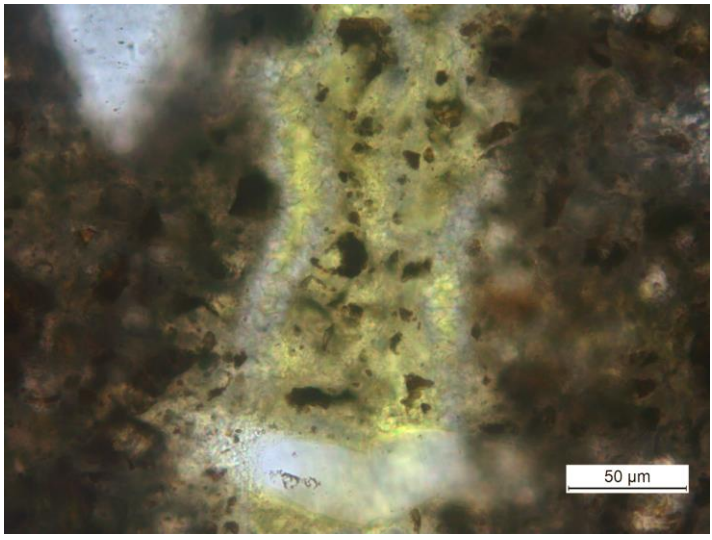

Figure 5.43. Thin section of the interior of a crack filled with healing products after second autogenous healing. The scale bar is 50 µm.

During the formation of calcium carbonate crystals, an amount of Ca^{2+} needs to leach out from the cementitious matrix. The matrix in the vicinity of a crack may thus look brighter in comparison to the plain matrix (Figure 5.44; clearly marked with the boundaries). In the interior of the crack, crystals are clearly formed. TGA on material found in a crack showed that this was mainly $CaCO_3$ with also partly $Ca(OH)_2$ from further hydration. When this healed crack is opened again, the Ca^{2+} will need to travel from a further distance compared to the first healing cycle and the material will be less able to regain its properties as less crystals are able to be formed. But, if the surface is sealed fast, the crystallization in the interior of a cracked specimen can still occur if the ions are not fully consumed. This led to the regain in mechanical properties at the second healing stage.

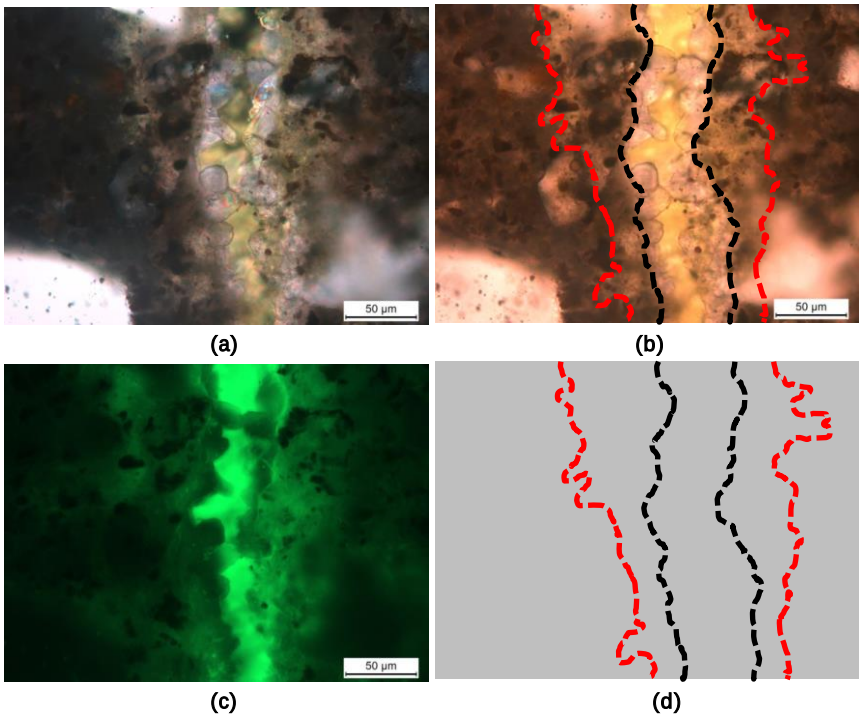

Figure 5.44. Thin section of a crack in a cementitious material under cross-polarized light **(a)**, normal light **(b)** and fluorescent light **(c)**. The crack boundary is shown with a black dashed line and the boundary of the region where Ca^{2+} has leached out with a red dashed line **(b, d)**. The scale bars are 50 µm.

5.9 X-ray microtomography

The mechanism of further hydration and calcium-carbonate crystallization may seal a crack at first and can result in the regain of mechanical properties. The regain is mostly measured by means of repeating mechanical tests and comparing the strength before and after healing, and the closure of cracks is studied quantitatively by means of light microscopy at the crack surface. But, almost no results of the healing inside a specimen can be given by such a microscopic test, unless the sample is destroyed. Thin sections for example need sawing of the specimen, possibly damaging the formed crystals in the crack. Characterization of the healing only from the surface is not sufficient to evaluate or verify the extent of healing throughout the entire specimen. This information, however, is very important to give insight in the extent of healing and its effectiveness, as the healing efficiency relies on the amount and distribution of the formed healing products. Therefore, one needs to quantify the amount in the whole specimen, in three dimensions, but without disturbing the formed healing products. High-resolution X-ray computed microtomography (X-ray µCT) becomes therefore useful. It is a non-destructive technique which generates three-dimensional images by combining a series of cross-sectional micrographs. Those micrographs are based on the attenuation of X-rays at different positions and depend on the atomic number and density of the material (Cnudde & Jacobs, 2004). The total amount and the distribution of the healing products in the cementitious matrix can hereby be investigated without disturbing the formed hydration products inside the crack. In addition, because X-ray µCT is non-destructive, the internal structure of the same sample can be compared and analysed before and after healing.

An X-ray study already proved bio-deposition (De Muynck et al., 2011) and bacterial-based self-healing and provided a nice quantification of the amount of healing products (Wang et al., 2014a; Wang et al., 2014b). This bacterial healing occurs to a higher extent compared to autogenous healing as its mechanism not only depends on the available reagents in the cementitious matrix, but it is a result of the bacterial metabolism. Sealing by precipitation in high-strength low-permeability concrete was already studied by means of micro-focus X-ray CT (Fukuda et al., 2012). It was found that precipitation occurred only near the exterior (at the surface) of the specimen and only the first 0 till 50-200 µm of the cracks (crack width of 100 µm) was filled with precipitation. However, the test specimens were stored in seawater. The observed precipitation could thus also be the result of a combination of autogenous healing and salt formation, and the formation of other healing products due to specific ions present in seawater (Palin et al., 2015). A recent µCT study (Fan & Li, 2015) gave results on the healing properties of strain-hardening materials. It was found that the extent and rate of healing strongly depended on the initial surface crack width. Also, the region of a crack close to the surface (from 0 to 50-150 µm below the surface) could be sealed quickly with crystalline precipitates. At greater depths, the healing process takes longer and is more likely due to continued hydration and pozzolanic reactions. The study was done on V-shaped cracks after performing four-point-bending tests and Fan & Li studied two average crack widths (31 µm and 102 µm) under wet/dry cycles (24h in water and 24h at 50% RH). For the 102 µm average crack, the total

crack volume decreased 2.4%, 7.2% and 10.8% after 1, 5 and 10 wet/dry cycles, respectively. In the 31 µm average crack, this was 13.2%, 55.3% and 73.1%, respectively. Smaller cracks are able to close by autogenous healing. For the large crack, 30% of the crack was healed in the region from the surface to 50-150 µm below the top surface. Beyond this shallow region, the extent of healing had a dramatic drop.

5.9.1 Studied specimens and X-ray beam line

The aim is to investigate the effective use of superabsorbent polymers to stimulate autogenous healing. The self-healing efficiency was studied in the interior of the specimen by means of X-ray µCT and the healing products were visualized three-dimensionally. The amount of healing within the cracks was quantified as a function of the distance from the surface. The formed healing products were additionally studied by means of scanning electron microscopy and energy-dispersive X-ray spectroscopy for elemental mapping/analysis.

For the X-ray µCT scanning, small cylindrical specimens (mixtures in Table 5.1 and storage conditions described in paragraph 5.3) with a height of 10 mm and a diameter of 6 mm were drilled from the casted specimens (160 × 40 × 10 mm^3) along their height. After drilling, the cylinders were taped around their sides to prevent collapse during crack creation. Those cracks were created manually at an age of 28 days by putting the samples in a screw jack and performing a Brazilian splitting test. The crack widths were measured ten times along the top and bottom of the specimens (interval distance 500 µm). The crack widths were approximately 100 µm (98 ± 20, 101 ± 17, 101 ± 14, 94 ± 19, 105 ± 11 µm for two REF and three SAP (1 m% of SAP B) specimens, respectively). The sides of the sample were partly crushed, but the interior did show a stable crack.

Only one specimen for each series in the different healing conditions was used due to the large amount of scanning time and time-consuming data-processing work per sample. Three samples with SAPs and two without SAPs were first scanned at an age of 28 days and were subsequently studied in three different curing conditions (Figure 5.45). The specimens were stored at a relative humidity (RH) of 60%, of more than 90% and in wet/dry cycles (1 hour in water and subsequently 23 hours in standard laboratory conditions at 60% RH). The temperature was always 20 ± 2°C. The two reference samples without SAPs were only stored in a RH > 90% and in wet/dry cycles. If such a reference specimen would be stored at 60% RH, there would not be any noteworthy verifiable form of autogenous healing. After 28 days of healing (at an age of 56 days) all specimens were scanned again. The specimens were dry when tested.

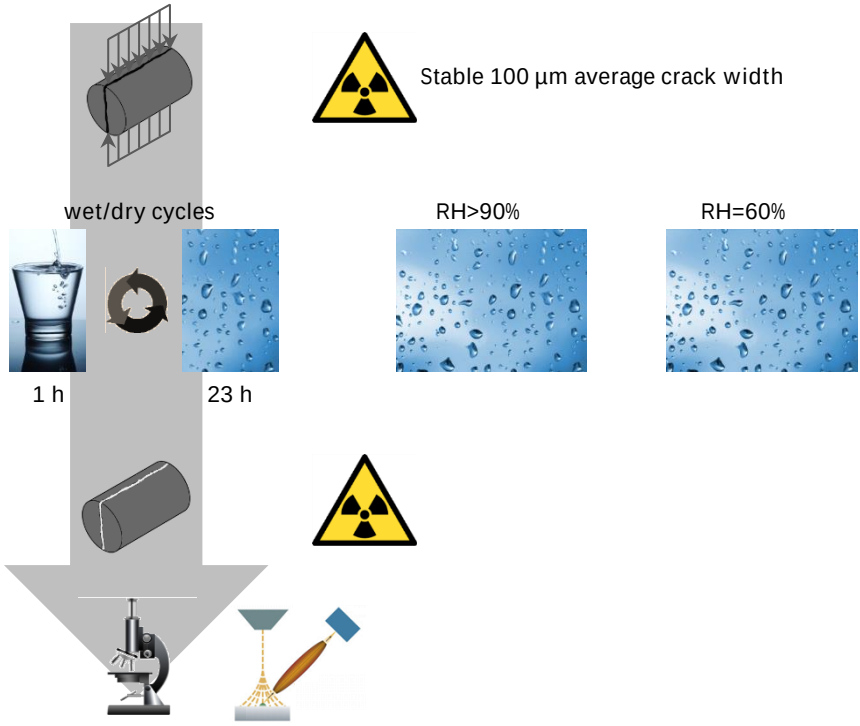

Figure 5.45. Testing sequence used for X-ray computed microtomography measurements.

The X-ray µCT scans were performed at the Centre for X-ray computed tomography of Ghent University (UGCT) (Masschaele et al., 2007) (Figure 5.46). The obtained resolution is an important factor to consider. As the X-ray beam used was conical, larger objects are imaged at a lower magnification and consequently at an inferior resolution than smaller samples. In this research 6 mm-sized specimens were investigated. The cylindrical specimen with a diameter of 6 mm was positioned between an X-ray source and an X-ray detector. CT requires a rotational motion of the sample relative to the source-detector system. For all samples, 2001 projections over 360° were taken with an exposure time of 1000 ms for each projection (PerkinElmer Camera). An aluminium filter (1 mm) was used to optimally match the detected spectrum with the attenuation behaviour of the sample. The X-ray tube was set at a voltage of 160 kV with a tube current around 62.5 µA. The obtained voxel size for the cylindrical cores was 6 µm. Taking this voxel size into account, features smaller than 12 µm were not visible in the reconstructed volumes. Because the samples had to be scanned before and after healing, the same acquisition parameters (filter, exposure time, number of projections, etc.) were chosen for each scan. After obtaining the raw projections, reconstructions of the samples, before and after the healing cycles, were performed using the software Octopus (Vlassenbroeck et al., 2007). After this reconstruction step, the volumes before and after were registered using VG Studio Max 2.1 and Dataviewer (Brucker; www.skyscan.be).

Figure 5.46. Sample within the concrete chamber and used beam line (Hector).

Quantification of the reconstructed slices was done using Octopus Analysis (formerly Morpho+) (Brabant et al., 2011). Before analysing the porosity, a bilateral filter was applied to remove the influence of noise. Afterwards, the porosity could be determined as the voids and plain cementitious material have a clearly different attenuation and corresponding grey value, and the value of threshold was chosen to be the minimum point in the grey histogram (the same values for all samples). It was thus possible to threshold the porosity on the reconstructed images. After thresholding, isolated foreground and background pixels were removed. An example of an original image from microtomography and its corresponding segmented binary image is shown in Figure 5.47. By calculating the equivalent diameter, pores with different sizes could be selected. This ranged from smaller capillary pores towards larger macro pores, taking into account that pores smaller than 12 µm could not be reliably thresholded. The biggest 'pore' was the crack itself and voids in connection with the crack structure.

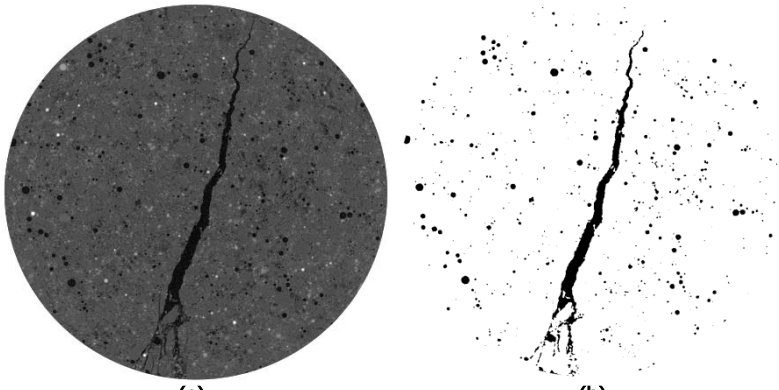

Figure 5.47. Original image obtain from microtomography **(a)** and corresponding segmented binary image **(b)**. The diameter of the specimen is 6 mm.

The healing products could be separated from the cementitious matrix by subtracting the reconstructions obtained after the healing period and the reconstructions before healing. The differential volume represented the formed healing products. Afterwards, a bilateral filter was applied to remove the influence of noise. After thresholding, isolated foreground and background pixels were removed. The precipitation as a function of depth inside the sample core was calculated with a step size of 6 µm.

The three obtained data sets per specimen (original un-healed specimen, porosity with equivalent diameter and healing products) were visualized three-dimensionally by means of the software VG Studio Max 2.1.

5.9.2 Visualising the formed healing products

The X-ray µCT measurements resulted in a direct visualization of the healing products as a function of the crack depth. By subtracting the images after and before healing, the amount of healing could be quantified. The images of the porosity and the formed healing products along the vertical axis of the cylindrical specimens at the top, middle and bottom of the sample are shown in Figure 5.48. The porosity and the crack are depicted in black and the new formed healing products after 28 days of healing conditions are in yellow. Also, in one part of the figure (SAP specimen stored at 60% RH), some SAP particles are highlighted in blue. The SAP particles could be visualized as the equivalent diameter of the porosity was determined using the software Octopus Analysis. The larger pores were the macro pores formed by the SAPs.

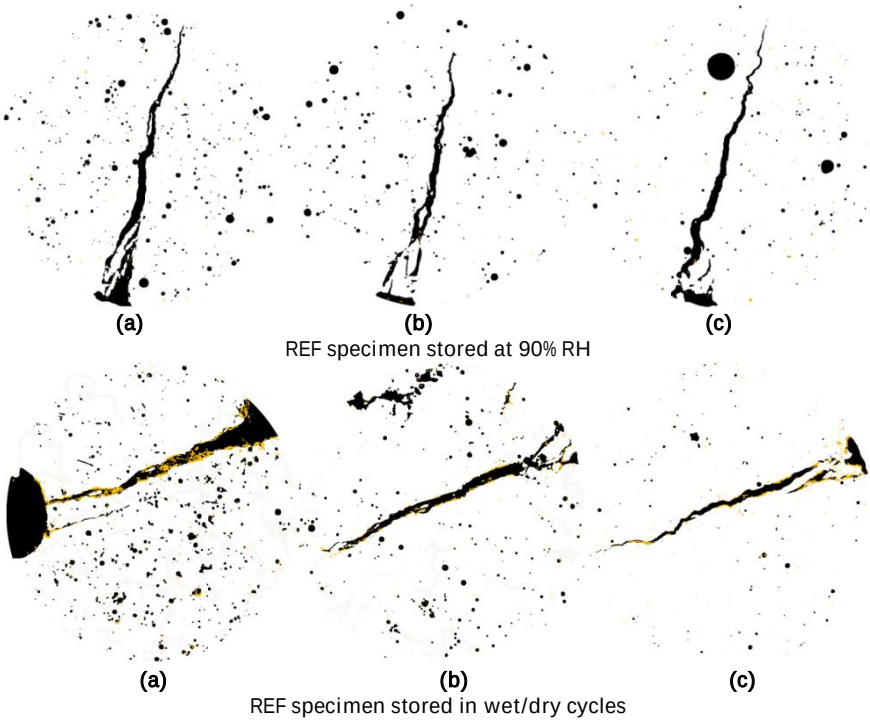

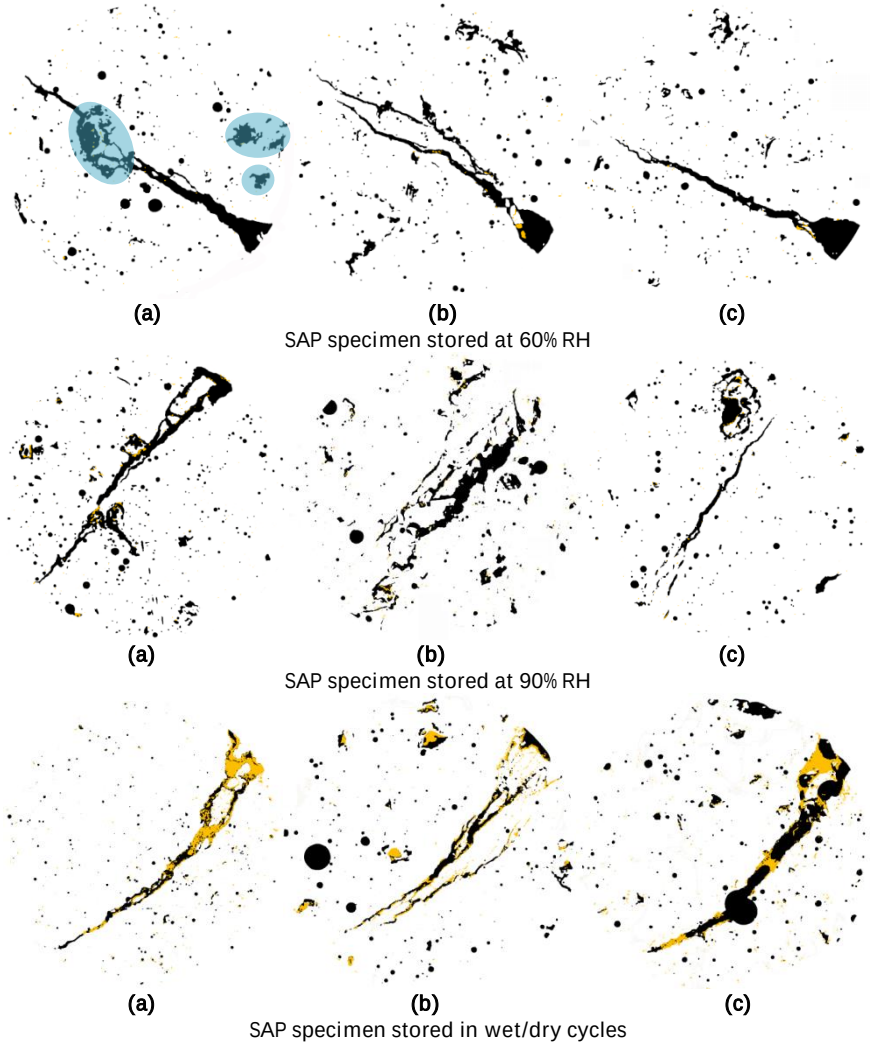

Figure 5.48. Cross-sections of the specimens with and without superabsorbent polymers stored in different curing conditions, at the top **(a)**, middle **(b)** and bottom **(c)** of the specimen. Black depicts the porosity and the crack, and yellow the formed healing products. In **(a)** some SAP particles are coloured in blue (SAP specimen stored at 60% RH). The diameter of the specimen is 6 mm.

It is clear that specimens healed under wet/dry cycles exhibit the best healing as a fair amount of water is available for autogenous healing in the form of further hydration, pozzolanic activity and calcium-carbonate crystallization. If superabsorbent polymers are added, the amount of healing after performing wet/dry cycles is higher. It is possible that the superabsorbent polymers are shifted in position due to the increase in mass during moisture uptake and that small loose particles shift due to handling. Precautions were made to safely move the specimens without disturbing them too much during transportation. Loose

particles are present in all specimens and this effect should be averaged out of the obtained results. All specimens could be compared as they were handled in the same way.

At a relative humidity of more than 90%, the healing is far less compared to the healing in wet/dry cycles as almost no fluid water is present. However, specimens with superabsorbent polymers show partial healing. At a relative humidity of 60%, only the mixtures with SAPs show partial healing and it was decided not to study the reference sample as there would not be significant healing.

The regain in mechanical properties for V-shaped cracks and its repeatability was already studied on the same mixtures. Samples with SAPs show hereby a higher regain in first-cracking-strength than the SAP-free samples under all studied healing conditions. The regained first-cracking-strength for the samples healed in wet/dry-cycles is higher (46% REF; 75% SAP) than for those healed in an environment with a RH > 90% (20% REF; 58% SAP) which, in turn, is higher than for those healed in an environment with a RH = 60% (7% REF; 45% SAP).

To verify the amount of additional water, a simple study can be conducted correlated to the amount of air pores, following the method described in (Laustsen et al., 2015). Based on a microscopic analysis, only considering the size of the macro pores, it was found earlier that the sizes of macro pores were 827 ± 173 µm (n = 100) for the SAP mixtures. The sizes if 8.9 g mixing water/g SAP were used, are 922 ± 102 µm (theoretical size if perfect spherical particles are assumed). This value was calculated starting from the initial size towards the final size by volume-based calculations. Both sizes correspond to the approximate size in the cross-sections highlighted in blue in Figure 5.48 (SAP specimen stored at 60% RH). The amount of additional water was thus the right one to be used since it was indeed absorbed by the SAP as appeared from the volume of the pores.

After calculating all porosity, i.e. the crack and the pores, and the healing products, the amount could be visualized in depth throughout the complete specimen. These results are shown in Figure 5.49. The complete matrix is presented in light grey, the porosity in dark grey and the healing products in yellow. The porosity in the specimens can be subdivided in the volume of pores, the crack volume and the volume of macro pores formed by the SAP particles. The amount of pores is approximately 2%, and the crack volume is approximately 2% (100 µm average crack width and 6 mm long). The amount of macro pores could be calculated based on the amount of entrained water to be added and this amount is 5%. The total amount of pores should therefore be approximately 9% in case of SAP mixtures and 4% in case of reference mixtures without SAPs. This is the case in the studied specimens; 4.89% for the REF sample stored in more than 90% RH, 5.21% in wet/dry cycles, 8.94% for the SAP specimen stored in 60% RH, 8.60% in more than 90% RH and 8.86% in wet/dry cycles.

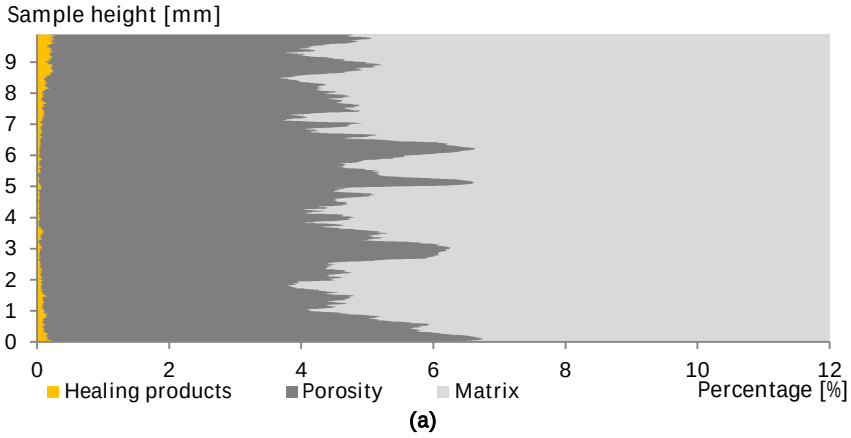
Sample height [mm]
0
1
2
3
4
5
6
7
8
9
0
2
4
6
8
10
12
Healing products
Porosity
Matrix
Percentage [%]

(a)

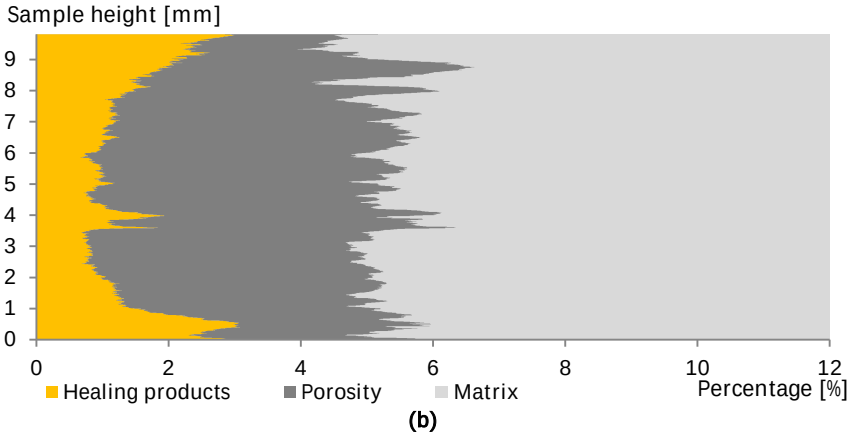
Sample height [mm]
0
1
2
3
4
5
6
7
8
9
0
2
4
6
8
10
12
Healing products
Porosity
Matrix
Percentage [%]

(b)

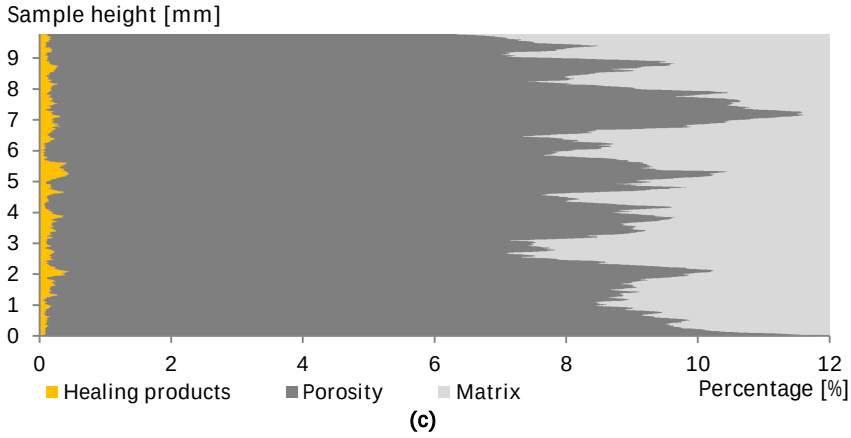
Sample height [mm]
0
1
2
3
4
5
6
7
8
9
0
2
4
6
8
10
12
Healing products
Porosity
Matrix
Percentage [%]

(c)

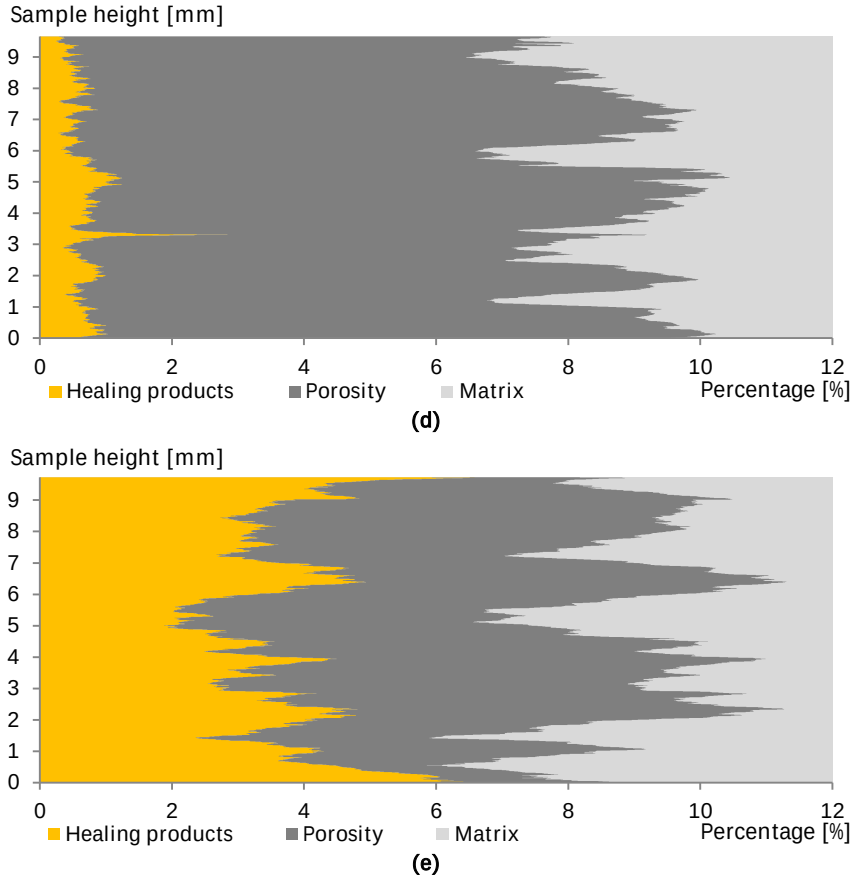

Figure 5.49. Amount of healing products coloured in yellow and un-healed part coloured in dark grey over the total area of the specimen as a function of the height of the specimen [%] for specimens without SAPs stored at 90% RH **(a)**, in wet/dry cycles **(b)**, specimens with SAPs stored at 60% RH **(c)**, at 90% RH **(d)**, and in wet/dry cycles **(e)**. The light grey depicts the solid cementitious matrix.

In specimens with SAPs in a healing condition of 60% RH (Figure 5.49c), the healing is limited but uniform throughout the complete specimen. A total of 2.0% of the porosity is healed. This amount is increased in a RH condition of more than 90%. Here 7.9% of the porosity is sealed with healing products. This amount is higher than the 1.8% healing found in a RH>90% in reference specimens without SAPs. Again, the uptake of moisture by the SAP particles proves to be useful for the healing of the cementitious material. In reference specimens without SAPs in wet/dry conditions, about 26.5% of the crack and porosity is closed, which is higher than a value of 10.8% found in literature for comparable conditions (Fan & Li, 2015). This amount is lower than the 40.4% found in SAP specimens. The polymers thus increase the self-healing potential of the material. Visually, the average 100 µm crack near the surface in SAP specimens stored in wet/dry cycles closed completely. This was also the case for V-shaped cracks in specimens with the same composition. It was found that cracks in SAP samples stored in wet/dry cycles

visually closed 80-100%, reference samples in wet/dry cycles 30%, SAP samples in RH>90% 10-20%, in RH=60% 0-10% and reference samples in RH conditions 0-1% (Figure 5.28). These findings are in agreement with the above-mentioned results. It is possible that after the healing period of 28 days, the reference and SAP samples would show additional healing. But, generally, the largest amount of healing occurs after only a few wet/dry cycles. Also, as we want to have a fast sealing/healing of the cracks, a healing period of 28 days was studied.

Figure 5.50a shows the remaining porosity of the reference material and it is clear that the top and bottom of the specimen heal faster compared to the centre of the specimen. Further inside the sample, the precipitation is randomly spread in the matrix and is concentrated in the crack. This is also the case in SAP specimens (Figure 5.50b). The amount of healing increases from a RH=60% over RH>90%, till wet/dry cycles as the amount of available water is increased as well. The calculated healing amount of all specimens can be compared using Figure 5.50c, where it is clear that the amount of healing increases with following order: REF RH>90%, SAP RH=60%, SAP RH>90%; REF wet/dry and SAP wet/dry, due to the availability of water and/or moisture.

Most of the healing product is formed at the top and bottom of the specimen near the surface of the crack. This is the case from 0 till 800-1000 µm inside the crack. The highest amount is found in the region 0-100 µm below the surface. In the interior of a crack, the amount of healing products is less and only at some distinct places, the healing products bridge a crack, probably in the vicinity of a fibre (as they act as a nucleation site for the calcium carbonate crystals). As the crack is sealed at the surface from intruding water, the crystallization comes to a hold in the interior of the crack. Less healing products are therefore found in the interior of the sample as for example the carbon dioxide will preferably be used at the surface where it dissolves in the water layer during the wet/dry cycles. Also Fan & Li (2015) showed that the region close to the surface (0-150 µm) had a high amount of crystalline products ($CaCO_3$), as studied by means of µCT tomography on specimens without SAPs. At greater depths, there was a lower amount of healing products (especially due to further hydration and pozzolanic reactions). Jonkers (2011) showed that precipitation mainly occurred near the crack rim leaving major parts of the 150 µm crack unhealed. On thin-sections it was also shown that crystals in SAP specimens form from 0 till 400-1000 µm inside a crack (Figure 5.42). Information obtained from microscopic analysis only provides insight into the healing at the surface of a specimen and of a crack. Thin sections provide information about the extent of healing perpendicular to a crack, but are destructive tests. Also, not all information is provided as it is a captured moment of a part of the crack. With X-ray computed tomography, it was possible to visualize the extent of healing in the interior of the crack and even to quantify it. The only drawback, even though it is a high-resolution X-ray, is the resolution itself. As the voxel size of a 6 mm sample was 6 µm, artefacts and areas smaller than 12 µm could not be seen. If a lower voxel size is needed, the sample needs to be smaller, but this would lead to non-representative results.

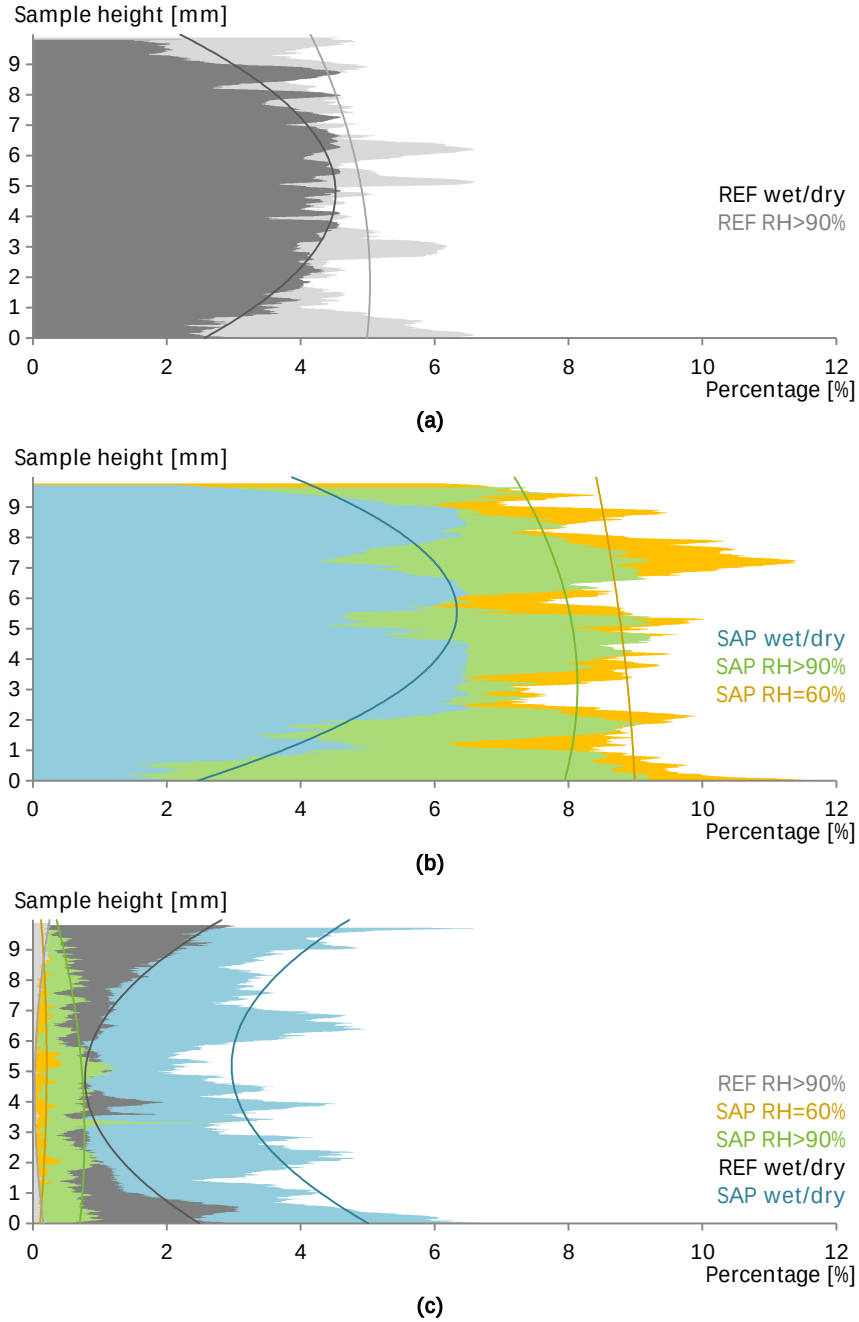

Figure 5.50. Comparison of the remaining percentage of the open porosity for the reference samples without SAPs **(a)**, and the specimens with SAPs **(b)** stored at the different curing conditions, and the healed crack volume versus the total sample volume for all studied samples **(c)** with their respective trend line.

5.9.3 Three-dimensional autogenous healing promoted by SAPs

All found results on the porosity, the crack and the formed healing products of the 2D reconstructed slices were rendered in 3D to obtain insight in the distribution of the healing products throughout the cementitious matrix and the overall crack. The three-dimensional visualizations are given in Figure 5.51. The original volume was rendered together with the thresholded porosity (as a function of the equivalent diameter) and the thresholded healing products. The original volume is shown in grey, the smaller porosity in dark grey, the SAP macro pores together with larger spherical air voids in blue (part a), the crack in red (part b) and the healing products in yellow (part c). Some precipitation may also be background noise by performing the test. This is almost impossible to avoid but is mostly removed thanks to the applied bilateral filter.

The porosity is similar in all studied specimens. Some bigger air pores can be seen as spherical air bubbles. Besides that, some irregular pores are visible as well and these are macro pores due to the mixing water uptake by the SAP particles. For better comparison, those macro pores are visualized by means of a blue colour (however, the spherical air voids are coloured in blue as well). These macro pores are homogenously distributed throughout the cementitious matrix. The sizes are the expected size considering the uptake of mixing water, as commented above. The SAP particles and macro pores adjacent to the crack are not visualized as they are considered to be part of the crack itself (based on the equivalent diameter criterion). The SAP particles are, however, present at the crack faces as they are stress initiators (Yao et al., 2011). This is beneficial for self-sealing and self-healing as the polymers are available to the intruding fluids and usable where they are effectively needed. The crack appears to be a steady-state through-going crack and the crack width is approximately 100 µm throughout the complete specimen.

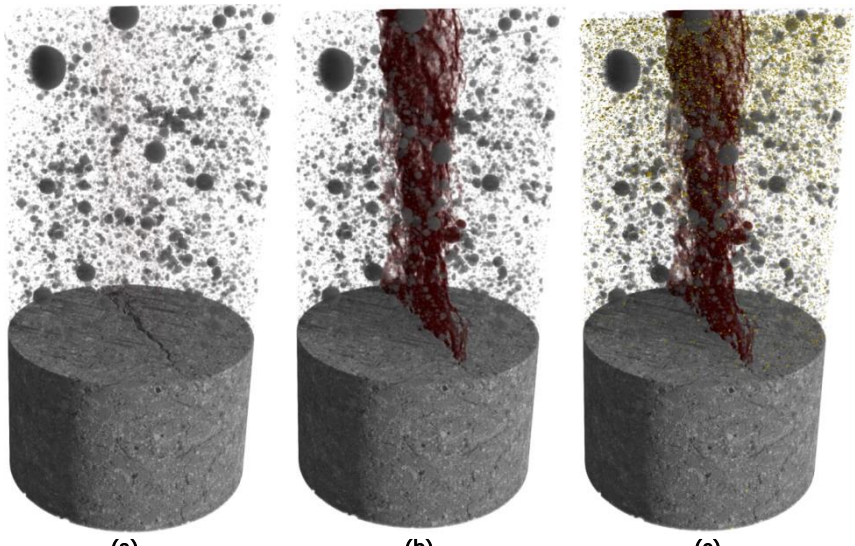

REF specimen stored at 90% RH

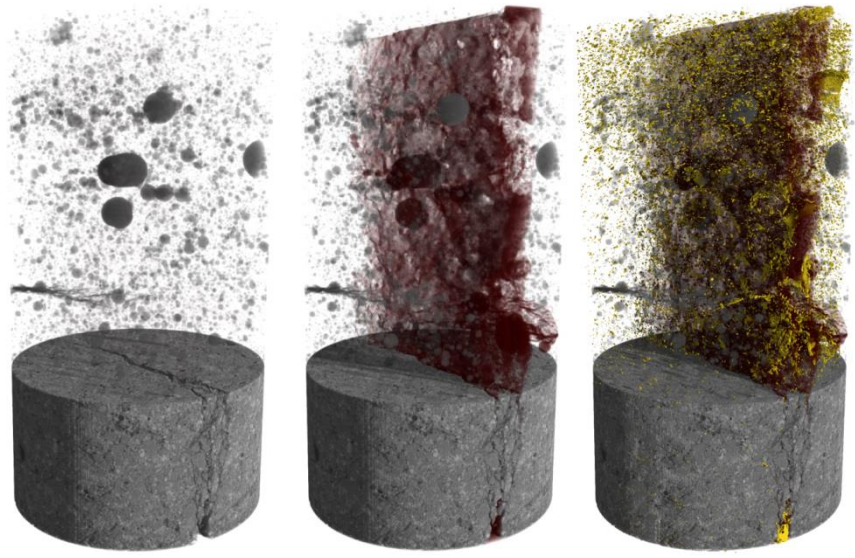

(a) (b) (c)

REF specimen stored in wet/dry cycles

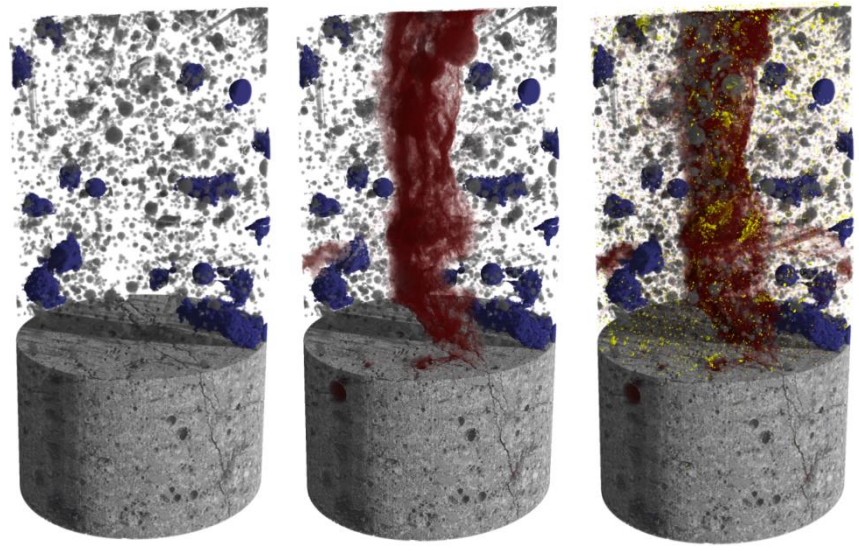

(a) (b) (c)

SAP specimen stored at 60% RH

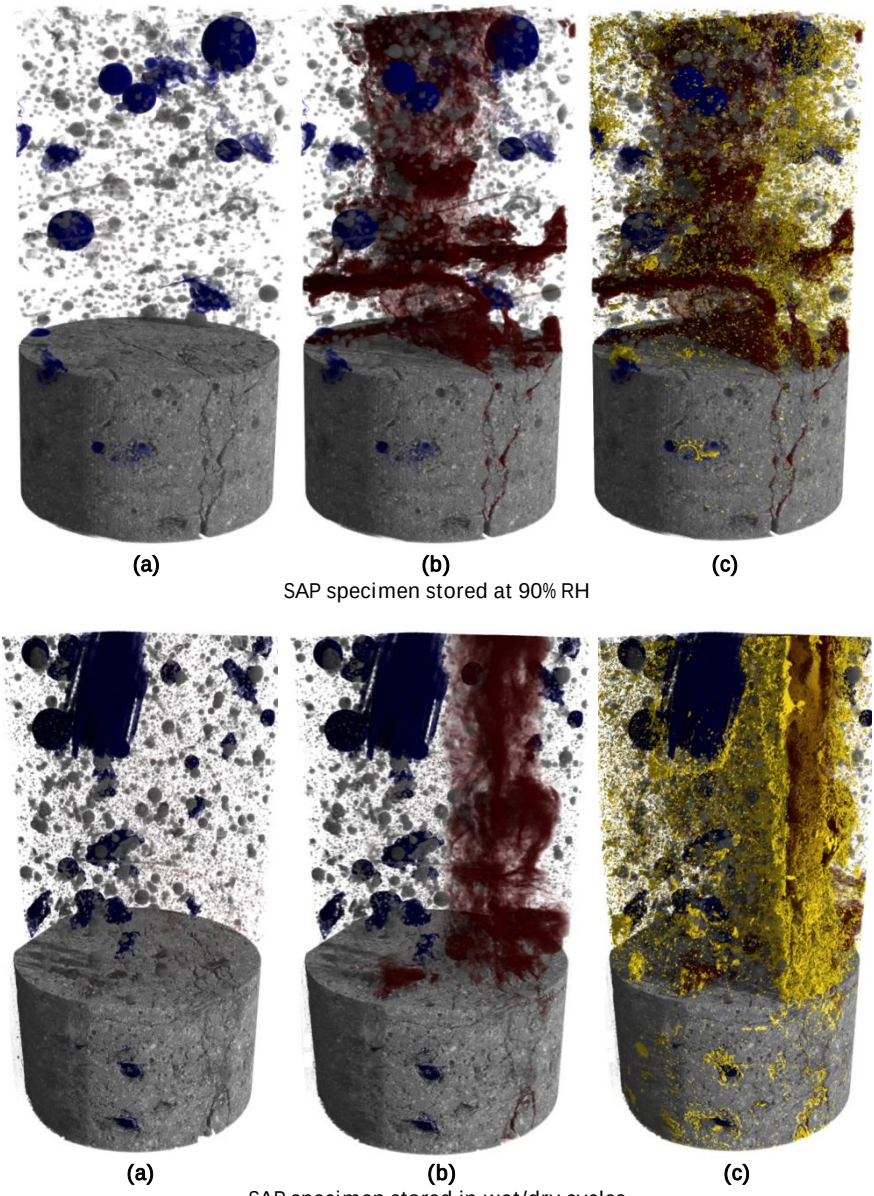

Figure 5.51. Three-dimensional cross-sections of the specimen with or without superabsorbent polymers stored in different curing conditions, with the porosity in grey and blue **(a)**, the crack in red **(b)** and the formed healing products in yellow **(c)**. The diameter of the specimen is 6 mm.

Abundant healing products formation can be seen in the cracks of specimens stored in wet/dry cycles and decreases with decreasing relative humidity. The cementitious materials are best healed in wet/dry cycles and when SAP particles are mixed in, mainly due to the availability of water. Some healing product

formation can be found near SAP particles stored in a RH condition. This can be the formation of healing products due to the release of moisture from the SAP to the local cementitious matrix. The big blue part at the top in the SAP specimen stored in wet/dry cycles is a broken off part of the specimen itself. Near the bottom of this void, some crystal formation due to self-healing is found.

5.9.4 Scanning electron microscopy and elemental analysis

A cracked specimen was also studied by means of scanning electron microscopy. A 160 × 40 × 10 mm³ specimen with healed (28 wet/dry cycles after being cracked at an age of 28 days) multiple cracks obtained from the mixture with SAPs, but loaded under four-point-bending, was impregnated with a low-viscosity epoxy resin (100 g Conpox Harpiks BY 158 and 28 g of Hærder HY 2996) under vacuum and subsequently cured for 48 h at 40°C. The specimen (perpendicular to the crack plane) was ground on a rotating wheel using a SiC abrasive paper (No. 320-grit) and water until the epoxy layer was removed and the particles became visible. Subsequently, the specimen was impregnated a second time. The specimen was then polished with SiC abrasive paper (No. 320-grit) and water until the same plane section became uncovered. Next, the specimen was polished with SiC abrasive paper (No. 2400-grit) and DP-lubricant brown (Struers). Subsequently, the specimen was polished with diamond paste (3 µm, then 1 µm and 0.25 µm) and methanol. In between each polishing step, the specimen was cleaned by submersion in methanol to remove all loose particles. At the end, the specimen was cleaned with a soft cloth to remove all impurities.

Another cracked (steady-state) specimen (160 × 40 × 10 mm³) was dry-sawn into four pieces of approximately 10 × 10 × 10 mm³ around a specific crack. The first sample was left untouched, the second was put in one wet/dry cycle, the third in two and the fourth in three wet/dry cycles. These specimens were not impregnated with epoxy and served to study the healing products formed at the surface of the crack.

Prior to the electron microscope analysis, the impregnated and polished healed sample together with four unpolished and not-impregnated samples (surface crack after 0, 1, 2 and 3 wet/dry cycles, respectively) were coated with a thin gold layer (approximately 20 nm) by means of a plasma magnetron sputter coater after vacuum conditioning. Scanning Electron Microscope (SEM) analysis was performed on a JEOL JSM-5600. The apparatus was used in the secondary electron mode (SEI) and the back scattered electron mode (BSE). The instrument was equipped with a BSE detector operating in the compositional contrast mode at an acceleration voltage of 20 kV. Next, the SEM apparatus was equipped with an electron microprobe JED 2300 and an EDS (Energy-Dispersive Spectroscopy) detector for elemental analysis. Here, the SEM-EDS apparatus was used in the mapping mode. Distinct spectra were made of the healing product formed at three distinct different places in the crack of the cementitious material. The magnification used was x4000 and x1000 in the SEI mode and x500 in the BSE mode.

Figure 5.52a shows the sheet-like structures, typical for a cementitious matrix, and a crack just after formation (the crack is perpendicular to the studied surface). The healing mechanism of $CaCO_3$ crystals at the surface of the specimen shows

teeth-like structures, expanding towards each other and eventually making a solid bridge over the crack (Figure 5.52). After only three wet/dry cycles, the crack near the surface (in this case a 10-15 µm crack), was healed completely (Figure 5.52d). Also the surface of the specimen was covered with crystals as the carbon dioxide and water are present there as well.

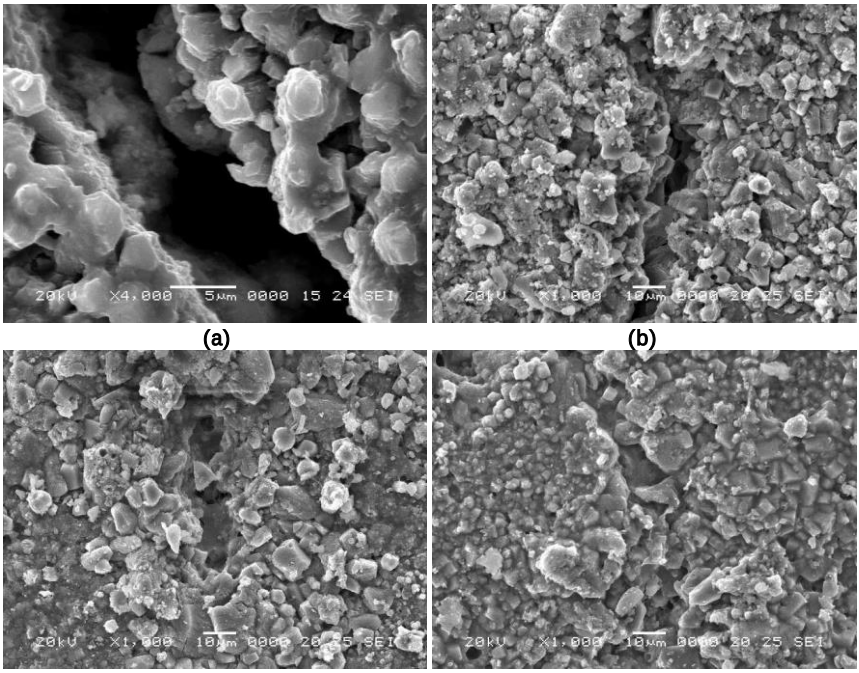

Figure 5.52. Scanning electron images of a new crack of approximately 10 µm **(a)**, the same crack after one **(b)**, two **(c)** and three **(d)** wet/dry cycle(s), showing the precipitation of healing products.

A study of two healed cracks by means of back-scattered scanning electron microscopy and mapping elemental analysis (Figure 5.53) showed the abundant presence of calcium ions in the formed crack (as shown by dashed lines), at it is the main constituent of the healed products. A teeth-like structure of $CaCO_3$ crystal formation is found at the right hand side. The blue regions in the middle are carbon ions from the used epoxy (Figure 5.53d). At the top of the bigger crack there is epoxy as well as there is a lower amount of healing products. This occurred near the red region showing silicate ions from sand particles. As less (almost no) Ca^{2+} ions are present from the cementitious matrix near the sand particles, as they do not contain such leachable ions, there is also less possibility of healing product formation. That is why there is less healing near aggregates. Just above these sand particles, there is again some healing present. This was also found in literature (Ahn & Kishi, 2010).

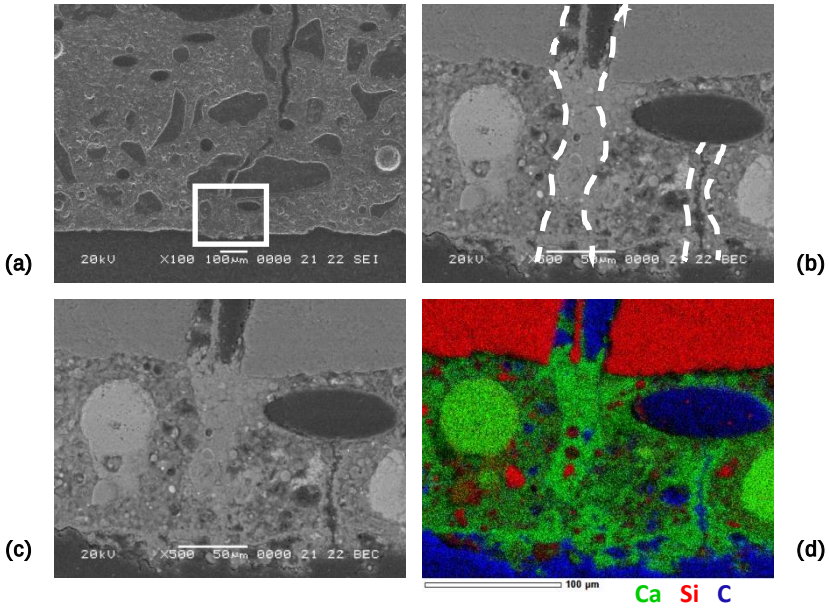

Figure 5.53. Scanning electron micrographs **(a)** and backscattered mapping **(b-c)** of two healed cracks of approximately 50 µm and 20 µm with the calcium elements in green, the siliceous elements in red and the carbon elements in blue **(d)**.

Energy-Dispersive X-ray analysis (Figure 5.54) was done on the middle region of three different healed cracks. The Energy-Dispersive Spectrum (EDS) results showed that the particles were mainly composed of three elements, namely Ca, C and O. The weight ratio was comparable to the one of $CaCO_3$, together with a small portion of $Ca(OH)_2$. Self-healing is attributed to the formation of C-S-H, the dissolution and re-deposition of $Ca(OH)_2$ and calcite formed from the carbonation of calcium hydroxide (see thermogravimetric analysis in paragraph 4.5). Au is also visible as it served as the coating layer for conductivity. Furthermore, Na, Mg, K and Fe are found as they are ions present in the cementitious matrix and basic constituents of the used cement. These other constituents are scattered results from the plain matrix and they could have been washed out from the matrix. In Figure 5.53d, small broken-off silica sand particles are dislodged and found in the crack, leading to the partial blockage and helping the overall sealing of the crack. Al and Si are present as well, and together with Ca and H ions, they may form C-S-H or calcium-aluminium-silicate-hydrates (C-A-S-H). The C-S-H healing product is preferred as it is the main source of mechanical strength while $CaCO_3$ crystals are weaker. This further hydration is expected to be one of the main mechanisms of autogenous healing in the interior of the specimen as less carbon dioxide will be present. At the outer region, it is mainly calcium carbonate crystallization.

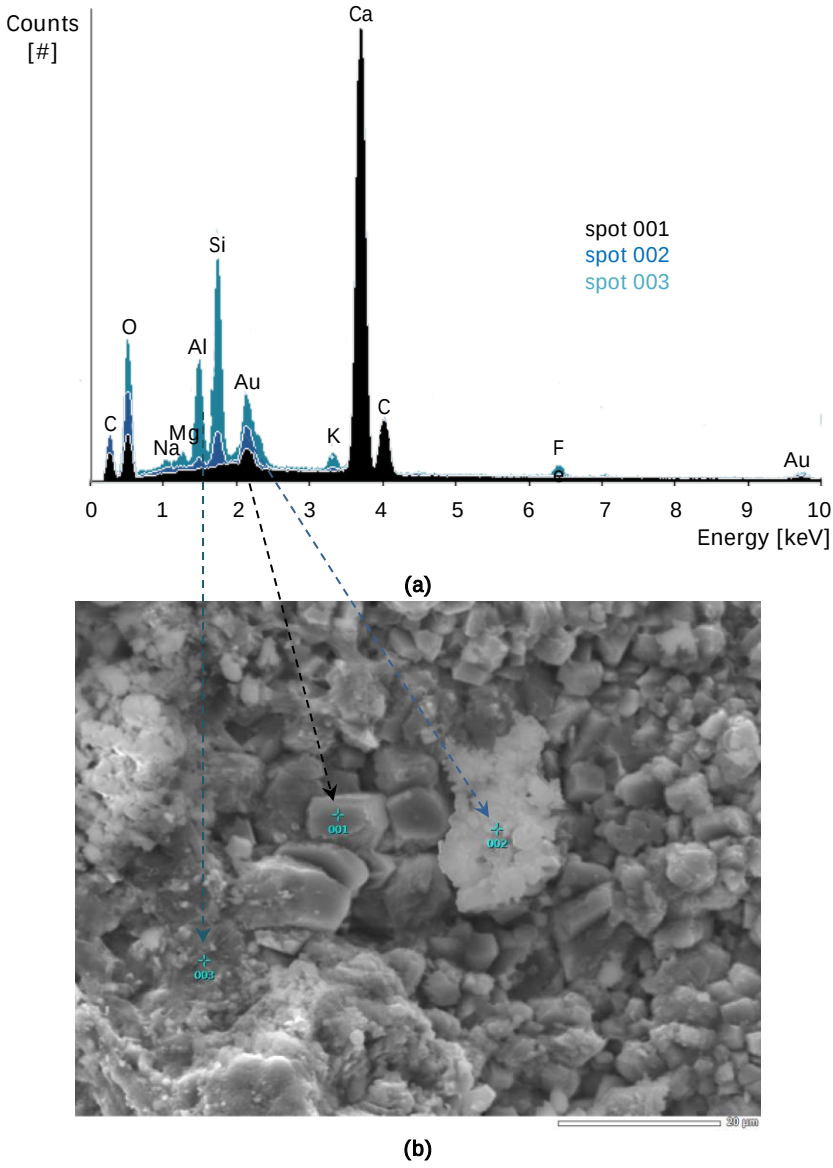

Figure 5.54. Backscattered spectra results of the healing products formed in a crack. The graph is a combination of three different spectra found in the crack **(a)**. The locations where the spectra were taken are also shown **(b)**. The scale bar amounts to 20 µm.

5.10 Conclusions

Micro-fibre reinforced strain-hardening cementitious materials are durable and provide reliable tensile ductility and crack-controlling capability to prevent localized cracking failure often observed in concrete structures. Their small cracks are interesting in terms of autogenous healing where only small cracks are able to heal completely. Autogenous healing was independent of the fibre type but was mainly dependent on the initial crack width. Small crack widths (<30 µm) often healed completely. Wider cracks (50-150 µm) only partially healed in specimens without superabsorbent polymers. Larger cracks (>150 µm) did not show a noteworthy form of autogenous healing. At early age (7 days), the main healing mechanism is the stitching of a crack by further hydration. After an age of 28 days more calcium carbonate is seen, and after 3 months of age, this calcium carbonate crystallization is the main healing mechanism.

The best overall self-healing mixture had a fly-ash-to-cement ratio of 1, a sand-to-binder ratio of 0.35, a water-to-binder ratio of 0.30, a superplasticizer-to-binder ratio of 0.0097 and 2 v% of oil-coated PVA microfibres.

Natural fibres

The use of flax and hemp fibres in cementitious composites resulted in mixtures with tensile strain-hardening and extensive multiple cracking properties. The best overall results were found in the technical flax mixtures, giving an average of 4.7 cracks per sample, with an average crack width of 28 µm and a multiple cracking amount of 0.76%.

The properties were further improved by chemically treating the fibres prior to mixing. The best results were obtained by mercerization with 2 m% NaOH of technical flax and slightly-retted hemp, providing respective averages of 7.5 and 6.8 cracks per sample, with average crack widths of 28 µm and 53 µm, respectively. A treatment with a silane primer, with benzoylperoxide, with acetic acid and with acetylation was not useful in terms of multiple cracking. The cottonisation process of flax partly removes the hemicellulose, responsible for the delay in hardening. This partial removal was confirmed by means of thermogravimetric analysis.

The findings show the great potential of flax and hemp fibres for use in cementitious composites. The most important downside to the use of these fibres remains the degradation in alkaline cementitious environment, as almost no strength remained after storing the untreated natural fibres in cement filtrate for six months. Chemical treatment improved the resistance of the natural fibres in an alkaline environment and the tensile properties were still present. Generally, flax and hemp fibres appear to be a good replacement for synthetic fibres and flax/hemp-fibre reinforced cementitious materials are an interesting alternative for future building applications.

Superabsorbent polymers

All types of SAPs are beneficial as they can promote autogenous healing. When cracking occurs and SAP particles are exposed to a humid environment, the particles swell and close the crack (see Chapter 4). The water permeability diminishes in time and the cracks are self-sealed. Furthermore, SAP particles

promote the self-healing ability by release of their absorbed water upon crack formation and this leads to a regain in mechanical properties. SAPs can sustain hydration by yielding their absorbed water for further hydration and for the precipitation of calcium carbonate. This was visually seen as cracks up to 130 µm were able to close when stored in wet/dry cycles. When not completely submerged in water, only samples containing SAPs showed self-healing properties due to moisture uptake.

To a certain degree the autogenous healing capability of cementitious materials is maintained during subsequent loading cycles. Cracks heal and close during a second healing cycle and there is a regain in first-cracking-strength of specimens stored in wet/dry cycles. The plain material without superabsorbent polymers is able to regain 46% of its first-cracking-strength after a first healing cycle. After the second healing cycle, this regain is 28%. When superabsorbent polymers are used, the regain is 75% and 66%, respectively. This increase is possibly due to the retained pore fluid and the reduced permeation through the crack. This causes the ideal conditions for promoted autogenous healing in the form of further hydration and calcium carbonate crystallization.

Analysis of thin sections and thermogravimetric analysis showed that crystals are mainly formed near the crack mouth and are likely to be calcium carbonate. The $CaCO_3$ crystallization at the first healing stage is mostly surface-controlled and the one at second healing is mostly diffusion-controlled. This is due to the consummation of Ca^{2+}-ions due to autogenous healing itself during the first healing cycles. As the ions are used near the crack faces, additional Ca^{2+}-ions will need to diffuse further through the matrix before being used in the crystallization process. X-ray computed microtomography was an extremely useful non-destructive technique to study the extent and amount of autogenous healing of a strain-hardening cementitious material. The results confirmed the overall findings. The amount of healing increased in following order:

REF RH>90% < SAP RH=60% < SAP RH>90% < REF wet/dry < SAP wet/dry

The extent of healing in wet/dry cycles depends on the position along the crack depth. A shallow region about 0 till 800-1000 µm from the surface is completely healed when using SAP particles. In the interior of the specimen, the healing amount was less.

Introducing 1 m% of SAP B relative to the cement weight gives the best results, considering no decrease in overall mechanical properties of the virgin material, which are similar as for the reference, and the superior self-sealing and self-healing capacity.

SAPs can be useful in regions with almost no rain, or for structures not exposed to direct rainfall, because they absorb the least amount of moisture and provide it to the cementitious matrix for healing. In regions with wet/dry cycles, water remains present in the SAPs during the dry periods. Therefore, self-healing can prevail at all times. Generally, the overall healing and closure of a crack may lead to less ingress of potentially harmful substances, thus possibly increasing the durability and service life of civil structures. This feature is enhanced due to the swelling action of the superabsorbent polymers and the subsequent better crystallization in a crack.

Chapter 6

Conclusions

| Thin application as a Voronoi structure, showing the endless possibilities

“It has been said something as small as the flutter of a butterfly's wing
can ultimately cause a typhoon halfway around the world.”

– *Chaos Theory*

6.1 Conclusions

In this PhD dissertation, there were three general objectives; excluding the teething problems due to mixing in superabsorbent polymers, optimizing an under-used technique for sorption measurements and designing a smart self-sealing and self-healing cementitious material independent from conditions. These objectives will be discussed in the next paragraphs.

6.1.1 To 'water' or not to 'water', that is the question

As superabsorbent polymers take up part of the mixing water, they influence the workability and thus also the fresh and hardened properties. The method by comparing the different flow values to determine the amount of additional superplasticizer or additional water is a good way to counteract the loss in workability and the change in microstructure. The amount of additional water was confirmed to be in accordance with measurements by means of optical microscopy on the size of the macro pores found. The amount of mixing water absorbed by the SAP seemed to be independent of the mixture composition. The experimentally determined amounts of additional water to be added are valid for the cement, fly ash and blast-furnace slag mixtures.

In both fly ash and blast-furnace slag systems mixtures with a water-to-binder ratio of 0.30, internal curing by means of SAP A (Ø = 100.0 ± 21.5 µm) seems to be successful, independent of the long-term higher rate of shrinkage in mixtures with supplementary cementitious materials. The particle size of SAP B (Ø = 477 ± 53 µm) was too big to ideally mitigate autogenous shrinkage, but the shrinkage was reduced nevertheless.

The use of superplasticizer (Glenium 51) used in this research to counteract the loss in workability by the superabsorbent polymers caused a postponing of the setting times, as determined by means of penetration tests and ultrasonic wave transmission measurements. The results show that one needs to be careful in the use of specific types of superplasticizer as a compensation for the loss in workability. If additional water is used (to compensate for the loss in workability), the setting is approximately the same as for a reference sample without SAPs and with the same effective water-to-cement ratio.

Not the total water-to-cement ratio, but the effective water-to-cement ratio is important in case of the capillary porosity. Additional water thus needs to be considered when using superabsorbent polymers if one aims to maintain approximately the same global microstructure. But afterwards, the additional water will cause further hydration too. This will cause a small reduction (not significant) of the amount of capillary pores. A comparison of the luminosity of thin sections under fluorescent light showed the same microstructural properties between the reference mixture and mixtures with SAPs and additional water, with the same effective water-to-cement ratio.

The bending and compressive strength are mostly governed by the formation of macro pores by the SAPs in mortars with high amounts of SAPs (up to 0.5-1 m% of cement weight). In case of bending strength, there is no conclusive difference (additional water has both positive as negative effects on the bending strength

properties), but the compressive strength is lower if additional water is used. SAP A caused a significant decrease in strength and SAP B only showed a moderate influence on the strength. If a superplasticizer is used to compensate for the loss in workability, the strength is not significantly different.

Depending on the foreseen application, additional water or superplasticizer should be used. In terms of porosity this is additional water, but in terms of strength, this should be superplasticizer. The teething problems by mixing in SAPs were addressed and counteracted.

6.1.2 Sorption to characterize the porous structure

The ideal drying technique, which can preserve the microstructure and can remove only the non-bound water, does unfortunately not exist. All drying techniques affect the microstructure in their own way. Water vapour sorption measurements have given additional experimental evidence that the best techniques to dry the cementitious samples are vacuum-drying and the solvent-exchange-method with isopropanol. Freeze-drying changed the microstructure due to thermo-mechanical stress in the inner calcium-silicate-hydrates (C-S-H). Oven-drying removed part of the non-evaporable water, dehydrated C-S-H, monosulfoaluminate (AFm) and ettringite (AFt) phases, and caused thermo-hydric stresses due to differential expansion. Capillary stresses due to receding water menisci may also induce a modification of the textural properties of the sample. Oven-drying and air-drying proved to cause carbonation, which has its impact on the microstructure. Oven-drying is thus an unsuitable drying technique to preserve the fragile microstructure of cement-based materials. Also, oven-drying at 105°C and air drying in the presence of silica gel led to the removal of part of the C-S-H phase, thus modifying the structural and textural properties of the sample. Methanol reacted with C-S-H (only upon heating) but isopropanol seemed to be inert with cementitious compounds.

Results from the static and dynamic water vapour sorption experiments could be compared and similar results were obtained. The static tests are time-consuming and the dynamic test is a fast test to determine the sorption properties of the material. The agreement between the results obtained by the two sorption techniques reveals that water sorption can be used as a characterization technique of the porous structure of cementitious materials. Cement pastes with SAPs and without additional water show a slight decrease in the micro- and mesopore range and have a similar microstructure as a cement paste with the same effective water-to-cement ratio. Cement pastes with SAPs and with additional water show no significant difference in the micropore range and a slight increase in larger mesopore range. Dynamic water vapour sorption, together with the Dubinin-Radushkevich and Barrett-Joyner-Halenda models, is a promising technique to characterize the pore structure in the micro- and mesopore range of cementitious materials.

6.1.3 Superabsorbent polymers prevent water movement: self-sealing

When cracking occurs and water enters a crack, the SAPs will swell and block the crack, resulting in a decrease in water permeability. In this way, the water flow is prevented. The drop in water permeability was both shown by low-pressure and high-pressure water permeability tests. The low-pressure water permeability of samples with 1 m% of SAP B was found to be nearly the same as for un-cracked specimens. Generally, SAP B is preferred over SAP A due to the larger particle size, less influencing all properties and showing the best results considering the self-sealing capacity. The best size of polyacrylates is approximately 500 µm in diameter. The swelling is dependent on the chemical composition of the SAPs.

Neutron radiography was used to visualize the water permeability on small scale. It is a powerful and non-destructive tool to quickly show the water in cementitious specimens and to determine the water distribution and the penetration depth of water in concrete cracks as a function of time and with a high spatial resolution. Due to the swelling capability of SAP particles, SAPs will block the crack. Not only the capillary water absorption but also the permeability of cracked concrete decreases. The water head in the small permeability tests on specimens without SAP decreases rapidly. The water head on specimens with SAPs, however, did barely change in time. In this way, harmful substances dissolved in fluids will penetrate the structure to a lower extent. Mortar samples containing SAPs show a lower total moisture uptake in a crack in comparison to samples without SAPs, due to their swelling capacity. SAP particles are thus able to retain the fluid within their structure and the crack is self-sealed autonomously.

In summary, SAP particles are able to prevent water movement through a crack, thus reducing the uptake of harmful substances, most likely leading to an enhanced long-term durability and normal service life.

6.1.4 A self-healing material independent from conditions

Microfibre-reinforced cementitious materials are durable and provide reliable tensile ductility and crack-controlling capability to prevent localized cracking failure often observed in concrete structures. The crack width is limited to 30 µm.

The use of flax and hemp fibres in cementitious composites resulted in mixtures with tensile strain-hardening and extensive multiple cracking properties. Mixtures with natural fibres show a lower workability due to their mixing-water uptake. Mixtures with cottonised flax hardened faster than mixtures with technical flax. This means that the cottonisation process partly removes the hemicellulose, responsible for the delay in hardening. This partial removal was confirmed by the thermogravimetric analysis results. The best overall results were found in the technical flax mixtures. The properties were further improved by chemically treating the fibres prior to mixing. The best results were obtained by mercerization with 2 m% NaOH of technical flax and slightly-retted hemp, providing respective averages of 7.5 and 6.8 cracks per sample, with average crack widths of 28 µm and 53 µm, respectively. Treatments with a silane primer, with benzoylperoxide, with acetic acid and with acetylation were not useful in terms of multiple cracking. The findings show the great potential of flax and hemp fibres for use in cementitious

composites. The most important downside to the use of these fibres remains the degradation in alkaline cementitious environment, as almost no strength remained after storing the untreated natural fibres in cement filtrate for six months. Chemical treatment (especially the mercerization with 2 m% NaOH) improved the resistance of the natural fibres in an alkaline environment and the tensile properties were still present.

Autogenous healing was independent of the fibre type but was mainly dependent on the initial crack width. If the crack widths remained small, this allowed autogenous healing. Small crack widths (< 30 µm) often healed completely. Wider cracks (50-150 µm) only partially healed. Larger cracks (>150 µm) did not show a noteworthy form of autogenous healing.

Generally, natural fibres appear to be a good replacement for synthetic fibres and flax fibre reinforced cementitious materials are an interesting alternative for future building applications.

When cracking occurs and SAP particles are exposed to a humid environment, the particles swell and close the crack. The water permeability diminishes in time and the cracks are sealed. The combination of microfibres and superabsorbent polymers leads to self-healing of small cracks as SAPs can sustain hydration by yielding their absorbed water and provide water to the cementitious matrix. Specimens healed after storing them in wet/dry cycles, exhibit the best healing as a fair amount of water is available for autogenous healing in the form of further hydration, pozzolanic activity and calcium carbonate crystallization. If superabsorbent polymers are added, the amount of healing is higher due to the higher availability of water, especially during dry conditions in wet/dry cycles and due to the moisture uptake capacity at certain relative humidity. At a relative humidity of more than 90%, the healing is far less compared to the healing in wet/dry cycles as almost no water is present. However, specimens with superabsorbent polymers do show partial healing. X-ray computed microtomography (µCT) is hereby an extremely useful non-destructive technique to study the extent and amount of autogenous healing of a strain-hardening cementitious material. The amount of healing increased in following order:

REF RH>90% < SAP RH=60% < SAP RH>90% < REF wet/dry < SAP wet/dry

Cracks in specimens containing SAPs are able to close up to crack widths of 130 µm when stored in wet/dry cycles. Analysis of thin sections and µCT showed that crystals are mainly formed near the crack mouth in a shallow region about 0 till 800-1000 µm from the surface and are likely to be calcium carbonate. The $CaCO_3$ crystallization at the first healing stage is mostly surface-controlled and the one at second healing is mostly diffusion-controlled. This is due to the consummation of Ca^{2+} ions due to autogenous healing itself during the first healing cycles. As the ions are used near the crack faces, additional Ca^{2+} ions will need to diffuse further through the matrix before being used in the crystallization process. In the interior of the specimen, the healing amount was less. The found healing products were $CaCO_3$, together with a small portion of $Ca(OH)_2$, C-S-H and C-A-S-H.

SAP particles promote the self-healing ability by renewed internal curing upon crack formation and this leads to regain of mechanical properties such as the first-cracking-strength, the modulus of elasticity and the amount of multiple cracking.

In wet/dry cycles, the plain material without superabsorbent polymers is able to regain 46% of its first-cracking-strength after a first healing cycle. After the second healing cycle, this regain is 28%. When superabsorbent polymers are used, the regain is 75% and 66%, respectively. This increase is possibly due to the retained pore fluid and the reduced permeation through the crack. This causes the ideal conditions for promoted autogenous healing. When not completely submerged in water, only samples containing SAPs showed self-healing properties due to moisture uptake. Even in an environment with a RH > 90%, there is a non-negligible healing capacity noticeable, due to their moisture uptake capacity.

Introducing 1 m% of SAP B relative to the cement weight gives the best results, considering the mechanical properties of the virgin material, which are similar as for the reference, and the superior self-sealing and self-healing capacity. Even though the active cross-section is reduced due to the macro pores resulting in a smaller first-cracking-strength, this effect is not significant when using larger SAP particles. The innovative smart material with SAP B is thus an excellent material to use in future building applications as the healing extent is improved.

SAPs can be useful in regions with almost no rain, or for structures not exposed to direct rainfall, because they absorb the least amount of moisture and provide it to the cementitious matrix for healing. In regions with wet/dry cycles, water remains present in the SAP during the dry periods. Therefore, self-healing can prevail at all times.

Generally, the sealing and healing of a crack may lead to less ingress of potentially harmful substances, thus increasing the durability and service life of civil structures. This feature is enhanced due to the multiple cracking induced by synthetic microfibres and the swelling action of the superabsorbent polymers in a crack and the subsequent better healing of the crack (Figure 6.1).

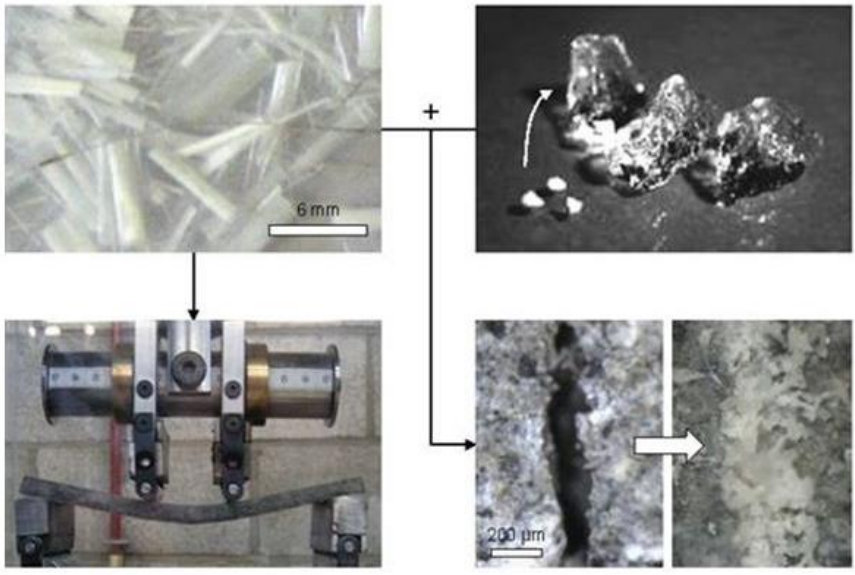

Figure 6.1. General overview of the combination of microfibres and SAPs to receive multiple cracking with small healable cracks and the stimulation of autogenous healing.

6.2 Perspectives and future

6.2.1 But at what cost?

Current practice requires regular inspection, maintenance and repair, to ensure structural safety over the service life of the structure. These practices involve large direct and indirect costs, such as economic losses from traffic jams. Additionally, not all structures are easy to access for inspection and repair. It would thus be an enormous advantage if the concept of self-healing could be translated to our engineering materials, such as concrete. For specific applications (large concrete structures as public works, industrial complexes - places which are inaccessible or difficult to reach as works underground, works under water - structures where liquid-tightness is important as tunnels, basements, waste storage structures, bridge decks, industrial floors), self-healing concrete could reduce the costs drastically. Since the maintenance and repair costs are reduced and the service life is increased, this results in a financially positive situation.

Several self-healing mechanisms can be applied. These are; bacterial healing (encapsulation in diatomaceous earth, microcapsules or hydrogels) (Wang, 2013), autonomous polymeric healing (Van Tittelboom, 2012) and the use of superabsorbent polymers to promote autogenous healing with or without combination of microfibres. All of them have their advantages and disadvantages. Considering the additional cost per m³ of concrete, the following calculation can be made.

Capsules polyurethane (PU):
dosage of microencapsulated PU: 3% relative to the volume of concrete;
cost of microencapsulated PU: 5 €/kg (PU) + 15 €/kg (capsules) = 20 €/kg;
total: 20 €/kg · 1050 kg/m³ (density polyurethane) · 3% = **630 €/m³**.

Bacterial vegetative cells (B_v) and diatomaceous earth (DE):
dosage of DE: 1-5% of cement;
cost of DE: 0.6 €/kg · 300 kg/m³ · 1-5% = 1.8-9 €/m³;
dosage of B_v: 5% of DE;
cost of B_v: 30 €/kg · 300 kg/m³ · 5% · 1-5% = 4.5-22.5 €/m³;
dosage of bio-reagents (Yeast extract, urea and $Ca(NO_3)_2$): 1-4% of cement;
cost: 1.6 €/kg · 300 kg/m³ *1-4% = 4.8-19.2 €/m³;
electricity cost immobilization; €0.2;
total: 1.8-9 €/m³ + 4.5-22.5 €/m³ + 4.8-19.2 €/m³ + €0.2 = **11.3-50.9 €/m³**.

Bacterial spores (B_s) and microcapsules:
dosage of microencapsulated spores: 1-3% of cement;
cost of microencapsulated spores: 50 €/kg · 300 kg/m³ · 1-3% = 150-450 €/m³;
dosage of bio-reagents (Yeast extract, urea and $Ca(NO_3)_2$): 1-4% of cement;
cost: 1.6 €/kg · 300 kg/m³ · 1-4% = 4.8-19.2 €/m³;
total: 150-450 €/m³ + 4.8-19.2 €/m³ = **154.8-469.2 €/m³**.

Bacterial spores (B_s) and hydrogels:
dosage of hydrogel: 1-2% of cement;
cost: 5 €/kg · 300 kg/m³ · 1-2% = 15-30 €/m³;
dosage of Bs: 0.5-1% of hydrogel (dry weight);
cost: 30 €/kg · 300 kg/m³ · 1-2%* 0.5-1% = 0.9-1.8 €/m³;
dosage of bio-reagents (Yeast extract, urea and $Ca(NO_3)_2$): 1-4% of cement;
cost: 1.6 €/kg · 300 kg/m³ · 1-4% = 4.8-19.2 €/m³;
cost for immobilization: 5 €/kg · 300kg/m³ · 1-2% = 15-30 €/m³;
total: 15-30 €/m³ + 0.9-1.8 €/m³ + 4.8-19.2 €/m³ + 15-30 €/m³ = **35.7-81 €/m³**.

Superabsorbent polymers (SAPs) for quick self-sealing:
dosage of SAPs sodium polyacrylate BASF: 1% of cement;
cost of SAPs sodium polyacrylate BASF: 3 €/kg;
total: 3 €/kg · 300 kg/m³ · 1% = **9 €/m³**.

Microfibres and superabsorbent polymers (SAPs):
dosage of PVA microfibres: 2% of volume = 26 kg/m³;
cost of PVA fibres: 1 €/kg;
dosage of SAPs sodium polyacrylate BASF: 1% of cement;
cost of SAPs sodium polyacrylate BASF: 3 €/kg;
Higher amounts of cement: 571 instead of 300 kg/m³ (100 €/ton) = €27.1;
total: 26 kg/m³ · 1 €/kg + 571 kg/m³ · 3 €/kg · 1% + €27.1 = **70.23 €/m³**.

Manual injection of one crack per m³ concrete (which is realistic) in a tunnel will cost 120-140 €/m³, so this is more expensive than applying a self-healing material (except for the PU solution), even without the indirect costs for closing the tunnel, etc. Even when self-healing increases the design life with only 20%, a lower life cycle cost will be obtained.

At the moment, without optimizing the production costs of the materials, the application of the strain-hardening cementitious material proves to be acceptable considering the cost. The increase in costs in the application with microfibres and superabsorbent polymers is due to the higher amount of cement, the use of the synthetic fibres and the superabsorbent polymer. But, these costs do not outweigh the savings made by excluding maintenance and repair costs. The problem may be the initial budget saving, which is always a problem. People think about the past, live in the present and only think about the near future. They should also act towards the not so imminent future. A small cost to be made now can save a lot in this future. Another problem is the governmental system. As a government is mostly only appointed for several years, it sometimes does not matter which solution is chosen, as long as it works within the legacy time. Unfortunately, this is always the cheapest solution. It is a current constitutional spiral which is not easily stopped. The material is pretty new to the conservative construction area, so a sensibilisation needs to occur before actual matters can be undertaken. The future, however, looks bright and promising to use this kind of material. The general public interest is an example for this and can ultimately stimulate the use of these new and innovative materials.

6.2.2 What does the future look like?

Possible applications of the self-sealing and self-healing material are widely spread. Water-retaining structures may benefit and other construction companies may be interested.

Furthermore, due to the self-compacting properties of the strain-hardening mixture, thin forms are achievable. Nature fits form to function, rewards cooperation and curbs excess form within. This is also true for this material; the accretion of material to places where it is most needed, resulting in adaptive structures. The form should be ideal to transfer loads, so that an excess of material can be removed. Also, both the microfibres and the superabsorbent polymers are working together to receive optimal conditions for self-sealing and self-healing.

The shape of a tree is the history of the forces which were acting on it while it grew. These same sensory mechanisms are found in animals, such as in their bone structure. Both their slender lightness and apparent fragility are only a facade. It is their ability to adapt shape and structure quickly to changing loads that make them robust and strong. This adaptiveness to changing forces and circumstances during its lifetime, many of which may be unpredictable, is a key feature. Such adaptiveness has also been called smart or intelligent behaviour (Beukers & Van Hinte, 1998). The strain-hardening material is also changing its properties in time, after for example imposed loading and autogenous healing. It should not be compromised by losing its load-bearing capacity. The new and smart material is able to transfer loads once again. This material will result in lighter and safer structures, leading to a reduced safety factor as the structure may reach its optimal design.

The principle of using superabsorbent polymers for internal curing has its possible applications for the industry. Contractors are searching for a way to decrease shrinkage cracks and to obtain a watertight structure. This is especially important for tunnel elements, underground parking garages, basements, liquid containing structures, pavements, etc. Nowadays, they are often forced to apply crack repair right after construction, due to the formation of shrinkage cracks and thermal cracks at early age. The shrinkage could be overcome by using superabsorbent polymers as they may provide internal curing to the construction element: they absorb water in the fresh concrete mix, and provide it to the cement particles at the right moment in the hydration process, in this way reducing the autogenous shrinkage. In hardened concrete, they may seal occurring cracks, as they swell in contact with intruding water. This will lead to more watertight structures. The SAPs will subsequently promote autogenous healing of the crack since they provide water for further hydration of yet unhydrated cement particles and calcium carbonate precipitation, leading to even more tight structures and possible regain of the mechanical properties.

Fibre-reinforced cementitious composites possess the qualities of a high strength concrete combined with crack width control and energy absorption capacity. Combined with self-healing it is a durable material and very promising to use in the future. However, performance-based durability concepts are still required to get a durability design framework for these strain-hardening materials

(Altmann & Mechtcherine, 2013). The possible use of natural fibres may give a low-cost alternative for the synthetic fibres. In the end, this may lead to a greener composite for autogenous healing.

Even bacteria can be added to a hydrogel, further improving the overall amount of healing products (Wang et al., 2014b).

Water is a key parameter next to the restriction in crack width. This needs to be taken into account as not every spot of a concrete structure will be exposed to rain/water. Superabsorbent polymers prove to be useful in this respect since they will promote autogenous healing. In the presence of fluids, the cementitious material is able to heal, further hydrate, increasing its durability. This healing is thus an extension of the life-like quality.

With these new composites, new healing agents and new techniques, the self-healing material will be used more in the future. The role of autogenous healing on corrosion prevention will be important in the future. If cracks are not sealed, water containing aggressive substances will break down the passive film on the reinforcements. This aspect needs to be considered when autogenous healing is used in real-time structures. The maintenance and longevity of these structures is hereby very important.

One general conclusion can be made; one should continue to build with nature's rules. The bleeding (healing agents), blood cells (microcapsules), blood flow vascular network (porous concrete), blood clothing (polymerization), skeleton and bone healing (crystallization) are only a few properties studied in the field of construction healing. By mimicking nature to enhance performance, more durable constructions will be designed, leading to a higher service life and better overall life quality.

References

116-PCD, RILEM TC. (1999). Recommendation of TC 116-PCD: Tests for gas permeability of concrete. Materials and Structures, 32(217), 174-179.

225-SAP, RILEM TC. (2012). Application of Superabsorbent Polymers (SAP) in Concrete Construction. In V. Mechtcherine & H.W. Reinhardt (Eds.), RILEM State-of-the-Art Report Prepared by Technical Committee 225-SAP, pp. 165.

Abrams, D.A. (1913). Test of a 40 ft. reinforced concrete highway bridge. In ASTM Proceedings (Ed.), (Vol. 13). Philadelphia: American Society for Testing Materials, 884–922.

Adolphs, J. (2008). Interaction of Water Vapour with Hardened Cement Paste - Specific Effects at 30%RH. Restoration of Buildings and Monuments, 14(4), 251-258.

Adolphs, J., Heine, P., & Setzer, M.J. (2002). Changes in Pore Structure and Mercury Contact Angle of Hardened Cement Paste Depending on Relative Humidity. Materials and Structures, 35(8), 477-486.

Aggelis, D.G., & Philippidis, T.P. (2004). Ultrasonic wave dispersion and attenuation in fresh mortar. NDT&E International, 37(8), 617-631.

Agopyan, V., Savastano Jr., H., John, V.M., & Cincotto, M.A. (2005). Developments on vegetable fibre-cement based materials in São Paulo, Brazil: an overview. Cement and Concrete Composites, 27(5), 527-536.

Ahn, T.-H., & Kishi, T. (2010). Crack Self-healing Behavior of Cementitious Composites Incorporating Various Mineral Admixtures. Journal of Advanced Concrete Technology, 8(2), 171-186.

Ahs, M.S. (2008). Sorption scanning curves for hardened cementitious materials. Construction and Building Materials, 22(11), 2228-2234.

Akers, S.A.S., & Studinka, J.B. (1989). Ageing behaviour of cellulose fibre cement composites in natural weathering and accelerated tests. International Journal of Cement Composites and Lightweight Concrete, 11(2), 93-97.

Akhavan, A., Shafaatian, S.-M.-H., & Rajabipour, F. (2012). Quantifying the effects of crack width, tortuosity, and roughness on water permeability of cracked mortars. Cement and Concrete Research, 42(2), 313-320.

Aldea, C., Shah, S., & Karr, A. (1999). Effect of Cracking on Water and Chloride Permeability of Concrete. Materials in Civil Engineering, 11(3), 181-187.

Aldea, C., Wong, W., Popovics, J.S., & Shah, S.P. (2000). Extent of Healing of Cracked Normal Strength concrete. Materials in Civil Engineering, 12(1), 92-96.

Altmann, F., & Mechtcherine, V. (2013). Durability design strategies for new cementitious materials. Cement and Concrete Research, 54, 114-125.

Andonian, R., Mai, Y.W., & Cotterel, B. (1979). Strength and fracture properties of cellulose fibre reinforced cement composites. Cement Composites, 1(4), 151-158.

Andry, H., Yamamoto, T., Irie, T., Moritani, S., Inoue, M., & Fujiyama, H. (2009). Water retention, hydraulic conductivity of hydrophilic polymers in sandy soil as affected by temperature and water quality. Journal of Hydrology, 373(1-2), 177-183.

Antheunis, H., van der Meer, J.-C., de Geus, M., Heise, A., & Koning, C.E. (2010). Autocatalytic Equation Describing the Change in Molecular Weight during Hydrolytic Degradation of Aliphatic Polyesters. Biomacromolecules, 11(4), 1118-1124.

Aono, Y., Matsushita, F., Shibata, S., & Hama, Y. (2007). Nano-structural Changes of C-S-H in Hardened Cement Paste during Drying at 50°C. Journal of Advanced Concrete Technology, 5(3), 313-323.

Assmann, A. (2013). Physical properties of concrete modified with superabsorbent polymers. Stuttgart University, Stuttgart, pp. 199.

Aveston, J., Cooper, G.A., & Kelly, A. (1971). Single and multiple fractures. Paper presented at the NPL Conference on The Properties of Fibre Composites, science and Technology Press Ltd., 15-24.

Aziz, M.A., Paramasivam, P., & Lee, S.L. (1981). Prospects for natural fibres reinforced concretes in construction. International Journal of Cement Composites and Lightweight Concrete, 3(2), 123-132.

Baert, G., Hoste, S., De Schutter, S., & De Belie, N. (2008). Reactivity of fly ash in cement paste studied by means of thermogravimetry and isothermal calorimetry. Journal of Thermal Analysis and Calorimetry, 94(2), 485-492.

Baetens, R., Jelle, B.P., & Gustavsend, A. (2010). Phase change materials for building applications: A state-of-the-art review. Energy and Buildings, 42(9), 1361-1368.

Baley, C. (2002). Analysis of the flax fibres tensile behaviour and analysis of the tensile stiffness increase. Composites, Part A, 33(7), 939-948.

Bang, S.S., Galinat, J.K., & Ramakrishnan, V. (2001). Calcite precipitation induced by polyurethane-immobilized Bacillus pasteurii. Enzyme and Microbial Technology, 28(4-5), 404-409.

Baroghel-Bouny, V. (2007). Water vapour sorption experiments on hardened cementitious materials - Part I: Essential tool for analysis of hygral behaviour and its relation to pore structure. Cement and Concrete Research, 37(3), 414-437.

Baroghel-Bouny, V., Mounanga, P., Khelid, A., Loukili, A., & Rafaï, N. (2006). Autogenous deformations of cement pastes: Part II. W/C effects, micro–macro correlations, and threshold values. Cement and Concrete Research, 36(1), 123-136.

Barrett, E.P., Joyner, L.G., & Halenda, P.P. (1951). The determination of pore volume and area distributions in porous substances. I - computations from nitrogen isotherms. Journal of the American Chemical Society, 73(1), 373-380.

Bary, B., & Sellier, A. (2004). Coupled moisture-carbon dioxide-calcium transfer model for carbonation of concrete. Cement and Concrete Research, 34(10), 1859-1872.

Batson, G. (1976). Steel fiber reinforced concrete. Materials Science and Engineering, 25(SEP-O), 53-58.

Beaudoin, J.J. (1979). Porosity measurement of some hydrated cementitious systems by high pressure mercury intrusion - microstructural limitations. Cement and Concrete Research, 9(6), 771-781.

Beaudoin, J.J. (1987). Validity of using methanol for studying the microstructure of cement paste. Materials and Structures, 20(1), 27-31.

Beaudoin, J.J., Gu, P., Marchand, J., Tamtsia, B.T., Myers, R.E., & Liu, Z. (1998). Solvent Replacement Studies of Hydrated Portland Cement Systems: The Role of Calcium Hydroxide. Advanced Cement Based Materials, 8(2), 56-65.

Beaudoin, J.J., Sato, T. & Tumidajski, P.J. (2006). The Thermal decomposition of $Ca(OH)_2$ Polymorphs. Paper presented at the 2nd International symposium on Advances in Concrete through Science and Engineering, Québec, 1-15.

Beaudoin, J.J., & Tamtsia, B.T. (2004). Effect of drying methods on microstructural changes in hardened cement paste: an a.c. impedance spectroscopy evaluation. Journal of Advanced Concrete Technology, 2(1), 113-120.

Behl, M., & Lendlein, A. (2007). Shape-memory polymers. Materials Today, 10(4), 20-28.

Bentur, A., & Akers, S.A.S. (1989). The microstructure and ageing of cellulose fibre reinforced cement composites cured in a normal environment. International Journal of Cement Composites and Lightweight Concrete, 11(2), 99-109.

Bentur, A., Ben-Bassat, M., & Schneider, D. (1985). Durability of Glass-Fiber-Reinforced Cements with Different Alkali-Resistant Glass Fibers. Journal of the American Ceramic Society, 68(4), 203-208.

Bentur, A., & Mindess, S. (1990). Fibre Reinforced Cementitious Composites. Modern Concrete Technology Series, London and New-York: E & FN Spon, pp. 625.

Bentz, D.P. (2008). A review of early-age properties of cement-based materials. Cement and Concrete Research, 38(2), 196-204.

Bentz, D.P., & Turpin, R. (2007). Potential applications of phase change materials in concrete technology. Cement and Concrete Composites, 29(7), 527-532.

Bentz, D.P., & Weiss, W.J. (2011). Internal Curing: A 2010 State-of-the-Art Review. In NIST Interagency (Ed.), No. 7765, pp. 82.

Betterman, L.R., Ouyang, C., & Shah, S.P. (1995). Fiber-matrix interaction in microfiber-reinforced mortar. Advanced Cement Based Materials, 2(2), 53-61.

Beukers, A., & Van Hinte, E. (1998). Lightness. The inevitable renaissance of minimum energy structures. Rotterdam: 010 Publishers, pp. 191.

Bijen, J. (1990). Improved mechanical properties of glass fibre reinforced cement by polymer modification. Cement and Concrete Composites, 12(2), 95-101.

Bilba, K., Arsene, M., & Ouensanga, A. (2003). Sugar cane bagasse fibre reinforced cement composites. Part I. Influence of the botanical components of bagasse on the setting of bagasse/cement composite. Cement and Concrete Composites, 25(1), 91-96.

Bledzki, A.K., Fink, H.P., & Specht, K. (2004). Unidirectional Hemp and Flax EP- and PP-composites: Influence of Defined Fiber Treatments. Applied Polymer Science, 93(5), 2150-2156.

Bledzki, A.K., & Gassan, J. (1999). Composites reinforced with cellulose based fibres. Progress in Polymer Science, 24(2), 221-274.

Bodros, E., & Baley, C. (2008). Study of the tensile properties of stinging nettle fibres (Urtica dioica). Materials Letters, 62(14), 2143-2145.

Boel, V. (2006). Microstructure of self-compacting concrete in relation with gas permeability and durability. Ghent University, Ghent, pp. 448.

Boghossian, E., & Wegner, L.D. (2008). Use of flax fibres to reduce plastic shrinkage cracking in concrete. Cement and Concrete Composites, 30(10), 929-937.

Borges, P.H.R., Costa, J.O., Milestone, N.B., Lynsdale, C.J., & Streatfield, R.E. (2010). Carbonation of CH and C-S-H in composite cement pastes containing high amounts of BFS. Cement and Concrete Research, 40(2), 284-292.

Bos, H., Van den Oever, M., & Peters, O. (2002). Tensile and compressive properties of flax fibres for natural fibre reinforced composites. Materials Science, 37(8), 1683-1692.

Bos, K. (2004). The potential of flax fibres as reinforcement for composite materials. Eindhoven University of Technology, Eindhoven, pp. 209.

Bourmaud, A., & Baley, C. (2009). Rigidity analysis of polypropylene/vegetal fibre composites after recycling. Polymer Degradation & Stability, 94(3), 297-305.

Brabant, L., Vlassenbroeck, J., De Witte, Y., Cnudde, V., Boone, M., Dewanckele, J., & Van Hoorebeke, L. (2011). Three-dimensional analysis of high-resolution X-ray computed tomography data with Morpho+. Microscopy and Microanalysis, 17(2), 252-263.

Brandt, A.M. (2008). Fibre reinforced cement-based (FRC) composites after over 40 years of development in building and civil engineering. Composite Structures, 86(1-3), 3-9.

Brandt, A.M. (2009). Cement based composites - materials, mechanical properties and performance: Oxon, Taylor and Francis, pp. 535.

Brüdern, A.E., & Mechtcherine, V. (2010). Multifunctional use of SAP in strain-hardening Cement-based Composites. Paper presented at the International RILEM Conference on Use of Superabsorbent Polymers and Other New Additives in Concrete, Lyngby, RILEM Publications S.A.R.L., 11-22.

Brunauer, S. (1962). Tobermorite gel - the heart of concrete. American Scientist, 50(1), 210-229.

Brunauer, S., Deming, L.S., Deming, W.E., & Teller, E. (1940). On the theory of the van der Waals adsorption of gases. Journal of the American Chemical Society, 62(7), 1723-1732.

Brunauer, S., Emmett, P.H., & Teller, E. (1938). Adsorption of Gases in Multimolecular Layers. Journal of the American Chemical Society, 60(2), 309-319.

Buchholz, F.L., & Graham, A.T. (1998). Modern superabsorbent polymer technology. New-York: Wiley-VCH, pp. 279.

Butler, M., Hempel, S., & Mechtcherine, V. (2011). Modelling of ageing effects on crack-bridging behaviour of AR-glass multifilament yarns embedded in cement-based matrix. Cement and Concrete Research, 41(4), 403-411.

Campbell, M.D., & Coutts, R.S.P. (1980). Wood fibre-reinforced cement composites. Journal of Materials Science, 15(8), 1962-1970.

Castellón, C., Medrano, M., Roca, J., Nogués, M., Castell, A., & Cabeza, L.F. (2007). Use of Microencapsulated Phase Change Materials in Building Applications. Building, X, 1-7.

Cai, W., & Bisschop, J. (2012). Optical method for measuring slow crack growth in cementitious materials. Materials and Structures, 45(11), 1613-1623.

Chappuis, J. (1999). A new model for a better understanding of the cohesion of hardened hydraulic materials. Colloids and Surfaces A: Physicochemical and Engineering Aspects, 156(1-3), 223-241.

Cho, S.H. (2006). Polydimethylsiloxane-based Self-healing Composite and Coating Materials. University of Illinois, Urbana-Champaign, pp. 127.

Clear, C.A. (1985). The Effects of Autogenous Healing upon the Leakage of Water through Cracks in Concrete. In Cement and Concrete Association (Ed.). Buckinghamshire: Cement and Concrete Association, Wexham Spring, pp. 31.

Cnudde, V., Dierick, M., Vlassenbroeck, J., Masschaele, B., Lehmann, E., Jacobs, P., & Hoorebeke, L.V. (2008). High-speed neutron radiography for monitoring the water absorption by capillarity in porous materials. Section B of Nuclear Instruments and Methods in Physics Research, 266(1), 155-163.

Cnudde, V., & Jacobs, P. (2004). Monitoring of weathering and conservation of building materials through non-destructive X-ray computed microtomography. Environmental Geology, 46(3-4), 477-485.

Cohen, M.D., & Menashi, D. (1986). Morphological developments of high- and low-alkali cement paste at the glass fiber-cement interface. Paper presented at the Proceedings of Durability of Glass Fiber Reinforced Concrete Symposium, Illinois, Precast/Prestressed Concrete Institute, 158-173.

Colliec-Jouault, S., Chevolot, L., Helley, D, Ratiskol, J., Bros, A., Sinquin, C., Roger, O., & Fischer, A.-M. (2001). Characterization, chemical modifications and in

vitro anticoagulant properties of an exopolysaccharide produced by Alteromonas infernus. Biochimica et Biophysica Acta, 1528(2-3), 141-151.

Collier, N.C., Sharp, J.H., Milestone, N.B., Hill, J., & Godfrey, I.H. (2008). The influence of water removal techniques on the composition and microstructure of hardened cement pastes. Cement and Concrete Research, 38(6), 737-744.

Colombo, I.G., Colombo, M., & di Prisco, M. (2015). Tensile behavior of textile reinforced concrete subjected to freezing-thawing cycles in un-cracked and cracked regimes. Cement and Concrete Research, 73, 169-183.

Cook, D.J. (1980). Cement and concrete composites reinforced with natural fibres. Paper presented at the Symposium on Fibrous Concrete, London, The construction Press, 99-114.

Cook, R.A., & Hover, K.C. (1999). Mercury porosimetry of hardened cement pastes. Cement and Concrete Research, 29(6), 933-943.

Costache, M.C., Wang, D., Heidecker, M.J., Manias, E., & Wilkie, C.A. (2006). The thermal degradation of poly(methyl methacrylate) nanocomposites with montmorillonite, layered double hydroxides and carbon nanotubes. Polymers for Advanced Technologies, 17(4), 272-208.

Coutts, R.S.P., & Campbell, M.D. (1979). Coupling agents in wood fibre-reinforced cement composites. Composites, 10(4), 228-232.

Craeye, B., & De Schutter, S. (2006). Experimental evaluation of mitigation of autogenous shrinkage by means of a vertical dilatometer for concrete. Paper presented at the International RILEM conference on Volume changes of hardening concrete: testing and mitigation, Lyngby, RILEM Publications S.A.R.L., 21-30.

Day, R.L. (1981). Reactions between methanol and Portland cement paste. Cement and Concrete Research, 11(3), 341-349.

de Andrade Silva, F., Butler, M., Hempel, S., Tolêdo Filho, R.D., & Mechtcherine, V. (2014). Effects of elevated temperatures on the interface properties of carbon textile-reinforced concrete. Cement and Concrete Composites, 48, 26-34.

de Beer, F.C., le Roux, J.J., & Kearsley, E.P. (2005). Testing the durability of concrete with neutron radiography. Nuclear Instruments and Methods in Physics Research Section A, 542(1-3), 226-231.

de Beer, F.C., Strydom, W.J., & Griesel, E.J. (2004). The drying process of concrete: a neutron radiography study. Applied Radiation and Isotopes, 61(4), 617-623.

De Belie, N., Baert, G., & De Schutter, S. (2011). Modelling of microstructure of Portland cement: fly ash binders based on calorimetric and thermogravimetric experiments. Paper presented at the Chemistry of Cement, XIII ICCC International congress, Madrid, 1-7.

De Belie, N., Kratky, J., & Van Vlierberghe, S. (2010). Influence of pozzolans and slag on the microstructure of partially carbonated cement paste by means of water vapour and nitrogen sorption experiments and BET calculations. Cement and Concrete Research, 40(12), 1723-1733.

De la Varga, I., Castro, J., Bentz, D.P., & Weiss, W.J. (2012). Application of internal curing for mixtures containing high volumes of fly ash. Cement and Concrete Composites, 34(9), 1001-1008.

De Lhoneux, B., Kalbskopf, R., Kim, P., Li, V.C., Lin, Z., Vidts, D., Wang, S., & Wu, H. (2002). Development of High Tenacity Polypropylene Fibres for Cementitious Composites. Paper presented at the JCI International Workshop on Ductile Fiber Reinforced Cementitious Composites (DFRCC) - Application and Evaluation, Takayama, JCI – Tokyo, 121-132.

De Muynck, W., Cox, K., De Belie, N., & Verstraete, W. (2008a). Bacterial carbonate precipitation as an alternative surface treatment. Construction and Building Materials, 22(5), 875-885.

De Muynck, W., De Belie, N., & Verstraete, W. (2010). Microbial carbonate precipitation in construction materials: A review. Ecological Engineering, 36(2), 118-136.

De Muynck, W., Debrouwer, D., De Belie, N., & Verstraete, W. (2008b). Bacterial carbonate precipitation improves the durability of cementitious materials. Cement and Concrete Research, 38(7), 1005-1014.

De Muynck, W., Leuridan, S., Van Loo, D., Verbeken, K., Cnudde, V., De Belie, N., & Verstraete, W. (2011). Influence of pore structure on the effectiveness of a biogenic carbonate surface treatment for limestone conservation. Applied and Environmental Microbiology, 77(19), 6808-6820.

de Rooij, M.R., Van Tittelboom, K., De Belie, N., & Schlangen, E. (2013). Self-Healing Phenomena in Cement-Based Materials, State-of-the-Art Report of RILEM Technical Committee 221-SHC: Self-Healing Phenomena in Cement-Based Materials, Springer, Dordrecht, pp. 256.

Delgado, M., Lázaro, A., Mazo, J., & Zalba, B. (2012). Review on phase change material emulsions and microencapsulated phase change material slurries: Materials, heat transfer studies and applications. Renewable and Sustainable Energy Reviews, 16(1), 253-273.

Derluyn, H., Derome, D., Carmeliet, J., Stora, E., & Barbarulo, R. (2012). Hysteretic moisture behavior of concrete: Modeling and analysis. Cement and Concrete Research, 42(10), 1379-1388.

Diamond, S. (2000). Mercury porosimetry: An inappropriate method for the measurement of pore size distributions in cement-based materials. Cement and Concrete Research, 30(10), 1517-1525.

Diamond, S. (2003). A discussion of the paper "Effect of drying on cement-based materials pore structure as identified by mercury porosimetry - a comparative study between oven-, vacuum- and freeze-drying" by C. Gallé. Cement and Concrete Research, 33(1), 169-170.

Dias, W.P.S. (2000). Reduction of concrete sorptivity with age through carbonation. Cement and Concrete Research, 30(8), 1255-1261.

Dick, J., De Windt, W., De Graef, B., Saveyn, H., Van der Meeren, P., De Belie, N., & Verstraete, W. (2006). Bio-deposition of a calcium carbonate layer on degraded limestone by Bacillus species. Biodegradation, 17(4), 357-367.

Dry, C. (1994). Matrix Cracking Repair and Filling using Active and Passive Model for Smart Time Release of Chemicals from Fibers into Cement Matrixes. Journal of Smart Materials and Structures, 3(2), 118-123.

Dry, C. (1996). Procedures Developed for Self-Repair of Polymer Matrix Composite Materials. Composite Structures, 35(3), 263-269.

Du Prez, F., & Dubruel, P. (2011). Polymer materials. Ghent: Ghent University, pp. 195.

Dubina, E., Wadsö, L., & Plank, J. (2011). A sorption balance study of water vapour sorption on anhydrous cement minerals and cement constituents. Cement and Concrete Research, 41(11), 1196-1204.

Dubinin, M.M. (1960). The potential theory of adsorption of gases and vapors for adsorbents with energetically non-uniform surfaces. Chemical Reviews, 60(2), 235-241.

Dubinin, M.M. (1975). Physical adsorption of gases and vapors in micropores. Progress in Surface and Membrane Science, Academia Press, 9, 1-70.

Dudziak, L., & Mechtcherine, V. (2008). Mitigation of volume changes of Ultra-High Performance Concrete (UHPC) by using Super Absorbent Polymers. Paper

presented at the 2nd international symposium on Ultra High Performance Concrete, Kassel, Kassel University Press GmbH, 425-432.

Dudziak, L., & Mechtcherine, V. (2010). Enhancing early-age resistance to cracking in high-strength cement based materials by means of internal curing using super absorbent polymers. Paper presented at the International RILEM Conference on Material Science, Aachen, RILEM Publications S.A.R.L., 129-139.

Dunstan, I. (1986). Fibre reinforced cement and concrete: research into practice. Materials and Structures, 20(2), 147-150.

Edvardsen, C. (1999). Water Permeability and Autogenous Healing of Cracks in Concrete. ACI Materials Journal, 96(4), 448-454.

Entrop, A.G., Brouwers, H.J.H., & Reinders, A.H.M.E. (2011). Experimental research on the use of micro-encapsulated Phase Change Materials to store solar energy in concrete floors and to save energy in Dutch houses. Solar Energy, 85(5), 1007-1020.

Erşan, Y.C., De Belie, N., & Boon, N. (2015). Microbially induced CaCO3 precipitation through denitrification: An optimization study in minimal nutrient environment. Biochemical Engineering Journal, 101, 108-118.

Espinosa, R.M., & Franke, L. (2006). Influence of the age and drying process on pore structure and sorption isotherms of hardened cement paste. Cement and Concrete Research, 36(10), 1969-1984.

Esteves, L.P. (2012). An ongoing investigation on modelling the strength properties of water-entrained cement-based materials. Paper presented at the Proceedings of the 3rd International Conference on Concrete Repair, Rehabilitation and Retrofitting, Cape Town, Taylor & Francis Group, 1450-1455.

European Union Road Federation, International Road federation. (2007). European Road Statistics, pp. 88.

Evans, R., & Tarazona, P. (1984). Theory of condensation in narrow capillaries. Physical Review Letters, 52(7), 557-560.

Everett, D.H. (1979). Characterisation of Porous Solids. London, Society of Chemical Industry, pp. 229.

Fan, S., & Li, M. (2015). X-ray computed microtomography of three-dimensional microcracks and self-healing in engineered cementitious composites. Smart Materials and Structures, 24(1), 015021.

Farage, M.C.R., Sercombe, J., & Gallé, C. (2003). Rehydration and microstructure of cement paste after heating at temperatures up to 300°C. Cement and Concrete Research, 33(7), 1047-1056.

Feldman, R.F., & Beaudoin, J.J. (1991). Pre-treatment of hardened hydrated cement pastes for mercury intrusion measurements. Cement and Concrete Research, 21(2-3), 297-308.

Feldman, R.F., & Sereda, P.J. (1970). A new model for hydrated Portland cement and its practical implications. Engineering Journal, 53(8-9), 53-59.

Ferrara, L. (2014). Crystalline admixtures in cementitious composites: from porosity reducers to catalysts of self healing. Paper presented at the International RILEM Conference on the Application of Superabsorbent Polymers and Other New Admixtures in Concrete Construction, Dresden, RILEM Publications S.A.R.L., 311-324.

Ferrara, L., Krelani, V., & Carsana, M. (2014). A "fracture testing" based approach to assess crack healing of concrete with and without crystalline admixtures. Construction and Building Materials, 68, 535-551.

Friedemann, K., Stallmach, F., & Kärger, J. (2006). NMR diffusion and relaxation studies during cement hydration—A non-destructive approach for

clarification of the mechanism of internal post curing of cementitious materials. Cement and Concrete Research, 36(5), 817-826.

Fukuda, D., Nara, Y., Kobayashi, Y., Maruyama, M., Koketsu, M., Hayashi, D., Ogawa, H., & Kanedo, K. (2012). Investigation of self-sealing in high-strength and ultra-low-permeability concrete in water using micro-focus X-ray CT. Cement and Concrete Research, 42(11), 1494-1500.

Furmaniak, S., Gauden, P.A., Terzyk, A.P., & Rychlicki, G. (2008). Water adsorption on carbons. Critical review of the most popular analytical approaches. Advances in Colloid and Interface Science, 137(2), 82-143.

Gagné, R., & Argouges, M. (2012). A study of the natural self-healing of mortars using air-flow measurements. Materials and Structures, 45(11), 1625-1638.

Gallé, C. (2001). Effect of drying on cement-based materials pore structure as identified by mercury intrusion porosimetry - A comparative study between oven-, vacuum- and freeze-drying. Cement and Concrete Research, 31(10), 1467-1477.

Gallé, C. (2003). Reply to the discussion by S. Diamond of the paper "Effect of drying on cement-based materials pore structure as identified by mercury intrusion porosimetry: a comparative study between oven-, vacuum- and freeze-drying". Cement and Concrete Research, 33(1), 171-172.

Garci Juenger, M.C., & Jennings, H.M. (2001). The use of nitrogen adsorption to assess the microstructure of cement paste. Cement and Concrete Research, 31(6), 883-892.

Gassan, J., & Bledzki, A.K. (2001). Thermal Degradation of Flax and Jute Fibers. Applied Polymer Science, 82(6), 1417-1422.

Gerlach, G., Guenther, M., Sorber, J., Suchaneck, G., Arndt, K.-F., & Richter, A. (2005). Chemical and pH sensors based on the swelling behavior of hydrogels. Sensors and Actuators B, 111-112, 555-561.

Geymayer, H.G., & Cox, F.B. (1970). Bamboo-reinforced concrete. ACI journal, 67(10), 841-846.

Gil, A., & Grange, P. (1996). Application of the Dubinin-Radushkevich and Dubinin-Astakhov equations in the characterization of microporous solids. Colloids and Surfaces, A: Physicochemical and Engineering Aspects, 113(1-2), 39-50.

Gollapudi, U.K., Knutson, C.L., & Islam, M.R. (1995). A new method for controlling leaching through permeable channels. Chemosphere, 30(4), 695-705.

Gram, H.E. (1983). Durability of natural fibres in concrete. Stockholm: Swedish Cement and Concrete Research Institute, pp. 255.

Granger, S., Loukili, A., Pijaudier-Cabot, G., & Chanvillard, G. (2007). Experimental characterization of the self-healing of cracks in an ultra-high performance cementitious material: Mechanical tests and acoustic emission analysis. Cement and Concrete Research, 37(4), 519-527.

Granju, J.-L., & Balouch, S.U. (2005). Corrosion of steel fibre reinforced concrete from the cracks. Cement and Concrete Research, 35(3), 572-577.

Gregg, S.J., & Sing, K.S.W. (1982). Adsorption, surface area and porosity (Vol. 2). London - New-York: Academic Press Inc, pp. 313.

Gruyaert, E. (2011). Effect of blast-furnace slag as cement replacement on hydration, microstructure, strength and durability of concrete. Ghent University, Ghent, pp. 345.

Gruyaert, E., Robeyst, N., & De Belie, N. (2010). Study of the hydration of Portland cement blended with blast-furnace slag by calorimetry and thermogravimetry. Journal of Thermal Analysis and Calorimetry, 102(3), 941-951.

Gruyaert, E., Tittelboom, K., Rahier, H., & Belie, N. (2014). Activation of the pozzolanic or latent-hydraulic reaction by alkalis in order to repair cracks in concrete. Journal of Materials in Civil Engineering, 04014208.

Gruyaert, E., Van Tittelboom, K., De Backer, P., Moerman, W., Dekeyser, B., & De Belie, N. (2013). Self-Healing of Thermal Cracks in Sandwich Panels. Paper presented at the International Conference on Self-Healing Materials, Gent, 196-200.

Guezennec, J., Pignet, P., Lijour, Y., Gentric, E., Ratiskol, J., & Colliec-Jouault, S. (1998). Sulfation and depolymerization of a bacterial exopolysaccharide of hydrothermal origin. Carbohydrate Polymers, 37(1), 19-24.

Gulrez, S.K.H., S., aphwan Al-Assaf, & O'Phillips, G. (2011). Chapter 5: Hydrogels: Methods of Preparation, Characterization and Applications. In A. Carpi (Ed.), Progress in Molecular and Environmental Bioengineering - From Analysis and Modeling to Technology Applications.

Hagymassy Jr., J., Brunauer, S., & Mikhail, R. Sh. (1969). Pore structure analysis by water vapor adsorption - I. t-curves for water vapor. Journal of Colloid and Interface Science, 29(3), 485-491.

Hagymassy Jr., J., Odler, I., Yudenfreund, M., Skalny, J., & Brunauer, S. (1972). Pore Structure Analysis by Water Vapor Adsorption III. Analysis of Hydrated Calcium Silicates and Portland Cements. Journal of Colloid and Interface Science, 38(1), 20-34.

Hancock, R.D., & Martell, A.E. (1989). Ligand Design for Selective Complexation of Metal Ions in Aqueous Solution. Chemical Reviews, 89(8), 1875-1914.

Hanehara, S., & Yamada, K. (1999). Interaction between cement and chemical admixture from the point of cement hydration, absorption behaviour of admixture, and paste rheology. Cement and Concrete Research, 29(8), 1159-1165.

Hanna, K., Odler, I., Brunauer, S., Hagymassy Jr., J., & Bodor, E.E. (1973). Pore Structure Analysis by Oxygen Adsorption I. t-Curves and Methods of Analysis. Journal of Colloid and Interface Science, 45(1), 27-37.

Hannant, D.J., & Keer, J.G. (1983). Autogenous healing of thin cement-based sheets. Cement and Concrete Research, 13(3), 357-365.

Hanžič, L., & Ilić, R. (2003). Relationship between liquid sorptivity and capillarity in concrete. Cement and Concrete Research, 33(9), 1385-1388.

Harbottle, M.J., Zhang, J., & Gardner, D.R. (2013). Combined physical and biological gel-based healing of cementitious materials. Paper presented at the ICSHM 2013: Proceedings of the 4th International Conference on Self-Healing Materials, Ghent, 206-210.

Hasholt, M.T., Jensen, O.M., Kovler, K., & Zhutovsky, S. (2012). Can superabsorbent polymers mitigate autogenous shrinkage of internally cured concrete without compromising the strength? Construction and Building Materials, 31, 226-230.

Hasholt, M.T., Jespersen, M.H.S., & Jensen, O.M. (2010). Mechanical properties of concrete with SAP part I: Development of compressive strength. Paper presented at the International RILEM Conference on Use of Superabsorbent Polymers and Other New Additives in Concrete, Lyngby, RILEM Publications S.A.R.L., 117-126.

Hassanein, R. (2006). Correction methods for the quantitative evaluation of thermal neutron tomography. ETH Zurich, Zurich, No. 16809, pp. 149.

Hassanein, R., Meyer, H.O., Carminati, A., Estermann, M., Lehmann, E., & Vontobel, P. (2006). Investigation of water imbibition in porous stone by thermal neutron radiography. Journal of Physics D: Applied Physics, 39(19), 4284-4291.

Hearn, N. (1998). Self-sealing, autogenous healing and continued hydration: what is the difference? Materials and Structures, 31(212), 563-567.

Hennink, W.E., & van Nostrum, C.F. (2002). Novel crosslinking methods to design hydrogels. Advanced Drug Delivery Reviews, 54(1), 13-26.

Hilloulin, B., Van Tittelboom, K., Gruyaert, E., De Belie, N., & Loukili, A. (2015). Encapsulation by polymeric capsules for self-healing concrete. Cement and Concrete Composites, 55, 298-307.

Hoffman, A.S. (2002). Hydrogels for biomedical applications. Advanced Drug Delivery Reviews, 54(1), 3-12.

Homma, D., Mihashi, H., & Nishiwaki, T. (2009). Self-Healing Capability of Fibre Reinforced Cementitious Composites. Advanced Concrete Technology, 7(2), 217-228.

Horkay, F., Tasaki, I., & Basser, P. (2001). Effect of monovalent-divalent cation exchange on the swelling of polyacrylate hydrogels in physiological salt solutions. Biomacromolecule, 2(1), 195-199.

Hosoda, A., Higuchi, T., Eguchi, M., Yoshida, H., & Aoki, H. (2012). Self Healing of Longitudinal Cracks in Utility Concrete Pole. Journal of Advanced Concrete Technology, 10(8), 278-284.

Hunger, M., Entrop, A.G., Mandilaras, I., Brouwers, H.J.H., & Founti, M. (2009). The behavior of self-compacting concrete containing micro-encapsulated phase change materials. Cement and Concrete Composites, 31(10), 731-743.

Igarashi, S., & Watanabe, A. (2006). Experimental study on prevention of autogenous deformation by internal curing using super-absorbent polymer particles. Paper presented at the International RILEM Conference on Volume Changes of Hardening Concrete: Testing and Mitigation, Lyngby, RILEM Publications S.A.R.L., 77-86.

IUPAC. (1972). Manual of Symbols and Terminology, Appendix 2, Pt.1, Colloid and Surface Chemistry. Pure Applied Chemistry, 31(1), 578-680.

Jacobsen, S., Marchand, J., & Hornain, H. (1995). SEM observations of the microstructure of frost deteriorated and self-healed concrete. Cement and Concrete Research, 25(8), 55-62.

Jacobsen, S., & Sellevold, E.J. (1996). Self-healing of high-strength concrete after deterioration by freeze/thaw. Cement and Concrete Research, 26(1), 55-62.

Jefferson, A., Joseph, C., Lark, R., Isaacs, B., Dunn, S., & Weager, B. (2010). A new system for crack closure of cementitious materials using shrinkable polymers. Cement and Concrete Research, 40(5), 795-801.

Jennings, H.M., & Bullard, J.W. (2011). From electrons to infrastructure: Engineering concrete from the bottom up. Cement and Concrete Research, 41(7), 727-735.

Jensen, O.M. (2008). Use of superabsorbent polymers in construction materials. Paper presented at the International Conference on Microstructure Related Durability of Cementitious Composites, Nanjing, RILEM Publications S.A.R.L., 757-764.

Jensen, O.M. (2011). Water absorption of superabsorbent polymers in a cementitious environment. Paper presented at the International RILEM Conference on Advances in Construction Materials through Science and Engineering, Hong Kong SAR, RILEM Publications S.A.R.L., 22-35.

Jensen, O.M., & Hansen, P.F. (1996). Autogenous Deformation and Change of the Relative Humidity in Silica Fume-Modified Cement Paste. ACI Materials Journal, 93(6), 539-543.

Jensen, O.M., & Hansen, P.F. (2001). Water-entrained cement-based materials I. Principles and theoretical background. Cement and Concrete Research, 31(4), 647-654.

Jensen, O.M., & Hansen, P.F. (2002). Water-entrained cement-based materials II. Experimental observations. Cement and Concrete Research, 32(6), 973-978.

Jensen, O.M., & Lura, P. (2006). Techniques and materials for internal water curing of concrete. Materials and Structures, 39(9), 817-825.

Jia, H.Y., Wei, C., Ming, X.Y., & Yang, E.-H. (2010). The Microstructure of Self-Healed PVA ECC Under Wet and Dry Cycles. Materials Research, 13(2), 225-231.

John, M.J., & Anandjiwala, R.D. (2008). Recent developments in chemical modification and characterization of natural fiber-reinforced composites. Polymer Composites, 29(2), 187-207.

Jonkers, H.M. (2008). Self Healing Concrete: A Biological Approach. In S. van der Zwaag (Ed.), Self Healing Materials. An Alternative Approach to 20 Centuries of Materials Science (Vol. 100, pp. 195-204): Springer.

Jonkers, H.M. (2011). Bacteria-based self-healing concrete. Heron, 56(1/2), 1-12.

Jonkers, H.M., Thijssen, A., Muyzer, G., Çopuroğlu, O., & Schlangen, E. (2010). Application of bacteria as self-healing agent for the development of sustainable concrete. Ecological Engineering, 36(2), 230-235.

Jooss, M. (2001). Leaching of Concrete under Thermal Influence. Otto-Graf-Journal, 12, 51-68.

Joseph, C., Gardner, D., Jefferson, T., Isaacs, B., & Lark, B. (2011). Self-healing cementitious materials: a review of recent work. Construction Materials, 164(CM1), 29-41.

Joseph, K., Thomas, S., & Pavithran, C. (1996). Effect of chemical treatment on the tensile properties of short sisal fibre-reinforced polyethylene composites. Polymer, 37(23), 5139-5149.

Juergen, G., Buenger, D., & Topuz, F. (2012). Hydrogels in Sensing Applications. Progress in Polymer Science, 37, 1678-1719.

Kalia, S., Kaith, B.S., & Kaur, I. (2009). Pre-treatments of natural fibers and their application as reinforcing material in polymer composites - A review. Polymer Engineering & Science, 49(7), 1253-1272.

Kamada, T., Uchida, S., & Rokugo, K. (2005). Non-destructive evaluation of setting and hardening of cement paste based on ultrasonic propagation characteristics. Journal of Advanced Concrete Technology, 3(3), 343-353.

Kan, L., & Shi, H. (2012). Investigation of self-healing behavior of Engineered Cementitious Composites (ECC) materials. Construction and Building Materials, 29, 348-356.

Kanda, T. (1998). Design of Engineered Cementitious Composites for Ductile Seismic Resistant Elements. University of Michigan, Ann Arbor, pp. 329.

Kandare, E., Deng, H., Wang, D., & Hossenlopp, J. (2006). Thermal stability and degradation kinetics of poly(methyl methacrylate)/layered copper hydroxy methacrylate composites. Polymers for Advanced Technologies, 17(4), 312-319.

Kanematsu, M., Maruyama, I., Noguchi, T., Iikura, H., & Tsuchiya, N. (2009). Quantification of water penetration into concrete through cracks by neutron radiography. Section A of Nuclear Instruments and Methods in Physics Research, 605(1-2), 154-158.

Kessler, M.R., Sottos, N.R., & White, S.R. (2003). Self-healing structural composite material. Composites Part A: Applied Science and Manufacturing, 34(8), 743-753.

Khare, A.R., & Peppas, N.A. (1995). Swelling-deswelling of anionic copolymer gels. Biomaterials, 16(7), 559-567.

Kim, D.J., Kang, S.H., & Ahn, T.-H. (2014). Mechanical Characterization of High-Performance Steel-Fiber Reinforced Cement Composites with Self-Healing Effect. Materials, 7(1), 508-526.

Kim, J.S., & Schlangen, E. (2010). Super absorbent polymers to simulate self healing in ECC. Paper presented at the 2nd International Symposium on Service Life Design for Infrastructures, Delft, RILEM Publications S.A.R.L., 849-858.

Konecny, L., & Naqvi, S.J. (1993). The effect of different drying techniques on the pore size distribution of blended cement mortars. Cement and Concrete Research, 23(5), 1223-1228.

Korpa, A., & Trettin, R. (2006). The influence of different drying methods on cement paste microstructures as reflected by gas adsorption: Comparison between freeze-drying (F-drying), D-drying, P-drying and oven-drying methods. Cement and Concrete Research, 36(4), 634-649.

Krelani, V. (2015). Self-healing capacity of cementitious composites. Politecnico Di Milano, Milano, pp. 256.

Kunieda, M., Choonghyun, K., Ueda, N., & Nakamura, H. (2012). Recovery of Protective Performance of Cracked Ultra High Performance Strain Hardening Cementitious Composites (UHP-SHCC) due to Autogenous Healing. Journal of Advanced Concrete Technology, 10(8), 313-322.

Kunieda, M., & Rokugo, K. (2006). Recent Progress on HPFRCC in Japan. Journal of Advanced Concrete Technology, 4(1), 19-33.

Langmuir, I. (1916). The constitution and fundamental properties of solids and liquids. Part I. Solids. Journal of the American Chemical Society, 38(11), 2221-2295.

Larner, L.J., Speakman, K., & Majumdar, A.J. (1976). Chemical interactions between glass fibres and cement. Journal of Non-Crystalline Solids, 20(1), 43-74.

Lauer, K.R., & Slate, F.O. (1956). Autogenous Healing of Cement Paste. ACI Materials Journal, 52(10), 1083-1097.

Laustsen, S., Bentz, D.P., Hasholt, M.T., & Jensen, O.M. (2010). CT measurement of SAP voids in concrete. Paper presented at the International RILEM Conference on Use of Superabsorbent Polymers and Other New Additives in Concrete, Lyngby, RILEM Publications S.A.R.L., 153-162.

Laustsen, S., Hasholt, M.T., & Jensen, O.M. (2015). Void structure of concrete with superabsorbent polymers and its relation to frost resistance of concrete. Materials and Structures, 48(1-2), 357-368.

Lee, H.K., Lee, K.M., Kim, Y.H., Yim, H., & Bae, D.B. (2004). Ultrasonic in-situ monitoring of setting process of high-performance concrete. Cement and Concrete Research, 34(4), 631-640.

Lee, H.X.D., Wong, H.S., & Buenfeld, N.R. (2010a). Potential of superabsorbent polymer for self-sealing cracks in concrete. Advances in Applied Ceramics, 109(5), 296-302.

Lee, H.X.D, Wong, H.S., & Buenfeld, N.R. (2010b). Self-sealing cement-based materials using superabsorbent polymers. Paper presented at the International RILEM Conference on Use of Superabsorbent Polymers and Other New Additives in Concrete, Lyngby, RILEM Publications S.A.R.L., 171-178.

Lee, K.M., Lee, H.K., Lee, S.H., & Kim, G.Y. (2006). Autogenous shrinkage of concrete containing granulated blast-furnace slag. Cement and Concrete Research, 36(7), 1279-1285.

Lehmann, E., Vontobel, P., & Wiezel, I. (2001). Properties of the radiography facility NEUTRA at SINQ and its use as European reference facility. Nondestructive Testing And Evaluation, 16(2-6), 191-202.

Lendlein, A., & Kelch, S. (2002). Shape-Memory Polymers. Angewandte Chemie, 41(12), 2034-2057.

Lepech, M.D. (2006). A paradigm for integrated structures and materials design for sustainable transportation infrastructure. University of Michigan, Michigan, pp.333.

Lepech, M.D., & Li, V.C. (2005). Water Permeability of Cracked Cementitious Composites. Paper presented at the Proceedings of International Conference on Fracture 11, Turin, No. 4539.

Lewis, G., & Mirihagalia, P. (1970). Natural vegetable fibres as reinforcement in cement sheet. Magazine of Concrete Research, 31(107), 104-108.

Li, M., & Li, V.C. (2011). Cracking and Healing of Engineered Cementitious Composites under Chloride Environment. ACI Materials Journal, 108(3), 333-340.

Li, S. (1999). Hydrolytic degradation characteristics of aliphatic polyesters derived from lactic and glycolic acids. Journal of Biomedical Materials Research, 48(3), 342-353.

Li, V.C. (2008). Engineered Cementitious Composites (ECC) – Material, Structural, and Durability Performance. In E. Nawy (Ed.), Concrete Construction Engineering Handbook, CRC Press, pp. 78.

Li, V.C., & Herbert, E. (2012). Robust Self-Healing Concrete for Sustainable Infrastructure. Journal of Advanced Concrete Technology, 10(6), 207-218.

Li, V.C., & Leung, C.K.Y. (1992). Steady state and multiple cracking of short random fiber composites. ASCE Engineering Mechanics, 188(11), 2246-2264.

Li, V.C., Lim, Y.M., & Chan, Y.W. (1988). Feasibility study of a passive smart self-healing cementitious composite. Composites Part B, 29(6), 819-827.

Li, V.C., Stang, H., & Krenchel, H. (1993). Micromechanics of Crack Bridging in Fibre-Reinforced Concrete. Materials and Structures, 26(8), 486-494.

Li, V.C., Wang, S., & Wu, C. (1997). Tensile strain-hardening behavior of polyvinyl alcohol engineered cementitious composites (PVA-ECC). ACI Materials Journal, 98(6), 483-492.

Li, V.C., Wu, C., Wang, S., Ogawa, A., & Saito, T. (2002). Interface Tailoring for Strain-Hardening Polyvinyl Alcohol - Engineered Cementitious Composites (PVA-ECC). ACI Materials Journal, 99(5), 463-472.

Li, V.C., & Wu, H.C. (1992). Conditions for Pseudo Strain-Hardening in Fiber Reinforced Brittle Matrix Composites. Applied Mechanics Review, 45(8), 390-398.

Lienhart, W., & Brunner, F.K. (2003). Monitoring of Bridge Deformations using Embedded Fiber Optical Sensors. Paper presented at the 11th FIG Symposium on Deformation Measurements, Santorini, 555-561.

Lin, Z., Kanda, T., & Li, V.C. (1999). On interface property characterization and performance of fiber-reinforced cementitious composites. Concrete Science and Engineering, 1(3), 173-184.

Litvan, G.G. (1976). Variability of the nitrogen surface area of hydrated cement paste. Cement and Concrete Research, 6(1), 139-143.

Liu, C., Qin, H., & Mather, P.T. (2007). Review of progress in shape-memory polymers. Journal of Materials Chemistry, 17(16), 1543-1558.

Lodewyckx, P. (2010). The effect of water uptake in ultramicropores on the adsorption of water vapour in activated carbon. Carbon, 48(9), 2549-2553.

Lodewyckx, P., Raymundo-Piñero, E., Vaclavikova, M., Berezovska, I., Thommes, M., Béguin, F., & Dobos, G. (2013). Suggested improvements in the parameters

used for describing the low relative pressure region of the water vapour isotherms of activated carbons. Carbon, 60, 556-558.

Ludirdja, D., Berger, R.L., & Young, J.F. (1989). Simple Method for Measuring Water Permeability of Concrete. ACI Materials Journal, 86(5), 433-439.

Luković, M., Dong, H., Šavija, B., Schlangen, E., Ye, G., & van Breugel, K. (2014). Tailoring strain-hardening cementitious composite repair systems through numerical experimentation. Cement and Concrete Composites, 53, 200-213.

Lura, P., Durand, F., Loukili, A., Kovler, K., & Jensen, O.M. (2006). Compressive strength of cement pastes and mortars with superabsorbent polymers. Paper presented at the International RILEM Conference on Volume Changes of Hardening Concrete: Testing and Mitigation, Lyngby, RILEM Publications S.A.R.L., 117-125.

Lura, P., Jensen, O.M., & Igarashi, S. (2007). Experimental observation of internal curing of concrete. Materials and Structures, 40(2), 211-220.

Lura, P., van Breugel, K., & Maruyama, I. (2001). Effect of curing temperature and type of cement on early-age shrinkage of high-performance concrete. Cement and Concrete Research, 31(12), 1867-1872.

Lura, P., Ye, G., Cnudde, V., & Jacobs, P. (2008). Preliminary results about 3D distribution of superabsorbent polymers in mortars. Paper presented at the International Conference on Microstructure Related Durability of Cementitious Composites, Nanjing, 1341-1348.

Maalej, M., Hashida, T., & Li, V.C. (2012). Effect of fiber volume fraction on the off-crack plane energy in strain-hardening engineered cementitious composites. Journal of the American Ceramic Society, 78(12), 3369-3375.

Maes, M., Van Tittelboom, K., & De Belie, N. (2014). The efficiency of self-healing cementitious materials by means of encapsulated polyurethane in chloride containing environments. Construction and Building Materials, 71, 528-537.

Maltais, Y., & Marchand, J. (1997). Influence of curing temperature on cement hydration and mechanical strength development of fly ash mortars. Cement and Concrete Research, 27(7), 1009–1020.

Mangat, P.S., & Gurusamy, K. (1988). Corrosion resistance of steel fibres in concrete under marine exposure. Cement and Concrete Research, 18(1), 44-54.

Mark, H.F., & Kroschwitz, J.I. (2003). Encyclopedia Of Polymer Science and Technology. New-York: John Wiley & Sons, pp. 3005.

Masschaele, B., Cnudde, V., Dierick, M., Jacobs, P., Van Hoorebeke, L., & Vlassenbroeck, J. (2007). UGCT: new X-ray radiography and tomography facility. Nuclear Instruments and Methods in Physics Research Section A, 580(1), 266-269.

Matou, S., Colliec-Jouault, S., Galy-Fauroux, I., Ratiskol, J., Sinquin, C., Guezennec, J., Fischer, A.-M., & Helley, D. (2005). Effect of an oversulfated exopolysaccharide on angiogenesis induced by fibroblast growth factor-2 or vascular endothelial growth factor in vitro. Biochemical Pharmacology, 69(5), 751-759.

McCarter, W.J., & Vennesland, Ø. (2004). Sensor systems for use in reinforced concrete structures. Construction and Building Materials, 18(6), 351-358.

Mechtcherine, V. (2012). Towards a durability framework for structural elements and structures made of or strengthened with high-performance fibre-reinforced composites. Construction and Building Materials, 31, 94-104.

Mechtcherine, V. (2013). Novel cement-based composites for the strengthening and repair of concrete structures. Construction and Building Materials, 41, 365-373.

Mechtcherine, V., de Andrade Silva, F., Butler, M., Zhu, D., Mobasher, B., Gao, S.-L., & Mäder, E. (2011). Behaviour of strain-hardening cement-based composites under high strain rates. Journal of Advanced Concrete Technology, 9(1), 51-62.

Mechtcherine, V., de Andrade Silva, F., Müller, S., Jun, P., & Tolêdo Filho, R.D. (2012). Coupled strain rate and temperature effects on the tensile behavior of strain-hardening cement-based composites (SHCC) with PVA fibers. Cement and Concrete Research, 42(11), 1417-1427.

Mechtcherine, V., Dudziak, L., & Hempel, S. (2009). Mitigating early age shrinkage of Ultra-High Performance Concrete by using Super Absorbent Polymers (SAP). Paper presented at the Creep, Shrinkage and Durability Mechanics of Concrete and Concrete Structures, Ise-Shima, Taylor & Francis, 847-853.

Mechtcherine, V., Dudziak, L., Schulze, J., & Stärhr, H. (2006). Internal curing by Super Absorbent Polymers - Effects on material properties of self-compacting fibre-reinforced high performance concrete. Paper presented at the international RILEM conference on Volume Changes of Hardening Concrete: Testing and Mitigation, Lyngby, RILEM Publications S.A.R.L., 87-96.

Mechtcherine, V., Gorges, M., Schröfl, C., Assmann, A., Brameshuber, W., Bettencourt Ribeiro, V., Cusson, D., Custódio, J., Fonseca da Silva, E., Ichimiya, K., Igarashi, S., Klemm, A., Kovler, K., Lopes, A., Lura, P., Nguyen, V.T., Reinhardt, H.W., Toledo Filho, R.D., Weiss, J., Wyrzykowski, M., Ye, G., & Zhutovsky, S. (2014). Effect of Internal Curing by Using Superabsorbent Polymers (SAP) on Autogenous Shrinkage and Other Properties of a High-performance Fine-grained Concrete: Results of a RILEM Round-robin Test, TC 225-SAP. Materials and Structures, 47(3), 541-562.

Mehling, H., & Cabeza, L.F. (2008). Heat and cold storage with PCM: An up to date introduction into basics and applications. Berlin: Springer, pp. 308.

Meshgin, P., & Xi, Y. (2012). Effect of phase change materials on properties of concrete. ACI Materials Journal, 109(1), 71-80.

Meznarich, N.A.K. (2012). Effect of Ternary Solutes on the Evolution of Structure and Gel Formation in Amphiphilic Copolymer Solutions. The University of Michigan, Ann Arbor, pp. 120.

Mignon, A., Graulus, G.-J., Snoeck, D., Martins, J., De Belie, N., Dubruel, P., & Van Vlierberghe, S. (2015). pH-sensitive superabsorbent polymers: a potential candidate material for self-healing concrete. Journal of Materials Science, 50(2), 970-979.

Mihashi, H., Kaneko, Y., Nishiwaki, T., & Otsuka, K. (2000). Fundamental study on development of intelligent concrete characterized by self-healing capability for strength. Transactions of the Japan Concrete Institute, 22, 441-450.

Mihashi, H., & Nishiwaki, T. (2012). Development of Engineered Self-Healing and Self-Repairing Concrete State-of-the-Art Report. Journal of Advanced Concrete Technology, 10(8), 170-184.

Mindess, S., & Young, J.F. (1981). Concrete. Englewood Cliffs, New-York: Prentice-Hall, pp. 671.

Mönnig, S. (2005). Water saturated super-absorbent polymers used in high strength concrete. Otto-Graf-Journal, 16, 193-202.

Mönnig, S. (2009). Superabsorbing additions in concrete – applications, modelling and comparison of different internal water sources. The University of Stuttgart, Stuttgart, pp. 180.

Mönnig, S., & Lura, P. (2007). Superabsorbent polymers - An additive to increase the freeze-thaw resistance of high strength concrete. In C.U. Grosse (Ed.),

Advances in Construction Materials. Berlin: Springer Berlin Heidelberg, 351-358.

Mortensen, B.M., Haber, M.J., DeJong, J.T., Caslake, L.F., & Nelson, D.C. (2011). Effects of environmental factors on microbial induced calcium carbonate precipitation. Journal of Applied Microbiology, 111(2), 338-349.

Moukwa, M., & Aïtcin, P.C. (1988). The effect of drying on cement pastes pore structure as determined by mercury porosimetry. Cement and Concrete Research, 18(5), 745-752.

Muller, A.C.A., Scrivener, K.L., Gajewicz, A.M., & McDonald, P.J. (2013a). Densification of C-S-H Measured by ^{1}H NMR Relaxometry. Physical Chemistry C, 117(1), 403-412.

Muller, A.C.A., Scrivener, K.L., Gajewicz, A.M., & McDonald, P.J. (2013b). Use of bench-top NMR to measure the density, composition and desorption isotherm of C-S-H in cement paste. Microporous and Mesoporous Materials.

Na, S.H., Hama, Y., Taniguchi, M., Katsura, O., Sagawa, T., & Zakaria, M. (2012). Experimental Investigation on Reaction Rate and Self-healing Ability in Fly Ash Blended Cement Mixtures. Journal of Advanced Concrete Technology, 10(8), 240-253.

Nair, K.C.M., Thomas, S., & Groeninckx, G. (2001). Thermal and dynamic mechanical properties of polystyrene-sisal fiber composites. Composites Science and Technology, 61(16), 2519-2529.

Nanayakkara, A. (2003). Self-healing of Cracks in Concrete subjected to Water Pressure. Paper presented at the Symposium on new technologies for urban safety of mega cities in Asia, Tokyo, 125-132.

Neville, A. (2002). Autogenous healing - A concrete miracle? Concrete International, 24(11), 76-82.

Nguyen, C., & Do, D.D. (2001). The Dubinin–Radushkevich equation and the underlying microscopic adsorption description. Carbon, 39(9), 1327-1336.

Nilsson, L.O. (2002). Durability concept; pore structure and transport processes (Vol. 2). Advanced concrete technology book, Vol 2 – Durability. London: Butterworth Heinemann, pp. 352.

Nishiwaki, T., Koda, M., Yamada, M., Mihashi, H., & Kikuta, T. (2012). Experimental Study on Self-Healing Capability of FRCC Using Different Types of Synthetic Fibers. Journal of Advanced Concrete Technology, 10(8), 195-206.

Nishiwaki, T., Mihashi, H., Jang, B.K., & Miura, K. (2006). Development of Self-Healing System for Concrete with Selective Heating around Crack. Advanced Concrete Technology, 4(2), 267-275.

Nishiyama, Y., & Okano, T. (1998). Morphological changes of ramie fiber during mercerization. Journal of Wood Science, 44(4), 310-313.

Nizovtsev, M.I., Stankus, S.V., Steryagov, A.N., Terekhov, V.I., & Khairulin, R.A. (2008). Determination of moisture diffusivity in porous materials using gamma method. International Journal of Heat and Mass Transfer, 51(17-18), 4161-4167.

Obla, K.H., & Li, V.C. (1995). A Novel Technique for Fiber-Matrix Bond Strength Determination for Rupturing Fibers. Cement and Concrete Composites, 17(3), 219-227.

Odler, I. (2003). The BET-specific surface area of hydrated Portland cement and related materials. Cement and Concrete Research, 33(12), 2049-2056.

Odler, I., Hagymassy Jr., J., Yudenfreund, M., Hanna, K.M., & Brunauer, S. (1972). Pore structure analysis by water vapor adsorption. IV. Analysis of

hydrated Portland cement pastes of low porosity. Journal of Colloid and Interface Science, 38(1), 265-276.

Ohba, T., & Kaneko, K. (2007). Cluster-associated filling of water molecules in slit-shaped graphitic nanopores. Molecular Physics, 105(2-3), 139-145.

Okwadha, G.D.O., & Li, J. (2010). Optimum conditions for microbial carbonate precipitation. Chemosphere, 81(9), 1143-1148.

Olson, R.A., & Jennings, H.M. (2001). Estimation of C-S-H content in a blended cement paste using water adsorption. Cement and Concrete Research, 31(3), 351-356.

Olson, R.A., Neubauer, C.M., & Jennings, H.M. (1997). Damage to the Pore Structure of Hardened Portland Cement Paste by Mercury Intrusion. Journal of the American Ceramic Society, 80(9), 2454-2458.

Omidian, H., Hashemi, S.A., Sammes, G., & Meldrum, I. (1999). Modified acrylic-based superabsorbent polymers (dependence on particle size and salinity). Polymer, 40(7), 1753-1761.

Orlowsky, J., Raupack, M., Cuypers, H., & Wastiels, J. (2005). Durability modelling of glass fibre reinforcement in cementitious environment. Materials and Structures, 38(2), 155-162.

Ozomaka, O.J. (1976). Characteristics of akwara as a reinforcing fibre. Magazine of Concrete Research, 28(96), 162-167.

Pacheco-Torgal, F., & Jalali, S. (2011). Cementitious building materials reinforced with vegetable fibres: A review. Construction and Building Materials, 25(2), 575-581.

Palacios, M., & Puertas, F. (2005). Effect of superplasticizer and shrinkage-reducing admixtures on alkali-activated slag pastes and mortars. Cement and Concrete Research, 35(7), 1358-1367.

Palin, D., Wiktor, V., & Jonkers, H.M. (2015). Autogenous healing of marine exposed concrete: Characterization and quantification through visual crack closure. Cement and Concrete Research, 73, 17-24.

Park, S.Y., Lee, Y., Bae, K.H., Ahn, C.-H., & Park, T.G. (2007). Temperature/pH-Sensitive Hydrogels Prepared from Pluronic Copolymers End-Capped with Carboxylic Acid Groups via and Oligolactide Space. Macromolecular Rapid Communications, 28(10), 1172-1176.

Parra-Montesinos, G. (2003). HPFRCC in earthquake-resistant structures: Current knowledge and future trends. Paper presented at the High performance fibre reinforced cement composites (HPFRCC4), Bagneux, RILEM Publications S.A.R.L., 453-472.

Parrott, L.J., Hansen, W., & Berger, R.L. (1980). Effect of first drying upon the pore structure of hydrated alite paste. Cement and Concrete Research, 10(5), 647-655.

Paul, A., Joseph, K., & Thomas, S. (1997). Effect of surface treatments on the electrical properties of low-density polyethylene composites reinforced with short sisal fibers. Composites Science and Technology, 57(1), 67-79.

Pease, B.J., Scheffler, G.A., & Janssen, H. (2012). Monitoring moisture movements in building materials using X-ray attenuation: Influence of beam-hardening of polychromatic X-ray photon beams. Construction and Building Materials, 36, 419-429.

Peippo, K., Hauranen, P., & Lund, P.D. (1991). A multicomponent PCM wall optimized for passive solar heating. Energy and Buildings, 17(4), 259-270.

Phillipson, M.C., Baker, P.H., Davies, M., Ye, Z., McNaughtan, A., Galbraith, G.H., & McLean, R.C. (2007). Moisture measurement in building materials: an overview of current methods and new approaches. Building Services Engineering Research and Technology, 28(4), 303-316.

Picandet, V., Khelidj, A., & Bellegou, H. (2009). Crack effects on gas and water permeability of concretes. Cement and Concrete Research, 39(6), 537-547.

Pielichowski, K., & Flejtuch, K. (2005). Non-oxidative thermal degradation of poly(ethylene oxide): kinetic and thermoanalytical study. Journal of Analytical and Applied Pyrolysis, 73(1), 131-138.

Postma, A., Davis, T.P., Donovan, A.R., Li, G., Moad, G., Mulder, R., & O'Shea, M.S. (2006). A simple method for determining protic end-groups of synthetic polymers by ^{1}H NMR spectroscopy. Polymer, 47(6), 1899-1911.

Powers, T.C., & Brownyard, T.L. (1948). Studies of the physical properties of hardened Portland cement paste (Vol. 22). Cornell: Portland Cement Association, Research Laboratories, pp. 892.

Pugliesi, R., & Andrade, M.L.G. (1997). Study of Cracking in Concrete by Neutron Radiography. Applied Radiation and Isotopes, 48(3), 339-344.

Qi, M., Liu, M., Chen, Z., & Zhang, F. (2008). Study on the swelling kinetics of superabsorbent using open circuit potential measurement. European Polymer Journal, 44(3), 743-754.

Qian, S.Z., Zhou, J., de Rooij, M.R., Schlangen, E., Ye, G., & van Breugel, K. (2009). Self-healing behavior of strain hardening cementitious composites incorporating local waste materials. Cement and Concrete Composites, 31(9), 613-621.

Qian, S.Z., Zhou, J., & Schlangen, E. (2010). Influence of curing condition and precracking time on the self-healing behavior of Engineered Cementitious Composites. Cement and Concrete Composites, 32(9), 686-693.

Racines, P.G. (1977). Development of low cost roofing material from sugarcane bagasse. Asian Institute of Technology, Bangkok.

Ramm, W., & Biscoping, M. (1998). Autogenous healing and reinforcement corrosion of water-penetrated separation cracks in reinforced concrete. Nuclear Engineering and Design, 179(2), 191-200.

Ranaivomanana, H., Verdier, J., Sellier, A., & Bourbon, X. (2011). Toward a better comprehension and modeling of hysteresis cycles in the water sorption-desorption process for cement based materials. Cement and Concrete Research, 41(8), 817-827.

Ravikumar, M., & Srinivasan, P.S.S. (2008). Phase Change Material as a Thermal Energy Storage Material for Cooling of Building. Journal of Theoretical and Applied Information technology, 4(6), 503-511.

Redon, C., Li, V.C., Wu, C., Hoshiro, H., Saito, T., & Ogawa, A. (2001). Measuring and Modifying Interface Properties of PVA fibres in ECC Matrix. ASCE Materials in Civil Engineering, 13(6), 399-406.

Reinhardt, H.W., & Assmann, A. (2009). Enhanced durability of concrete by superabsorbent polymers. Paper presented at the International Symposium Brittle Matrix Composites 9, Warsaw, Woodhead Publishing, 291-300.

Reinhardt, H.W., & Grosse, C.U. (2004). Continuous monitoring of setting and hardening of mortar and concrete. Construction and Building Materials, 18(3), 145-154.

Reinhardt, H.W., & Jooss, M. (2003). Permeability and Self-healing of Cracked Concrete as a Function of Temperature and Crack Width. Cement and Concrete Research, 33(7), 981-985.

Richardson, I.G. (2004). Tobermorite/jennite- and tobermorite/calcium hydroxide-based models for the structure of C-S-H: applicability to hardened pastes of tricalcium silicate, h-dicalcium silicate, Portland cement, and blends of Portland cement with blast-furnace slag, metakaolin, or silica fume. Cement and Concrete Research, 34(9), 1733-1777.

Robeyst, N., Grosse, C.U., & De Belie, N. (2009). Measuring the change in ultrasonic p-wave energy transmitted in fresh mortar with additives to monitor the setting. Cement and Concrete Research, 39(10), 868-875.

Robeyst, N., Gruyaert, E., Grosse, C.U., & De Belie, N. (2008). Monitoring the setting of concrete containing blast-furnace slag by measuring the ultrasonic p-wave velocity. Cement and Concrete Research, 38(10), 1169-1176.

Roels, S., & Carmeliet, J. (2006). Analysis of moisture flow in porous materials using microfocus X-ray radiography. International Journal of Heat and Mass Transfer, 49, 4762-4772.

Roels, S., Carmeliet, J., Hens, H., Adan, O., Brocken, H., Verny, R., Pavlik, Z., Ellisa, T., Hall, C., Kumaran, K., Pel, L., & Plagge, R. (2004). A comparison of different techniques to quantify moisture content profiles in porous building materials. Journal of Building Physics, 27(4), 361-376.

Roig-Flores, M., Moscato, S., Serna, P., & Ferrara, L. (2015). Self-healing capability of concrete with crystalline admixtures in different environments. Construction and Building Materials, 86, 1-11.

Romualdi, J.P., & Batson, G. (1963). Mechanics of crack arrest in concrete. Journal of the Engineering Mechanics Division, 89(EM3), 147-168.

Romualdi, J.P., & Mandel, J.A. (1964). Tensile strength of concrete affected by uniformly distributed and closely spaced short lengths of wire reinforcement. ACI journal, 61(6), 657-670.

Rong, M.Z., Zhang, M.Q., Liu, Y., Yang, G.C., & Zeng, H.M. (2001). The effect of fiber treatment on the mechanical properties of unidirectional sisal-reinforced epoxy composites. Composites Science and Technology, 61(10), 1437-1447.

Rosa, F., Bordado, J., & Casquilho, M. (2013). Synthesis, swelling capacity, and texture of polymers from monomers of sulfonic acid and acrylamide. Polymer Engineering & Science, 53(8), 1728-1733.

Rouquerol, J., Avnir, D., Fairbridge, C.W., Everett, D.H., Haynes, J.H., Pernicone, N., Ramsay, J.D.F., Sing, K.S.W., & Unger, K.K. (1994). Recommendations for the characterization of porous solids (Technical Report). Pure Applied Chemistry, 66(8), 1739-1758.

Ruiz Velasco, C., Baud'huin, M., Sinquin, C., Maillasson, M., Heymann, D., Colliec-Jouault, S., & Padrines, M. (2011). Effects of a sulfated exopolysaccharide produced by Altermonas infernus on bone biology. Glycobiology, 21(6), 781-795.

Şahmaran, M., Christianto, H.A., & Yaman, İ.Ö. (2006). The effect of chemical admixtures and mineral additives on the properties of self-compacting mortars. Cement and Concrete Composites, 28(5), 432-440.

Şahmaran, M., Lachemi, M., Hossain, K.M.A., Ranade, R., & Li, V.C. (2009). Influence of aggregate type and size on ductility and mechanical properties of engineered cementitious composites. ACI Materials Journal, 106(6), 308-316.

Şahmaran, M., & Li, V.C. (2009). Influence of microcracking on water absorption and sorptivity of ECC. Materials and Structures, 42(5), 593-603.

Şahmaran, M., Yildirim, G., & Erdem, T.K. (2013). Self-healing capability of cementitious composites incorporating different supplementary cementitious materials. Cement and Concrete Composites, 35(1), 89-101.

Sal'nikov, V.V., Ageeva, M.V., Yumashev, V.N., & Lozovaya, V.V. (1993). The ultrastructure of bast fibres. Russian Journal of Plant Physiology, 40(1), 458-464.

Sangadji, S., & Schlangen, E. (2012). Self Healing of Concrete Structures - Novel Approach Using Porous Network Concrete. Journal of Advanced Concrete Technology, 10(5), 185-194.

Sangadji, S., & Schlangen, E. (2013). Mimicking Bone Healing Process to Self Repair Concrete Structure Novel Approach Using Porous Network Concrete. Procedia Engineering, 54, 315–326.

Sant, G., Lothenbach, B., Juilland, P., Le Saout, G., Weiss, W.J., & Scrivener, K.L. (2011). The origin of early age expansions induced in cementitious materials containing shrinkage reducing admixtures. Cement and Concrete Research, 41(3), 218-229.

Savastano Jr., H., & Agopyan, V. (1999). Transition zone studies of vegetable fibre-cement paste composites. Cement and Concrete Composites, 21(1), 49-57.

Savastano Jr., H., Warden, P.G., & Coutts, R.S.P. (2000). Brazilian waste fibres as reinforcement for cement-based composites. Cement and Concrete Composites, 22(5), 379-384.

Šavija, B., Luković, M., Hosseini, S.A.S., Pacheco, J., & Schlangen, E. (2015). Corrosion induced cover cracking studied by X-ray computed tomography, nanoindentation, and energy dispersive X-ray spectrometry (EDS). Materials and Structures, 1-20.

Sawpan, M.A., Pickering, K.L., & Fernyhough, A. (2011). Effect of various chemical treatments on the fibre structure and tensile properties of industrial hemp fibres. Composites Part A: Applied Science and Manufacturing, 42(8), 888-895.

Schossig, P., Henning, H.-M., Gschwander, S., & Haussmann, T. (2005). Micro-encapsulated phase-change materials integrated into construction materials. Solar Energy Materials and Solar Cells, 89(2-3), 297-306.

Schröfl, C., Mechtcherine, V., & Gorges, M. (2012). Relation between the molecular structure and the efficiency of superabsorbent polymers (SAP) as concrete admixture to mitigate autogenous shrinkage. Cement and Concrete Research, 42(6), 865-873.

Schröfl, C., Mechtcherine, V., Kaestner, A., Vontobel, P., Hovind, J., & Lehmann, E. (2015). Transport of water through strain-hardening cement-based composite (SHCC) applied on top of cracked reinforced concrete slabs with and without hydrophobization of cracks - Investigation by neutron radiography. Construction and Building Materials, 76, 70-86.

Scrivener, K.L. (2004). Backscattered electron imaging of cementitious microstructures: understanding and quantification. Cement and Concrete Composites, 26(8), 935-945.

Sedan, D., Pagnoux, C., Smith, C., & Chotard, T. (2008). Mechanical properties of hemp fibre reinforced cement Influence of the fibre matrix interaction. European Ceramic Society, 28(1), 183-192.

Sierra-Beltran, M.G., Jonkers, H.M., & Schlangen, E. (2014). Characterization of sustainable bio-based mortar for concrete repair. Construction and Building Materials, 67(C), 344-352.

Silakhori, M., Naghavi, M.S., Metselaar, H.S.C., Mahlia, T.M.I., Fauzi, H., & Mehrali, M. (2013). Accelerated Thermal Cycling Test of Microencapsulated Paraffin Wax/Polyaniline Made by Simple Preparation Method for Solar Thermal Energy Storage. Materials, 6(5), 1608-1620.

Silva, F. (2015). Up-scaling the production of bacteria for self-healing concrete application. Ghent University, Ghent, pp. 220.

Sisomphon, K., Çopuroğlu, O., & Koenders, E.A.B. (2012). Self-healing of surface cracks in mortars with expansive additive and crystalline additive. Cement and Concrete Composites, 34(4), 566-574.

Slate, F.O. (1976). Coconut fibres in concrete. Engineering Journal of Singapore, 3(1), 51-54.

Snellings, R., De Schepper, M., De Buysser, K., Van Driessche, I., & De Belie, N. (2012). Clinkering reactions during firing of recyclable concrete. Journal of the American Ceramic Society, 95(5), 1741-1749.

Snoeck, D., & De Belie, N. (2012). Mechanical and self-healing properties of cementitious composites reinforced with flax and cottonised flax, and compared with polyvinyl alcohol fibres. Biosystems Engineering, 111(4), 325-335.

Snoeck, D., & De Belie, N. (2015a). Effect of superabsorbent polymers, superplasticizer and additional water on the setting of cementitious materials. International Journal of 3R's (Repair, Restoration and Renewal of Built Environment), 5(3), 721-729.

Snoeck, D., & De Belie, N. (2015b). From straw in bricks to modern use of microfibres in cementitious composites for improved autogenous healing – a review. Construction and Building Materials, 95, 774-787.

Snoeck, D., & De Belie, N. (2015c). Repeated autogenous healing in strain-hardening cementitious composites by using superabsorbent polymers. Journal of Materials in Civil Engineering, 04015086, 1-11.

Snoeck, D., Dewanckele, J., Cnudde, V., & De Belie, N. (2015a). X-ray computed microtomography to study autogenous healing of cementitious materials promoted by superabsorbent polymers. Cement and Concrete Composites, 1-11. DOI: 10.1016/j.cemconcomp.2015.10.016

Snoeck, D., Dubruel, P., & De Belie, N. (2012a). Superabsorbent polymers to prevent water movement in cementitious materials. International Journal of 3R's (Repair, Restoration and Renewal of Built Environment), 3(3), 432-440.

Snoeck, D., Jensen, O.M., & De Belie, N. (2015b). The influence of superabsorbent polymers on the autogenous shrinkage properties of cement pastes with supplementary cementitious materials. Cement and Concrete Research, 74, 59-67.

Snoeck, D., Priem, B., Dubruel, P., & De Belie, N. (2015c). Encapsulated Phase-Change Materials as additives in cementitious materials to promote thermal comfort in concrete constructions. Materials and Structures. doi: 10.1617/s11527-014-0490-5

Snoeck, D., Schaubroeck, D., Dubruel, P., & De Belie, N. (2014a). Effect of high amounts of superabsorbent polymers and additional water on the workability, microstructure and strength of mortars with a water-to-cement ratio of 0.50. Construction and Building Materials, 72, 148-157.

Snoeck, D., Smetryns, P.-A., & De Belie, N. (2015d). Improved multiple cracking and autogenous healing in cementitious materials by means of chemically-treated natural fibres. Biosystems Engineering, 139, 87-99.

Snoeck, D., Steuperaert, S., Van Tittelboom, K., Dubruel, P., & De Belie, N. (2012b). Visualization of water penetration in cementitious materials with superabsorbent polymers by means of neutron radiography. Cement and Concrete Research, 42(8), 1113-1121.

Snoeck, D., Van Tittelboom, K., Steuperaert, S., Dubruel, P., & De Belie, N. (2014b). Self-healing cementitious materials by the combination of microfibres and superabsorbent polymers. Journal of Intelligent Material Systems and Structures, 25(1), 13-24.

Snoeck, D., Vandenhaute, M., Vanderleyden, E., De Belie, N., Van Vlierberghe, S., & Dubruel, P. (2015e). Stable cross-linked Pluronic hydrogels: reality or utopia? Journal of Materials Science, submitted.

Snoeck, D., Velasco, L.F., Mignon, A., Van Vlierberghe, S., Dubruel, P., Lodewyckx, P., & De Belie, N. (2014c). The influence of different drying techniques on the water sorption properties of cement-based materials. Cement and Concrete Research, 64, 54-62.

Snoeck, D., Velasco, L.F., Mignon, A., Van Vlierberghe, S., Dubruel, P., Lodewyckx, P., & De Belie, N. (2015f). The effects of superabsorbent polymers on the microstructure of cementitious materials studied by means of sorption experiments. Cement and Concrete Research, 77, 26-35.

Song, X.F., Wei, J.F., & He, T.SH. (2009). A method to repair concrete leakage through cracks by synthesizing super-absorbent resin in situ. Construction and Building Materials, 23(1), 386-391.

Soroka, I. (1993). Concrete in hot environments. Modern Concrete Technology Series. London: E & FN Spon, pp. 251.

South, A.B., & Lyon, L.A. (2010). Autonomic Self-Healing of Hydrogel Thin Films. Angewandte Chemie, 49(4), 767-771.

Sreekala, M.S., Kumaran, M.G., Joseph, S., Jacob, M., & Thomas, S. (2000). Oil palm fibre reinforced phenol formaldehyde composites: influence of fibre surface modifications on the mechanical performance. Applied Composites Materials, 7(5-6), 295-329.

St John, D.A., Poole, A.B., & Sims, I. (1998). Concrete Petrography: a handbook of investigative techniques. London: Arnold, Hodder Headline Group, pp. 432.

Stamboulis, A., Baillie, C. A., & Peijs, T. (2001). Effects of environmental conditions on mechanical and physical properties of flax fibres. Composites, Part A, 32(8), 1105-1115.

Stocks-Fischer, S., Galinat, J.K., & Bang, S.S. (1999). Microbiological precipitation of $CaCO_3$. Soil Biology and Biochemistry, 31(11), 1563-1571.

Swift, D.G., & Smith, R.B.L. (1979). The flexural strength of cement based composites using low modulus sisal fibres. Composites, 10(3), 145-148.

Tada, S., & Watanabe, K. (2005). Dynamic determination of sorption isotherm of cement based materials. Cement and Concrete Research, 35(12), 2271-2277.

Talaiekhozan, A., Keyvanfar, A., Shafaghat, A., Andalib, R., Abd Majid, M.Z., Fulazzaky, M.A., Zin, R.M., Lee, C.T., Hussin, M.W., Hamzah, N., Marwar, N.F., & Haidar, H.I. (2014). A Review of Self-healing Concrete Research Development. Journal of Environmental Treatment Techniques, 2(1), 1-11.

Tanaka, D., & Fillmore, D.J. (1979). Kinetics of swelling of gels. Journal of Chemical Physics, 70(3), 1214-1218.

Tang, W., Kardani, O., & Cui, H. (2015). Robust evaluation of self-healing efficiency in cementitious materials - A review. Construction and Building Materials, 81, 233-247.

Taylor, H.F.W. (1990). Cement chemistry. London: Thomas Telford Publishing, pp. 491.

ter Heide, N. (2005). Crack Healing in Hydrating Concrete. Delft University of Technology, Delft, pp. 128.

Termkhajornkit, P., Nawa, T., Nakai, M., & Saito, T. (2005). Effect of fly ash on autogenous shrinkage. Cement and Concrete Research, 35(3), 473-482.

Termkhajornkit, P., Nawa, T., Yamashiro, Y., & Saito, T. (2009). Self-healing ability of fly ash-cement systems. Cement and Concrete Composites, 31(3), 195-203.

Thao, T.D.P., Johnson, T.J.S., Tong, Q.S., & Dai, P.S. (2009). Implementation of self-healing in concrete - Proof of concept. The IES Journal Part A: Civil & Structural Engineering, 2(2), 116-125.

Thiéry, M., Faure, P., Morandeau, A., Platret, G., Bouteloup, J.-F., Dangla, P., & Baroghel-Bouny, V. (2011). Effect of carbonation on the microstructure and moisture properties of cement-based materials. Paper presented at the 12DBMC - 12th International Conference on Durability of Building Materials and Components, Porto, 1-8.

Thomas, J.J., Hsieh, J., & Jennings, H.M. (1996). Effect of Carbonation on the nitrogen BET surface area of hardened Portland cement paste. Advanced Cement Based Materials, 3(2), 76-80.

Thommes, M. (2010). Physical adsorption characterization of nanoporous materials. Chemie Ingenieur Technik, 82(7), 1059-1071.

Tiwari, R. (2008). Thermal Techniques for Material Characterization, Ceramic Industry.

Tolêdo Filho, R.D., Scrivener, K.L., England, G.L., & Ghavami, K. (2000). Durability of alkali-sensitive sisal and coconut fibres in cement mortar composites. Cement and Concrete Composites, 22(2), 127-143.

Trask, R.S., & Bond, I.P. (2006). Biomimetic self-healing of advanced composite structures using hollow glass fibres. Smart Materials and Structures, 15(3), 704-710.

Trtik, P., Muench, B., Weiss, W.J., Herth, G., Kaestner, A., Lehmann, E., & Lura, P. (2010). Neutron tomography measurements of water release from superabsorbent polymers in cement paste. Paper presented at the International RILEM Conference on Material Science, Aachen, RILEM Publications S.A.R.L., 175-185.

Trtik, P., Münch, B., Weiss, W.J., Kaestner, A., Jerjen, I., Josic, L., Lehmann, E., & Lura, P. (2011). Release of internal curing water from lightweight aggregates in cement paste investigated by neutron and X-ray tomography. Nuclear Instruments and Methods in Physics Research Section A, 651(1), 244-249.

Trtnik, G., Turk, G., Kavčič, F., & Bosiljkova, V.B. (2008). Possibilities of using the ultrasonic wave transmission method to estimate initial setting time of cement paste. Cement and Concrete Research, 38(11), 1336-1342.

Tsuji, M., Shitama, K., & Isobe, D. (1999). Basic studies on simplified curing technique, and prevention of initial cracking and leakage of water through cracks of concrete by applying superabsorbent polymers as new concrete admixture. Journal of the Society of Materials Science, 48(11), 1308-1315.

Tsukamoto, M., & Woener, J.D. (1991). Permeability of cracked fibre-reinforced concrete. Darmstadt Concrete, 6, 123-135.

Tzvetkov, G., Graf, B., Wiegner, R., Raabe, J., Quitmann, C., & Fink, R. (2008). Soft X-ray spectromicroscopy of phase-change microcapsules. Micron, 39(3), 275-279.

Valckenborg, R.M.E., Pel, L., Hazrati, K., Kopinga, K., & Marchand, J. (2001). Pore water distribution in mortar during drying as determined by NMR. Materials and Structures, 34(10), 599-604.

van Breugel, K. (2007). Is There a Market for Self-healing Cement-based Materials? Paper presented at the 1st International Conference on self-healing Materials, Noordwijk, RILEM Publications S.A.R.L., 1-9.

Van De Velde, K., & Kiekens, P. (2001). Thermal degradation of flax: the determination of kinetic parameters with thermogravimetric analysis. Applied Polymer Science, 83(12), 2634-2643.

Van den Heede, P. (2014). Durability and sustainability of concrete with high volumes of fly ash. Ghent University, Ghent, pp. 340.

Van den Heede, P., Maes, M., & De Belie, N. (2014). Influence of active crack width control on the chloride penetration resistance and global warming

potential of concrete slabs made with fly ash + silica fume concrete. Construction and Building Materials, 67(Part A), 74-80.

Van Tittelboom, K. (2012). Self-healing concrete through incorporation of encapsulated bacteria- or polymer-based healing agents. Ghent University, Ghent, pp. 344.

Van Tittelboom, K., Adesanya, K., Dubruel, P., Van Puyvelde, P., & De Belie, N. (2011a). Methyl methacrylate as a healing agent for self-healing cementitious materials. Smart Materials and Structures, 20(12), 125016.

Van Tittelboom, K., & De Belie, N. (2013). Self-Healing in Cementitious Materials - A Review. Materials, 6(6), 2182-2217.

Van Tittelboom, K., De Belie, N., De Muynck, W., & Verstraete, W. (2010). Use of bacteria to repair cracks in concrete. Cement and Concrete Research, 40(1), 157–166.

Van Tittelboom, K., De Belie, N., Lehmann, F., & Grosse, C.U. (2012a). Acoustic emission analysis for the quantification of autonomous crack healing in concrete. Construction and Building Materials, 28(1), 333-341.

Van Tittelboom, K., De Belie, N., Van Loo, D., & Jacobs, P. (2011b). Self-healing efficiency of cementitious materials containing tubular capsules filled with healing agent. Cement and Concrete Composites, 33(4), 497–505.

Van Tittelboom, K., Gruyaert, E., De Backer, P., Moerman, W., & De Belie, N. (2014). Self-repair of thermal cracks in concrete sandwich panels. Structural Engineering.

Van Tittelboom, K., Gruyaert, E., Rahier, H., & De Belie, N. (2012b). Influence of mix composition on the extent of autogenous crack healing by continued hydration or calcium carbonate formation. Construction and Building Materials, 37, 349-359.

Van Tittelboom, K., Snoeck, D., Vontobel, P., Wittmann, F.H., & De Belie, N. (2012c). Use of neutron radiography and tomography to visualize the autonomous crack sealing efficiency in cementitious materials. Materials and Structures.

Van Tittelboom, K., Tsangouri, E., Van Hemelrijck, D., & De Belie, N. (2015). The efficiency of self-healing concrete using alternative manufacturing procedures and more realistic crack patterns. Cement and Concrete Composites, 57, 142-152.

Vandenhaute, M., Schelfhout, J., Van Vlierberghe, S., Mendes, E., & Dubruel, P. (2014). Cross-linkable, thermo-responsive Pluronic® building blocks for biomedical applications: Synthesis and physico-chemical evaluation. European Polymer Journal, 53, 126-138.

Verhoeven, L., & Lodewyckx, P. (2001). Comparison of Dubinin-Radushkevich micropore volumes obtained from N_2, CO_2 and H_2O-adsorption isotherms. Paper presented at the Carbon 2001, Lexington, American Carbon Society, 1-6.

Villain, G., Thiéry, M., & Platret, G. (2007). Measurement methods of carbonation profiles in concrete: Thermogravimetry, chemical analysis and gammadensimetry. Cement and Concrete Research, 37(8), 1182-1192.

Vlassenbroeck, J., Dierick, M., Masschaele, B., Cnudde, V., Van Hoorebeke, L., & Jacobs, P. (2007). Software tools for quantification of X-ray microtomography at the UGCT. Nuclear Instruments and Methods in Physics Research Section A, 580(1), 442-445.

Völkl, J.J., Beddoe, R.E., & Setzer, M.J. (1987). The specific surface of hardened cement paste by small-angle X-ray scattering effect of moisture content and chlorides. Cement and Concrete Research, 17(1), 81-88.

Vontobel, P., Lehmann, E., Hassanein, R., & Frei, G. (2006). Neutron tomography: method and applications. Physica B: Condensed Matter, 385-386(1), 475-480.

Wang, J. (2013). Self-healing concrete by means of immobilized carbonate precipitating bacteria. Ghent University, Ghent, pp. 303.

Wang, J., De Belie, N., & Verstraete, W. (2012a). Diatomaceous earth as a protective vehicle for bacteria applied for self-healing concrete. Journal of Industrial Microbiology and Biotechnology, 39(4), 567-577.

Wang, J., Dewanckele, J., Cnudde, V., Van Vlierberghe, S., Verstraete, W., & De Belie, N. (2014a). X-ray computed tomography proof of bacterial-based self-healing in concrete. Cement and Concrete Composites, 53, 289-304.

Wang, J., Snoeck, D., Van Vlierberghe, S., Verstraete, W., & De Belie, N. (2014b). Application of hydrogel encapsulated carbonate precipitating bacteria for approaching a realistic self-healing in concrete. Construction and Building Materials, 68, 110-119.

Wang, J., Soens, H., Verstraete, W., & De Belie, N. (2014c). Self-healing concrete by use of microencapsulated bacterial spores. Cement and Concrete Research, 56, 139-152.

Wang, J., Van Tittelboom, K., De Belie, N., & Verstraete, W. (2012b). Use of silica gel or polyurethane immobilized bacteria for self-healing concrete. Cement and Building Materials, 26(1), 532-540.

Wang, K., Jansen, D.C., Shah, S.P., & Karr, A.F. (1997). Permeability study of cracked concrete. Cement and Concrete Research, 27(3), 381–393.

Wang, S. (2005). Micromechanics Based Matrix Design for Engineered Cementitious Composites. University of Michigan, Ann Arbor, pp. 221.

Wang, S., & Li, V.C. (2006). Polyvinyl alcohol fiber reinforced engineered cementitious composites: material design and performances. Paper presented at the International RILEM Workshop on High Performance Fiber Reinforced Cementitious Composites in Structural Applications, RILEM Publications S.A.R.L., 65-73.

Wang, Y., Backer, S., & Li, V.C. (1987). An experimental study of the synthetic fibre reinforced cementitious composites. Journal of Materials Science, 22(12), 4281-4291.

Wanka, G., Hoffmann, H., & Ulbricht, W. (1994). Phase Diagrams and Aggregation Behavior of Poly(oxyethylene)-Poly(oxypropylene)-Poly(oxyethylene) Triblock Copolymers in Aqueous Solutions. Macromolecules, 27(15), 4145-4159.

Wei, B., Cao, H., & Song, S. (2010). Environmental resistance and mechanical performance of basalt and glass fibers. Materials Science and Engineering A, 527(18), 4708-4715.

White, S.R., Sottos, N.R., Geubelle, P.H., Moore, J.S., Kessler, M.R., Sriram, S.R., Brown, E.N., & Viswanathan, S. (2001). Autonomic healing of polymer composites. Nature, 409, 794-797.

Wiktor, V., & Jonkers, H.M. (2011). Quantification of crack-healing in novel bacteria-based self-healing concrete. Cement and Concrete Composites, 33(7), 763-770.

Winnefeld, F., Becker, S., Pakusch, J., & Götz, T. (2007). Effects of the molecular architecture of comb-shaped superplasticizers on their performance in cementitious systems. Cement and Concrete Composites, 29(4), 251-262.

Wittmann, F.H., Zhang, P., Lehmann, E., & Zhao, T.J. (2011). Visualisation of frost damage in concrete by means of neutron radiography. Paper presented at the Proceedings of a Workshop on Basic Research on Concrete and Applications, Geneva, ASMES Aedification Publishers, 155-174.

Wood, G.O. (2001). Affinity coefficients of the Polanyi/Dubinin adsorption isotherm equations: A review with compilations and correlations. Carbon, 39(3), 343-356.

Wu, M., Johannesson, B., & Geiker, M. (2012). A review: Self-healing in cementitious materials and engineered cementitious composite as a self-healing material. Construction and Building Materials, 28(1), 571-583.

Wyrzykowski, M., & Lura, P. (2014). Reduction of autogenous shrinkage in OPC and BFSC pastes with internal curing. Paper presented at the XIII International Conference on Durability of Building Materials and Components, São Paulo, 1010-1017.

Yan, P., & Chen, Z. (2014). Autogenous shrinkage of fly ash concrete with different water-binder ratios. Journal of the Chinese Ceramic Society, 42(5), 585-589.

Yang, E.-H. (2008). Designing added functions in Engineered Cementitious Composites. University of Michigan, Ann Arbor, pp. 293.

Yang, E.-H., Yang, Y., & Li, V.C. (2007a). Use of High Volumes of Fly Ash to Improve ECC Mechanical Properties and Material Greenness. ACI Materials Journal, 104(6), 303-311.

Yang, H., Yan, R., Chen, H., Lee, D.H., & Zheng, C. (2007b). Characteristics of hemicellulose, cellulose and lignin pyrolysis. Fuel, 86(12-13), 1781-1788.

Yang, H., Yan, R., Chen, H., Zheng, C., Lee, D.H., & Liang, D.T. (2006). In-depth investigation of biomass pyrolysis based on three major components: hemicellulose, cellulose and lignin. Energy and Fuels, 20(1), 388-393.

Yang, Y., Lepech, M.D., Yang, E.-H., & Li, V.C. (2009). Autogenous Healing of Engineered Cementitious Composites under Wet-dry Cycles. Cement and Concrete Research, 39(5), 382-390.

Yang, Y., Yang, E.-H., & Li, V.C. (2011). Autogenous healing of engineered cementitious composites at early age. Cement and Concrete Research, 41(2), 176-183.

Yao, Y., Zhu, Y., & Yang, Y. (2011). Incorporation of SAP particles as controlling pre-existing flaws to improve the performance of ECC. Construction and Building Materials, 28(1), 139-145.

Ye, G. (2003). Experimental study and numerical simulation of the development of the microstructure and permeability of cementitious materials. PhD, Technical University Delft, Delft, pp. 186.

Yildirim, G., Şahmaran, M., & Ahmed, H. (2014). Influence of Hydrated Lime Addition on the Self-Healing Capability of High-Volume Fly Ash Incorporated Cementitious Composites. Journal of Materials in Civil Engineering, 04014187, 1-11.

Yilmaz, V.T., & Glasser, F.P. (1991). Reaction of alkali-resistant glass fibres with cement. I, Review, assessment, and microscopy. Glass technology, 32(3), 91-98.

Zalba, B., Marín, J.M., Cabeza, L.F., & Mehling, H. (2003). Review on thermal energy storage with phase change: materials, heat transfer analysis and applications. Applied Thermal Engineering, 23(3), 251-283.

Zeronian, S.H., & Nevell, T.P. (1985). Cellulose Chemistry and its Application. Halsted Press, John Wiley, Chichester, UK, pp. 552.

Zhang, J., & Scherer, G.W. (2011). Comparison of methods for arresting hydration of cement. Cement and Concrete Research, 41(10), 1024-1036.

Zhang, L., & Glasser, F.P. (2000). Critical examination of drying damage to cement pastes. Advances in Cement Research, 12(2), 79-88.

Zhang, P., Wittmann, F.H., & Zhao, T.J. (2011a). Quantitative determination of capillary absorption of concrete. Paper presented at the Proceedings of a

Workshop on Basic Research on Concrete and Applications, Geneva, ASMES, Aedificatio Publishers, 9-20.

Zhang, P., Wittmann, F.H., Zhao, T.J., & Lehmann, E. (2010a). Neutron imaging of water penetration into cracked steel reinforced concrete. Physica B: Condensed Matter, 405(7), 1866-1871.

Zhang, P., Wittmann, F.H., Zhao, T.J., Lehmann, E., Tian, L., & Vontobel, P. (2010b). Observation and quantification of water penetration into Strain Hardening Cement-based Composites (SHCC) with multiple cracks by means of neutron radiography. Nuclear Instruments and Methods in Physics Research Section A, 620(2-3), 414-420.

Zhang, P., Wittmann, F.H., Zhao, T.J., Lehmann, E.H., & Vontobel, P. (2011b). Neutron radiography, a powerful method to determine time-dependent moisture distributions in concrete. Nuclear Engineering and Design, 241(12), 4758-4766.

Zhao, H., & Darwin, D. (1992). Quantitative backscattered electron analysis of cement paste. Cement and Concrete Research, 22(4), 695-706.

Zhou, J., Qian, S.Z., Sierra-Beltran, M.G., Ye, G., van Breugel, K., & Li, V.C. (2010). Development of engineered cementitious composites with limestone powder and blast furnace slag. Materials and Structures, 43(6), 803-814.

Zhou, J., Qian, S.Z., Ye, G., Copuroglu, O., van Breugel, K., & Li, V.C. (2012). Improved fiber distribution and mechanical properties of engineered cementitious composites by adjusting the mixing sequence. Cement and Concrete Composites, 34(3), 342-348.

Zhou, Z., Ou, G., Hang, Y., Chen, G., & Ou, J. (2009). Research and development of plastic optical fiber based smart transparent concrete. Paper presented at the Smart Sensor Phenomena, Technology, Networks, and Systems, San Diego, Society of Photo-Optical Instrumentation Engineers SPIE, 72930F, 1-6.

Zhou, Z.H., Li, Z.Q., Xu, D.Y., & Yu, J.H. (2011). Influence of Slag and Fly Ash on the Self-Healing Ability of Concrete. Advanced Materials Research, 306-307, 1020-1023.

Zhu, D., Gencoglu, M., & Mobasher, B. (2009). Low velocity flexural impact behavior of AR glass fabric reinforced cement composites. Cement and Concrete Composites, 31(6), 379-387.

Zhu, Q., Barney, C.W., & Erk, K.A. (2014). Effect of ionic crosslinking on the swelling and mechanical response of model superabsorbent polymer hydrogels for internally cured concrete. Materials and Structures, 1-16.

Zlopasa, J., Koenders, E.A.B., & Picken, S.J. (2014). A novel bio-based curing compound for cement-based materials. Paper presented at the PRO 95: International RILEM Conference on the Application of Superabsorbent Polymers and Other New Admixtures in Concrete Construction, Dresden, RILEM Publications S.A.R.L., 47-54.

Zohuriaan-Mehr, M.J., & Kabiri, K. (2008). Superabsorbent Polymer Materials: a Review. Iranian Polymer Journal, 17(6), 451-477.

Zollo, R.F. (1997). Fiber-reinforced concrete: an overview after 30 years of development. Cement and Concrete Composites, 19(2), 107-122.

Zweers, M.L.T., Engbers, G.H.M., Grijpma, D.W., & Feijen, J. (2004). In vitro degradation of nanoparticles prepared from polymers based on dl-lactide, glycolide and poly(ethylene oxide). Journal of Controlled Release, 100(3), 347-356.

Curriculum vitae

Personal information

Name	Didier Snoeck
Date of birth	February 27th 1988
Place of birth	Ghent - Belgium
Nationality	Belgian
Address	Hukkelgemwegel 29, 9820 Merelbeke
E-mail	Didier.Snoeck@UGent.be

Education

University

2011 - 2015 Doctorate (PhD) in Civil Engineering
Faculty of Engineering and Architecture at Ghent University

Title:
Self-healing and microstructure of cementitious materials with microfibres and superabsorbent polymers

Specialist courses:
Polymer materials (Ghent University)
Concrete microscopy course (Delft University of Technology)
Self-healing materials (Delft University of Technology)
High-performance fibre-reinforced cement-based composites (Technical University of Dresden)

Seminars in transferable skills:
Effective scientific communication
Quality research skills / research methodology
Basic assistant training
Workshop: to upgrade your lessons
Water-tightness of concrete structures: design/implementation

2006 - 2011 Bachelor and Master of Science in Civil Engineering
Major: Construction Design
Faculty of engineering and architecture at Ghent University
Graduated summa cum laude

MSc thesis:
Self-healing concrete by the combination of microfibres and reactive substances

Secondary

2000 - 2006 Latin and mathematics
Don Bosco College Zwijnaarde
Graduated summa cum laude

Employment

2011- 2015	Research Assistant of the Research Foundation-Flanders (FWO-Vlaanderen) Researcher at the department of Structural Engineering, Faculty of Engineering and Architecture at Ghent University Magnel Laboratory for Concrete Research *Teaching activities:* Introduction to Strength of Materials Statics *Services:* Tests on products for the protection and repair of concrete structures Tutor of 9 Master Dissertations *Committees:* RILEM TC RSC: Recommendations for use of superabsorbent polymers in concrete construction RILEM TC 225-SAP: Application of superabsorbent polymers in concrete construction Organizing committee of the International Conference on Self-Healing Materials (ICSHM2013)
March- April 2014	Guest researcher at the Technical University of Denmark Department of Building Materials

Scientific prizes

2015	Best Oral Presentation - Hard Matter, ICSHM, Duke University
2011	First prize ENCI Study Award, Heidelberg Cement Group
2011	Honourable Mention BBG Study Award, Belgian Concrete Group
2011	Last round VABOR study award for maintenance and repair of concrete
2011	Shortlist Flemish Thesis Prize: Technology and Innovation: Agoria Award
2011	Shortlist Flemish Thesis Prize: Best beta-thesis: EOS Award
2011	Nominated for the ie-net Prizes, Community of Engineers
2006	Diploma 18th Flemish Physics-Olympiad
2006	Diploma 23rd Flemish Chemistry Olympiad
2005	Laureate and finalist Flemish Mathematics Olympiad as a fifth grader

Scientific publications

A1 publications

Snoeck, D., Dewanckele, J., Cnudde, V., & De Belie, N. (2015). X-ray computed microtomography to study autogenous healing of cementitious materials promoted by superabsorbent polymers. Cement and Concrete Composites, 1-11. DOI: 10.1016/j.cemconcomp.2015.10.016

Wang, J., Mignon, A., **Snoeck, D.**, Wiktor, V., Boon, N. & De Belie, N. (2015). Application of modified-alginate encapsulated carbonate producing bacteria in concrete: a promising strategy for crack self-healing. Frontiers in Microbiology, 6, 1088, 1-14.

Snoeck, D., Smetryns, P.-A., & De Belie, N. (2015). Improved multiple cracking and autogenous healing in cementitious materials by means of chemically-treated natural fibres. Biosystems Engineering, 139, 87-99.

Snoeck, D. & De Belie, N. (2015). From straw in bricks to modern use of microfibres in cementitious composites for improved autogenous healing – A review. Construction and Building Materials, 95, 774-787.

Snoeck, D., Velasco, L.F., Mignon, A., Van Vlierberghe, S., Dubruel, P., Lodewyckx, P. & De Belie, N. (2015). The effects of superabsorbent polymers on the microstructure of cementitious materials studied by means of sorption experiments. Cement and Concrete Research, 77, 26-35.

Mignon, A., **Snoeck, D.**, Schaubroeck, D., Luickx, N., Dubruel, P., Van Vlierberghe, S. & De Belie, N. (2015). pH-responsive superabsorbent polymers: opening a pathway to self-healing of mortar, or is it closing a pathway? Reactive and Functional Polymers, 93, 68-76.

Snoeck, D. & De Belie N. (2015). Repeated autogenous healing in strain-hardening cementitious composites by using superabsorbent polymers. Journal of Materials in Civil Engineering, 04015086, 1-11.

Snoeck, D., Jensen, O.M., & De Belie, N. (2015). The influence of superabsorbent polymers on the autogenous shrinkage properties of cement pastes with supplementary cementitious materials. Cement and Concrete Research, 74, 59-67.

Snoeck, D., Priem, B., Dubruel, P. & De Belie, N. (2015). Encapsulated Phase-Change Materials as additives in cementitious materials to promote thermal comfort in concrete constructions. Materials and Structures, published online, 1-15. DOI: 10.1617/s11527-014-0490-5.

Mignon, A., Graulus, G.-J., **Snoeck, D.**, Martins, J., De Belie, N., Dubruel, P., & Van Vlierberghe, S. (2015). pH-sensitive superabsorbent polymers: a potential candidate material for self-healing concrete. Journal of Materials Science, 50(2), 970-979.

Snoeck, D., Schaubroeck, D., Dubruel, P., & De Belie, N. (2014). Effect of high amounts of superabsorbent polymers and additional water on the workability, microstructure and strength of mortars with a water-to-cement ratio of 0.50. Construction and Building Materials, 72, 148-157.

Snoeck, D., Velasco, L.F., Mignon, A., Van Vlierberghe, S., Dubruel, P., Lodewyckx, P., & De Belie, N. (2014). The influence of different drying techniques on the water sorption properties of cement-based materials. Cement and Concrete Research, 64, 54-62.

Wang, J., **Snoeck, D.**, Van Vlierberghe, S., Verstraete, W., & De Belie, N. (2014). Application of hydrogel encapsulated carbonate precipitating bacteria for approaching a realistic self-healing in concrete. Construction and Building Materials, 68, 110-119.

Van Tittelboom, K., **Snoeck, D.**, Vontobel, P., Wittmann, F.H., & De Belie, N. (2013). Use of neutron radiography and tomography to visualize the autonomous crack sealing efficiency in cementitious materials. Materials and Structures, 46(1-2),105-121.

Snoeck, D., Steuperaert, S., Van Tittelboom, K., Dubruel, P., & De Belie, N. (2012). Visualization of water penetration in cementitious materials with superabsorbent polymers by means of neutron radiography. Cement and Concrete Research, 42(8), 1113-1121.

Snoeck, D., Van Tittelboom, K., Steuperaert, S., Dubruel, P., & De Belie, N. (2014). Self-healing cementitious materials by the combination of microfibres and superabsorbent polymers. Journal of Intelligent Material Systems and Structures, 25(1), 13-24.

Snoeck, D., & De Belie, N. (2012). Mechanical and self-healing properties of cementitious composites reinforced with flax and cottonised flax, and compared with polyvinyl alcohol fibres. Biosystems Engineering, 111(4), 325-335.

Submitted A1 publications

Mignon, A., **Snoeck, D.**, D'Halluin, K., Balcaen, L., Vanhaecke, F., Dubruel, P., Van Vlierberghe, S. & De Belie, N. (2015). Alginate biopolymers: a smart cure for cracked concrete. Construction and Building Materials, submitted.

Vandenhaute[1st] M., **Snoeck[1st] D.**, Vanderleyden E., De Belie N., Van Vlierberghe S. & Dubruel P. (2015). Stable cross-linked Pluronic hydrogels: reality or utopia? Journal of Materials Science, submitted.

Mechtcherine V., Schröfl, C., Wyrzykowski, M., Gorges, M., Cusson, D., Margeson, J., De Belie, N., **Snoeck, D.**, Ichimiya, K., Igarashi, S.-I., Falikman, V., Friedrich, S., Bokern, J., Kara, P., Lura, P., Marciniak, A., Reinhardt, H.-W., Sippel, S., Ribeiro, A.B., Custódio, J., Ye, G., Dong, H. & Weiss, J. (2015). Effect of superabsorbent polymers (SAP) on the freeze-thaw resistance of concrete: results of a RILEM round-robin test. Materials and Structures, submitted.

Van Tittelboom, K., Wang, J., Gomes De Araújo, M.A., **Snoeck, D.**, Gruyaert, E., Debbaut, B., Derluyn, H., Cnudde, V., Tsangouri, E., Van Hemelrijck, D. & De Belie, N. (2015). Comparison of different approaches for self-healing concrete in a large-scale lab test. Construction and Building Materials, submitted.

Maes, M., **Snoeck, D.**, & De Belie, N. (2015). Chloride penetration in cracked mortar and the influence of autogenous crack healing. Construction and Building Materials, submitted.

A2 publications

Snoeck, D. & De Belie, N. (2015). Effect of superabsorbent polymers, superplasticizer and additional water on the setting of cementitious materials. International Journal of 3R's (Repair, Restoration and Renewal of Built Environment), 5(3), 721-729.

Snoeck, D., Dubruel, P., & De Belie, N. (2012). Superabsorbent polymers to prevent water movement in cementitious materials. International Journal of 3R's (Repair, Restoration and Renewal of Built Environment), 3(3), 432-440.

A3 publications

Snoeck, D. (2012). Zelfhelend beton: Zelfheling door combinatie van microvezels en reactieve stoffen. Cement, Uitgeverij Æneas, 2012:4, p.95 & p.128, 3 p. paper online.

B2 book chapters

Çopuroglu, O., Schlangen, E., Nishiwaki, T., Van Tittelboom, K., **Snoeck, D.**, De Belie, N. & de Rooij, M.R. (2013). Chapter 3: Experimental techniques used to verify healing. In: de Rooij, M.R., Van Tittelboom, K., De Belie, N. and Schlangen, E. (Eds.) Self-Healing Phenomena in Cement-Based Materials: State-of-the-Art Report of RILEM Technical Committee 221-SHC. Vol. 11, ISBN 978-94-007-6623-5, 256 p.

Reinhardt, H.W., Jonkers, H., Van Tittelboom, K., **Snoeck, D.**, De Belie, N., De Munck, W., Verstraete, W., Wang, J. & Mechtcherine, V. (2013). Chapter 4: Recovery against environmental actions. In: de Rooij, M.R., Van Tittelboom, K., De Belie, N. and Schlangen, E. (Eds.) Self-Healing Phenomena in Cement-Based Materials: State-of-the-Art Report of RILEM Technical Committee 221-SHC. Vol. 11, ISBN 978-94-007-6623-5, 256 p.

Li, V.C. Sakulich, A.R., Reinhardt, H.W., Schlangen, E., Van Tittelboom, K., **Snoeck, D.**, De Belie, N., Joseph, C., Gardner, D.R., Lark, R.J., Mihashi, H. & Nishiwaki, T. (2013). Chapter 5: Recovery against mechanical actions. In: de Rooij, M.R., Van Tittelboom, K., De Belie, N. and Schlangen, E. (Eds.) Self-Healing Phenomena in Cement-Based Materials: State-of-the-Art Report of RILEM Technical Committee 221-SHC. Vol. 11, ISBN 978-94-007-6623-5, 256 p.

C1/P1 publications

Van Tittelboom, K., Wang, J., Gomes De Araújo, M.A., **Snoeck, D.**, Gruyaert, E., Debbaut, B. & De Belie, N. (2015). Real-scale testing of the efficiency of self-healing concrete. In: Proceedings of the 4th International Conference on Concrete Repair, Rehabilitation and Retrofitting (ICCRRR), Leipzig, 5-7 October 2015, 1-8.

Snoeck, D. & De Belie, N. (2015). Effect of fibre type and superabsorbent polymers on the self-healing properties of strain-hardening cementitious materials. In: Brandt, A.M., Olek, J., Glinicki, M.A., Leung, C.K.Y. and Lis, J. (Eds.). Proceedings of the International Symposium on Brittle Matrix Composites, BMC11, Warsaw, 28-30 September 2015, 213-222.

Snoeck, D., Velasco, L.F., Mignon, A., Vervaet, C., Van Vlierberghe, S., Dubruel, P., Lodewyckx, P. & De Belie, N. (2015). The effects of superabsorbent polymers on the water vapour sorption properties of cementitious materials. In: Proceedings of the 27th Biennial National Conference of the Concrete Institute of Australia, Concrete 2015, Melbourne, 30 August – 2 September 2015, 805-813.

Snoeck, D., Dewanckele, J., Dierick, M., Van Hoorebeke, L., Cnudde, V., Dubruel, P. & De Belie, N. (2015). Autogenous healing of cementitious materials promoted by superabsorbent polymers studied by means of X-ray computed microtomography. In: Proceedings of the 5th International

Conference on Self Healing Materials, Durham, 21-24 June 2015, 4 p CEMT O20-31.

Mignon, A., **Snoeck, D.**, Velasco, L.F., Lodewyckx, P., Dubruel, P., Van Vlierberghe, S. & De Belie, N. (2015). Smart superabsorbent polymers for self-sealing and -healing of mortar. In: Proceedings of the 5th International Conference on Self Healing Materials, Durham, 21-24 June 2015, 4 p CEMT O18-54.

De Belie, N., Van Tittelboom, K, Tsangouri, E., Karaiskos, G. **Snoeck, D.**, Wang, J., Gomes De Araújo, M.A. & Van Hemelrijck, D. (2015). Autonomous regeneration of concrete structures by incorporation of self-healing mechanisms. In: Proceedings of the International Conference on the Regeneration and Conservation of Concrete Structures, Nagasaki, 1-3 June 2015, 1-10.

Snoeck, D., Smetryns, P.-A. & De Belie, N. (2014). Chemical treatment of natural fibres to obtain multiple cracking and self-healing in cementitious materials. In: Schlangen, E., Sierra-Beltran, M.G., Luković, M. and Ye, G. (Eds.). Proceedings of the 3rd International RILEM Conference on Strain Hardening Cementitious Composites, Dordrecht, 3-5 November 2014, 185-192.

Snoeck, D., Dubruel, P. & De Belie, N. (2014). How to seal and heal cracks in cementitious materials by using superabsorbent polymers. In: Mechtcherine, V. and Schröfl, C. (Eds.). Proceedings of the International Conference on Application of Superabsorbent Polymers and Other New Admixtures in Concrete Construction Dresden, 15-17 September 2014, 375-384.

Mignon, A., **Snoeck, D.**, Van Vlierberghe, S., Dubruel, P. & De Belie, N. (2014). Comparing pH-sensitive with commercial superabsorbent polymers in cementitious materials. In: Mechtcherine, V. and Schröfl, C. (Eds.). Proceedings of the International Conference on Application of Superabsorbent Polymers and Other New Admixtures in Concrete Construction Dresden, 15-17 September 2014, 37-46.

Snoeck, D., Debaecke, S. & De Belie, N. (2014). Repeated autogenous healing in cementitious composites with microfibres and superabsorbent polymers. In: Quattrone, M. and John, V.M. (Eds.). Proceedings of the XIII International Conference on Durability of Building Materials and Components, São Paulo, 3-5 September 2014, 73-80.

Snoeck, D., Velasco, L.F., Mignon, A., Van Vlierberghe, S., Dubruel, P., Lodewyckx, P. & De Belie, N. (2013). Effect of the drying technique on the sorption properties in cementitious materials. In: Proceedings of the TRANSCEND Conference on Water transport in cementitious materials, Guildford, 3-6 November 2013, 84-87.

Snoeck, D. & De Belie, N. (2013). The influence of superabsorbent polymers on the microstructure and permeability of cementitious materials. In: Li, Z.J., Sun, W., Miao, C.W., Sakai, K., Gjørv, O.E. and Banthia, N. (Eds.) Proceedings of the Seventh International Conference on Concrete under Severe Conditions - Environment and Loading, Nanjing, 23-25 September 2013, 363-373.

Snoeck, D., Dubruel, P. & De Belie, N. (2013). Microfibres and hydrogels to promote autogenous healing in cementitious materials. In: De Belie, N., van der Zwaag, S., Gruyaert, E., Van Tittelboom, K. and Debbaut, B. (Eds.). Proceedings of the 4th International Conference on Self Healing Materials, Ghent, 16-20 June 2013, 17-20.

Van Tittelboom, K., **Snoeck, D.**, Wang, J. & De Belie, N. (2013). Most recent advances in the field of self-healing cementitious materials. In: De Belie, N., van der

Zwaag, S., Gruyaert, E., Van Tittelboom, K. and Debbaut, B. (Eds.). Proceedings of the 4th International Conference on Self Healing Materials, Ghent, 16-20 June 2013, 406-413.

Snoeck, D., Steuperaert, S., Van Tittelboom, K., Dubruel, P. & De Belie, N. (2012). The use of superabsorbent polymers as a crack sealing and crack healing mechanism in cementitious materials. In: Alexander, M.G., Beushausen, H.-D., Dehn, F. and Moyo, P. (Eds.). Proceedings of the 3rd International Conference on Concrete Repair, Rehabilitation and Retrofitting, Cape Town, 3-5 September 2012, 152-157.

De Belie, N., Van Tittelboom, K., **Snoeck, D.** & Wang, J. (2012). Smart additives for self-sealing and self-healing concrete. In: Proceedings of the International symposium on concrete with smart additives and supplementary cementitious materials, Cancun, 12-17 August 2012, 1-12.

De Belie, N., Van Tittelboom, K., **Snoeck, D.** & Wang, J. (2012). More durable concrete structures by autonomous repair of damage. In: Proceedings of the International Congress on Durability of Concrete, Trondheim, 17-21 June 2012, 1-14.

De Belie, N. & **Snoeck, D.** (2011). Assessment of the performance of cottonised flax in natural fibre reinforced cementitious composites. In: Godbout, A. and Potvin, L. (Eds.). Proceedings of the 7th International Symposium on Concrete for a Sustainable Agriculture (CSA), Québec, 18-21 September 2011, 156-165.

C3 publications

Velasco, L.F., **Snoeck, D.**, Mignon, A., Van Vlierberghe, S., Dubruel, P., De Belie, N. & Lodewyckx, P. (2015). Towards a global model for describing the low relative pressure region of water vapour isotherms on porous materials. In: Proceedings of the 6th International Conference on Carbon for Energy Storage/Conversion and Environment Protection, CESEP, Poznam, 18-22 October 2015, 1-2.

Van Tittelboom, K., **Snoeck, D.**, Wang, J., Van Belleghem, B., Dewanckele, J., Dierick, M., Cnudde, V., Van Hoorebeke, L. & De Belie, N. (2015). Use of X-ray radiography and tomography to evaluate self-healing concrete. In: Proceedings of the 2nd UGCT seminar, Ghent, 10 September 2015, 1-2.

Mignon, A., **Snoeck, D.**, Dubruel, P., Balcaen, L., De Belie, N. & Van Vlierberghe, S. (2015). Biopolymers for self-sealing and -healing of mortar. In: Proceedings of the XXIV International Materials Research Congress, Cancun, 12-17 August 2012, abstract on CD.

Velasco, L.F., **Snoeck, D.**, Mignon, A., Van Vlierberghe, S., Dubruel, P., De Belie, N. & Lodewyckx, P. (2015). Role of the surface chemistry of the adsorbent on the initialization step of the water sorption process. In: Proceedings of the World Conference on Carbon, Dresden, 12-17 July 2015, 2 p abstract 5.

Velasco, L.F., **Snoeck, D.**, Mignon, A., Van Vlierberghe, S., Dubruel, P., De Belie, N. & Lodewyckx, P. (2014). Influence of the surface oxygen content of the material on the specific interactions taking place at the first stages of water sorption. In: Proceedings of the World Conference on Carbon, Jeju, 29 June - 4 July 2014, 2 p POT7-23.

Velasco, L.F., **Snoeck, D.**, Mignon, A., Van Vlierberghe, S., Dubruel, P., De Belie, N. & Lodewyckx, P. (2014). Correlating the water adsorption mechanism at low relative pressures of activated carbons with cements. In: Proceedings of

the 10th International Symposium on the Characterization of Porous Solids (COPS-X), Granada, 11-14 May 2014, p. 242.

Mignon, A., **Snoeck, D.**, Van Vlierberghe, S., Dubruel, P. & De Belie, N. (2013). Application of pH-sensitive hydrogels for concrete applications. In: Proceedings of the TRANSCEND Conference on Water transport in cementitious materials, Guildford, 3-6 November 2013, p. 140.

Velasco, L.F., **Snoeck, D.**, Mignon, A., Van Vlierberghe, S., Dubruel, P., De Belie, N. & Lodewyckx, P. (2013). Broadening the water vapour adsorption modeling of activated carbons towards cementitious materials. In: Proceedings of the 5th International Conference on Carbon for Energy Storage/Conversion and Environment Protection, CESEP, Mülheim a.d. Ruhr, 22-26 September 2013, PP28.

Snoeck, D. (2012). Self-healing cementitious materials by the combination of microfibres and superabsorbent polymers. In: Proceedings of the 3rd Magnel Research Seminar, Beervelde, 31 May 2013, 29-30.

Steuperaert, S., **Snoeck, D.**, Van Vlierberghe, S., Dubruel, P. & De Belie, N. (2012). Superabsorbent polymers as a sealing agent in concrete. In: Proceedings of the SIM User Committee Meeting, Antwerp, 7 December 2012.

Snoeck, D. (2012). Concrete which repairs itself. In: Proceedings of the 13th FEA PhD Symposium, Stirring researchers, shaking ideas, Ghent, 5 December 2012.

Snoeck, D., Van Tittelboom, K. & De Belie, N. (2012). Smart additives for self-sealing and self-healing. In: Proceedings of the XXI International Materials Research Congress, Cancun, 12-17 August 2012, abstract on CD.

Dejonghe, P., De Belie, N., Steuperaert, S. & **Snoeck, D.** (2011). The behaviour of superabsorbing polymers in concrete as a sealing agent: absorption kinetics, degradation and water permeability testing. In: Proceedings of the 3rd International Conference on Self-healing materials, Bath, 27-29 June 2011, 1-2.